

DTIC FILE COPY

①

AGARD-CP-437 Vol.2

AGARD-CP-437 Vol.2

AD-A211 894

ADVISORY GROUP FOR AEROSPACE RESEARCH & DEVELOPMENT

AGARD CONFERENCE PROCEEDINGS No.437

**Validation of Computational Fluid
Dynamics
Volume 2 — Poster Papers**

NORTH ATLANTIC TREATY ORGANIZATION



DISTRIBUTION AND AVAILABILITY
ON BACK COVER

89 3 17 079

AGARD-CP-437
Volume 2

NORTH ATLANTIC TREATY ORGANIZATION
ADVISORY GROUP FOR AEROSPACE RESEARCH AND DEVELOPMENT
(ORGANISATION DU TRAITE DE L'ATLANTIQUE NORD)

AGARD Conference Proceedings No.437
VALIDATION OF COMPUTATIONAL FLUID DYNAMICS
Volume 2: POSTER PAPERS

Volume 1 contains the Symposium papers
and Round Table Discussion presented at
the Symposium



A-1

Poster Papers presented at the Symposium of the Fluid Dynamics Panel in
Lisbon, Portugal, 2-5 May 1988.

THE MISSION OF AGARD

According to its Charter, the mission of AGARD is to bring together the leading personalities of the NATO nations in the fields of science and technology relating to aerospace for the following purposes:

- Recommending effective ways for the member nations to use their research and development capabilities for the common benefit of the NATO community;
- Providing scientific and technical advice and assistance to the Military Committee in the field of aerospace research and development (with particular regard to its military application);
- Continuously stimulating advances in the aerospace sciences relevant to strengthening the common defence posture;
- Improving the co-operation among member nations in aerospace research and development;
- Exchange of scientific and technical information;
- Providing assistance to member nations for the purpose of increasing their scientific and technical potential;
- Rendering scientific and technical assistance, as requested, to other NATO bodies and to member nations in connection with research and development problems in the aerospace field.

The highest authority within AGARD is the National Delegates Board consisting of officially appointed senior representatives from each member nation. The mission of AGARD is carried out through the Panels which are composed of experts appointed by the National Delegates, the Consultant and Exchange Programme and the Aerospace Applications Studies Programme. The results of AGARD work are reported to the member nations and the NATO Authorities through the AGARD series of publications of which this is one.

Participation in AGARD activities is by invitation only and is normally limited to citizens of the NATO nations.

The content of this publication has been reproduced directly from material supplied by AGARD or the authors.

Published December 1988

Copyright © AGARD 1988
All Rights Reserved

ISBN 92-835-0489-5 Vol.1
ISBN 92-835-0490-9 Vol.2
ISBN 92-835-0491-7 Set of 2 Vols.



*Printed by Specialised Printing Services Limited
40 Chigwell Lane, Loughton, Essex IG10 3TZ*

PREFACE

The aerospace community has come to realize that Computational Fluid Dynamics offers great potential as an analysis and design tool for air vehicles as well as components. Great strides have been made in recent years in development of both computer hardware and solution algorithms as well as pioneering applications. Design applications are being made in today's developments. In general, CFD methods of today can simulate flows about complex geometries with simplified flow physics or flows about simple geometries with complex flow physics, however, they cannot simulate both in many cases. Significant progress still has to be made to help resolve these issues.

The ultimate goal of CFD development is a fully mature design and analysis capability that is user friendly, cost effective, numerically accurate and fully verified by detailed experimental or analytical comparisons. A critical step, as far as practical applications of CFD are concerned, is the thorough validation or calibration of the CFD tools. Through validation the design user of CFD can gain the high level of confidence that is needed to permit the capability to realize its full potential as a design tool.

AGARD's Fluid Dynamics Panel has sponsored a Symposium with the specific intent of examining activities, both computational and experimental, directed toward validating or calibrating CFD codes over a broad spectrum of fluid-dynamics study areas. The objectives of the Symposium were to identify the level of agreement of numerical solution algorithms and physical models with experimental and/or analytical data, to identify regions of validity for given flow solvers, and to identify flow regions where significant gaps exist and further work is warranted.

Due to the intense interest in this subject, a large number of paper abstracts were submitted to the FDP "Call for Papers". The Programme Committee decided to accommodate this intense response by inviting authors to prepare "Poster Papers" for a special session. Poster Papers were mounted on large display stands and authors informally inter-acted with interested participants during a two hour period. This stimulating discussion period proved to be highly successful. Volume 2 contains the formal written versions of the Poster Papers. Volume 1 contains the Symposium papers and the concluding Round Table Discussion.

* * *

La communauté aérospatiale est en voie de se rendre compte des possibilités énormes offertes par le calcul en dynamique des fluides en tant qu'outil d'analyse et de conception. Des progrès considérables ont été enregistrés au cours des dernières années dans le développement du matériel informatique et des algorithmes de résolution ainsi que des applications originales et des applications d'études sont en cours.

En règle générale, les nouvelles méthodes de CDF permettent soit de simuler des écoulements autour de géométries complexes selon des lois physiques d'écoulement simplifiées, soit de simuler des écoulements autour de géométries simplifiées, selon des lois de physique d'écoulement complexes, mais non pas les deux, dans bien des cas. Des efforts importants sont encore demandés afin de résoudre ces problèmes.

Le but ultime recherché par ces travaux de développement du CDF serait la réalisation d'un système d'analyse et de conception à l'épreuve de toute défaillance, et qui serait en même temps convivial, d'un bon rapport qualité/prix, précis du point de vue numérique et confirmé rigoureusement par des expérimentations détaillées. En ce qui concerne les applications pratiques du CDF, la validation poussée, ou l'étalonnage des codes CDF représente une étape critique. La validation assure à l'utilisateur du CDF le niveau de fiabilité élevé dont il a besoin, et elle doit permettre à cet outil de réaliser tout son potentiel en tant qu'aide à la conception.

Le Panel AGARD de la dynamique des fluides a organisé ce symposium pour permettre un examen des travaux de calcul ainsi que des travaux expérimentaux qui sont en cours à l'heure actuelle et dont l'objet serait de valider ou d'étalonner les codes CDF, et ceci pour la quasi-totalité des domaines de recherche en dynamique des fluides.

Le symposium a eu pour objectif principal de déterminer le niveau de concordance entre les méthodes physiques et les algorithmes de résolution numériques d'une part, et les données expérimentales d'autre part, ainsi que l'identification des domaines de validation pour des solveurs d'écoulements spécifiques et l'identification des régimes d'écoulement pour lesquels il existe des lacunes importantes, et où des recherches supplémentaires seraient justifiées.

Etant donné le vif intérêt du sujet de nombreux résumés de communications ont été soumis à l'approbation du Comité chargé du programme. Pour répondre à cette demande importante le Comité a donc décidé d'inviter des auteurs à préparer une session spéciale permettant une exposition de leurs communications. Ces communications ont été présentées sur de grands et larges supports et les auteurs se sont tenus à la disposition des participants pendant environ deux heures. Cette exposition a stimulé des discussions vivantes et bénéfiques pour tous.

Le Volume 2 contient les textes complets des présentations faites lors de cette exposition et le Volume 1 contient les communications du Symposium et les conclusions de la Table Ronde.

AGARD FLUID DYNAMICS PANEL

Chairman: Mr D.H.Peckham
Superintendent AE2 Division
Royal Aerospace Establishment
R141 Building
Farnborough, Hants GU14 6TD
United Kingdom

Deputy Chairman: Dr W.J.McCroskey
Senior Staff Scientist
US Army Aero Flightdynamics
Directorate (AVSCOM)
Ames Research Center N258-1
Moffett Field, CA 94305
United States

PROGRAMME COMMITTEE

Dr R.G.Bradley, Jr. (Co-Chairman)
Director, Aerospace Technology Dept.
GD/FW-MZ 2888
Fort Worth Division
P.O. Box 748 Fort Worth, TX 76101, USA

Professor Ir. J.W.Slooff
National Aerospace Laboratory, NLR
Anthony Fokkerweg 2
1059 Amsterdam, Netherlands

Dr W.Schmidt (Co-Chairman)
Deputy Director-Dornier 328 Program
Dornier GmbH, EY
Postfach 1420
D-7990 Friedrichshafen
Federal Republic of Germany

Professor H.Norstrud
Appt. 24
27 rue Noulet
F-31400 Toulouse, France

M. l'Ing. en Chef B.Monnerie
Directeur Adjoint
Direction Aérodynamique
B.P. 72
ONERA
92322 Châtillon, France

Professor A.F. de O.Falcao
Pavilhao de Maquinas
Instituto Superior Tecnico
1096 Lisboa Codex, Portugal

Professor D.Papailiou
Department of Mechanical Engineering
University of Patras
Rio 26001
Patras, Greece

Mr P.R.Bignell
BAe PLC, Sowerby Research Centre
Naval Weapons Division
FPC 067, P.O. Box 5
Filton
Bristol BS12 7QW, UK

Dr Ing. G.Bucciantini
Aeritalia-Societa Aerospaziale Italiana
Gruppo Velivoli Combattimento
Corso Marche 41
10146 Torino, Italy

Dr R.A.Graves
Director, Aerodynamics Div.
NASA/HQ/Mail Code RF
Washington D.C. 20546, USA

PANEL EXECUTIVE

From Europe:
Mr M.C.Fischer
AGARD-OTAN
7 rue Ancelle
92200 Neuilly-sur-Seine, France
Tel (1) 4738 5775 — Telex 610176 (France)

From USA and Canada:
AGARD-NATO
APO New York 09777

CONTENTS

	Page
PREFACE	iii
FLUID DYNAMICS PANEL	iv
	Reference
POSTER PAPER SESSION	
Chairman: R.A.Graves	
VALIDATION OF A MULTI-BLOCK EULER FLOW SOLVER WITH PROPELLER-SLIPSTREAM FLOWS by Bu A.Amendola, R.Fognaccini, J.W.Boerstael and A.Kassies	P1
INVESTIGATION OF THE SURFACE FLOW ON CONICAL BODIES AT HIGH SUBSONIC AND SUPERSONIC SPEEDS by W.J.Bannink, E.M.Houtman and S.P.Ottochian	P2
DESIGN AND VALIDATION OF A 2D EULER CODE by B.Favini, F.Sabetta and L.Zannetti	P3*
FINITE DIFFERENCE METHODS IN RECIRCULATING FLOWS by J.C.F.Pereira and F.Durst	P4
THE DESIGN OF THE GARTEUR LOW ASPECT-RATIO WING FOR USE IN THE VALIDATION OF SHEAR LAYER AND OVERALL FLOW PREDICTION METHODS by M.C.P.Firmin and M.A.McDonald	P5
SLENDER CONE CFD AND EXPERIMENTAL DATA COMPARISONS IN HYPERSONIC FLOW by J.Y.Baltar and E.Tjonneland	P6
VALIDATION OF A USER-FRIENDLY CFD CODE FOR PREDICTION OF THE AERODYNAMIC CHARACTERISTICS OF FLIGHT VEHICLES by M.Fortier	P7
COMPARISON OF THEORY AND EXPERIMENT FOR FOUR SUPERCRITICAL, LOW DRAG AIRFOILS by D.J.Jones, M.Khalid and B.Eggleston	P8
SOLUTION ERROR ESTIMATION IN THE NUMERICAL PREDICTIONS OF TURBULENT RECIRCULATING FLOWS by R.Kessler, M.Peric and G.Scheuerer	P9
DETAILED FLOWFIELD MEASUREMENTS OVER A 75-DEGREE SWEEPED DELTA WING FOR CODE VALIDATION by S.O.Kjelgaard and W.L.Sellers, III	P10
EXPERIMENTS AND CODE VALIDATION FOR JUNCTURE FLOWS by L.R.Kubendran, C.-H.Sung and C.-I.Yang	P11
ACCURACY AND EFFICIENCY OF A TIME MARCHING APPROACH FOR COMBUSTOR MODELING by A.A.Boretti and F.G.Martelli	P12
LARGE-SCALE VISCOUS SIMULATION OF LAMINAR VORTEX FLOW OVER A DELTA WING by B.Müller and A.Rizzi	P13
INVESTIGATION OF THE ACCURACY OF FINITE VOLUME METHODS FOR 2- AND 3-DIMENSIONAL FLOWS by C.Rossow, N.Kroll, R.Radspieler and S.Scherr	P14

* Not available at the time of printing.

**DOCUMENTATION OF SEPARATED FLOWS FOR COMPUTATIONAL FLUID
DYNAMICS VALIDATION**
by D.Hummel

Page

P15

**OVERVIEW OF CFD METHODS AND COMPARISONS WITH FLIGHT AEROTHERMAL
DATA**
by K.Sutton, E.V.Zoby and H.H.Hamilton

P16

VALIDATION OF A MULTI-BLOCK EULER FLOW SOLVER WITH PROPELLER-SLIPSTREAM FLOWS

by

A. Amendola, R. Tognaccini

Aeritalia/GVT, Transport Aircraft Group
Aerodynamic Dept.
80038 Pomigliano (Napoli)
Viale dell'Aeronautica, Italia

J.W. Boerstoeel, A. Kassies

National Aerospace Laboratory NLR
PO Box 90502, 1006 BM Amsterdam
The Netherlands

SUMMARY

A new computer-program system for the numerical simulation of subsonic and transonic flows around complex aircraft configurations is described. This system computes Euler flows on multi-blocked grids. The system consists of four major parts:

- a block decomposer for the subdivision of flow domains into blocks,
- a grid generator for blocked flow domains,
- a flow solver for blocked grids, and
- a flow visualizer for flows on blocked grids.

These parts are interfaced by files with simple formats. Special attention was given to provide this package of software products with:

- excellent portability (the system was tested on various front-end and supercomputers),
- modularity (with respect to physical and numerical subtasks, and with respect of subdividing the total simulation task in loosely coupled subtasks).

The system has good growth potential towards a Navier-Stokes simulation environment.

The system is being validated with various test cases. Results of one of these test cases (the wing/nacelle/propeller configuration tested in a NASA-Langley wind-tunnel, NASA CR 172605) show that the system performs reasonably from the point of view of both accuracy and operational manageability. However, the current block-decomposition/grid-generation procedure must be made more flexible in order to allow:

- everywhere in the flow domain sufficient numerical accuracy,
- sufficient short turn-around times in procedures for redesigns of block decompositions and of blocked grids, and
- more efficient central-memory and calculation management in supercomputers.

1. INTRODUCTION

About two and a half years ago, NLR and AIT/GVT started jointly the development of a computer-program system for the numerical simulation of subsonic and transonic flows around complex aircraft configurations. This development is expected to cover a period of four years. The list of functional, operational, and accuracy requirements, that was defined at the start of the project, mentioned as one of the prime functional requirements, the simulation of propulsion-system effects on the flows around configurations with a complexity representative for industrial applications. The emphasis was placed on the analysis of propeller/slipstream effects on the flows around wings, nacelles, and fuselages. Various test cases were selected to validate the system (2D airfoils, 3D flows). One of the test case is the wing/nacelle/propeller configuration tested in a wind-tunnel at NASA-Langley (Ref. 1). The complexity of this test case is representative for the engineering practice in aircraft industry, in fact the geometry is complex and the tested flow conditions cover many interesting features, like a propeller slipstream over a wing, a cold exhaust jet, transonic flow, slip layers, swirl and vorticity, total pressure variations, large viscous effects on the rear loaded wing. In this paper, this test case is used to analyze the current performance of the simulation system.

This paper gives an overview of the current layout and performance of the flow simulation system. The paper consists of the following parts:

- section 2, simulation-system overview,
- section 3, geometry definition, block decomposition, and grid generation,
- section 4, flow calculation,
- section 5, visualization and post-processing,
- section 6, conclusions

Results of testing the system with test cases are presented in section 3 through 6.

The development of the computer program system was funded by NLR (The Netherlands), Aeritalia/GVT Naples (Italy) and the Netherlands Agency for Aerospace Program NIVR.

2. FLOW-SIMULATION SYSTEM OVERVIEW

An overview of the structure of the multiblock Euler-flow simulation system is presented in this section.

Mathematically, a flow simulation boils down to solving numerically an initial-boundary-value problem for the Euler conservation equations on a flow domain bounded by the aircraft surfaces. Initial and boundary conditions are numerically specified to obtain a well-posed problem.

The simulation may then be considered to consist of the execution of the three mathematical tasks of e.g. 2.1 :

- construction of a computational grid in the flow domain,
- discretisation of the conservation equations and of the initial and boundary conditions and
- numerical solution of the resulting discrete equation system.

The mathematical model of the flow simulation is mapped into a flow simulation system like that of fig.2.2. Such a system is a collection of computer codes, data interfaces and procedures, that is operational on a computer network.

The major function of the system is to produce, for a given aircraft configuration, results of flow simulations of sufficient accuracy in acceptable turn-around times. However, in inverse design calculations, parts of the aircraft geometry have to be computed as a function of e.g. a given pressure distribution. In such a case, the shape of domain is not completely known.

At NLR the Euler-flow-solver system is operational in batch on the front-end computer Cy 180-855 and on the NEC SX-2 supercomputer. The NEC SX-2 vector supercomputer has a control processor and an arithmetic vector processor, 16 Mwords central memory (64-bit), and 96 Mwords extended memory (operating like a solid-state disk). At AIT/GVT (Naples), the system is operational in batch on the Cy 180-860 on site, and on the CRAY X-MP/48-SSD supercomputer of CINECA (Italy) as remote connection. This CRAY installation has 4 vector processors, 8 Mwords central memory and 32 Mwords solid-state disk memory.

Well-designed vector programs coded in portable ANSI-Fortran/77 were measured to have average speeds of 100-400 Mflops on the NEC SX-2, and 50-100 Mflops on the CRAY with a single processor.

The block decomposition occurs at present with a commercially available software package (PATRAN). This package is operated interactively from terminals on the front-end computers via low-speed networks (10-40 Kbits). The grid-generator code is currently run interactively from terminals on front-end computers for the grid-design work (mesh-size tuning), and in batch on front-end or supercomputers if the mesh-size tuning is known. Both the block-decomposition and the grid-generation task will undergo in this year a major upgrade. It will become possible to run these codes interactively via a medium-speed network (0.1-1 Mbits). The flow visualizer is used for the graphical inspection on terminals of flow- and grid-calculation results. Auxiliary functions are production of tables and files for further post-processing. The flow visualizer is being upgraded to be operated from workstations. These workstations are connected to the mainframe computers via a medium- and high-speed networks.

3. GRID GENERATION

It is now generally recognized that the difficulties in the generation of grid around complex geometries have limited the flow simulation for practical configurations. Most of the production codes now widely in use in industry are based on simple grid-generation procedures that have proven valuable in producing high-quality grids for a restricted range of problems (wing, wing-body). The fundamental problem connected with the grid generation for general configuration, as reported by Weatherill (Ref. 2), is that each component in the configuration has its own natural topology, and usually these topologies are incompatible with each other.

3.1 MULTIBLOCK APPROACH, DESIGN PRINCIPLES

To connect different topologies Atta and Vadyak (Ref. 3) generate independently the grid for each component, no attempt being made to ensure continuity, so producing overlapped regions and requiring an interpolation procedure to transfer the flow variables. More recently Jameson and Baker (Ref. 4) tried to eliminate the limitation of hexahedral cell shape leading to a grid without inherent structure (unstructured).

Although a structured grid seems to be a natural choice to perform flow calculations about simple geometries, it can be a restriction for grid generation around practical configurations, so that the unstructured approach could be attractive. Extensive research is still required in both the areas of grid generation and flow solvers. However, the multiblock approach, adopted herein, consists of a preliminary topological subdivision of the complete flow domain into a limited number of large hexahedral elements called blocks (Ref. 5). The collection of blocks fills the space without gap or overlap so that a face can be shared by different blocks. The behavior of the grid lines at block interfaces is an important characteristic that differentiates the methods falling in this class. These methods are attractive on account of several reasons that are interesting to examine. First of all it is possible to produce inside each block a smooth grid using one of the currently available techniques (elliptic, parabolic, algebraic). As a consequence it is possible to solve the flow equations using well known algorithms developed for single-block grids.

Block decomposition will also facilitate the use of different flow models in different blocks and the same applies for different mesh refinement strategies. It is also quite evident that no-overlapping is a consistent advantage for communication between different blocks. In fact only boundary conditions for 2D data structure are required. This simplifies the logic and gives possibilities of efficient calculation too.

Topology subdivision -

The subdivision of the physical domain into a number of subdomains (blocks) is a process depending on its topological and geometrical properties. Basically each block is an hexahedral volume (fig. 3.1) to be defined topologically by means of the specification of the vertex-edge-face connectivity and geometrically using a set of parametric relations for edge-faces and with vertex coordinates. Several kind of degeneracies are allowed to make the procedure more flexible (fig. 3.2), but a one-to-one face coupling is assumed. The last assumption simplifies the programming logic and the mathematical model of coupling boundary conditions both for the grid generator and the flow solver and reduces the risk of problems in stability and convergence at a cost of an increase in the number of blocks required.

Grid generation -

It is clear from literature that the elliptic and algebraic techniques are efficient and conceptually attractive. A simple algebraic technique has been adopted herein to generate an initial grid distribution used as starting solution for a relaxation algorithm that solves an elliptic problem. The elliptic grid-generator contains a mesh control capability so that it can perform a fine tune on the grid inside each block. At block interfaces continuity in the grid lines is assured but no condition is imposed on the line slope. The elliptic equations are:

$$(w_1^2 \|P_\xi\| P_\xi)_\xi + (w_2^2 \|P_\eta\| P_\eta)_\eta + (w_3^2 \|P_\zeta\| P_\zeta)_\zeta = 0 \quad 3.1$$

$$P = [x, y, z]^T; \quad P_\xi = [x_\xi, y_\xi, z_\xi]^T \quad 3.2$$

with $w_i = w_i(\xi, \eta, \zeta)$ positive weight functions that provide the direct control on cells size and smoothness. A surface grid points distribution on the block faces provides a Dirichlet BC for these PDEs. The surface grid on each face is produced as solution of two coupled equations that can be written down, for two generic parametric directions, without loss of generality, as follows:

$$(p_s)^T [(w_2 P_\eta)_\eta + (w_3 P_\zeta)_\zeta] = 0 \quad 3.3a$$

$$(p_t)^T [(w_2 P_\eta)_\eta + (w_3 P_\zeta)_\zeta] = 0 \quad 3.3b$$

where:

$$p_s = P_s \|P_s\|^{-1}; \quad P_s = \partial P(s, t) / \partial s \quad 3.4a$$

$$p_t = P_t \|P_t\|^{-1}; \quad P_t = \partial P(s, t) / \partial t \quad 3.4b$$

with (s, t) curvilinear parametric coordinates. Dirichlet BCs are provided by a grid points distribution on the edges of the face. The grid distribution on each edge is produced as solution of a one-dimensional ODE of the form:

$$(p_u)^T (w_3 P_\zeta)_\zeta = 0 \quad 3.5a$$

$$p_u = P_u \|P_u\|^{-1}; \quad P_u = \partial P(u) / \partial u \quad 3.5b$$

with u a curvilinear parametric coordinate.

Mesh size control

Mesh size control is provided in the PDEs (3.1), (3.3), (3.5) by means of the weight functions w_i . These weight functions are user-defined, positive everywhere in the computational domain (ξ, η, ζ) . A tricubic Hermite operator is used to model the functions starting from a number of vertex-values and coefficients. Given these weight functions a grid is completely defined as solution of the above PDEs. Further, the grid quality can be sufficiently controlled. No control of grid skewness and cell-volume variation is applied, to avoid over-specification.

3.2 GRID-GENERATION PROCEDURE

Euler solvers can be used to produce reliable aerodynamic predictions, but unfortunately the large scale industrial applications of these technologies could be strongly affected by high turn-around time and manpower required for each single calculation. To alleviate this problem the grid generation process has been designed to make extensive use of interactive graphic and supercomputer facilities. For the same reason it is also useful to reach a complete integration between different software modules with the available graphic packages used to perform special functions. To analyze the mesh generation procedure first we observe that it can be broken down into a number of steps:

- 1) topological block decomposition
- 2) geometrical block decomposition
- 3) grid initialization
- 4) weight-function definition
- 5) tuning of a number of coarse grids
- 6) tuning of the fine grid

Topological block decomposition (step 1) may be viewed as decomposing a particular solid, the finite flow domain, into smaller solids by inserting new faces, edges and vertices in the starting solid. A graphic pa-

ckage (PATRAN) has proven useful in performing this operation being able to handle topological information as lists of identifiers and connectivity properties (fig. 3.3). Interface codes are used to easily transfer the information between the package and the grid-generator. Geometrical block decomposition (step 2) in practice consists of the construction of the geometrical model for the configuration. This problem is well known for CFD applications, but additional requirements are necessary for multiblock solutions. For instance topological elements (edges, faces) that are in the flow field need to be defined too. Further, the points distribution generated from the analytical model should meet more severe restrictions in order to assure an accurate geometry description inside the codes. Several packages are today available for surface modelling (CATIA, CV, AEROLIS) and in principle each one can be used provided that an efficient and general interface could be constructed. It is also useful to stress the strong connection between topological and geometrical decomposition and the heavy impact they have on the grid quality. A bad decomposition will have severe effects on the grid that cannot be repaired by the mesh control in the grid-generator but will force the user to redesign the block decomposition. The weight functions definition (step 4) requires an iterative process, with the man inside the loop, involving also grid initialization (step 3) and elliptic PDEs solutions on coarse grids (step 5). The weight function coefficients are modified semi-interactively until the grid is satisfactory. The coefficients are modified following some general criteria, for instance a reduction in the weight vertex value causes a local increase of grid points density. The tuning of the final grid is carried out via a single batch-run using the weights coefficients defined previously on coarse grids. A fast and reliable grid inspection has been obtained by means of a graphic post-processing designed for the general purpose of flow data visualization and analysis.

3.3 ACHIEVEMENTS AND FUTURE IMPROVEMENTS

In principle the grid generation method described here is capable to handle every complex practical configuration. Further the modular organization of the software has been built to reach a full integration within a pre-existing CAD/CAE environment in order to reduce the time scale for a single calculation. The ideal situation should be that the required time for a complete grid-generation and successive flow analysis be well inside a typical aircraft design cycle with affordable manpower investment. On the basis of our current experience it seems that the basic design principles are valid. The system developed will be really able to satisfy the demand for a routine Euler codes application in an industrial environment, but still some work must be done to optimize and improve it.

3.4 EXAMPLES

A collection of examples of grid generated with the present method is examined below.

NACA 0012 in a wind tunnel

To simulate a two-dimensional flow field around an airfoil a finite wing mounted wall-to-wall into a wind tunnel has been used. A subdivision based on 6 blocks has been adopted driving an O-type grid topology. An enlarged window of the grid (figg. 3.4-5) allows to see the effect of the mesh refinement close to the airfoil and the skewness of the grid lines at blocks interfaces. A H-type grid has been produced by simple changing the block subdivision (figg. 3.6-7).

Nacelle-propeller SR-2

Some test runs have been carried out on a nacelle-propeller configuration to analyse stability behaviour of the propeller boundary conditions. A grid has been produced around this 3D configuration using a subdivision in 14 blocks. Fig. 3.8 shows the far field region of this grid while in fig. 3.9 there is an enlarged view.

Wing-prop-nacelle

From a practical point of view an interesting problem is the treatment of a wing mounted nacelle including the aerodynamic interference of propeller slipstream. The geometry and the topology of this kind of configurations are very complex and could be considered a valid test for a grid-generator. For these reasons the configuration of (Ref. 1) was selected. The availability of a large amount of experimental data was also considered useful for the aerodynamic validation of the codes. The subdivision has been performed using 96 blocks for the complete domain (48 for half domain), while the total number of cells used is 800000 (1.1 million of grid points). A number of pictures of the grid can be found in figg. 3.10 through 3.15. Note the H-type structure of mesh at wing-intersection, where it should be also noted that the geometry has been modelled slightly differently from that in (Ref. 1).

4. FLOW CALCULATIONS

For solving the Euler equations on a multiblock structured domain an explicit finite volume approach with central space discretization and explicit adaptive viscosity has been used. The basic algorithm is widely described in literature and has been tested successfully on various configurations (Ref. 8). The conservative Euler equations in differential form are :

$$\frac{\partial W}{\partial t} + \frac{\partial F_1}{\partial x} + \frac{\partial F_2}{\partial y} + \frac{\partial F_3}{\partial z} = 0 \quad 4.1$$

$$W^T = [\rho, \rho u, \rho v, \rho w, \rho E]$$

$$F_1^T = [\rho u, \rho u^2 + p, \rho v, \rho w, \rho H u]$$

$$F_2^T = [\rho v, \rho uv, \rho v^2 + p, \rho wv, \rho H v]$$

$$F_3^T = [\rho w, \rho uw, \rho vw, \rho w^2 + p, \rho H w]$$

where W is the independent variable vector (density, components of mass flux in the three cartesian directions, total energy for unit volume) and F_1, F_2, F_3 are the corresponding flux vectors.

Equations (4.1) can be discretized in space by writing the integral balance equations for each grid cell (i,j,k) with volume h_{ijk} :

$$\frac{d}{dt} (h_{ijk} W_{ijk}) + Q_{ijk} - D_{ijk} = 0 \quad 4.2$$

where Q_{ijk} represents the net flux out of the cell which is balanced by the rate of change of W in the cell volume, and D_{ijk} is the artificial dissipative divergence added to avoid the well-known odd-even decoupling of the solution and to provide good shock capturing without overshoots. Q_{ijk} is computed by evaluating the flux values at face centers using arithmetic averages of flow variables at cell centres.

Specifying ξ, η, ζ the three curvilinear coordinate directions and $\mathbf{e}_\xi, \mathbf{e}_\eta, \mathbf{e}_\zeta$ respectively the forward and backward difference operators, the artificial dissipative term is:

$$D_{ijk} = (D_\xi + D_\eta + D_\zeta) W_{ijk} \quad 4.3a$$

where:

$$D_\xi W_{ijk} = (D_\xi^{(2)} - D_\xi^{(4)}) W_{ijk} \quad 4.3b$$

and:

$$D_\xi^{(2)} W_{ijk} = \nabla_\xi (\lambda_{i+1/2}^{(2)} W_{ijk}) \Delta_\xi W_{ijk} \quad 4.3c$$

$$D_\xi^{(4)} W_{ijk} = \nabla_\xi (\lambda_{i+1/2}^{(4)} W_{ijk}) \Delta_\xi \nabla_\xi \Delta_\xi W_{ijk}$$

The operators D_η and D_ζ are defined in a similar manner. Particular care has been taken in the definition of the scaling factors λ of artificial terms in the coordinate directions.

In the basic formulation of Jameson the scaling factors were defined with an isotropic behaviour, which means independent scaling from the curvilinear direction. Using linear Von Neumann stability analysis we found that the stability domain, the highest frequencies error damping and accuracy are improved by using scaling factors according to the physical wave speed. An estimate of the wave speed components is obtained by computing the spectral radii of the three Jacobian matrices $\partial F_1 / \partial W, \partial F_2 / \partial W, \partial F_3 / \partial W$:

$$\begin{aligned} \lambda_\xi &= q \cdot \mathbf{s}^{(\xi)} + c |\mathbf{s}^{(\xi)}| & q &: \text{velocity vector} \\ \lambda_\eta &= q \cdot \mathbf{s}^{(\eta)} + c |\mathbf{s}^{(\eta)}| & c &: \text{speed of sound} \\ \lambda_\zeta &= q \cdot \mathbf{s}^{(\zeta)} + c |\mathbf{s}^{(\zeta)}| & \mathbf{s}^{(\xi)} &: \text{cell-area vector} \end{aligned} \quad 4.4$$

which are also the scaling factors used in our formulation.

At boundaries dissipative boundary conditions for viscous operators are applied. Specifying n , index 0 the layer of halo cells just outside the boundary face,

$$W_{-1jk} - 2W_{0jk} + W_{1jk} = 0; \Delta_\xi W_{1/2jk} = W_{1jk} - W_{0jk} \quad 4.5$$

gives Dirichlet BCs for the 4th-order operator and Neumann BCs for the 2nd-order one.

A key role in multiblock approach for complex configurations is played by boundary conditions at the internal block faces. The Euler equations are time-integrated in each block, while the exchange of information among them is assured by means of boundary conditions at the internal block interfaces. This condition specifies the unknowns W in the layer of halo grid points outside the boundary of a block.

In the Euler solver, only 0-continuity of grid lines across internal block-face boundaries is required, large discontinuities of slopes are accepted. A general coupling procedure is applied for preserving accuracy and conservation at internal faces. Condition for conservative coupling of blocks is (fig. 4.1):

$$W_w = 1/2 (W_i + W_{ex})_1 = 1/2 (W_j + W_{ex})_2 \quad 4.6a$$

while an auxiliary relation for determining the halo cells variables can be:

$$1/2 (W_{ex1} + W_{ex2}) = 1/2 (W_{i1} + W_{j2}) + \frac{q_w}{c_w} \frac{\partial W}{\partial \xi} \quad 4.6b$$

so only an evaluation of the gradient vector at the internal face is required. This formulation gives satisfactory results for high skewness and high stretching between cells at both sides of the face.

The propeller is modelled as an actuator disk across which the flow undergoes discontinuous changes that represent the effect of the propeller on the flow through the disk. The mass flux is continuous across it, but the three momentum fluxes and the energy flux have in general discontinuity jumps across the disk. The discontinuities are usually defined by specifying jumps over the disk in other variables. Two actuator-disk models are applied.

- a) In the first model the jumps are defined by prescribing the distributions of local pressure coefficient $dc_p(r)$ and local thrust coefficient $dc_t(r)$ as a function of the dimensionless radius r of the disk.
- b) In the second model, the jumps are defined by prescribing the distributions of the total pressure $P_t(r)$ and of the swirl unit vector $d(r)$ at the downstream side of the disk.

The time iteration procedure at the propeller disk is made according to characteristic theory. When the flow is locally subsonic four variables are extrapolated at disk from the upstream values and one BC relation is applied (mass conservation), downstream of the disk four BC relations are applied and one extrapolation is made from downstream state.

When an exhaust jet is present in the Euler flow calculation, boundary conditions must be specified over an outlet surface where the exhaust jet enters the flow domain. Total pressure, total temperature and swirl of flow are assumed to be given as a function of the position in the outlet surface. Furthermore, the absolute value of velocity is extrapolated from the flow field.

In the current flow solver, degenerated block faces are allowed (fig. 3.2). To avoid inaccuracies because of the large different scales of grid cell edges, a special treatment for cells at degenerated block faces has been introduced. For instance, when a block face is degenerated into an edge, no coupling with other blocks is required because fluxes at the block face are zero. A flow state is computed in the domain represented in fig. 4.2 by the dotted lines, imposing in it the conservation of flow variables. The net fluxes, both physical and artificial, can be easily computed by summation of fluxes at cells that build up the domain.

In the halo and first inner layer, the state is assumed constant and equal to that one defined above.

In the case of far field boundary conditions the flow state is computed according to characteristic theory using the Riemann variables while for a solid wall linear extrapolation of pressure is applied.

The set of ordinary differential equation systems is solved by using a standard four stage multistep scheme. In order to improve stability and convergence speed enthalpy damping and residual averaging techniques are used.

Useful informations about accuracy and stability of the numerical algorithm are given by a study of the linear 2D model equation in a cartesian grid:

$$u_t + c \cdot \nabla u + D^{(4)} = 0 \quad 4.7$$

where c is the characteristic wave speed and $D^{(4)}$ the 4th-order dissipative term (4.3). It is interesting to perform a Fourier analysis (Ref. 9) of the behaviour of the error amplification factor module of the scheme in the plane of phase angles. It is then possible to observe how some grid properties modify the error damping in the numerical scheme. In fig. 4.4 the effects of aspect ratios of grid cells are illustrated for $\Delta x/\Delta y=1$ and for $\Delta x/\Delta y=100$. In fig. 4.4.a and b the characteristic speed is inclined at 45° with respect to the x direction while in fig. 4.4.c it is aligned with it.

The first tests of the multiblock Euler code were made on the six blocks grid around NACA 0012 airfoil already described. The fig. 4.4 shows convergence history and pressure coefficient on the airfoil and in the flow field for a transonic case. The last example of flow calculations showed here are around the NASA-Langley propeller-wing-nacelle configuration of fig. 3.10-15. The fig. 4.5 represents the convergence histories for a propeller off/on case ($M = 0.70$, $\alpha = -1.3^\circ$) on two grid levels.

The incidence has been slightly changed to compare data at the same lift coefficient of the windtunnel experiment at 0. Mach number distributions are shown in fig. 4.6-8 while in fig. 4.9-10 comparison with experimental data is plotted.

The flow calculations are correct and convergence acceptable. The effect of enthalpy damping is still under investigation.

5. VISUALIZATION

The calculation of 3D flows on blocked grids produces results with a simple regular data structure. The inspection of these results can only be done efficiently by means of graphical tools. The visualization task is divided into two major subtasks.

- Selection task (code ESELB). This offers the possibility to reduce the amount of data to be sent over (file) transfer networks by selecting those parts of grid-generator data and, optionally, the flow-solver data needed for visualization. In general the code ESELB runs on the same computer as the grid-generator and the flow-solver codes.
- Visualization task (code VISU3D). This task uses selected data and produces plots of them. In general, the VISU3D code runs on a workstation or on a mainframe/terminal combination.

The interface between the selection and the visualization code is assured with a standard file containing visualization data, VISDAT.

This file contains all data needed for the visualization and can be sent in short transfer times over transfer networks.

The standard VISDAT file plays a key role in the visualization. It allows any grid generator and any flow solver to be interfaced with the visualization codes, via a selection code. The general structure of the

file is as follows:

- each file consists of a number of pictures
- each picture contains identification data, optionally a structure, and an object in 3D space (possibly moving in time)
- each object consists of a number of parts
- each part is a geometrical entity, given by an array of points in 3D space, like a (part of a) block (volume in 3D), a surface segment in 3D, or a line segment in 3D.

At each point of an object, the coordinates (x,y,z) are given and, optionally, the value of a number of selected variables, like pressure coefficient, Mach number, entropy, etc. For a steady object, the variables can be time-varying, but object and variables can be both time-varying.

Each structure is a tree with nodes. With these nodes, the parts of an object can be arranged in a hierarchical organization. This structure is available to express a user view to how object parts are grouped in to objects. Moreover the nodes can contain a 4D transformation matrix, that can be used to specify one or more symmetries in the object. This option simplifies the manipulation of object parts, and allows the reduction of the amount of data when symmetries are present.

Examples of plots produced with ESELB/VISU3D codes are given in section 3 and 4.

To compare computed results with windtunnel measurement data, an interface with the EDIPAS software package (Ref. 7) is available.

EDIPAS is a system for the processing and analysis of engineering data, based upon a data base management system. It is well-suited for the storage and maintenance of data from different sources, and has a powerful selection mechanism. For the results see section 4.

A recent development is the implementation of parts of the VISU3D visualization concepts on graphic workstations Cy 910 (Iris 3000). Up till now, an animation module has been designed. It is used to visualize the convergence of Euler-flow calculations as a function of the iteration-step number of the numerical time integration scheme.

6. CONCLUSION

A new computer program system for the calculation of three-dimensional Euler flows around complex aerodynamic configurations was tested with among others a propeller-wing-nacelle configuration. The test results are already quite acceptable, but it is desirable that for such complex flows, the accuracy of the computational results is further analysed.

An overview of the system is presented in section 2. It consists of a grid generator for blocked grids, an Euler-flow simulator, and a graphical visualizer.

The system is operational on various computer networks, and in both industrial and in research environments. The design principles for the construction of blocked grids are presented in section 3. Mesh-size tuning is done with a new elliptic procedure, with user-defined weight functions for mesh-size control. Grid lines are over block faces continuous, but in general slope discontinuous. Examples of blocked grids are illustrated.

The central difference scheme with explicit artificial viscosity for the Euler flow simulator is sketched in section 4. Iteration to a steady state is done with a 4-stage Runge-Kutta time integration scheme with local time stepping, residual averaging and enthalpy damping. A conservative coupling of blocks with slope-discontinuous grid lines is presented. Test calculations were converging and qualitatively correct, but the accuracy of the results should be analyzed further for complex flows.

The grids and flow data are visualized with a VISU3D code. A standard file, containing objects to be visualized, is used to couple this code with flow simulators, grid generators, and other codes.

At present, the computer program system is already a powerful means for the aerodynamic analysis and design of many standard two and three-dimensional aerodynamic configurations. It is expected that it will rapidly grow out to a useful numerical simulation and design system for very complex configurations and flows.

7. REFERENCES

1. Bartlett G. W., "An experimental investigation of propfan installations on an unswept supercritical wing at transonic Mach numbers " NASA CR 172605, 1985
2. Weatherill N.P., Forsey C.R., "Grid generation and flow calculations for complete aircraft geometries using a multi-block scheme" AIAA-84-1665, 1984
3. Atta E.H. Vadyak J., "A grid interfacing zonal algorithm for three-dimensional transonic flows about aircraft configurations " AIAA-82-1017, 1982
4. Jameson A., Baker T.J., "Improvement to the aircraft Euler method " AIAA-87-0452, 1987
5. Boerstel J.W., "Preliminary design and analysis of procedures for the numerical generation of 3D block-structured grids " NLR TR 86-102 U
6. Thompson J.F., Thames F.C., Mastin C.W., "Automatic numerical grid generation of body-fitted curvilinear coordinate system for field containing any arbitrary two-dimensional bodies "

- J. Comp. Physics, 15, 1974, pp 299-319
7. EDIPAS-CCBmembers, " EDIPAS user's reference manual " NLR Memorandum IN-83-007 U
 8. Jameson A., Schmidt W., Turkel E., "Numerical solution of the Euler equations by Finite Volume Methods using Runge-Kutta time stepping" AIAA-81-1259, 1981
 9. Vichnevetsky R., Bowles J.B., " Fourier Analysis of Numerical approximations of hyperbolic equations" SIAM Philadelphia, 1982

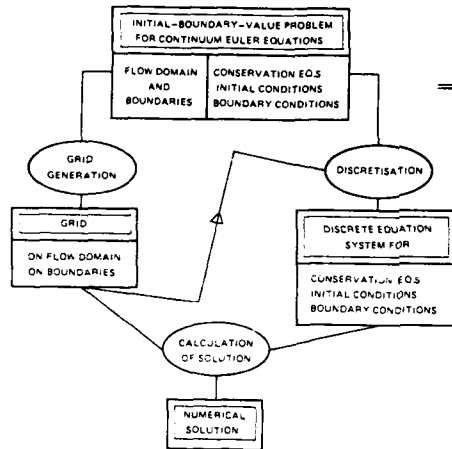


Fig. 2.1—Euler flow simulation as the execution of mathematical tasks.

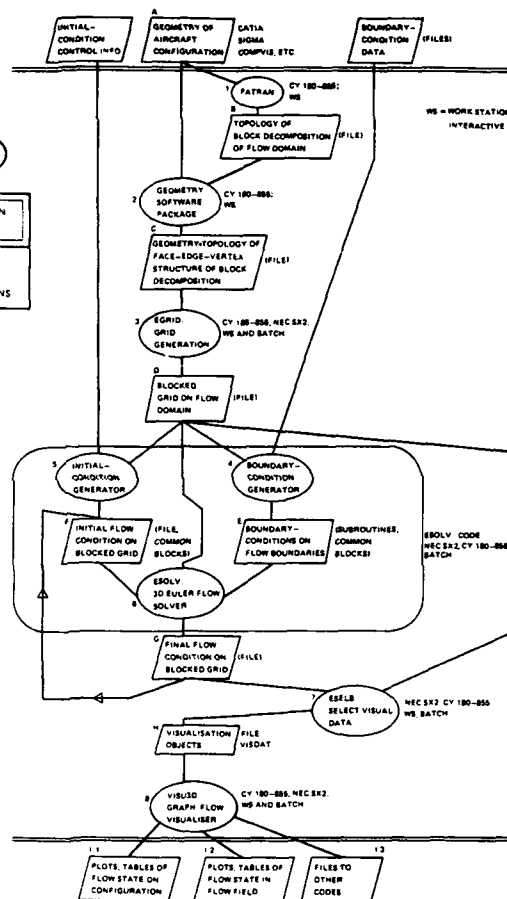
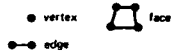
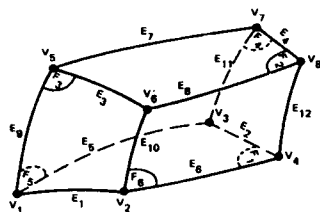
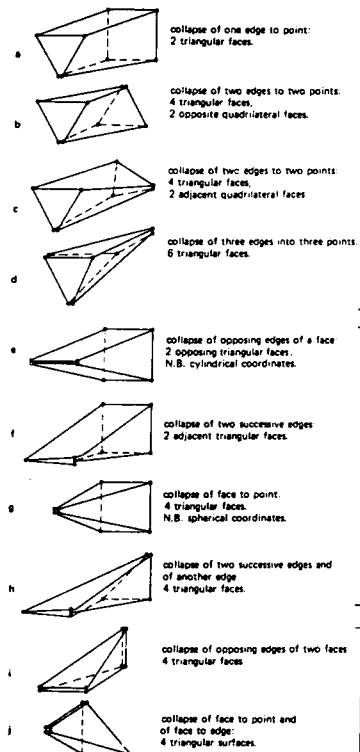


Fig. 2.2—Task decomposition and subtask data interfaces in Euler-flow simulation system (on NLR network).



block volume enclosed by bounding surface consisting of
6 faces F_1, \dots
12 edges E_1, \dots
8 vertices V_1, \dots
connectivity properties as shown

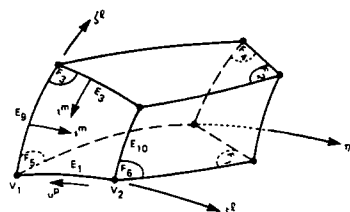
Fig. 3.1 - Topology of a block (hexaedron).



HEXAHEDRA
(6 FACES)

PENTAHEDRA
(5 FACES)

TETRAHEDRA
(4 FACES)



IN BLOCK

$$B^L = (F_1, F_2, F_3, F_4, F_5, F_6)$$

$$z^L = 0, z^L = 1, r^L = 0, r^L = 1, z^L = 0, z^L = 1$$

$$(z^L, r^L, z^L) \in [0, 1]^3$$

IN FACE F_3

$$F_m = (E_9, E_{10}, E_3, E_1), m = 3$$

$$s^m = 0, s^m = 1, t^m = 0, t^m = 1$$

$$(s^m, t^m) \in [0, 1]^2$$

IN EDGE E_1

$$E_p = (V_2, V_1), p = 1$$

$$u^p = 0, u^p = 1$$

$$(u) \in [0, 1]$$

Fig. 3.3 - Definition of boundary conforming local coordinate system in blocks by pairing and ordering labels in arrays specifying connectivity relations.

Fig. 3.2 - Geometrical-ly degenerated blocks.

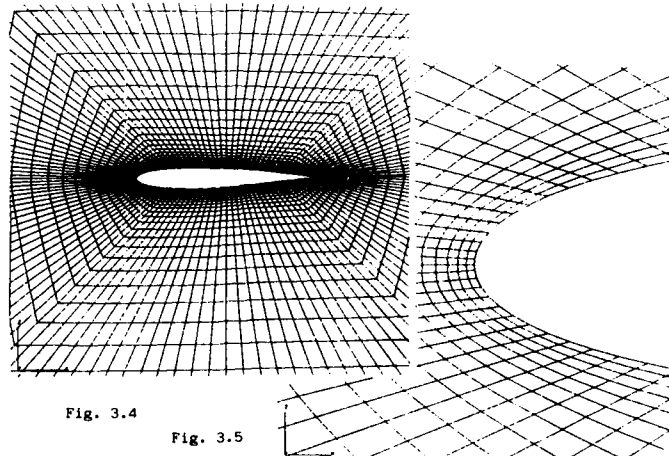


Fig. 3.4

Fig. 3.5

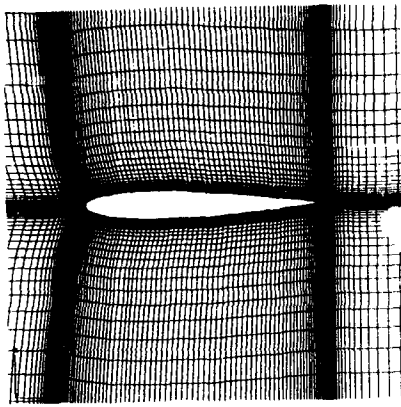


Fig. 3.6

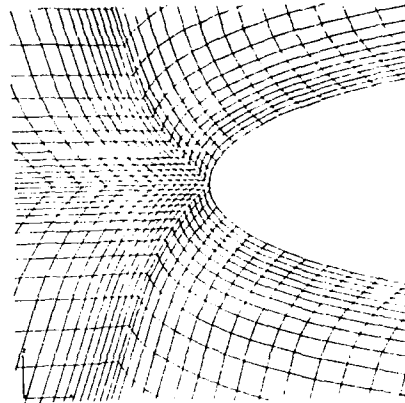


Fig. 3.7

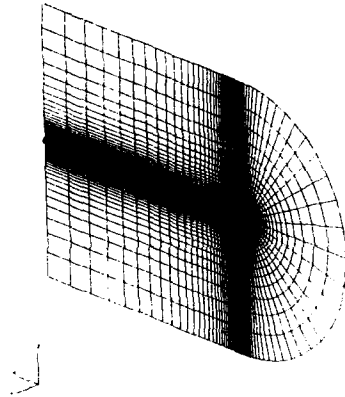


Fig. 3.8

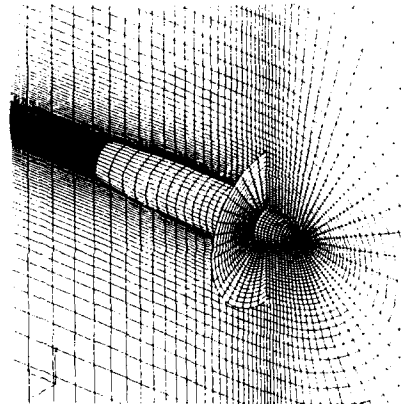


Fig. 3.9

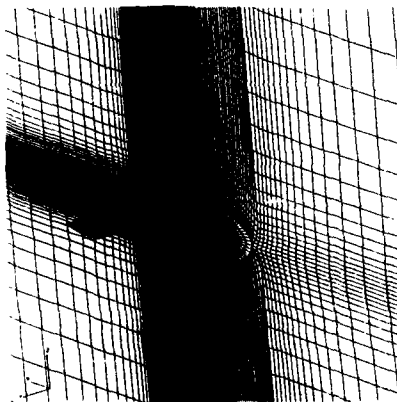


Fig. 3.10

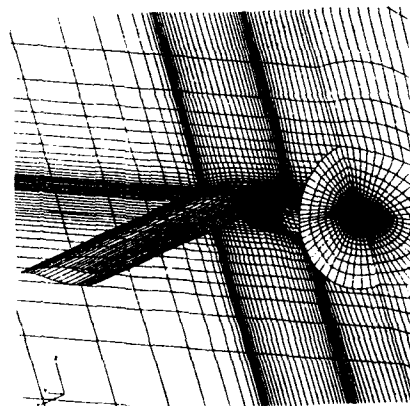


Fig. 3.11

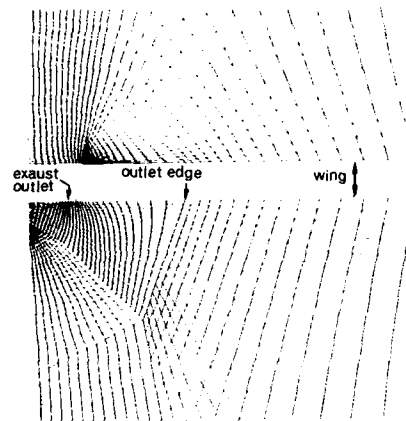


Fig. 3.12

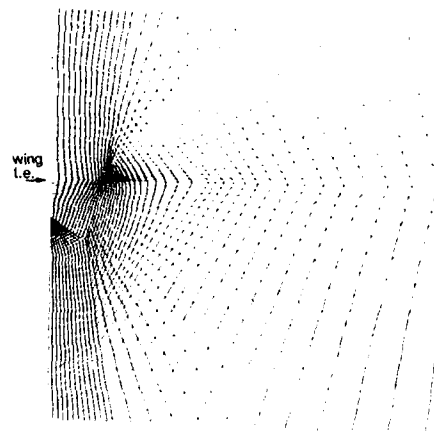


Fig. 3.13

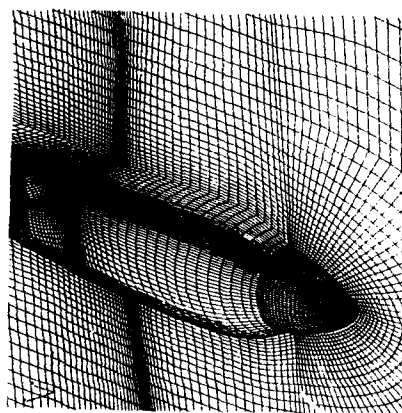


Fig. 3.14

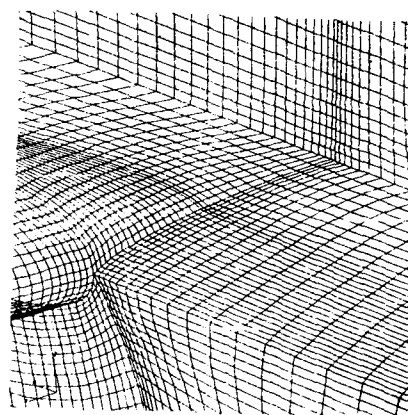


Fig. 3.15

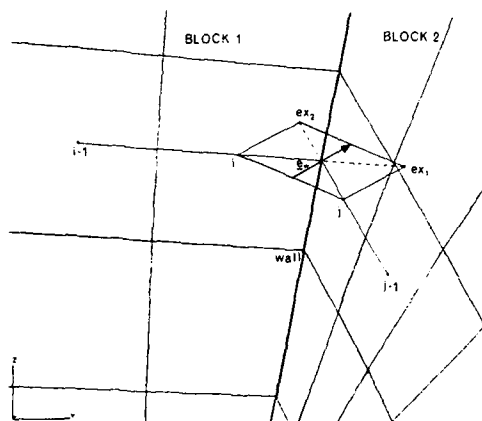


Fig. 4.1- A 2D view of block coupling.

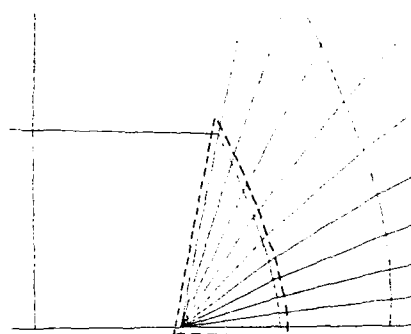
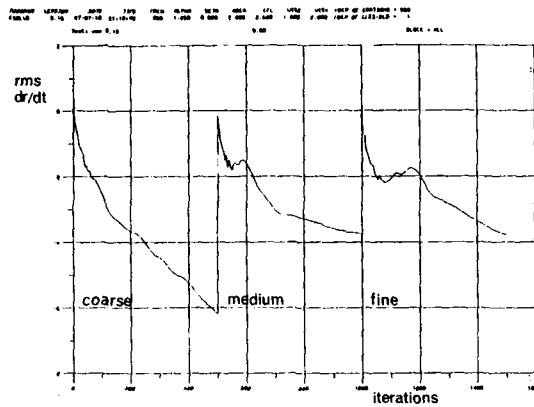
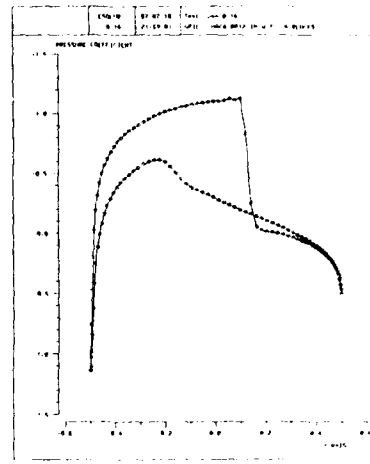


Fig. 4.2 - Boundary conditions' domain for degenerated face into an edge.



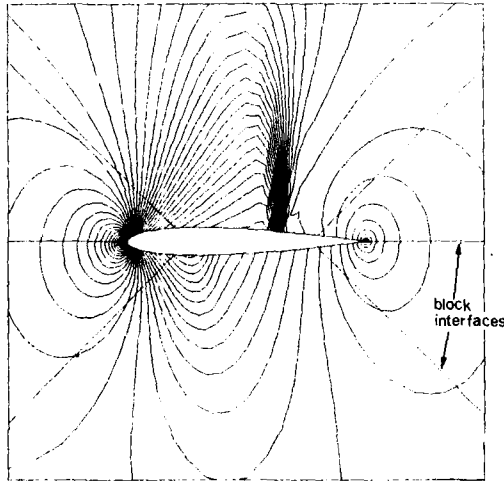
(a)



(b)

Fig. 4.4 - Results for a 6-blocks topology subdivision of a NACA-0012 airfoil.

- (a) convergence history
- (b) pressure distribution
- (c) iso-cp (contour step .05),
(136 cells around the airfoil).



(c)

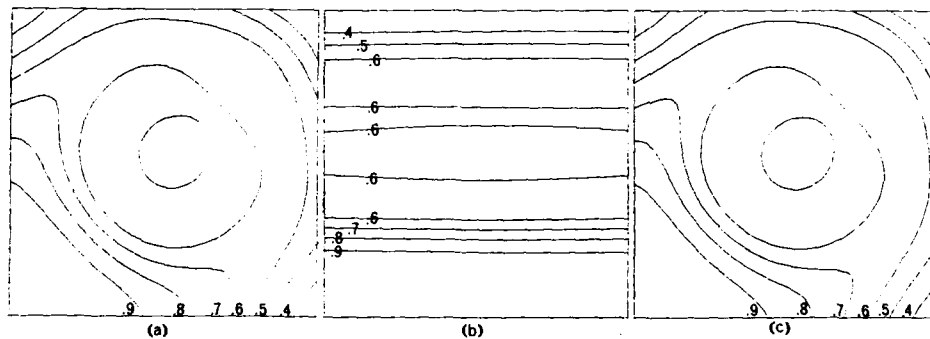


Fig. 4.4 - Isocurves of error amplification factor module of the scheme in the plane of phase angles, $(0 \leq p \leq \pi, 0 \leq q \leq \pi)$; 4-stage scheme; (a) $\Delta x/\Delta y=1, c_x=c_y=1$; (b) $\Delta x/\Delta y=100, c_x=c_y=1$; (c) $\Delta x/\Delta y=100, c_x=.99, c_y=.01$.

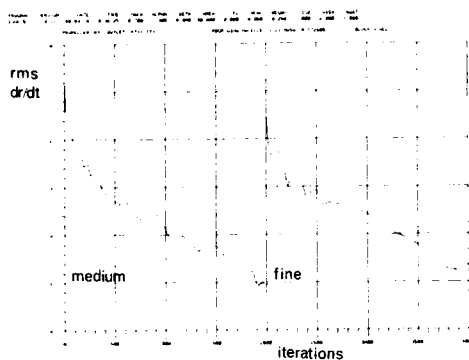


Fig. 4.5a - Convergence history for the prop-wing-nacelle, propeller off.

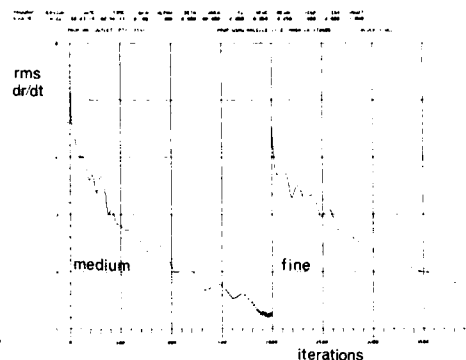


Fig. 4.5b - Convergence history for the prop-wing-nacelle, propeller on.

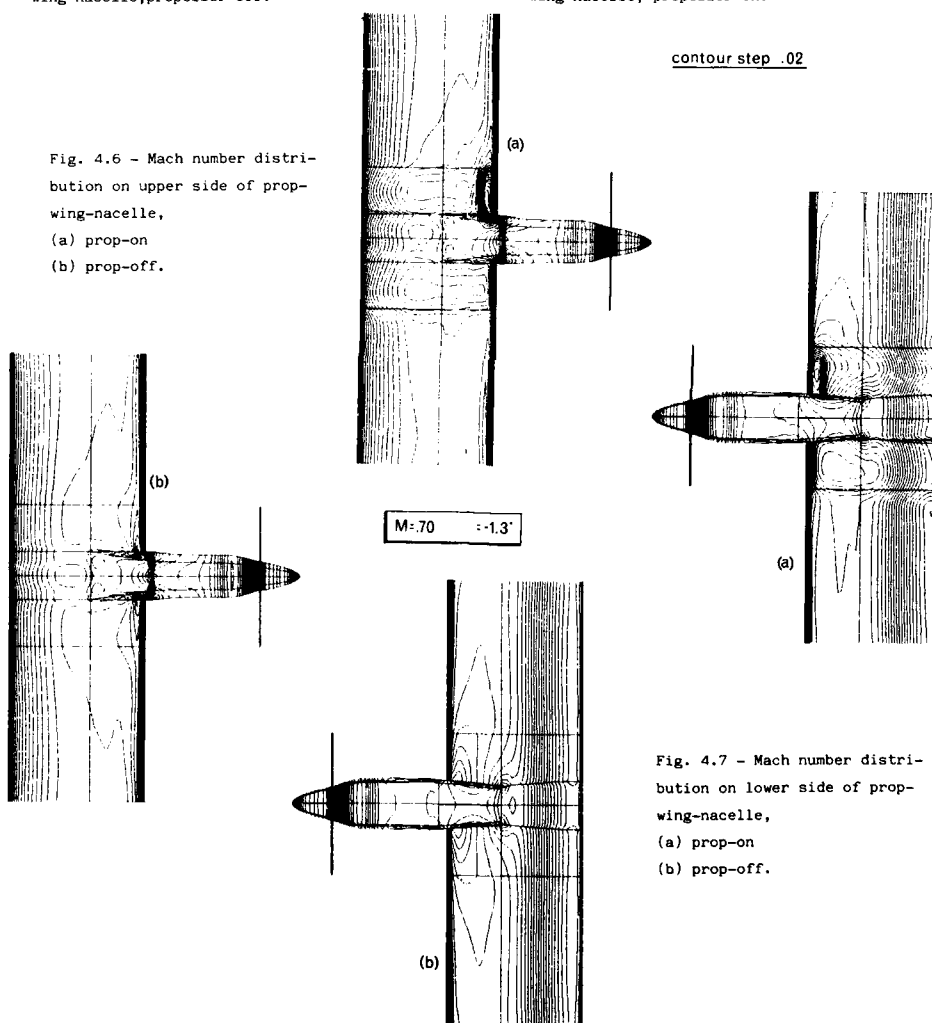


Fig. 4.6 - Mach number distribution on upper side of prop-wing-nacelle,
(a) prop-on
(b) prop-off.

Fig. 4.7 - Mach number distribution on lower side of prop-wing-nacelle,
(a) prop-on
(b) prop-off.

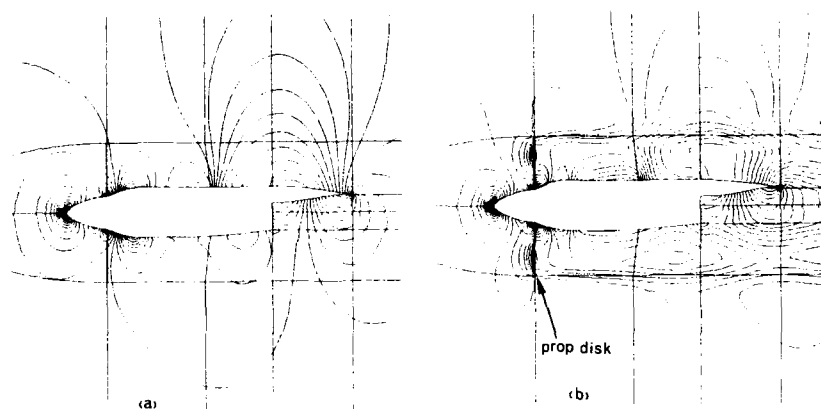


Fig. 4.8 - Iso-mach on the symmetry plane of the prop-wing-nacelle, (a) prop-off, (b) prop-on, contour step .02 .

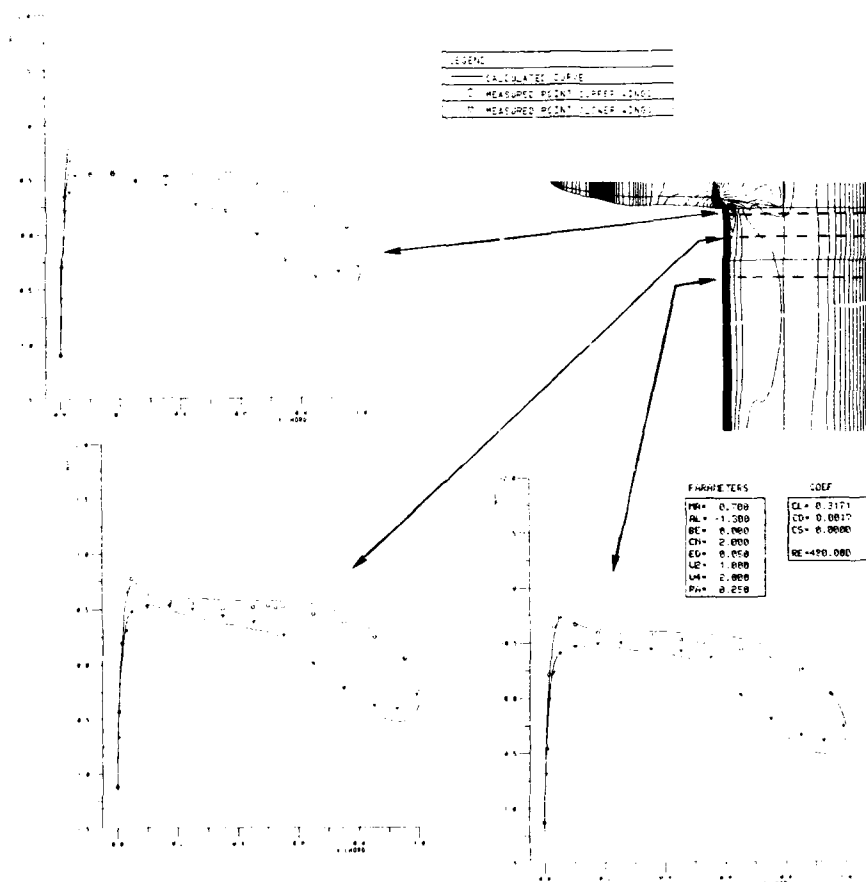


Fig. 4.9 - Theory-experiment comparison for the prop-wing-nacelle test, prop-off.

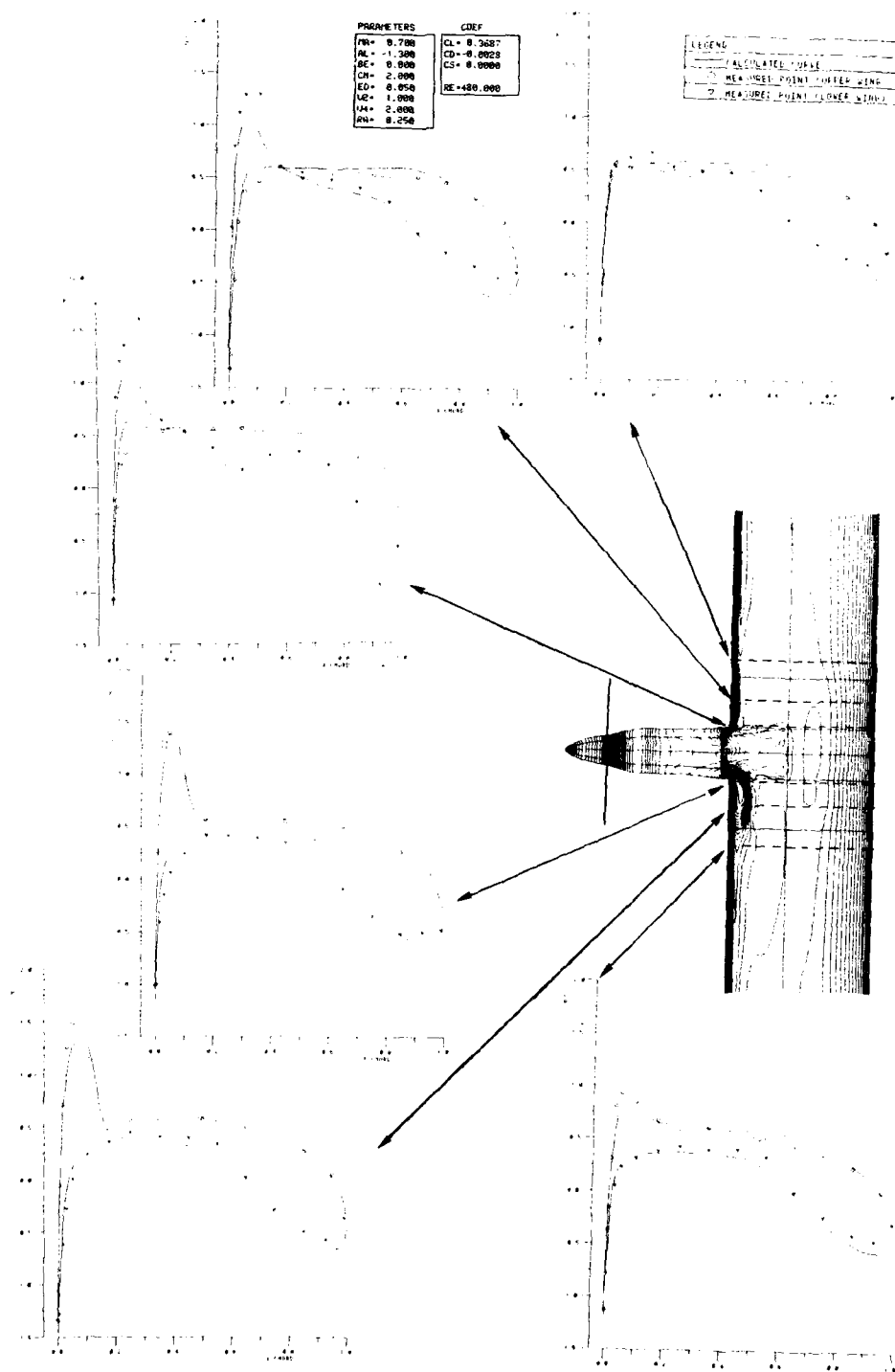


Fig. 4.10 - Theory-experiment comparison for the prop-wing-nacelle test, prop-on ($J=3.026$).

INVESTIGATION OF THE SURFACE FLOW ON CONICAL BODIES AT HIGH SUBSONIC AND SUPERSONIC SPEEDS

W.J. Bannink, E.M. Houtman and S.P. Ottochian
Faculty of Aerospace Engineering, Delft University of
Technology, Kluyverweg 1, 2629 HS Delft, The Netherlands

SUMMARY

Turbulent boundary layer calculations have been performed of the flow on the leeward side of two conical bodies at moderate to high angles of attack. A sharp-edged planar 65° sweep delta wing at high subsonic speeds up to $M_\infty=0.85$ and angles of attack up to 15° and a 7.5° semi-apex angle circular cone at $M_\infty=2.95$ at 14° angle of attack are used. The boundary layer method, based on a finite difference predictor-corrector algorithm, assumes a conical external flow and applies a local (Blasius) similarity concept in radial direction from the apex. The solution marches in cross-direction from the reattachment line toward the location of separation and to the symmetry line on the body. In order to check whether the method produced correct results with respect to the location of separation and the surface flow inclination, experimental pressure distributions are used to generate the inviscid solutions at the edge of the boundary layer. The predicted surface flow on both bodies are in close agreement with the experimental results. In particular the location of the separation lines were very close to those observed in oil flow patterns. That the approximate flow model (conical) produces such good results in the case of the delta wing is due to the relatively large spanwise pressure gradients compared to the chordwise gradients.

NOTATION

E	ratio of total enthalpy, Eq. (18)	γ	ratio of specific heats
F,G	velocity ratios, Eq. (15)	δ	boundary layer thickness
H	total enthalpy, Eq. (5)	c_m, c_{m1}, c_{m0}	eddy viscosity coefficients, Eqs. (8a), (9), (10)
M	Mach number	c_H	eddy conductivity coefficient, Eq. (8b)
Pr	Prandtl number, Eq. (4)	n	transformed z-coordinate, Eq. (13)
Pr _t	'turbulent' Prandtl number, Eq. (8b)	θ_c	cone semi-apex angle
R	gas constant	μ	dynamic viscosity coefficient, kg/ms
Re _r	Reynolds number, Eq. (23)	ν	kinematic viscosity coefficient, m ² /s
T	temperature	ρ	density
U _∞	free stream velocity	σ	= $\rho\mu$, Eq. (23)
C_{f_r}, C_{f_θ}	skin-friction coefficients, Eqs. (21), (22)	τ	shear stress
C_p	surface pressure coefficient	τ_t	turbulent shear stress
C_r	rootchord of delta wing	ϕ, ψ	stream functions, Eq. (14)
p	pressure	φ	angle of velocity vector on surface z=const., Eq. (30)
q	= $(u^2 + v^2)^{1/2}$, Eq. (30)	ψ	circumferential angle on cone surface, Fig. 1
r, θ , z	cylindrical coordinates, Fig. 1	<u>Subscripts</u>	
u, v, w	velocity components in r, θ , z directions, respectively, Fig. 1	e	edge of boundary layer
u _{ref}	reference velocity, Eq. (14b)	t	tangential
x, y, z'	cartesian coordinates, Fig. 1	w	wall
α	angle of attack	∞	free stream conditions

1. INTRODUCTION

The interest in the flow around conical bodies such as delta wings and cones at high angles of attack is considerably increased in the last few years. The reason may not only be found in the aerodynamics of fast manoeuvrable aircraft or missiles, but a large portion of the growing interest can be attributed to the capability to compute complex flow fields. However, even if one confines oneself to simple geometries like a planar triangular wing with sharp leading edges or a circular cone it is a rather difficult task to obtain realistic computational results for such bodies at high angles of attack. This holds in particular for high speed free stream conditions. An important role plays the viscosity in all speed regimes, as may be illustrated by a comparison of experiments with the results of many computations using the Euler equations. An extensive compilation of this may be found in the recently published proceedings of the International Vortex Flow Experiment on Euler Code Validation, Ref. 1.

For a clear understanding of the flow around bodies at high angles of attack, understanding of the flow separation process is a prerequisite. The rolling up of free shear layers, whether they emanate from the leading edge of a wing or from a smooth surface like a cone, has a major effect on the entire 3D flow field and consequently on the aerodynamic characteristics of the wing or body. The primary vortices from sharp leading edges of a delta wing may be captured by an Euler code. This is not so for the vortices shed off from a smooth surface. The latter are of an entirely viscous nature, since they are generated at those locations where the boundary layer no longer can sustain an adverse pressure gradient and will separate. Of course the status of the boundary layer is important: a turbulent boundary layer will be attached over a longer distance than a laminar one.

The present paper presents the computation of the location of separation on a sharp-edged planar delta wing at high subsonic speeds and that on a circular cone in supersonic flow. The computations were made using a quasi 3D boundary layer method, developed by the second author in Ref. 2, which is based on the assumption of conical inviscid external flow. This assumption is valid for the supersonic problem but needs justification for the high subsonic delta wing problem. The latter will be discussed at the presentation of results. Although the method has been developed for application with solutions of conical

inviscid flow codes, we use here experimental pressure distributions to generate the conical inviscid flow. The method may be seen as a modification and an extension of the methods described in Refs. 3,4. Since pressure distributions beyond 30% wing or body length have been employed only turbulent boundary layers are considered in the present paper. The experimental data with which the numerical results are compared were obtained from measurements in the transonic-supersonic wind tunnel of the Delft University of Technology, Faculty of Aerospace Engineering. One model was a 65° swept planar delta wing tested at free stream Mach numbers between 0.6 and 0.9 at angles of attack of 5°-22° (Ref. 5). Of this model calculations were made for $M_\infty=0.6, 0.7$ and 0.85 and for angles of attack of 5°, 10° and 15°. The other model was a circular cone of 7.5° semi-apex angle tested at $M_\infty=2.95$ at $\alpha=5^\circ-22^\circ$ (Ref. 6). Calculations were made for $\alpha=14^\circ$.

2. GOVERNING EQUATIONS

The boundary layer equations for steady, compressible, laminar and turbulent flow will be described in an orthogonal curvi-linear (r, θ, z) coordinate system, fit to a conical body, see Fig. 1. In this system z is normal to the surface, r is measured along the body (and normal to z) and θ is the angle on the conical body between a generator and a fixed reference generator, for example in the symmetry plane (thus θ is the angle on the unwrapped surface). The velocity components u, v, w are in r, θ, z directions, respectively. In this coordinate system the boundary layer equations may be written, according to Ref. 7, as follows:

$$\frac{\partial}{\partial r} (r\rho u) + \frac{\partial}{\partial \theta} (\rho v) + \frac{\partial}{\partial z} (r\rho w) = 0 \quad (1)$$

r -momentum

$$\rho u \frac{\partial u}{\partial r} + \frac{\rho v}{r} \frac{\partial u}{\partial \theta} + \rho w \frac{\partial u}{\partial z} - \frac{\rho v^2}{r} = \rho_e u_e \frac{\partial u_e}{\partial r} + \frac{\rho_e v_e}{r} \frac{\partial u_e}{\partial \theta} - \frac{\rho_e v_e^2}{r} + \frac{\partial}{\partial z} (\mu \frac{\partial u}{\partial z} - \rho w'w')$$

θ -momentum

$$\rho u \frac{\partial v}{\partial r} + \frac{\rho v}{r} \frac{\partial v}{\partial \theta} + \rho w \frac{\partial v}{\partial z} + \frac{\rho uv}{r} = \rho_e u_e \frac{\partial v_e}{\partial r} + \frac{\rho_e v_e}{r} \frac{\partial v_e}{\partial \theta} + \frac{\rho_e u_e v_e}{r} + \frac{\partial}{\partial z} (\mu \frac{\partial v}{\partial z} - \rho v'w')$$

energy

$$\rho u \frac{\partial H}{\partial r} + \frac{\rho v}{r} \frac{\partial H}{\partial \theta} + \rho w \frac{\partial H}{\partial z} = \frac{\partial}{\partial z} (\frac{\mu}{Pr} \frac{\partial H}{\partial z} + \mu (1 - \frac{1}{Pr}) \frac{\partial}{\partial z} (\frac{u^2 + v^2}{2}) - \rho w'H')$$

where H is the total enthalpy defined by

$$H = \frac{\gamma}{\gamma-1} \frac{p}{\rho} + \frac{u^2 + v^2 + w^2}{2} \quad (5)$$

As usual p and ρ are the static pressure and static density, respectively and μ is the dynamic viscosity coefficient. The subscript e denotes conditions at the edge of the boundary layer. The Prandtl number is taken as a constant, $Pr=0.71$ and μ will be determined according to Sutherland's law. Further we have the Reynolds decomposition where the randomly changing flow variables are replaced by time averages plus

fluctuations about the average, e.g. $\rho w = \bar{\rho w} + \rho'w'$.

The boundary conditions for Eqs. (1)-(4) are

$$z=0: u, v, w=0; \frac{\partial H}{\partial z} = 0 \text{ (adiabatic wall) or } H = H_w(r, \theta) \quad (6)$$

$$z=\delta: u = u_e(r, \theta); v = v_e(r, \theta); H = H_e(r, \theta) \quad (7)$$

where δ is the boundary layer thickness and the subscript w denotes quantities taken at the wall ($z=0$). For turbulent flows it is necessary to make closure assumptions for the Reynolds stresses. Here the two layer eddy-viscosity concept of Cebeci (Ref. 8), where the Reynolds stresses are related to the mean velocity and total enthalpy profiles, is used

$$-\rho u'w' = \rho c_m \frac{\partial u}{\partial z}; -\rho v'w' = \rho c_m \frac{\partial v}{\partial z} \quad (8a)$$

$$-\rho w'H' = \rho c_H \frac{\partial H}{\partial z} = \rho \frac{c_m}{Pr_t} \frac{\partial H}{\partial z} \quad (8b)$$

c_m is the eddy-viscosity coefficient, c_H the eddy-conductivity coefficient and Pr_t is the 'turbulent'

Prandtl number, $Pr_t = \frac{c_m}{c_H}$. c_m is defined in an inner region near the surface by

$$c_{m1} = [0.4 z (1 - \exp(-\frac{z}{A}))]^2 \left(\left(\frac{\partial u}{\partial z} \right)^2 + \left(\frac{\partial v}{\partial z} \right)^2 \right)^{1/2} \quad (9)$$

where

$$A = 26 \frac{v}{u_\tau} \left(\frac{\rho_w}{\rho} \right)^{1/2}; u_\tau = \left(\frac{\tau_{tw}}{\rho_w} \right)^{1/2}; \tau_{tw} = \mu_w \left[\left(\frac{\partial u}{\partial z} \right)_w^2 + \left(\frac{\partial v}{\partial z} \right)_w^2 \right]^{1/2}$$

In the outer region ϵ_m is defined by

$$\epsilon_m = 0.0168 \left| \int_0^m (u_{te} - u_t) dz \right| \quad (10)$$

$$\text{where } u_t = (u^2 + v^2)^{1/2}$$

The influence between the two layers is established by continuity of the two eddy-viscosity relations. According to Ref. 9 the turbulent Prandtl number is taken constant, $Pr_t = 0.90$. In order to reduce the number of dependent variables two streamfunctions are introduced, analogous to Ref. 6, such that

$$r\rho u = \frac{\partial \Psi}{\partial z}, \quad \rho v = \frac{\partial \Phi}{\partial z} \quad (11)$$

Satisfying the continuity equation, Eq. (1), we obtain

$$r \frac{\partial \Psi}{\partial r} = - \frac{\partial \Psi}{\partial r} - \frac{\partial \Phi}{\partial \theta} \quad (12)$$

We also transform the z coordinate into a nondimensional quantity by

$$\eta = \left(\frac{u_e}{\rho_e \mu_e r} \right)^{1/2} \int_0^z \rho dz \quad (13)$$

Then, two nondimensional functions may be derived satisfying

$$f(r, \theta, \eta(z)) = (\rho_e \mu_e u_e r)^{-1/2} \frac{1}{r} \Psi(r, \theta, \bar{z}) \quad (14a)$$

$$g(r, \theta, \eta(z)) = \frac{u_e}{u_{ref}} (\rho_e \mu_e u_e r)^{-1/2} \Phi(r, \theta, \bar{z}) \quad (14b)$$

where u_{ref} is a reference velocity that here is set equal to v_e . Using Eqs. (11)-(14) we may derive

$$u = u_e \frac{\partial f}{\partial \eta} = u_e F \quad (15a)$$

$$v = v_e \frac{\partial g}{\partial \eta} = v_e G \quad (15b)$$

Eqs. (8) and (11)-(15) may now be substituted into the boundary layer equations Eqs. (2)-(4) and the boundary conditions Eqs. (6), (7). Before doing so we first make the assumption of a conical inviscid external flow. In such a flow the flow quantities are independent of r . Then, the laminar boundary layer equations allow similarity solutions along rays $\theta = \text{constant}$. The similarity transformation is equivalent to the Blasius transformation for a flat plate. Such a concept is not valid for a turbulent boundary layer since the eddy-viscosity term is dependent on r . Here we adopt the idea of local similarity introduced in Refs. 10, 11 which means that the eddy-viscosity term is assumed to be locally independent of r , while it is evaluated at its local r position. The validity of this assumption relies essentially on the property that the flow quantities in the boundary layer vary sufficiently slow with r . As we will see in the problems considered here the variation of flow quantities such as pressure and speed in spanwise direction (θ -coordinate) is much larger than in streamwise direction (r -coordinate). Under the just mentioned local similarity restriction a transformation of the boundary layer equations Eqs. (2)-(4) into a parabolic system may be accomplished. The coordinate r serves as a parameter and θ is the time-like marching direction. Thus, for a conical inviscid external flow the equations become

$$\frac{\partial}{\partial \eta} \left[b \frac{\partial F}{\partial \eta} \right] + \left(Q + \frac{v_e}{u_e} \frac{\partial g}{\partial \theta} \right) \frac{\partial F}{\partial \eta} - \frac{v_e}{u_e} G \frac{\partial F}{\partial \theta} = R_1 \quad (16)$$

$$\frac{\partial}{\partial \eta} \left[b \frac{\partial G}{\partial \eta} \right] + \left(Q + \frac{v_e}{u_e} \frac{\partial g}{\partial \theta} \right) \frac{\partial G}{\partial \eta} - \frac{v_e}{u_e} G \frac{\partial G}{\partial \theta} = R_2 \quad (17)$$

$$\frac{1}{Pr} \frac{\partial}{\partial \eta} \left[b \frac{\partial E}{\partial \eta} \right] + \left(Q + \frac{v_e}{u_e} \frac{\partial g}{\partial \theta} \right) \frac{\partial E}{\partial \eta} - \frac{v_e}{u_e} G \frac{\partial E}{\partial \theta} = - \frac{\partial R_3}{\partial \eta} \quad (18)$$

where

$$Q = \frac{3}{2} f + \left(\frac{v_e}{2u_e \sigma_e} \frac{d\sigma_e}{d\theta} + \frac{d}{d\theta} \left(\frac{v_e}{u_e} \right) \right) g$$

$$\begin{aligned}
\sigma_e &= \rho_e \mu_e u_e \\
E &= H/H_e \\
b &= \frac{\rho \mu}{\rho_e \mu_e} \left(1 + \frac{\rho_e}{\mu} \right) \\
R_1 &= \left(\frac{v_e}{u_e} \right)^2 \left(\frac{1}{v_e} \frac{du_e}{d\theta} FG - G^2 \right) \\
R_2 &= FG + \frac{1}{u_e} \frac{dv_e}{d\theta} G^2 - \frac{\rho_e}{\rho} \left(1 + \frac{1}{u_e} \frac{dv_e}{d\theta} \right) \\
R_3 &= \frac{u_e^2 \left(1 - \frac{1}{Pr} \right) \rho \mu}{\rho_e \mu_e H_e} \left(F \frac{\partial F}{\partial \eta} + \frac{v_e^2}{u_e^2} G \frac{\partial G}{\partial \eta} \right)
\end{aligned}$$

The boundary conditions are

$$\eta=0: f=F=0; g=G=0; \frac{\partial E}{\partial \eta} = 0 \text{ (adiabatic wall) or } E = E_w \quad (19)$$

$$\eta=\eta_e: F=G=E=1 \quad (20)$$

Eqs. (16)-(20) are solved starting at a reattachment line where $v=v_e=0$ and $\frac{dv_e}{d\theta} > 0$. The solution is marched in θ -direction (locally streamwise) until separation is reached. In conical flow this means that the skin-friction coefficient in θ -direction becomes zero. The skin-friction coefficient in r and θ -directions are defined by

$$c_{f_r} = \frac{2(\mu \frac{\partial u}{\partial z})_w}{\rho_w u_w^2} = \frac{2}{(Re_r)^{1/2}} \left(\frac{u_e}{u_w} \right)^2 \left(\frac{\sigma_w}{\sigma_e} \right)^{1/2} \left(\frac{\rho}{\rho_w} \frac{\mu}{\mu_w} \frac{\partial F}{\partial \eta} \right)_w \quad (21)$$

$$c_{f_\theta} = \frac{2(\mu \frac{\partial v}{\partial z})_w}{\rho_w u_w^2} = \frac{2}{(Re_r)^{1/2}} \frac{u_e v_e}{u_w^2} \left(\frac{\sigma_w}{\sigma_e} \right)^{1/2} \left(\frac{\rho}{\rho_w} \frac{\mu}{\mu_w} \frac{\partial G}{\partial \eta} \right)_w \quad (22)$$

where

$$Re_r = \frac{\rho_w u_w r}{\mu_w} \text{ and } \sigma = \rho \mu u \quad (23)$$

However, on the reattachment line $G = \frac{v}{v_e}$ is indeterminate and we have to taken the limit at this position. It may be shown that G is finite at the reattachment line and that the starting solutions may be obtained from Eqs. (16)-(18). They reduce to the ordinary differential equations

$$\frac{d}{d\eta} \left(b \frac{dF}{d\eta} \right) + Q \frac{dF}{d\eta} = 0 \quad (24)$$

$$\frac{d}{d\eta} \left(b \frac{dG}{d\eta} \right) + Q \frac{dG}{d\eta} = FG + \frac{1}{u_e} \frac{dv_e}{d\theta} G^2 - \left(G^2 - \frac{\rho_e}{\rho} \right) - \frac{\rho_e}{\rho} \quad (25)$$

$$\frac{1}{Pr} \frac{d}{d\eta} \left(b \frac{dE}{d\eta} \right) + Q \frac{dE}{d\eta} = \frac{u_e^2 \left(1 - \frac{1}{Pr} \right)}{H_e} F \frac{dF}{d\eta} \frac{\rho \mu}{\rho_e \mu_e} \quad (26)$$

3. INVISCID VELOCITY FROM EXPERIMENTAL PRESSURE DISTRIBUTION

As boundary conditions for the boundary layer calculation method we need the velocity components u_e and v_e . They can be obtained by an inviscid flow code or by a given pressure distribution. For a conical external flow the velocity vector may be derived from a spanwise pressure distribution. On the body surface ($z=0, w=0$) the inviscid conical equations may be written as

$$\frac{du}{d\theta} - v = 0 \quad (27)$$

$$v \frac{dv}{d\theta} + uv + \frac{1}{\rho} \frac{dp}{d\theta} = 0 \quad (28)$$

$$\frac{\gamma}{\gamma-1} \left(\frac{p}{\rho} - \frac{p_\infty}{\rho_\infty} \right) + \frac{1}{2} (u^2 + v^2 - U_\infty^2) = 0 \quad (29)$$

If we transform the velocity components into

$$u = q \cos \varphi, \quad v = q \sin \varphi \quad (30)$$

where q is the speed of the inviscid surface flow and φ the angle of the velocity vector with a conical ray, we obtain from Eqs. (27) and (28) for isentropic flow

$$\frac{q^2}{U_\infty^2} = 1 + \frac{2}{\gamma-1} \frac{1}{M_\infty^2} \left(1 - \left(\frac{p}{p_\infty} \right)^{\frac{\gamma-1}{\gamma}} \right) \quad (31)$$

and

$$\left(1 + \frac{d\varphi}{d\theta} \right) \tan \varphi + \frac{\frac{1}{p_\infty} \frac{dp}{d\theta}}{\gamma \left(\frac{p}{p_\infty} \right)^{1/\gamma} \left[M_\infty^2 + \frac{2}{\gamma-1} \left(1 - \left(\frac{p}{p_\infty} \right)^{\frac{\gamma-1}{\gamma}} \right) \right]} = 0 \quad (32)$$

Eq. (32) can be solved numerically for a given spanwise pressure distribution and given starting values of φ and $\frac{d\varphi}{d\theta}$. On a reattachment line this equation is indeterminate. This problem may be dealt with by differentiation of Eq. (32). The result on the reattachment line is

$$\frac{d\varphi}{d\theta} = -\frac{1}{2} + \frac{1}{2} \left[1 - \frac{\frac{4}{p_\infty} \frac{d^2 p}{d\theta^2}}{\gamma \left(\frac{p}{p_\infty} \right)^{1/\gamma} \left[M_\infty^2 + \frac{2}{\gamma-1} \left(1 - \left(\frac{p}{p_\infty} \right)^{\frac{\gamma-1}{\gamma}} \right) \right]} \right]^{1/2} \quad (33)$$

4. FINITE DIFFERENCE METHOD

The boundary layer equations Eqs. (16)-(18) with the boundary conditions Eqs. (19) and (20) are solved using a marching procedure. Since we are dealing with parabolic equations an implicit scheme is preferred because it is unconditionally stable. In a fully implicit scheme the nonlinear terms have to be linearized with a Newton method; this implies an iteration procedure. In the present solution method an alternative is applied by using a predictor-corrector linearization as proposed by Matsuno (Ref. 3) and DeJarnette and Woodson (Ref. 4). Such a scheme is half-implicit, second-order accurate, unconditionally stable (Ref. 3) and no iteration procedure is needed. To determine the initial profiles Eqs. (24)-(26) are solved using finite differences in an iteration procedure at each grid point where successive improvements to the previous solution are applied by a Newton linearization. For the solution of the boundary layer equations, Eqs. (16)-(18), the following notations are used

$$U_{i,j} = U(\theta_i, \eta_j) \quad (34)$$

where

$$\theta_{i+1} = \theta_i + \Delta\theta_i \quad ; \quad i = 1, 2, \dots, \text{IMAX}-1 \quad (35a)$$

$$\eta_{j+1} = \eta_j + \Delta\eta_j \quad ; \quad j = 1, 2, \dots, \text{JMAX}-1 \quad (35b)$$

The central difference operators are defined by

$$\delta_n U_{i,j} = \frac{U_{i,j+1} - U_{i,j-1}}{\Delta\eta_j + \Delta\eta_{j-1}} \quad (36)$$

$$\delta_n U_{i,j+\frac{1}{2}} = \frac{U_{i,j+1} - U_{i,j}}{\Delta\eta_j} \quad (37)$$

$$\delta_\theta U_{i+\frac{1}{2},j} = \frac{U_{i+1,j} - U_{i,j}}{\Delta\theta_i} \quad (38)$$

$$\delta_n (b_{i,j} \delta_n U_{i,j}) = \frac{2}{\Delta\eta_j + \Delta\eta_{j-1}} \left(b_{i,j+\frac{1}{2}} \frac{U_{i,j+1} - U_{i,j}}{\Delta\eta_j} - b_{i,j-\frac{1}{2}} \frac{U_{i,j} - U_{i,j-1}}{\Delta\eta_{j-1}} \right) \quad (39)$$

with $b_{i,j+\frac{1}{2}} = \frac{1}{2} (b_{i,j} + b_{i,j+1})$.

For the predictor step the backward difference operator

$$\nabla_\theta U_{i+\frac{1}{2},j} = \frac{U_{i+\frac{1}{2},j} - U_{i,j}}{\frac{1}{2}\Delta\theta_i} \quad (40)$$

is used.

The discretization of $\frac{\partial f}{\partial n} = F$ becomes

$$\delta_n f_{i,j+1/2} = \frac{f_{i,j+1} - f_{i,j}}{\Delta n_j} = \frac{1}{2} (F_{i,j+1} - F_{i,j})$$

from which we may write

$$f_{i,j+1} = f_{i,j} + \frac{1}{2} \Delta n_j (F_{i,j} + F_{i,j+1}) \quad (41)$$

A similar expression holds for $g_{i,j+1}$.

The predictor stage for Eqs. (16)-(18) becomes

$$\delta_n (b_{i,j} \delta_n F_{i+1/2,j}) + (Q_{i,j} + \frac{v_e}{u_e} \frac{1}{2} \nabla_\theta g_{i+1/2,j}) \Delta_n F_{i,j} - \frac{v_e}{u_e} \frac{1}{2} G_{i,j} \nabla_\theta F_{i+1/2,j} = (R_1)_{i,j} \quad (42)$$

$$\delta_n (b_{i,j} \delta_n G_{i+1/2,j}) + (Q_{i,j} + \frac{v_e}{u_e} \frac{1}{2} \nabla_\theta g_{i+1/2,j}) \Delta_n G_{i,j} - \frac{v_e}{u_e} \frac{1}{2} G_{i,j} \nabla_\theta G_{i+1/2,j} = (R_2)_{i,j} \quad (43)$$

$$\frac{1}{Pr} \delta_n (b_{i,j} \delta_n E_{i+1/2,j}) + (Q_{i,j} + \frac{v_e}{u_e} \frac{1}{2} \nabla_\theta g_{i+1/2,j}) \Delta_n E_{i,j} - \frac{v_e}{u_e} \frac{1}{2} G_{i,j} \nabla_\theta E_{i+1/2,j} = -\delta_n (R_3)_{i,j} \quad (44)$$

The relation between f, g and F, G , respectively, is obtained from Eq. (41) and a similar one for g . For the corrector-stage the equations are

$$\delta_n (b_{i+1/2,j} \delta_n (\frac{F_{i,j} + F_{i+1,j}}{2})) + (Q_{i+1/2,j} + \frac{v_e}{u_e} \frac{1}{2} \nabla_\theta g_{i+1/2,j}) \Delta_n F_{i+1/2,j} - \frac{v_e}{u_e} \frac{1}{2} G_{i+1/2,j} \delta_\theta F_{i+1/2,j} = (R_1)_{i+1/2,j} \quad (45)$$

$$\delta_n (b_{i+1/2,j} \delta_n (\frac{G_{i,j} + G_{i+1,j}}{2})) + (Q_{i+1/2,j} + \frac{v_e}{u_e} \frac{1}{2} \nabla_\theta g_{i+1/2,j}) \Delta_n G_{i+1/2,j} - \frac{v_e}{u_e} \frac{1}{2} G_{i+1/2,j} \delta_\theta G_{i+1/2,j} = (R_2)_{i+1/2,j} \quad (46)$$

$$\frac{1}{Pr} \delta_n (b_{i+1/2,j} \delta_n (\frac{E_{i,j} + E_{i+1,j}}{2})) + (Q_{i+1/2,j} + \frac{v_e}{u_e} \frac{1}{2} \nabla_\theta g_{i+1/2,j}) \Delta_n E_{i+1/2,j} - \frac{v_e}{u_e} \frac{1}{2} G_{i+1/2,j} \delta_\theta E_{i+1/2,j} = -\delta_n (R_3)_{i+1/2,j} \quad (47)$$

Again f and g are related to F and G by equations of the type of Eq. (41).

The difference equations may be written in a block-tridiagonal matrix form having 5×5 matrices as entries. The system is solved by the modified Davis algorithm (Ref. 12). The solution marches in θ -direction until the skin-friction coefficient in that direction, c_{f_θ} (Eq. (22)), goes through zero when

the separation line is reached. The number of grid points across the boundary layer was 81 for the delta wing and 101 for the cone. A variable grid was employed according to (Ref. 12)

$$n_j = \frac{n_{jMAX} \{K(j-1)^{\Delta N/\Delta N_{O-1}}\}}{K^{1/\Delta N_{O-1}}} \quad (48)$$

where

$$n_{jMAX} = 6 \text{ (delta wing), } 7 \text{ (cone); } \Delta N = 1/80 \text{ (delta wing), } 1/100 \text{ (cone); } \Delta N_{O-1} = 0.1; K=1.5.$$

The number of gridpoints in θ -direction was 241 in the case of the delta wing and 151 for the cone. In

the delta wing calculations also the meshwidth $\Delta \theta$ was varied in such a way that the product $\frac{dv_e}{d\theta} \Delta \theta$ was

kept constant above a certain level of $\frac{dv_e}{d\theta}$. A maximum value of $\Delta \theta = 0.004$ was maintained in regions of

small $\frac{dv_e}{d\theta}$. For the cone a constant increment of $\Delta \theta = 0.00273$ was used throughout the entire computational domain.

5. EXPERIMENTS

The experimental results are obtained from two sets of experiments. One set (Ref. 5) were measurements on a delta wing with a flat upper surface and sharp 65° swept leading edges; the root chord was 120 mm. The results discussed in the present paper cover free stream Mach numbers of 0.6, 0.7 and 0.85 and angles of attack of 5, 10 and 15° . In these cases oil flow patterns and leeward surface pressure distributions were obtained. A spanwise row of pressure taps is located at 70% chord; also along the rootchord a row of taps from 30%-90% is located. Beginning at a chordwise position of 65% several rows of a few (4 or 5) pressure taps each were present (at 65, 75, 79, 83, 92% rootchord). These rows were applied in order to check the amount of concavity of the flow and, at the higher Mach numbers and angles of attack, the existence and if so the position of shock waves. The Reynolds number based on the root chord was 3-3.6 million, depending on the Mach number. The other set of experimental results were obtained from early circular cone flow tests (Ref. 6) made at a free stream Mach number of 2.95 at angles of attack between 5° and 22° . The cone had a semi-apex angle of 7.5° and a length of 150 mm. For the boundary layer computation we selected an angle of attack $\alpha = 14^\circ$, being a case where the flow was still 'smooth' that means no embedded shocks were observed in the experiments and for which the oil flow pattern showed separation lines. The circumferential pressure distributions at 53% and 85% of the cone length served as input for the method. The static

pressure distribution along a generator confirmed that the flow was very conical indeed. The Reynolds number based on the cone length was 5.1 million.

6. DISCUSSION OF RESULTS

Since the boundary layer computational model is essentially of the weak interaction type the computations can only be carried out up to separation. However, the method can sustain some steps downstream of it. Only turbulent boundary layers are computed since the pressure distributions used are measured in the turbulent region.

6.1. Delta wing results

The delta wing experiments showed that the pressure distribution along the rootchord is not conical. At angles of attack of interest for the present paper an almost linear pressure increase was measured from $\frac{x}{c_r} = 0.30-0.90$ (Ref. 5). The computed results, however, based mainly on the spanwise pressure distribution at 70% chord position, show an extremely good agreement with the experimental results, as will be discussed furtheron. As has been pointed out in the foregoing the spanwise variations of the flow quantities have a much larger influence on the separation phenomenon than the chordwise variation. Table 1 gives an indication of the largest observed pressure gradients in x and y directions at $\alpha = 15^\circ$.

$\frac{x}{c_r}$	$\frac{y}{c_r}$	$M_\infty = 0.6$			$M_\infty = 0.7$		
		C_p	$\frac{dC_p}{dx}$	$\frac{dC_p}{dy}$	C_p	$\frac{dC_p}{dx}$	$\frac{dC_p}{dy}$
			mm ⁻¹	mm ⁻¹		mm ⁻¹	mm ⁻¹
0.65	0	-0.143	} 0.006	-	-0.183	} 0.007	-
0.725	0	-0.087		-	-0.122		-
0.70	0.214	-1.327	-	} 0.215	-1.220	-	} 0.151
0.70	0.233	-0.827	-		-0.868	-	

Table 1. Experimental pressure gradients at $\alpha = 15^\circ$ (Ref. 5).

The largest deviations from conical flow were observed in the center part of the wing ($y/y_{ge} < 0.3$).

In Fig. 2 a sketch is shown of the vortex system above the delta wing and of the surface streamlines. Two main (primary) vortices are shed from the sharp leading edges. The flow reattaches on the wing surface at the reattachment line A1. With increasing angle of attack this line moves towards the wing symmetry line and they will eventually coincide. From the reattachment position towards the leading edge the surface flow first accelerates and reaches a suction peak and then decelerates due to an adverse pressure gradient. This unfavourable gradient may cause the surface flow to separate at the secondary separation line to form a secondary vortex in the field above the wing surface. The pressure distribution measured in such a flow is shown in Fig. 3, where they have been b-splined for the sake of the calculations. Also the inviscid velocity components derived from the pressure distribution using Eqs. (31)-(33) are presented in Fig. 3. It appears that the C_p -distribution is very closely related to the distribution of the velocity component normal to a conical ray (v_e). The spanwise variation of u_e is almost negligible in that respect. This relatively large distinction between the two velocity components has been observed in all cases calculated, also for the supersonic cone flow. It confirmed the findings of Table 1. In Fig. 4 the skin-friction coefficients defined by Eqs. (21) and (22) are shown. The coefficients are computed starting on the reattachment line and/or the rootchord. The secondary separation is taken as the position where C_{p_g} goes negative. On the separation line $C_{p_r} \neq 0$. As may be seen in Fig. 5 the 3D separation occurs at a location where the surface streamlines reveal a strong spanwise deflection. Qualitatively speaking there is not much difference between the distributions of the skin-friction coefficients in Figs. 4a and 4b, only the magnitude is different. Evidently this has to do with the analogy between the pressure distributions in both cases. The calculated streamline patterns are presented in Fig. 5. The theoretically obtained locations of the secondary separation are slightly inboard of the experimentally observed lines. With respect to this particular item the overall results are very good indeed as shows Table 2.

M_∞	α deg.	Second. Separ. % semi-span		Diff.
		exp.	comp.	
0.6	5	82.2	81.3	0.9
0.6	10	77.4	76.1	1.3
0.6	15	73.9	72.9	1.0
0.7	10	75.8	74.6	1.2
0.7	15	72.8	68.6	4.2
0.85	5	80.6	80.9	-0.7
0.85	10	73.2	70.5	3.2

Table 2. Location of secondary (turbulent) separation (Ref. 5).

Apparently, at the higher Mach numbers in combination with the larger angles of attack the difference between theoretical and experimental results increases, which is not unexpected considering the assumptions made in the flow model. For comparison the inviscid streamlines (at the edge of the boundary layer) are shown. They have been calculated by the method discussed in section 3. In Figs. 6 the flow angle ϕ with respect to a ray through the apex of the wing has been plotted versus the spanwise coordinate. Shown are the distributions for the skin-friction lines (surface streamlines) and for the inviscid streamlines (edge of the boundary layer). For comparison also the values of ϕ_w obtained from oil flow pictures have been plotted; the agreement with the numerical results is very good. A photograph of the oil flow pattern for $M_\infty=0.85$, $\alpha=10^\circ$, one of the cases calculated, is given in Fig. 7. If Fig. 5b is compared with Fig. 7, for example by superimposing them on each other, it would appear that the theoretical surface streamlines in the overall picture agree very well with the experimental results. Finally in Fig. 8 the spanwise development is sketched of the profile of the velocity component v normal to a conical ray. The computation could be continued just beyond separation so that a region of reverse flow appears.

6.2. Circular cone results

A physical picture of the flow about a cone at high angles of attack is depicted in Fig. 9. In this problem where there are no defined geometrical locations where the flow is likely to separate, the flow separates from the smooth cone surface due to a high adverse pressure gradient. This behaviour might be compared to the secondary separation on the delta wing.

The numerical results are shown in Figs. 10-13 and 15. Fig. 10, 11 and 13 should be interpreted looking into the direction of the local surface flow, i.e. the circumferential angle ψ (the abscissae in these figures) is measured from the windward symmetry generator, see Fig. 9. If the pressure distribution of Fig. 10 is compared to that of the delta wing (Fig. 5) it is obvious that the gradients are much lower and thus also the adverse pressure gradient causing separation. In observing the difference in gradient we should however take into account that the difference between the highest and lowest pressure levels of both cases is considerable as well. Fig. 11 shows that some influence of the lesser adverse pressure gradient is recognized in the decrease of the skin-friction coefficient prior to separation. As a matter of fact the Reynolds number had a large influence on the computational results (as it should). For local Reynolds numbers Re_ψ above 5 million the skin-friction coefficient c_f did not reach the zero level, but

only showed a positive minimum close to zero. A similar result was also obtained in Ref. 4 for an incompressible flow on a delta wing. In Fig. 12 the surface streamlines are plotted together with the inviscid ones obtained with the conical Euler equations. The figure shows the unwrapped cone surface cut at the windward symmetry generator; this generator appears as the two side edges in the figure. As before, the agreement with the experimental oil flow visualization results is nice as is demonstrated by the closeness of theoretical and experimental separation lines and also by comparing Fig. 12 as a whole with the wind tunnel result shown in Fig. 14. An aspect of this comparison is illustrated in Fig. 13 where the flow inclination angle ϕ is shown as function of the circumferential angle ψ . Again three quantities are considered: the computational value at the surface, the inviscid result at the edge of the boundary layer and the experimental value obtained from the oil flow pattern. The experimentally determined quantity has an uncertainty that is estimated to be $\pm 3^\circ$. It must be noted that no attempt has been made to compute the surface flow at the leeward side in between the two separation lines (Fig. 12) where the secondary separation takes place in the experiments. In conclusion in Fig. 15 some of the cross-flow velocity profiles v are collected. Just as for the delta wing the computation is continued slightly beyond the point where c_f passes the zero value. The velocity profiles show a bulging shape ($v > v_g$) inside the

boundary layer. This shape changes into more 'common' profiles as the separation line is approached. Unfortunately no boundary layer profiles have been measured to check the theoretical behaviour.

6.3. Status of the boundary layer

As discussed previously the boundary layer was assumed to be turbulent at the chordwise positions where the spanwise distributions were taken. Therefore all the calculations were carried out for a turbulent boundary layer. This is certainly valid in the case of the cone flow where the Reynolds number is 5 million; however, the delta wing results need some explanation. In order to demonstrate the possibilities of using a 'conical boundary layer' method in conjunction with realistic pressure distributions at a single chordwise position where a turbulent boundary layer is plausible, only a few cases have been considered in the present study. As long as no complicated flow phenomena as embedded shocks, trailing edge effects and tip effects, vortex bursting and the like are encountered, the method shows to give good agreement with experimental surface flow. The examples used as computational models belonged to the category where the above mentioned complications did not occur. The tests, however, were extended over a wider range of free stream Mach numbers and angles of attack, see Ref. 5. In a number of combinations of Mach number and angle of attack boundary layer transition could easily be established. Then the secondary separation line showed a non-conical transition from its laminar location to a more out board one. The transition started at x/C_r between 0.2-0.25, although it should be noted that it was not always as concealed as in Fig. 7. Outside the transitional region the secondary separation line was in the laminar as well as in the turbulent region straight to a very good approximation (Ref. 5). It will be evident that the non-conical transitional region cannot be covered by the present method.

7. CONCLUSIONS

From the computational and experimental investigations on conical bodies, viz. a planar sharp-edged delta wing at high subsonic speeds and a circular cone at supersonic speeds, at moderate to high angles of attack the following conclusions may be drawn.

- Oil flow visualization studies have shown that the surface flow on the bodies may be considered as conical (or nearly conical on the delta wing). For the delta wing certain reservations should be made. The free stream Mach number and/or the angle of attack should be limited in the sense that embedded shocks, upstream influence of trailing edge and wing tips, vortex breakdown must be absent. For both bodies applies that the boundary layer transitional region should be excluded.
- In the case of the delta wing the experimental pressure distribution did not entirely satisfy the requirement for conical flow. However, in the region of interest the spanwise pressure gradients were

at least 20 times larger than those in chordwise direction. This is the main reason for a nearly conical flow pattern.

- If the above mentioned reservations are met and if an accurate spanwise inviscid velocity distribution is used as boundary condition (in the present case obtained from a measured pressure distribution) the 'conical boundary layer' method provides a good possibility to compute the surface flow and to predict the separation lines on conical bodies.

REFERENCES

1. Elsenaar, A. and Eriksson, G., Eds., Proceedings of the Symposium on International Vortex Flow Experiment on Euler Code Validation, October 1-3, 1986, Stockholm, FFA, Bromma, Sweden.
2. Houtman, E.M., A General Method for Calculating Compressible Boundary Layers on Conical Surfaces with Conical Outer Flow, Delft University of Technology, Faculty of Aerospace Engineering, To be published 1988.
3. Matsuno, K., A Vector-Oriented Finite Difference Scheme for Calculating Three-Dimensional Compressible Laminar and Turbulent Boundary Layers on Practical Wing Configurations, AIAA Paper No. 81-1020, 1981.
4. DeJarnette, F.R. and Woodson, S.H., Numerical and Experimental Determination of Secondary Separation on Delta Wings in Subsonic Flow, AIAA Journ. Aircraft, Vol. 22, No. 7, pp. 602-608, 1985.
5. Ottochian, S.P., Bannink, W.J. and Houtman, E.M., Investigation of the Vortex Flow over a Sharp-Edged Delta Wing in the Transonic Speed Regime, Delft University of Technology, Faculty of Aerospace Engineering, To be published, 1988.
6. Bannink, W.J. and Nebbeling, C., Measurements of the Supersonic Flow Field Past a Slender Cone at High Angles of Attack, AGARD Conference Proceedings CP 247, Paper 22, 1979.
7. Cebeci, T., Kaups, K. and Ramsey, J.A., A General Method for Calculating Three-Dimensional Compressible Laminar and Turbulent Boundary Layers on Arbitrary Wings, NASA CR-2777, 1977.
8. Cebeci, T., Calculation of Three-Dimensional Boundary Layers. I. Swept Infinite Cylinders and Small Cross Flow, AIAA Journ., Vol. 12, No. 6, pp. 779-786, 1974.
9. Cebeci, T. and Smith, A.M.O., Analysis of Turbulent Boundary Layers, Academic Press, New York, 1974.
10. Adams, Jr., J.C., Finite-Difference Analysis of the Three-Dimensional Turbulent Boundary Layer on a Sharp Cone at Angle of Attack in a Supersonic Flow, AIAA Paper No. 72-186, 1972.
11. Bontoux, P. and Roux, B., Compressible Turbulent Boundary Layer on a Yawed Cone, AIAA Paper No. 75-858, 1975.
12. Blottner, F.G., Introduction to Computational Techniques for Boundary Layers, Sandia Laboratories, Albuquerque, Rep. 79-0893, 1979.

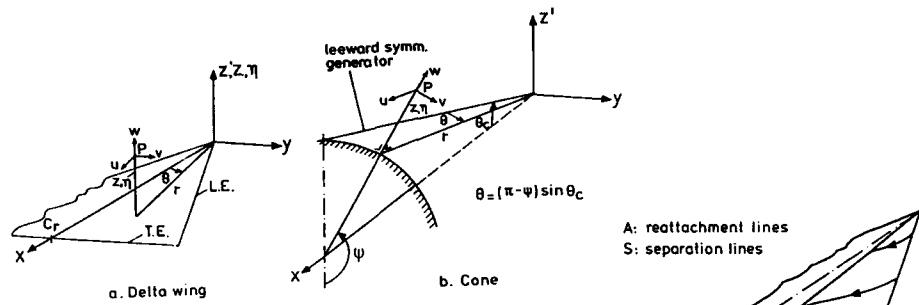


Fig.1. Coordinate systems.

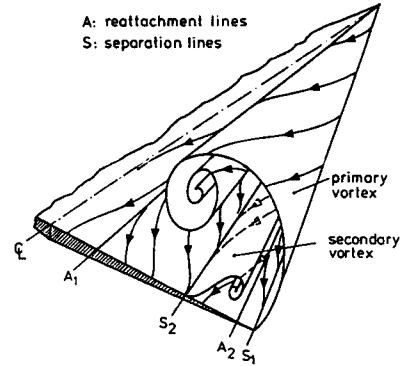


Fig.2. Delta wing leeward surface flow geometry.

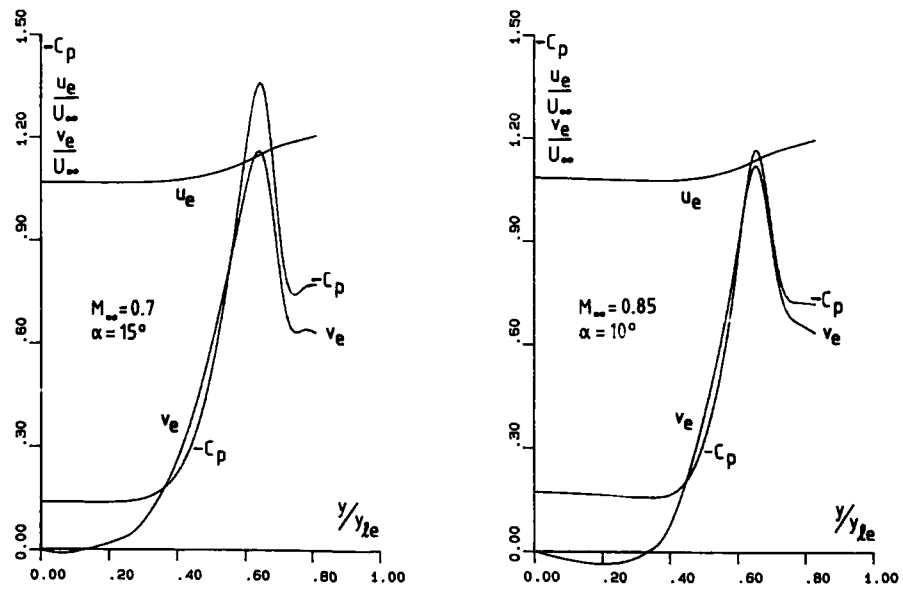


Fig.3. Experimental pressure coefficients and inviscid velocity components at leeward surface of delta wing.

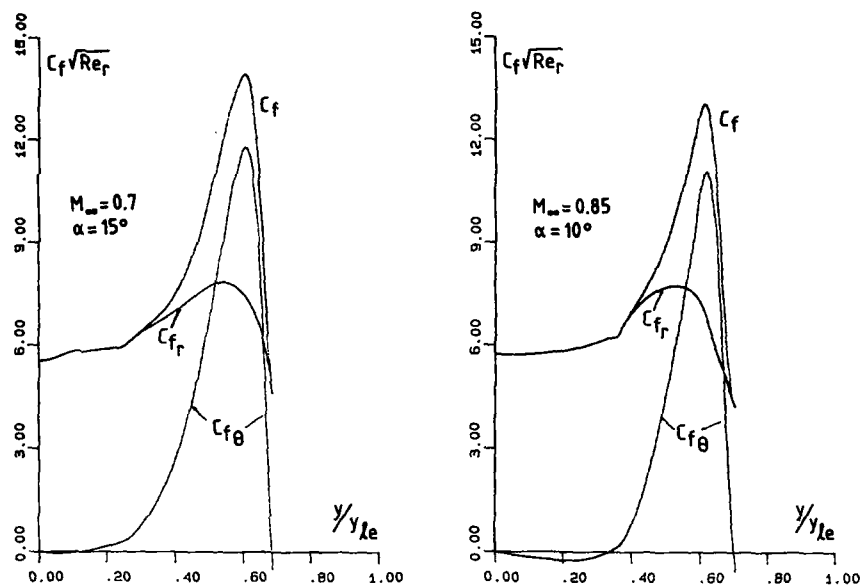


Fig.4. Skin friction coefficients on delta wing.

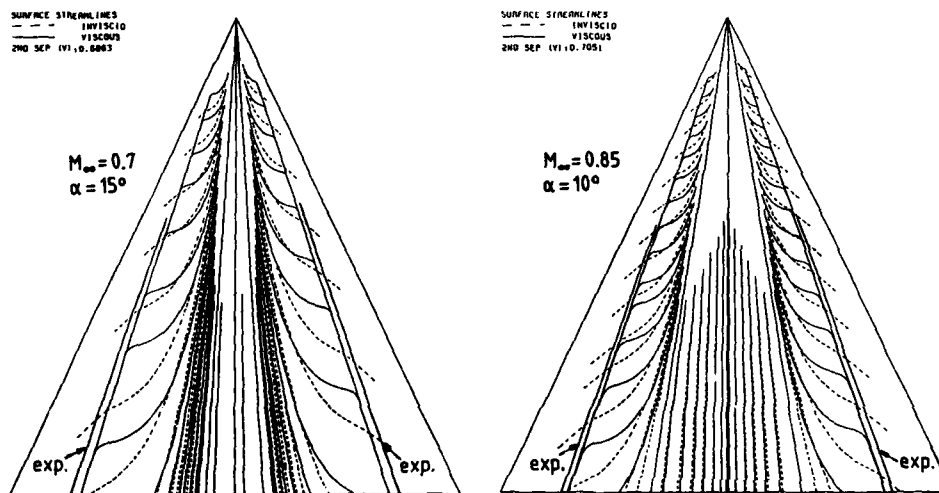


Fig.5. Surface streamlines and separation lines on delta wing.

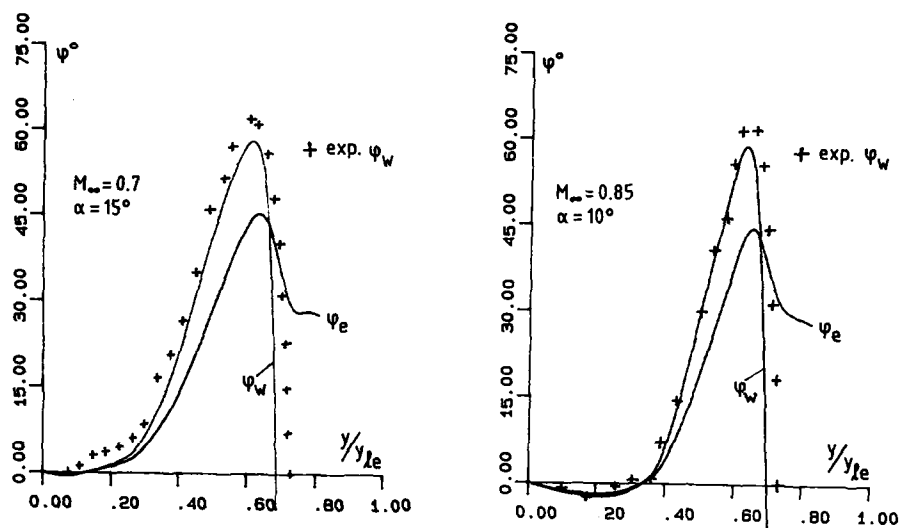


Fig. 6. Flow directions on delta wing.

Fig. 7. Oil flow pattern on delta wing at $M_\infty = 0.85$, $\alpha = 10^\circ$.

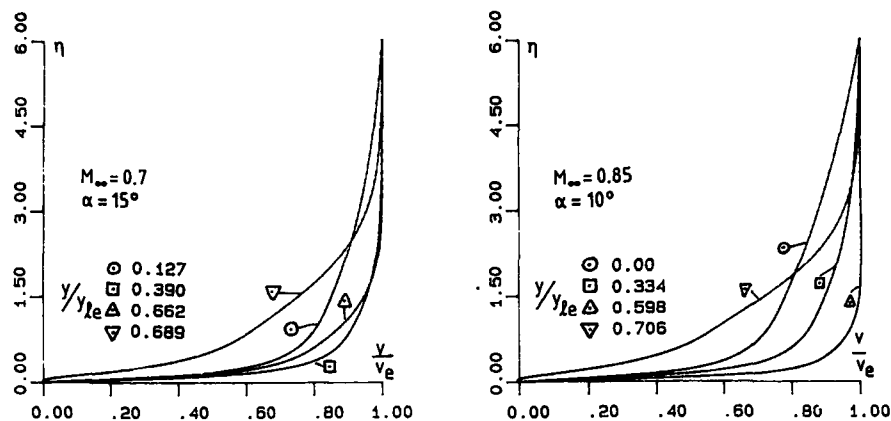


Fig. 8. Spanwise development of cross-flow velocity component in boundary layer on delta wing.

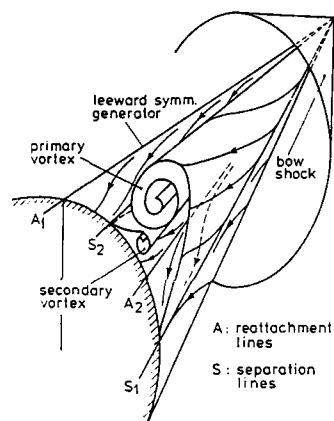


Fig. 9. Cone leeward surface flow geometry.

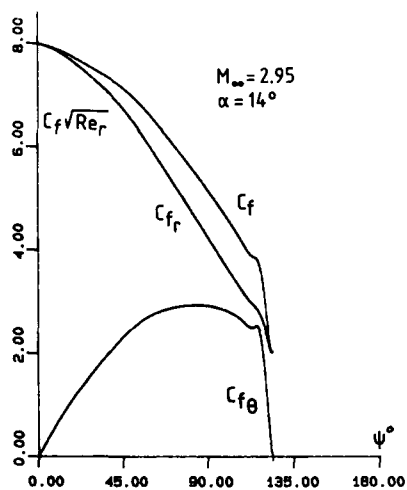


Fig. 11. Skin friction coefficients on cone.

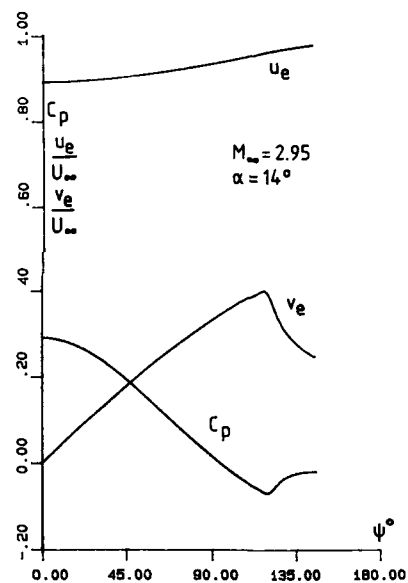


Fig. 10. Experimental pressure coefficient and inviscid velocity components at leeward surface of cone.

P2-14

SURFACE STREAMLINES
 --- INVISCID
 --- VISCIOUS
 2ND SEP 1971 123.9566

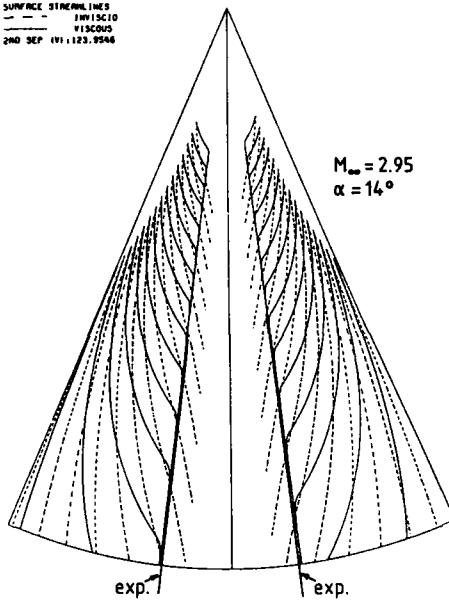


Fig.12. Surface streamlines and separation lines on cone.

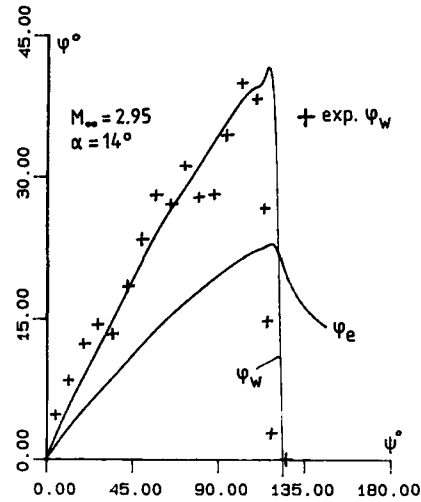


Fig.13. Flow directions on cone.

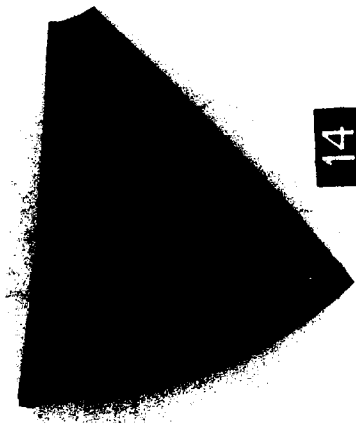


Fig.14. Oil flow pattern on cone;
 $M_{\infty} = 2.95, \alpha = 14^\circ$.

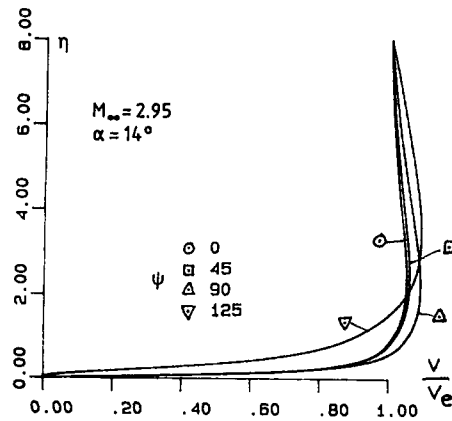


Fig.15. Spanwise development of cross-flow velocity component in boundary layer on cone.

FINITE DIFFERENCE METHODS IN RECIRCULATING FLOWS

J.C.F. Pereira
 Instituto Superior Técnico
 Dept. of Mechanical Engineering
 Av. Rovisco Pais
 1096 Lisbon Codex
 PORTUGAL
 and

F. Durst
 Lehrstuhl für Strömungsmechanik
 Universität of Erlangen-Nürnberg
 Egerlandstrasse, 13
 D-8520 Erlangen
 WEST GERMANY

SUMMARY

This paper presents numerical solutions of the two-dimensional Navier-Stokes equations using finite-difference approaches in which different numerical schemes for the discretization of the convective terms are used. The errors arising in the solution of the recirculating flows are mainly attributed to the convective discretization schemes and, hence, knowledge of different numerical schemes is essential to accurately predict complex recirculating flows. To assess the performance of prediction schemes, it is necessary to carry out predictions in carefully selected laminar flows. For this reason the flows examined in this paper are all in the laminar regime and emphasis is given to the evaluation of various discretization schemes and comparisons of the numerical solutions with laser-Doppler measurements.

INTRODUCTION

In recent years, large computers have become available that permit numerical solutions of two-dimensional recirculating flows to be obtained. As the flow geometry gets complex, even these large computers do not provide enough computational speed or storage space to carry out the flow predictions with the required accuracy. Numerical diffusion introduces errors into the prediction which are mainly attributed to the convection discretization schemes employed in the computations and once the assessment of turbulence models in recirculating flows is limited by the accuracy of the numerical treatment of the flow equations. Therefore there is an extensive interest in information on the best discretization scheme for particular class of flows. In the present study, laminar recirculating flows were considered and different discretization schemes were employed to carry out computations of laminar flows. The present report provides a brief summary of the outcome of this investigation. Numerical calculations have been performed with an intent to compare five finite different schemes for convection discretization. These are as follows:

- i) The Quadratic Upstream-Weighted Scheme (QUDS)
- ii) The Hybrid Central/Upwind Scheme (CUDS)
- iii) The Hybrid Power Law/Upwind Scheme (PLDS)
- iv) The Hybrid Central/Skew Upwind (CSUDS)
- v) The first order Upwind Scheme (UDS)

The test cases considered were the backward-facing step flow, the obstacle flow, the unsteady flow of a sudden type expansion and unsteady flow around a square obstacle. For all these flows, LDA- measurements were available and, hence, computations could be directly compared with measurements to assess the performance of the various discretization schemes.

GOVERNING FLOW EQUATIONS, NUMERICAL SCHEMES AND SOLUTION PROCEDURE

Governing equations

The partial differential equations (PDE) governing the steady recirculating flows presented in this study are the Navier-Stokes equations. Mass conservation also holds and this can be formulated to yield the continuity equation. The flows considered are two-dimensional and incompressible and, hence, the general PDEs describing the flow field are:

Continuity equation:

$$\frac{\partial \rho U}{\partial x} + \frac{\partial \rho V}{\partial y} = 0 \quad (1)$$

Momentum equations:

$$\begin{aligned} \frac{\partial \rho U}{\partial t} + \frac{\partial \rho U U}{\partial x} + \frac{\partial \rho V U}{\partial y} \\ = - \frac{\partial P}{\partial x} + \mu \left(\frac{\partial^2 U}{\partial x^2} + \frac{\partial^2 U}{\partial y^2} \right) + S_U \end{aligned} \quad (2)$$

$$\begin{aligned} \frac{\partial \rho V}{\partial t} + \frac{\partial \rho U V}{\partial x} + \frac{\partial \rho V V}{\partial y} \\ = - \frac{\partial P}{\partial y} + \mu \left(\frac{\partial^2 V}{\partial x^2} + \frac{\partial^2 V}{\partial y^2} \right) + S_V \end{aligned} \quad (3)$$

These equations can be written in the form of a general transport equation, as follows:

$$\begin{aligned} \frac{\partial \rho \phi}{\partial t} + \frac{\partial \rho U \phi}{\partial x} + \frac{\partial \rho V \phi}{\partial y} \\ = \Gamma_\phi \left(\frac{\partial^2 \phi}{\partial x^2} + \frac{\partial^2 \phi}{\partial y^2} \right) + S_\phi \end{aligned} \quad (4)$$

where ϕ denotes the U or V velocity components and S_ϕ represents the pressure gradient term in the x- and y-directions. The continuity equation results from this general transport equation by setting $\phi = 1$ and $S_\phi = 0$.

The transformation of the PDEs for the U- and V-momentum into the equivalent finite difference equations (FDEs) can be obtained by using the finite volume method. The application of the finite volume method requires discretizations of the convective and diffusive fluxes at each control volume face. In the present study, the diffusive fluxes were always approximated by central differences known to be of third order accuracy.

Numerical schemes for discretization of convective terms

The approximation of the convective fluxes in the momentum equations at each control volume face was performed with different numerical schemes. Five numerical schemes were used:

o The upwind differencing scheme (UDS) is the simplest unconditional stable scheme to approximate the convection terms. It, however, induces a truncation error which is felt like a diffusive term in the equations. This can lead to low accuracy in predicted solutions of flow fields. This discretization scheme approximates the -control volume face value by the nodal value taken in the upstream direction of the velocity.

o The hybrid central/upwind differencing scheme (CUDS), [1], is based on the exact solution of the linear one-dimensional steady convection-diffusion equation between any two neighbouring mesh nodes. The convective terms are

approximated by central differences for Peclet numbers ($Pe = \rho \Delta x U / T$), $|Pe| < 2$. For $|Pe| > 2$, the convection terms are approximated by UDS.

o The hybrid power law/upwind differencing scheme (PLDS), [2], in comparison to the above schemes, represents a better approximation of the exact solution of the one-dimensional convection-diffusion equation. In this approximation, 'a power law' is used for $|Pe| < 10$ and UDS for $|Pe| > 10$.

o The hybrid central/skew upwind differencing scheme (CSUDS), [3], strongly reduces the problem caused by the flow direction to grid line skewness. For Peclet number $|Pe| > 2$, this scheme tries to simulate a grid in which the coordinate grid lines are aligned with the local flow direction. It takes explicit account of the local flow angle by determining the velocity vector tangential to the streamline at the control volume face. For $|Pe| < 2$, the scheme uses central differences for the discretization of the convection terms in the equations.

o The quadratic weighted upstream differencing scheme (QUDS), [4], is based on a local quadratic interpolation at the -surface for estimating both the convective and diffusive flux terms on each control volume face individually. For non-uniform grid distributions the local quadratic interpolations were derived taking into account the non-uniformity between mesh points.

Table I lists the discretization schemes considered and gives a brief summary of each of them.

Solution procedure

All computations presented in this paper were performed with an appropriately modified version of a computer code TEACH designed to solve two-dimensional elliptic flow problems in terms of the primitive hydrodynamic variables U , V and P . The code, in its original form, uses CUDS and is based on the so-called SIMPLE solution algorithm for the solution of the final set of linear equations. As a first step in solving a specified flow problem, the TEACH program computes a preliminary velocity field by solving discretized versions of the momentum equations employing a guessed pressure field. This field is then improved by solving the pressure-correction equation which contains a dilatation term (i.e. the local mass imbalance) as a source. In the present study, the system of algebraic equations was always solved by the 'strongly implicit method' (see [5])

NUMERICAL SCHEME	REFERENCE	COMPUTATIONAL GRID	INTERPOLATION PRACTICES AT $i+1/2, j$ FACE WALL	APPROXIMATION $\phi_{i+1/2, j}$	TRUNCATION ERROR τ_E
WIND SCHEME (DS)	Chou et al (1953)			$\phi_{i+1/2, j} = \frac{U_{i+1/2, j}^+ \phi_{i+1, j} + U_{i+1/2, j}^- \phi_{i, j}}{U_{i+1/2, j}^+ + U_{i+1/2, j}^-}$	$\tau_E _{U, \text{convec}} = \frac{1}{2} \left[U \frac{\partial^2 \phi}{\partial x^2} \right]_{i+1/2, j}$ $= (V/\delta y) \phi_{yy} _{i+1/2, j} = \text{NOT}$
HYBRID CENTRAL/UPWIND SCHEME (UDS)	Spalding (1972)			$\phi_{i+1/2, j} = \frac{\phi_{i+1, j} + \phi_{i, j}}{2}$ $\phi_{i+1/2, j} = U^+ \phi_{i+1, j} + U^- \phi_{i, j}$	$\tau_E _{U, \text{convec}} = \frac{1}{8} \left[-U \frac{\partial^2 \phi}{\partial x^2} \right]_{i+1/2, j}$ $V \frac{\partial^2 \phi}{\partial y^2} = \frac{U \phi_{yy}^2}{2} \phi_{yy}$ $= \frac{U \phi_{yy}^2}{2} \phi_{yy} _{i+1/2, j} = \text{NOT}$
HYBRID POWER LAW/UPWIND SCHEME (DS)	Patankar (1980)			$\phi_{i+1/2, j} = (\phi_{i+1, j} - \phi_{i, j}) \cdot (1 - 0.5 Pe)^{0.5} + 0.5 Pe^{0.5} - 1 \cdot \phi_{i, j}$ $\phi_{i+1/2, j} = U^+ \phi_{i+1, j} + U^- \phi_{i, j}$	$\tau_E _{U, \text{convec}} = \frac{1}{8} \left[U \frac{\partial^2 \phi}{\partial x^2} \right]_{i+1/2, j}$ $= V \frac{\partial^2 \phi}{\partial y^2} = \frac{U \phi_{yy}^2}{2} \phi_{yy} _{i+1/2, j} = \text{NOT}$

NUMERICAL SCHEME	REFERENCE	COMPUTATIONAL STAR	INTERPOLATION PRACTICES AT $(i+1/2, j)$ FACE WALL	APPROXIMATION OF $\phi_{i+1/2, j}$	TRUNCATION ERROR τ_k
HYBRID CENTRAL / BREW UPWIND SCHEME (CBUDS)	Rothby (1976)			$\phi_{i+1/2, j} = U^* \nabla^2 \phi_{i+1, j-1} + (1-C) \phi_{i+1, j} +$ $+ U^* \nabla^2 \phi_{i+1, j-1} + 2C \phi_{i+1, j-1} + U^* \nabla^2 \phi_{i+1, j+1} + (1-C) \phi_{i+1, j+1} +$ $+ U^* \nabla^2 \phi_{i+1, j+1} + 2C \phi_{i+1, j+1} + U^* \nabla^2 \phi_{i-1, j-1} + (1-C) \phi_{i-1, j-1} +$ $+ U^* \nabla^2 \phi_{i-1, j-1} + 2C \phi_{i-1, j-1} + U^* \nabla^2 \phi_{i-1, j+1} + (1-C) \phi_{i-1, j+1} +$ $+ U^* \nabla^2 \phi_{i-1, j+1} + 2C \phi_{i-1, j+1}$ $U^* = \frac{U_{i+1/2, j}}{20}$ $C = \frac{\Delta x}{20 \Delta y} \left(\frac{U_{i+1/2, j}}{U_{i+1/2, j}} \right)$ $a = \frac{1}{2} (1 + \frac{1}{2}) \quad b = \frac{1}{2} (1 - \frac{1}{2})$ $g^2 = \frac{(1-C) \pm (1-C)}{2(1-C)}$	$\tau_k [U, V, \text{correct}] = \frac{1}{8} \left[\frac{U^2 \Delta x^2}{2} + \frac{U^2 \Delta y^2}{2} \right]$ $V_{12} \phi_{yy} = 2(U) \phi_{yy} =$ $V_{12} \phi_{yy} = 2(U) \phi_{yy} =$
QUADRATIC UPSTREAM WEIGHTED SCHEME (QUDS)	Leonard (1979)			$\phi_{i+1/2, j} = \frac{\phi_{i+1, j-1} - \phi_{i-1, j-1}}{2} - \frac{U_{i+1/2, j}}{20 \Delta x} \left(\frac{U_{i+1/2, j}}{U_{i+1/2, j}} \right)$ $+ \left[\frac{1}{8} \phi_{i+1, j} + \frac{1}{8} \phi_{i-1, j} - \frac{1}{8} \phi_{i+1, j-1} - \frac{1}{8} \phi_{i-1, j-1} - \frac{1}{8} \phi_{i+1, j+1} - \frac{1}{8} \phi_{i-1, j+1} \right] -$ $- \frac{U_{i+1/2, j}}{20 \Delta x} \left(\frac{U_{i+1/2, j}}{U_{i+1/2, j}} \right) \left[\frac{1}{8} \phi_{i+1, j} + \frac{1}{8} \phi_{i-1, j} - \frac{1}{8} \phi_{i+1, j-1} - \frac{1}{8} \phi_{i-1, j-1} - \frac{1}{8} \phi_{i+1, j+1} - \frac{1}{8} \phi_{i-1, j+1} \right] -$ $- \frac{1}{8} \phi_{i+1, j-1} - \frac{1}{8} \phi_{i-1, j-1} - \frac{1}{8} \phi_{i+1, j+1} - \frac{1}{8} \phi_{i-1, j+1}$	$\tau_k [U, V, \text{correct}] = \frac{1}{8} \left[\frac{U^2 \Delta x^2}{2} + \frac{U^2 \Delta y^2}{2} \right]$ $+ \frac{U^2 \Delta x^2}{2} \phi_{yyy} + \frac{U^2 \Delta y^2}{2} \phi_{yyy}$ $+ \frac{U^2 \Delta x^2}{2} \phi_{yyy} + \frac{U^2 \Delta y^2}{2} \phi_{yyy}$

TABLE 1 - Numerical schemes used for convection discretisation.

and [6]) instead of the tri-diagonal matrix algorithm. The reason for using the strongly implicit method was the faster convergence achieved by the strongly implicit method for well-conditioned matrices, as in the case of the pressure correction equation.

RESULTS AND COMPARISON

Steady State Flows

The geometrical configurations of the backward-facing step and flow over a fence or an obstacle are shown in Figure 1.

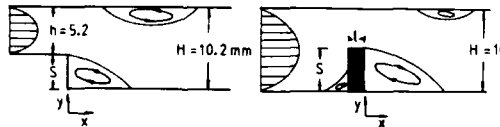


Figure 1 - Geometry for backward facing step flow over a fence.

For the backward facing step flow, a fully developed inlet profile at $x/s = -2$ was prescribed. At the exit plane, $x/s = 44$, a zero velocity gradient for U and V was assumed. The definition of the Reynolds number, which was used in this study, is based on the mean inlet velocity and hydraulic diameter of the inlet channel. For comparison purposes, all the schemes were applied with the same non-uniform grid comprising 55×53 grid points. After the step, an expansion ratio of 1.1 was used. For the same reasons the grid was kept unchanged for all Reynolds number. Grid dependence studies showed that for $Re < 420$, relative coarse grids with high expansion ratios were appropriate to predict the flow. For $Re > 420$, multiple recirculations occur, and the UDS, CUDS and PLDS schemes showed to require a much higher grid nodes than the presently used of 55×53 to achieve grid independent flow predictions.

Figures 2a), b) c) show the computed and measured locations of separation and reattachment x_1 , x_2 , x_3 for $50 \leq Re \leq 1000$. They also show calculations of other authors [8] and [9], using much higher grid points. All the schemes predicted correctly the appearance of the top recirculation region. The results obtained with UDS for $Re < 400$ displayed a shorter reattachment x_1 than the ones predicted with the other schemes. This was due to the false diffusion introduced by the first order Upwind discretization. For this range of Re , the CUDS and PLDS schemes used central differences in large regions of the computational domain, and therefore they presented better results than the UDS. However, for $Re > 550$ the UDS displayed higher values of x_1 than the CUDS and PLDS schemes. For this range of Re ,

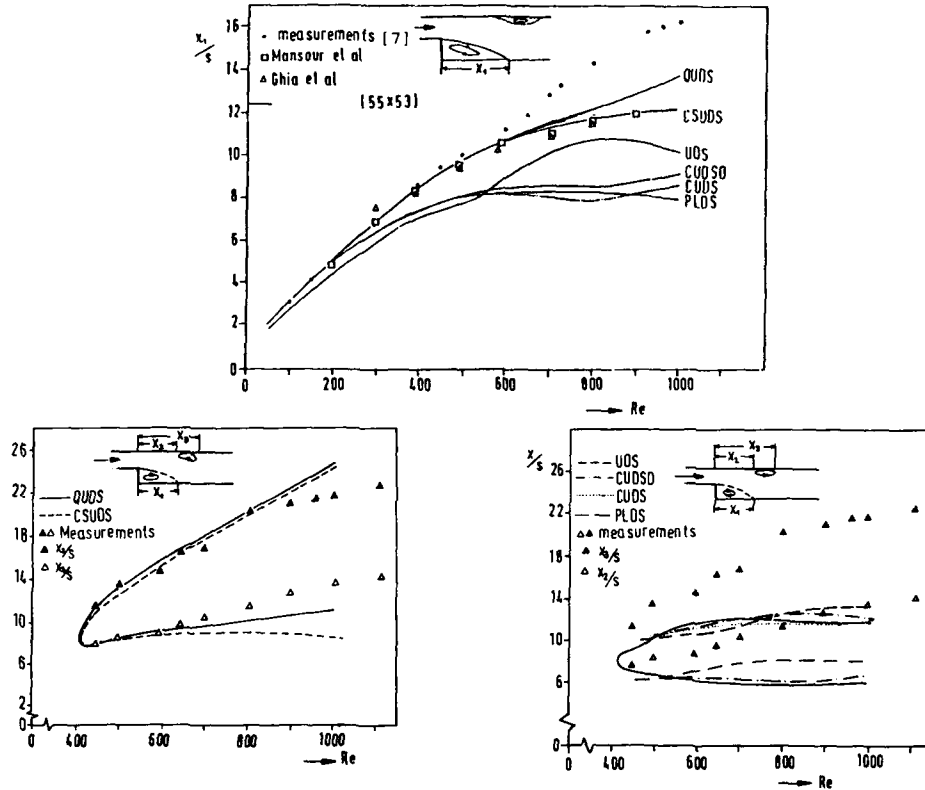


Figure 2 - Comparison of predicted and measured reattachment lengths for backstep flow.

a large recirculation region on the top channel wall arose. In this recirculation region, very low Peclet numbers ($|Pe| < 2$) were present. The false diffusion induced by the UDS in the surrounding and inside the top recirculation region yielded the destruction of this region. Thus the UDS predicts a much shorter top bubble in both x and y co-ordinate directions than the CUDS and PLDS. As a consequence, the main recirculation region predicted by the UDS was larger than the one predicted by the CUDS and PLDS. The excellent performance of QUOS is also demonstrated by the direct comparison of predicted and measured velocity profiles shown in Figure 3a) and 3b) for $Re = 389$ and $Re = 603$. The Hybrid Scheme CUDS is not capable of computing the flow with sufficient accuracy.

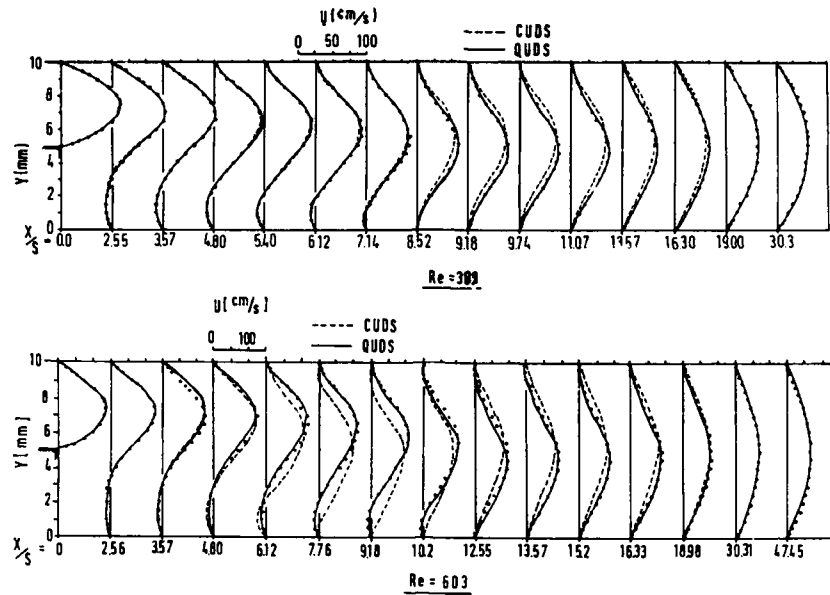


Figure 3 - Comparison of the U-velocity field predicted with the CUDS and QUDS and measurements. a) $Re = 389$; b) $Re = 603$

As a final result for the backward-facing step flow the prediction of the locations of the detachment and reattachment lines are shown in Figure 4. In the Re-region of the flow where two-dimensionality could be maintained in the experiments, good agreement between QUDS-predictions and experiments was obtained.

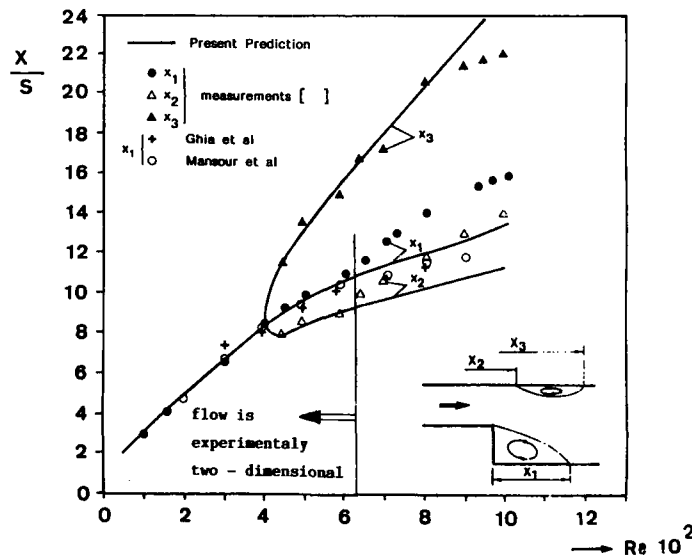


Figure 4 - Comparison of predicted and measured reattachment lengths using QUDS scheme.

The essential findings for the backward-facing step flow basically repeat themselves for the laminar flow over a fence, see [10]. Again, the QUDS scheme is able to capture the strong variation of the velocity profiles, as indicated in Figure 5. Also the length of the separation region attached to the fence is predicted reasonably well with the QUDS, see Figure 6. All the other schemes perform poorly.

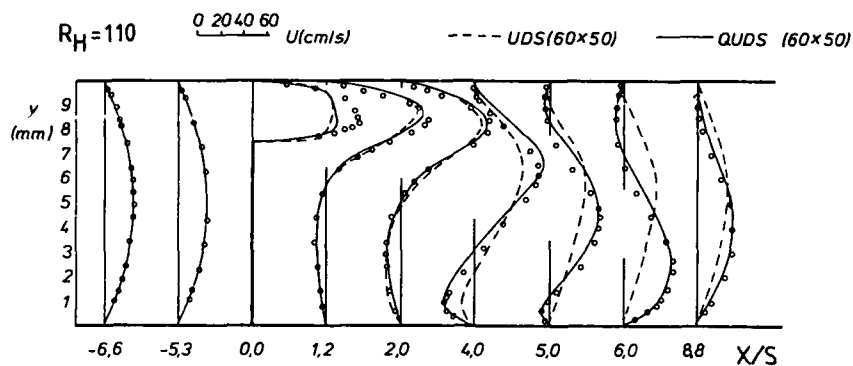


Figure 5 - U-velocity profiles measured and calculated with the UDS and QUDS schemes for flow over a fence $Re = 110$.

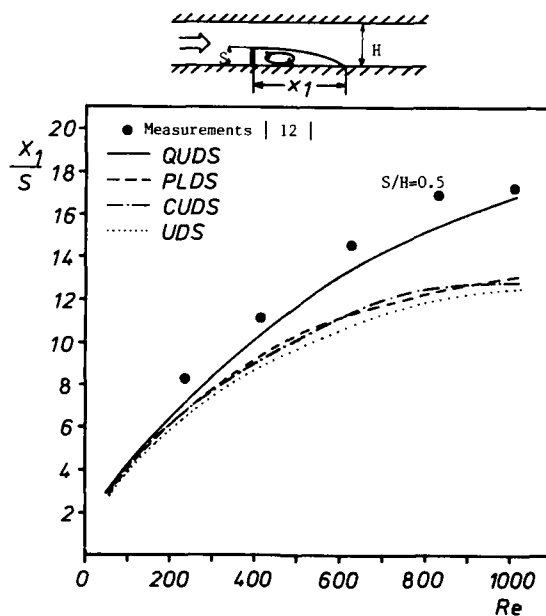


Figure 6 - Comparison of reattachment lengths predicted and measured function of Reynolds number.

UNSTEADY FLOWS

Good performance of the QUDS encouraged the application or the extension of the computer programme to unsteady flows using a fully implicit temporal discretization. The predictions were carried out for a geometry indicated in figure 7 which represents a sudden pipe expansion. The impulsively started flow was obtained by the piston displacement in the larger tube. The grid expands with piston displacement as proposed by [11]. When the piston moves to the right, fluid enters from the inlet tube into the cylinder and flow separation occurs at the sudden expansion and this was measured and predicted, see [12], [13].

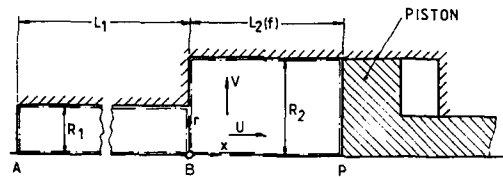


Figure 7 - Flow geometry of unsteady flow in a pipe expansion.

The test case considered corresponds to a maximum piston velocity of 11.9 mm/s, equivalent to a Reynolds number $Re = 2 U R_2 / \nu$ of 98, the initial clearance of the piston, i.e. the distance between the plane $x = 0$ and the piston surface, was 40 mm. Figure 8 shows a comparison of the predicted and measured velocity components at a time $t = 0.71$ s. Note, that the scale for the U-velocity is four

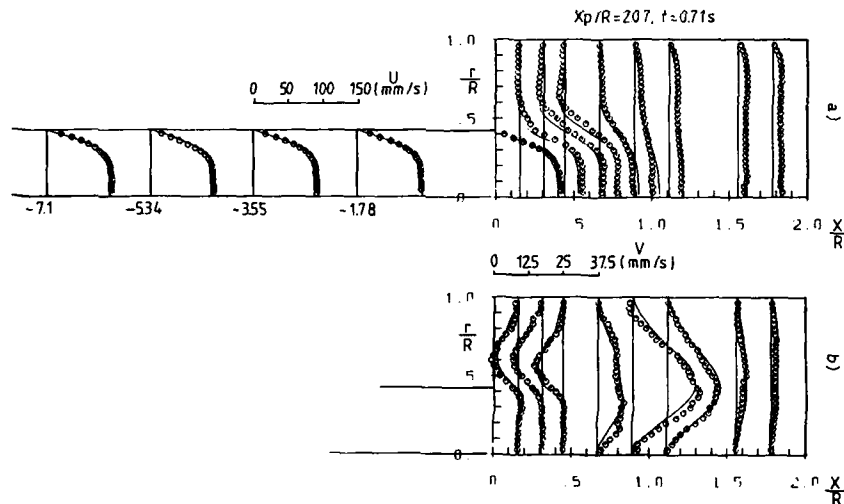


Figure 8 - Comparison of predicted and measured velocity profiles at $t = 0.71$ s, a) axial velocity; b) radial velocity.

times the one for the V-velocity. The agreement between the experimental axial velocities and the predictions in the inlet tube ($x < 0$) is very good, see Fig. 8a. This is due to the relatively small time-steps used in the calculations (0.005 s) leading to a high accuracy of the implicit temporal discretization,

but also, and more important, to the diminishing back-influence of the flow in the larger tube at the piston position ($L_2/R_2 = 2.07$) where the comparison is made. At earlier times or smaller piston displacements L_2 , the flow in the piston-tube exerted a noticeable influence on the velocity profile at the inlet section $x = 0$, and then the agreement between experiments and predictions was not as good as is shown in Fig. 8. In general it was found that the chosen inlet profiles influenced the prediction in the piston-tube substantially. For instance, in an earlier stage of the work, profiles corresponding to a fully developed flow and a constant velocity are employed. In both cases serious deviations from the experimental results were obtained. This sensitivity to the inlet conditions should be felt in more complex, practical applications also (e.g. the flow in reciprocating engines), and makes predictions for design purposes extremely difficult.

All the predictions shown so far were obtained with the quadratic upstream weighted discretization scheme above, the reason being the reduction of numerical diffusion. To emphasize this property of the discretization method comparative calculations were performed with the conventional hybrid-scheme. Fig. 9 shows streamlines calculated with the two schemes and compares them to

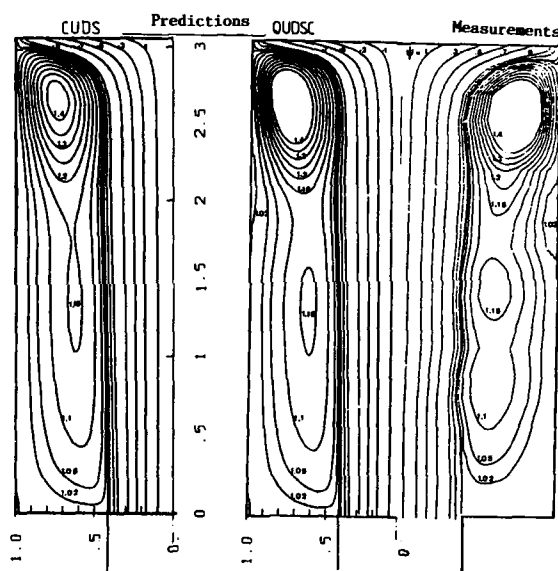


Figure 9 - Comparison of predicted and measured streamline at $t = 2.92$ s, a) hybrid-scheme; b) quadratic upstream scheme; c) data.

the measured ones. For the low Reynolds numbers considered here, the differences are not too dramatic. It can be seen, however, that the secondary flow on the cylinder wall is not resolved by the hybrid scheme. Also, inside the recirculation region, where very small velocities occur, qualitative differences between the two schemes arise. The only explanation for these discrepancies is the presence of false diffusion due to the use of first-class order upwind differencing in the hybrid-scheme. It causes a more pronounced spreading of the inlet jet close to the piston surface. As a consequence, negative velocities inside the vortex are smaller than predicted by quadratic upstream interpolation or measured. These small differences are responsible for the absence of the recirculation flow region on the cylinder wall.

Similar good agreement between experimental and numerical studies using the quadratic upstream scheme for convection discretization was obtained for the unsteady flow around a square obstacle. Figure 10 shows a summary of the results

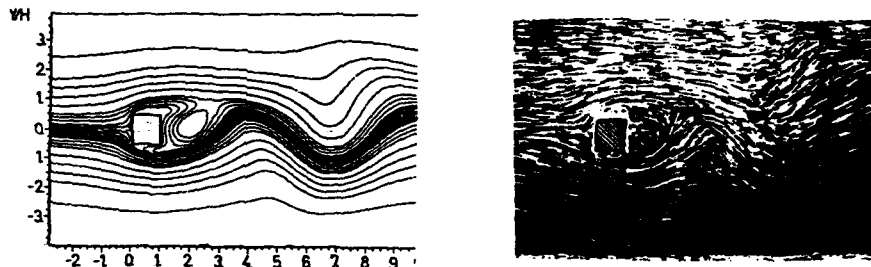


Figure 10 - Comparison of calculated instantaneous streamlines and flow visualization results for $Re = 500$.

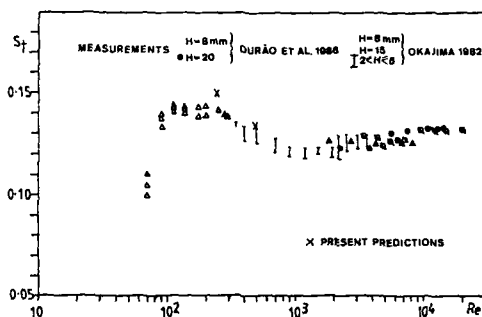


Figure 11 - Comparison of calculated Strouhal number with experimental data.

computed and visualized near wake flow for $Re = 500$. Figure 11 shows the comparisons of computed predominant frequency and experimental values in terms of Strouhal number for two sets of data, see [14] and [15]. The calculated values of the Strouhal number for flow Reynolds number, $Re = 250$ and $Re = 500$, display good agreement with the experiments.

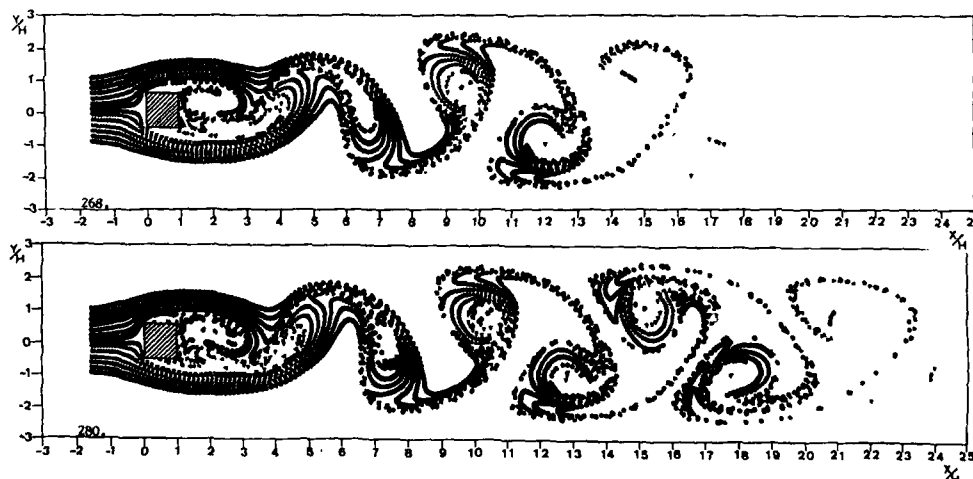


Figure 12 - Streakline plots of the flow around a square obstacle at $t = 268$ s and $t = 280$ s, $Re = 250$.

Figure 12 shows streakline plots, and they were obtained by the introduction of 14 passive markers upstream of the square obstacle. They were injected at every two time iterations. The massless particles provide an excellent means for visualizing the motion of the large coherent structures and good comparison was obtained with flow visualization.

Figure 13 shows a comparison between the results obtained with the quadratic upstream and central/upwind schemes for convection discretization. The figure clearly shows the effect of false diffusion induced by first order upwind. The results were obtained after 2400 time steps and the particles were injected every two time steps after 2000 iterations.

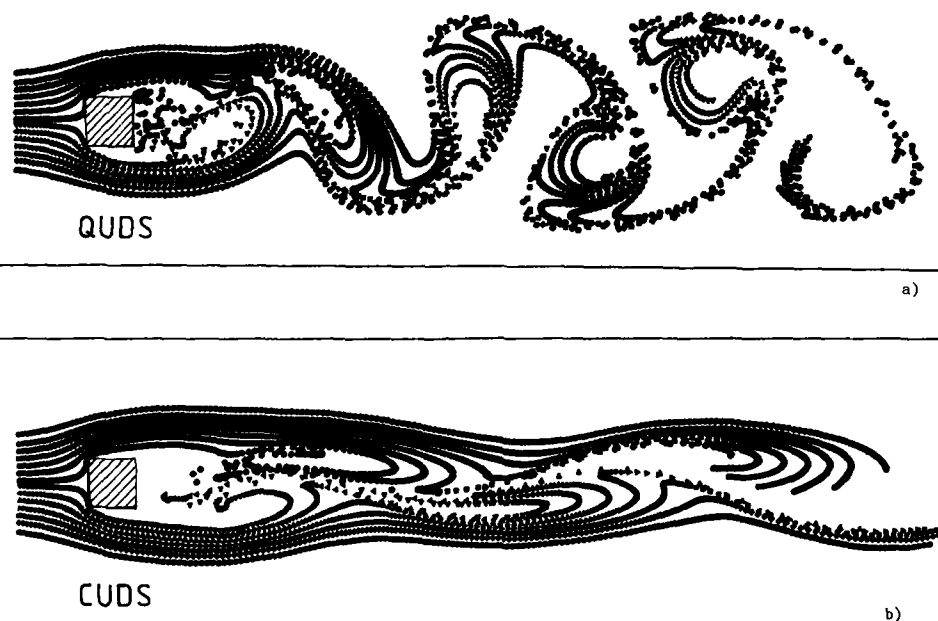


Figure 13 - Streakline plots of the flow around a square obstacle at $t = 192$ s, a) quadratic upstream; b) central/upwind. $Re=250$

CONCLUSIONS

Calculations of the steady laminar backward facing step for $50 \leq Re \leq 1000$ and of the flow over a fence for different Reynolds numbers showed that the quadratic upstream weighted scheme QUDS or the hybrid central/skew upwind scheme CSUDS are more accurate than the standard upwind scheme or the schemes that revert into it, i.e., the hybrid central/upwind or the hybrid power law/upwind schemes.

For unsteady recirculating flow calculations the use of first order implicit temporal discretization together with the third order accurate quadratic upstream scheme for spatial approximation showed to be a simple and accurate solution algorithm for unsteady recirculating flows as long as very small time steps are used to decrease errors induced by the first order temporal discretization. The unsteady flow at a sudden pipe expansion driven by the

impulsively start of a piston and the unsteady periodic flow around a square cylinder were well predicted with the present method.

The comparison of the predicted results with the experimental data shows that in general the quadratic upstream interpolation scheme yielded a much more reliable simulation of the flow pattern than the hybrid scheme and it is suggested to employ this scheme for turbulent analogous flows.

REFERENCES

- [1] SPALDING, D.B., A novel finite difference formulation for differential expressions involving the first and second derivatives. *Int. J. Num. Meth. Eng.*, Vol. 4, 1972, pp. 551-559.
- [2] PATANKAR, S.V., Numerical Heat Transfer and Fluid Flow. Hemisphere Publishing Corp., Washington, 1980.
- [3] RAITHEY, G.D., Skew upstream differencing schemes for problems involving fluid flow. *Comp. Meth. App. Mech. Eng.*, Vol. 9, 1976, pp. 153-164.
- [4] LEONARD, B.P., A stable and accurate convective modelling procedure based on quadratic upstream interpolation. *Comp. Meth. Appl. Mech. Eng.*, Vol. 19, 1979, pp. 59-98.
- [5] STONE, H.L., Iterative solution of implicit approximations of multidimensional partial differential equations. *SIAM J. Num. Anal.* Vol. 5, Nr. 3, 1968, pp. 530-558.
- [6] AZEVEDO, J.L.T., DURST, F., and PEREIRA, J.C.F. (1986). Comparison of strongly implicit procedures for the solution of the fluid flow equations in finite difference form. To be published in *J. Mathematical Modelling*.
- [7] ARMALY, B.F., DURST, F., PEREIRA, J.C.F. and SCHONUNG, B., Experimental and theoretical investigations of backward facing step flow. *J. Fluid Mech.*, Vol. 127, 1983, pp. 473-496.
- [8] MANSOUR, N.N., KIM, J. and MOIN, P., Computation of turbulent flows over a backward facing step. *Proc. of Turbulent Shear Flows IV*, 1983, Karlsruhe.
- [9] GHIA, N.N., OSSWALD, G.A. and GHIA, U., A direct method for the solution of unsteady two-dimensional incompressible Navier-Stokes equations. *Aerodynamic Flows*, Jan. 1983.
- [10] DURST, F., FOUNTI, M., GACKSTATTER, R., PEREIRA, J.C.F. and TROPEA, C., The wall reattaching flow over two-dimensional obstacles. *2nd Symp. on Appl. of Laser Anem. to Fluid Mech.*, Lisbon, Portugal 1984a.
- [11] GOSMAN, A.D. and WATKINS, A.P., A computer prediction method for turbulent flow and heat transfer in piston/cylinder assemblies. *Proc. Symp. on Turbulent Shear Flows I*, Pennsylvania State University, 1977, p. 523.
- [12] PEREIRA, J.C.F., Experimentelle und numerische Untersuchungen stationaerer und instationaerer laminarer Stroemungen mit Abloesung. *Dissertation Universitat Erlangen Nuernberg*, 1985.
- [13] DURST, F., PEREIRA, J.C.F. and SCHEURER, G., Calculations and experimental investigations of the laminar unsteady flow in a pipe expansion. In Finite Approximations in Fluid Mechanics, pp. 43-56, ed. Ernst Heinrich Hirschel, Friedr. Vieweg & Sohn, 1986.
- [14] DURAO, D.F.G., HEITOR, M.V. AND PEREIRA, J.C.F. The flow around a square obstacle. *AGARD - Advanced Instrumentation for Aero Engine Components*, Proc. N° 399, 1986.
- [15] OKAJIMA, A. Strouhal numbers of rectangular cylinders, *J. Fluid Mech.* 123, pp 379-398, 1982.

THE DESIGN OF THE GARTEUR LOW ASPECT-RATIO WING FOR USE IN THE VALIDATION OF
SHEAR LAYER AND OVERALL FLOW PREDICTION METHODS

by

M. C. P. Firmin
M. A. McDonald
Royal Aircraft Establishment
Farnborough
Hampshire, GU14 6TD
England

SUMMARY

A low aspect-ratio wing has been designed, for use in the critical analysis of computational methods for three-dimensional shear layers, following the guidelines agreed by GARTEUR Action Group AD(AG07). The aim of the paper is to give details of the design processes used and to indicate the flow conditions which will be explored in the detailed shear-layer tests to be made in the NLR LST (3.0 x 2.25 m) and ONERA (1.8 x 1.4 m) low-speed wind tunnels, as part of the GARTEUR programme. Calculations have been made, using a selection of boundary layer methods which indicate that the design should provide very challenging tests for methods. Pilot model tests, made at NLR, have suggested that the wing has been designed successfully and these have encouraged the Action Group to proceed with the main test programme.

NOTATION

c	local streamwise chord
C _f	skin friction coefficient based on local flow conditions
C _L	lift coefficient for streamwise section
C _p	surface pressure coefficient based on freestream conditions
H	δ ₁ /θ ₁₁ , streamwise shape factor for boundary layer
Re	Reynolds number based on geometric mean chord
u	component of velocity within the boundary layer measured in the direction of local external flow
x	local streamwise distance
z	distance normal to wing surface
α	angle of incidence, measured with respect to local chord at η = 0
β (BETA)	angle of twist within the boundary layer, ie angular change in flow direction between the external streamline and the limiting streamline at the surface
δ	boundary layer thickness
δ ₁	streamwise displacement thickness = $\frac{1}{\rho_e u_e} \int_0^\delta (\rho_e u_e - \rho u) dz$
η (ETA)	spanwise distance as a fraction of local semi-span
θ ₁₁ (THETA)	streamwise momentum thickness = $\frac{1}{\rho_e u_e^2} \int_0^\delta \rho u (u_e - u) dz$
λ _{TE}	angle of sweep of trailing edge
ρ	density
Suffixes, etc	
e	value at the edge of boundary layer
*	location of section of maximum twist and camber.

1 INTRODUCTION

Progress in computational methods for the calculation of flows over aerofoils and wings has been rapid during the last decade and in consequence the need for reliable experimental evidence, suitable for the validation and improvement of methods, has become acute. Up to the present the most advanced methods being envisaged for transonic flows at high subsonic speeds are ones involving either solutions of the Reynolds-averaged Navier-Stokes equations or the Euler equations coupled with an advanced method for calculating the flow in the shear layers. It is likely that these classes of methods will eventually become the main computational tools used within the aircraft industry for detailed design purposes. Generally the limitations on the accuracy of predicting the flow come from two main causes, first, the numerical algorithms for solving the inviscid region of the flow, particularly for complex geometries, and second, the turbulent shear layers, the modelling of which is to some extent empirical. Progress in the understanding of turbulence has been slow and the prospects for the development of a universal model are not good; hence for the foreseeable future, it seems inevitable that the use of multifarious turbulence models, or alternatively ones which change between different regions of the flow, has to be accepted. Thus experimental data of high quality are needed for the flows of most interest; in particular, for wing flows, information is required on the turbulent properties of three-dimensional boundary layers and wakes. Although a large number of wind-tunnel experiments of three-dimensional turbulent boundary layers have been undertaken, it appears that only a small number are close to practical wing flows to be of real interest¹⁻⁴ in the development of 'engineering' methods.

In 1983 a meeting was held in Stockholm to discuss possible collaboration on experiments concerned with three-dimensional turbulent shear flows⁵. Two experiments were suggested, a fundamental one with the aim of improving the understanding of turbulent flows, and another on a wing flow to provide data of more immediate practical interest. The proposed wing-flow experiment was to be at low speed because of the difficulties in making turbulence measurements in flows at high subsonic speeds. It was thought that the main features of practical interest could be simulated and the work envisaged complemented that already being undertaken at RAE⁶ on a low aspect-ratio wing at high subsonic speeds, where mean-flow measurements of the shear layers are being made. It was proposed that the experiment be conducted under the auspices of GARTEUR (Group for Aeronautical Research and Technology in Europe). For this investigation Sweden (FFA) was to be included as an associate member in addition to France, Federal Republic of Germany, The Netherlands and the United Kingdom. A GARTEUR Exploratory Group was set up to define an experimental programme to be performed on a shared basis between the member countries. The subsequent Action Group, which is responsible for the conduct of the experiment, started work in the middle of 1986, with the RAE being given the responsibility for the design of the wing, following the guidelines agreed by the members. There are to be three models of the wing, two full models to be tested at NLR and ONERA, and a 'pilot' model. The models are all being manufactured by FFA. All the participating countries, represented by DFVLR, FFA, NLR, ONERA and RAE will be involved in the measurements. It is intended that the work should be completed within about four years.

The aim of this paper is to give details of the wing design, including the methods used in the design process, and to indicate the flow conditions which should be encountered in the detailed measurements of the shear layers. The wing design is arranged so that detailed results can be obtained for the boundary layer and wake development in conditions of:

- (a) extreme three-dimensionality within the boundary layer for at least part of the flow, and
- (b) incipient separation near to the trailing edge of the upper surface.

The pilot model has already been made by FFA and tested in a small NLR tunnel. These pilot tests indicate that the flow required of the design has been achieved.

2 DESIGN REQUIREMENTS

The requirements for a low aspect-ratio wing to be tested at low speeds in the NLR (3.0×2.25 m) and ONERA (1.8×1.4 m) wind tunnels were laid down in broad terms, in the discussions on the overall experiment in 1985 by the GARTEUR Exploratory Group.

It was decided that the test set-up would consist of a swept-wing half-model attached to a test section wall of a low-speed wind tunnel. Ideally, the wing was to have an aspect ratio for the half wing of 1.5, taper ratio of 0.5, a quarter-chord sweep angle of 30 degrees, with the wing half-span of 0.8b, where b is the greater of the two dimensions of the tunnel cross-section. Setting the wing span parallel to the wider walls of the tunnel ensures a larger wing chord and correspondingly thicker boundary layers. Geometric similarity within the working sections has been achieved as far as possible by having separate models for each tunnel, although there remain some dissimilarities because the working sections do not scale exactly, and other minor geometrical differences may result in different scaling of the boundary layer flow on the tunnel walls. The requirement on the wing span results in a model that is much larger than ones normally tested in low-speed tunnels, and makes it essential to use a method for the design which adequately represents the effect of the walls of the working section. The Reynolds number based on the geometric mean wing chord for the design is to be 3×10^6 , which is achievable in both the NLR and ONERA wind tunnels. It was also planned to perform tests using the pilot model in a smaller tunnel at NLR at a slightly lower Reynolds number, but maintaining geometric similarity with the set-up for the main tests. The aim of the pilot model tests is to check on the flow achieved but no attempt is to be made to measure any shear layers.

The Action Group also decided that in addition to the above geometric requirements, the flow on the swept wing should aim at satisfying the following requirements:

- (a) The pressure distribution on the wing surfaces should be similar to that on a modern transonic wing with rear loading.
- (b) The adverse pressure gradients on the rear part of the wing upper surface should lead to a three-dimensional separation region over part of the span (Fig 1).
- (c) On the wing lower surface the flow should remain attached but be close to separation upstream of the trailing edge and prior to the favourable pressure gradients associated with rear loading.
- (d) Significant spanwise variations in the viscous flow should occur on both the upper and lower surfaces of the wing.

If possible, transition of the boundary layer was to be caused by leading-edge contamination using a 'trip' on the attachment line near the wing root, otherwise the boundary layer was to be tripped at about 5% chord on both upper and lower surfaces of the wing.

The authors were given the responsibility for the design within the above requirements, as a contribution to the collective GARTEUR experiments.

3 DESIGN PROCESS

The design of a wing of moderate sweep, with separated boundary-layer flow over part of the upper surface close to the trailing edge is an unusual requirement and not one normally undertaken by wing designers. It is also unusual to test such a wing in conditions where the wind-tunnel walls are only about half a root chord or less away from the wing surfaces, and the wing tip is also quite close to the tunnel walls (see Fig 1).

Several methods for the design of a wing in low speed flow are available at RAE, but it was considered to be essential for the method used to account adequately both for the viscous effects and the close proximity of the wind-tunnel walls. For these requirements the BAE (SPARV) panel method⁷⁻⁹ was ideal, although it needed further development in the representation and storage of the boundary conditions for the viscous effects, and in common with all other available codes it cannot yet be used for separated flow on wings.

The steps undertaken in the design process are as follows:

- (a) Accept the planform and arrangement of the wing in the wind tunnel, as specified in section 2.
- (b) Decide on a basic aerofoil section which can be modified to give the required flow.
- (c) Decide on the spanwise form of the changes to the thickness, camber and wing twist to provide sufficient spanwise variation in the flow.
- (d) Make an estimate of the boundary-layer growth and therefore the displacement effect (ie transpiration velocity distribution) based on some target flow.
- (e) Run the BAE (SPARV) panel program in order to obtain the surface pressure distribution for 'inviscid' flow, and for a 'first' calculation of the boundary layers. Here the calculation for 'inviscid' flow will include fixed boundary conditions which allow for some account to be made of the viscous effects based on the target flow. The 'first' calculation of the boundary layers gives an estimate of the boundary-layer growth based on the 'inviscid' flow pressure distribution.
- (f) Modify the basic thickness distribution or the spanwise changes in thickness, camber and wing twist in order to achieve more closely the required flow characteristics. For this step simple sweep relationships are used and an aerofoil design code used for modification to the thickness and camber distribution of the basic aerofoil section.
- (g) Repeat steps (b) to (f) as necessary, then use the BAE (SPARV) panel program in a modified form such that the wing surface and wake boundary conditions are revised using under-relaxation from the initial chosen starting conditions. By this means the calculated pressure distribution and the boundary conditions will become more consistent. This step will be successful only if the pressure distribution generated results in calculated boundary layers for fully attached flow on both wing surfaces, and adequate under-relaxation is used in the determination of the boundary conditions.
- (h) Once steps (b) to (f) result in a converged solution, with the final target flow achieved, then an increase in wing incidence may be used in an attempt to provoke the required flow separation. The results from this scheme can only be checked experimentally because the existing calculation method has not yet been extended successfully to admit even small regions of separated flow. Alternatively, a boundary-layer method may be used in an inverse mode to determine a surface pressure distribution which is compatible with the required separated flow. The BAE (SPARV) method may then be used in a design mode to determine the wing thickness distribution that is compatible with both the boundary-layer flow and the surface pressure distribution. In order for this scheme to be successful, the required pressure distribution has to be compatible with an actual wing flow, so some iteration is necessary, though convergence is not guaranteed. As will be shown later an increase in incidence was used to generate the required flow, because use of the BAE (SPARV) design method resulted in fairly rapid changes in the surface curvature in the region of separation, a feature which was likely to make some of the shear layer measurements more difficult to perform.

3.1 Programs used

3.1.1 Viscous panel method^{7,8}

This is a surface source and vorticity panel method developed at BAE, for obtaining the potential flow over arbitrary geometries. It is known by the acronym SPARV which stands for Source Patch And Ring Vortex. Unlike a number of other panel methods it does not require a specification of the vorticity distribution in advance as it obtains this as part of the solution for wing-like or lifting surface flows. The method uses constant source panels and constant doublet panels (vortex rings) placed together on the surface. The strengths of the source and doublet panels are determined by making them to be equal on the upper and lower surfaces of the wing. An implicit Kutta condition is applied by making the bound vorticity zero along the trailing edge. This is achieved by imposing a horseshoe vortex at the trailing edge with the same strength as that for the panel ahead of it. For our application, where a wing is mounted in a wind tunnel, the boundary conditions at the tunnel walls are satisfied by a distribution of source panels alone, and viscous effects on these boundaries are neglected. For the wing flow the boundary layers are accounted for by modifying the boundary conditions to represent displacement effects by transpiration at the wing surface and along the wake.

The development of the shear layers is determined using an entrainment method due to Cross⁹. This is an integral method based on a velocity profile family which uses a modified form of the Cole's law of the wall and wake for both the streamwise and crosswise components of the boundary-layer flow. The method permits a distortion of the shape of the 'wake' function of the standard Cole's profile to allow for effects of strong departures from equilibrium¹⁰. No allowance is made for the normal pressure gradients through either the boundary layer or wake.

The panel method was modified specially for this work so that it could be used in a design mode, while maintaining a fixed transpiration boundary condition over the wing and wake surfaces to account for the shear layer displacement effects. Details of the basic design mode are given by Sinclair¹¹. The essence of the method is that for 'thick wing' type of components the nonlinear effects of geometry change in the standard panel method are replaced by linear thin wing theory applied to the expected small differences between the calculated and required pressure distribution. The output is the required change to the thickness and camber distribution. A normal direct calculation with fixed boundary conditions is executed to determine the final pressure distribution. The method is based on the work of Fray and Slooff¹² at NLR.

3.1.2 Aerofoil method¹³

This is a panel method, developed at RAE by Fiddes and Hogan, for the design of aerofoils starting from a guessed shape and a required pressure distribution. It is an improved version of the method described by Chen¹⁴. The method uses flat panels each carrying a linearly-varying vorticity distribution and placed between the ordinates defining the aerofoil shape. The contribution of each panel to the stream function is calculated, and the condition that the aerofoil surface be a streamline is applied at the ends of the panels. This determines the vorticity distribution on the panels and hence the achieved pressure distribution. The desired and achieved pressure distributions are then compared at the same points as where the aerofoil is defined, and the shape modified accordingly. Chen uses constant vorticity panels, and is thus constrained to compare desired and achieved pressures at the mid-points of panels. This leads to an awkward interpolation process between panel edges and mid-points during the design procedure which can lead to an unstable iteration process. This is avoided in the RAE method.

4 CALCULATIONS

4.1 Development of wing

Initially a NACA 632015 aerofoil, modified to have a wedge-shaped region near the trailing edge, was chosen as the basic streamwise section for the wing, together with spanwise variation of additional thickness, incidence and camber taking the form

$$\Delta Z_n = \frac{1}{2} \Delta Z_{n*} \left[1 + \sin \left\{ \frac{\pi}{2} \left(\frac{2n}{n*} - 1 \right) \right\} \right], \quad (1)$$

so that the maximum changes from the basic section occur at $n = n^*$, and the section remains unchanged at the root. The basic streamwise section is symmetrical, has a 15% thickness-to-chord ratio with the maximum thickness at about 35% chord, and a roof-top pressure distribution on the upper surface for a lift coefficient of about 0.2. Attempts were made to obtain the required flow by increasing the wing thickness and camber, but keeping the combined camber and incidence small over the front of the wing. The aim was to keep the peak velocities fairly low in the region close to the leading edge, so that changes in incidence of the wing could be used to modify the flow in setting up the experimental conditions without any danger of large suction peaks, or laminar separation occurring near to the leading edge. For these calculations a rather arbitrary limit of 20% was placed upon the maximum streamwise thickness-to-chord ratio and n^* was set equal to 0.6 (i.e. 60% of the span of the half wing).

During the first series of calculations for the design it became clear that the restrictions imposed were too severe and the following conclusions were reached:

- (a) Suitable flows could be generated for the wing lower surface with adequate rear loading.
- (b) It did not appear to be possible to obtain flows for the upper surface which approached separation with distance along the chord*, slowly enough to achieve an exacting test case for the shear-layer development.
- (c) As could be expected, it was not possible to generate shear-layer flows typical of transonic flow conditions behind shock waves by developing the required pressure gradients without excessively large and undesirable changes in the surface curvature occurring.

For the second series of calculations the condition on camber and incidence near to the leading edge was relaxed but the limit on the maximum streamwise thickness-to-chord ratio for the section was maintained. No further attempt was made to generate locally strong adverse pressure gradients, because excessive surface curvature in the measurement area would cause difficulties in the experimental work.

These new calculations suggested that:

- (i) Suitable flows could now be generated for the upper surface of the wing by allowing the peak suction to increase towards the nose, without generating excessively large velocity gradients near the attachment line.
- (ii) The rather arbitrary limit on the streamwise thickness-to-chord ratio for the sections rendered it impossible to generate a suitable flow for both the upper and lower surfaces at one incidence, while maintaining a reasonable wing thickness in the region of the rear loading.

These two sets of initial calculations indicated that it should be possible to generate the required flow using the spanwise form for the changes in camber and incidence used already, provided the limit on maximum thickness-to-chord ratio was relaxed. It would also be desirable to have a large leading edge radius with the maximum thickness well forward on the wing. The results also suggested that a major change was required to the basic streamwise section.

The third stage in the design process was to choose a desirable inviscid pressure distribution for the section at $n = n^*$, to convert this to the equivalent for two-dimensional flow using a simple sweep relationship, and then to run the RAE aerofoil method¹³ to obtain the aerofoil shape. Here the upper surface pressure distribution was chosen from the second series together with the lower surface pressure distribution from the first series at suitable conditions as the basis; in the knowledge that these were likely to give the required boundary-layer flows on both surfaces of the wing. The resulting aerofoil, after making modifications to get a reasonably smooth shape is given in Fig 2a. The detailed shape in the region of the stagnation point was not acceptable initially, and the difficulties in this region were

* is either the skin friction falls to zero or the surface flow direction becomes parallel to the wing generator.

avoided by specifying the sparse distribution of points as shown. The final ordinates used for the basic section (see Fig 2b) were then obtained by interpolation using a cubic spline fit. The aerofoil shape was converted to a form suitable for the wing using the simple sweep relationship. The full section was used at $\eta = \eta^* = 0.6$, but a symmetrical section of the same thickness form was used for the basic section at the root (ie $\eta = 0.0$). The changes in camber and incidence across the span are given by equation (1).

The third stage in the design was repeated several times until a satisfactory flow was generated using the scheme described in section 3. The aerofoil section used in the final design was much thicker than originally envisaged, being of the order of 30% for the maximum thickness-to-chord ratio. As will be seen later this results in a wing with a thickness-to-chord ratio of 26% for the streamwise section.

4.2 Final design for incipient separation

Using the scheme detailed in section 3, and the development of the wing outlined in section 4.1, it was possible to generate a wing design with most of the required aerodynamic characteristics. The flow will be fully attached to the wing at the design condition but with incipient separation close to the trailing edge on the outer part of the upper surface. Some final improvements were made to the design of the lower surface, in order to increase the rear loading, without altering the upper surface shape. These relatively small changes were applied using equation (1), but this resulted in the streamwise sections at different parts of the span not having exactly the same thickness distribution. A selection of the chordwise pressure distributions are given in Fig 3, it is noticeable that the loading on the wing increases from the root to a maximum in the region of $\eta = \eta^* = 0.6$, as might be expected; detailed predictions for the lift coefficient are given in Table 1.

In order to obtain a solution close to incipient separation a large number of iterations were performed using a very low relaxation factor ($\omega = 0.075$) in the coupling between the calculated results for the transpiration velocities from the boundary layer and wake method, and the boundary conditions for the panel method. The overall results appear to be well converged over most of the upper and lower surfaces of the wing except in a small region close to the trailing edge on the outer part of the upper surface, where the flow is close to separation and the pressure level changes gradually as the iterations proceed. The cross-over in the pressures near to the trailing edge at $\eta = 0.792$ is symptomatic of the problem. The lack of convergence is possibly a sign of reaching the limit of successful application of the direct mode of coupling, although it could also be caused by known inadequacies in the flow modelling in the region of the trailing edge. The pressure distributions appear to be similar for the different streamwise sections, except for the significant increase in loading over the middle of the span mentioned earlier. In spite of this, substantial changes in camber and twist do exist across the span as indicated by the three streamwise sections of the wing shown in Fig 4, and the calculated boundary-layer characteristics do suggest that the flow should be highly three-dimensional in form.

In Fig 5a the streamwise shape factors (H) are given for the upper surface boundary layers. The values calculated for the region of the root of the wing, which were kept reasonably low by selecting a symmetrical section at zero incidence in that region, do not exceed 1.65, thus minimising the risk of the boundary layers in the junction between the tunnel wall and the wing root separating because of adverse pressure gradients over the rear of the wing. Other potential problems with the junction flow were left to be overcome in the pilot model tests because no account has been taken of the tunnel-wall boundary-layer flow. Further out on the wing, eg at mid semi-span, the shape factor reaches 2.15 by the trailing edge, which past experience with first order boundary layer methods suggests is close to incipient separation for two-dimensional flow over aerofoils. Outboard of this the values are even higher close to the trailing edge reaching values as high as 2.4, at 80% of the semi-span. The values near the trailing edge outboard of this station appear to be increasingly affected by what is likely to be inadequate representation of the boundary-layer flow near to the wing tip. For the boundary-layer calculations the Reynolds number based on the mean chord is 3×10^6 and transition is fixed at 3% chord on both surfaces, although in practice it is possible that the transition will occur at the attachment line. If spanwise turbulent contamination of the laminar boundary layer does occur at the attachment line then it would be expected that the flow will be even more likely to separate at the design condition.

For the lower surface (see Fig 5b) the boundary layers are, like the upper surface, well away from possible separation at the root of the wing. The effect of the rear loading is noticeable for this surface with peak values for the shape factors occurring at about 70% chord, where the adverse pressure gradients are relaxing in a chordwise direction before becoming favourable aft of about 80% of the local chord. A peak value of H of 1.8 is reached at $\eta = \eta^* = 0.6$ for the streamwise shape factor, a value high enough to ensure an interesting lower surface flow. This peak value appears to be well away from possible incipient separation, but during the development of the wing it was found that an attempt to increase this value to 1.9 failed because the boundary layer did not recover to lower values further outboard, as they do for the results shown here, suggesting that the flow may be in a sensitive state. Towards the tip, the flow is basically outboard so the problems encountered for the upper surface do not appear to exist. No attempt was made to improve the modelling near the tip, other than to exclude an inflow in the boundary layer from the tip. It was not possible to increase the total number of panels available with the version of the program used.

The calculated magnitude of local skin friction coefficient ($\times 1000$) is given for the upper and lower surface in Fig 6a&b. Contours of equal skin friction coefficient are given for

$$3.9 > C_f \times 1000 > 0.0$$

These figures show trends very similar to those deduced from the results for the shape factors. The additional point that emerges is that the skin friction coefficient does not ever get lower than 0.0006 even towards the trailing edge on the upper surface. This is probably because large angles of twist are generated within the boundary layers and consequently the displacement thickness does not grow as rapidly as in two dimensions, and the skin friction coefficient remains positive.

A calculation has been undertaken, using the skin friction coefficient and the direction of the flow at the surface of the wing, to obtain the streamlines in the lower part of the boundary layers. The results of these calculations are given in Fig 7a&b. For the upper surface, Fig 7a, away from the leading-edge region, the streamlines tend to run towards the root on the forward part of the wing, because the inviscid flow has been accelerated in a direction normal to the wing generators and there is very little twist within the boundary layer.

Further aft the streamlines become dominated by the boundary-layer flow and they tend to turn towards the tip. The turning increases in severity along the chord, with divergence of the streamlines over the rear of the inboard part of the wing, while over the outer part there is some convergence with rapid turning of the streamlines close to the trailing edge where there is either incipient separation and/or a breakdown of the boundary-layer calculation. For the lower surface, Fig 7b, the streamlines are rather as might be expected, significant twist being generated in the boundary layers in the region of adverse pressure gradients with some recovery when the boundary layers are subjected to favourable pressure gradients. The severity of the boundary-layer twist increases to a maximum where the section has maximum rear loading and camber. The influence of the tip is noticeable for both upper and lower surfaces. On the upper surface it tends to cause the flow to turn streamwise with a consequential increase in boundary layer thickness, whereas on the lower surface the reverse is true. The calculated surface streamlines suggest that the flow should prove to be a testing one for the calculation methods, if these conditions are satisfactorily reproduced in the experimental investigation.

4.3 Experimental verification

Since the wing has been developed for the validation of computational methods, with special requirements placed on the boundary-layer flow, it is not surprising that the shape of the wing surface is rather unconventional. The requirement that the boundary layers, under the test conditions in a low-speed tunnel, should be representative of those likely to be found on both the upper and lower surfaces of a wing at the design condition for high subsonic speed has resulted, as stated earlier, in an exceptionally thick wing with a thickness to chord ratio of about 0.26. In addition the risk of complicated 'root' and 'tip' flows dominating the boundary layers over the main surfaces of the wing has been minimised by reducing the loading in the region of the intersection of the wing with the wind-tunnel wall, and at the wing tip; thus resulting in the maximum angle of wing twist and the maximum camber of the streamwise sections occurring at mid semi-span. The pilot model was manufactured at FFA, and a photograph, taken on completion, is shown in Fig 8*. It shows the upper surface viewed from outboard and behind the trailing edge of the wing. The features built into the design by the requirements on the flow are clearly visible from this angle of view although the wing does appear to be grossly foreshortened.

The pilot model has been tested in a small NLR wind tunnel, and Fig 9** shows the wing mounted in the working section. The measurements made have been limited to surface pressures at two chordwise stations and surface oil flows. The evidence provided by NLR, had indicated that the design has been successful in providing a wing which has extreme three-dimensionality within the boundary layer for at least part of the flow, and incipient separation close to the trailing edge on the outer part of the upper surface. The boundary-layer flow is found to be sensitive to the form of transition fixing used in the region of the leading edge. For these tests, at a Reynolds number of 2.5×10^6 based on the geometric mean chord, laminar flow exists at the attachment line or relaminarization occurs in the favourable pressure gradient near the nose. The boundary layer was tripped with a sparse distribution of carborundum particles, at 8% of the mean chord from the flow attachment line on the upper side, but measured round the surface of the streamwise section. The corresponding position for the lower surface is 6%. These positions, measured in the chordwise direction are between the nose and 4% local chord for the upper surface and between 1% and 4% local chord on the lower surface, depending on the spanwise location of the section. With this transition fixing, which is nearly always further forward than for the calculations, the surface oil flow suggests that the boundary layer is remarkably similar to that predicted in the design calculations. Unfortunately, the oil-flow studies indicated that the wing tip had too strong an influence on the way separation develops over the rear of the upper surface on the outer part of the wing as the angle of incidence is increased. To reduce the effect of the tip on the boundary-layer flow in the region of 90% semi-span, it was decided to modify the tip by changing its spanwise section shape from a circular to a 2:1 elliptic form, so increasing the semi-span. The larger changes in span occur close to the maximum thickness, but the trailing-edge span remains almost unchanged. This modification made only a small difference to the flow at the design condition, but did reduce the tendency for the separated region to be dominated by the tip flow, and therefore will be used for the main models. In order to avoid the formation of a small scarf vortex at the wing root, formed because of the intersection of the wing with the boundary layer on the wall of the wind tunnel, a small fairing has been designed, which will also be incorporated on the main models.

In Fig 10**, photographs are presented showing the surface oil flow at the design incidence. If the oil flow streak lines are compared with the surface flow predicted for the design (Fig 7) it does appear that the three-dimensionality within the boundary layers is underestimated by the calculations for both the upper and lower surfaces. This is unlikely to be explained fully by the pilot model tests being done at a slightly lower Reynolds number, with boundary-layer transition not exactly the same as assumed for the design. For the main tests in the larger wind tunnels, detailed shear layer flow measurements are to be made at the design condition, or at an incidence which gives a surface flow at least as severe as that observed during the tests on the pilot model. The experimental evidence suggests that the flow on the lower surface of the wing changes only slowly with incidence, so it will be possible to achieve a flow closely similar to the one required by making a small alteration to the angle of incidence of the wing.

* published by courtesy of FFA

** published by courtesy of NLR

5 BOUNDARY LAYER PREDICTIONS

One of the main aims of the design has been to provide a wing that generates a flow field which will prove to be an important test case for computational methods. Previous evidence from other wing flow experiments is very sparse and other more general comparisons made between results from calculation methods for turbulent boundary layers¹⁵⁻¹⁸ suggest that significant differences occur between predictions of the flow development as the shear layers approach separation. The boundary-layer method used for the design was, as mentioned earlier, an entrainment integral method due to Cross⁹. Several other calculations have been performed using the design pressure distribution as the basis for the comparison in order to check if the flow at the design condition is sufficiently demanding for the calculation methods. These methods are split into two types, those involving solutions of equations describing the development of boundary layer integral quantities^{10,19,20} and those involving solutions of the mean-flow boundary layer differential equations^{21,22}. A sample of the results obtained for both the upper and lower surfaces of the wing are given in Fig 11, where they are compared with the original predictions from the BAE (SPARV) program. The integral methods are all of the entrainment type and the calculations were performed for the basic methods. The RAE lag-entrainment* method uses an additional equation to determine the entrainment but the same velocity profile family as for the RAE Thompson entrainment method. The relationship for the streamwise shape factor is given by Lock as equation (105) in Ref 10. The ONERA-CERT method is different from the others in both the entrainment relationship and the profile family. In this method it is also arranged that the turbulent shear stress vector is not necessarily aligned with the direction of the local velocity gradient. The differences between the methods make quite large changes to the predicted results. The RAE lag-entrainment method shows the least tendency to predict flow separation either in terms of the shape factor (H) or through the twist generated within the boundary layer (δ). Analysis of the surface oil flows from the pilot model test (Fig 10) would suggest that all the integral methods generally underestimate the twist within the boundary. However, in none of the methods is account taken of 'secondary' effects which would tend to increase H and consequently δ . It has been found that when these effects are included in the lag-entrainment method, accurate predictions are obtained for the flow over two-dimensional aerofoils²⁴. The predictions using differential boundary layer methods show an even larger spread between the results, although all the calculations are limited to ones with turbulence models of the eddy viscosity type. The NLR and ARA methods, using a 'Cebeci-Smith' type of modelling give results similar in some respects to those obtained from the RAE lag-entrainment method, apparently underestimating the twist within the three-dimensional boundary layers. The NLR method uses a turbulence model due to Michel²⁵, whereas the ARA method uses the standard turbulence model of Cebeci-Smith²⁶. The ARA method, with a modified 'Cebeci-Smith' turbulence model, was developed by Johnston²¹ to improve comparisons with the experiment of van den Berg and Elsenaar²⁷ in the region of high crossflow but with no change to the standard form for two-dimensional flows. This modification appears to improve the predictions considerably for this case. It is based on an empirical observation that the outer eddy viscosity is decreased by the three-dimensionality of the flow. Other calculations have been made at NLR using their method, which also confirm the predictions as being very sensitive to the assumptions made about the magnitude of the mixing length. Attempts to obtain results from the methods using other turbulence models are not yet available; even so, the evidence presented suggests that the flow to be studied is likely to be an exacting and interesting test case for computational methods. Furthermore, they indicate that it may be unnecessary to increase the wing incidence in the main tests to provide a fully separated flow, as suggested originally, in order to provide a severe test for the methods, since the conditions for incipient separation may be sufficiently difficult and challenging.

6 DESIGN FOR SEPARATED FLOW

The original plan, as detailed in section 3, was to accept either a design for incipient separation and then to induce the required flow by a small increase in incidence, or to attempt to modify the design in a limited region by the use of a boundary-layer method in an inverse mode and to determine the wing shape by use of the BAE (SPARV) program in a design mode. The Action Group decided to adopt the former approach because this resulted in a much flatter wing surface in the region where separation was likely to occur.

Prior to this an attempt to obtain a design for separated flow was made as follows:

- (a) Data from work on the NACA 4412 aerofoil²⁸ was analysed to determine the form of the shape factor versus chordwise position (x/c) which has resulted in a plateau in the surface pressure distribution for the separated region of a two-dimensional flow. The aerofoil has, in the region of separation, a reasonably flat but convex surface, typical of many wings. The information used is given in Fig 12, where a hyperbola has been fitted to the data.
- (b) A correlation is formed from the boundary layer data extracted from the results for the present design for the variation of the boundary-layer twist (δ) with the streamwise shape factor (H) for the flow over the rear of the upper surface of the wing. This correlation, limited to data close to the region of incipient separation, would not be expected to be valid generally but can be used as a guide to the values of δ compatible with the values of H used (Fig 13).
- (c) Choose a region of the wing where H and δ are to be modified to simulate separated flow.
- (d) Decide on the required values of H and δ using the correlation between H and δ (Fig 13) and the form of H along the chord of the NACA 4412 aerofoil (Fig 12).
- (e) Use an inverse form of a three-dimensional integral boundary-layer method to determine a revised distribution for the input velocities in the design method, and new transpiration velocities.
- (f) Revise the starting points used for each streamwise station in step (d), and so improve the uniformity of the pressure distribution in the chosen region of separation. Repeat this step until a satisfactory pressure distribution is achieved.

* with no secondary influences included²³

† such as pressure gradients normal to the surface, and Reynolds normal stresses, etc

(g) Run the BAE (SPARV) program in the design mode with the given transpiration velocity distribution determined in step (f) in order to obtain the new wing geometry.

The region chosen for the separated flow extended from about 80% chord at $\eta = 0.71$ reaching the trailing edge between $\eta = 0.46$ and $\eta = 0.88$.

The method has several weaknesses; firstly, the form of the pressure distribution chosen may not be compatible with a genuinely separated flow in three dimensions and consequently it may take many attempts to obtain a consistent overall solution. Secondly, changes in pressure distribution towards the trailing edge on the lower surface and also in the wake, needed in order to match the new upper surface values, had to be guessed, and so there may be a need for a number of attempts to obtain satisfactory values.

The results obtained were only partly successful in that the design method in step (g) did not fully converge, but they did indicate that significant changes may be necessary to the wing design if the chosen separated region of flow was to be generated. Three of the modified sections are given in Fig 14 where it can be seen that the revised sections are significantly thicker and the surface curvature is increased quite markedly where the separation starts. Because some of the experimental work envisaged requires a relatively flat surface, this wing design is unlikely to be an improvement over selecting the wing for incipient separation at the trailing edge and then increasing the wing incidence by trial until a suitable flow is achieved.

7 CONCLUSIONS

A low aspect-ratio wing has been designed, based on the requirements of the GARTEUR Action Group AD(AC07), for testing in two European low-speed wind tunnels using separate models. The evidence obtained during this programme of work should provide some much needed detailed shear stress and mean flow data of high quality for conditions of severe three-dimensionality in the shear layers, and result in improvements to turbulence modelling for this restricted range of flows. The measurements will provide data for conditions which are shown to be difficult to calculate, and thus should prove to be an important challenge to the Computational Fluid Dynamics community and provide a formidable test case.

The method used for the design employed viscous/inviscid matching techniques for a wing flow at conditions close to incipient separation. An attempt was made to extend the design to include a limited region of separated flow. In order to achieve the required flow the wing is much thicker than most wings and it has an unusual wing twist and camber distribution.

A pilot model, using the design for incipient separation, has been tested in a small low-speed wind tunnel at NLR and successful results from these tests have encouraged the GARTEUR Action Group to proceed with the main test programme using larger versions of the same design of wing, but modified at the root and tip.

Table 1
SPANWISE LIFT DISTRIBUTION -
DESIGN FOR INCIPIENT SEPARATION

STN	η	CL
1	0.042	0.306
2	0.125	0.332
3	0.208	0.371
4	0.292	0.417
5	0.375	0.467
6	0.458	0.516
7	0.542	0.554
8	0.625	0.573
9	0.708	0.562
10	0.792	0.518
11	0.875	0.448
12	0.958	0.332

Copyright ©, Controller HMSO London, 1988

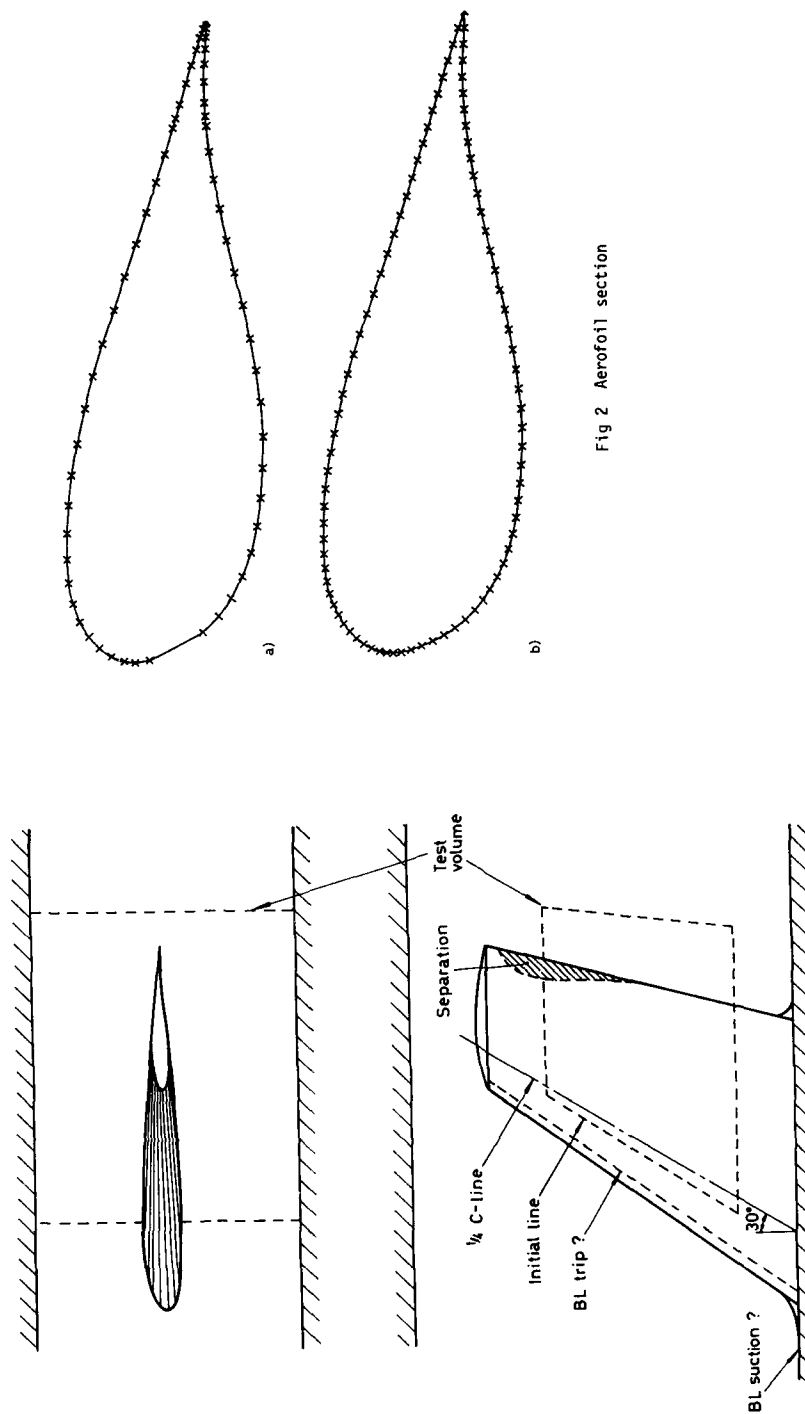
REFERENCES

- 1 J.P. Johnston, 'Experimental studies in three-dimensional boundary layers.' Thermoaciences Div, Stanford Univ. Report MD-34, July 1976
- 2 D.A. Humphreys and B. van den Berg. 'Evaluation of flow 0250: the three-dimensional turbulent boundary layer.' In: Complex turbulent flows; comparison of computation and experiment. The 1980/1 AFSOR-HTM Stanford Conference (1981)
- 3 P. Bradshaw and N.S. Pontikas. 'Measurements in the turbulent boundary layer on an "Infinite" swept wing.' Journal of Fluid Mechanics, 159, pp 105-130, October 1985
- 4 S.D. Anderson and J.K. Eaton. 'Experimental study of a pressure-driven three-dimensional, turbulent boundary layer.' AIAA Journal, 25, No.8, pp 1086-1092, August 1987
- 5 D.A. Humphreys. 'Report on the first meeting of EUROEXPT - Joint European three-dimensional turbulent boundary layer experiment.' FFAP-65 (1983)

- 6 M.C.P. Firmin. 'Application of RAE viscous flow methods near separation boundaries for three-dimensional wings in transonic flow.' AGARD CP 412 - paper 26, April 1986
- 7 J.A.H. Petrie. 'A surface source and vorticity panel method.' Aeronautical Quarterly, Vol. XXIX, November 1978
- 8 J.A.H. Petrie. 'Development of an efficient and versatile panel method for aerodynamic problems.' Degree Thesis, Dept of Applied Mathematical Studies, University of Leeds, March 1979
- 9 A.G.T. Cross. 'Calculation of compressible three-dimensional turbulent boundary layers with particular reference to wing and bodies.' BAe, Brough, Report YAD 3379 (1979)
- 10 R.C. Lock. 'Prediction of the drag of wings at subsonic speeds by viscous/inviscid interaction techniques.' AGARD Lecture Series on 'Drag prediction and reduction'. AGARD Report 723 (1985)
- 11 P.M. Sinclair. 'Development of a subcritical design program based on the panel program SPARV.' BAe, Brough. Note YAD 5012, January 1983
- 12 J.M.J. Fray and J.W. Slooff. 'A constrained inverse method for the aerodynamic design of thick wings with a given pressure distribution in subsonic flow.' NLR MP 80017U (1980). AGARD Symposium on Subsonic/Transonic Configuration Aerodynamics, Munich, May 1980
- 13 S.P. Fiddes and M. Hogan. 'A low speed aerofoil design method: description and application.' (RAE Report in preparation.)
- 14 A.W. Chen. 'The determination of geometries for multiple element aerofoils optimised for maximum lift coefficient.' Thesis, University of Illinois (1972)
- 15 L.F. East. 'Computation of three-dimensional turbulent boundary layers: Euromech 60, Trondheim 1975.' FFA TN AE-1211 (1975)
- 16 D.A. Humphreys. 'Comparison of boundary layer calculations for a wing: the May 1978 Stockholm Workshop test case.' FFA TN AE-1522 (1979)
- 17 J.P.F. Lindhout, B. van den Berg and A. Elsenaar. 'Comparison of boundary layer calculations for the root section of a wing: the 1979 Amsterdam Workshop test case.' NLR MP 80028U (1980)
- 18 B. van den Berg, D.A. Humphreys, E. Krause and J.P.F. Lindhout. 'Three-dimensional turbulent boundary layers - calculations and experiments: analysis of an EUROVISC Workshop.' VIEWEG Series Notes on Numerical Fluid Mech., 19 (1987)
- 19 J. Cousteix. 'Theoretical analysis and prediction methods for a three-dimensional turbulent boundary layer.' ONERA NT 157 (1974). English Translation ESA TT 238 (1976)
- 20 P.D. Smith. 'Calculation with the three-dimensional lag-entrainment method.' Proc. SSPA-ITTC Workshop on Ship Boundary Layers 1980. Lars Larsson (Ed). SSPA No.90 (1981)
- 21 L.J. Johnston. 'A numerical method for three-dimensional compressible turbulent boundary-layer flow.' 5th Int. Conf. on Numerical Methods in Laminar and Turbulent Flow. Montreal, Quebec, Canada, 6-10 July 1987
- 22 J.P.F. Lindhout, G. Moek, D.E. de Boer and B. van den Berg. 'Method for the calculation of three-dimensional boundary layers on practical wing configurations.' J. Fluid Engineering, 103, p 104 (1981)
- 23 J.E. Green, D.G. Weeks and J.W.F. Brooman. 'Prediction of turbulent boundary layers and wakes in compressible flow by a lag-entrainment method.' ARC R&M 3791 (1973)
- 24 P.R. Ashill, D.J. Weeks and J.L. Fulker. 'Wind tunnel experiments on aerofoil models for the assessment of computational flow methods.' Symposium on 'Validation of computational fluid dynamics', Lisbon, 2-5 May 1988.
- 25 R. Michel, C. Quémard and R. Durant. 'Application d'un schéma de longueur de mélange à l'étude des couches limites turbulentes d'équilibre.' ONERA TN 154 (1969)
- 26 T. Cebeci and A.M.O. Smith. 'Analysis of turbulent boundary layers.' Academic Press (1974)
- 27 B. van den Berg and A. Elsenaar. 'Measurement in a three-dimensional incompressible turbulent boundary layer in an adverse pressure gradient under infinite swept wing conditions.' NLR TR 72092U (1972)
- 28 R.C. Hastings and B.R. Williams. 'Studies of the flow field near a NACA 4412 aerofoil at nearly maximum lift.' Aero J., 91, 901, pp 29-44 (1987)

ACKNOWLEDGMENT

The authors wish to acknowledge the assistance of Mr J.S. Smith, RAE, and staff at BAe, Brough, with the initial work on the BAe (SPARV) program. The cooperation of the members of the GARTEUR Action Group (B. van den Berg, NLR; A. Bertabrud/E. Totland, FFA; J. Cousteix/C. Gleyzes, ONERA, H.U. Meier/H.P. Kneplin, DFVLR) is gratefully acknowledged, especially for providing data from their own work.



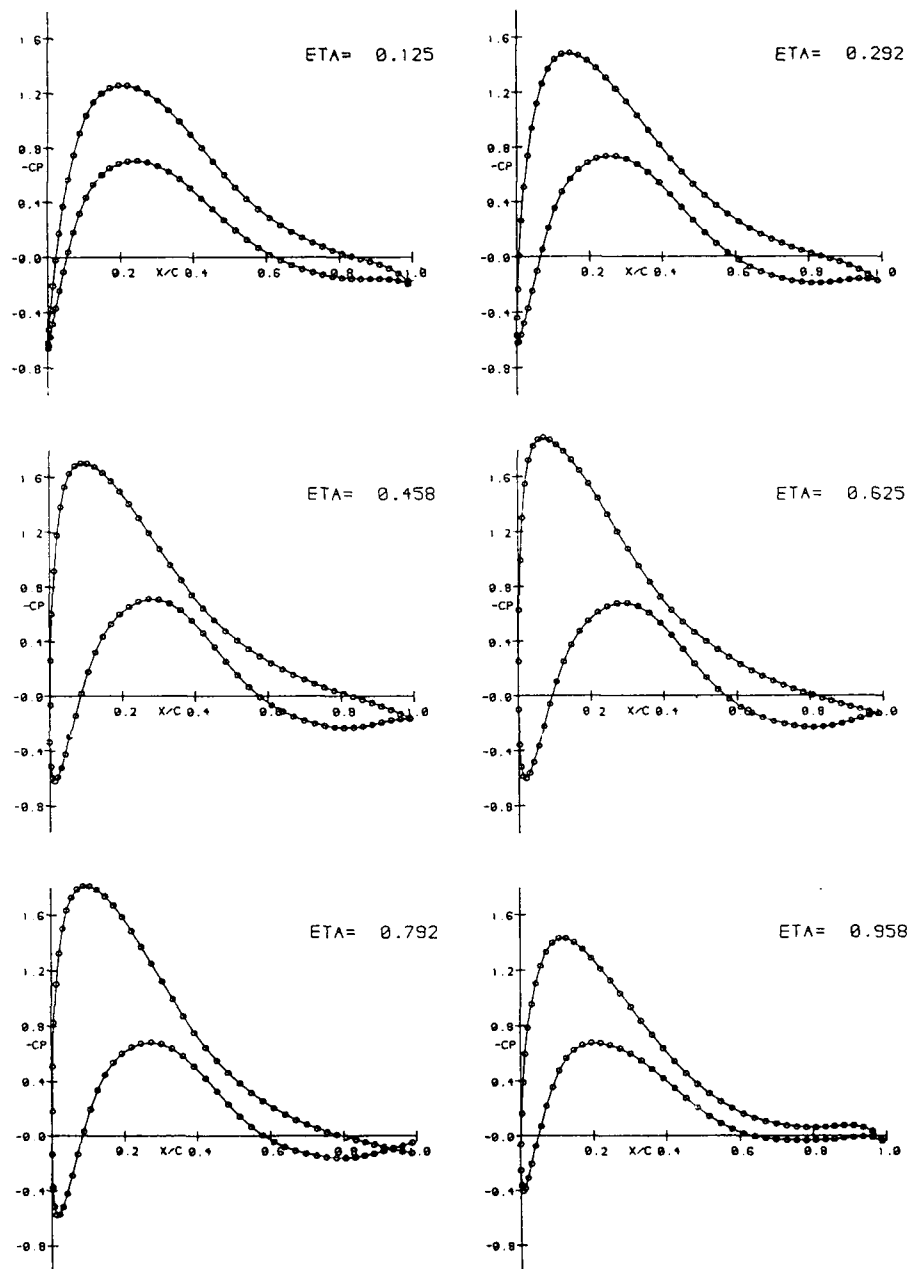


Fig 3 Calculated surface pressure distributions

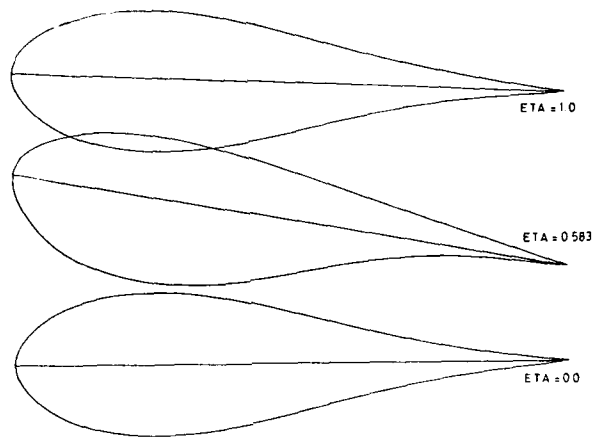
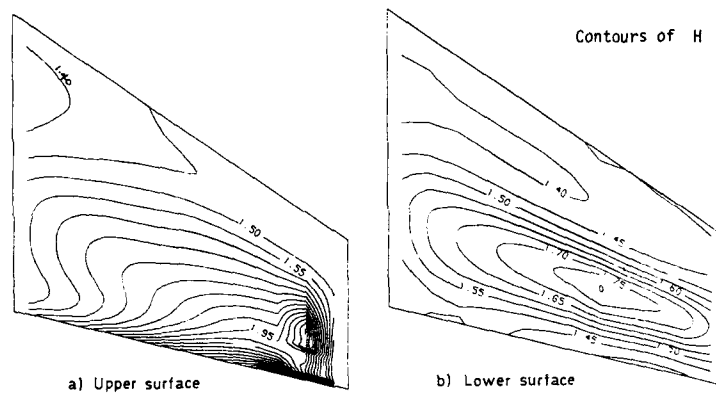


Fig 4 Streamwise sections - wing design for incipient separation



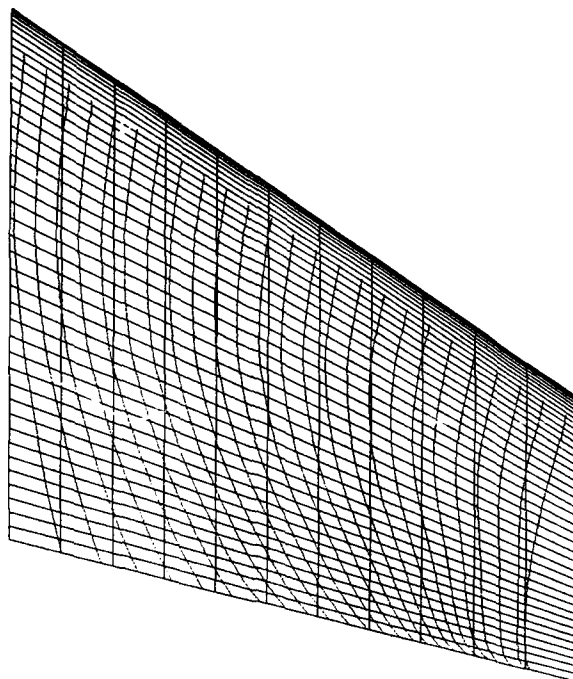


Fig 7a Surface streamlines - upper surface

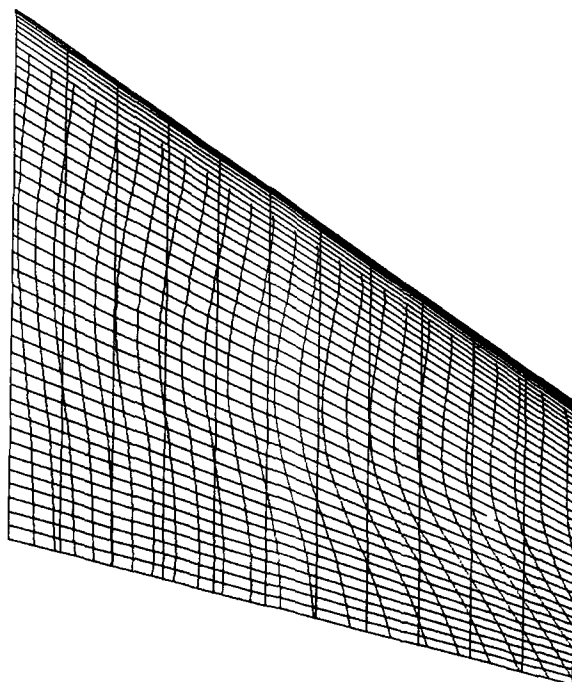


Fig 7b Surface streamlines - lower surface



Fig 10a Surface oil flow - upper surface - $Re = 2.5 \times 10^6$,
 $\alpha = 0$ degrees



Fig 10b Surface oil flow - lower surface - $Re = 2.5 \times 10^6$,
 $\alpha = 0$ degrees



Fig 8 The pilot model - showing upper surface

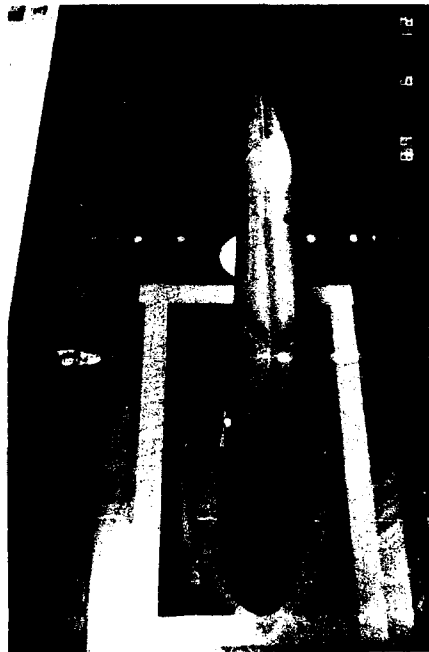


Fig 9 The pilot model mounted in small NLR LST

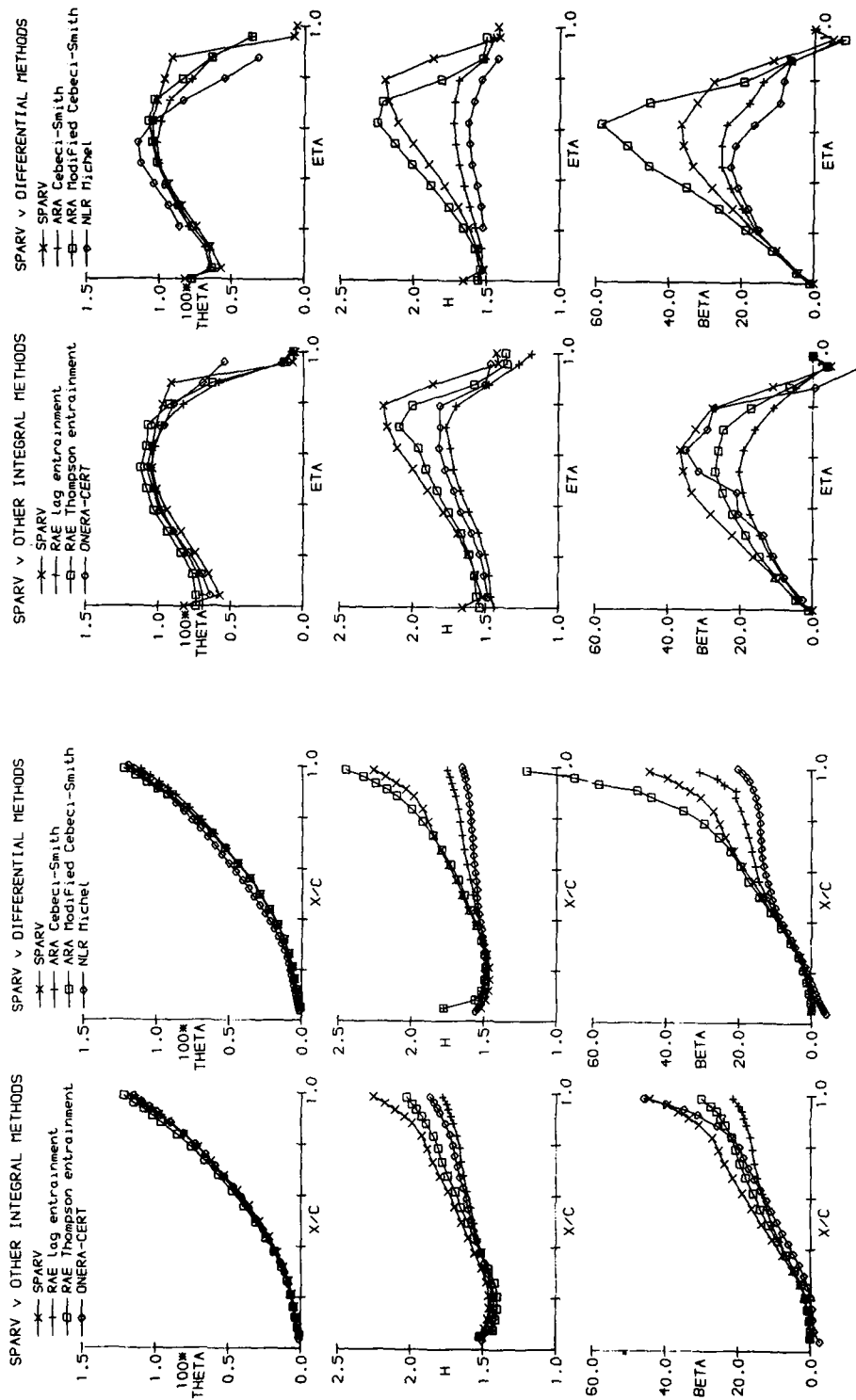


Fig 11a Comparison of results at $ETA = 0.625$. Upper surface.

Fig 11b Comparison of results at $X/C = 0.935$. Upper surface.

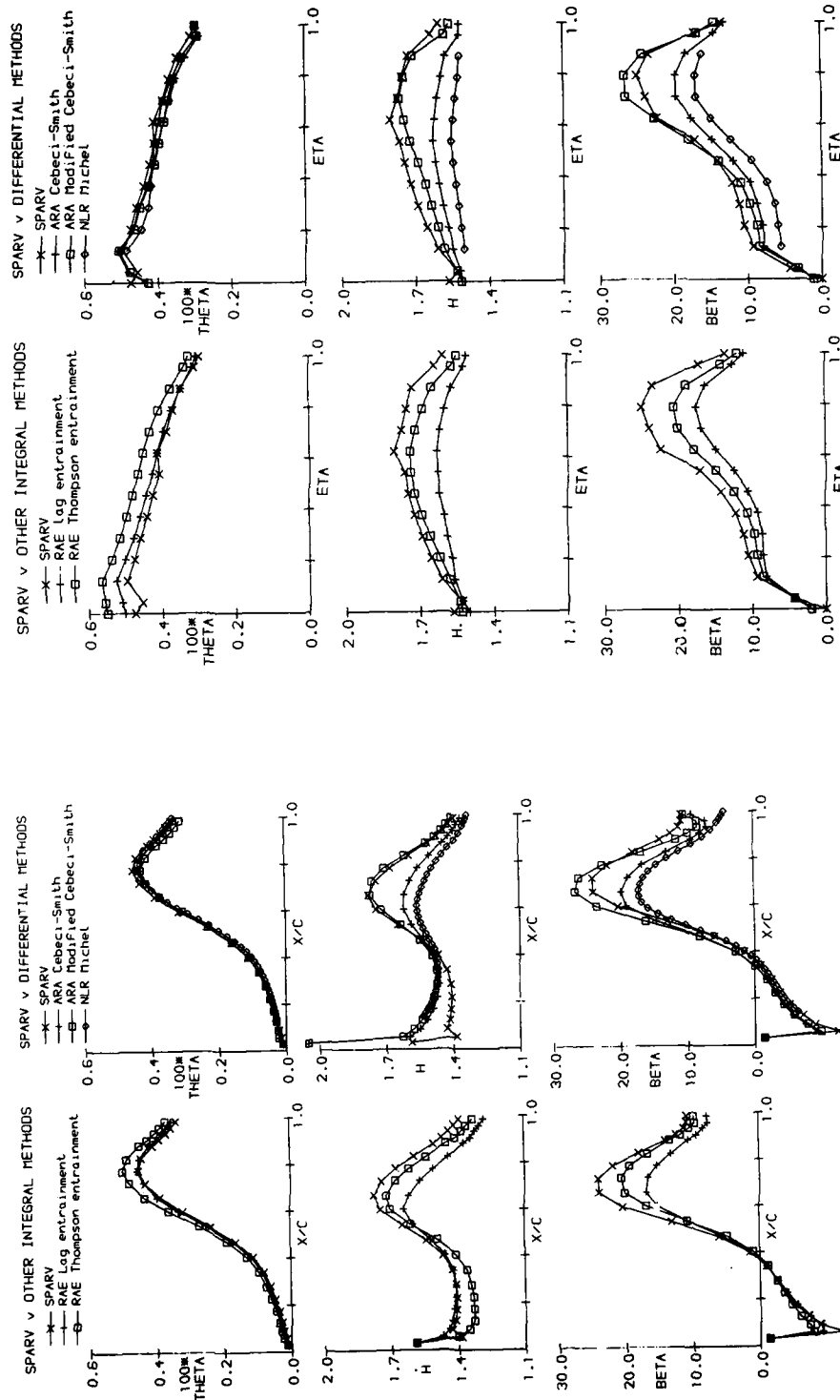

Fig 11d Comparison of results at $X/C = 0.67$. Lower surface.

Fig 11c Comparison of results at $X/C = 0.71$. Lower surface.

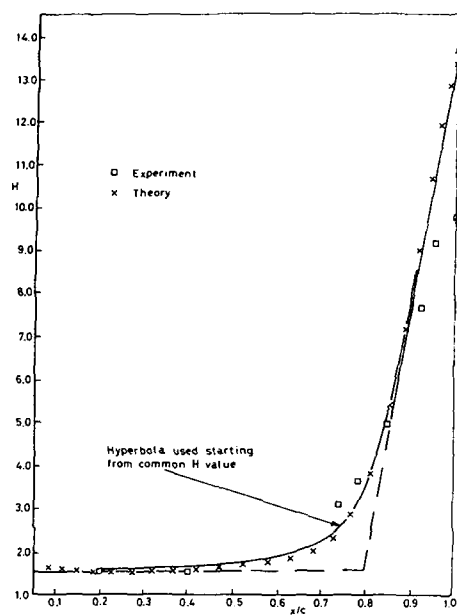


Fig 12 Development of H on upper surface of NACA 4412 aerofoil

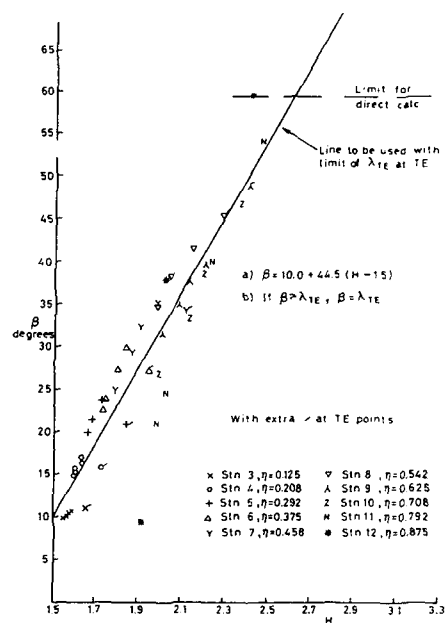


Fig 13 Correlation of β for wing design

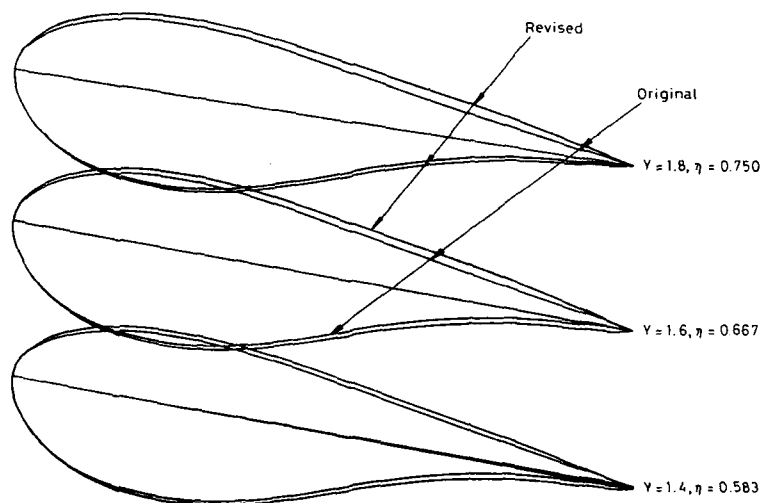


Fig 14 Selection of revised sections

SLENDER CONE CFD AND EXPERIMENTAL DATA COMPARISONS IN HYPERSONIC FLOW

by

J.Y. BALTAR
E. TJONNELAND
BOEING ADVANCED SYSTEMS
P.O. BOX 3703
SEATTLE, WASHINGTON 98124, USA

SUMMARY

A zonal Navier-Stokes / Parabolized Navier-Stokes (NS/PNS) computational fluid dynamics (CFD) analysis of the flow field about sharp and slightly blunted cones at Mach 18.7 was made. The results were compared with experimental measurements from the Princeton High Pressure Hypersonic Nitrogen Tunnel. Plots are shown comparing predicted and measured shock locations, surface pressures, surface heat transfer, and several flow field properties. Contour plots of the overall flow field are shown for cones with two nose radii. The agreement between the CFD results and experiment was fair considering that several important aspects of the flow physics in the tunnel were not properly modelled. The most important of these are the axial variation in wind tunnel static pressure and the gas characteristics of the nitrogen in the test section. The experimental data set, including data up to Mach 26.5, has proven to be valuable for improving the understanding of the flow physics on slender cones at hypersonic speeds.

1.0 INTRODUCTION

The initial purpose of this study was to validate a zonal NS/PNS CFD analysis through comparisons with slender cone experimental data at high Mach numbers. A number of difficulties with both the experimental data and the CFD analysis prevented this. This paper will present the significant aspects of and lessons learned about CFD analysis and experimental data needs for understanding slender body hypersonic flow regimes.

The experimental data chosen is from the Reference 1 Ph.D. thesis. This data set was chosen because the test conditions reported spanned the range of continuum flow to near non-continuum flow. The simple cone geometry was tested at 0 degrees angle-of-attack. It would therefore be easy to define and generate a grid that could be analyzed axisymmetrically. The reported results included multiple measurements of the flow field in addition to the surface measurements that are usually reported.

Since the majority of the flow field over the cone was supersonic, a CFD code which takes advantage of the parabolic nature of the flow was utilized. The 3D PNS code SPEAR, which solves the flow equations in a single marching pass, was chosen to analyze the flow field (in an axisymmetric mode) for the model with the exception of the blunt nose regions. An initial solution plane is required to start the PNS solution procedure. For sharp cones, this can be generated internally by the code as uniform freestream conditions. For blunt cones, elliptic effects are important in the subsonic regions near the stagnation point so an initial solution plane must be supplied externally. These effects can be modelled with the full Navier-Stokes code BLUNT which is designed for analysis of 2-D blunt geometries.

2.0 REVIEW OF THE EXPERIMENT

In the Reference 1 thesis, the results of an experimental investigation of the study of the flow field about sharp and slightly blunted conical bodies at hypersonic speeds were presented. The Mach number for the three conditions in the thesis ranged from 18.7 to 26.5 and the unit Reynolds number ranged from 37800/in. to 1500/in., respectively. The former case is in the continuum regime while the latter case is near the non-continuum limit. The models tested (see Figure 1) had a half-angle of 10 degrees with nose radii ranging from sharp ($R_n = 0.002$ in) to slightly blunted ($R_n = 0.075$ inches). The test medium was ultra-pure nitrogen and the flow remained laminar throughout the test due to the very low Reynolds numbers. The surface temperature was cooled to a nominal $T_{wall} / T_{total} = .15$. Shock location, surface pressure and surface heat transfer were measured at the locations shown in Figure 2. Flow field measurements were made of pitot pressure, stagnation temperature, heat flux, and density. An experimental accuracy of $\pm 5\%$ was claimed in Reference 1.

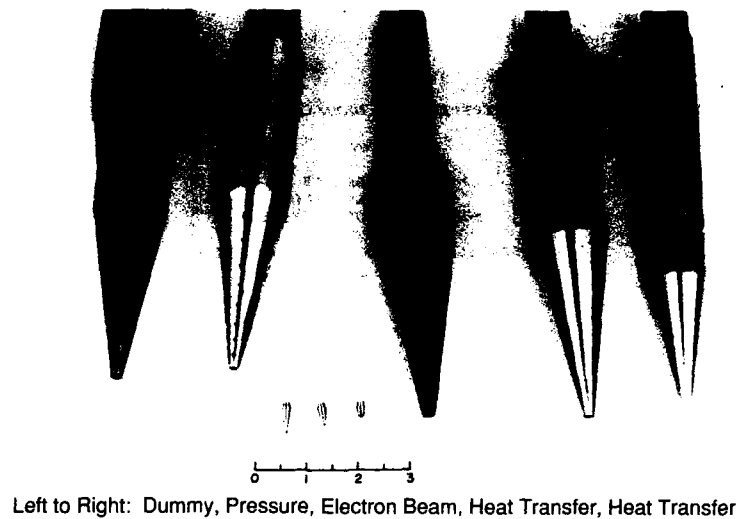


Figure 1. Photograph of Models with Replaceable Tips

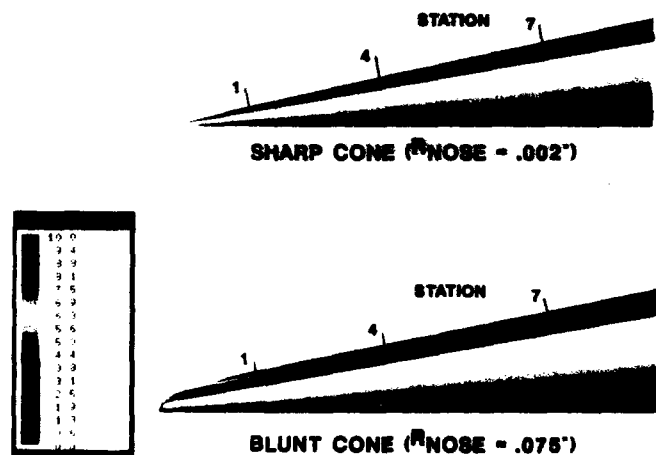


Figure 2. Mach Number Contours

Other flow field properties, such as Mach number, static temperature, density and velocity, were calculated in the thesis from these measurements by four methods:

- A. P_t (meas) + p (assumed) + $U(T)$ (Crocco relationship assumed)
- B. P_t (meas) + p (assumed) + T_t (meas)
- C. P_t (meas) + p (assumed) + q (meas)
- D. P_t (meas) + T_t (meas) + density (meas).

Method C results were not consistent throughout the thesis and the Method D results were only good for the lower Reynolds number cases so they will not be shown in this study.

For the Mach 18.7 case, the freestream molecular mean free path (λ) was 7.4E-4 inches giving a Knudsen number (λ / L) of 0.37 and 0.01 based on the sharp and blunt nose radii, respectively, and $Kn = 0.0002$ based on the cone length. For the Mach 26.5 case, the freestream mean free path was 0.026 inches giving Knudsen numbers of 13., 0.34, and 0.0065 based on the respective lengths. Knudsen numbers below 0.03 are considered to be in the continuum regime where the Navier-Stokes equations are valid while a Knudsen number above 1.0 is in the non-continuum regime. Knudsen numbers between these limits are in a transition region where the validity of the Navier-Stokes equations is in question.

Comparisons were made in the thesis between the measurements and various analyses which were available at that time. These were briefly described in the thesis and results from them are shown in the plots presented later. A one line description of each is given here. A more detailed description of the analysis procedures is available in Reference 1.

- Rubin - finite difference, single set of NS equations (may be PNS)
- Mayne - inviscid / B.L. iteration
- Cheng - thin layer NS, numerical solution
- Garvine - finite difference, inviscid-viscous equations (may be PNS)
- Rakich - blunt body inviscid finite difference

3.0 DESCRIPTION OF THE CFD CODES

The BLUNT code (Reference 2) solves the Reynolds-averaged Navier-Stokes equations on 2-D planar or axisymmetric blunt bodies. The procedure is based on an implicit upwind differencing method with special logic to make the code efficient and reliable. The code includes the Tannehill equilibrium air model and the Baldwin/Lomax algebraic turbulence model. An internal algebraic mesh generator with some capability for adapting the mesh to the flow properties is utilized. Curve fits of previous inviscid cases are used for initial conditions along with a graduated grid procedure to allow the solution to converge more rapidly. All shocks are captured as part of the solution.

The SPEAR/3D code (Reference 3) can model external and internal supersonic/hypersonic viscous flow fields with thin subsonic wall layers. The numerical method incorporates a second order accurate alternating direction implicit algorithm to solve the Parabolized Navier-Stokes equations with a single marching pass. The equations have been transformed into a generalized 3-D non-orthogonal coordinate system that can conform to arbitrarily shaped boundaries. In regions where elliptic effects are important, the solution can be coupled to an elliptic pressure solver. The code includes the Tannehill equilibrium air model and the Baldwin/Lomax algebraic turbulence model or a two-equation k-epsilon turbulence model. The bowshock may be fitted or captured as part of the solution. All internal shocks are captured. The lower boundary is always defined as a wall which may be adiabatic or isothermal and have regions of suction or blowing. Radiation from the wall can also be modelled. An internal algebraic mesh generator is available for use on simple geometries or an externally generated mesh may be supplied for complicated geometries. An interpolator is included in the code that may be used to change the mesh as the solution is marched down the body or to interpolate a starting solution from a converged BLUNT solution. Both SPEAR/3D and BLUNT were developed by Amtec Engineering of Bellevue, Washington.

4.0 DETAILS OF THE CFD ANALYSIS

The Reference 1 thesis includes results for runs at three Mach number conditions for conical bodies with three different nose radii. The original plan for this study was to analyze the sharpest and bluntest cones at the highest and lowest Mach number conditions to study the effects of the rarefied gas regime on CFD codes based on the continuum flow assumption. Due to the problems encountered with low Reynolds number stability, only the low Mach number cases were completed in the time allotted. The details of these two analyses are describe here.

A. Sharp Cone

The BLUNT code would not converge for a fine-mesh cold-wall solution on the "sharp" cone with a 0.002 inch spherical nose. This may have been caused by the low Reynolds number based on the nose radius or else because of roundoff problems associated with the small nose radius.

SPEAR was started very close to the virtual tip of the cone with initial conditions of freestream values at all nodes except the no-slip fixed wall temperature (540 R) boundary condition. The outer boundary of the 21 radial node mesh is set so that the shock is initially captured and the shock will run into the outer boundary where it will be fitted within 20 axial steps. SPEAR is then restarted with 41 radial mesh points and marched 210 steps downstream to an axial distance of 4 inches. A mesh refinement study of the sharp-nose start case was performed. Step size, near-wall cell height and number of radial nodes were varied in the starting region and for the downstream region to determine the effects on the solution. The finest mesh solution was chosen for the starting region, but the surface properties and profiles in the downstream region did not show much variation with mesh changes.

The initial runs for this case were run using the ideal gas ($\gamma = 1.4$) model since the freestream static temperature is 43.7 degrees R. An equilibrium air case was run since the peak static temperature in the boundary layer was about 960 degrees R. During the study of the effects of freezing the flow properties at the nozzle throat, γ was varied from 1.3 to 1.45. The shock location and surface pressure varied moderately and the peak static temperature in the boundary varied considerably with these changes but the heat transfer did not vary much. Since the actual properties of the nitrogen gas in the test section have not been determined, the $\gamma = 1.4$ results will be presented in this paper.

B. Blunt Cone

The graduated grid method described in Reference 2 was utilized to converge a fine mesh (40x50) laminar adiabatic wall solution using BLUNT for the Mach 18.7 case with the 0.075" nose radius. The wall temperature was then gradually lowered to the desired wall temperature of 540 R. This case converged when the sharp nose case did not because the Reynolds number based on the nose radius was 2835 instead of 75. The BLUNT solution was run with the 1st order upwind algorithm.

SPEAR was started from the cold wall solution and run to the end of the 4 inch cone using 41 radial points and 104 axial steps. Several runs were made to determine how to interface the captured BLUNT shock solution and the fitted SPEAR shock solution and to check the mesh resolution.

5.0 DISCUSSION

5.1 COMPARISON OF CFD AND EXPERIMENTAL RESULTS

A. Sharp Cone

A comparison of the shock location from the CFD results with the four experimental methods of locating the shock for the sharp cone case is shown in Figure 3. The CFD results are in good agreement with the data. The heat flux measurement, which was says is the least reliable, shows the worst agreement with the CFD results. The larger disagreement near the leading edge may be caused by the uniform profile starting procedure used with SPEAR which does not accurately model the viscous interaction near the tip. A summary of the percent differences between CFD and experiment for the various measurements is given in Table 1.

A comparison of predicted and measured surface pressures is shown in Figure 4. The CFD results are higher than the data but are in better agreement with the calculations of Mayne. The experimental results fall below the inviscid value toward the rear of the model because there is an axial static pressure gradient in the tunnel. The CFD analysis was performed for uniform external flow and appears to be approaching a constant value for an inviscid cone with a displacement thickness added.

Sharp Cone		
	At station 1	At station 7
Shock location:	-10%	0%
Surface pressure:	+8%	+20%
Wall heat transfer:	+33%	+27%
P static variation:	4% max	4% max
Pitot profile:	+100% max	+50% max
Mach number profile:	+40% max	+25% max
T static peak:	-15% max	-9% max
Blunt Cone		
	At station 1	At station 7
Shock location:	-5%	-4%
Surface pressure:	-17%	+15%
Wall heat transfer:	+40%	+66%
P static variation:	30% max	7% max
Pitot profile:	+50% max	+100% max
Mach number profile:	+33% max	+48% max
T static peak:	-15% max	0% max

Table 1. Comparison of CFD Results with Experimental Data (Experiment is Base)

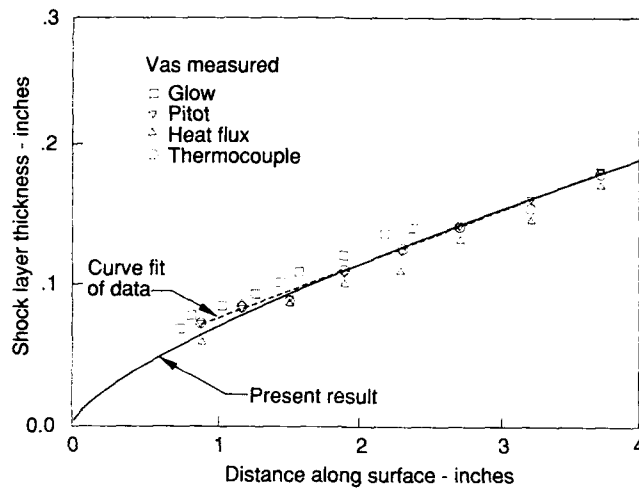


Figure 3. Shock Layer Thickness - Sharp Cone

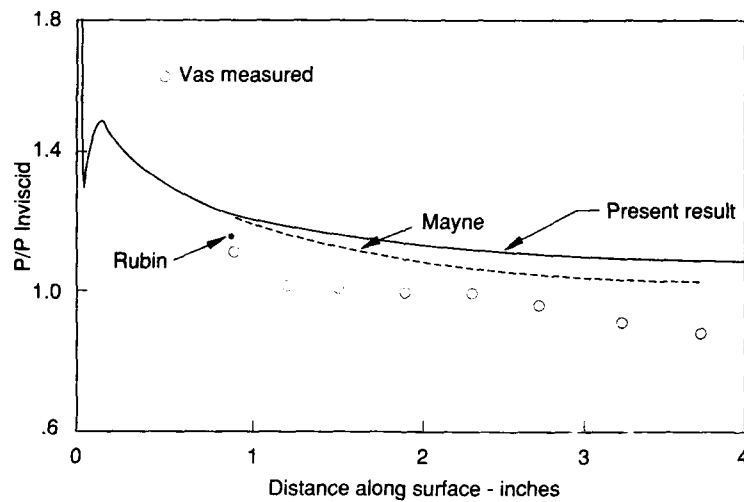


Figure 4. Surface Pressure - Sharp Cone

A comparison of predicted and measured surface heat transfer results is shown in Figure 5. The CFD results are higher than the data. This may be caused by rarefied gas effects since using the continuum assumption in a non-continuum region would tend to over-predict wall shear stress and heat transfer. In an attempt to resolve the differences in the heat transfer comparisons, many SPEAR runs were made varying the Prandtl number, ratio of specific heats, wall temperature, viscosity equation, and axial and radial mesh density. Slight changes in the wall heat transfer were noted when the viscosity was calculated by the equations given in Reference 1 rather than Sutherland's law. The other variations had a negligible effect on the wall heat transfer. One affect that has not been investigated is the axial variation in the model wall temperature. In the photograph in Figure 6, the tip of the model (and the pitot probe) appears to be glowing from the high temperature since the replaceable tips (about .25 to .5 inches long) could not be cooled.

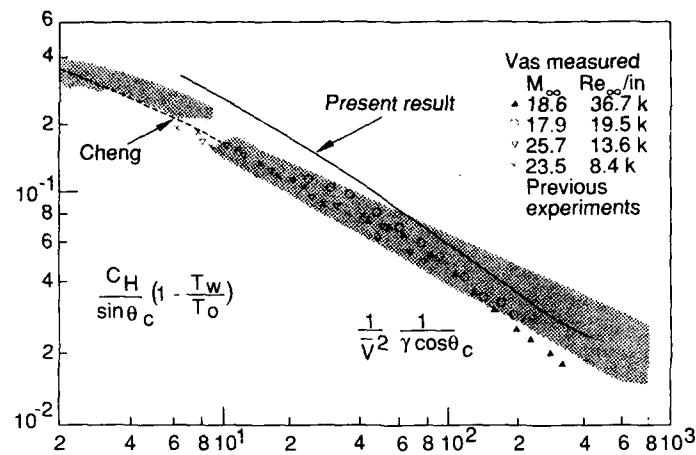


Figure 5. Surface Heat Transfer - Sharp Cone



Figure 6. Photograph of Blunt Cone Showing the Shock Layer and Pitot Probe

Figures 7a,b & c present the flow field static pressure profiles calculated by SPEAR and the measured wall static pressures. The CFD results are shown at the three stations (shown in Figure 2) at which Vas compared the data with other analyses. For the other analyses, only Rubin calculated flow field static pressure and this was only up to Station 1. No flow field static pressures were measured, so Vas assumed the wall static pressure was constant through the shock layer for all subsequent calculations. The CFD profile results show a maximum variation from the wall value of static pressure of 4% which could result in a variation in local Mach number of 0.2 at Mach 10 according to NACA 1135. Therefore the CFD results show that the constant pressure assumption is good for the sharp cone.

Figures 8a,b, & c are comparisons between the pitot profiles calculated using SPEAR and the measured pitot pressures at three measuring stations. The SPEAR pitot pressures were calculated using the predicted local static pressure and Mach number. Vas has noted that the measured pitot pressures are invalid within about 0.020 inches of the wall due to probe interactions with the wall. It should be noted that the height of the pitot probe was about 0.010 inches and the entire shock layer at station 1 is only about 0.070 inches thick.

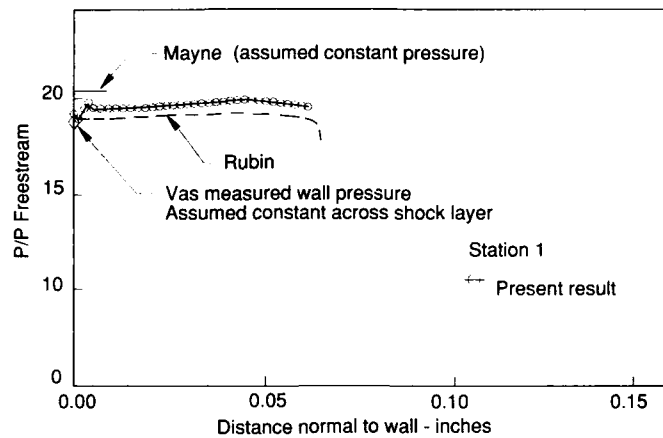


Figure 7a. Flow Field Static Pressure, Station 1 - Sharp Cone

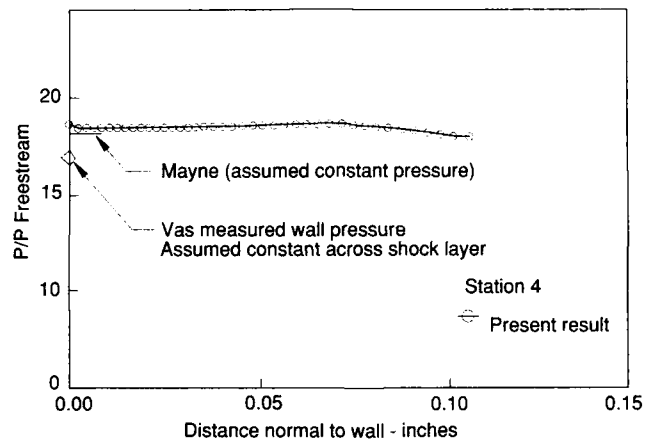


Figure 7b. Flow Field Static Pressure, Station 4 - Sharp Cone

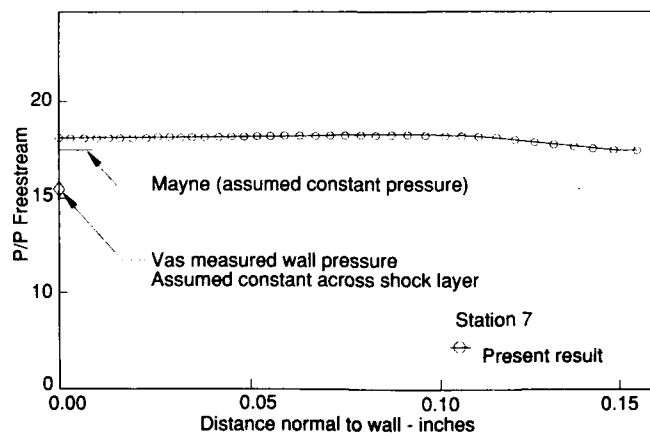


Figure 7c. Flow Field Static Pressure, Station 7 - Sharp Cone

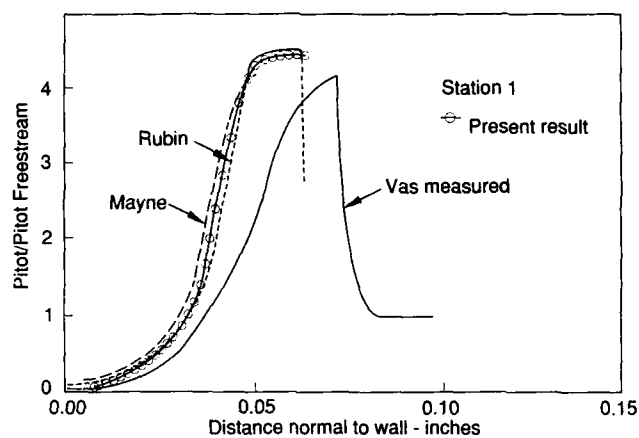


Figure 8a. Flow Field Pitot Pressure, Station 1 - Sharp Cone

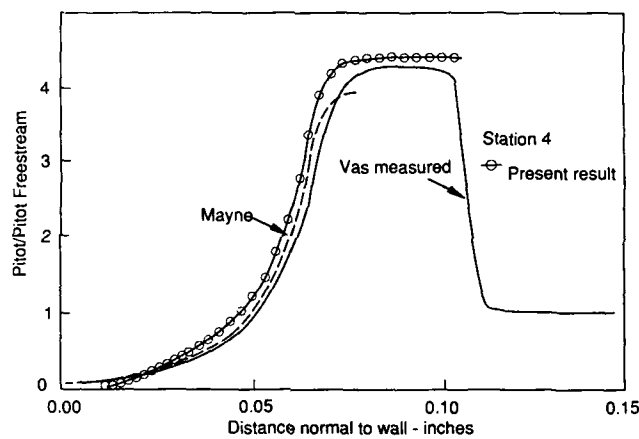


Figure 8b. Flow Field Pitot Pressure, Station 4 - Sharp Cone

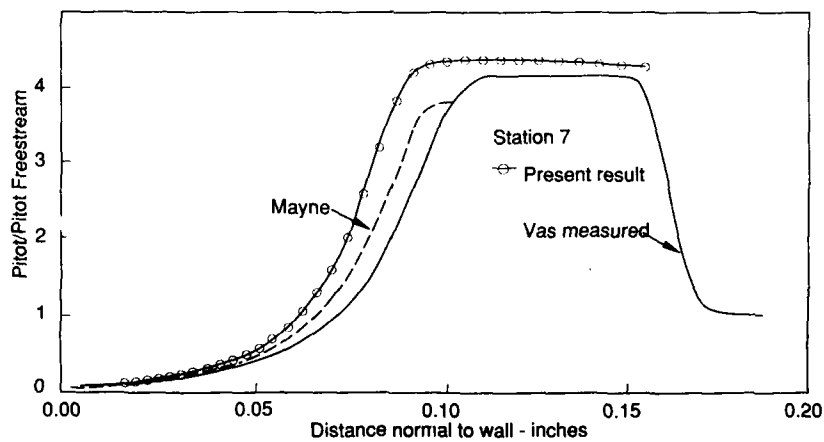


Figure 8c. Flow Field Pitot Pressure, Station 7 - Sharp Cone

The Mach number and static temperature profiles from SPEAR were compared to the profiles calculated from the data by Methods A and B. The results of these comparisons are not plotted but are summarized in Table 1. The SPEAR Mach number is calculated from the local velocities and speed of sound, which is a function of the local static temperature and the gas properties. Vas calculates Mach number from the measured pitot pressure, the (assumed constant) wall static pressure and the gas properties using the Rayleigh-pitot formula. The peak in the boundary layer static temperature calculated by SPEAR was strongly dependent on the variations listed under heat transfer. Large differences between CFD and experiment would be expected if the proper gas properties were not used.

At station 1, the present CFD results agree very well with the other CFD results shown in the thesis for most variables but do not agree as well with the results from the experiment. Therefore, it would appear that some aspect of the flow physics near the nose is not being properly modelled in the various CFD analysis methods. By station 4, the CFD and experimental results agree well for most parameters but then start to diverge again by station 7 possibly because of the axial pressure gradient in the tunnel. In general, the CFD results agree better with the calculated results presented in Vas' thesis than with the experimental results.

B. Blunt Cone

A comparison of the shock location from the CFD results with the four experimental methods of locating the shock for the blunt cone case is shown in Figure 9. The CFD results are slightly below the data. This indicates that the CFD codes are probably under-predicting the viscous effects.

A comparison between predicted and measured surface pressures is shown in Figure 10. The CFD results are higher than the data but agree very closely with the calculations of Garvine. As for the sharp cone, the CFD calculated pressures appear to be approaching a constant value for an inviscid cone with a displacement thickness added.

A comparison between predicted and measured surface heat transfer results is shown in Figure 11. As with the sharp cone case, the CFD results are higher than the data. Since these results are very similar to the sharp nose case heat transfer results, the starting procedure is probably not the reason for the poor heat transfer comparison.

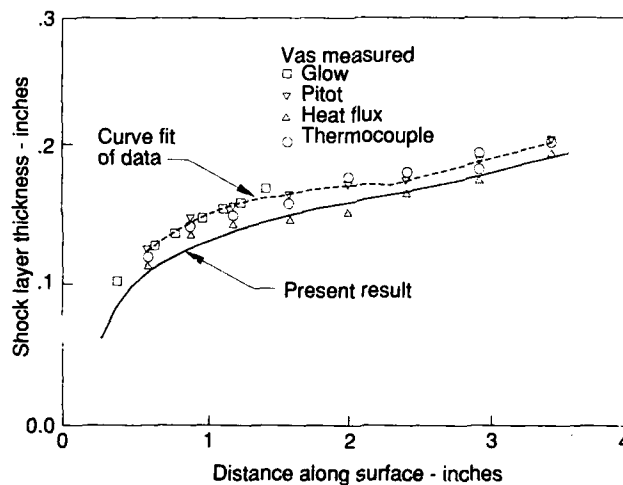


Figure 9. Shock Layer Thickness - Blunt Cone

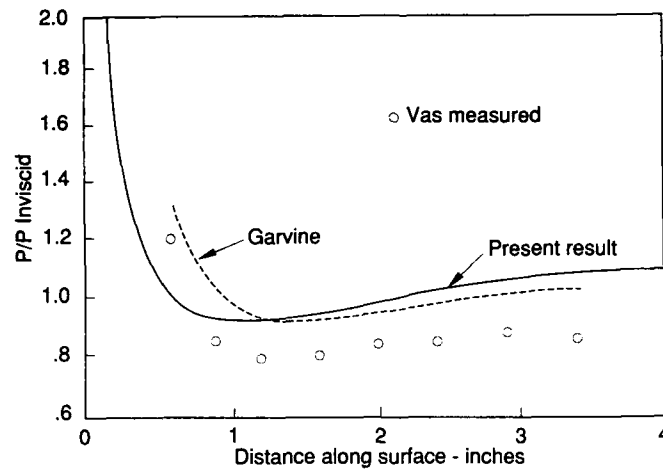


Figure 10. Surface Pressure - Blunt Cone

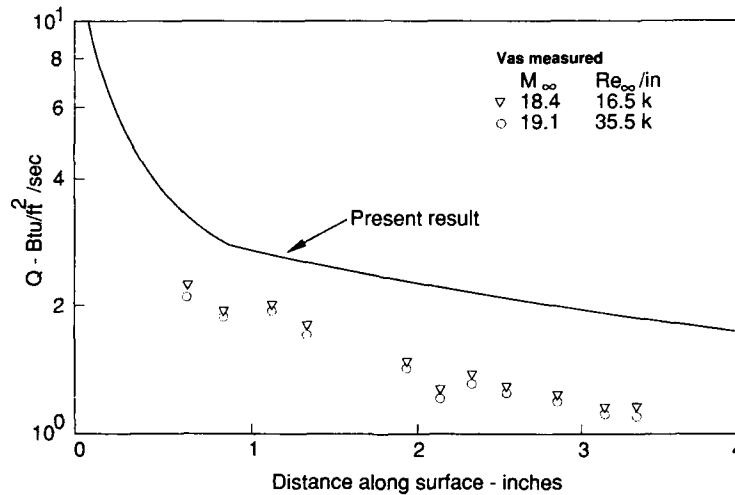


Figure 11. Surface Heat Transfer - Blunt Cone

Figures 12 and 13 present the CFD results for flow field static and pitot pressure for the blunt cone case compared with the measured and calculated profiles from the thesis. In Figure 12a, the CFD results show a variation in the flow field static pressure from the wall value of about 30% which could result in a variation in Mach number of 1.5 at Mach 10 according to NACA 1135. Vas notes that the constant static pressure assumption should not be valid in the nose region of a blunt cone and the CFD results confirm this. By station 4, the static pressure profile is more representative of cone flow and thus the same level of static pressure variation across the shock layer that was predicted in the sharp cone case is predicted here. The Mach number and static temperature profiles were also compared and these results are summarized in Table 1. In general, the profile shapes are similar between CFD and experiment but the CFD analysis consistently predicts a thinner boundary layer region and a larger inviscid region. The percent differences shown in Table 1 are large because the property gradients are very steep.

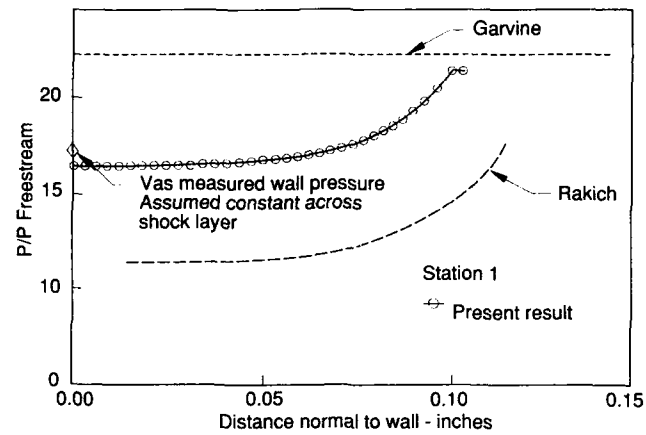


Figure 12a. Flow Field Static Pressure, Station 1 - Blunt Cone

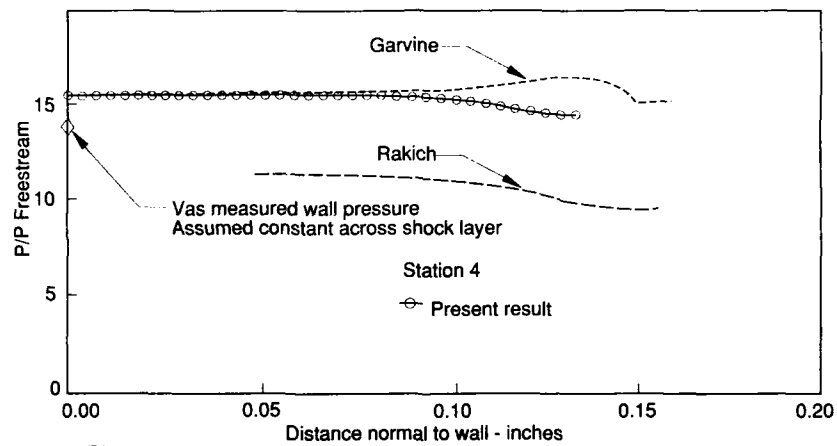


Figure 12b. Flow Field Static Pressure, Station 4 - Blunt Cone

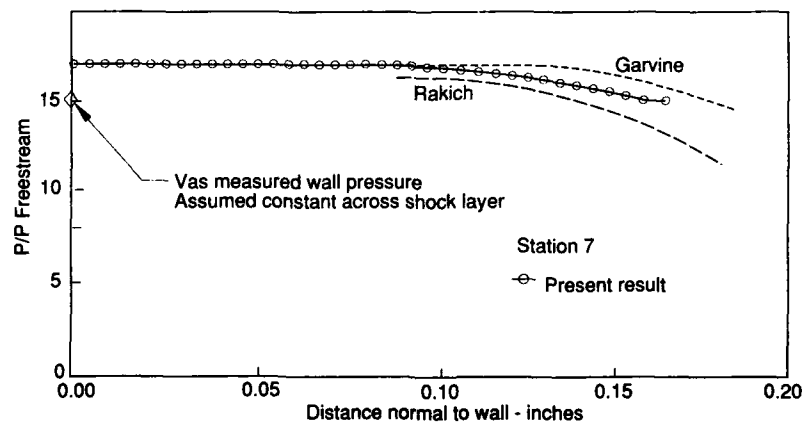


Figure 12c. Flow Field Static Pressure, Station 7 - Blunt Cone

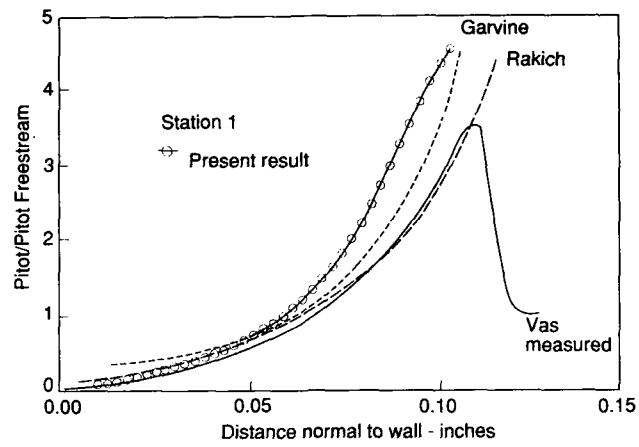


Figure 13a. Flow Field Pitot Pressure, Station 1 - Blunt Cone

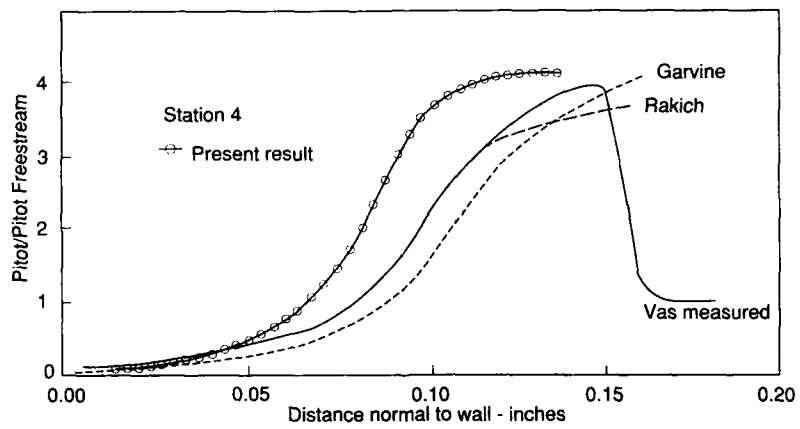


Figure 13b. Flow Field Pitot Pressure, Station 4 - Blunt Cone

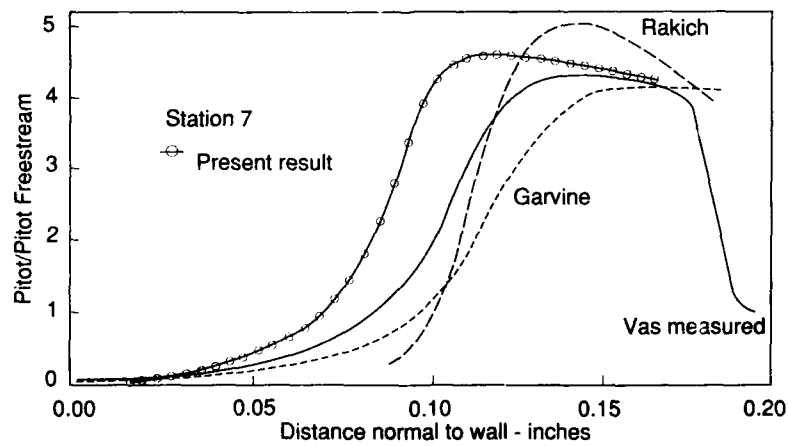


Figure 13c. Flow Field Pitot Pressure, Station 7 - Blunt Cone

5.2 EXPERIMENTAL DATA CONCERNS

Several aspects of the wind tunnel flow and measuring equipment that have raised concerns during this study are briefly enumerated below.

1. There is an axial static pressure gradient in the tunnel (documented in Reference 4) which causes a Mach number gradient of 0.3 Mach per inch as shown in Figure 14. For the 4 inch model tested, this is a change of over 1 Mach number from the tip to the last measuring station.
2. As shown in Figure 15, even for the high Reynolds number case the nose of the model is near the non-continuum regime. The assumption of continuum flow must be investigated.
3. The properties of the nitrogen are not documented in the thesis. The tunnel calibration document calculates a "frozen" temperature (which occurs just downstream of the wind tunnel throat) at which the properties in the test section are frozen due to vibrational non-equilibrium. The effect of this is to change the ratio of specific heat for an ideal gas assumption. To properly model the non-equilibrium effects, a finite rate chemistry code should be run for the wind tunnel nozzle conditions or the flow properties should be measured at the start of the test section.

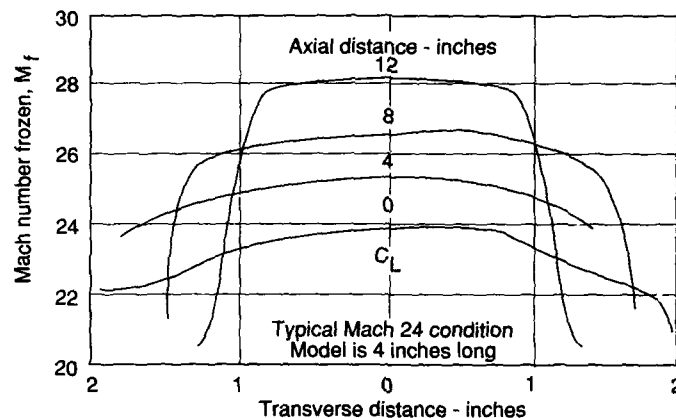


Figure 14. Non-Uniform Wind Tunnel Conditions

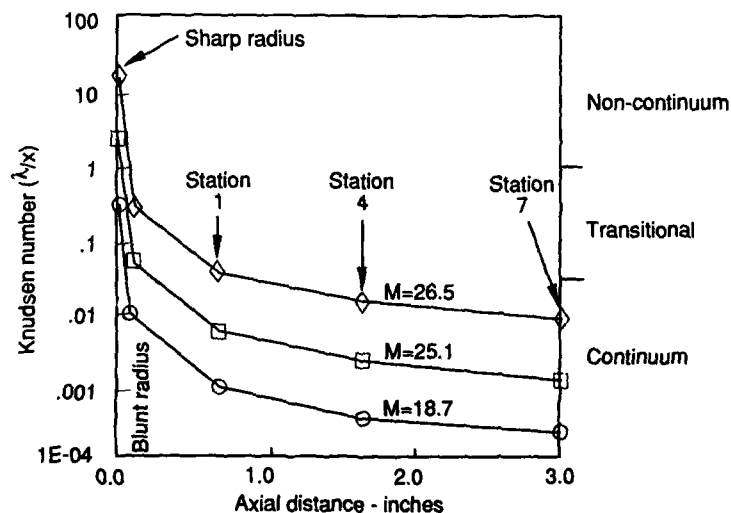


Figure 15. Rarefied Gas Near Tip of Models

4. The size of the pitot probe head is about 0.010 inches while the entire shock layer is only 0.070 inches near the first measuring station. The relative sizes of the pitot probe head and the shock layer can be seen from the photo in Figure 6. In a steep gradient region the pressure being measured by the pitot probe may actually be some average of the pitot pressure of the flow.
5. The model surface temperature was not measured. CFD studies were performed that showed that wall heat transfer was not very sensitive to changes in the constant wall temperature of about 80 degrees R. However, the effect of any axial temperature gradients caused by the inability to cool the replaceable tips (about .25 to .5 inches long) is unknown.

5.3 CFD ANALYSIS LIMITATIONS

The major limitations of these two CFD codes for analyzing this experiment are enumerated here.

1. There is no model currently in the codes for the properties of the nitrogen gas that is valid from the high pressures and temperatures in the stagnation chamber to the low static pressure and temperatures in the test section. A model of these properties is probably available in the literature but time restrictions have not permitted searching for and implementing a model.
2. The axial static pressure variation in the tunnel could not be modelled with the present boundary conditions in SPEAR. A change to allow for an axially varying outer boundary condition must be made to improve the simulation beyond the present results.
3. The Mach 18.7 case analyzed is in the continuum regime, however it is approaching the rarefied gas regime, and the effects of the continuum assumptions on flow properties at these conditions is not known. The Mach 26.5 case (which is in the rarefied gas regime) could be run and a comparison would indicate the magnitude of rarefied gas effects.
4. Previous investigators (for example Reference 5) have encountered trouble obtaining CFD solutions with Navier-Stokes codes below a minimum Reynolds number limit. For the Reference 5 problem, the minimum Reynolds number based on nose radius was found to be about 90. The reason for this limit is not known. A similar problem was encountered in this study when trying to converge the BLUNT code on a 0.002" spherical nose when the Re based on nose radius was about 75.

6.0 CONCLUSIONS AND RECOMMENDATIONS

The experimental data set presented in the Reference 1 thesis has proven to be valuable for improving the understanding of the flow physics on slender bodies at hypersonic speeds near the non-continuum regime. Other experimental data sets are available for CFD validation at hypersonic speeds but these usually include only surface measurements. Very few experimental data sets are available that include flow field measurements of pitot pressure and total temperature. The data at Mach 25.1 and 26.5 with unit Reynolds numbers of 10,000 and 1,500, respectively, can be used in a study of the validity of the continuum assumption for CFD as the flow approaches the non-continuum regime.

Evaluation of the CFD codes used in the present study proved more difficult than expected for a number of reasons. CFD code evaluation using experimental data such as Reference 1 would be more definitive with CFD codes capable of modelling all the physical processes that are present, including the test media chemistry (in this case nitrogen), the variations of flow characteristics in the tunnel, rarefied gas effects, instrumentation size effects and temperature gradients in the model.

Future wind tunnel studies should be designed with CFD validation studies in mind. Specifically, experimental data must accurately measure all of the initial and boundary conditions (including all gas properties) needed to complete a computational solution. Since this data would provide an upstream boundary condition to the test section, it would not be necessary to analyze the flow field upstream of the test section. Ideally, the measurements of the flow field upstream of and in the test section would be acquired by non-intrusive techniques.

REFERENCES

1. Vas, I.E., Ph.D. Thesis, "An Experimental Study of the Flow about a Slender Cone at Hypersonic Speeds", May 1970, New York University.
2. Peery, K.M., S.T. Inlay and J.T. Katsandres, "Real-Gas Blunt-Body Flow Simulations", June 1987, AIAA-87-2179.
3. Yaghmaee, S. and D.W. Roberts, "Modelling Shock/Boundary Layer Interactions with a Partially Parabolic Navier-Stokes Analysis", June 1987, AIAA-87-2178.
4. Vas, I.E. and G. Koppenwallner, "The Princeton University High Pressure Hypersonic Nitrogen Tunnel N-3", July 1964, Princeton University Report No.690.
5. Bartel, T.J. et al, "Comparisons of Monte-Carlo and PNS Calculations for Rarefied Flows Over Reentry Vehicle Configurations", January 1988, AIAA-88-0465.

**VALIDATION OF A USER-FRIENDLY CFD CODE
FOR PREDICTION OF THE AERODYNAMIC CHARACTERISTICS OF FLIGHT VEHICLES**

by
Michel Fortier
Leader, Ballistics Group
Defence Research Establishment Valcartier
P.O. Box 8800
Courcellette, Quebec G0A 1R0
Canada

SUMMARY

A computational fluid dynamics code based on the development of small perturbation theory for the solution of inviscid irrotational compressible fluid flow around flight vehicle configurations is described. The user-friendly feature of the code is illustrated by a guided weapon canard configuration for which are displayed computed pressure distributions on selected components. Five test cases including a simple wing shape and more complex guided weapon and aircraft configurations are presented, to demonstrate the capabilities and limitations of the code. Theoretical pressure, force and moment coefficients are compared to wind tunnel data obtained from various facilities including the DREV transonic indraft wind tunnel. The results of the comparison show the capabilities of the code in the subsonic and supersonic speed regimes for simple and complex configurations at low incidences, and its limitations at transonic speeds and at high angles of attack.

SYMBOLS

ac	aerodynamic center
c	wing local chord
\bar{c}	wing mean aerodynamic chord
c_l	wing sectional lift coefficient
c_p	pressure coefficient
C_L	lift coefficient
C_m	pitching moment coefficient
C_N	normal force coefficient
C_Y	side force coefficient
$C()_\alpha$	coefficient of force or moment due to angle of attack
$C()_\beta$	coefficient of force or moment due to sideslip angle
$C()_\delta$	coefficient of force or moment due to control deflection
M	Mach number
q	dynamic pressure
S	surface area
u, v, w	perturbation velocities
x, y, z	Cartesian coordinates
α	angle of attack
β	sideslip angle
δ	control surface deflection angle
ζ, η	integration variables
ϕ	velocity potential
$[\]$	square matrix
$\{ \}$	column matrix

1. INTRODUCTION

A computerized aerodynamic analysis capability is essential for the development of modern flight vehicles such as guided weapons and supersonic fighter aircraft. In the exploratory phase of a development, numerous configurations are studied to evaluate concepts, and design iterations are made to optimize selected configurations on the basis of stated performance, stability and control requirements. This dictates the choice of an aerodynamic analysis code which is not only accurate but also fast and user-friendly.

During the past few years, advances in computational fluid dynamics (CFD) and the introduction of supercomputers have rendered feasible the computation of 3-dimensional viscous flow fields around complete aircraft configurations (Refs. 1 and 2). However, this capability was achieved at the expense of professional and computer resources which are still measured respectively in weeks and hours to run a single case.

The purpose of this paper is therefore to describe briefly a user-friendly CFD code which offers the advantage of requiring only moderate computer resources, and to present the results of test cases which were used for its validation.

2. CFD CODE DESCRIPTION

FAD is a finite element aerodynamic code which is based on the development of small perturbation theory for the solution of partial differential equations governing potential flow fields around flight vehicle configurations at subsonic and supersonic speeds. The theory is valid for a fluid flow which is steady, nonviscous, compressible, irrotational and isentropic.

The code is linked to the ANVIL-4000 computer aided design and manufacturing (CAD/CAM) system (Ref. 3) to facilitate the process of defining the geometry of multi-component configurations which are approximated by grids of finite elements. The computational procedure is coded in FORTRAN IV on a Honeywell DPS 8/70C digital computer and is illustrated by a general flowchart in Fig. 1. For a given configuration and Mach number, FAD calculates a downwash matrix, an aerodynamic influence coefficient matrix, a panel force matrix, a panel pressure coefficient matrix and a set of stability derivatives.

The configuration planform is approximated by a grid of small quadrilateral panels as shown in Fig. 2. The coordinates of the panel corner points define the boundaries of constant pressure surface vortex singularities which are used to represent planform incidence and interference effects. The potential function for this type of singularity is given by

$$\phi = \frac{K}{\pi} \iint \frac{z(x-\zeta)d\zeta dn}{[(y-n)^2 + z^2]^{3/2} [(x-\zeta)^2 + (1-M^2)(y-n)^2 + z^2]^{3/2}} + \frac{1-K}{\pi} \iint \frac{zd\zeta dn}{(y-n)^2 + z^2} \quad [1]$$

where $K = 0.5$ for $M < 1.0$ (subsonic flow), $K = 1.0$ for $M > 1.0$ (supersonic flow) and which satisfies Prandtl's linearized equation, for small perturbations, of a steady irrotational flow of a non-viscous compressible fluid. Prandtl's equation is written as

$$(1-M^2) \frac{\partial^2 \phi}{\partial x^2} + \frac{\partial^2 \phi}{\partial y^2} + \frac{\partial^2 \phi}{\partial z^2} = 0 \quad [2]$$

The three velocity components of the perturbed flow field can therefore be obtained by differentiation of the potential function, i.e.

$$u = \frac{\partial \phi}{\partial x}, \quad v = \frac{\partial \phi}{\partial y} \quad \text{and} \quad w = \frac{\partial \phi}{\partial z} \quad [3]$$

The solutions of these equations are given in Ref. 4. The particular solution for the velocity component normal to a corner element of a panel is given by

$$w = -\frac{K(\Delta p/q)}{4\pi} [(1^2 + 1 - M^2)F_2 - L(F_1 - F_3) - y F_6] \quad [4]$$

where $(\Delta p/q)$ is a unit non-dimensional pressure and L, F_1, F_2, F_3, F_6 are functions which depend on Mach number (M) and geometry. The downwash velocity induced at a panel control point (i) by a singularity of unit strength on panel (j) is thus computed by superposition of corner element solutions such that

$$w_{ij} = w_{ij1} - w_{ij2} - w_{ij3} + w_{ij4} \quad [5]$$

For a symmetric planform, the net downwash at (i) is obtained by adding the downwash of the image point to that of the control point. The elements of the downwash matrix are then expressed as follows

$$w_{ij}^1 = w_{ij} + \bar{w}_{ij} \quad [6]$$

where \bar{w}_{ij} represents the downwash at an image point. For an unsymmetric planform, $\bar{w}_{ij} = 0$. The aerodynamic influence coefficient (AIC) matrix is defined such that

$$\{a_{ij}\} = \{S_i\} \{w_{ij}^1\}^{-1} \quad [7]$$

where $\{S_i\}$ is a column matrix of panel areas and where each element of the AIC matrix represents the load induced on panel (i) per unit incidence of panel (j), divided by dynamic pressure. The total aerodynamic load on a panel is then equal to the sum of the loads on the panel caused by all the other panels such that

$$\{L_i\} = q \{a_{ij}\} \{a_j\} \quad [8]$$

where q is the dynamic pressure and $\{a_j\}$ is a column matrix of panel incidences. The pressure coefficient of a panel is then given by

$$\{c_{p_i}\} = q^{-1} \{L_i\} / \{S_i\} \quad [9]$$

The aerodynamic forces acting on a multi-component configuration such as the one given in Fig. 2 are determined by integration of the load distributions given by eq. 8. Filling the matrix $\{a_j\}$ with equal panel deflections is equivalent to setting the configuration planform at an angle of attack and the calculation of the corresponding stability derivatives follows thereof. Control derivatives are obtained by setting all the elements of the matrix $\{a_j\}$ equal to zero, with the exception of those elements corresponding to the panels of the selected control surface.

FAD incorporates interactive subroutines with colour graphics, for flow visualization on the complete configuration, and options to select the configuration components for which the computed pressure distributions are to be displayed. Examples are given in Figs. 3 to 5, where pressure distributions are shown for the body, canard control surface and tail surface of the guided weapon of Fig. 2.

3. CFD CODE VALIDATION

Test cases which were used to validate the FAD code range from simple wing shapes to more complex guided weapon and aircraft configurations. Five cases, listed in Table I, are presented to demonstrate the main capabilities and limitations of the code.

TABLE I
FAD Code Validation Test Cases

TEST CASE	PITCH	YAW	CONTROL	MACH
ONERA M6 Wing	✓			0.70, 0.84
AGARD Model "B"	✓			Sub, Trans, Super
USAF Guided Weapon	✓		✓	✓ ✓
NASA Cruise Missile	✓	✓		✓ ✓ ✓
CP-13A Aircraft	✓		✓	0.4, 1.2, 1.6

3.1 Test Case 1: ONERA M6 Wing

The ONERA M6 wing is a research wing with a simple trapezoidal planform of low sweep (30° at leading edge) and moderate aspect ratio (3.8). Its planform was approximated by the grid shown in Fig. 6. The wing pressure and sectional lift coefficient distributions were computed for two different lifting cases: a subcritical case ($M=0.70$, $\alpha=6^\circ$) and a supercritical case ($M=0.84$, $\alpha=3^\circ$). The computed pressure distributions are shown in Figs. 7 and 8. The computed spanwise distributions of the sectional lift coefficients are given in Figs. 9 and 10, where they are compared to those available from the wind tunnel data of Ref. 5. As shown in Fig. 9, very good agreement between theory and experiment was obtained for the subcritical case. The agreement between theory and experiment is not as good for the supercritical case, as shown in Fig. 10. However it is fairly reasonable, considering that the computed value of the wing lift coefficient (0.234) is 8% above that obtained from the wind tunnel.

3.2 Test Case 2: AGARD Model "B"

The AGARD model B is a wing-body calibration model which was standardized for high speed wind tunnel testing, but for which exists a wealth of data down to Mach 0.7 (Refs. 6 to 8). Its geometry is given in Fig. 11. The cylindrical body is 8.5 caliber long with a 3.0 caliber ogive nose. The wing has a delta planform with a 60° leading-edge sweep. The model normal force and pitching moment slopes due to angle of attack (C_{N_α} and C_{m_α}) were computed for subsonic, transonic and supersonic Mach numbers. The variation with Mach number of the computed C_{N_α} and C_{m_α} derivatives are compared to wind tunnel data (Refs. 6 and 7) in Figs. 12 and 13. As shown in these figures, the variation with Mach number of both derivatives is well predicted by the FAD code. The computed values are well within the bounds of the experimental data for subsonic and transonic speeds, but on the outer edge for supersonic. Considering that only 28 elements were used to model the wing, a finer grid would have yielded better accuracy.

3.3 Test Case 3: USAF Guided Weapon

The USAF guided weapon, which is shown in Fig. 2, features a symmetrical canard configuration with movable cruciform control surfaces located on the forward body and mounted in line with fixed cruciform tail surfaces of low sweep and moderate aspect ratio. The configuration angle of attack and control deflection derivatives were computed for subsonic and low transonic Mach numbers. The computed values of C_{N_α} and C_{m_α} are compared to those of wind tunnel data in Figs. 14 and 15. The wind tunnel data was obtained from Ref. 9. The comparison shows good agreement between theory and experiment up to Mach 0.8 where the results start to diverge because of theory limitations. The theory being linear it is also valid only in the low-angle-of-attack region of attached flow where viscous effects are small. This is shown in Fig. 16, where the theoretical and experimental variations with α of the configuration normal force coefficient are given at Mach 0.6. No disagreement is noticeable between theory and experiment for angles of attack below 5° . However, the theoretical predictions fall short of the experimental data above this value. The experimental normal force coefficient is 15% higher than its predicted value at the test maximum α of 13° . The development of a vertical vortex sheet at the tip of the tail surface may account for the difference. As the angle of attack increases, the vortex sheet starts to act as an endplate changing the tail lift distribution over its planform. In the outboard region of the tail the local lift is increased and the net effect is to raise the value of the normal force coefficient above its value predicted by linear potential flow theory.

3.4 Test Case 4: NASA Cruise Missile

The NASA cruise missile model, which is shown in Fig. 17, has a wing with 58° of leading-edge sweep and conventional aft tail surfaces with 63° of leading-edge sweep. The wing and tail surfaces are attached to a body of circular cross section. A simulated equipment fairing is attached along the center line on the underside of the body. The configuration longitudinal and lateral aerodynamic characteristics were computed as outlined in Section 2.0 for subsonic, transonic and supersonic Mach numbers. The results for the lift-curve slope, C_{L_α} , and the aerodynamic center, ac , are given in Figs. 18 and 19, while those for the sideslip derivative, C_{Y_β} , and the lateral center of pressure, c.p., are given in Figs. 20 and 21. Overall, the comparison of the theoretical results with the wind tunnel data of Ref. 10 reveals the agreement between theory and experiment even in the transonic region. This is due in part to the high sweep angle of the wing and tails. The location of the ac , expressed in percent of wing mean aerodynamic chord, was especially well predicted by theory. As shown in Fig. 19, the ac location is constant over the subsonic range, and shifts rearward about 25% from subsonic to supersonic speeds.

3.5 Test Case 5: CF-18A Aircraft

The CF-18A Hornet is a single-place, twin-engine supersonic fighter/attack aircraft built by McDonnell Douglas Corporation. Its configuration is characterized by a mid-wing with a large highly swept leading-edge extension, all-moving horizontal tail surfaces and twin vertical tails. The wing is moderately swept (20° at $c/4$) and its aspect ratio is equal to 3.5. The finite element grid which was used to approximate the aircraft configuration planform is shown in Fig. 22. Planform subsonic and supersonic load distributions were computed for unit angle of attack and horizontal tail control deflection cases. Longitudinal aerodynamic characteristics were determined by integration of the load distributions. Computed values of the aircraft lift-curve slope and aerodynamic center are given in Table II at $M=1.2$ and 1.6 , for which wind tunnel data was available (Ref. 11). As shown in this table, the discrepancy between theoretical and experimental data is less than 5% for the lift-curve slope. Also, the location of the aerodynamic center was predicted within 10% of the wing mean aerodynamic chord. The aircraft theoretical incremental pressure coefficient distribution due to a one degree deflection of the horizontal tail surfaces is shown in Fig. 23 for a low speed condition. Experimental horizontal tail power data was available only for this condition. Computed horizontal tail control effectiveness and power coefficients are given in Table III and compared to the experimental data. The comparison shows excellent agreement between theoretical and experimental data, the discrepancy between the two sets of data being less than 5%.

TABLE II
FAD Code Validation Test Case 5
CF-18A Aircraft
Supersonic Lift-Curve Slope and AC

DATA	C_{L_α} (deg^{-1})		ac ($\% \bar{c}$)	
	$M=1.2$	$M=1.6$	$M=1.2$	$M=1.6$
Theory	0.100	0.075	49	64
Wind Tunnel	0.100	0.072	58	58
% Discrepancy	0	4	9	6

TABLE III
FAD Code Validation Test Case 5
CF-18A Aircraft
Low Speed Horizontal Tail Power

DATA	$C_{L_{\delta_H}}$ (deg^{-1})	$C_{m_{\delta_H}}$ (deg^{-1})
theory	0.0146	- 0.0175
Wind Tunnel	0.0150	- 0.0180
% Discrepancy	3	3

4. CONCLUDING REMARKS

A computational fluid dynamics code has been described and some test cases which were used for its validation have been presented. The combination of small perturbation theory and finite element techniques has been shown to provide valid results in the subsonic and supersonic speed regimes for simple and complex configurations at low incidences. Limitations at transonic speeds and at high angles of attack have been discussed. Based on the results of the validation, it is concluded that this CFD code can be used with confidence during the exploratory phase of a project, to predict some of the aerodynamic characteristics of flight vehicles of fairly complex shapes such as guided weapons and supersonic fighter aircraft.

5. REFERENCES

1. Paul Kutler, "A Perspective of Theoretical and Applied Computational Fluid Dynamics", AIAA Journal, March 1985.
2. "Applications of Computational Fluid Dynamics in Aeronautics", AGARD Conference Proceedings No. 412, November 1986.
3. "ANVIL-4000 Reference Manual", Manufacturing and Consulting Services Inc., July 1985.
4. F.A. Woodward, "Analysis and Design of Wing-Body Combinations at Subsonic and Supersonic Speeds", Journal of Aircraft, November - December 1968.
5. V. Schmitt, D. Destarac and B. Chaumet, "Viscous Effects on a Swept Wing in Transonic Flow", ONERA T.T. No. 1983-73, July 1983.
6. H. Valk and J.J. Van der Zwaan, "A Review of Measurements on AGARD Calibration Model B in the Transonic Speed Range", NLR Report MP 197, 1960.
7. J.P. Hartzuiker, "A Review of Measurements on AGARD Calibration Model B in the Mach Number Range from 1.4 to 8", NLR Report MP 200, 1961.
8. "Commissioning Report of the DREV 2 ft. Indraft Tunnel", DSMA Report No. 695/912, March 1977.
9. Eglin Air Force Base, unpublished wind tunnel data, 1969.
10. M.L. Spearman and I.K. Collins, "Aerodynamic Characteristics of a Swept-Wing Cruise Missile at Mach Numbers from 0.50 to 2.86", NASA TN D-7069, November 1972.
11. G.E. Peters, S.L. Parker, C.M. Pully, B.R. Williams, "F/A-18 Basic Aerodynamic Data", McDonnell Douglas Corp. Report No. MDC A8575, March 1984.

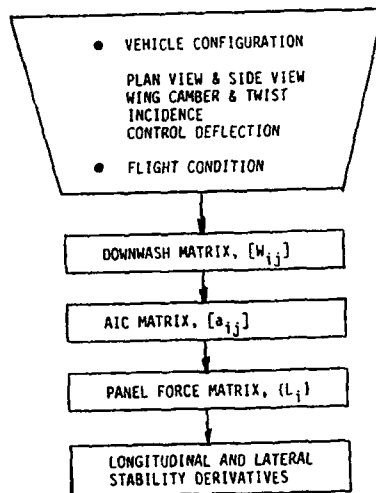


FIGURE 1 - FAD: Finite element aerodynamics program

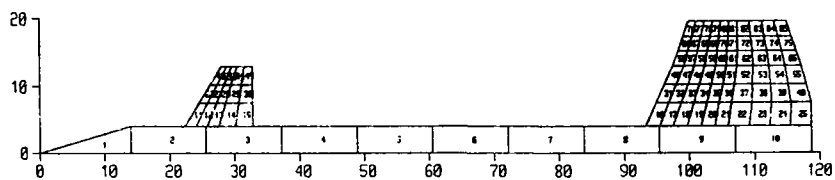
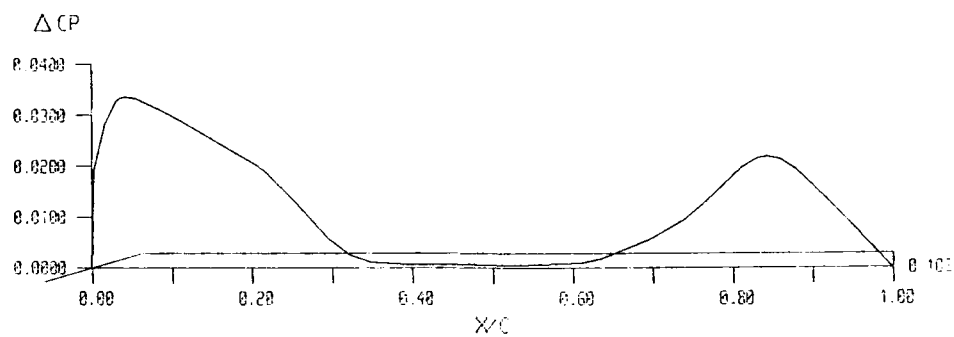


FIGURE 2 - Guided weapon aerodynamic grid

FIGURE 3 - Guided weapon body pressure distribution ($M=0.6$, $\alpha=1^\circ$)

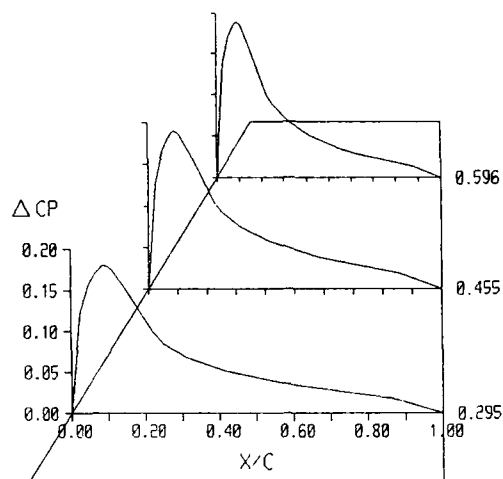


FIGURE 4 - Guided weapon canard pressure distribution ($M=0.6$, $\alpha=1^\circ$)

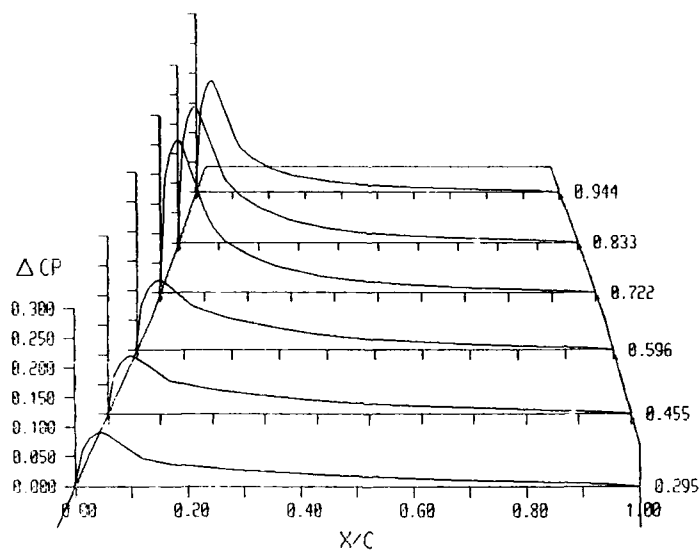


FIGURE 5 - Guided weapon tail pressure distribution ($M=0.6$, $\alpha=1^\circ$)

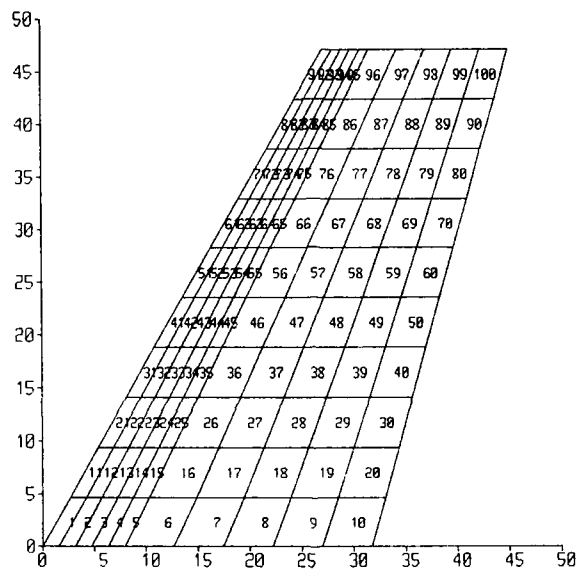


FIGURE 6 - ONERA M6 wing aerodynamic grid

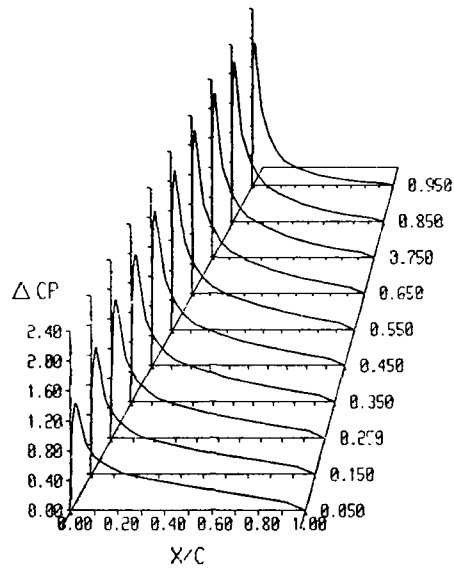


FIGURE 7 - ONERA M6 wing planform pressure distribution ($M=0.7$, $\alpha=6^\circ$)

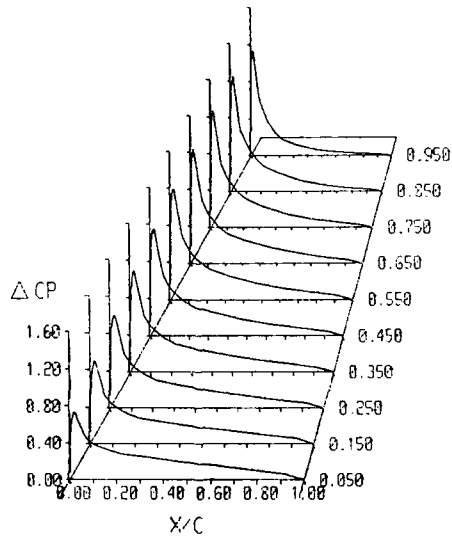
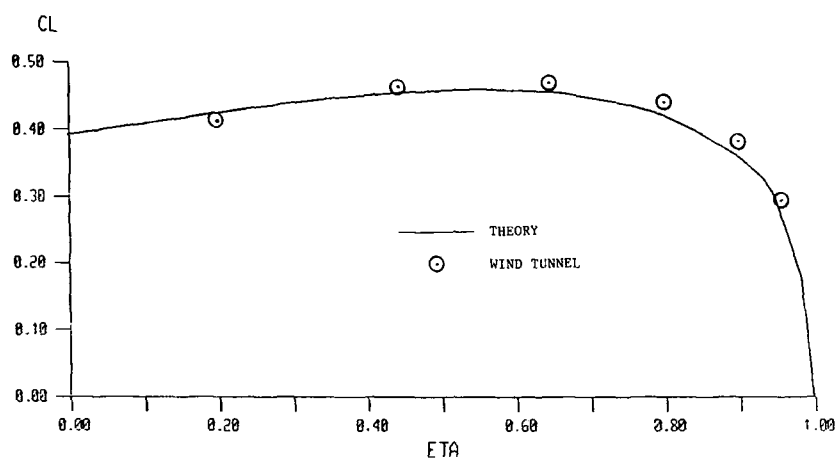
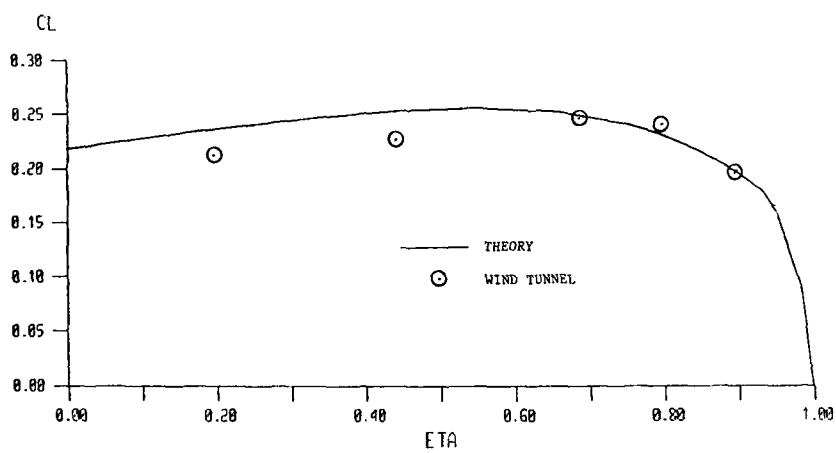


FIGURE 9 - ONERA M6 wing planform pressure distribution ($M=0.84$, $\alpha=3^\circ$)

FIGURE 9 - ONERA M6 wing spanwise lift distribution ($M=0.7$, $\alpha=6^\circ$)FIGURE 10 - ONERA M6 wing spanwise lift distribution ($M=0.84$, $\alpha=3^\circ$)

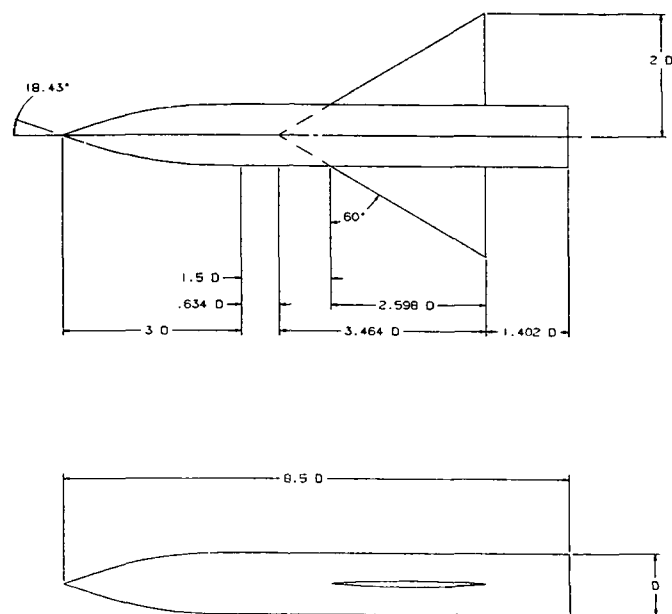


FIGURE 11 - AGARD model "B" geometry

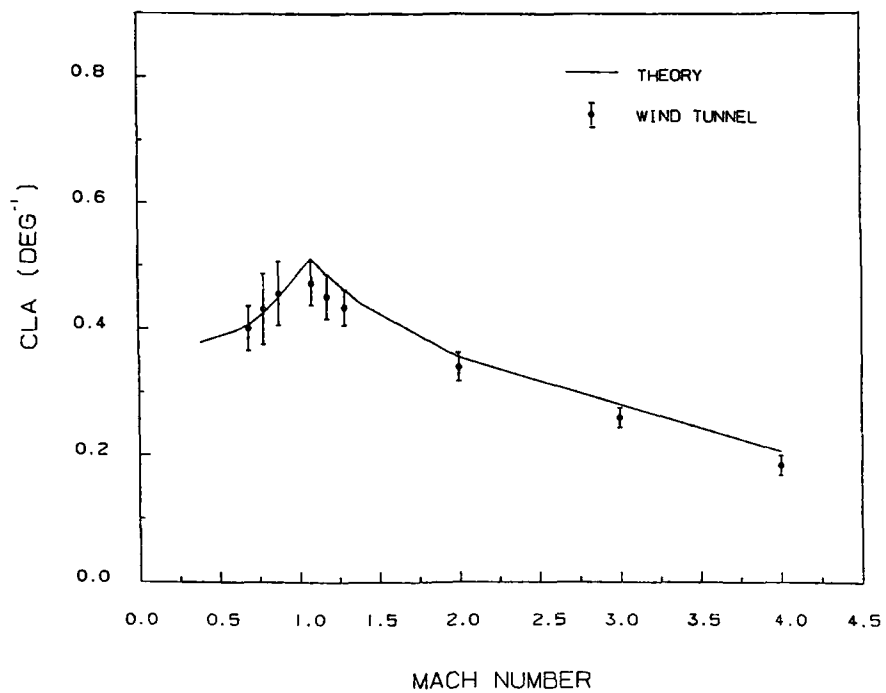


FIGURE 12 - AGARD model "B" normal force slope vs Mach number

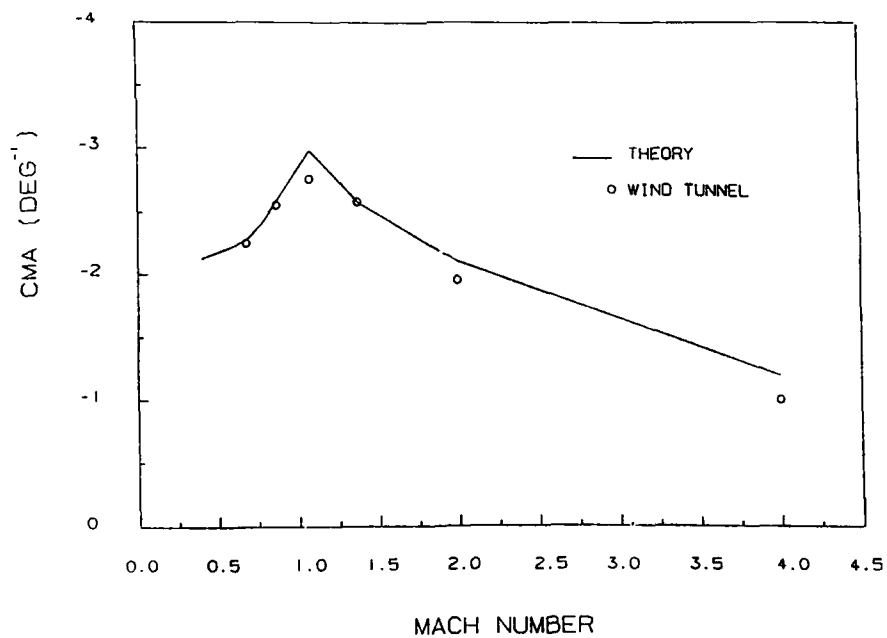


FIGURE 13 - AGARD model "B" pitching moment slope vs Mach number

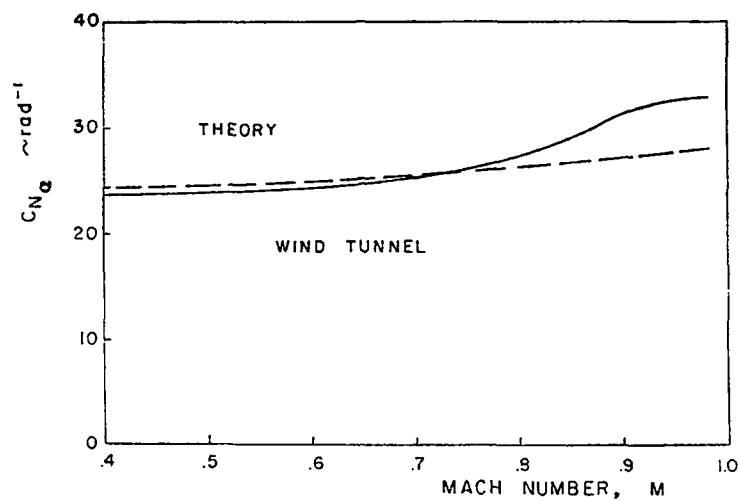


FIGURE 14 - Guided weapon normal force slope vs Mach number

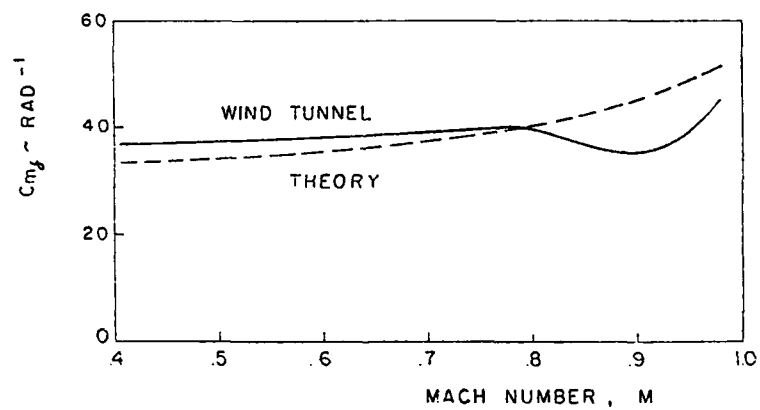


FIGURE 15 - Guided weapon canard control power vs Mach number

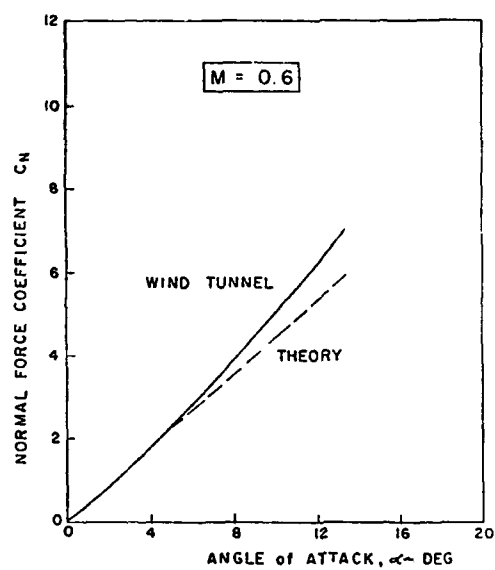


FIGURE 16 - Guided weapon normal force vs angle of attack

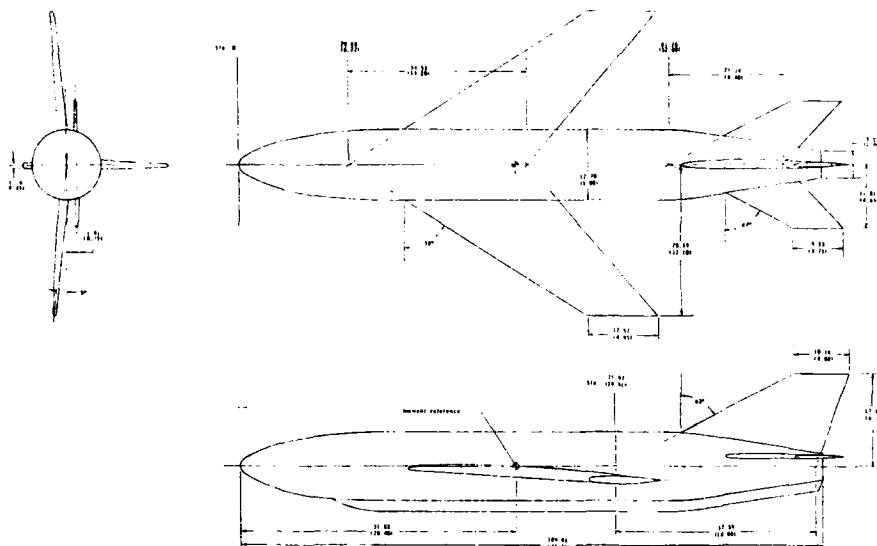


FIGURE 17 - NASA cruise missile model general arrangement

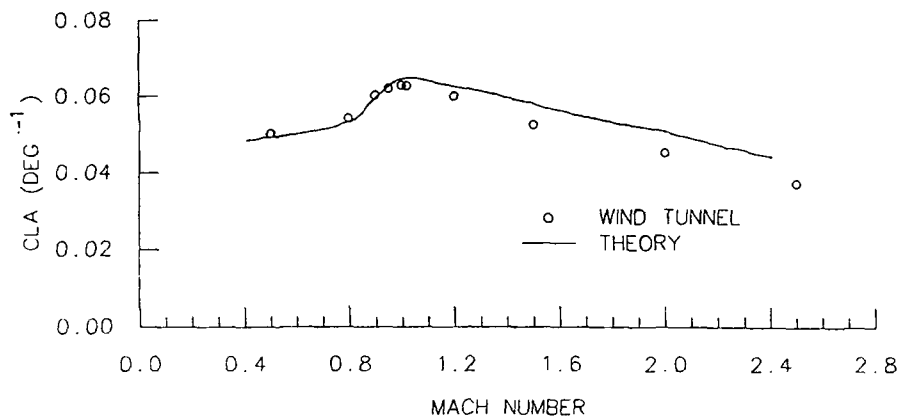


FIGURE 18 - NASA cruise missile model lift-curve slope vs Mach number

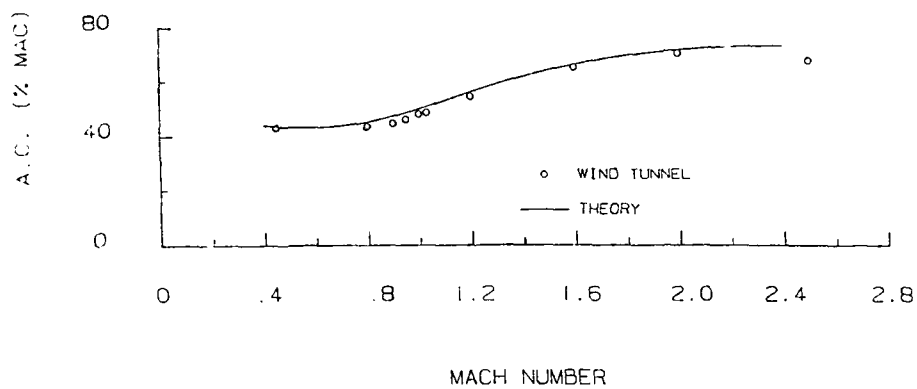


FIGURE 19 - NASA cruise missile model aerodynamic center vs Mach number

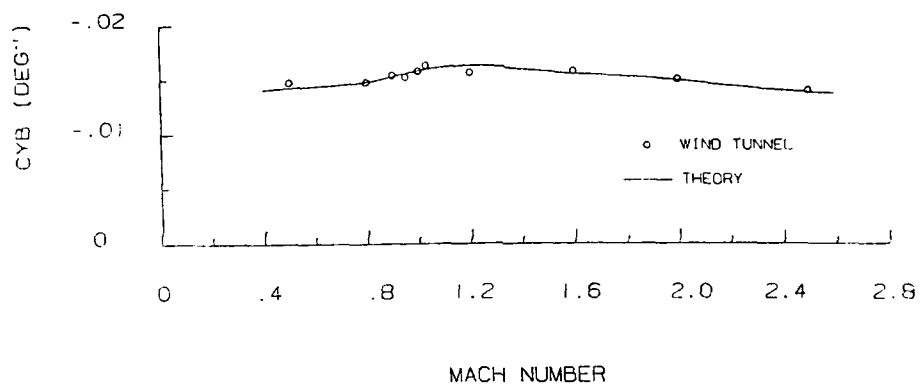


FIGURE 20 - NASA cruise missile model sideslip force derivative vs Mach number

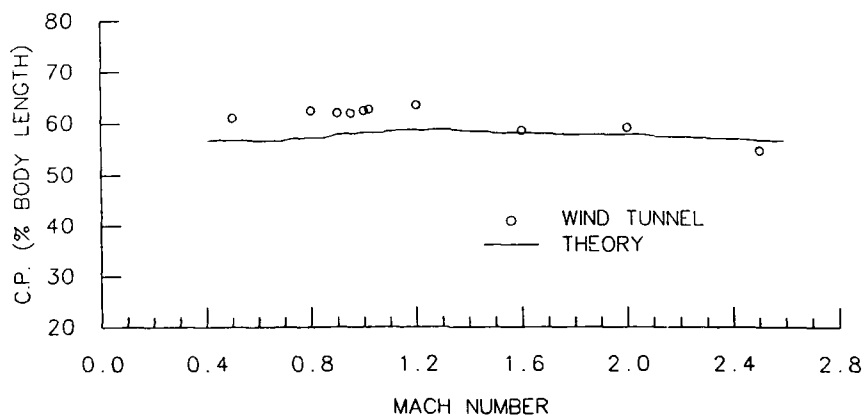


FIGURE 21 - NASA cruise missile model lateral center of pressure vs Mach number

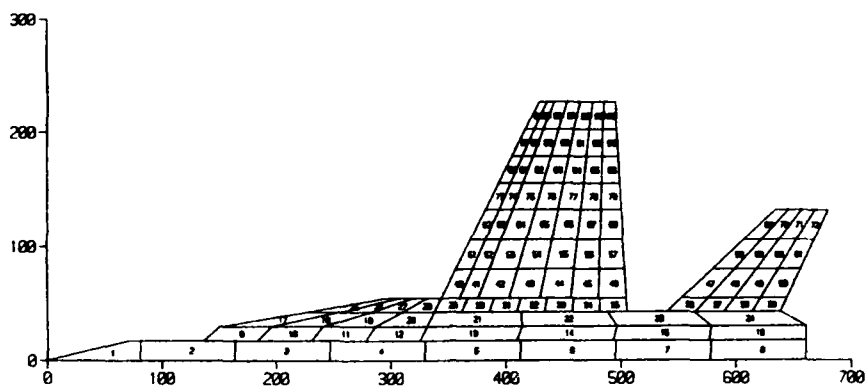
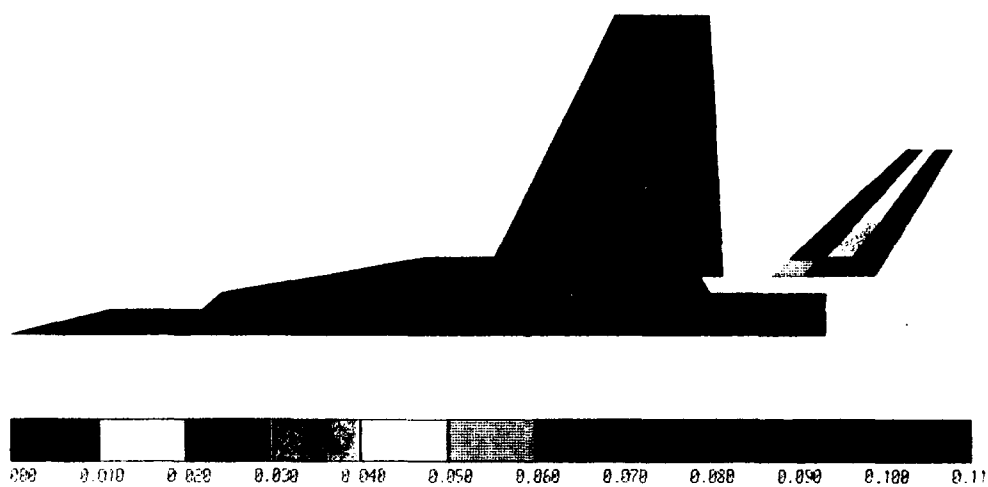


FIGURE 22 - CF-18A aircraft aerodynamic grid

FIGURE 23 - CF-18A aircraft pressure distribution due to horizontal tail deflection
 $M=0.4$, $\alpha=0$, $\delta_H=1^\circ$

Comparison of Theory and Experiment for Four Supercritical, Low Drag Airfoils

D.J. Jones, M. Khalid
National Aeronautical Establishment
National Research Council
Montreal Road
Ottawa, Canada
K1A 0R6

and

B. Eggleston
deHavilland Aircraft
Downsview, Ontario
Canada

Summary

A comparison of a revised BGK code, GRUMFOIL, and the DRELA code from MIT (modified by Boeing) is here presented. The results are compared against experimental data for four different airfoils with relative thickness from 10% to 21%.

Nomenclature

b	tunnel width	k_m	parameter used in sidewall correction
c	chord (12" for 16% airfoil, otherwise 10")	$M_{c,b}$	Barwell's sidewall corrected Mach
C_D	drag coefficient	number	
C_{D_v}	viscous drag in GRUMFOIL	$M_{c,m}$	Murthy's sidewall corrected Mach
C_{D_w}	drag measured by traversing the wake	number	
C_L	lift coefficient	M_T	tunnel Mach number
C_{L_B}	lift coefficient measured by the balance	M_∞	freestream Mach number
C_{L_c}	corrected lift coefficient	P_0	stagnation pressure
C_{L_p}	pressure integrated lift coefficient	P_∞	freestream static pressure
C_M	quarter chord pitching moment	R_c	chord Reynolds number
C_p	pressure coefficient	x	chordwise distance
C_{p_c}	corrected pressure coefficient, also $C_{p,c}$	α	angle of incidence
$C_{p,m}$	pressure coefficient corrected according to Murthy	β	$\sqrt{1-M_\infty^2}$
H	boundary layer shape factor	δ^*	boundary layer thickness
k	parameter used in sidewall correction	$\Delta\alpha$	α correction
		ΔM	Mach number correction ($M_\infty = M_T + \Delta M$)
		ΔM_m	sidewall correction to Mach number according to Murthy

1. Introduction

This paper shows a comparison of three different two-dimensional transonic airfoil theories and compares them to experimental data obtained in the NAE 1.5 m x 1.5 m blowdown wind tunnel with a 38 cm wide 2-D insert. Four different airfoils of 10, 13, 16 and 21% maximum thickness are considered in the study.

Previous comparisons made at NAE have been made using a revised Bauer, Garabedian and Korn (BGK) [1] code. The comparison of theory and experiment after applying an upper and lower wall correction has always looked fairly reasonable in most cases, even though BGK uses the non-conservative formulation. Recently, however, GRUMFOIL [2,3] was made available to NAE through a cooperative project with NASA, Langley on the CAST 10 airfoil. We were therefore interested in studying the predictive capability of GRUMFOIL for our current four airfoils. Lynch [4,5] had previously compared GRUMFOIL results against Douglas data obtained in the NAE tunnel and had found good agreement if a four wall correction procedure, due to Murthy [6], was applied to the wind tunnel results. The necessity for the four wall correction, rather than the standard upper and lower wall correction only [7], is not clear since the sidewall boundary layer growth is controlled in the NAE tunnel by applying sidewall suction close to, and around, the airfoil. The suction is intended to control the boundary layer so that it is roughly parallel to the sidewalls and hence keep the flow two-dimensional. This two-dimensionality has been confirmed many times with flow visualisation. Nevertheless, in order to be consistent with Lynch's analysis we have here applied the same four wall correction when comparing with GRUMFOIL.

The third code used in the comparison is an MIT code due to DRELA [8,9] and modified by Boeing Commercial Airplane Co. [10]. This is a full Euler code with boundary layer accounted for by the displacement thickness. With this code it was also found necessary to apply the four wall correction procedure in order to obtain a meaningful match of theory and experiment. A major feature of the DRELA code, unlike the others, is the inverse design capability, which is easy to use and is consistent with the analysis mode - making it a powerful tool for airfoil development.

The four airfoils used in the comparison were designed over the past several years beginning with the thicker foils (16 and 21%). At that time NAE and deHavilland were interested in thick wing supercritical wing technology at a lift coefficient of about 0.6. They were designed with slightly favourable pressure gradients up to the shock so that laminar flow would be encouraged. They were also designed to have good drag performance under turbulent flow conditions. The earlier results were encouraging enough to prompt a design of the thinner 10 and 13% sections.

Complete tests of all four airfoils were made for Reynolds numbers from about 6 million (based on chord) up to 20 million and for a Mach number range from about 0.2 to beyond drag rise. Lift coefficients from zero to post $C_{L_{max}}$ were covered in most cases.

Since the NLF feature of these airfoils was the main part of the study, very few transition fixed runs were made for the thinner airfoils (perhaps 6 runs for each). However, rather than assess the airfoil codes under more complicated transition free cases, we decided in this paper to concentrate solely on the transition fixed data. The computer codes were then much more robust and results could be obtained relatively easily. Transition was fixed in all cases at 7% and 15% chord on the upper and lower surfaces respectively.

Similar comparisons to those made here were reported in a recent viscous transonic airfoil workshop [11]. Several computer codes were compared with experimental data. These codes included inviscid-boundary layer coupling methods including GRUMFOIL and ISES (DRELA and Giles) and a non-conservative code by Desai and Rangarajan [12]. Also several Navier-Stokes codes were included. The experimental data was taken from tests on NACA0012 and RAE2822. Also a 'Jones' airfoil was included for which there was no experimental data.

In his concluding remarks on the workshop [11] Holst, rather wisely, left specific conclusions about which methods are superior or inferior to the reader. The only obvious conclusion apparent to the present authors is that the non-conservative formulation [12], similar to BGK in that respect, generally showed a trailing edge pressure that was too high. This is confirmed by our own experiences as shown later.

The present paper starts by describing the airfoil computer codes. The geometry of the four airfoils is then outlined followed by a description of the wind tunnel facility. Next an interesting method for extracting experimental wave drag and viscous drag is presented and finally results of the comparison are given.

2. THE THREE AIRFOIL CODES

The first code used [1] is that developed by Bauer, Garabedian and Korn, which was later modified to include Jameson's fast solver method. The method is non-conservative and uses, in our case, Green's lag entrainment boundary layer method [13] for the turbulent flow and a compressible Thwaites method for laminar flow. This is in contrast to the original code which used the Nash-MacDonald theory with no allowance for laminar boundary layer growth. The viscous effects are simulated by boundary-layer displacement additions to the airfoil surface while the wake is modelled as a constant thickness extension of the trailing edge. An iterative inviscid-boundary layer approach is used on both a coarse and fine mesh, the latter having 161 points on the airfoil. Due to the code being non-conservative mass is created at the shock but a mass-flux correction is applied to the drag. This code will be designated BGK for future reference in the paper.

Melnik's GRUMFOIL code [2,3] was also used in the comparison. This is a fully conservative formulation using a modified Green's lag-entrainment method and Thwaites' integral method for the laminar flow up to transition. The turbulent boundary layer solution employs Carter's semi-inverse scheme and a revised form of Green's method which is used on the airfoil and is continued into the wake. The wake, wake curvature effects and the interaction effects at the trailing edge are all incorporated into the code although the analysis is strictly true only for airfoils with cusped trailing edges. A surface source velocity method is used to account for boundary layer effects. In order to be specific in the options used with GRUMFOIL they were: IM1NB = 3, INCE = 2 and ICF = 2 (as identified in Ref. 3).

The final code used was the Drela code [8] (referred to as DRL on the graphs but also known as ISES [9]). This code was developed by Drela as a Ph.D. thesis at M.I.T. Its use was made available to the present authors through the courtesy of the Boeing Commercial Airplane Company in Seattle. The Boeing version of the code is slightly different to the original version. In the original form Drela solves the full Euler equations but in a streamline coordinate system which has the advantage of reducing the number of unknowns per grid node from four to two. In the supersonic zone artificial dissipation is included by using upwinded velocities. The turbulent boundary layer and wake region are solved from the compressible momentum integral formulation with a lag-dissipation closure. In the laminar region a two-equation model is used rather than the more usual Thwaites' one-equation model; this is shown to give better accuracy than the latter when compared to a full finite difference solution. Transition is predicted using a spatial amplification theory based on the Orr-Sommerfeld equation. The program does not model the shock-boundary layer interaction explicitly nor does it account for the wake curvature aft of the trailing edge. Displacement thickness addition is used to account for the boundary layer.

Drela solves the entire equation set including the inviscid, viscous and matching conditions as a coupled system by a global Newton method. In practice the method is quite efficient (about one minute on a Cray 2) and fairly robust particularly when doing a sweep of α or C_L values.

In their modification of the code Boeing [10] have incorporated a better modelling of the dissipation coefficient in the integral turbulent boundary layer equation. They show that their improvement gives better agreement with experiment than the original code and also they show improvement over BGK results (Program H, ref 1) when a comparison is made for several airfoils including RAE 2822.

3. THE FOUR AIRFOILS

The four airfoils under study (Fig. 1) were designed jointly by NAE and deHavilland. The study of this family of natural laminar flow airfoils has been continuing since 1982. References 14, 15, and 16 describe some of the work carried out on the 16 and 21% airfoils while a report to be shortly released covers the total series [17].

The airfoils are of 10, 13, 16 and 21% maximum thickness to chord ratios, designated NAE 80-060-10(1), NAE 76-060-13(1), NAE 72-060-16(1) and NAE 68-060-21(1) respectively. The digits express design conditions for Mach Number, lift coefficient and maximum thickness to chord ratio. They were all designed using the modified BGK [1] computer code with user interaction to modify the profile shapes such that the pressure distributions in the 'roof top' regions were relatively flat or favourable. This was expected to, and did, give gradients favourable enough to encourage natural laminar flow leading to very low drag figures [16]. Design pressure plots are shown in Fig. 2.

The majority of the tests were done with free transition but a comparison of the codes using fixed transition only is covered in this paper. This is considered as a starting point for further investigation with free transition conditions. We fixed transition strips at 0.07 x/c on the upper surface and at 0.15 x/c on the lower surface. This fixing was done using #320 grit on a strip about 1/10" chordwise.

Some features to note in the geometry of the four airfoils are firstly the trailing edge thickness which is 0.5% in the earlier designs i.e. the 16 and 21% foils while it is 0.2% and 0.1% for the later designs i.e. the 13 and 10% foils. This very thin trailing edge was considered advantageous in drag reduction for NLF airfoil design. The second feature to note is the trailing edge angle which is 6.4°, 6.4°, 9.0° and 11.4° for the 10, 13, 16 and 21% foils respectively. Clearly GRUMFOIL, which is accurate only for small trailing edge angles, may have problems with the latter two airfoils.

4. THE EXPERIMENTAL FACILITY

All the airfoil experiments were carried out in the NAE 1.5 m x 1.5 m wind tunnel with a 38 cm x 1.5 m 2-D insert (Fig. 3). Sidewall suction is applied to control the boundary layer growth on the tunnel sidewalls and so give good two dimensional flow. The tunnel interference effects of the porous top and bottom walls are accounted for by using Mokry and Ohman's theory [7]. The tunnel is capable of high Reynolds number operation due to the high pressures that can be attained. Further information can be found in References 18 and 19.

4.1 WALL CORRECTION PROCEDURES

Our standard NAE correction procedure is based solely on the top and bottom wall corrections of Mokry and Ohman [7]. We surmise that this procedure, although essentially only for top and bottom wall effects also includes any residual (after suction) sidewall effects since these would change the vortex strength (from the lift) and be noticeable in the far field solution which is used in Mokry and Ohman's theory. So far this has yielded satisfactory data which has compared reasonably well with the BGK code for some airfoils.

However, it is known [20] that GRUMFOIL and, it transpired, the DRELA code require an extra correction to the Mach number M_c to provide satisfactory agreement with experimental data. Lynch made a thorough study [4,5] of Douglas data from the NAE tunnel and compared to GRUMFOIL and BGK, with the conclusion that a four wall correction procedure based on Murthy's work [6,7] gave an extra ΔM and so obtained a good comparison of theory and experiment with GRUMFOIL. BGK results, using the two wall correction, were not so good.

The four wall correction procedure used by Lynch and developed by Murthy is based on the earlier work of Barnwell [21] and Sewall [22]. The so called sequential procedure has been applied by Kemp [23] and Murthy [6]. In this procedure the freestream tunnel Mach number is modified for the sidewall boundary layer growth according to the formula

$$\frac{M_{c,b}}{(1-M_{c,b}^2)^{3/4}} = \frac{M_T}{(1-M_T^2+k)^{3/4}}$$

$$k = \frac{2\delta^*}{b} \left(2 + \frac{1}{H} M_T^2\right) \quad (1)$$

The boundary layer properties δ^* and H are measured along the empty tunnel sidewall at the model location. Barnwell and Sewall also modify the pressure coefficients by a factor

$$\left(\frac{M_T}{M_{c,b}}\right)^{2/3}$$

and correspondingly modify force and moment coefficients, in particular C_L . These modified C_L and C_p wall values are then used to compute the top and bottom wall interference corrections. Kemp [23] uses the TWINTAN small disturbance code.

Murthy [6] extended Barnwell and Sewall's theory for the sidewall boundary layer correction to allow for a more realistic variation of the boundary layer induced spanwise velocities. His theory leads to the correction formula.

$$M_{c,m} = \frac{M_T}{(1+k)^{1/2}} \quad (2)$$

Murthy states that this is valid from subsonic to transonic speeds and agrees with Barnwell-Sewall correction at transonic speeds for small values of k . Now k in the NAE tunnel is fairly constant (little variation with M_T) and has a value of about 0.04. Thus in our case the Barnwell-Sewall correction to Mach number would be typically -0.017 while Murthy would give about -0.014.

In addition to computing the corrected Mach number from (2) Murthy also corrects pressures and forces by the factor

$$\begin{aligned} (1+k)^{1/2} & \text{ for subsonic speeds} \\ (1+k)^{1/3} & \text{ for transonic speeds} \end{aligned} \quad (3)$$

Unfortunately in the wind tunnel environment we cannot correct M_T and C_p independently since C_p is determined from a static pressure measurement p_s , a stagnation pressure p_0 and a corrected Mach number as follows. Freestream static and dynamic pressures become

$$p_{s,c} = p_0 / (1 + \frac{1}{5} M_c^2)^{3.5}$$

$$q_{s,c} = 0.7 p_{s,c} M_c^2$$

$$C_{p,c} = \frac{p_s - p_{s,c}}{q_{s,c}}$$

Comparing the corrected C_p to the uncorrected value ($C_{p,T}$) gives

$$C_{p,c} = A C_{p,T} + B \quad (4)$$

where

$$A = \frac{M_T^2}{M_c^2} \left\{ \frac{1 + \frac{1}{5} M_c^2}{1 + \frac{1}{5} M_T^2} \right\}^{3.5}$$

and

$$B = \frac{(1 + \frac{1}{5} M_T^2)^{-3.5} - (1 + \frac{1}{5} M_c^2)^{-3.5}}{0.7 (1 + \frac{1}{5} M_c^2)^{-3.5} M_c^2}$$

Clearly the C_p correction from (4) is quite different to that of Murthy's (3) since (4) involves a shift as well as a scaling. Numerically B is about -0.034 ($M_T = 0.8$, $M_c = 0.785$) which seems to be a significant amount. Likewise A is about 1.023. In contrast Murthy's factor $(1+k)^{1/3}$ is 1.013. This shows that there is a significant difference between Murthy's C_p correction formula and the true wind tunnel correction for C_p . One can see that for $C_{p,T} = -1$ for example (close to a 'rooftop' value) the following values would be obtained.

$$C_{p,m} = -1.013$$

$$C_{p,c} = -1.057$$

Thus it is doubtful to the present authors that the Murthy corrections to C_p are consistent (except for first order small perturbation theory) since a correction to freestream Mach number must lead to a scaling and shifting of the C_p data.

Now if the C_p values were to be modified according to (4) i.e. consistent with a corrected Mach number, we could then compute corrected rail pressures and corrected lift. Then following the sequential approach of Murthy [6] and others [23], we could then apply corrections to account for the upper and lower walls. The method of correction at NAE, due to Mokry and Ohman [7], involves a fast Fourier transform to compute ΔH and $\Delta \alpha$.

However, making such a sidewall correction to M_T and $C_{p,T}$ at the rails will, in Mokry's theory, produce the same final result M_c as if no sidewall correction had been applied. This property is known as autoconvergence or autocorrective and has been noted previously (GARTEUR action group [24]). As a check that this property does hold in practice with actual data we computed one case with differing M_T . The results of this are shown in Table 1. It can be seen that the final Mach number in case A is 0.763 while in case B it is 0.764. Thus in practice the autocorrective feature is confirmed to within 0.001 of Mach number.

It appears then that sequential approach of Murthy [6] will not change the final corrected Mach number obtained after applying Mokry's top and bottom wall correction procedure. Lynch [4] in his comparison of NAE wind tunnel data assumed the correction due to Murthy was simply additive to the top and bottom wall correction of Mokry. This implied that an extra correction, possibly due to local sidewall boundary layer thinning in front of the airfoil, of about 0.014 is also subtracted from M_T as well as Mokry's ΔM which is also of order 0.014 for higher lift cases. Fig. 4 shows the correction to Mach number according to Murthy's formula based on NAE δ^* and H measurements. These were used in comparisons shown later.

Lynch [4] corrected the C_p surface values by first using Mokry's correction to ΔM (as in equation (4)) and then scaled C_p according to the apparently inconsistent formula

$$C_{p,m} = C_{p,T} (1+k)^{1/2} \quad (5)$$

The reason for using the power 1/2 rather than Murthy's 1/3 in transonic cases is not clear. Lynch showed very good agreement between his experimental data and results of GRUMFOIL. We will be doing a similar comparison in this paper to try and repeat Lynch's good agreement for our airfoils, albeit in the knowledge that the scaling (5) is not consistent.

It is worth noting that Murthy [25] later modified his theory to account for the finite aspect ratio of the model width to chord. In this case the k given in (1) is modified to be

$$k_m = 2 \frac{\delta^*}{b} \left(2 + \frac{1}{H} M_T^2 \right) \frac{k_2}{\sinh k_2}$$

where

$$k_2 = \frac{\pi \delta b}{\ell}$$

Murthy recommends using the length scale ℓ equal to $2c$. Numerically this has the effect of making k_m about 0.03 ($k \approx 0.04$) and reducing the Mach Number correction from about 0.014 to about 0.011.

5. EXTRACTION OF VISCOUS DRAG AND WAVE DRAG

Elfstrom's symmetric wake approach [26] is used to extract the individual wave drag and viscous drag contributions to the total drag. This method assumes that the unequal momentum deficit coming from the upper and lower surfaces of the airfoil quickly interact through high viscous shearing forces to produce a symmetrical wake pattern, provided that there are no shock waves present. This assumption was validated by both Lynch [4] and the present authors by examining many profiles. Typical examples are shown in Fig. 5. Scans 2 through 5 are almost symmetric about the peak and thus indicate very little drag due to the shock wave. This is confirmed by looking at the pressure plots, Fig. 6, which show no shocks or very weak ones for these scans.

A further assumption is made that the momentum deficit due to the shock wave is not spread out appreciably by the viscous shearing forces but rather produces a 'tail' in the wake drag curve as shown in Fig. 5. Thus by subtracting the symmetrical part of the drag (usually twice the lower side contribution) from the total wake drag one can evaluate the wave drag. Table 2 shows the breakdown of total drag into viscous and wave drag for the same cases as Fig. 5.

A comparison is made later on of the viscous and wave drag contributions from the three codes and compared to experimental data extracted as outlined above. To extract the two contributions from the theories we used the authors' methods as follows.

For the BGK code the wave drag is computed according to Garabedian's formula given in Ref. 27 (as incorporated in Program H and modified in SCWIII [1]). The boundary layer effects though are computed using Green's boundary layer method [13], rather than Nash-MacDonald in the original code. The viscous drag in the BGK code is computed from the Squire-Young formula.

In GRUMFOIL [2,3] C_D is computed from integration of pressure and skin friction over the airfoil surface. The viscous drag is denoted by C_{D_v} and is computed from the wake momentum thickness far downstream (i.e. 28_∞). It is stated [2] that the difference between C_D and C_{D_v} is a relatively accurate measure of the wave drag. Thus we use Grumfoil's C_{D_v} and $C_D - C_{D_v}$ to represent the viscous and wave drags respectively.

In the DRELA code [8] the total drag is calculated from the momentum deficit obtained by integrating vertically at a station far downstream. The integration includes the viscous wake effect as well as the 'entropy' wake due to the shock. To compute the drag due to the shock wave alone a similar integration is made using local stagnation conditions. In this case we define 'viscous' drag as the difference between total drag and wave drag.

6. RESULTS

6.1 PRESSURE DISTRIBUTION AND DRAG

Firstly, the codes and their operating conditions are summarized below.

BGK - same M_∞ and C_L as experimental M_∞ and C_{Lc}

GRM (GRUMFOIL) - M_∞ determined by applying an extra ΔM to M_∞ , see Fig. 4. This correction is due to Murthy [6] and was used by Lynch [4]. It is thought to be due to sidewall boundary layer effects near the airfoil. This phenomenon is currently under study at NAE.

The lift is obtained by scaling C_{Lc} by $(1+k)^{1/2}$. Experimental pressures C_{pc} are also scaled by the same factor. As pointed out earlier the present authors consider this inconsistent; however Lynch [4] did show good agreement with GRUMFOIL when using this scaling.

DRL (Drela modified by Boeing)

The same adjustments to M_∞ and C_L were made as for GRUMFOIL. Note that small differences may sometimes appear due to slightly different interpretation of ΔM_∞ .

Now, using the above scaling of C_{pc} yields different experimental data (C_{pc} for BGK but $(1+k)^{1/2}C_{pc}$ for GRM and DRL) thus making plots on the same graph difficult. To get around this problem we simply use the same C_{pc} (experimental) on the graph but scale the results of GRM and DRL by $(1+k)^{-1/2}$.

On the plots to follow the notation below has been used.

- M freestream Mach number. Mokry and Ohman correction for the experiment and BGK. A further ΔM correction, possibly sidewall, for GRM and DRL.
- CLP pressure integrated lift value. For GRM and DRL scaled by $(1+k)^{1/2}$.
- RN scaled by approximately $\frac{M_\infty}{M_c}$ for GRM and DRL
- ALP angle of incidence corrected by Mokry and Ohman formula [7]. BGK, GRM and DRL computed to keep the lift at the required value (corrected as above).
- CMP pitching moment from pressure integration
- CDW drag due to the shock wave (see earlier section)
- CDNW drag due to viscous effects (total drag minus CDW)
- CDT total drag
- MMAX maximum Mach number on the upper surface
- MSH Mach number before the shock
- XSH location of shock wave, taken where $M_L = 1.1$

NAE 80-060-10 (1)

A typical almost shockless result is shown in Fig. 7 and a supercritical result in Fig. 8. It can be seen that GRUMFOIL and DRELA give, in the weak shock case, a better prediction of surface pressures. BGK shows lower C_p 's on the upper and lower surfaces and higher pressures in the 'cove' region on the lower surface as well as a higher trailing edge C_p . In the supercritical case GRUMFOIL gives the best prediction of shock location and is generally good overall. BGK shows a post shock acceleration which is typical in other cases also.

As the lift is increased just beyond the linear portion of C_L - α it can be seen (Fig. 9) that GRUMFOIL is generally good except for a strong overshoot aft of the shock. The DRELA code in this case predicts the shock too far forward while BGK is fairly representative of the pressure distribution except for post shock behaviour and the usual lower surface 'cove' region overprediction and trailing edge pressure too high.

In order to draw global conclusions about the comparison of the codes with experiment we present in Fig. 10 charts which show MSH, XSH, MMAX, CDT, CDW and CDNW plotted with experimental values vertically and theoretical values horizontally. An exact match would, of course, have all the points on the 45° line. Note that MSH is not always easy to ascertain as the theoretical shock is spread over 3 mesh points and there may be pressure variation just prior to the shock; likewise in the experiment there may be some amounts of scatter. On the other hand XSH and MMAX are well defined so more trust can be put in these comparisons. Looking at the results for MMAX it is clear that GRM is the best with the other two codes underpredicting maximum Mach number. Also GRM gives very good shock wave predictions except for shocks at around 60-70%.

In the total drag comparison BGK and DRL are generally about 7 counts too low while GRM shows more scatter with a mean about 8 counts too high.

NAE 76-060-13(1)

A typical comparison of C_p is shown in Fig. 11. Again BGK shows a large acceleration after the shock. Both GRM and DRL show very good agreement in this case.

Overall, as shown in Fig. 12, GRM and DRL appear to give the best prediction of MMAX and XSH. For total drag, BGK is about 12 counts too low, DRL 10 counts too low and GRM again shows more scatter and is about 8 counts too high.

NAE 72-060-16(1)

A typical comparison is shown in Fig. 13. It can be seen that BGK is still predicting too high a C_p in the lower surface cove region and at the trailing edge; the post shock acceleration is also present, but this shows now also in the experiment. GRM seems still to give a reasonable prediction with DRL somewhat further from the experiment.

Overall BGK now shows a prediction of XSH and MMAX equally as good as GRM (see Fig. 14) while DRL seems to have far more scatter further from the 45° line.

Drag scatter is in this case far greater than for the 10 and 13% airfoils. BGK indicates levels about 16 counts too low, DRL about 6 counts too low while GRM is very scattered but with a mean close to the 45° line.

NAE 68-060-21(1)

A result near the design condition is shown in Fig. 15. BGK is predicting the shock too far back while GRM seems to give a fair overall pressure prediction (which is surprising given that the airfoil has an 11.4° trailing edge angle). DRL is now showing a larger discrepancy than previously observed.

However at lower incidences where the flow is only just supercritical (Fig. 16) it can be seen that both GRM and DRL do a poor job near the leading edge with too much acceleration on the upper surface and too little on the lower surface. Also GRM is predicting separation at the start of the lower surface cove at about 60% chord. BGK on the other hand is generally well behaved except for over-prediction in the lower surface cove area.

Because of the poor performance of the codes for this airfoil overall plots were not attempted.

6.2 DRAG RISE PREDICTION

For the 10% and 16% airfoils there was sufficient data to estimate drag rise at $C_L = 0.6$, see Fig. 17. It can be seen that drag rise prediction is very good for both airfoils except for BGK being somewhat too low in the case of the thicker foil.

GRM is consistently high in drag levels. BGK is too low up to drag rise while DRL is very good for the 16% foil but too low in drag level for the 10% airfoil.

7. CONCLUSIONS

Three theoretical computer codes - a modified BGK, GRUMFOIL, and the DRLEA code from MIT (modified by Boeing) - have been used and the results compared to data obtained in the NAE 1.5 m x 1.5 m wind tunnel facility. Four different relative thickness airfoils, ranging from 10% to 21%, were considered in the study. Only transition fixed cases were included.

For the 10 and 13% airfoils the GRUMFOIL code seemed to give the best prediction when scaling pressure coefficients and lift by the Murthy factor $(1+k)^{1/2}$ and also changing freestream Mach number again by Murthy's extra correction. This extra correction may be due to sidewall boundary layer growing or diminishing along the sidewall; this is currently under study at NAE. The present authors do not agree with the $(1+k)^{1/2}$ scaling of the pressure coefficient as Murthy but certainly this scaling does produce a good prediction from the GRUMFOIL code as found also by Lynch [4].

For the 16% airfoil the correlations were not quite as good as for the thinner foils; BGK and GRUMFOIL showed equally well in the comparisons.

In the case of the 21% airfoil none of the codes was satisfactory. GRUMFOIL showed a reasonable prediction near the design condition but gave a poor prediction at lower lift conditions particularly near the leading edge.

Further studies are being undertaken to determine whether a Mach number correction due to the sidewall boundary layer is needed. If so, then correct scaling of C_p must be applied and further correlations made.

The present study attempted to isolate wave drag from viscous drag following the process described by Elfstrom [26]. This may be a useful method for future analysis of drag components.

8. REFERENCES

1. Bauer, F., Garabedian, P.R. and Korn D. Supercritical Wing Sections III. Lecture Notes in Economics and Mathematical Systems. No. 150, 1977.
2. Meirik, R.E., Chow, R.R., Mead, H.R. and Jameson, A. An Improved Viscid/Inviscid Interaction Procedure for Transonic Flow over Airfoils. NASA CR-3805, October 1985.
3. Mead, H.R. and Meirik, R.E. GRUMFOIL: A Computer Code for the Viscous Transonic Flow over Airfoils. NASA CR-3806, October 1985.
4. Lynch, F.T., Bui, M.H. and Patel, D.R. Some Fundamental Concepts in the Design, Analysis and Testing of Transonic Airfoils. Douglas Aircraft Co. Paper 7579, October 1985.
5. Lynch, F.T. and Johnson, C.B. Wind Tunnel Sidewall Boundary Layer Effects in Transonic Airfoil Testing - Some Correctable but Some Not. Paper No. 18. Agard Symposium on Aerodynamic Data Accuracy and Quality. Sept. 1987.
6. Murthy, A.V. A Simplified Fourwall Interference Assessment Procedure for Airfoil Data Obtained in the Langley 0.3 Meter Transonic Cryogenic Tunnel. NASA CR-4042. Jan. 1987.
7. Mokry, M. and Ohman, L.H. Application of the Fast Fourier Transform to Two-Dimensional Wind Tunnel Wall Interference. Journal of Aircraft, Vol. 17, June 1980.
8. Drela, M. Two-Dimensional Transonic Aerodynamic Design and Analysis Using the Euler Equations. Ph.D. Thesis, MIT, 1985.
9. Drela, M. and Giles, M.B. ISES: A Two-Dimensional Viscous Aerodynamic Design and Analysis Code. AIAA Paper 86-0424. Jan. 1987.
10. Depak Om. Private Communication with Boeing Commercial Airplane Co.
11. Holst, T.L. Viscous Transonic Airfoil Workshop Compendium of Results. AIAA Paper 87-1460.
12. Desai, S.S. and Rangarajan, R. Viscous Transonic Flow over Airfoils Using Transonic Full Potential Equation in a System of Cartesian Coordinates. AIAA Paper 87-0411, Jan. 1987.
13. Green, J.E., Weeks, D.J., and Brooman, J.W.F. Prediction of Turbulent Boundary Layers and Wakes in Compressible Flow by a Lag-Entrainment Method. RAE-TR-72231, 1973.
14. Jones, D.J. and Khalid, M. Analysis of Experimental Data for a 21% Thick Natural Laminar Flow Airfoil, NAE 68-060-21:1. NRC Report NAE-AN-34, Oct. 1985.
15. Khalid, M. and Jones, D.J. Further Studies on the 21% Thick, Supercritical NLF Airfoil NAE 68-060-21:1. NRC Report NAE-AN-41, Sept. 1986.
16. Eggleston, B., Poole, R.J.D., Jones, D.J. and Khalid, M. Thick Supercritical Airfoils with Low Drag and Natural Laminar Flow. J. of Aircraft, Vol. 24, No. 6, June 1987, 405-411.
17. Khalid M. and Jones D.J. Experimental and Theoretical Studies of a Family of Natural Laminar Flow Airfoils. NRC Report to be published.
18. Ohman L.H. The NAE 15" x 60" Two-Dimensional Test Facility; New Features and Some Related Observations, Results of New Centreline Calibration at 20.5% Porosity. NRC Report LTR-HA-15, 1973.
19. Ohman L.H., Brown D., Bowker A.J. and Ellis F.A. Recent Improvements to the NAE 5 ft x 5 ft Blowdown Wind Tunnel. NRC Report AN-31, 1985.
20. Meirik R.E. Private communication
21. Barnwell R.W. Similarity Rule for Sidewall Boundary-Layer Effect in Two-Dimensional Wind Tunnels. AIAA J1., Vol. 18, Sept. 1980, pp. 1149-1151.
22. Sewall, William G. The Effects of Sidewall Boundary-Layer in Two-Dimensional Subsonic and Transonic Wind Tunnels. AIAA J1. Vol. 20, Sept. 1982, pp. 1253-1256.
23. Kemp, W.B., Jr., Combined Four-Wall Interference Assessment in Two-Dimensional Wind Tunnel Tests. AIAA Paper 82-0586.
24. GARTEUR Action Group AD (AG-23) Two-Dimensional Transonic Testing Methods. NLR TR-83086U, July 1981.
25. Murthy, A.V. Effect of Aspect Ratio on Sidewall Boundary Layer Influence in Two-Dimensional Airfoil Testing. NASA CR-4008. Sept. 1986.
26. Elfstrom, G.M. Extraction of Wavedrag from Airfoil Wake Measurements. AIAA Paper No. 81-0291, Jan. 1981.
27. Garabedian, P.R. Computation of Wave Drag for Transonic Flow. Journal d'Analyse Mathematique, Vol. 30 1976.

9. ACKNOWLEDGEMENTS

The authors wish to thank the Boeing Commercial Airplane Company for permitting the deHavilland Division to use the modified DRELA code at the Boeing Computer Services facility in support of this work.

CASE A. RUN 32966

	M	α	Q	C_{LB}	C_M
Uncorrected	0.771	3.39	39.93	0.704	-0.0867
Corrected	0.763	2.72	39.41	0.714	-0.0879

CASE B. RUN 32966

Uncorrected	0.748	3.39	38.39	0.732	-0.0902
Corrected	0.764	2.69	39.43	0.714	-0.0878

TABLE 1. Effect of Different M_p on the Top and Bottom Wall Correction Using Mokry and Ohman's Theory [7].

RUN	PROBE				DRAG		
	SCAN	VISC.	AVG.	WAVE	AVG.	TOTAL	AVG.
31278	1	1	0.0125		0.0022		0.0147
31278	1	2	0.0118		0.0016		0.0134
31278	1	3	0.0106	0.0116	0.0013	0.0017	0.0120
31278	1	1	0.0109		0.0002		0.0110
31278	1	2	0.0106		0.0007		0.0112
31278	1	3	0.0101	0.0105	0.0007	0.0005	0.0107
31278	1	1	0.0106		0.0004		0.0110
31278	1	2	0.0107		0.0004		0.0111
31278	1	3	0.0101	0.0105	0.0003	0.0004	0.0104
31278	1	1	0.0108		0.0003		0.0111
31278	1	2	0.0110		0.0001		0.0111
31278	1	3	0.0106	0.0108	0.0002	0.0002	0.0108
31278	1	1	0.0111		0.0001		0.0113
31278	1	2	0.0101		0.0011		0.0112
31278	1	3	0.0109	0.0107	0.0001	0.0005	0.0110
31278	1	1	0.0114		0.0002		0.0116
31278	1	2	0.0125		0.0003		0.0129
31278	1	3	0.0110	0.0116	0.0015	0.0007	0.0124
31278	1	1	0.0104		0.0045		0.0149
31278	1	2	0.0118		0.0042		0.0160
31278	1	3	0.0108	0.0110	0.0042	0.0043	0.0151
31278	1	1	0.0127		0.0073		0.0200
31278	1	2	0.0122		0.0087		0.0209
31278	1	3	0.0129	0.0126	0.0061	0.0074	0.0190
31278	1	1	0.0204		0.0187		0.0391
31278	1	2	0.0130		0.0183		0.0313
31278	1	3	0.0113	0.0149	0.0150	0.0173	0.0263
31278	1	1	0.0423		0.0251		0.0674
31278	1	2	0.0382		0.0182		0.0563
31278	1	3	0.0164	0.0323	0.0229	0.0221	0.0393

TABLE 2. Drag, CDW, on Three Wake Probes Downstream of the Model (the fourth, nearest the wall, is ignored)

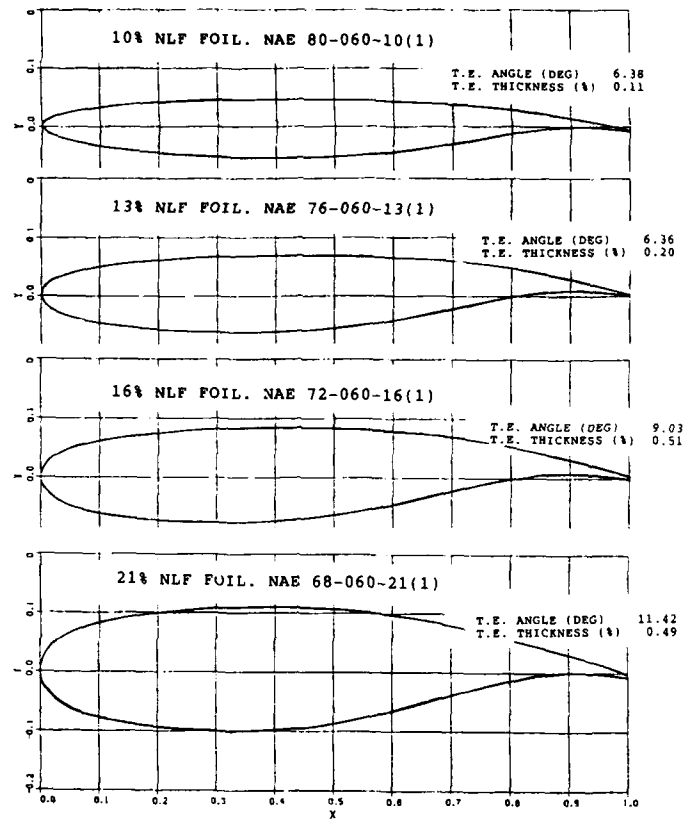


FIG 1. The Four Airfoils Tested in the NAE Facility

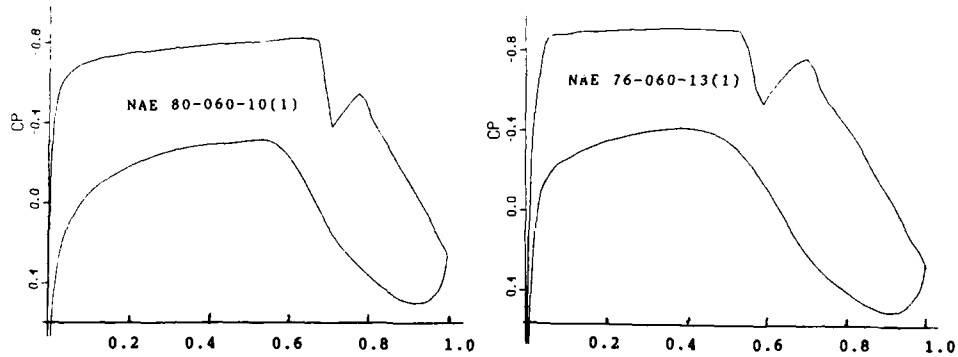


FIG 2. Design Pressure Distributions for the Four Airfoils (BGK prediction) . . . continued

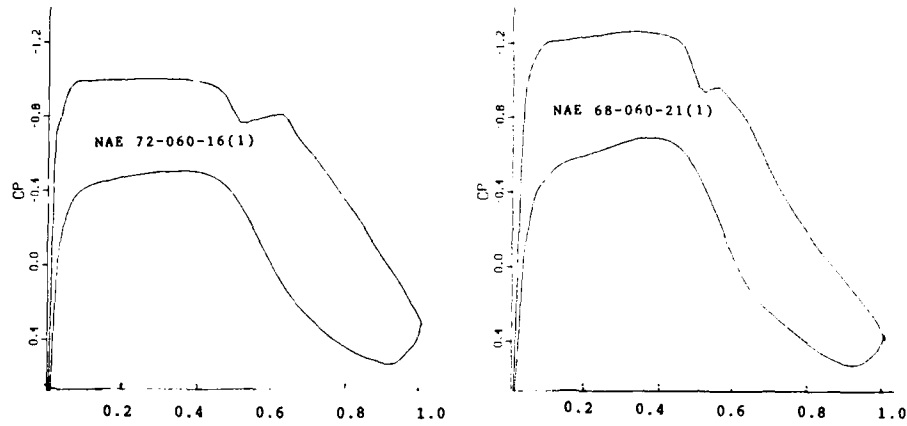


FIG 2. (continued) Design Pressure Distributions for the Four Airfoils (BGK prediction)

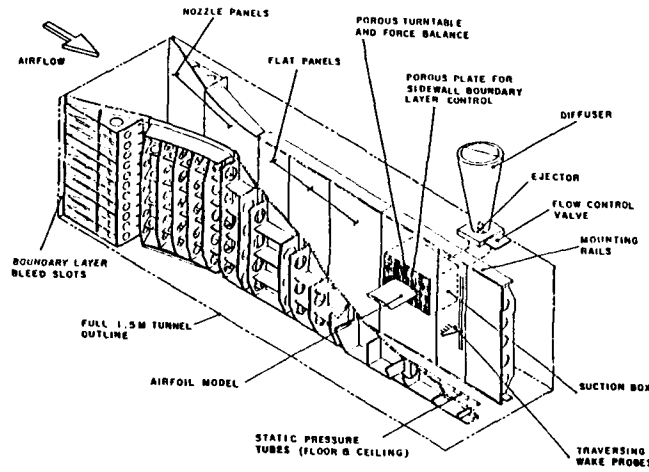


FIG. 3: NAE 2 DIMENSIONAL TEST SECTION

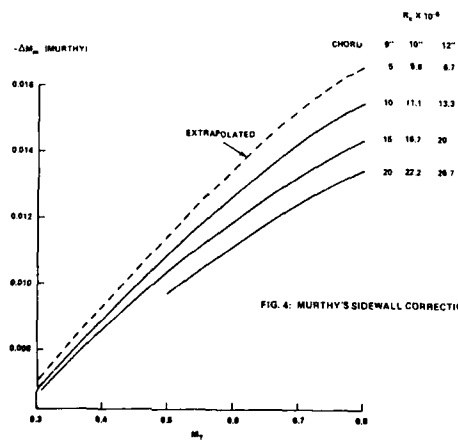


FIG. 4: MURTHY'S SIDEWALL CORRECTION TO MACH NUMBER FOR THE NAE TEST FACILITY

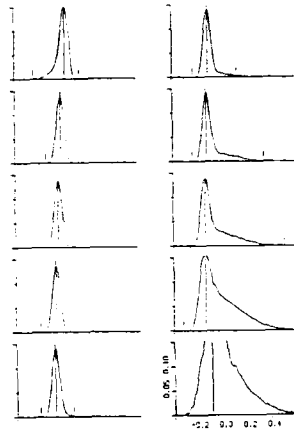


FIG 5.
Typical Wake Profiles for 13% Airfoil.
NAE Run 31278, Probe 1. (Dashed line is
the Reflection, about the peak, of the
Opposite Portion).

RUN 31278 SECN 2											
H	C _L	RN	ALP	CHP	CDN	CDNW	CDT	MPX	MSH	XSH	
0.804	0.258	12.9	-0.15	-0.115	0.0001	0.0085	0.0287	1.05	0.00	0.00	EXP
0.804	0.258	12.9	-0.01	-0.120	0.0000	0.0077	0.0277	1.07	0.00	0.00	SGK
0.799	0.304	12.6	-0.80	-0.112	0.0005	0.0088	0.0293	1.06	0.00	0.00	GRM
0.787	0.325	12.5	-0.86	-0.113	-0.0001	0.0079	0.0279	1.06	0.00	0.00	DRL

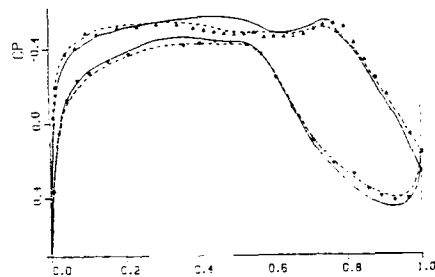


FIG 7.
Pressure Distribution of the 10% Airfoil -
Slightly Supercritical Case.

H	C _L	RN	ALP	CHP	CDN	CDNW	CDT	MPX	MSH	XSH	
0.803	0.471	12.9	0.45	-0.123	0.0005	0.0052	0.0088	1.14	1.14	0.57	EXP
0.803	0.471	12.9	-0.29	-0.120	0.0007	0.0060	0.0087	1.15	1.15	0.52	SGK
0.799	0.462	12.5	-0.16	-0.113	0.0013	0.0050	0.0100	1.16	1.16	0.56	GRM
0.787	0.462	12.5	-0.22	-0.120	0.0001	0.0081	0.0082	1.14	1.13	0.52	DRL

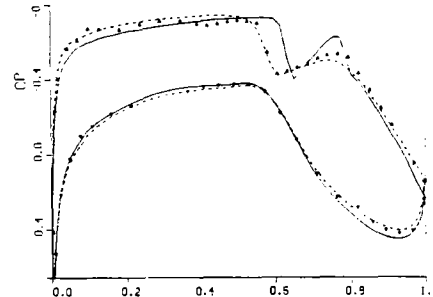


FIG 8. Pressure Distribution of the 10% Airfoil -
Medium Strength Shock.

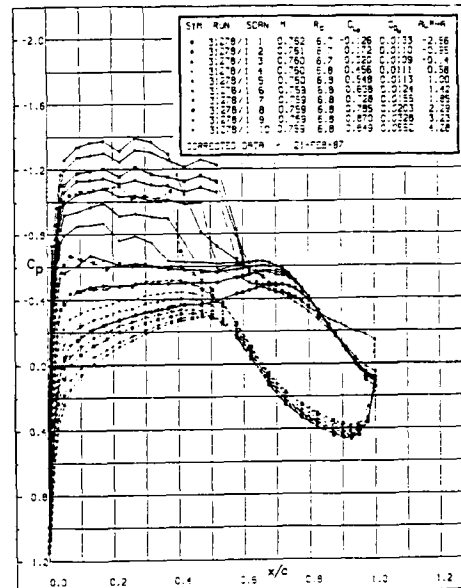


FIG 6.
Surface Pressure Distributions Corresponding
to the Wake Probe Plots of Fig 5.

RUN 31278 SECN 2 SECN 6											
H	C _L	RN	ALP	CHP	CDN	CDNW	CDT	MPX	MSH	XSH	
0.802	0.796	12.9	2.17	-0.151	0.0121	0.0136	0.0264	1.32	1.32	0.73	EXP
0.802	0.791	12.9	1.19	-0.153	0.0097	0.0098	0.0194	1.30	1.30	0.76	SGK
0.797	0.814	12.5	1.12	-0.183	0.0159	0.0115	0.0274	1.35	1.35	0.76	GRM
0.787	0.814	12.5	2.07	-0.129	0.0167	0.0162	0.0326	1.35	1.35	0.65	DRL

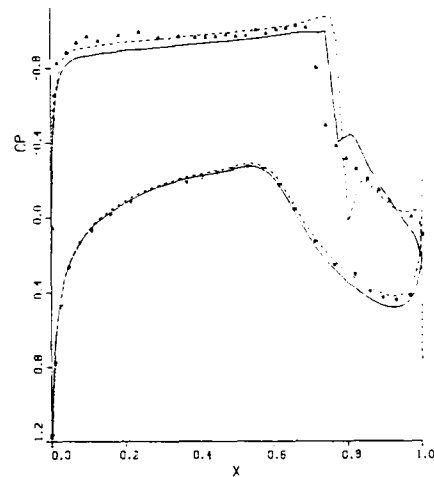


FIG 9. Pressure Distribution of the 10%
Airfoil - Strong Shock.

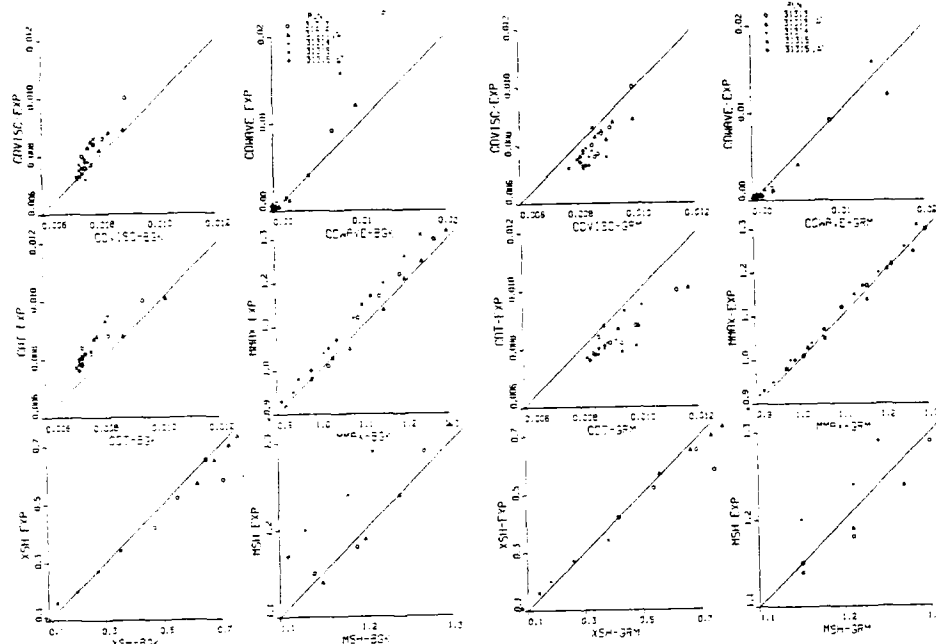


FIG 10(a). Comparison of XSH, MSH etc. for 10% Airfoil - BGR Predictions

FIG 10(b). Comparison of XSH, MSH etc. for 10% Airfoil - GRM Predictions

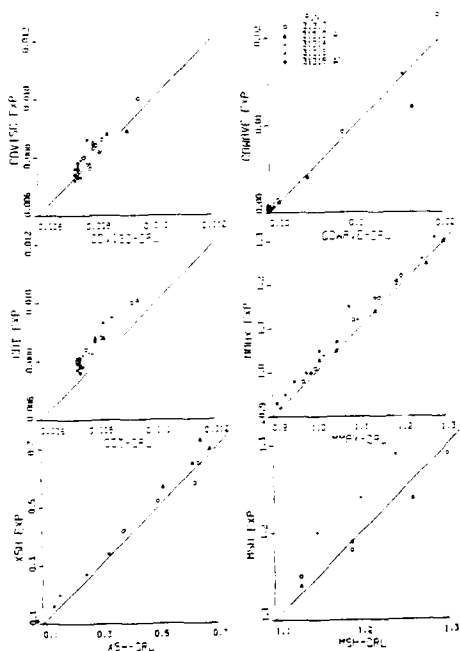


FIG 10(c). Comparison of XSH, MSH etc. for 10% Airfoil - DRL Predictions

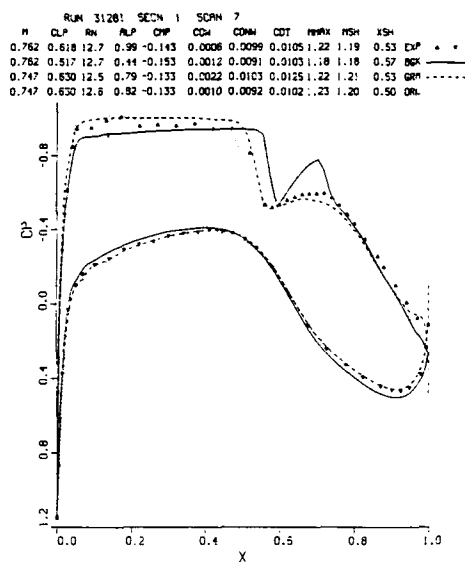


FIG 11 Pressure Distribution on 13% Airfoil

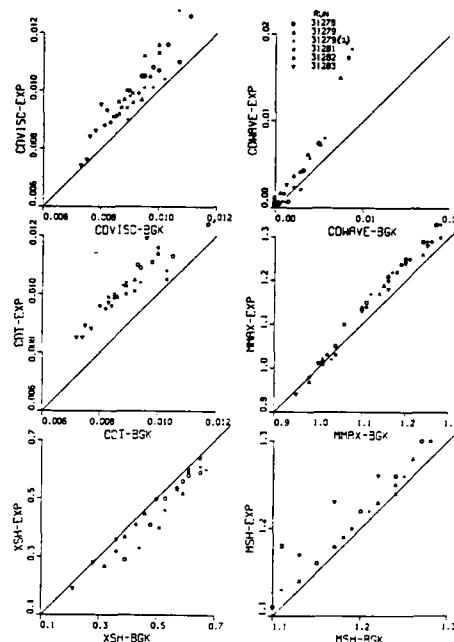


FIG 12(a). Comparison of XSH, MSH etc. for 13% Airfoil - BGK Predictions

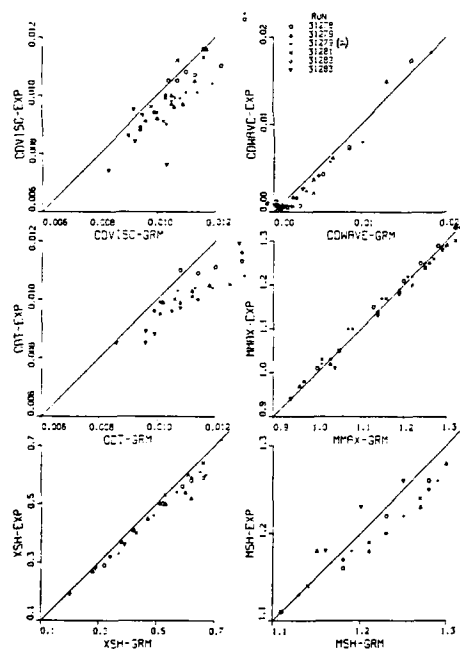


FIG 12(b). Comparison of XSH, MSH etc. for 13% Airfoil - GRM Predictions

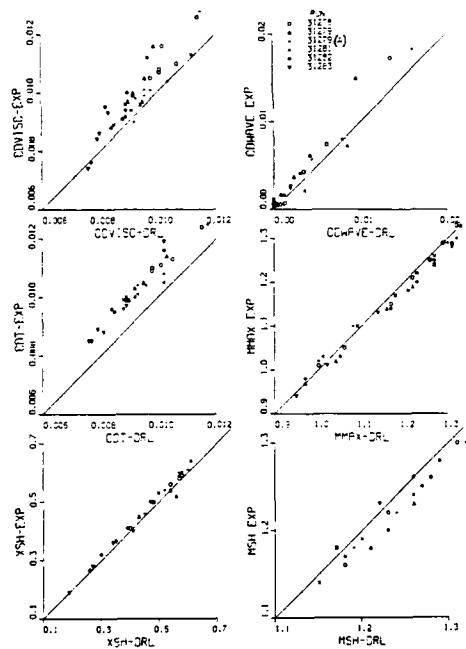


FIG 12(c). Comparison of XSH, MSH etc. for 13% Airfoil - DRL Predictions

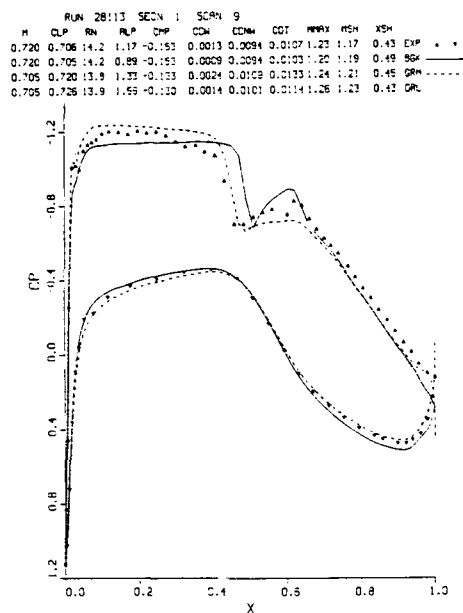


FIG 13. Pressure Distribution on the 16% Airfoil

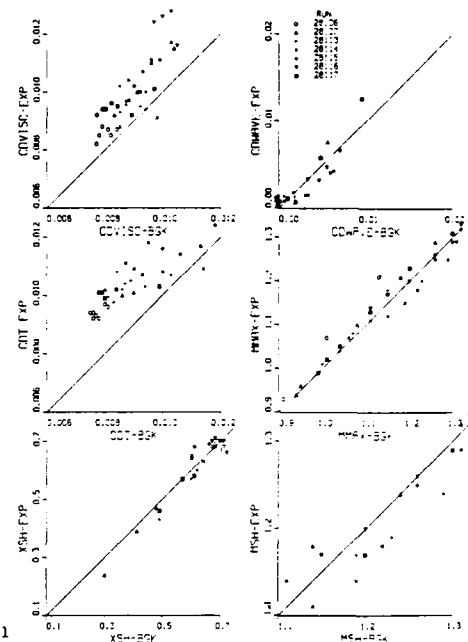


FIG 14(a). Comparison of XSH, MSH etc. for 16% Airfoil - BGK Predictions

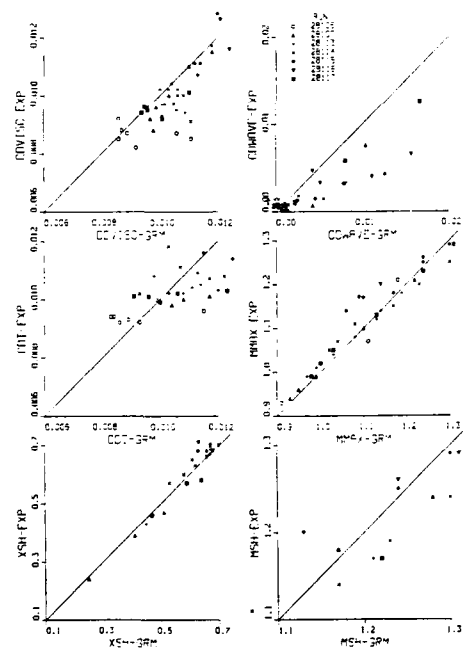


FIG 14(b). Comparison of XSH, MSH etc. for 16% Airfoil - GRM Predictions

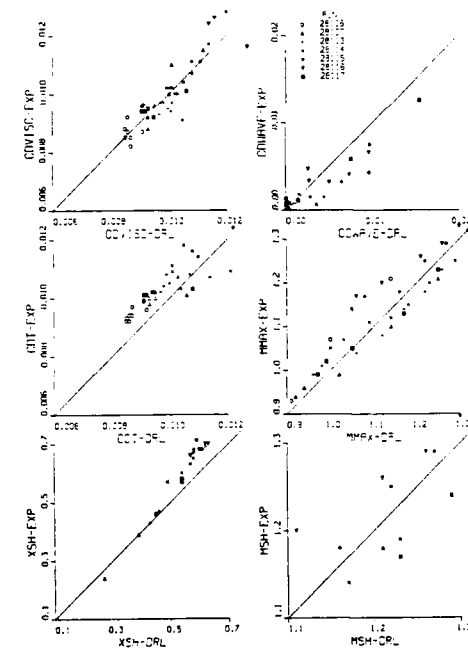


FIG 14(c). Comparison of XSH, MSH etc. for 16% Airfoil - DRL Predictions

RUN 29769 SECN 1 SCRN 9

N	CLP	RM	PLP	CHP	CDM	CDMM	CDT	PMAX	PMH	XSH
0.680	0.577	12.6	0.38	-0.124	0.0013	0.0117	0.0130	1.18	1.14	0.38 EXP
0.680	0.577	12.6	0.37	-0.124	0.0001	0.0109	0.0110	1.18	1.14	0.45 BOK
0.666	0.508	12.4	1.07	-0.104	0.0025	0.0139	0.0164	1.18	1.16	0.37 GRM
0.667	0.594	12.3	2.06	-0.095	0.0005	0.0136	0.0141	1.22	1.20	0.35 DRL

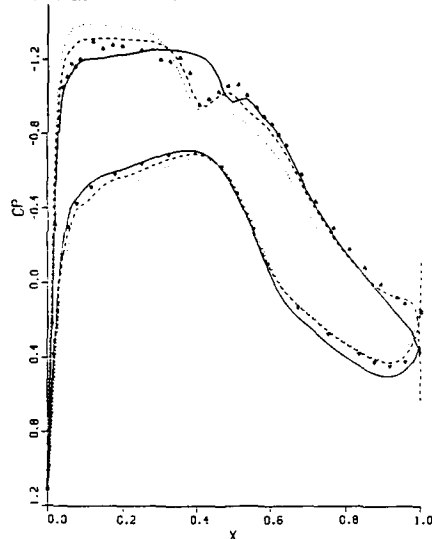


FIG 15. Pressure Distribution on 21% Airfoil - Medium Strength Shock.

RUN 29769 SECN 1 SCRN 6

N	CLP	RM	PLP	CHP	CDM	CDMM	CDT	PMAX	PMH	XSH
0.681	0.357	12.6	-0.32	-0.124	0.0009	0.0117	0.0126	1.05	0.00	0.00 EXP
0.681	0.358	12.6	-0.74	-0.126	-0.0002	0.0104	0.0103	1.06	0.00	0.00 BOK
0.667	0.364	12.4	0.12	-0.095	0.0008	0.0152	0.0160	1.06	0.00	0.00 GRM
0.667	0.367	12.3	0.61	-0.100	0.0000	0.0124	0.0124	1.06	0.00	0.00 DRL

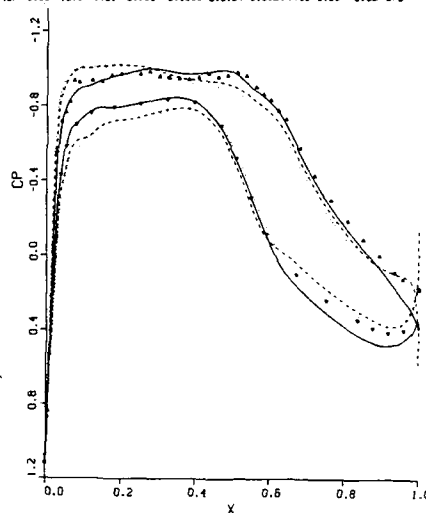


FIG 16. Pressure Distribution on 21% Airfoil - Slightly Supercritical Case.

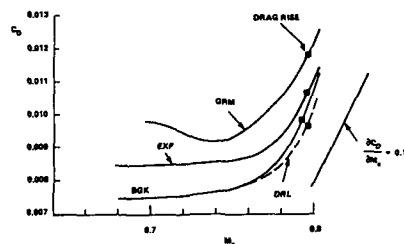


FIG 17a: C_D vs M , 10% AIRFOIL, $C_{L_{max}} = 0.8$, $R_e = 12.8 \times 10^6$

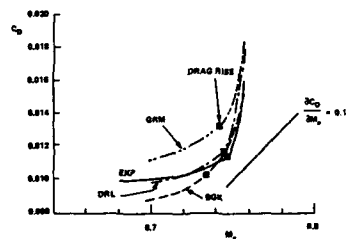


FIG 17b: C_D vs M , 18% AIRFOIL, $C_{L_{max}} = 0.8$, $R_e = 14.7 \times 10^6$

Solution error estimation in the numerical predictions of turbulent recirculating flows

R. Kessler, M. Peric, G. Scheuerer

Lehrstuhl für Strömungsmechanik
University of Erlangen-Nürnberg
Egerlandstr. 13
D-8520 Erlangen, FRG

SUMMARY

The paper presents an efficient method for numerical solution error estimation and its application to numerical predictions of turbulent recirculating flows. A finite volume method with colocated variable arrangement is employed to solve the flow and k-ε turbulence model equations. The two-dimensional, turbulent flow over an obstacle in a plane channel is selected to demonstrate the necessity of the error estimation. Recent laser Doppler measurements are available for this geometry. The error estimation method, which is applied to each solution variable, serves two purposes. Firstly, it aids in the construction of an optimum numerical grid. Secondly, the information on the location and magnitude of the numerical errors is essential to draw reliable conclusions from comparisons of numerical results and experimental data. The procedure outlined in the paper is based on Richardson extrapolation and enables an accurate assessment of the performance of the employed turbulence model and, hence, of the complete numerical solution method.

1. INTRODUCTION

Despite the development and use of high performance supercomputers, turbulence models will have to be employed for calculating high Reynolds number flows of practical interest in the near future. Therefore, the study and assessment of the performance of turbulence models is of great importance. Turbulence models usually are assessed by comparing the calculated results with reliable experimental data. However, the numerical results do not only depend on the mathematical model used, but are also influenced by the solution errors produced by the numerical scheme. The experimental results used for comparison are imperfect too, e.g. due to inaccuracies of the test section, measurement errors and deviations from idealized assumptions (2-D flow, boundary conditions, etc.). Numerical errors do not always increase the discrepancy between numerical results and experimental data. For example, numerical dissipation produced by inadequate grids in connection with first order differencing can hide possible shortcomings of a turbulence model and pretend a good agreement of the calculated results and the measured data. For this reason, a comparison of the numerical results and experimental data and an estimation of both the solution errors and the measurement uncertainties is necessary to evaluate and - in turn - further increase the performance of turbulence models.

Solution errors in numerical calculations depend on many facts, e.g. the numerical grid used, the order of the discretization scheme and the particular physical problem. A simple method to obtain quantitative information about solution errors is the Richardson extrapolation. In this paper, the successful application of an error estimation based on this technique is shown by calculating the turbulent flow over an obstacle in a plane channel. A finite volume method is used for solving the two-dimensional mean flow equations in connection with the k-ε turbulence model. The results demonstrate clearly that extremely fine grids are necessary to reduce the solution errors below a reasonable value. The comparison of the accuracy-checked numerical results with the experimental data shows the shortcomings of the turbulence model employed and thus gives a sound basis for further turbulence model developments.

2. MATHEMATICAL MODEL

The results presented in this paper are based on the two-dimensional, time-averaged equations for the conservation of mass and momentum. Assuming incompressible flows these equations read:

$$\begin{aligned} (1) \quad & \frac{\partial(\rho U)}{\partial x} + \frac{\partial(\rho V)}{\partial y} = 0 \\ (2) \quad & \frac{\partial(\rho U^2)}{\partial x} + \frac{\partial(\rho UV)}{\partial y} = -\frac{\partial P}{\partial x} - \frac{\partial(\rho \bar{u}^2)}{\partial x} - \frac{\partial(\rho \bar{u} \bar{v})}{\partial y} \\ (3) \quad & \frac{\partial(\rho UV)}{\partial x} + \frac{\partial(\rho V^2)}{\partial y} = -\frac{\partial P}{\partial y} - \frac{\partial(\rho \bar{u} \bar{v})}{\partial x} - \frac{\partial(\rho \bar{v}^2)}{\partial y} \end{aligned}$$

with the mean velocity components U and V in the x- and y-direction, respectively, the

mean pressure P and the constant density ρ . The velocity component fluctuations are represented by the lower case letters u and v ; overbars indicate the time-averaged quantities. The viscous terms in Eqs. (2) and (3) have been dropped due to the assumption of a high turbulence Reynolds number.

The Reynolds stresses $-\rho\overline{u^2}$, $-\rho\overline{v^2}$ and $-\rho\overline{uv}$ appearing in the momentum equations result from averaging the nonlinear convective terms. They are related to known quantities by a turbulence model. In the present paper the k - ϵ turbulence model proposed by Launder and Spalding [1] is employed. This model uses the eddy viscosity concept to relate the turbulent stresses and the mean strain rates:

$$(4) \quad -\rho\overline{u^2} = 2\mu_t \frac{\partial U}{\partial x} - \frac{2}{3}\rho k$$

$$(5) \quad -\rho\overline{v^2} = 2\mu_t \frac{\partial V}{\partial y} - \frac{2}{3}\rho k$$

$$(6) \quad -\rho\overline{uv} = \mu_t \left(\frac{\partial U}{\partial y} + \frac{\partial V}{\partial x} \right)$$

The eddy viscosity μ_t is made up by the turbulent kinetic energy $k = 1/2 (\overline{u^2} + \overline{v^2} + \overline{w^2})$ and its dissipation rate ϵ :

$$(7) \quad \mu_t = c_\mu \rho \frac{k^2}{\epsilon}$$

where c_μ is an empirical constant given below. The distribution of k and ϵ is determined by semi-empirical transport equations for these quantities:

$$(8) \quad \frac{\partial(\rho U k)}{\partial x} + \frac{\partial(\rho V k)}{\partial y} = \frac{\partial}{\partial x} \left(\frac{\mu_t}{\sigma_k} \frac{\partial k}{\partial x} \right) + \frac{\partial}{\partial y} \left(\frac{\mu_t}{\sigma_k} \frac{\partial k}{\partial y} \right) + P_k - \rho \epsilon$$

$$(9) \quad \frac{\partial(\rho U \epsilon)}{\partial x} + \frac{\partial(\rho V \epsilon)}{\partial y} = \frac{\partial}{\partial x} \left(\frac{\mu_t}{\sigma_\epsilon} \frac{\partial \epsilon}{\partial x} \right) + \frac{\partial}{\partial y} \left(\frac{\mu_t}{\sigma_\epsilon} \frac{\partial \epsilon}{\partial y} \right) + \frac{\epsilon}{k} (c_{\epsilon 1} P_k - \rho c_{\epsilon 2} \epsilon)$$

$$(10) \quad P_k = \mu_t \left[2 \left(\frac{\partial U}{\partial x} \right)^2 + 2 \left(\frac{\partial V}{\partial y} \right)^2 + \left(\frac{\partial U}{\partial y} + \frac{\partial V}{\partial x} \right)^2 \right]$$

Equations (1)-(10) form a closed system to calculate the five unknowns U , V , P , k and ϵ . The empirical constants appearing in these equations are set to the standard values suggested by Launder and Spalding [1]:

$$(11) \quad c_\mu = 0.09, \quad c_{\epsilon 1} = 1.44, \quad c_{\epsilon 2} = 1.92, \quad \sigma_k = 1.0, \quad \sigma_\epsilon = 1.3$$

3. NUMERICAL METHOD

A finite volume method (FV) is employed to solve the continuity, momentum and turbulence model equations. In this section, the main features of this numerical method are discussed briefly. A more detailed description is given by Peric et al. [2].

Contrary to many conventional FV methods (e.g. Patankar [3]) employing a staggered variable arrangement to avoid oscillatory pressure and velocity fields, the present method is based on a colocated variable arrangement. The velocity components as well as all scalar variables are stored in the geometrical centre of the control volumes (CV). The grid, storage locations and labelling scheme are shown in Fig. 1. The colocated

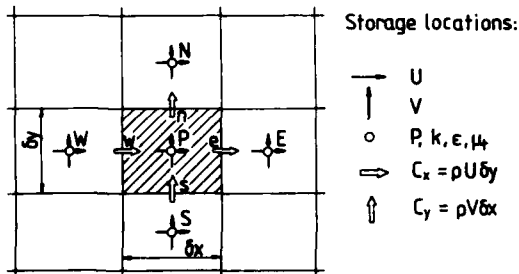


Fig. 1 :

Location of the control volumes, the variables and the convective fluxes C_x and C_y .

variable arrangement facilitates the treatment of boundary conditions especially around sharp corners. The main advantages of the colocated arrangement become apparent when extensions such as multigrid techniques and non-orthogonal grids are considered (Becker et al. [4]; Peric [5]).

In order to ensure the stability of the method, special provision is made for the coupling of the velocities and the pressure. Otherwise, the well-known checkerboard instability would occur. A special interpolation formula for the calculation of the velocity components at the control volume faces is used in the continuity equation for efficient suppression of the numerical instability. A detailed comparison of the FV methods with colocated and staggered variable arrangement confirms the identical stability behaviour of both versions (Peric et al. [2]). The number of iterations required for a converged solution as well as the solution itself are almost identical for both methods.

In the discretization process the convective and diffusive fluxes through the boundaries of each control volume must be related to the nodal values. Here, the diffusive terms are discretized with central differences. Two different schemes are employed to approximate the convective fluxes: the first order upwind differencing scheme (UDS) and the second order central differencing scheme (CDS). The resulting algebraic equation for a control volume is arranged in the deferred correction manner suggested by Rhosla and Rubin [6]:

$$(12) \quad \sum_m A_m^u \phi_m = S_\phi - \gamma \left[\sum_m (A_m^c - A_m^u) \phi_m \right]$$

where ϕ is any of the dependent variables and S_ϕ is the source term of the respective equation. The coefficients arising from upwind and central differencing of the convective terms are denoted by the symbols A_m^u and A_m^c , respectively, where the subscript m indicates the four nearest neighbours of a grid point, see Fig 1. The weighting factor γ allows a smooth change of the discretization scheme for the convective fluxes from pure UDS ($\gamma = 0$) to CDS ($\gamma = 1$). Only the UDS part of coefficients is treated implicitly. The correction term at the right hand side of Eq. (12) ensures the chosen discretization iteratively. This procedure extends the range of stable solutions with CDS and reduces the number of iterations needed for convergence.

The velocities and the pressure in the discretized equations are linked via the SIMPLE algorithm of Patankar and Spalding [7] including the modified interpolation practice discussed above. Using the continuity constraint yields a pressure-correction equation of the Poisson type, with a discrete form similar to that of Eq. (12). Due to the non-linearity and coupling of the equations, under-relaxation has to be used to ensure convergence (cf. Patankar, [3]). The rate of convergence depends strongly on the choice of the underrelaxation parameters for the velocities α_u and the pressure-correction α_p . A nearly optimum rate of convergence for a wide range of applications can be achieved for $\alpha_p = 1 - \alpha_u$ and values of 0.7 - 0.8 for α_u . All the calculations presented in this paper were made with a value of 0.75 for the underrelaxation of the velocities as well as for the turbulence model equations, and a value of 0.25 for the underrelaxation of the pressure-correction.

The algebraic subsystems resulting from the individual differential equations are solved sequentially for U , V , P' , k and ϵ by the incomplete LU factorization method of Stone [8]. The coefficients A_m are held constant in the course of this cycle (outer iteration). Only one relaxation with the algorithm of Stone is made per outer iteration for solving the equations of U , V , k and ϵ . The pressure-correction equation is iterated up to six times per cycle, unless its residuals have dropped by a factor of five. After updating the coefficients, the whole cycle is repeated until convergence is achieved.

The sums of the absolute residuals of the continuity and the momentum equations are used for monitoring convergence. The iteration process is terminated after the residual sums, normalized by the inlet mass or momentum fluxes, fall below 10^{-3} . In the present calculations about 1200 iterations were required using the UDS and a 95×60 CV grid. For the finer grid with 190×120 CV and CDS the necessary number of iterations increased to about 6000.

4. SOLUTION ERROR ESTIMATION

As pointed out in the introduction, information about the solution errors produced by the numerical method is essential for a meaningful assessment of the calculated results and especially for testing and developing turbulence models. A simple and efficient method to obtain estimates of the magnitude and the spatial distribution of the solution errors is the Richardson extrapolation technique proposed by Caruso et al. [9]. This method is based on Taylor series expansion of the solution error ϵ_h , defined as the difference between the exact solution ϕ and the numerical solution ϕ_h calculated on a grid with spacing h . For first order methods the corresponding Taylor series is :

$$(13) \quad \epsilon_h = \phi - \phi_h = a_1 h + a_2 h^2 + \dots$$

For higher order methods, one or more of the leading coefficients a_1, a_2, \dots in the expansion disappear. A numerical solution on a coarser grid with spacing $2h$ yields the solution error ϵ_{2h} :

$$(14) \quad \epsilon_{2h} = \phi - \phi_{2h} = a_1 2h + a_2 4h^2 + \dots$$

Subtraction of Eqs. (14) and (13) results in

$$(15) \quad \phi_h - \phi_{2h} = a_1 h + a_2 3h^2 + \dots \approx \epsilon_h$$

The first terms of the series in Eqs. (15) and (13) are identical. Hence, the difference between the fine and coarse grid solutions is a good estimate for the solution error of the fine grid solution.

In the FV method employed for the present calculations a coarse grid control volume is always made up out of four fine grid control volumes. Therefore, the calculation nodes of the coarse and fine grids do not coincide, and the fine grid solution ϕ_h is interpolated bilinearly prior to the application of Eq. (15). This procedure results in an error estimate for the fine grid solution located at the grid points of the coarse grid.

The additional numerical work for the solution error estimation is negligible compared with the computing time required for the fine grid solution. Therefore, this error estimation method is a good tool for a reliable assessment of any numerical calculations.

5. GEOMETRY AND BOUNDARY CONDITION

The turbulent flow over a quadratic obstacle in a plane channel is an appropriate example to demonstrate the gain from the application of the error estimation method presented above. In spite of the relatively simple geometry the ensuing flow is very complex, featuring three different recirculation zones. Such an obstacle flow has recently been investigated by Tropea and Dimaczek [10], who made extensive laser Doppler measurements. The Reynolds number, based on the maximum inlet velocity and the height H of their water channel, was 95.000, ensuring a fully turbulent flow. Profiles of the mean velocities and the Reynolds stresses $-\rho \overline{u^2}$, $-\rho \overline{v^2}$, $-\rho \overline{w^2}$ and $-\rho \overline{uv}$ are measured in the midplane of the channel at various streamwise locations. The ratio of the spanwise extent and the height of the channel was approximately 10. In the centre region of the channel most measurements indicate two-dimensional flow. This will be discussed in more detail in the next section.

The geometry of the computational domain is shown in Fig. 2. The height h of the quadratic obstacle is half the height of the channel. The obstacle is located $3h$ downstream from the inlet boundary. The length of the whole computation domain is set to 12 times the height of the channel. Three different boundary types appear in this problem: inlet and outlet sections and walls. The treatment of these boundaries is discussed in this order.

The measured data for U , V and k are prescribed at the inlet plane to simulate the experiment as closely as possible. These boundary conditions ensure that the relatively short computational domain upstream of the obstacle as well as the asymmetries in the experimental profiles can not impair the comparison. No data are available for the dissipation rate ϵ . Therefore the inlet values are calculated using the eddy viscosity assumptions (6), (7) and the measured profiles of U , \overline{uv} and k :

$$(16) \quad \epsilon = c_\mu \frac{-\overline{uv} \partial U}{k^2 \partial y}$$

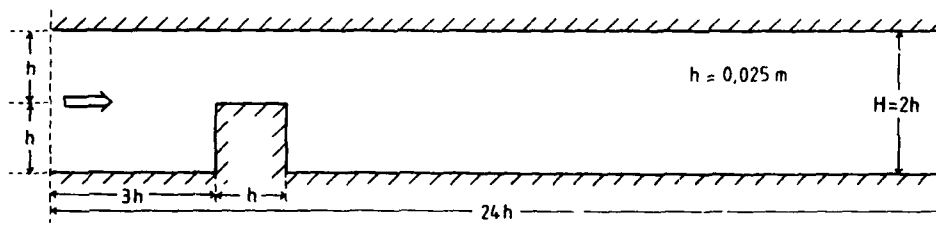


Fig. 2 : Sketch of the calculation domain.

The experimental data are fitted by appropriate algebraic functions, in order to ensure smooth inlet profiles and to avoid unrealistic values due to measurement scatter.

The outlet plane must be located far enough from the obstacle to avoid any unwanted effects of the outlet boundary conditions on the upstream region. In order to limit the computational effort, a reasonable compromise is to locate the outlet plane at $x = 12H$, i.e. at approximately four reattachment lengths downstream of the obstacle. The derivatives in the x-direction of the velocity components and the turbulence quantities are set to zero there. This is a reasonable approximation in view of the relatively small x-dependence of the channel flow in this region. Test calculations with different lengths of the computational domain confirm the reliability of this boundary condition.

Defining boundary conditions for turbulent, separated flows at rigid walls is a particular difficulty. The use of the no-slip condition requires a very fine grid in the vicinity of the wall with at least few grid points located in the viscous sublayer. For high Reynolds number flows, the numerical effort will increase tremendously because the viscous sublayer becomes progressively thinner as the Reynolds number increases. Moreover, a low Reynolds number turbulence model would have to be used and these models are yet not well proven for separated flows. In order to avoid these difficulties, the near-wall regions are commonly bridged by so-called wall functions. This technique is also used in the present calculations. As we deal with a finite volume method, the wall fluxes have to be specified. For the wall-parallel velocities, these are the wall shear stresses. They are calculated from a relation given by Launder and Spalding [1]:

$$(17) \quad \tau_w = \frac{\rho U_c k_c^{1/2} c_\mu^{1/4} \kappa}{\ln(y_c^+) + C}$$

where the dimensionless wall distance is defined as follows:

$$(18) \quad y^+ = \frac{y_c k_c^{1/2} c_\mu^{1/4} \rho}{\mu}$$

The subscript c denotes variables at the grid nodes adjacent to the wall. Values of 0.41 and 5.2 are assigned to the von Karman constant κ and the constant C, respectively. Equations (17) and (18) are based on the assumptions of a logarithmic velocity profile, local equilibrium of the production and the dissipation rates of the turbulent kinetic energy and a constant stress layer. Using the same assumptions, the production and dissipation rates P_k and ϵ , respectively, for the near-wall control volumes are expressed as:

$$(19) \quad P_{k,c} \approx \tau_w \frac{\partial U}{\partial y} = \frac{\tau_w^2}{\rho y_c k_c^{1/2} c_\mu^{1/4} \kappa}$$

$$(20) \quad \epsilon = c_\mu^{3/4} \frac{k^{3/2}}{\kappa y_c}$$

The convective and diffusive wall fluxes of k and ϵ are set to zero. The value of ϵ at the near-wall nodes is computed directly from Eq. (20). The application of the wall functions described above leads to reasonable results for flows in which the above assumptions are approximately satisfied. However, in separated flows these assumptions are no longer valid, especially in the regions around the separation and reattachment points. The consequences of these shortcomings of wall functions when applied to separated flows are not well known and will be discussed briefly in the following section.

6. RESULTS

The solution errors and their dependence on the grid and the discretization scheme are discussed first. The calculations were performed with two different grids, comprising 95×60 and 190×120 CV, respectively. The grids are Cartesian and nonuniform, with a high concentration in the regions near the leading and trailing edges of the obstacle, where considerable variations of the gradients of all variables are expected. In the interest of a clear graphic presentation, Fig. 3 shows the left part of the coarse grid. Table 1 gives the employed grid expansion factors, defined as the length ratio of adjacent control volumes, and the dimensions of the smallest control volumes located near the edges of the obstacle showing the high resolution of the fine grid near the obstacle. The values of the expansion factors are chosen close to unity in order to avoid additional inaccuracies due to different lengths of neighbour control volumes.

The error estimation method described in Section 4 can easily be modified for application to CDS calculations. However, the calculations employing the second order CDS yield a converged solution only on the fine grid. A stable solution could not be achieved with the CDS on the coarse grid, due to oscillations occurring at high grid Peclet numbers. For this reason the error estimation can only be applied to the UDS solutions.

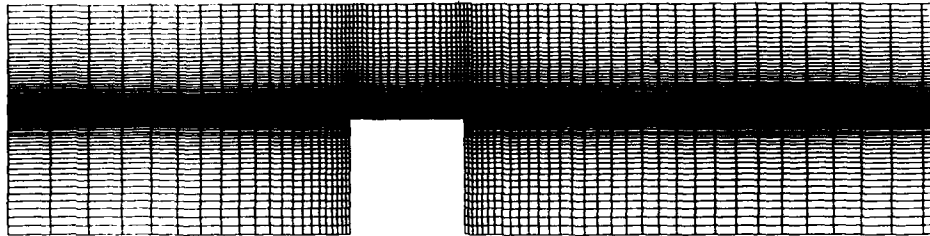


Fig. 3 : Coarse grid in the vicinity of the obstacle, 95x60 control volumes.

	σ_x	Δx $\cdot 10^{-4}[\text{m}]$	σ_y	Δy $\cdot 10^{-4}[\text{m}]$
95 x 60 CV	1.093	7.9	1.128	3.7
190 x 120 CV	1.045	3.8	1.062	1.9

Table 1 : Grid expansion factors σ_x , σ_y and smallest control volume length of the coarse and fine grid.

Fig. 4 shows the computed solution errors of the fine grid UDS solution. Contour plots of the solution errors are made for the two mean velocity components and for the turbulent kinetic energy. For all three variables remarkably large solution errors occur in the vicinity of the leading edge of the obstacle, although the resolution of the 190 x 120 grid is highest there. The solution error of the U-component (Fig. 4 a), normalized with the maximum inlet velocity, exceeds 10 % in a limited region. Apart from a second maximum of the error located near the bottom wall in front of the obstacle, the solution error is 1 % or lower elsewhere. The solution errors of the V-component are

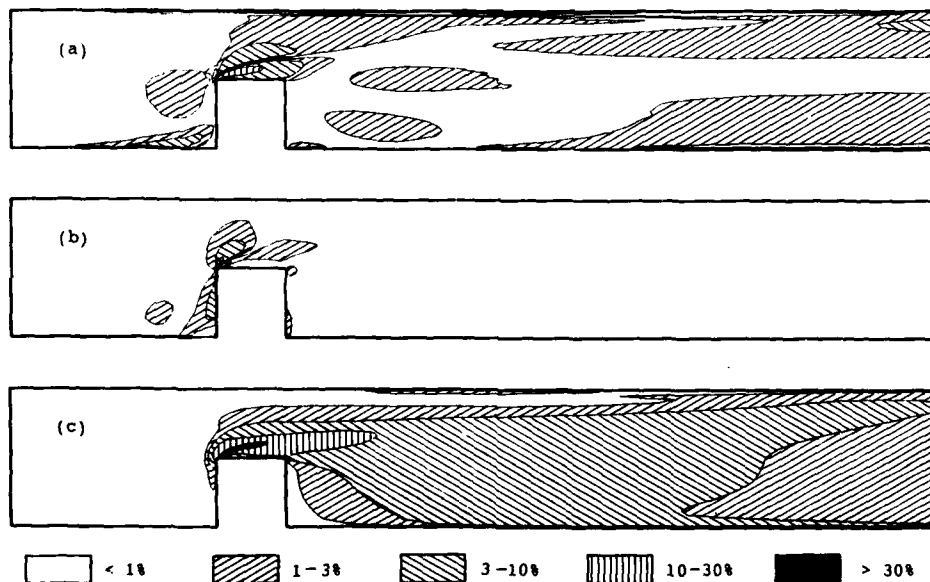


Fig. 4 : Estimated error distribution of the fine grid upwind solution, 190x120 control volumes. (a) U-velocity, (b) V-velocity, (c) turbulent kinetic energy k.

normalized with the maximum inlet velocity too. Values of more than 3 % are detected in a small region near the leading edge of the obstacle (Fig. 4b). Elsewhere, the solution errors of V are below 1%, as the V -component itself is smaller than U in most of the flow domain. The solution errors of the turbulent kinetic energy above the obstacle are largest. They are normalized with the maximum value of k calculated on the fine grid and exceed 30 % in a small region and 10 % up to one obstacle height downstream. Due to the dominant convective transport, the solution errors remain larger than 3 % even far downstream.

This example demonstrates that UDS solutions can contain considerable numerical errors even when very fine grids, with a high concentration of control volumes in critical regions, are used. The numerical errors for the turbulence quantities can be substantially higher than the errors for the mean velocities. This fact has to be kept in mind when these quantities are compared with measurements.

The requirement of very fine grids cannot be circumvented in all cases by using the more accurate second order central differencing scheme for the convective terms. This is due to the fact that the higher order schemes like CDS often produce oscillatory solutions or do not converge at all on coarse grids. Although CDS can be employed in many cases at Peclet numbers significantly higher than 2 (the upper limit derived from the one-dimensional convection-diffusion equation), some damping has to be applied if the grid is not sufficiently fine. In our case pure CDS solution could be obtained on the finest grid; on coarser grids UDS had to be blended with CDS (cf. Eq. (12)), achieving stability at the expense of accuracy.

Since a coarse grid CDS solution could not be obtained, we compare the fine grid CDS solution with the corresponding UDS solution. This comparison is shown in Fig. 5 in terms of normalized differences of the two solutions. The normalization factors are the same as for the solution errors in Fig. 4. Upstream and in the vicinity of the obstacle, the contour lines of the solution differences in Fig. 5 are rather similar to the contour lines of the solution errors discussed above. Hence, it can be concluded that the differences in this part of the computational domain are mainly caused by the inaccuracies of the UDS solution and the errors of the CDS solution are essentially lower. A somewhat different behaviour emerges for the downstream regions shown in Figs. 4 and 5. There, the estimated errors for U and V are of the order of 1 % or less, suggesting high accuracy (Fig. 4). However, differences between the UDS and CDS solutions of more than 3 % for the U -component appear in Fig. 5 up to the outlet plane. The same is observed for the V -component and the turbulent kinetic energy. The reason for these relatively large differences between the UDS and CDS solutions is the dominating convective transport. The solution errors produced in the vicinity of the obstacle influence the entire flow in the downstream region and are only weakly damped. The estimation method underpredicts these solution errors far downstream, probably due to the dominating nonlinear term in this region.

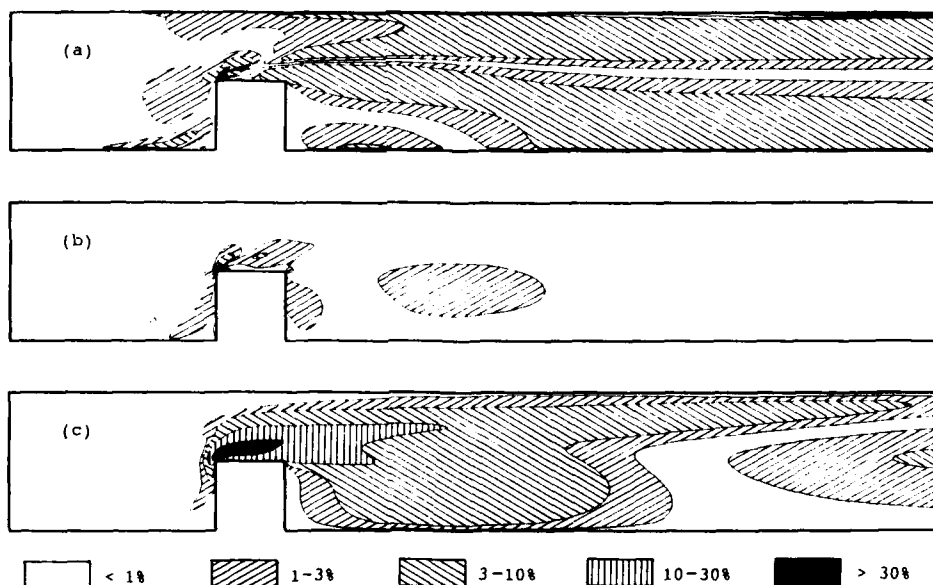


Fig. 5 : Comparison of the fine grid upwind and central differencing solutions, 190×120 control volumes. (a) U-velocity, (b) V-velocity, (c) turbulent kinetic energy k .

After these numerical considerations, some physical aspects of the predicted flow field, based on the most accurate CDS solution are discussed. The calculated streamlines are shown in Fig. 6a. A small separation zone appears in front of the obstacle. A further separation point is located at the leading corner of the obstacle. The following recirculation zone is very flat and the flow reattaches just at the trailing edge of the obstacle. At this point the main recirculating zone begins. A small secondary separation can be seen at the lower corner of the obstacle. The same flow structure has been observed in experiments. However, the recirculation zone at the top of the obstacle is somewhat thicker in the experiments, so that the flow does not reattach at the top wall and the two separation zones are connected with each other.

Contour lines of the turbulent kinetic energy k are plotted in Fig. 6b. The turbulence level of the fully developed channel flow at the inlet plane is small. Above the obstacle, the accelerated flow together with the thin recirculation zone cause a steep profile of the U-component near the top wall of the obstacle. This leads to high production rates of the turbulent kinetic energy k , documented by the absolute maximum value of k in this region. Downstream the obstacle a second smaller maximum of the k is observed, which is caused by the shear layer of the large recirculating mass flow. Far downstream the turbulent kinetic energy decreases only slowly due to the dominating convective transport. Hence, the values of k at the outlet plane are still far from the level known from fully developed channel flows.

The location of the points of separation and reattachment is of special interest in many fluid flow problems. For this reason, numerical methods and the turbulence models implemented are often appraised by their capability to predict the separation length well. The calculated reattachment lengths, normalized with the obstacle height, are presented in Table 2 together with the experimental value given by Tropea and Dimaczek [10]. Both UDS solutions overpredict the reattachment length, with decreasing tendency as the resolution is increased. However, the more accurate CDS solution underpredicts the reattachment length by about 5 %. The latter can be regarded as the correct value produced by the k - ϵ turbulence model.

The comparison of the reattachment lengths calculated by the various discretization schemes with different resolution makes clear, that the good prediction of a single physical quantity without any further information about numerical errors may lead to erroneous conclusions with respect to the performance of the employed turbulence model. For the present problem, the measured value of the reattachment length can be predicted exactly by variations of the grid size and the discretization scheme (eg. by blending UDS and CDS in a suitable proportion). In this case, the shortcomings of the turbulence model are compensated by the numerical errors of computational scheme. It is therefore essential to know the order of the numerical errors before any conclusions can be made.

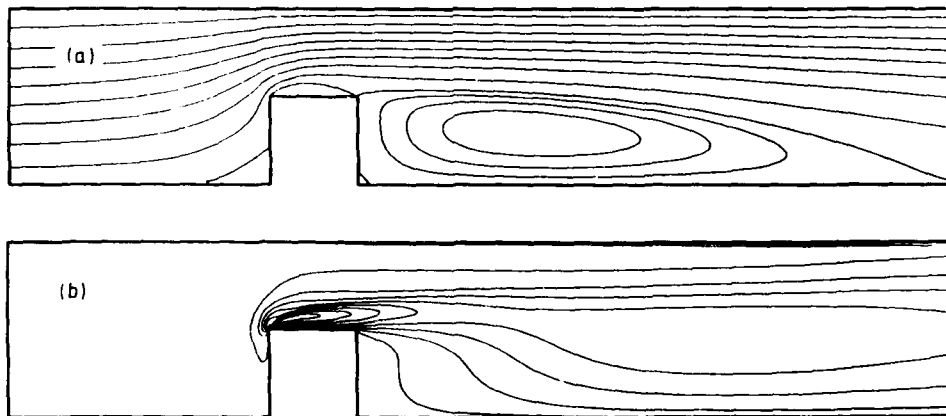


Fig. 6 : (a) Streamlines and (b) contour lines of the turbulent kinetic energy k , central differencing scheme, 190x120 control volumes.

experiment		7.12h	
upwind differencing	95x60 CV	7.59h	+6.9%
upwind differencing	190x120 CV	7.40h	+4.2%
central differencing	190x120 CV	6.77h	-4.6%

Table 2 : Comparison of the predicted and measured reattachment lengths.

Some weak points of the $k-\epsilon$ turbulence model can be detected by comparing the CDS solution with the data of Tropea and Dimaczek [10]. The profiles of U , V , k and \overline{uv} at three streamwise locations in the flow field are selected for this purpose. In addition to the most accurate CDS solution - in the following diagrams marked by solid lines - the results of the UDS calculations are also shown (dashed lines).

The first cross section is located upstream of the obstacle (in the first recirculation zone), at $x/H = 1.3$. Due to this separation, the profile of U -velocity has three inflection points, which are well simulated by the numerical solution (cf. Fig. 7a). A somewhat larger discrepancy between calculations and experiment observed for the V profile (Fig. 7b), is in the range of uncertainty of the experimental data. The turbulent kinetic energy k , shown in Fig. 7c, increases strongly in the lower part of the channel, which cannot be produced by the numerical calculations. The reason for this discrepancy is probably a three-dimensional flow structure in the vicinity of the separation zone. Measurements of non-zero W -components and a corresponding pattern of the wall shear stress indicate periodic structures in the spanwise direction. More detailed measurements are required before this phenomenon can be discussed in detail. The absolute values of the Reynolds stress \overline{uv} in this section (cf. Fig. 7d) are too small, compared to the expected uncertainty to draw any conclusion from its profile.

The second cross-section for comparing the profiles of U , V , k and \overline{uv} is located at $x/H = 1.54$, close to the leading edge of the obstacle. The beginning of the thin recirculation zone is indicated by the negative U values near the wall. The calculated negative values of U exceed the measured data by a factor of two. Moreover, the maximum of the backward flow is located closer to the wall than in the measurement (cf. Fig. 8a). This dislocation of the maximum in the backward flow of a recirculation zone is due to the $k-\epsilon$ turbulence model and is also observed in calculations of other flow configurations, see Obi et al. [11]. The reason for this behaviour of the turbulence model is not completely clear. However, the wall functions do not seem to be responsible for these effects. At this section the flow achieves its maximum deflection. Thus the value of the V -component exceeds the maximum inlet velocity. The shape of the V profile is well predicted by the calculations (Fig. 8b), but the values of V are 20 % smaller than the measured ones. This underprediction of the V -component is typical for all calculated V profiles downstream of the obstacle. The predicted value of maximum turbulent kinetic energy k agrees astonishingly well with the measured data at this section (Fig. 8c). In the upper part of the channel the measured values are very small, whereas the computed values are essentially higher. This is one reason for the opposite behaviour of the computed and measured profiles of the Reynolds stress \overline{uv} shown in Fig. 8d.

The comparison of the numerical results and experimental data in this section as well as the error estimations clearly indicate the difficulties in studying the

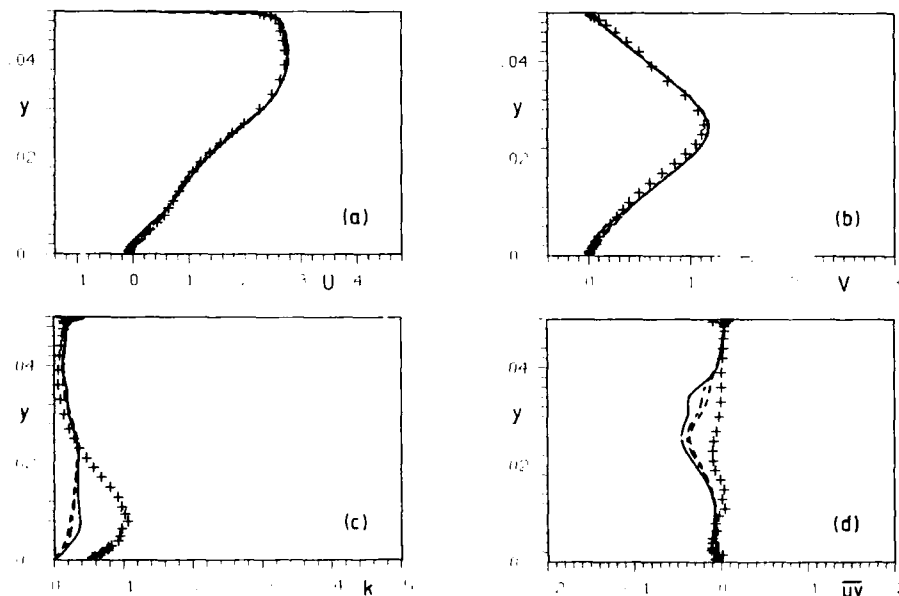


Fig. 7 : Comparison of measured and predicted profiles of the U -velocity (a), the V -velocity (b), the turbulent kinetic energy k (c) and the turbulent shear stress \overline{uv} (d) at $x/H = 1.3$. — CDS fine grid, ---- UDS fine grid, ----- UDS coarse grid, + experiments (Tropea, Dimaczek [10]).

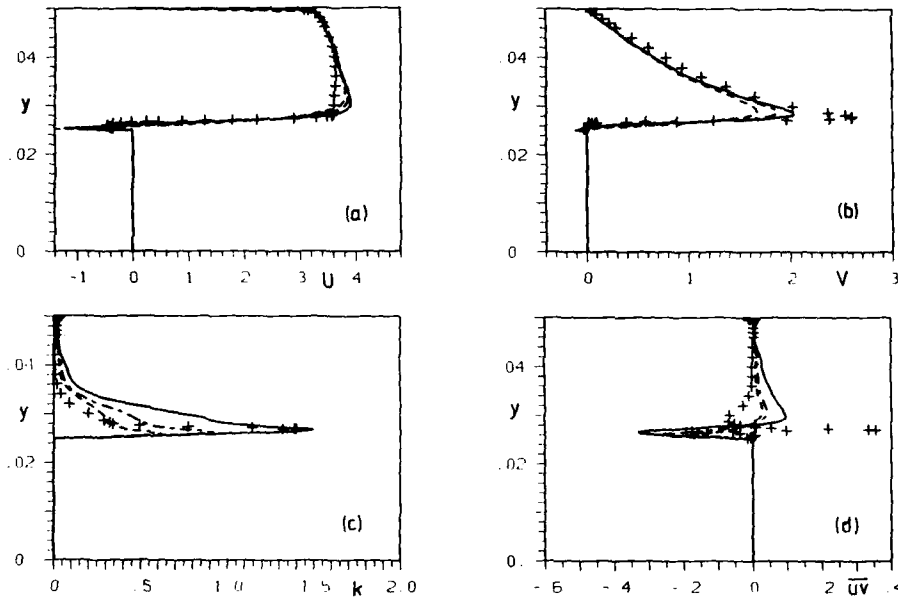


Fig. 8 : Comparison of measured and predicted profiles of the U-velocity (a), the V-velocity (b), the turbulent kinetic energy k (c) and the turbulent shear stress \overline{uv} (d) at $x/H = 1.54$. — CDS fine grid, ---- UDS fine grid, -.-.- UDS coarse grid, + experiments (Tropea, Dimaczek [10]).

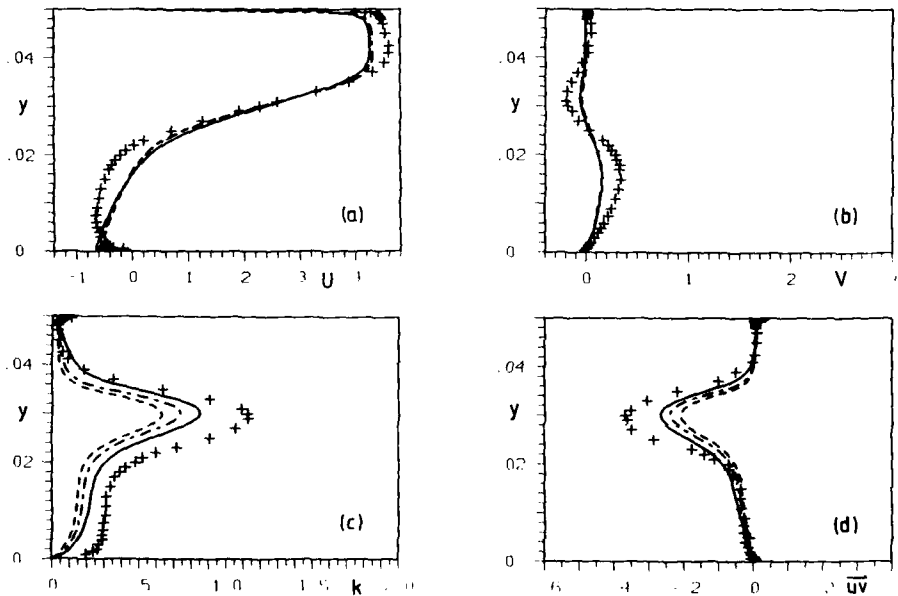


Fig. 9 : Comparison of measured and predicted profiles at $x/H = 2.5$.

turbulent flow in the region above the leading edge of the obstacle. This is true for the numerical method and the turbulence model as well as for the experimental investigations of this flow regime. For a reliable discussion of the flow phenomena in this region, improved calculations together with further, more accurate measurements are urgently required.

The third section selected for comparison is located downstream from the obstacle within the large recirculation zone. Figure 9a shows the computed profiles of the U-velocity, which deviates clearly from the experimental data. The predicted U values are smaller than the measured data nearly everywhere, indicating a smaller recirculating mass flow. This fact is confirmed by the underprediction of the V-component plotted in Fig. 9b. Moreover, the predicted maximum negative U-velocity is dislocated to the wall. A similar effect has been reported above for the previous cross section. The turbulent kinetic energy k and the Reynolds stress \overline{uv} are shown in Figs. 9c and 9d, respectively. Both of the turbulence quantities are underpredicted by the $k-\epsilon$ turbulence model. Therefore, the turbulent transport of momentum normal to the streamwise direction is too small. The lack of this turbulent momentum transport is the reason for the significantly slower mass flow in the recirculation region. This obvious shortcoming of the $k-\epsilon$ turbulence model remains far downstream and leads to the slower flow recovery.

7. SUMMARY AND CONCLUDING REMARKS

A finite volume method is used to predict the rather complex fully turbulent flow over an obstacle in a plane channel. The two-dimensional time-averaged flow equations are solved in connection with the $k-\epsilon$ turbulence model equations. An efficient error estimation technique based on the Richardson extrapolation is employed, which gives helpful information about the accuracy of the numerical solutions. The numerical results, computed on different grids with various discretization schemes, are compared with recent laser Doppler measurements.

The error estimation technique provides qualitative and quantitative information about the distribution of the numerical solution errors and can thus aid the grid refinement strategy. However, the most important point is that this method allows the separation of pure numerical and turbulence model errors. This is a basic requirement for the scientific evaluation of the turbulence model performance. Comparing the predicted and measured values of only one quantity - e.g. the reattachment length - often leads to erroneous conclusions about the accuracy of the global numerical solution, as is clearly shown in the present calculations.

First order discretization methods are shown to require very fine meshes to yield sufficiently small solution errors. The solution error detected in the present first order upwind solution on the finest grid cannot be neglected, although the non uniform 190×120 grid yields a high resolution near the obstacle. In general, the solution errors of the turbulence quantities are significantly higher than the errors of the mean velocities. The second order central differencing calculations performed on the fine grid are found to yield a solution with acceptably small numerical errors. From this point of view, the results of many previous studies, employing first order methods on coarse grids, have to be appraised carefully.

The comparisons of the predicted and measured data disclose some shortcomings of the $k-\epsilon$ turbulence model, when applied to separated flows. However, to identify the sources of these errors, more detailed and accurate experimental data - including triple correlations, production and dissipation rates - are required. Based on such improved data, further developments in turbulence modelling (e.g. Reynolds stress models, low Reynolds number models) will be promoted and more reliable tests and assessments could be performed.

8. REFERENCES

- [1] Launder, B. E.; Spalding, D. B., "The Numerical Computation of Turbulent Flow", Comp. Meth. Appl. Mech. and Eng., vol. 3, (1974), pp. 269-289.
- [2] Peric, M.; Kessler, R.; Scheuerer, G., "Comparison of Finite-Volume Numerical Methods with Staggered and Collocated Grids", (1987), Rept. No. 163/t/87, Lehrst. f. Strömungsmechanik, University of Erlangen-Nürnberg, FRG, also to appear in Computers and Fluids (1988).
- [3] Patankar, S. V., "Numerical Heat Transfer and Fluid Flow", McGraw Hill, New York, (1980).
- [4] Becker, C.; Ferziger, J. H.; Peric, M.; Scheuerer, G., "Finite Volume Multigrid Solutions of the Two-Dimensional Incompressible Navier-Stokes Equations", 4th GAMM-Seminar on 'Robust Multigrid Methods', Kiel, (1988), FRG.
- [5] Peric, M., "A Finite Volume Method for the Prediction of Three-Dimensional Fluid Flow in Complex Ducts", PhD Thesis, University of London, (1985).

- [6] Khosla, P. K.; Rubin, S. G., "A Diagonally Dominant Second-Order Accurate Implicit Scheme", *Computers and Fluids*, Vol. 2, (1974), pp. 207.
- [7] Patankar, S. V.; Spalding, D. B., "A Calculation Procedure for Heat, Mass and Momentum Transfer in Three-Dimensional Parabolic Flows", *Int. J. Heat Mass Transfer*, Vol. 15, (1972), pp. 1787-1806.
- [8] Stone, H. L., "Iterative Solution of Implicit Approximations of Multi-Dimensional Partial Differential Equations", *SIAM J. Num. Anal.*, Vol 5, (1968), pp. 530-558.
- [9] Caruso, S. C.; Perziger, J. H.; Oliger, J., "Adaptive Grid Techniques for Elliptic Flow Problems", Rept. No. TF-23, Thermosc. Div., Stanford University, (1985).
- [10] Tropea, C.; Dimaczek, G., Private communications, Lehrst. f. Strömungsmechanik, University Erlangen-Nürnberg, FRG, (1988).
- [11] Obi, S.; Peric, M.; Scheuerer, G., "Finite Volume Calculations of a High Reynolds Number Backward Facing Step Flow Employing a Colocated Variable Arrangement", Proc. 2nd Int. Symp. Transport Phenomena in Turbulent Flows, The University of Tokyo, 25-29 Oct. 1987.

9. ACKNOWLEDGEMENTS

The work reported in this paper has largely benefitted from discussions with Prof. J. H. Ferziger during his sabbatical leave from Stanford University. The authors are grateful for this. The support of the Deutsche Forschungsgemeinschaft within its program "Physik abgelöster Strömungen" is also gratefully acknowledged.

Detailed Flowfield Measurements Over A 75° Swept Delta Wing For Code Validation

Scott O. Kjølgaard
William L. Sellers III

NASA Langley Research Center
Hampton, VA

Summary

Selected results from an experimental investigation documenting the flowfield over a 75° swept delta wing at an angle-of-attack of 20.5° are presented. Results obtained in the investigation include surface flow visualization, off-body flow visualization, and detailed flowfield surveys for various Reynolds numbers. Flowfield surveys at Reynolds numbers of 0.5, 1.0 and 1.5 million were conducted with both a pitot pressure probe and a 5-hole pressure probe; and 3-component laser doppler velocimeter surveys were conducted at a Reynolds number of 1.0 million. The pitot pressure surveys were obtained at 5 longitudinal stations, the 5-hole probe surveys were obtained at 3 longitudinal stations and the laser doppler velocimeter surveys were obtained at one station. The accuracy of each instrumentation system is discussed, as well as, discrepancies in the calculation of vorticity using various algorithms.

Nomenclature

a	speed of sound, ft/sec
b	local span of model, inches
C_p	Static pressure coefficient, $\frac{P_s - P_{s\infty}}{q}$
C_{pt}	Pitot pressure coefficient, $\frac{P_t - P_{t\infty}}{q}$
D	diameter, ft
L	length of model (22.392 inches)
M	Mach number, U_∞/a
r	vortex core radius
Rn	Reynolds number, $U_\infty L/\nu$
P_s	static pressure, lb/ft ²
P_t	pitot pressure, lb/ft ²
St	Stokes number, $\frac{1}{18} \frac{\rho_p U_s D_p D_p}{\rho \nu r}$
q	dynamic pressure, $\frac{1}{2} \rho U_\infty^2$, lb/ft ²
U_∞	freestream velocity, ft/sec
U_s	swirl velocity near vortex core, ft/sec
u, v, w	velocity components in body axis system, ft/sec
$\tilde{u}, \tilde{v}, \tilde{w}$	velocity components in tunnel axis system, ft/sec
u'	rms of fluctuating component of \tilde{u} velocity, ft/sec
\vec{V}	local flow velocity, ft/sec
x, y, z	distance from coordinate origin in body axis system, inches
$\tilde{x}, \tilde{y}, \tilde{z}$	distance from coordinate origin in tunnel axis system, inches
α	pitch angle measured by 5-hole probe, deg
β	yaw angle measured by 5-hole probe, deg
Γ	circulation, ft ² /sec
ν	kinematic viscosity, ft ² /sec
ρ	density, slugs/ft ³
θ	total flow angle, $\sin^{-1} \left(\frac{\sqrt{\tilde{v}^2 + \tilde{w}^2}}{\sqrt{\tilde{u}^2 + \tilde{v}^2 + \tilde{w}^2}} \right)$
ψ	yaw angle, deg
ω	vorticity, $\frac{L}{U_\infty} \left(\frac{\partial \tilde{u}}{\partial y} - \frac{\partial \tilde{v}}{\partial x} \right)$

Subscripts:

p	particle
t	transition
∞	at freestream conditions

Introduction

Computational methods are progressing rapidly toward the prediction of the three-dimensional flowfield about complex geometries at high angles-of-attack. These methods solve either the Euler or Navier-Stokes equations and, typically, some assumptions about the structure of the flowfield are made to make the solution more tractable. These computational methods require a large number of grid points to adequately model the flowfield, and they produce large amounts of information. To validate these methods, detailed experimental flowfield measurements are required. To date, few sets of experimental data exist which are of sufficient detail and completeness to allow a definitive validation of current computational methods.

This paper will describe an experimental effort at NASA-Langley Research Center to fully document the flowfield over a 75° swept delta wing at an angle-of-attack of 20.5° . This investigation was expressly directed toward obtaining a data base for code validation. The data obtained includes surface flow visualization at Reynolds numbers ranging from 0.5 to 2.0 million in increments of 250,000; pitot pressure surveys at 5 longitudinal stations at Reynolds numbers of 0.5, 1.0, and 1.5 million; 5-hole pressure probe surveys at 3 longitudinal stations at Reynolds numbers of 0.5, 1.0, and 1.5 million; and 3-component laser doppler velocimeter surveys at a Reynolds number of 1.0 million. Reynolds number variation was accomplished by changing the tunnel speed, which corresponds to a Mach number range of 0.04 to 0.11. Supersonic data were previously obtained with this same model in the NASA Langley Unitary Plan Wind Tunnel by Miller and Wood (reference 1) and compared with computational results in reference 2. A comparison of the results from this investigation with the results from the computational method described in reference 2 are presented in reference 3 for a Reynolds number of 0.5 million.

Test Facility and Data Acquisition System

The 75° swept delta wing was tested in the NASA-Langley Basic Aerodynamics Research Tunnel (BART). The BART is an open-return wind tunnel with a test section 28 inches high, 40 inches wide by 10 feet long. The maximum test section velocity is 220 ft/sec which yields a Rn/ft of 1.4 million. The airflow entering the test section is conditioned by a honeycomb, 4 anti-turbulence screens and an 11:1 contraction ratio. A photograph of the facility is shown in figure 1. The variation in the longitudinal component of turbulence intensity with test section q is presented in figure 2. The figure indicates that the turbulence intensity ranges from 0.05 to 0.08 percent at test section $q = 10$ and 45 psf, respectively.

Code validation requires large amounts of experimental flowfield data. The timely acquisition and reduction of this data dictates the use of a highly integrated and fully automated data acquisition and control system (DACS). The BART DACS consists of a desktop computer system which monitors and controls the tunnel instrumentation (voltages and pressures). Data acquisition software has been written which allows completely automated surveys of flowfields above models of arbitrary geometrical shape. Real-time color displays of the flowfield data are produced by the DACS to allow immediate interpretation of the test results. A minicomputer is used to control and acquire data from the 3 component laser doppler velocimeter (LDVDAS). This system communicates with the BART DACS to allow real-time color displays of the flowfield data. A block diagram showing the integration of the BART DACS with the LDVDAS is presented in figure 3.

Model Description

The model used in this investigation was a 75° swept delta wing. A sketch of the model is presented in figure 4. The model is constructed of aluminum and has a centerline length of 22.392 inches and a span of 12 inches. The upper surface of the delta wing was flat. The leading edge of the delta wing is sharp (.005 inch radius) with a chamfer of 10° normal to the leading edge. The model was attached to the model support system at $x/L = 0.64$ on the lower surface. Figure 5 shows the delta wing mounted in the test section. A row of 19 pressure ports were located at $x/L = 0.9$; however, they were not used in this investigation. Boundary layer transition was not fixed on either the upper or lower surfaces.

Experimental Techniques

Flow Visualization

Surface flow visualizations were conducted at Reynolds numbers ranging from 0.5 to 2.0 million in increments of 250,000. The upper surface of the model was covered with a black vinyl adhesive-backed paper. A mixture of titanium dioxide suspended in kerosene, with a small amount of oleic acid added as an anti-coagulant, was painted on the vinyl paper with a brush. The airspeed in the test section was brought to test conditions, and after the kerosene had evaporated, the TiO_2 was left deposited on the surface. The vinyl paper was then carefully lifted off the surface, placed on poster board, and photographed for a permanent record. Figure 6 shows a typical TiO_2 surface flow visualization.

Laser light sheet flow visualization was used to see if the vortices shed by the model were burst, and to determine if the probes used in this investigation had any visible effect on the vortices. The laser light sheet was produced using a 5-watt argon ion laser as the light source with a twin-mirrored galvanometer light sheet generator as described in reference 4. The smoke was produced by vaporizing propylene glycol at a temperature of 380° F and introduced into the tunnel circuit ahead of the honeycomb. Figure 7 shows a typical laser light sheet photograph and illustrates the capability of the system to produce simultaneous multiple light sheets.

Pitot Pressure Surveys

Pitot pressure surveys were conducted at $x/L = 0.3, 0.5, 0.7, 0.9$, and 1.1 in planes normal to the freestream direction for Reynolds numbers of 0.5, 1.0, and 1.5 million. The probe used was a boundary layer probe approximately 0.024 inches wide by .013 inches high with a wall thickness of 0.005 inches. The pitot pressure probe was always aligned in the freestream direction.

A computer-controlled probe-positioning system was used to traverse the probe through the flowfield above the delta wing. At the beginning of each survey and after the airspeed was brought to test condition, the model surface was located through the use of an electrical probe fouling circuit. This was done to lessen the effect of the probe and model deflections under aerodynamic loading. Once the model surface was located, the flowfield survey was conducted under complete computer control. A typical flowfield survey consisted of a grid of approximately 91 points horizontally by 31 points vertically (≈ 2800 data points per survey location) with a spacing between points equal to 1.67 percent of the local span. The time required to acquire one survey was approximately 2 hours. The data acquisition software also allowed the researcher to specify an 'embedded' survey grid in the survey just acquired. In this investigation, the embedded grid option was used for a more detailed survey of the left-hand (positive y/s) secondary vortex. The embedded grids typically contained 1700 data points with a grid spacing equal to 0.35 percent of the local span and required 75 minutes to complete.

Pressure data was measured using an electronic-scanning pressure system with 1 psid transducers. The accuracy of these transducers is ± 0.001 psi. This accuracy is a function of temperature (± 0.0005 psi/° F); therefore, the data acquisition system continuously monitored the temperature and automatically performed a recalibration when the temperature changed more than 2° F. After stepping to each measurement location and pausing 0.5 seconds, the mean pressure was determined by averaging 255 samples acquired over a 1 second time interval. The pitot pressure deficit was measured by referencing the pressure transducers to the total pressure downstream of the last anti-turbulence screen. The pitot pressure deficit was nondimensionalized by the freestream dynamic pressure to obtain the pitot pressure coefficient, C_{p_i} . Real-time color displays of the C_{p_i} were produced to insure there were no lead/lag errors induced by the movement of the probe through the flowfield.

5-Hole Probe Surveys

Five-hole probe surveys were conducted to measure flow angularity and velocity above the delta wing. These surveys were obtained at $x/L = 0.7, 0.9$, and 1.1 in planes normal to the freestream direction for Reynolds numbers of 0.5, 1.0, and 1.5 million.

The probe used in this investigation was a hemi-spherical tipped, 0.125 inch diameter 5-hole pressure probe. The probe was calibrated using equations derived from the potential flow about a sphere. The derivation of the calibration equations and the method of acquiring the calibration data are described in reference 5. The error in α , β , and q deduced from the 5-hole probe calibration data are presented in figure 8. The 5-hole probe was always aligned in the freestream direction and used the same probe positioning system and pressure measurement technique described above. The real-time display was updated to display the crossflow velocity vectors with the color of the vector reflecting the longitudinal component of velocity. A typical flowfield survey consisted of a grid similar to that

of the C_p measurements (≈ 3300 data points per survey location). However, due to the size of the 5-hole probe, the embedded survey grid option was not used to survey the secondary vortex.

Laser Doppler Velocimeter Surveys

The BART is equipped with a dedicated 3-component laser doppler velocimeter (LDV) system to enable the non-intrusive measurement of flowfields. The LDV is capable of obtaining accurate velocity measurements in flowfields with reverse flows, large shear gradients and velocity fluctuations. For this investigation, two LDV surveys were obtained at the longitudinal station $x/L = 0.9$ at a Reynolds number of 1.0 million for comparison with the 5-hole pressure probe results.

The BART LDV system is a three-color, orthogonal, crossed-fringe configuration with the receive optics mounted 90° off-axis. The 514.5, 496.5 and 476.5 nanometer wavelengths are used to measure the lateral (v), streamwise (u), and vertical (w) velocity components, respectively. Bragg cells are used to provide directional measurement capability in all three velocity components. The sample volume is spherical in shape and has been calculated to be approximately $150\text{-}\mu\text{m}$ in diameter. The optics and laser move as a unit on a traversing system that provides 1 meter of travel, with $10\text{-}\mu\text{m}$ resolution, in all three axes.

The flowfield was seeded with $0.8\text{-}\mu\text{m}$ polystyrene latex microspheres. The seed particles were suspended in a mixture of alcohol and water and were injected into the flow upstream of the honeycomb using an atomizing spray nozzle. Typically 500 to 4096 velocity samples were obtained at each measurement location in the flowfield. The actual number of samples depended on the particular location in the flowfield and the particle seeding rate.

The ability of a particle to track the streamlines in the flowfield, and thus the accuracy of the LDV, is directly related to the size of the particle. Theoretical predictions of particle trajectories in various flows were reported in references 6 through 9. Dring and Suo (reference 6) concluded that the particle trajectory in a free vortex swirling flow is governed primarily by the Stokes number (St) and when the Stokes number is less than 0.01, the particle will follow the circular streamlines of the free vortex.

The $0.8\text{-}\mu\text{m}$ particles used during this test have a density $\rho_p = 2.03727$ slugs/ft³. The Stokes number for the particles, based on the radius and the swirl velocity at the edge of the vortex core, is 0.007. The numerical procedure described by Dring (reference 6) was used to predict the particle trajectories for the vortices that were measured during this investigation. The predictions show that the particles used during this test, will follow the streamlines of the vortex with accuracy of about 1%.

Results and Discussion

Flow Visualization

A brief description of the flow over a swept delta wing will aid in the subsequent discussion of the results. At moderate to high angles-of-attack, the airflow separates at the sharp leading edge of a swept delta wing. The separated shear layer rolls up into two primary vortices as sketched in figure 9a (from reference 10). As the airflow rolls up and over the primary vortices it impinges on the surface along the attachment line and then flows outward. These two vortices induce additional velocities on the upper surface of the wing, which produce a suction pressure near the leading edges (figure 9b). Because of the steep adverse pressure gradients induced outboard of the primary vortex, the boundary layer separates and rolls up into smaller secondary vortices, which induce additional velocities on the surface and cause further modification of the wing pressure distribution. Depending on Reynolds number, additional tertiary separations may also occur. The secondary separation lines appear as rays emanating from the apex of the delta wing as shown in figure 9c. When the boundary layer transitions from laminar to turbulent, the position of the secondary separation shifts outward toward the leading edge as described by Hummel in reference 10. Vortex bursting may also cause a shift in the secondary separation line. In fact, Lambourne and Bryer (reference 11) described a situation in which the vortex bursting over the surface of the wing causes an outward shift or bending in the secondary separation line because of a reduction in the adverse pressure gradient and an increase in turbulence. This was not the case in this investigation since the laser light sheet flow visualization, as in figure 7, confirmed that the vortices were not burst over the entire Reynolds number range of the test.

The region where the boundary layer transitions from laminar to turbulent is important for validating computational methods, especially Reynolds-averaged Navier-Stokes codes which use turbulence models. Surface flow visualizations using titanium dioxide and kerosene were used to characterize the state of the boundary layer for Reynolds numbers between 0.5 and 2.0 million. The complete set of surface flow visualizations are presented in reference 12. The surface flow visualizations were digitized to obtain the location of the secondary separation lines

and these data are presented in figure 10. This figure shows the position of the right-hand secondary separation lines for the Reynolds numbers that were investigated. The transition Reynolds number is defined as,

$$Rn_t = x_t U_\infty / \nu$$

where x_t is the streamwise distance from the apex to where transition begins, ranged from 800,000 to 900,000. This agrees well with the results of Hummel presented in reference 10. The figure shows that the boundary layer transitions at the trailing edge of the wing at a Reynolds number of approximately 1.0 million and moves forward to $x/L \approx 0.4$ at a Reynolds number of 2.0 million.

Flowfield Surveys

Due to the large volume of off-body flowfield data that was obtained during this investigation, it is unfeasible to present the results for the entire test. Therefore, only the results for the Reynolds number of 1.0 million will be presented and discussed.

Pitot Pressure Coefficient, C_{pt}

Figure 11 presents contour plots of the pitot pressure coefficient data acquired over the 75° swept delta wing at $x/L = 0.3, 0.5, 0.7, 0.9$ and 1.1 for the Reynolds number of 1 million. The results indicate a high gradient in C_{pt} just outboard of the primary vortex core. It also shows two interesting regions where the C_{pt} measured in the flowfield are very nearly equal to the C_{pt} measured in the freestream. The first region appears as a hole between the free shear layer and the cores of the primary vortices. The second is a roughly triangular region at the centerline of the wing near the surface. These features were interesting because they were not apparent in the smoke patterns of the laser light sheet or in previous investigations on a similar geometry (reference 10).

Whenever a probe is introduced into a complex flowfield, the effect of the probe on the flowfield must be considered as well as the probe's own measurement characteristics. Flow visualization has confirmed that the presence of the probe did not cause premature bursting of the vortex or any perceptible disturbance to either the primary or secondary vortices. The pitot pressure probe used in this investigation was chosen because its extremely small size enabled measurements to be made with high spatial resolution in the flowfield. It was recognized at the outset of the investigation that the probe would not be capable of measuring the true total pressure since it is always aligned in the freestream direction and not in the direction of the local flow. Since the sensitivity of the pitot pressure probe is known, the measured data can be compared with computational results which predict pressure and velocity at all points in the flowfield. Figure 12 presents the pitot pressure measured by the probe versus the yaw angle. The figure shows that the probe has a plateau region of only $\pm 7^\circ$ and its response rolls off sharply outside of this range. The same response was measured for both pitch and yaw at multiple freestream dynamic pressures.

Results from the CFL3D Navier-Stokes code described in reference 2 were used to examine the effects of flow angularity on the measurement of total pressure. Figure 13 presents the total pressure coefficient contours predicted by the CFL3D code for $\alpha = 20.5^\circ$, $x/L = 0.7$ and $M = 0.3$. The total pressure coefficients were calculated using the static pressure and an isentropic deceleration of the total velocity component to stagnation. These contours indicate a vortical flow pattern similar to those obtained using the laser light sheet. Figure 14 presents the distribution of total flow angle calculated from the results of the CFL3D code. Total flow angles in the vortex flowfield reach a maximum of approximately 60° at this cross section and display characteristics similar to those seen in the experimental data. The velocity and static pressure field data were used to compute a "reduced total pressure coefficient", based on bringing only the component of the local velocity vector aligned with the freestream to rest. This reduced total pressure coefficient data is presented in figure 15a and includes at least the first order effect of the flow angularity on the present method of measuring total pressure. Figure 15a in comparison with the measured pitot pressures of figure 15b, shows that the calculated reduced total pressures contain all of the features of the measured pitot pressures. To provide a true quantitative comparison with theory and experiment, the actual measurement characteristics of the probe would need to be used to obtain the reduced total pressure instead of method described above.

Figure 16 presents typical C_{pt} data acquired during an embedded survey of the left-hand secondary vortex for $x/L = 0.9$, $Rn = 0.5, 1.0$, and 1.5×10^6 , respectively. The figure shows that the transition of the boundary layer from laminar to turbulent appears to change the structure of the secondary vortex. Figure 16a. ($Rn = 0.5$ million) shows a shear layer between the primary and secondary vortices with a corresponding large gradient in C_{pt} ; however, in figure 16c. ($Rn = 1.5$ million) this high gradient region does not appear.

Velocity Surveys

Velocity surveys were obtained for $x/L = 0.7, 0.9$, and 1.1 for the Reynolds numbers of $0.5, 1.0$, and 1.5 million. Figure 17 presents typical crossflow velocity vectors for the $x/L = 0.9$; $Rn = 1.0$ million. This figure shows the density with which the velocity data was acquired. Figure 18 presents contours of the u, v , and w components of velocity for the $x/L = 0.9$; $Rn = 1.0$ million data set.

Once again, one must consider the effect that the probe has on the flowfield as well as the probes ability to measure the flow angle and velocity in a non-uniform velocity field. As stated before, laser light sheet flow visualization showed that the probe had no visible effect on the position or structure of the primary or secondary vortex cores. Figure 8 presents the measurement errors for the 5-hole probe in a uniform flowfield. However, the flowfield over the 75° is obviously not uniform, as shown in figure 19. The figure presents the gradients in the v and w components of velocities. The flowfield has large gradients in both the v and w components (as high as 7000 ft/sec/ft). To assess the measurement errors of the 5-hole probe in this high gradient flowfield, a velocity survey was obtained using a three component LDV at the same points above the delta wing as the 5-hole probe. Figure 20 presents the differences between the LDV and the 5-hole probe results for the u, v , and w components of velocity. The figure shows that for regions of low velocity gradients (< 800 ft/sec/ft), the 5-hole probe does a reasonable job of measuring the flowfield quantities (probe error < 5 percent). In the core of the vortex, the 5-hole probe has errors in the u, v , and w components of velocity of $25, 17$, and 35 percent, respectively. The errors were calculated assuming that the LDV measurements were the reference. The equation used to calculate the u component error is show below:

$$u_{error} = 100 * \frac{(u_{LDV} - u_{5-hole})}{\sqrt{u_{LDV}^2 + v_{LDV}^2 + w_{LDV}^2}}$$

Vorticity

The velocity data obtained with the 5-hole probe were used to calculate the vorticity in the flowfield above the delta wing. These vorticity contours are presented in figure 21 for $x/L = 0.7, 0.9$, and 1.1 for a Rn of 1.0 million.

The vorticity calculated from a velocity field can vary significantly due to differences in algorithms, grid size and density. There are two commonly used techniques to calculate vorticity. The first method uses a finite difference algorithm to approximate the gradient terms $\frac{\partial \tilde{u}}{\partial y}$ and $\frac{\partial \tilde{v}}{\partial x}$ in the calculation of vorticity. The second method is based on Stokes theorem and calculates the circulation, $\Gamma = \oint \vec{V} \cdot d\vec{l}$ about a bounding path (typically a rectangle) and divides Γ by the enclosed area to compute the vorticity. The vorticity data presented in this paper were calculated using second order finite differencing on both interior and boundary points of the survey plane and was nondimensionalized by the root chord divided by the freestream velocity. This technique for calculation of vorticity is consistent with those commonly used by code developers.

A comparison was made between the vorticity calculated using both techniques during the course of this investigation. The maximum value of vorticity calculated from identical velocity fields was found to differ by as much as 50% . The vorticity calculated by the circulation method was consistently higher than that calculated by the finite difference method. Care must be exercised even when comparing the maximum vorticity levels from similar data sets using the same vorticity calculation technique. The maximum value of vorticity in a velocity field is very sensitive to grid size, placement and density and therefore, is not a good parameter for a detailed comparison. The vorticity data presented by Carcaillet in reference 13, provides a good example. The data was generated by a 75° swept delta wing at Reynolds numbers bracketing the present experiment. Even though very similar finite difference techniques were used and the survey grids were approximately the same, the data in reference 13 shows almost twice the maximum vorticity level in the core when compared to those measured in this experiment. Very good agreement is obtained, however, between vorticity contours just outside of the core. The results point to the fact that the experimentalist and computational code developers must be explicit in describing the technique for calculating vorticity and the geometry of the grid before the data can be used for detailed comparisons.

Concluding Remarks

Selected results from an experimental investigation documenting the flowfield over a 75° swept delta wing at an angle-of-attack of 20.5° are presented. Results obtained in the investigation include surface flow visualization, off-body flow visualization, and detailed flowfield surveys for various Reynolds numbers. Surface flow visualization was obtained at Reynolds numbers ranging from 0.5 to 2.0 million in increments of $250,000$. Flowfield surveys at

Reynolds numbers of 0.5, 1.0 and 1.5 million were conducted with both a pitot pressure probe and a 5-hole pressure probe; and 3-component laser doppler velocimeter surveys were conducted at a Reynolds number of 1.0 million. The pitot pressure surveys were obtained at 5 longitudinal stations, the 5-hole probe surveys were obtained at 3 longitudinal stations and the laser doppler velocimeter surveys were obtained at one station. Comparisons between the velocities measured by the 5-hole probe and those measured by the 3-component laser doppler velocimeter indicate that the 5-hole probe does a reasonable job of measuring flowfield quantities when the gradients in the flowfield are less than 800 ft/sec/ft. However, errors as high as 35 percent are seen in the region of the vortex core. Vorticity was calculated from the velocity data using two different algorithms and it was found to be sensitive to both algorithm, grid size and density.

References

1. Miller, D. S. and Wood, R. M.: *Lee-Side Flow Over Delta Wings at Supersonic Speeds*, NASA TP-2430, June 1985.
2. Thomas, J. L., Taylor, S. L., and Anderson, W. K.: *Navier-Stokes Computations of Vortical Flows Over Low Aspect Ratio Wings*, AIAA Paper 86-0207, January 1987.
3. Taylor, S. L.; Kjølgaard, S. O.; Weston, R. P.; Thomas, J. L. and Sellers, W. L. III: *Experimental and Computational Study of the Subsonic Flow About a 75° Swept Delta Wing*, AIAA Paper 87-2425, August 1987.
4. Rhodes, David B., Franke, John M., Jones, Stephen B., Leighty, Bradley D.: *A Twin-Mirrored Galvanometer Laser Light Sheet generator*, NASA TM 100587, 1988.
5. Kjølgaard, S. O.: *Description of the Theoretical Derivation and Calibration Technique for a Hemispherical-tipped 5-hole Probe*, NASA TM 4047, 1988.
6. Dring, R. P. and Suo, M.: *Particle Trajectories in Swirling Flows*, Journal of Energy, Vol. 2, No. 4, July-August 1978.
7. Dring, R. P., Caspar, J. R. and Suo, M.: *Particle Trajectories in Turbine Cascades*, Journal of Energy, Vol. 3, No. 3, May-June 1979.
8. Dring, R. P.: *Sizing Criteria for Laser Anemometry Particles*, Journal of Fluids Engineering, Vol. 104, March 1982.
9. Vorropoulos, G. and Wendt, J. F.: *Laser Velocimetry Study of Compressibility Effects on the Flow Field of a Delta Wing*, AGARD CP-342, April 1983.
10. Hummel, D.: *On the Vortex Formation Over a Slender Wing at Large Angles of Incidence*, AGARD CP-247, October 1978.
11. Lambourne, N.C. and Bryer, D.W.: *The Bursting of Leading Edge Vortices - Some Observations and Discussion of the Phenomenon*, Aeronautical Research Council, R&M No. 3282, 1961.
12. Kjølgaard, S. O., Sellers, W. L. III, and Weston, R. P.: *The Flowfield Over a 75 Degree Swept Delta Wing at 20.5 Degrees Angle-of-Attack*, AIAA Paper 86-1775, June 1986.
13. Carcaillet, R.; Manie, F.; Pagan, D.; and Solignac, J. L.: *Leading Edge Vortex Flow Over A 75° Swept Delta Wing: Experimental and Computational Results*, ONERA T.P. n° 1986-122, September 1986. (also presented at the 15th ICAS conference, London, 7-12 September 1986.)



Figure 1. Photograph of the Basic Aerodynamics Research Tunnel.

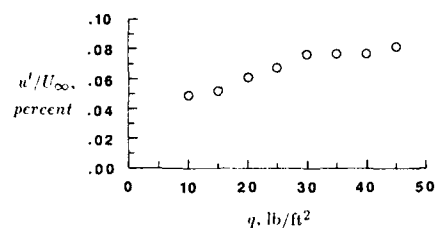


Figure 2. Variation in longitudinal turbulence intensity with q.

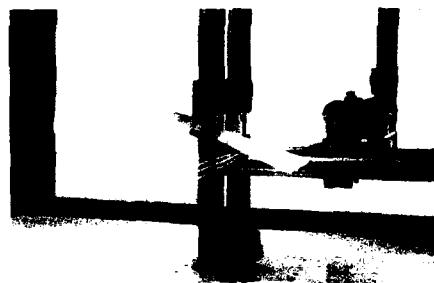
Figure 4. Sketch of 75° delta wing model.
(all dimensions in inches)

Figure 5. Photograph of the 75° delta wing model mounted in BART test section showing LDV laser beams.

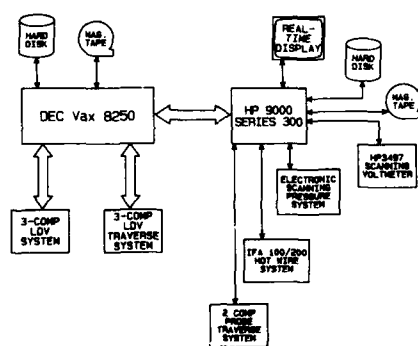


Figure 3. Schematic of the BART Data Acquisition System.

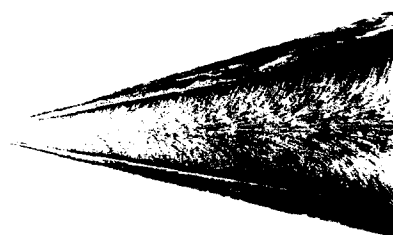
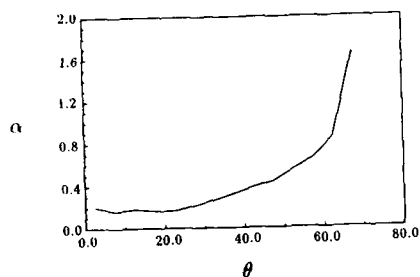
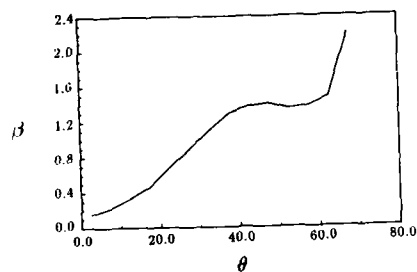
Figure 6. Surface flow visualization over 75° delta wing; $\alpha = 20.5^\circ$, $Re = 1.0$ million.



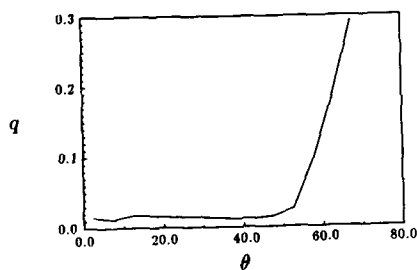
Figure 7. Photograph of laser light sheet flow visualization over 75° delta wing; $Rn = 0.5$ million.



a). Error in α versus total flow angle.



b). Error in β versus total flow angle.



c). Error in q versus total flow angle.

Figure 8. Characteristics of the 5-hole probe used in this investigation (uniform flow).

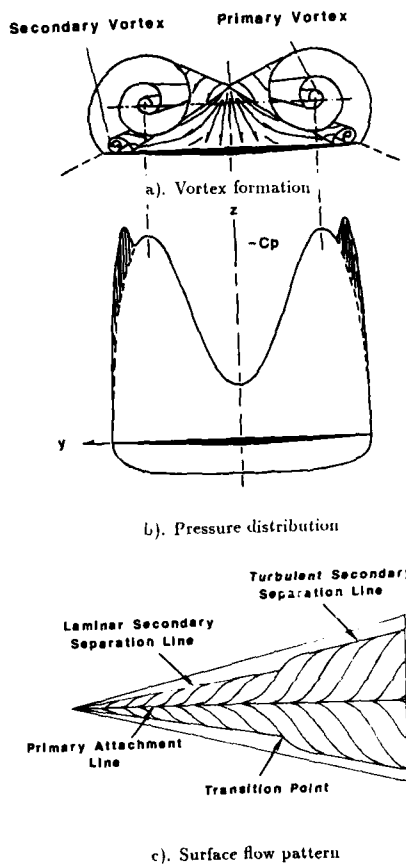


Figure 9. Schematic of the flow over a slender sharp-edged wing.

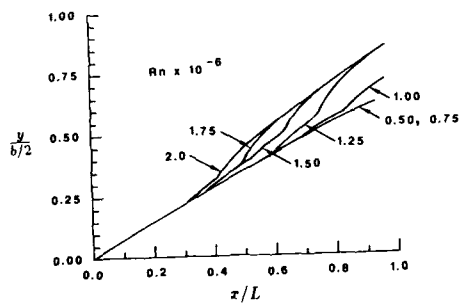


Figure 10. Secondary separation lines for right-hand side of 75° swept delta wing (Rn noted are $Rn \times 10^{-6}$).

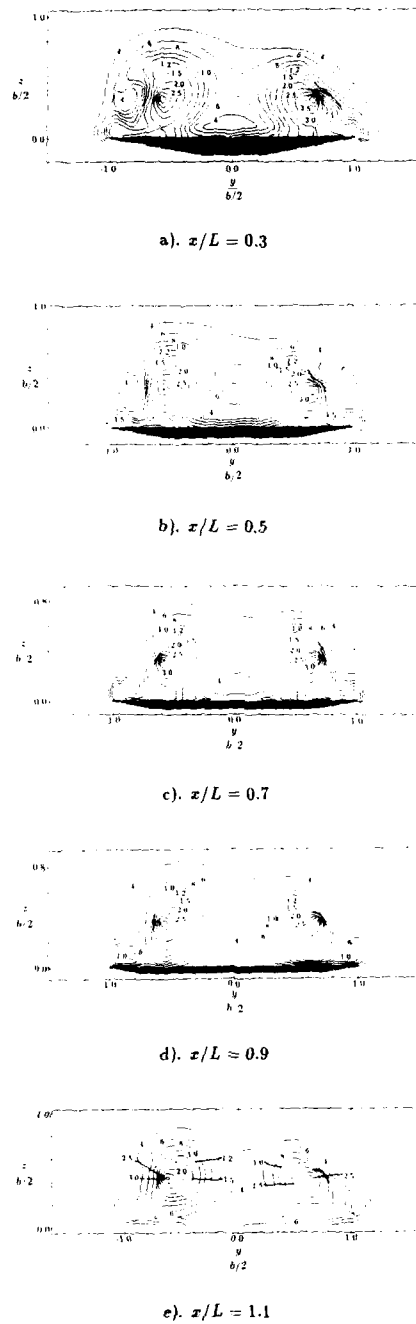


Figure 11. Contours of C_{pt} for $Re = 1.0$ million.

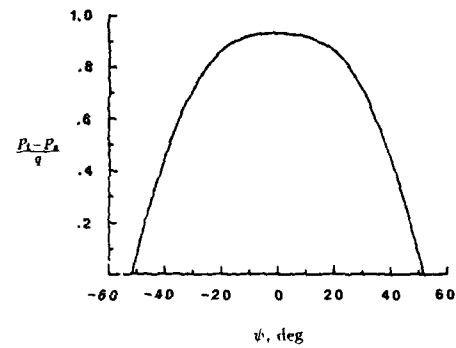


Figure 12. Sensitivity of pitot pressure probe to yaw angle.



Figure 13. Contours of total pressure coefficient from CFL3D Navier-Stokes code; $x/L = 0.7$, $M = 0.3$, $Re = 0.9$ million.



Figure 14. Contours of total flow angle from CFL3D Navier-Stokes code; $x/L = 0.7$, $M = 0.3$, $Re = 0.9$ million.

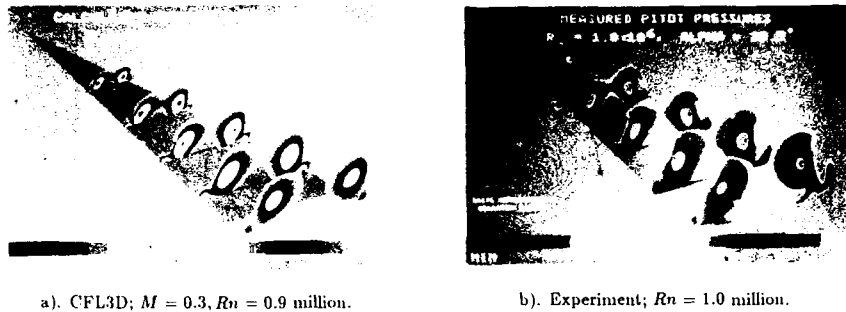
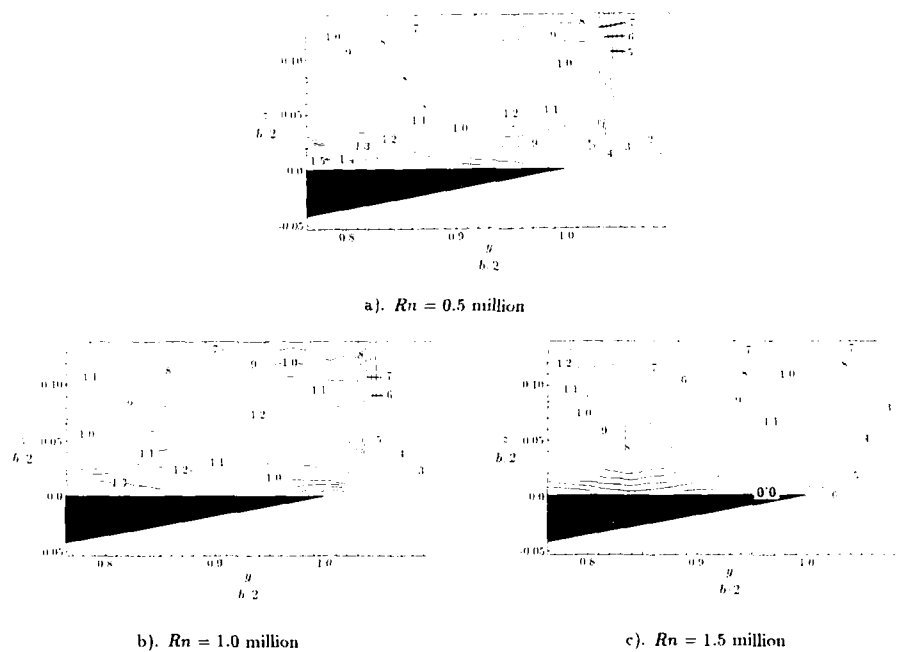
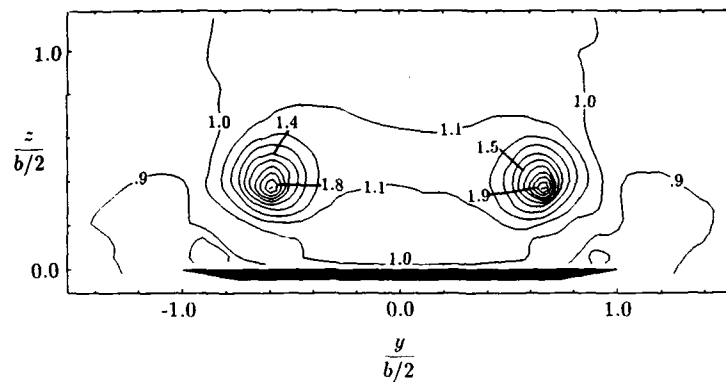
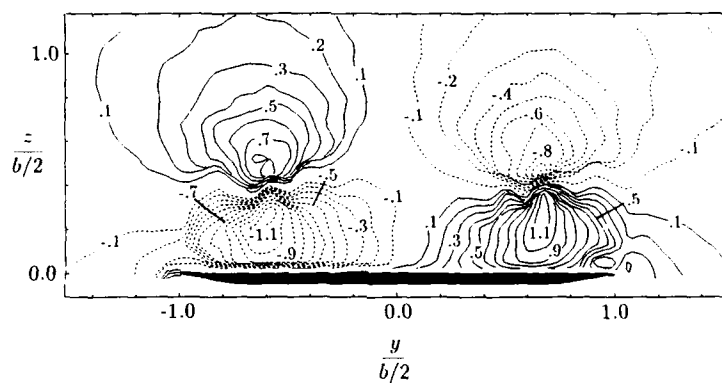


Figure 15. Comparison of reduced total pressure coefficient from CFL3D Navier-Stokes code with experimental results.

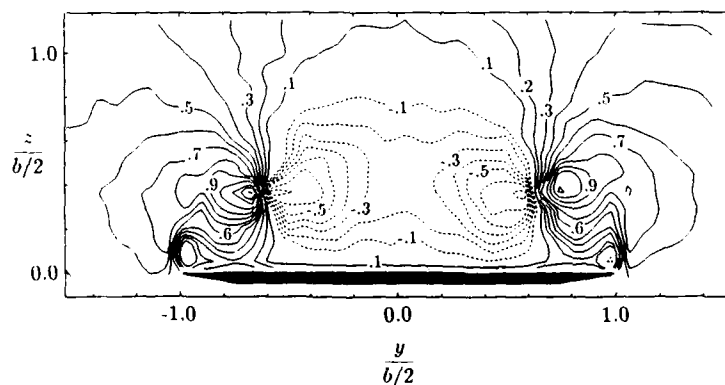




a). u/U_∞



b). v/U_∞



c). w/U_∞

Figure 18. Contours of the velocity data obtained with the 5-hole probe; $x/L = 0.9$, $Re = 0.9$ million.

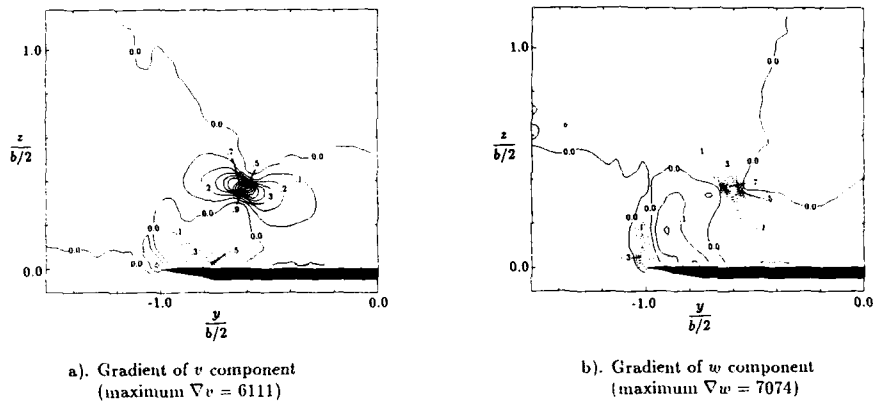


Figure 19. Contours of the velocity gradients in the flowfield over the 75° swept delta wing; $x/L = 0.9$, $Rn = 1.0$ million. (contour levels nondimensionalized by maximum gradient)

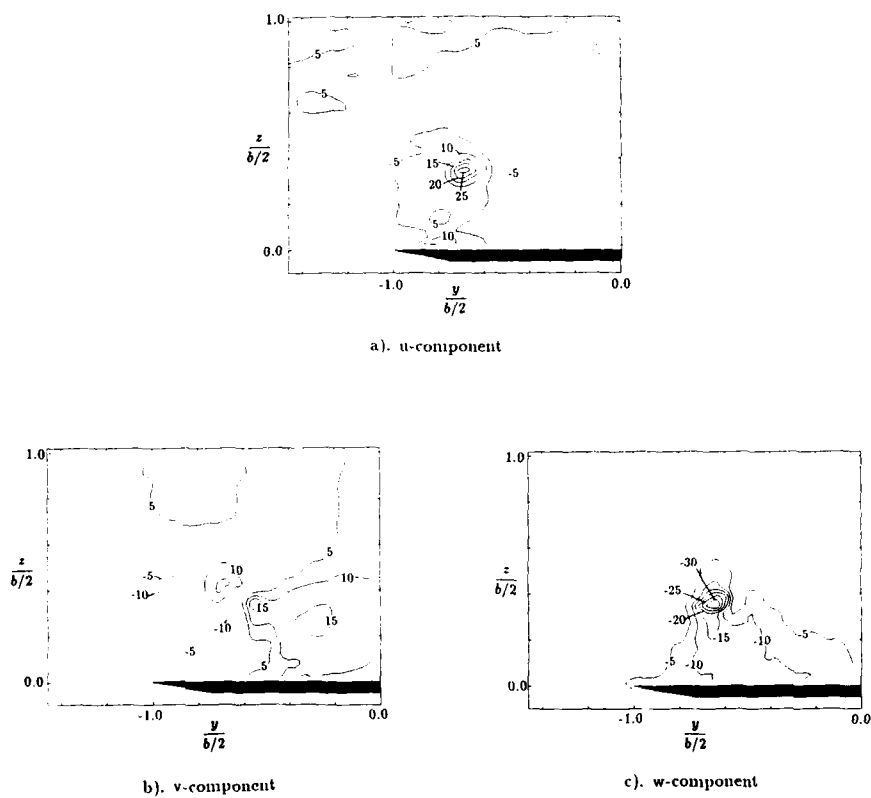
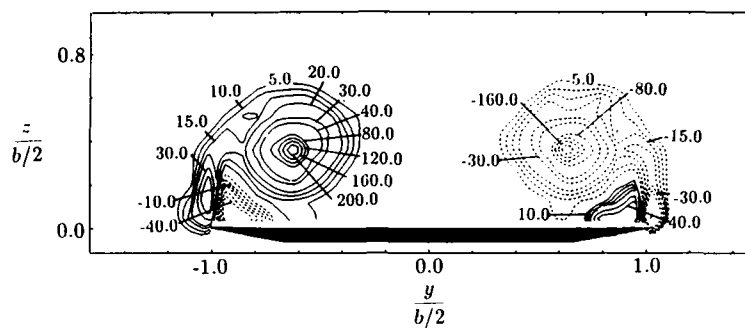
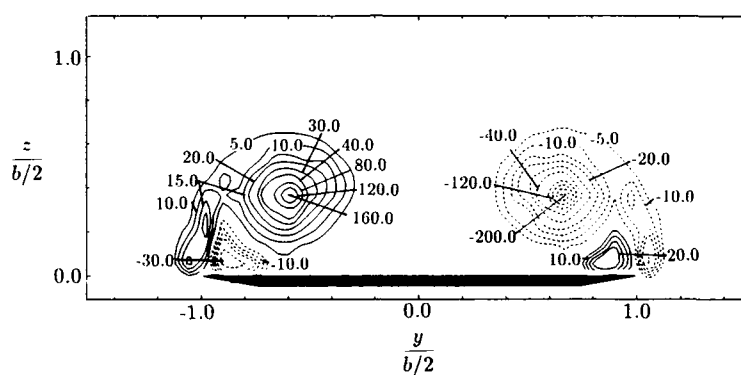
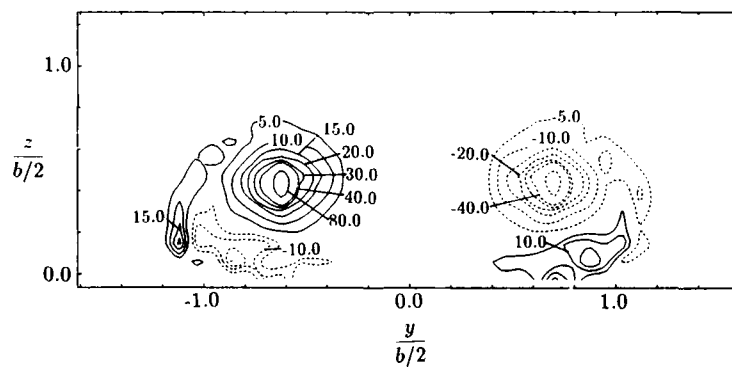


Figure 20. Per cent differences between measured velocities; $x/L = 0.9$, $Rn = 1.0$ million.

a). $x/L = 0.7$ b). $x/L = 0.9$ c). $x/L = 1.1$ Figure 21. Contours of vorticity derived from 5-hole probe data; $Rn = 1.0$ million.

EXPERIMENTS AND CODE VALIDATION FOR JUNCTURE FLOWS

L. R. Kubendran (AS&M, Inc.)
 NASA Langley Research Center
 Hampton, VA 23665, U.S.A.

and

C.-H. Sung and C.-I. Yang
 David Taylor Naval Ship R&D Center
 Bethesda, MD 20084, U.S.A.

SUMMARY

The turbulent flow around a juncture formed by an unswept wing and a flat plate has been experimentally studied, and the effectiveness of modifications near the wing leading edge in controlling the juncture flow field has been evaluated. The results are compared with numerical solutions of the incompressible Reynolds-averaged Navier-Stokes equations. The Baldwin-Lomax turbulence model is used in the computations. The numerical code is very time efficient, and it predicts the flow behavior well, including the detection of leading-edge vortex formation. It tends to over-predict the boundary layer thickness and the location of the vortex. Both the experiment and computations indicate that the leading edge flow separation is eliminated by the use of a leading-edge fillet designed in this study, resulting in drag reduction.

INTRODUCTION

A wing/fuselage-type juncture is typical of those found in aircraft, submarines, turbo-machinery, and aero/hydrodynamic test facilities. In this juncture, the turbulent boundary layer developing on the fuselage surface encounters an adverse pressure gradient as it nears the wing leading edge. The ensuing flow separates and forms a horseshoe vortex structure which surrounds the leading edge and trails downstream (fig. 1). In addition, a small counter-rotating vortex is also present very close to the wing/fuselage intersection. These vortices, together with the secondary flows that are present in any streamwise corner, lead to a truly complex three-dimensional flow. This vortex-dominated flow field becomes even more complicated when decelerating flow near the wing trailing edge separates.

The juncture vortex system can degrade the lift/drag characteristics of the juncture surfaces by modifying the regions of attached flow, and can affect the performance characteristics of the surfaces downstream. A clear understanding of the juncture flow is necessary for designers to assess or minimize the above-mentioned effects. Many groups of researchers have experimentally studied various aspects of this flow in different flow regimes (e.g., refs. 1-6). These studies have improved our understanding of the flow mechanisms in this field. But, it would be of great help to the designers if calculation methods existed in addition to these experimental results. Researchers involved in computational fluid dynamics consider the analysis of this flow challenging because of the presence of all six components of Reynolds stresses in turbulent flow junctures in addition to the secondary motion. Boundary-layer approximation methods are not adequate for solving this problem, and until recently, approaches based on Navier-Stokes equations could not be attempted because of insufficient computing resources. The advent of supercomputers is changing this situation.

With the availability of supercomputers such as CRAY-2 through nationwide computer networks, more and more Navier-Stokes solution procedures are being developed. Some of the recent computational studies related to this flow problem are detailed in references 7-9. But these and other codes will have to be validated against experimental results so that designers can confidently use them for evaluation of new concepts and for routine design analysis. With this in mind, an attempt has been made to validate a Navier-Stokes code in this paper.

The Numerical code has been developed at the David Taylor Naval Ship Research and Development Center (DTNSRDC). The experiments described here form the basis for a cooperative effort between NASA-Langley and DTNSRDC. The objectives of this program are two-fold: (1) viscous drag reduction by improvement of juncture flow field characteristics, and (2) validation of the DTNSRDC numerical code. Comparison between predictions of this code and the results of a previous DTNSRDC juncture flow experiment (ref. 6) has indicated good agreement (ref. 10).

In this paper, relevant results from the experiments conducted at NASA-Langley will be presented. The code will be validated against experimental static pressure distributions, and streamwise velocity measurements in the juncture and in the wake. An uncertainty analysis of the results will also be presented.

DESCRIPTION OF EXPERIMENTS

Facility and Instrumentation

The experimental facility was the 12 in. by 18 in. Low Speed Wind Tunnel at the NASA Langley 8-Ft. Transonic Pressure tunnel Complex. This open-circuit tunnel had an overall contraction ratio of 24:1. Two turbulence reduction screens and a honeycomb flow straightener were in the inlet section. This tunnel had an automated data acquisition system and a computer-controlled probe-traversing capability.

The probe rake used in this study had total- and static-pressure probes, and provision for a plug-in hot-wire sensor. The pressure probes were used for making all of the velocity measurements. The hot wire was used for checking the tunnel flow quality. All of the measurements were made at a nominal freestream velocity of 87 ft/s, corresponding to a unit Reynolds number of 520,000/ft. At this operating condition, the r.m.s. velocity fluctuation in the streamwise direction was measured to be about 0.15%.

Experimental Model

A schematic of the experimental setup is given in figure 2. The wing-fuselage juncture was simulated by mounting an unswept wing normal to a vertical splitter plate ("fuselage"). The wing had a chord length of six inches and a span of eight inches. For the smoke flow visualization and for making some preliminary measurements, an NACA 0012 wing was used, details of which are given in references 11 and 12. (Some relevant results from these experiments will be used here as needed.) For making detailed surveys, an NACA 0020 wing was used. The wing leading edge was located at 24 in. downstream of the plate leading edge. A flap at the plate trailing edge was used to adjust the stagnation point location near the plate leading edge. The plate boundary layer was tripped by means of a roughness strip near the leading edge. The plate was instrumented with wall static pressure orifices in the streamwise and lateral directions.

Leading-edge Flow Control

It has been observed in reference 5 that the wing leading edge shape or slenderness ratio (i.e., the ratio between maximum thickness and distance from leading edge to maximum thickness) is a major factor in determining the juncture flow field, and that the strength and location of the secondary vortex system can be controlled by suitably changing the leading edge. It is expected that leading-edge modifications near the wing root can lower the adverse pressure gradients encountered near the wing leading edge, and hence reduce vorticity in this region. Results from reference 13 indicate that a corner fillet of constant radius merely shifts the location of the secondary vortex, even though it has beneficial effects near the wing trailing edge location. Reference 14 demonstrates that wing sweep can sharply reduce pressure gradients upstream of the juncture in supersonic flows.

With the guidance provided by the above observations, the following criteria were used in the design of the fillet. The maximum height of the fillet above the plate surface should not significantly exceed the plate boundary layer thickness at the wing leading edge location. The thickness of the fillet should not exceed the maximum thickness of the wing since it was essential not to modify the juncture potential flow. In addition, it is preferable to use easily-developable surfaces, for ease of construction and installation on existing aircraft.

The modifications were restricted to the region upstream of the maximum thickness location. In the fillet design, a section of the wing near the root was stretched linearly so that the extension upstream of the leading edge was 2 in. at the root, and zero at a height of 1 in. from the root. The basic shape (NACA 4-digit series) of the airfoil (up to the maximum thickness point) was maintained at all heights above the plate surface. A removable fillet was fabricated using numerically-controlled machines. A photograph of the fillet used is shown in figure 3.

Measurement Locations

Pressure and streamwise velocity measurements, with and without leading-edge fillet, were made at the following stations: (1) two chord lengths

upstream of the leading edge, (2) at 50% chord location in the juncture, and (3) one chord length downstream of the wing trailing edge (fig. 2). Three sets of data were acquired at each of the above-mentioned measurement locations.

Measurement Uncertainties

An electrical model-detection circuit was used with the probe rake to accurately establish reference points on the plate and the wing. Backlash error was eliminated by traversing in one direction from the reference point. The uncertainties in locating x , y , and z are ± 0.05 in., ± 0.002 in., and ± 0.002 in., respectively. The accuracy of the differential pressure transducer used in the experiment is $\pm 0.25\%$ of the reading. The pressure instruments were calibrated as and when necessary, and their calibration factors were checked and adjusted for drift before making measurements on any given day. The estimated uncertainty in the wall static-pressure measurement is $\pm 0.4\%$. The uncertainty in the measurement of streamwise component of the velocity varied across the boundary layer. Near the surfaces, probe interference could have introduced an uncertainty of about $\pm 2.5\%$. Also, the measured streamwise velocities were not corrected for the influence of cross-stream flow velocities, which could have resulted in an overestimation of up to 3% . The total uncertainty in velocity for $y/c < 0.1$ is -2.5% to $+4.0\%$. For larger values of y , the uncertainty will be less than 1% .

EXPERIMENTAL RESULTS

In this section, some qualitative and quantitative results are presented to highlight the complex juncture flow. Smoke flow visualization results are from a related investigation (ref. 12). In that experiment, smoke-wire technique was used to visualize various x - z planes (planes parallel to the plate and slicing the wing) in a juncture formed by an unswept wing with NACA 0012 cross-section, mounted perpendicular to a flat plate. It should be noted here that the chord Reynolds number used in that study was 60000, with laminar flow on the plate. Still, the mechanism (adverse pressure gradient) that leads to vortex formation is the same in both laminar and turbulent flows, with the extent of separation being different.

Figure 4(a) presents visualization of the x - z plane located at y/δ (δ is the undisturbed plate boundary layer thickness at the wing leading edge). This picture clearly shows the flow separation upstream of the wing leading edge and the formation of horseshoe-type vortices. These vortices wrap around the wing and diffuse as they move downstream in the juncture. In the filleted case shown in figure 4(b), the leading-edge separation has been eliminated, and vorticity in the flow field has been effectively reduced. The fillet used is very similar to the one that was described earlier. Further details of this flow-visualization study are found in reference 12.

In the present experiment, surface oil-flow visualization was used to identify the regions affected by the use of leading-edge modification. The flow visualization shown in figure 5 is around the filleted juncture, and there is similarity between this picture and figure 4(b). Leading-edge flow separation, normally seen upstream of a blunt wing, has been essentially eliminated.

The downstream effects of this leading-edge device can be characterized from momentum measurements as shown in figure 6. There the wake momentum deficit (K_y) at a given y is calculated by integrating the momentum defect across a strip of wake measurement region, with z varying from -4 in. to 4 in. Also shown in this figure is the cumulative deficit (D_y), as determined by integrating K_y from the plate surface to a given y . This cumulative deficit, which is a measure of wake drag when y is large, is consistently lower with the fillet, indicating flow improvement. Similar quantitative results have also been obtained in a laminar juncture (ref. 12). These results reinforce the view that elimination of flow separation at inception can have large beneficial effects. Further research work is being carried out based on this conviction.

The following sections describe the numerical procedure used for calculating this flow, and give detailed comparisons of the code predictions with the experimental results.

DESCRIPTION OF CODE

A detailed description of the numerical procedure used to solve for the steady-state solution of the incompressible three-dimensional Reynolds-averaged Navier-Stokes equations can be found in reference 10. Only a brief outline is given here.

The governing equations to be solved are based on Turkel's preconditioned formulation (ref. 15) which is a generalization of Chorin's artificial compres-

sibility approach (ref. 16). The time derivative terms are preconditioned by multiplying an appropriate matrix in order to reduce the disparity in propagation speeds of fast-moving acoustic and slow-moving convective solutions.

The spatial discretization is based on the cell-centered central difference finite-volume formulation with the dependent variables located at the center of the computational cell. Then the governing equations are written in semi-discrete form at each cell center. The time-stepping scheme used is an explicit one-step four-stage Runge-Kutta method. This scheme is first-order accurate, has a Courant-Friedrichs-Lewy (CFL) number of 3, and has been shown to be computationally more efficient than the Runge-Kutta schemes used in references 17-19. A fourth difference artificial dissipation model has been incorporated to dampen spurious solutions.

In order to simplify the computation of viscous terms, a generalized version of the thin-layer approximation adequate for wing/fuselage-type junctures has been adopted. The Baldwin-Lomax turbulence model (ref. 20) is used. Techniques to accelerate the rate of convergence to a steady-state solution include the use of local time step, and the implicit residual smoothing. The use of the latter has raised the CFL number from 3 to 5 or 6. A great care must be exercised in the treatment of boundary conditions. The component of the momentum equations normal to the boundary surface written in curvilinear coordinates is used to set up the boundary conditions at the solid wall and the plane of symmetry. The non-reflecting boundary conditions using the characteristic variables are used for the farfield boundaries.

Computations

The computations were based on the Reynolds number used in the experiment. The computational domain was relatively small to avoid using a large computer memory. The inflow boundary was 1.7 chord lengths upstream of the leading edge of the airfoil, and the outflow boundary was at 2.0 chord lengths downstream of the trailing edge. The outer boundary was at 1.9 chord lengths from the x-y plane of symmetry, and the top boundary was at 0.7 chord lengths from the plate. The 3-D computational grid was constructed by stacking 2-D C-type grids.

The computations were performed on CRAY-2 of the Numerical Aerodynamic Simulation (NAS) Program at the NASA Ames Research Center. Computations were run in a coarse grid of $41 \times 25 \times 25$. Based on previous experience (ref. 10), a finer grid would have been necessary if the details of the small counter-rotating vortex needed to be resolved. The computations took 18 minutes of CPU time for 1500 time steps, and the solution did not change significantly after about 500 time steps (5 min. of CPU time). The root-mean-square residual of the pressure was reduced by three to four orders of magnitude. The solutions were second-order accurate in space. They were first-order accurate in time, which was considered adequate since only steady-state solutions were of interest. Computations of flow about junctures with fillets designed based on the criteria stated earlier are presented in reference 21.

ASSESSMENT OF CODE PREDICTIONS

In figure 7, the calculated wall static-pressure distributions in the plane of symmetry ($z=0$) upstream of the juncture configurations are compared with the experimental results. The agreement is considered quite good. In figure 7(a), the computations resolve the "hump" (local maximum at about $x/c = -0.1$) normally associated with the location of the separation vortex core. The experiments did not pick up this detail, mainly because of insufficient number of pressure orifices along the plate centerline. For the filleted case in figure 7(b), the calculations do not show any "hump" in the pressure distribution, confirming the experimental results (fig. 5) that the leading-edge separation has been eliminated or minimized.

Contours of streamwise component of the mean velocity u normalized with freestream velocity u_∞ are compared in figures 8 and 9. Figure 8 presents the results at the y-z plane in the juncture at $x/c=0.5$. The experimental results show that the leading-edge fillet causes significant changes in the flow behavior downstream in the juncture. The juncture vortex is much weaker for the filleted case, as indicated by the more uniform velocity contours in the juncture. The computed results exhibit a very similar trend, although the location of the vortex, as deduced from the contour distortions, is further away from the juncture. Similar computational problem has been reported in a recent report (ref. 22).

Figure 9 presents comparisons of velocity contours at the wake plane, $x/c=2.0$. Again, the improvements brought about by the elimination of leading-edge separation can be seen in figure 9(b) as reduction of contour distortions. The numerical results indicate a comparable behavior. But, they over-predict the boundary layer (or region) thickness. As stated earlier, freestream Reynolds number was the only constraint used in the computations of this flow.

The measured initial conditions could not be used in the calculations because of time limitations. This is believed to be one of the main reasons for over-prediction.

Individual velocity profiles are compared in figures 10 and 11. Since the computed location of the vortex is different from that of the experiment, one can expect differences in individual profile comparisons. Part of the differences between the experimental results and computations near the plate surface ($y/c < 0.1$) can be attributed to the measurement uncertainties (stated in a previous section), which can result in a fuller profile.

CONCLUSIONS

Elimination of leading-edge separation has considerable beneficial effects, as confirmed by the experiments and the computations described above. The numerical code is very time efficient, and it predicts the flow behavior well, including the detection of leading-edge vortex formation. It tends to over-predict the boundary layer thickness and the location of the vortex. Further comparisons for the wing at an angle of attack are being made, and the results will be published in future.

REFERENCES

1. Hubbartt, J.; McMahon, H.; and Oguz, E.: "Exploratory Tests of Flow in Wing-Root Junctions", Georgia Institute of Technology, School of Aerospace Engineering, Final Report, Contract No. P.O. CK27034P, Lockheed-Georgia Company, Marietta, Georgia, 1976.
2. Melling, A.; and Whitelaw, J. H.: "Turbulent Flow in a rectangular duct," *Journal of Fluid Mechanics*, Vol. 78, 1976, pp. 289-315.
3. Shabaka, I. M. M. A.; and Bradshaw, P.: "Turbulent Flow in an Idealized Wing-Body Junction," *AIAA Journal*, Vol. 19, No. 12, Feb. 1981.
4. Pierce, F. J.; Harsh, M. D.; and Menna, J. D.: "The Mean Flow Structure Around and Within a Turbulent Junction or Horseshoe Vortex," Virginia Polytechnic Institute and State University Report VPI-E-85-19, September 1985.
5. Kubendran, L. R.; McMahon, H. M.; and Hubbartt, J. E.: "Turbulent Flow Around a Wing/Fuselage-Type Junction," *AIAA Journal*, Vol. 24, No. 9, September 1986, pp. 1447-1452.
6. Dickinson, S. C.: "An Experimental Investigation of Appendage/Flat-Plate Junction Flow, Volume I: Description, Volume II: Elliptical Nose Appendage Data Base," David W. Taylor Naval Ship R&D Center Report 86/052, December 1986.
7. Kwak, D.; Rogers, S. E.; Kaul, U. K.; and Chang, J. L. C.: "A Numerical Study of Incompressible Junction Flows," NASA TM 88319, August 1986.
8. Briley, W. R.; Buggeln, R. C.; and McDonald, H.: "Solution of the Three-Dimensional Navier-Stokes equations for a Steady Laminar Horseshoe Vortex Flow," *AIAA Paper* 85-1520, 1985.
9. Baker, A. J.; and Orzechowski, J. A.: "An Interaction Algorithm for Three-Dimensional Turbulent Subsonic Aerodynamic Junction Region Flow," *AIAA Journal*, Vol. 21, April 1983, pp. 524-533.
10. Sung, C.-H.; Lin, C.-W.; and Hung, C. M.: "An Explicit Runge-Kutta Method for 3D Turbulent Incompressible Flows," 7th GAMM Conference on Numerical Methods in Fluid Mechanics, Belgium, Sept. 9-11, 1987.
11. Kubendran, L. R.; and Harvey, W. D.: "Juncture Flow Control Using Leading-Edge Fillets," *AIAA Paper* 85-4097, 1985.
12. Kubendran, L. R.; Bar-Sever, A.; and Harvey, W. D.: "Flow Control in a Wing/Fuselage-type Junction," *AIAA Paper* 88-0614, 1988.
13. Kubendran, L. R.; and Scheiman, J.: "Juncture Flow Measurements using Laser Velocimetry," *AIAA-85-1612*, 1985.
14. Price, E. A., Jr.; and Stalling, R. L., Jr.: "Investigation of Turbulent Separated Flows in the Vicinity of Fin-type Protuberances at Supersonic Mach Numbers," NASA TN D-3804, February 1967.
15. Turkel, E.: "Preconditioned Methods for Solving the Incompressible and Low Speed Compressible Equations," NASA ICASE Report 86-14, March 1986.

16. Chorin, A. J.: "A Numerical Method for Solving Incompressible Viscous Flow Problems," *Journal of Computational Physics*, Vol. 2, pp. 12-26, 1967.
17. Jameson, A.; Schmidt, W.; and Turkel, E.: "Numerical Solutions of the Euler Equations by Finite Volume Methods Using Runge-Kutta Time-Stepping Schemes," *AIAA Paper 81-1259*, 1981.
18. Rizzi, A.; and Eriksson, L.-E.: "Computation of Flow Around Wings Based on Euler Equations," *Journal of Fluid Mechanics*, Vol. 148, pp. 45-71, 1984.
19. Rizzi, A.; and Eriksson, L.-E.: "Computation of Inviscid Incompressible Flow with Rotation," *Journal of Fluid Mechanics*, Vol. 153, pp. 275-312, 1985.
20. Baldwin, B. S.; and Lomax, H.: "Thin-Layer Approximation and Algebraic Model for Separated Turbulent Flows," *AIAA Paper 78-257*, 1978.
21. Sung, C.-H.; and Lin, C.-W.: "Numerical Investigation on the Effect of Fairing on the Vortex Flows Around Airfoil/Flat-Plate Junctions," *AIAA Paper 88-0615*, 1988.
22. Burke, R. W.: "Numerical Calculation of Appendage-Flat Plate Junction Flow," *David W. Taylor Naval Ship R&D Center Report 87/002*, September 1987 (N88-15158).

ACKNOWLEDGMENT

The experiments were carried out at the Fluid Dynamics Branch of the Transonic Aerodynamics Division, NASA Langley Research Center, under NASA Contract NAS1-18235. The first author gratefully acknowledges the continuous support and directions provided for the juncture flow research by the Head of the Branch, Mr. William D. Harvey.

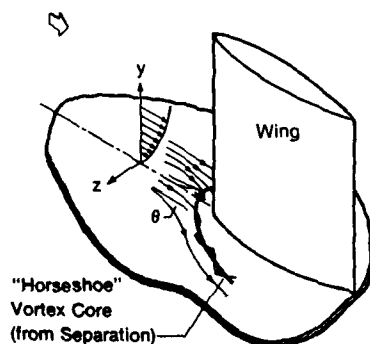


Figure 1.- Juncture flow schematic.

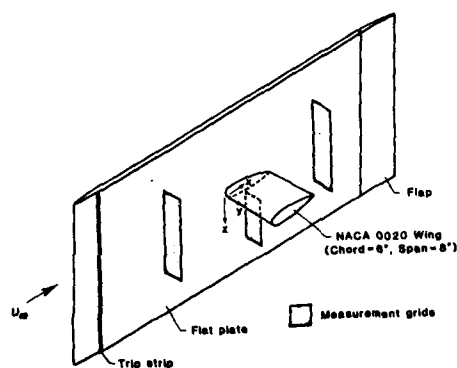


Figure 2.- Experimental setup.

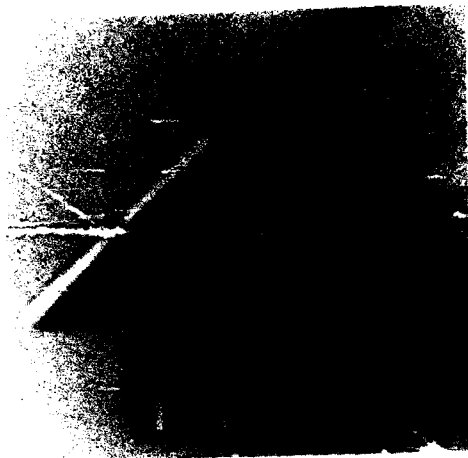


Figure 3.- Removable leading-edge fillet.

(a) No fillet



(b) With leading-edge fillet



Figure 4.- Junction flow visualization at $y/\delta=0.5$.



Figure 5.- Visualization of flow around filleted junction.

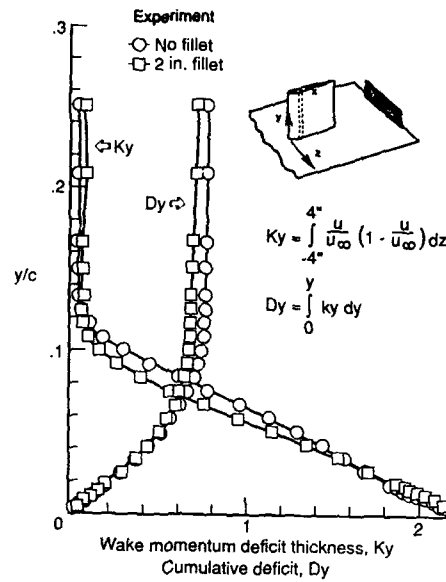


Figure 6.- Effect of leading-edge modification on wake flow (measurement plane: $x/c=2.0$).

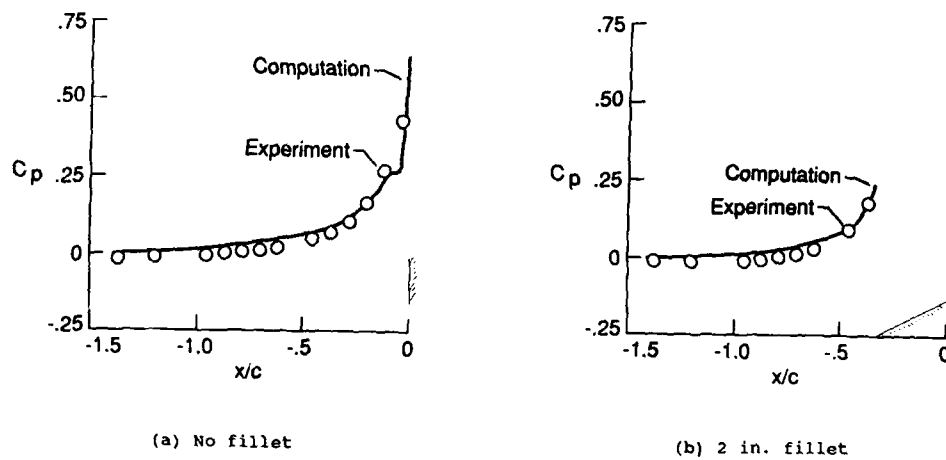


Figure 7.- Comparison of plate centerline static-pressure distribution upstream of wing leading edge.

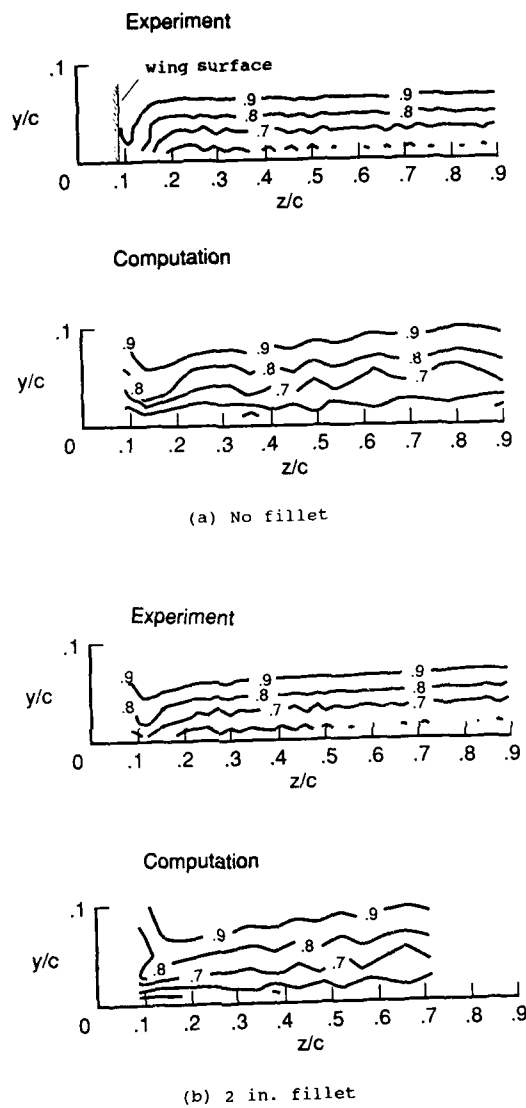
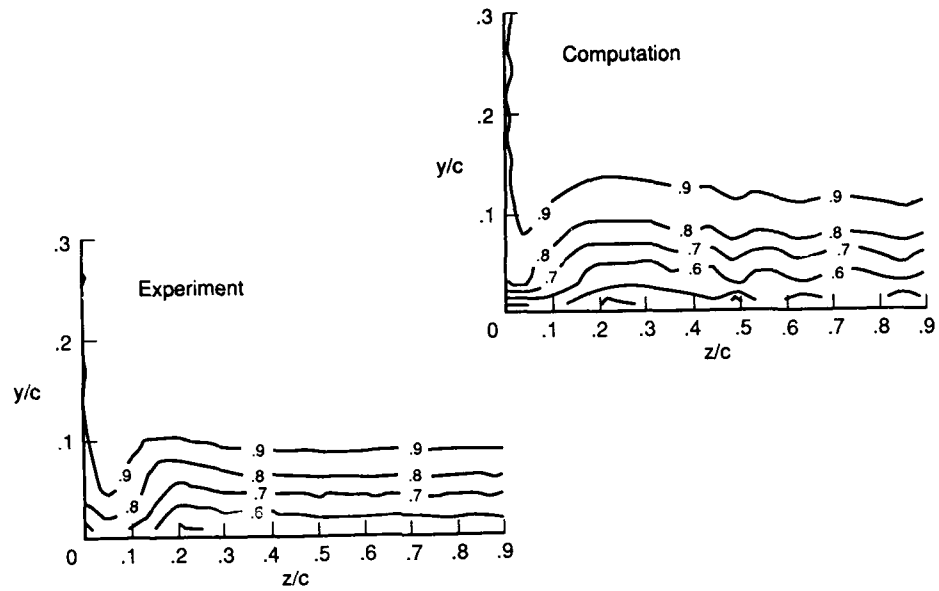
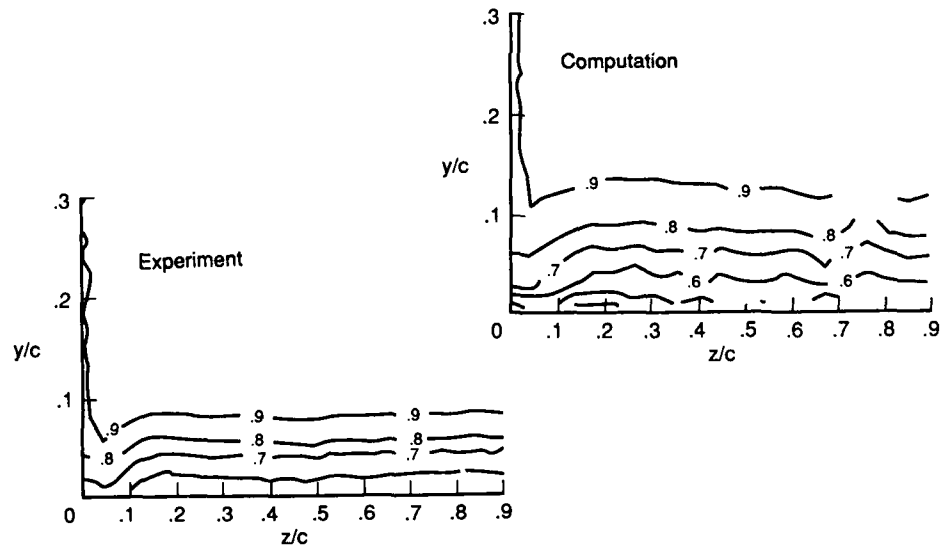


Figure 8.- Comparison of code predictions with experimental data (contours of streamwise velocity u/u_∞ at measurement plane $x/c=0.5$).



(a) No fillet



(b) 2 in. fillet

Figure 9.- Comparison of code predictions with experimental data (contours of streamwise velocity u/u_∞ at measurement plane $x/c=2.0$).

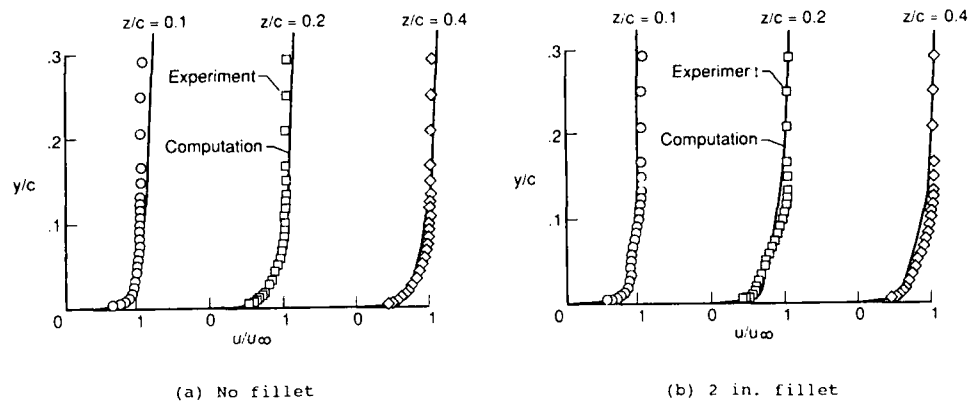


Figure 10.- Comparison of code predictions with experimental data (streamwise velocity profiles at measurement plane $x/c=0.5$).

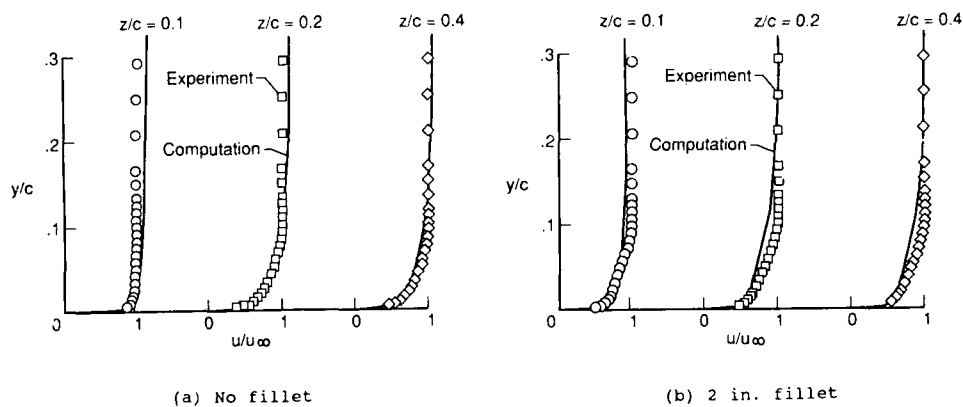


Figure 11.- Comparison of code predictions with experimental data (streamwise velocity profiles at measurement plane $x/c=2.0$).

ACCURACY AND EFFICIENCY OF A TIME MARCHING APPROACH FOR COMBUSTOR MODELING

A.A. Boretti and F.G. Martelli
Dipartimento di Energetica
Università di Firenze
Via di Santa Marta, 3
50139 Firenze, Italy

1. ABSTRACT

Research on numerical modeling of turbulent reactive gas flows is being conducted at the University of Florence Department of Energy Engineering (DEF) to provide improved analytical models of combustion devices. The objective is to develop adequate mathematical models of physical processes and a solution algorithm with suitable numerical properties. The paper describes in detail both the flow model and the numerical method adopted.

2. NOMENCLATURE

a	= speed of sound
a, a'	= coefficients
b, b'	= coefficients
A	= matrix of the quasilinear form
B	= matrix of the quasilinear form
c	= mean square fluctuating concentration
c_p	= constant pressure specific heat
C	= constant
D	= diffusion vector
e	= specific internal energy
E	= total specific energy
f	= unknown vector
f	= function
F	= axial flux vector
g	= perturbation vector or amplification factor
G	= radial flux vector
h	= unknown index
H	= heat released by the chemical reaction
H_{opt}	= optimization matrix
k	= thermal conductivity coefficient
K	= turbulence kinetic energy
i	= $\sqrt{-1}$
I	= identity matrix
j	= index of the spatial discretization
L	= length
m	= index of the time discretization
M	= Mach number
n	= index of the spatial discretization
N	= number of unknowns
p	= pressure
P	= turbulence kinetic energy production term
Pr	= reference Prandtl number, $\mu^* \cdot c_p / k^*$
q	= heat flux vector
R	= low Reynolds number term
Re	= reference Reynolds number, $V^* \cdot L^* \cdot \sigma^* / \mu^*$
Re_t	= turbulent Reynolds number
s	= stoichiometric ratio
S	= source vector
Sc	= reference Schmidt number, Γ^* / μ^*
t	= time
u	= axial velocity component
v	= radial velocity component
V	= velocity vector
x	= axial coordinate
y	= radial coordinate
Y	= mass fraction
w	= wave number
xx	= computational coordinate
zy	= computational coordinate
α	= specific heat ratio
β	= eigenvalue
Γ	= diffusion coefficient
σ	= density
μ	= viscosity coefficient
τ	= viscous stress tensor
ϕ	= conserved scalar

θ = complex scalar
 Ω = artificial viscosity coefficient
 δr = characteristic control surface dimension
 δt = timestep
 δx = mesh dimension
 δV = control surface area
 $\dot{\omega}$ = rate of chemical reaction
 ϵ = kinetic energy dissipation rate
 n = parameter for cartesian and axisymmetric coordinates

Subscripts

f_u = fuel
 l_{am} = laminar
 max = maximum
 min = minimum
 ox = oxidizer
 $turb$ = turbulent
 v = viscous sublayer
 w = wall

Superscripts

* = reference

3. INTRODUCTION

Numerical research on turbulent reacting flows is being conducted at the University of Florence Department of Energy Engineering (DEF) with the long range objective of bringing internal computational fluid dynamics to a level of practical application in designing combustion devices. Turbulent flows involving chemical reactions occur in many devices, from powerplants to jet engines. The requirements of increased combustion efficiency and decreased pollutant emissions in these applications have led to the need for designers to be able to predict quantitatively the behavior of turbulent reacting flows.

Classical empirical design methods show severe limitations in scaling combustion chambers. Furthermore, they are of little use when big jumps are required in the technology levels or in developing combustion chambers based on novel concepts. Nonetheless, the development of more suitable empirical-analytical design methods calls for significant advances in both physical modeling and numerics. The reliability of a numerical method is indeed mainly a function of both the adequacy of the physical process mathematical models and the numerical properties of the solution algorithm.

The basic equations that describe a multicomponent reacting gas mixture flow are assumed to be the Navier-Stokes conservation equations from a Eulerian standpoint, for overall mass, momentum, energy and species, amplified to include chemical source terms, and closed by chemical kinetics relationships and state relations.

Since even the fastest and most accurate computer available today cannot provide direct solution of these equations with adequate space and time resolutions, in most of the problems having engineering significance, it is customary to decompose the various quantities characterizing the flow into averaged values and fluctuating components. In turbulent flows, an averaging process is introduced in order to obtain the laws of motion for the averaged turbulent quantities (Reynolds averaged Navier-Stokes equations). For compressible flows, a density weighted average is preferred (Favre-averaged Navier-Stokes equations). Conversely, hypotheses are necessary to close conservation equations for averaged quantities.

Reactive gas flows are described as a mixture of three species, fuel, oxidizer and products, with combustion supposed to be controlled by a single step, irreversible chemical reaction where fuel and oxidizer combine in a fixed mass proportion to produce only a single product. This model represents a highly idealized description of practical chemical systems, but appears to be adequate for engineering purposes [8, 9].

In order to be able to properly describe turbulent reacting flows, it is necessary to develop mechanical turbulence and reaction rate models. The mechanical turbulence models developed by the authors range from a simple algebraic generalized mixing length model [10, 11] to a more sophisticated model with conservation equations for two turbulence quantities. The latter, described herein, utilizes turbulence kinetic energy K and its dissipation rate ϵ in a low Reynolds number formulation. While the algebraic approach has the notable advantage of simplicity, the two equation approach certainly represents a far more general model. In both cases, however, the level of approximation is always quite satisfactory for engineering purposes [10, 11, 15].

The averaged chemical source terms are modeled by using pseudo-eddy breakup mixing-controlled reaction rate expressions [8,9]. Fast kinetic assumptions appear to be particularly reliable in modeling turbulent reacting flows. The reaction rate models developed at DEF range from a model for only perfectly premixed flows to a model taking into account an imperfect premixing, currently under development and described herein.

Simple mixing-controlled reaction rate formulas allow a quantitative prediction of heat release due to chemical reactions [10, 11].

The main obstacles in advance numerics are the coupling and nonlinearity of equations, complexity of configurations, and the limitations of techniques, i.e., numerical discretization errors and instabilities in solution algorithms.

The spatial finite volume method (FVM) of discretization allows easy adaptability to different configurations. The method puts emphasis on the balance of flux integrals over control volumes, and conservation is ensured, since continuity of fluxes is maintained. A second-order accuracy on smoothly varied meshes is obtained by using hexagonal control volumes, with numerical errors vanishing at mesh refinement.

The explicit pseudo unsteady solution technique using artificial time-dependent equations exhibits good properties of stability, convergence, and ease of understanding. The procedure is particularly simple and robust, as required by the coupling between conservation equations and the non linearity. The physical implications are transparent and computing costs are reduced to acceptable levels.

This work involves a fluid dynamic study of steam generator boilers in large-size thermoelectric powerplants, where it is necessary to solve compressible viscous flow equations for exceedingly low Mach numbers. In fact, at such low speeds, compressible equations must be used to adequately account for the combustion-generated heat. Therefore, the paper deals with low speed regimes only.

Physical modeling and numerics are easier to perform in two-dimensional geometries. At present, we shall limit our attention to two-dimensional flows with both cartesian and axisymmetric coordinates.

4. FLOW MODEL

The following equations describing the flow model are written in the general two-dimensional form. A switching parameter Ω distinguishes between cartesian and axisymmetric coordinates.

4.1 BASIC CONSERVATION EQUATIONS

The basic conservation equations are the unsteady Navier-Stokes conservation equations, for mass, momentum, and energy. The unsteady form is required in the time marching approach to reach the steady solution. These equations are written in Favre-averaged form, with a first-order turbulence closure as follows [1, 2]

$$f_t + F_x + G_y = S$$

where f , F , G and S are four-component vectors and

$$f = \gamma^n \cdot (\sigma, \sigma \cdot u, \sigma \cdot v, \sigma \cdot E)^t$$

$$F = \gamma^n \cdot (\sigma \cdot u, \sigma \cdot u^2 + p - \tau_{xx}, \sigma \cdot u \cdot v - \tau_{xy}, (\sigma \cdot E + p) \cdot u - u \cdot \tau_{xx} - v \cdot \tau_{xy} - q_x)^t$$

$$G = \gamma^n \cdot (\sigma \cdot v, \sigma \cdot u \cdot v - \tau_{xy}, \sigma \cdot v^2 + p - \tau_{yy}, (\sigma \cdot E + p) \cdot v - u \cdot \tau_{xy} - v \cdot \tau_{yy} - q_y)^t$$

$$S = \gamma^n \cdot (0, 0, \Omega \cdot (p - \tau_{ee}) / \gamma^n, \sigma \cdot \epsilon - P + \rho f_u \cdot H)^t$$

where

$$\tau_{xx} = 2/3 \cdot \mu / Re \cdot (3 \cdot u_x - u_x - v_y - \Omega \cdot v / y) - 2/3 \cdot \sigma \cdot K$$

$$\tau_{xy} = \mu / Re \cdot (u_y + v_x)$$

$$\tau_{yy} = 2/3 \cdot \mu / Re \cdot (3 \cdot v_y - u_x - v_y - \Omega \cdot v / y) - 2/3 \cdot \sigma \cdot K$$

$$\tau_{ee} = 2/3 \cdot \mu / Re \cdot (3 \cdot v / y - u_x - v_y - v / y) - 2/3 \cdot \sigma \cdot K$$

$$q_x = \alpha \cdot k \cdot e_x / (Re \cdot Pr)$$

$$q_y = \alpha \cdot k \cdot e_y / (Re \cdot Pr)$$

$\Omega = 1$ or 0 for cartesian and axisymmetric coordinates respectively.

The Reynolds stresses have been expressed through an eddy viscosity model, following the Boussinesq assumption, by introducing an effective viscosity coefficient μ , the sum of a laminar and a turbulent part

$$\mu = \mu_{lam} + \mu_{turb}$$

Similarly, the turbulent flux vector has been modeled with a gradient assumption, by introducing an effective thermal conductivity coefficient k , the sum of a laminar

and a turbulent part

$$k = k_{lam} + k_{turb}$$

The turbulent viscosity coefficient is expressed according to the Prandtl-Kolmogorov expression

$$\mu_{turb} = \sigma \cdot C_k \cdot Re \cdot K^2 / \epsilon$$

while k_{turb} is assumed proportional to μ_{turb}

$$k = k_{lam} + k_{turb} = \mu_{lam} \cdot Pr / Pr_{lam} + \mu_{turb} \cdot Pr / Pr_{turb} \approx \mu$$

The production term for the turbulence kinetic energy is given as

$$P = \mu_{turb} / Re \cdot (2 \cdot [(u_x)^2 + (v_y)^2 + \rho \cdot (v/y)^2] + (v_x + u_y)^2)$$

For a perfect gas, the equation of state is

$$p = (\alpha - 1) \cdot \sigma \cdot e = (\alpha - 1) \cdot \sigma \cdot (E - \frac{1}{2} \cdot (u^2 + v^2))$$

and the speed of sound is written

$$a^2 = \alpha \cdot p / \sigma$$

Only one term involving an average of velocity and pressure gradient fluctuations is disregarded in the energy equation [1]. This assumption seems to be reasonable at Mach numbers below five, and certainly does not reduce accuracy in applications involving low speeds such as those under consideration.

The equations are written in dimensionless form. All the variables' characteristic values are constructed on the basis of a reference length L^* , velocity V^* , density σ^* , and values μ^* and k^* of the viscosity and thermal conductivity coefficients, whereas the other characteristic quantities are derived from: L^*/V^* for t , V^{*2} for e , E , K , H^* , P and $\sigma^* \cdot V^{*2}$ for q , $\sigma^* \cdot V^{*2}$ for p , $\mu^* \cdot V^*/L$ for τ , V^{*3}/L^* for ϵ

The physical flow domain is generally limited by inlet, exit, solid, and symmetry boundaries. A number of boundary conditions equal to the number of conservation equations minus one is imposed at inlet (u , v , e are known), while only one condition is imposed at exit (p is known). Along the solid boundaries the no-slip condition requires $u = v = 0$, while the heat-flux vector has to be specified (usually no-heat-flux conditions are adopted). At the plane of symmetry, the normal derivatives of all the flow parameters vanish. The only exceptions occur for those flow parameters which must be set equal to zero such as the normal velocity component.

4.2 LOW REYNOLDS NUMBER K- ϵ TURBULENCE MODEL

Over the past decade, two-equation models of turbulence have been widely used in modeling turbulence effects. Such models have certainly facilitated numerical studies of turbulent flows, though agreement of such predictions with experimental data has not been uniformly satisfactory. For wall flows, these models have been normally used in conjunction with empirical wall function. The wall function transfers the solid boundary conditions to points in the fluid removed from the wall. However, universal wall functions are not well established in many situations, and thus methods including an integration up to the wall appear preferable.

The no-slip boundary condition for flows over a solid wall ensures that viscous effects are important in the immediate wall vicinity. Standard K- ϵ models neglect any direct viscous effect on the turbulence structure, and hence are inapplicable in the viscous sublayer. In the viscous sublayer, the turbulence Reynolds numbers

$$R_i = \sigma \cdot K^2 \cdot Re / (\mu_{lam} \cdot \epsilon)$$

are low, the molecular transport is of the same order or greater than the turbulent transport, and the dissipative motions are strongly influenced by viscosity.

Low Reynolds number K- ϵ turbulence models are usually obtained according to a strategy of minimum change to high Reynolds number models. In the turbulence kinetic energy and kinetic energy dissipation rate conservation equations, the molecular diffusion term must be retained. Furthermore, an additional term significant at low Reynolds number is kept in the latter equation.

The unsteady conservation equations for K and ϵ are written, according to the previous general form, as

$$f = y'' \cdot (\dots, \sigma \cdot K, \sigma \cdot \epsilon)^t$$

$$F = y'' \cdot (\dots, \sigma \cdot u \cdot K - DK_x, \sigma \cdot u \cdot \epsilon - D\epsilon_x)^t$$

$$G = y'' \cdot (\dots, \sigma \cdot v \cdot K - DK_y, \sigma \cdot v \cdot \epsilon - D\epsilon_y)^t$$

$$S = y^6 \cdot (\dots, P - \sigma \cdot \epsilon, P \cdot C_{\epsilon 1} \cdot \epsilon / K - C_{\epsilon 2} \cdot \sigma \cdot \epsilon^2 / K + R_{\epsilon})^2$$

with

$$DK_x = f' / Re \cdot K_x / Sc_x$$

$$DK_y = f' / Re \cdot K_y / Sc_x$$

$$D\epsilon_x = f' / Re \cdot \epsilon_x / Sc_{\epsilon}$$

$$D\epsilon_y = f' / Re \cdot \epsilon_y / Sc_{\epsilon}$$

R_{ϵ} is a low Reynolds number term defined later on. The reference value for f' is f'' . Similarly to the previous assumption for k ,

$$f' = f'_{lamin} + f'_{turb} = \mu_{lamin} \cdot Sc / Sc_{lamin} + \mu_{turb} \cdot Sc / Sc_{turb} \approx \mu$$

The empirical constants appearing in the modeled equations are functions of R_t . From sublayer data obtained in high Reynolds number boundary layers, the function C_{μ} is given as

$$C_{\mu} = 0.09 \cdot \exp[-2.5 / (1 + R_t / 50)]$$

For decaying isotropic grid turbulence, a curve fit to experimental data gives

$$C_{\epsilon 1} = 1.43$$

$$C_{\epsilon 2} = 1.92 \cdot [1.00 - 0.33 \cdot \exp(-R_t^2)]$$

The Schmidt numbers should follow from a computer optimization. At present, the following values are used

$$Sc_{\epsilon} = 1.3$$

$$Sc_x = 1.0$$

but some adjustment is required.

Further modifications are needed for use near walls. Let y be the direction normal to the wall. Within the viscous sublayer, according to the classical representations of the near wall region such as the Chieng and Launder's two-layer model [3] reproduced in Figure 1, the velocity displays a linear variation, which we may write as

$$u = y \cdot Re \cdot \tau_w / \mu$$

where τ_w is the wall shear stress. Furthermore, the kinetic energy has a parabolic variation

$$K = K_v \cdot (y/y_v)^2$$

where y_v is the thickness of the viscous sublayer. (This corresponds to a linear increase in fluctuating velocity with distance from the wall.) The dominant contribution to the energy-generation rate is a term $\tau_{turb} \cdot u_y$, where τ_{turb} is the local turbulent shear stress. Since this stress is zero within the viscous sublayer, the generation of turbulence energy is zero. Unlike the generation, the dissipation rate is not zero, and the value is a constant equal to

$$2 \cdot \mu_{lamin} / (Re \cdot \sigma) \cdot (K^2_{,y})^2$$

On introducing the expression of K , we obtain

$$\epsilon = 2 \cdot \mu_{lamin} / (Re \cdot \sigma) \cdot K_v / y_v^2$$

In the immediate vicinity of a solid surface $\epsilon \approx$ constant, and therefore $\epsilon/K \rightarrow 0$ as $y \rightarrow 0$. The problem can be overcome by reinterpreting the dissipation equation so that it becomes an equation for

$$\epsilon^* = \epsilon - 2 \cdot \mu_{lamin} / Re \cdot (K^2_{,x} + K^2_{,y})^2$$

As a result, a term

$$R_{\epsilon} = -2 \cdot \mu_{lamin} / Re \cdot (K^2_{,x} + K^2_{,y})^2$$

is added as a source term in the kinetic energy conservation equation.

The term R_{ϵ} has been modeled as

$$R_{\epsilon} = -2 \cdot \mu_{lamin} / Re \cdot (\epsilon^2_{,x} + \epsilon^2_{,y})^2$$

The inclusion of the low Reynolds number terms in the conservation equations allows a $K = 0$, $\epsilon = 0$ wall boundary condition to be applied.

The proposed model appears to describe the flow in the immediate neighborhood of the wall in a reasonable way. The model basically differs from other low Reynolds number formulations such as those proposed by Chien and Launder [3] and Hassid and Poreh [4] in the form of the low Reynolds number terms R_τ and R_ϵ . The model does not take into account the preferential damping of velocity fluctuations in the direction normal to the wall, as in Chien [5] and Nagano and Hishida [4]. In comparison, the proposed formulation has the advantage of enhanced generality and programming ease.

Both K and ϵ have to be specified at inlet, while no condition is needed at exit. Inlet conditions are usually considered of lesser importance, but the imposed boundary conditions can lead to wrong conclusions about the performance of a turbulence model. The inlet profiles of K and ϵ can have significant effects on the downstream flow. In absence of experimental inlet profile data, careful choice of the inlet conditions is essential [6, 7]. Typical inlet conditions adopted in predictions are

$$K = C_K \cdot V^2$$

$$\epsilon = C_\epsilon \cdot K^{3/2} / L_\epsilon$$

with L_ϵ a fraction of the inlet duct height.

This model, now under development, is open to modification.

4.3 COMBUSTION MODEL

Let us consider a gas mixture of three species, fuel, oxidizer, and products. In the partially premixed case, all the species are known through solution of conservation equations for two reactive variables, let us say, the fuel mass fraction Y_F , and the conserved scalar ϕ

$$\phi = Y_{F,u} - Y_{O,x}/s$$

This scalar, an example of the Shvab-Zeldovich coupling function, is a flow property free from sources and sinks.

The solution of a conservation equation for ϕ or Y_F is perfectly identical for physical reasons, and the oxidizer mass fraction can be derived from ϕ and $Y_{F,u}$. However, the solution of a conservation equation without source and sinks is preferable for numerical reasons.

The conservation equations for Y_F and ϕ are written as follows

$$f = y'' \cdot (\dots, \sigma \cdot Y_{F,u}, \sigma \cdot \phi)^t$$

$$F = y'' \cdot (\dots, \sigma \cdot u \cdot Y_{F,u} - DY_x, \sigma \cdot u \cdot \phi - D\phi_x)^t$$

$$G = y'' \cdot (\dots, \sigma \cdot v \cdot Y_{F,u} - DY_y, \sigma \cdot v \cdot \phi - D\phi_y)^t$$

$$S = y'' \cdot (\dots, -\sigma \cdot \mu_{F,u}, 0)^t$$

with

$$DY_x = \tau / Re \cdot (Y_{F,u})_{,x} / Sc_r$$

$$DY_y = \tau / Re \cdot (Y_{F,u})_{,y} / Sc_r$$

$$D\phi_x = \tau / Re \cdot \phi_{,x} / Sc_r$$

$$D\phi_y = \tau / Re \cdot \phi_{,y} / Sc_r$$

The diffusion coefficient τ is assumed equal for all species. Its reference value is τ^* , and again $\mu_{F,u}$ is assumed proportional to $\mu_{F,u}^*$.

Both Y_F and ϕ have to be specified at inlet, while no condition is needed at exit. Along the solid boundaries, the diffusion vectors for species have to be specified (although usually no diffusion conditions are adopted).

The problem is completely closed when a formula for the (averaged) rate of chemical reaction for fuel is supplied. Because the chemical reactions can be considered in most cases very fast, it can be assumed that the rate of combustion will be determined by the rate of dissipation of the eddies. The fuel and oxidizer appear to be fluctuating intermittent quantities so that there is a relationship between the fluctuations and the average concentration of the species or their gradients. Therefore, the rate of dissipation can be expressed by the mean concentration of the species or by their gradients. In combustion controlled by turbulent mixing, the rate of chemical reaction is thus a function of both Y_F and ϕ , other than of a time characteristic for turbulent mixing K/ϵ .

As in the classical Eddy breakup models [8], we assume

$$\dot{c}_{rs} = C_{rsu} \cdot c \cdot \nabla^2 \cdot \epsilon / K$$

where C_{rsu} is a model constant and the variable c represent the mean square fluctuating component of fuel concentration. The reaction rate is thus directly proportional to a parameter representing reactant fluctuations and inversely proportional to a characteristic time for turbulent mixing.

While variable c may be obtained by solving its governing equation, it is preferable to assume that generation equals dissipation. Therefore, c can be evaluated from an algebraic equation written

$$c = C_0 \cdot [(Y_{rs})_{,x}^2 + (Y_{rs})_{,y}^2] \cdot K^2 / \epsilon^2$$

where C_0 is another model constant. The reaction rate is thus made dependent on the fuel mass fraction gradient.

The imperfect premixing is considered by introducing a limiting value for fluctuation, i.e., the smaller value between fuel and oxidizer concentration

$$c \leq Y_{rs}^2$$

$$c \leq (Y_{ox}/s)^2$$

As previously pointed out for the mechanical turbulence model, the proposed reaction rate model is still under development, so that further modifications in expressing c are likely to be necessary in order to obtain a fully satisfactory model for mixing controlled reactions.

The influence of temperature, disregarded in the proposed model, will soon be introduced in dealing with kinetically influenced processes. These processes can be easily considered by evaluating \dot{c}_{rs} as the lowest value obtained from the previous formulation and by an Arrhenius-type formulation [8, 9].

5. NUMERICAL METHOD

A numerical method has been developed for solving steady two-dimensional problems. It comprises a pseudo-unsteady solution, with artificial time-dependent equations, a finite volume spatial discretization, and an explicit corrected viscosity temporal discretization.

5.1 PSEUDO-UNSTEADY METHOD

The physical time dependent techniques (PTD), i.e., those solving the physical unsteady conservation equations, have the disadvantage of requiring a very large number of timesteps before convergence. To improve convergence, the physical unsteady conservation equations are replaced by artificial unsteady conservation equations. The artificial time-dependent techniques (ATD) solve unphysical unsteady conservation equations, constructed by adding purely artificial unsteady operators to the steady physical conservation equations, so as to lead to the correct steady solution in as small a number of timesteps as possible.

Let us consider a pseudo-unsteady solution of the following system of first-order equations

$$f_1 + A \cdot f_1 = C_0 \cdot I \cdot f + C_1 \cdot I \cdot f_{,xx}$$

where A is a matrix, possibly the function of the f_h 's ($h = 1, \dots, N$), but not of their derivatives, with N real eigenvalues β_h , transformable into diagonal form, and C_0 is a positive constant, and C_1 is constant, not necessarily positive).

The perturbation field can be expressed as follows [10]

$$g = g^* \cdot \exp(i \cdot w \cdot x) \cdot \exp(\theta \cdot t)$$

where g^* is a constant complex vector and θ a constant complex scalar. Substitution yields an algebraic equation, the solution of which furnishes N possible values of θ .

If $C_0 \neq 0$, $C_1 \neq 0$, the solution generally yields values of θ which are not wholly imaginary in that they have a positive or negative real part

$$\theta_h = -(C_1 \cdot w^2 - C_0) - i \cdot w \cdot \beta_h \quad (h = 1, \dots, N)$$

and the perturbation waves are consequently damped or amplified in accordance with C_0 is smaller or greater than $C_1 \cdot w^2$ respectively. In the specific case of $C_0 = 0$, $C_1 = 0$, the perturbation waves propagate at velocities β_h , without damping or amplification.

As a result of the previous analysis, suitable artificial time-dependent

conservation equations can be constructed by improving both the propagation and damping processes, obviously providing an unaltered steady solution. Examples of improved propagation are given in [12 - 15], while examples of improved damping are given in [10, 17]. The viscous terms always produce perturbation damping. Furthermore, emphasis must be placed upon the numerical treatment of the transport equations that contain source terms, i.e., energy, turbulence kinetic energy and its dissipation rate, and the fuel mass fraction. Under certain circumstances, these terms may give rise to perturbation amplification.

Suitable artificial time-dependent conservation equations can be constructed by improving the propagation processes, obviously providing an unaltered steady solution [12 - 15]. Assuming a successive explicit time-integration scheme, the timesteps are determined according to a local CFL condition. Therefore, the timesteps are assumed inversely proportional to the module of the maximum perturbation speed, β_{max} . To maximize the effect of the elimination process, the ratio between the speeds of slowest and fastest perturbations β_{min}/β_{max} should be as large as possible.

Thereafter, the physical time-dependent conservation equations were replaced by

$$f_{,t} + H_{PTD} f_{,x} + G_{,y} = S$$

where H_{PTD} is a matrix defined in order to optimize the rate of convergence toward the steady state.

The matrix expression is subject to several conditions [12]: 1) the coefficients of H_{PTD} must only be functions of f ; 2) the determinant should be nonzero; 3) the resultant system of conservation equations must be hyperbolic with respect to time; and 4) the number of negative eigenvalues must be equal to the number of boundary conditions given for the PTD equations.

In view of the great variety of admissible ATD equations, the systems are compared in terms of the best minimum and maximum perturbation speed ratios, with the further assumption of modifications to only one conservation equation. With those assumptions, H_{PTD} can be expressed in two-dimensional applications as [15]

$$H_{PTD} = \begin{pmatrix} 1 & 0 & 0 & 0 & \dots & 0 \\ 0 & 1 & 0 & 0 & \dots & 0 \\ 0 & 0 & 1 & 0 & \dots & 0 \\ M \cdot f_1 \cdot V^2 & -f_1 \cdot u & -f_1 \cdot v & f_2 & \dots & 0 \\ \dots & \dots & \dots & \dots & \dots & \dots \\ 0 & 0 & 0 & 0 & \dots & 1 \end{pmatrix}$$

where f_1, f_2 depend on the Mach number $M = V/a$,

$$f_1 = \min(M^2 - 1, 0),$$

$$f_2 = \max(f_1 + 1, C_r)$$

with C_r a small positive number.

The perturbation speed ratio for the PTD equations at low Mach numbers is given

$$\beta_{min}/\beta_{max} = 1/(1+1/M)$$

The perturbation speed ratio for the proposed ATD equations, again at low Mach numbers, is

$$\beta_{min}/\beta_{max} = 1/[(1 + M^2)/2 + \{(1 - M^2)/2\}^2 + 1]^{1/2}$$

Minimum and maximum perturbation speed ratios (a parameter regarded as a convergence speed indicator) are presented in Figure 2 for the PTD and ATD equations. The PTD equations appear to be unsuitable for flows with low Mach numbers, while the speed ratio appears to be significantly improved in low Mach number regions for the ATD equations [16].

5.2 SPACE DISCRETIZATION

The equations are discretized in space using a finite volume technique. The mesh is generally nonorthogonal and curvilinear, conforming to the domain boundaries and having lines intersecting at arbitrary angles. It is refined wherever high gradients are expected to occur. The discretization nodes, located at the line intersection, are the centers of hexagonal control volumes, obtained by connecting the six surrounding nodes, as represented in Figure 3.

The discretized version of the conservation equations with the fully irregular hexagonal control surface is a generalization of the classical hexagonal discretization proposed by Couston [18] for inviscid cascade flow calculations. Nonetheless, the classical discretization appears to be unsuitable for viscous calculations in complex geometries, mainly due to the requirements of constant mesh spacing in the direction normal to the wall.

A study of the consistency and order of accuracy of the discretization from hexagonal, trapezoidal, bitrapezoidal, and quadrilateral control surfaces conducted according to the procedure described in [19] shows that 1) discretizations of these types are generally only conditionally consistent and 2) the mesh requirements for consistency and second-order accuracy are easiest to satisfy for the hexagonal surface. In classical applications with nonuniform orthogonal meshes, discretization results unconditionally consistent with a second-order accuracy, and an ensuing mesh only admitting smooth variations.

With unconditionally consistent spatial discretization, numerical errors always vanish with mesh refinement. Furthermore, second-order accuracy on smoothly varied meshes is an important property of the scheme, since an error due to numerical diffusion of the first-order (as in the old upwind schemes) is frequently of such large magnitude that it overwhelms the turbulence model used in the calculations.

These control volumes allow use of flow parameters not specified by a boundary condition, according to the same numerical process inside the passage, through solution of conservation equations over half control volumes. However, half control volumes are used only along the solid boundaries, since a simpler extrapolation from the inner point is preferable along the inlet and outlet boundaries.

The approximation of the first-order derivatives of f is easily defined in terms of the coordinates and values of f in each node and its four neighbors [20]. If the cell of the center j,n belongs to a curvilinear system $zx(x,y) = \text{constant}$, $zy(x,y) = \text{constant}$, the derivatives f_x , f_y , required to express the viscous stress and the heat-flux and diffusion vectors can be written in terms of derivatives with respect to the curvilinear system; these can be easily approximated by means of standard centered differences.

5.3 TIME DISCRETIZATION

The equations are discretized in time using an explicit one-step corrected viscosity scheme. A semi-implicit character is introduced in the scheme previously adopted by the authors [10, 11] used to evaluate artificial viscosity. This improves stability properties without introducing additional difficulty.

The discretized version of the conservation equations is written

$$\begin{aligned} f^{m+1}_{j,n} = & -\delta t / 5V \cdot I(f_{\text{fluxes}}) + S_{j,n} \\ & + 1/6 \cdot (f^{m+1}_{j-1,n} + f^{m+1}_{j-1,n-1} + f^{m+1}_{j,n-1} + f^{m+1}_{j+1,n} + f^{m+1}_{j+1,n+1} + f^{m+1}_{j,n+1} - 6 \cdot f^{m+1}_{j,n}) \\ & - Q/6 \cdot (f^{m+1}_{j-1,n} + f^{m+1}_{j-1,n-1} + f^{m+1}_{j,n-1} + f^{m+1}_{j+1,n} + f^{m+1}_{j+1,n+1} + f^{m+1}_{j,n+1} - 6 \cdot f^{m+1}_{j,n}) \end{aligned}$$

where inviscid flux terms are evaluated at time $m \cdot \delta t$, while the viscous terms are evaluated at time $m \cdot \delta t$. In the latter time, quantities are evaluated only at fixed intervals and assumed constant between updating intervals.

The term f^{m+1} on the R.H.S., replacing a term f^m , means that the last updated value of f is used as it becomes available. This introduces a semi-implicit character, thereby improving the stability properties of the scheme. This modification does not introduce any difficulty, but, on the contrary, it results in a useful simplification. This allows to obtain an improved accuracy/convergence ratio, since numerical viscosity can be reduced for the same convergence rate.

In order to investigate the stability properties of the new scheme, let us consider the scalar equation

$$f_t + A \cdot f_x = 0$$

where A is a constant. The discretized version of this equation can be written

$$f^{m+1}_j = f^m_j - \delta t / \delta x \cdot A / 2 \cdot (f_{j+1}^m - f_{j-1}^m) + 1/2 \cdot (f_{j+1}^{m+1} + f_{j-1}^{m+1} - 2 \cdot f_j^m)$$

where a term f_{j-1}^{m+1} now replaces f_{j-1}^m on the R.H.S. This linear equation has a solution of the type

$$f_j^m = f^0(w) \cdot g^m \cdot \exp(i \cdot j \cdot w \cdot \delta x)$$

where f^0 represents the initial data and the superscript m in g means a power; g , the complex amplification factor, is given by

$$g = [-\delta t / \delta x \cdot A / 2 \cdot (\exp(i \cdot w \cdot \delta x) - \exp(-i \cdot w \cdot \delta x)) + \exp(i \cdot w \cdot \delta x) / 2] / [1 - \exp(-i \cdot w \cdot \delta x) / 2]$$

where angle $w \cdot \delta x$ varies between $-\pi$ and π , depending on the wavenumber w . According to the von Neumann stability criterion, the scheme is stable if $|g| \leq 1$ for all $w \cdot \delta x$, and unstable otherwise.

The amplification factor g is generally given, in a two-level scheme, by

$$(a + i \cdot a') \cdot g + (b + i \cdot b') = 0$$

where a, a', b, b' are all real coefficients dependent upon $w \cdot \delta x$. Therefore, if

$$g = |g| \cdot [\cos(\theta) + i \cdot \sin(\theta)]$$

then

$$|g|^2 = ([b \cdot a + b' \cdot a']^2 + [b \cdot a' - b' \cdot a]^2) / [a \cdot a + a' \cdot a']^2$$

In the specific case, the stability limit is given as

$$1/C_1 \cdot A \cdot \delta t / \delta x \leq 1$$

where C_1 is a number greater than unity. In the scheme previously adopted by the authors, the limit is simply

$$A \cdot \delta t / \delta x \leq 1$$

and therefore the new scheme gains in stability by a factor C_1 .

In the case where the model equation is a vector equation, f is a vector and A is a matrix that might be a function of the f_h 's ($h = 1, \dots, N$) but not of their derivatives, with N real eigenvalues β_h , the stability condition is replaced by

$$1/C_1 \cdot \beta_{max} \cdot \delta t / \delta x \leq 1$$

This condition can be expressed in the same fashion as the one adopted for the classical C.F.L. condition, i.e., the numerical domain of dependence of the scheme must contain the domain of dependence of the difference equation, although the latter is now reduced by a factor C_1 .

In the old scheme, the scalar viscosity coefficient Q is evaluated as

$$Q = C_{01} \cdot [1 - C_{02}/6 \cdot$$

$$| \phi_{j-1,2}^{n*} + \phi_{j-1,2}^{n*-1} + \phi_{j,2}^{n*} + \phi_{j,2}^{n*-1} + \phi_{j+1,2}^{n*} + \phi_{j+1,2}^{n*-1} - 6 \cdot \phi_{j,2}^{n*} |]$$

If $Q = 0$, the artificial viscosity is not corrected and its coefficient is of the order of $\delta r^2 / \delta t$, i.e., the artificial viscosity term introduces an error of the order of δr , which is unacceptable. If $Q = 1$, the error due to artificial viscosity is completely corrected, but the scheme reduces to unconditionally unstable for inviscid flows. If $Q = 1 - O(\delta r)$, a weak, often acceptable, residual viscosity is retained at the steady state; this viscosity is of the order of $(1-Q) \cdot \delta r^2 / \delta t$, i.e., only δr^2 .

It should be noted that the artificial viscosity is weak only at the steady state, but it is rather strong when required by the damping of perturbations during transient states.

Since a larger artificial viscosity coefficient improves convergence and since every conservation equation involves proper choice of the artificial viscosity coefficient to achieve a balance between stability and accuracy requirements, we shall introduce an artificial viscosity vector

$$Q = C_{01} \cdot [1 - C_{02}/6 \cdot$$

$$| \phi_{j-1,2}^{n*} + \phi_{j-1,2}^{n*-1} + \phi_{j,2}^{n*} + \phi_{j,2}^{n*-1} + \phi_{j+1,2}^{n*} + \phi_{j+1,2}^{n*-1} - 6 \cdot \phi_{j,2}^{n*} |]$$

where C_{01} and C_{02} have become two vectors, i.e., the viscosity coefficients are dependent on this particular equation. The end result is an improved accuracy/convergence ratio with respect to that of the previous scheme.

In the calculations, the terms referred to in iteration n^* are updated only at specific iterations and are assumed constants between two updatings. The updating rate is assumed equal to 20-25 iterations as a result of a numerical optimization. The viscosity coefficients are generally of the order of unity, but smaller values, producing a stronger artificial viscosity, are used in the mass conservation equation and in the energy conservation equation for nonreacting flows.

Lastly, it should be noted that special attention is focused to those source terms representing generation/destruction of turbulence kinetic energy or fuel consumption. The source terms representing generation/destruction in the transport equation for the turbulence kinetic energy and its dissipation rate are predominant with respect to transport and diffusion. Therefore, the oscillations of these terms have to be properly

reduced in order to avoid instabilities. The terms, suitably filtered, are evaluated only at set intervals and assumed constant during intervals. This results in a reduction of the oscillations and in enhanced convergence. The same applies to the source terms representing fuel consumption, especially the term appearing in the energy conservation equation due to the large values of the heat released by the chemical reaction $H \gg E$, where additional problems arise from the interaction between turbulence and combustion from the presence of K and ϵ in the fuel reaction rate expression.

6. RESULTS

The code is particularly economical with respect to both storage requirements and computing times. Calculations have been easily performed on an IBM PC AT. Computational time per node and per time step is of the order of $2 \cdot 10^{-3}$ s per conservation equation. The number of iterations to be performed obviously depends on the degree of accuracy. A residual source criterion is adopted to ensure that the procedure has converged. The unknown field satisfies the steady conservation equations to the required degree when the maximum pointwise residual for every conservation equation becomes smaller than values of the order of 10^{-3} - 10^{-6} . In typical calculations, convergence is reached in about 3000 - 4000 time steps.

6.1 NONREACTING FLOWS

The numerical method was first applied to the prediction of nonreacting flows. Several isothermal flows of engineering interest were computed and compared with experimental data, including plane and axisymmetric computations of recirculating flows (backward facing step flow, flow in a symmetric expansion, or double step, flow in a sudden pipe expansion; the flow domains are schematically illustrated in Figure 4).

Preliminary calculations were performed with a 25×35 computational grid. Grid size was dictated by available resources, although obviously better results can be obtained on finer grids. In particular, stronger mesh refinement should be used near the walls, mainly due to the low Reynolds number formulation of the $K-\epsilon$ turbulence model.

Calculations were performed for a flow over a backward facing step; experimental data obtained by Westphal et al. are given in [22]. The duct height upstream of the expansion is 76.2 mm, the step height is 50.8 mm, and the Reynolds number, based on step height is 42,000.

The mesh adopted is shown in Figure 5. The velocity field in Figure 6 exhibits the expected features, with the separated and reattachment region downstream of the step. A useful parameter for a quantitative evaluation of the prediction capability is comparison of the length of the recirculation region x_r , normalized by step height. The experimental reattachment length is about 7.33, the predicted reattachment length is 7.58.

In calculating backward facing step flow, standard $K-\epsilon$ models [6] underpredict the reattachment length by as much as 20%. This implies that the shear stress in the separated shear layer are overpredicted, i.e. the computed turbulent viscosity is higher than that existent in the region, which is probably the main reason for failure. Contrarily, the prediction obtained using the proposed $K-\epsilon$ model is quite accurate, despite the coarse grid adopted.

Calculations were also performed for a flow over an axisymmetric expansion (cfr. experimental data obtained by Moon and Rudinger [23]). The pipe diameter upstream of the expansion is 70 mm, the pipe diameter downstream of the expansion is 100 mm, and the Reynolds number, based on the small tube diameter, is 280,000.

The mesh adopted is shown in Figure 7. The velocity field in Figure 8 exhibits the expected features. Comparison of the length of the recirculation region x_r , normalized by the step height, gives an experimental reattachment length of about 8.0-8.5 with a predicted reattachment length of 8.04.

In contrast to the predictions for backward facing step flow, the standard $K-\epsilon$ models predict the reattachment length within experimental uncertainty [6], while the prediction obtained using the proposed $K-\epsilon$ model is again quite satisfactory.

The fairly good prediction of the flow in an abrupt pipe expansion and the underprediction of the recirculation length in the flow over a backward facing step, usually encountered using standard $K-\epsilon$ models are most likely due to an incorrect representation of the stabilizing effect of the top wall in these models. Within the limits of these applications, the proposed model seems to properly model the near wall region. Obviously, much more exploration is needed before final judgment can be passed.

Predicted and measured axial velocities are compared in Figures 9 - 11. While accuracy satisfactory for engineering purposes is obtained, better grid refinement should be adopted for fully satisfactory results.

6.2 REACTING FLOWS

The method was also applied to an extremely simplified configuration of turbulent flow with chemical reactions. In this configuration, mixing of two parallel streams, one of hot gases and the other of a fresh mixture of air and methane, in a constant area duct is considered. The hot jet causes a flame to be ignited and stabilized in the duct.

In the flow domain, schematically illustrated in Figure 12, the inlet duct, with a cross-section of $100 \times 100 \text{ mm}^2$, is split into two parts. The upper section ($80 \times 100 \text{ mm}^2$) is assigned to the fresh air and methane mixture, with a velocity of 65 m/s , a temperature of 580 K , and a mixture ratio of 0.8 ; the lower one ($20 \times 100 \text{ mm}^2$) one is assigned to the pilot flame made up of hot gases, with a velocity of 130 m/s and a temperature of 2000 K ; the walls are insulated.

This configuration has been studied both experimentally and theoretically; two sections, $x = 42 \text{ mm}$ and $x = 122 \text{ mm}$, were investigated with CARS measurements [25]. The authors studied the configuration using their simplified model, i.e., a generalized mixing-length mechanical turbulence model, with a formulation for the chemical source term to be used only in perfectly premixed flows [10, 11].

Preliminary calculations were performed on the 35×45 computational grid shown in Figure 13. Comparison of experimental and theoretical transverse temperature profiles in Figures 14 and 15 shows that agreement in both sections lies within engineering accuracy. At $x = 42 \text{ mm}$, the differences are very close to the limit of experimental uncertainty, since the influence of the reaction rate formulation is very small. At $x = 122 \text{ mm}$, the temperatures in the mixing layer are underestimated, with relatively large differences; this is attributable to a limited computer optimization of the model constants and to the lack of an ignition condition.

7. CONCLUSIONS

An artificial time-dependent technique (ATD) capable of solving the steady conservation equations governing partially premixed turbulent reacting gas flows has been presented.

Mechanical turbulence has been modeled using a low Reynolds number formulation of a $K-\epsilon$ turbulence model. This low Reynolds number terms and the dependence of the model constants on the turbulence Reynolds number allows a fairly good representation of the near wall region.

The chemical source term has been modeled according to classical fast kinetic assumptions. The formulation relates the chemical source term to the fuel mass fraction gradients, while making it possible to take into account imperfect premixing by introducing limiting values.

The proposed ATD equations, discretized by means of an explicit dissipative finite volume scheme, have been used to compute turbulent reacting and nonreacting flows. Results, obtained on coarse grids, are encouraging: The method appears to be simple, robust, and efficient, with computing costs reduced to acceptable levels.

8. REFERENCES

- [1] Hirsch, C., and Deconinck, H., "Description of Various Flow Models from Navier-Stokes to Potential Flow Models" in *Thermodynamics and Fluid Mechanics of Turbomachinery*, edited by Ucer, Stow, and Hirsch, Martinus Nijhoff Publishers, Boston, Massachusetts, 1985.
- [2] Hankey, W.L., Joseph, S.S., and Mikhail, A.G., "Computation of a Supersonic Flow Past an Axisymmetric Nozzle Boattail with Jet Exhaust," *AIAA Journal*, Vol. 18, No. 8, 1980, pp. 869-875.
- [3] Chieng, C.C., and Launder, B.E., "On the Calculation of Turbulent Heat Transport Downstream from an Abrupt Pipe Expansion," *Numerical Heat Transfer*, Vol. 3, 1980, pp. 189-205.
- [4] Nagano, Y., and Hishida, M., "Improved Form of the $K-\epsilon$ Model for Wall Turbulent Shear Flows," *Journal of Fluids Engineering*, Vol. 109, June, 1987, pp. 156-160.
- [5] Danberg, J.E., and Sahu, J., "Navier-Stokes Computations of Transonic Flows with a Two-Equation Turbulence Model," *AIAA Journal*, Vol. 24, No. 11, 1986, pp. 1744-1751.
- [6] Nallasamy, M., "Turbulence Models and Their Applications to the Prediction of Internal Flows: A Review," *Computers and Fluids*, Vol. 15, No. 2, 1987, pp. 151-194.

- [7] Sloan, D.G., Smith, P.J., and Smoot, L.D., "Modeling of Swirl in Turbulent Flow Systems," *Progress in Energy and Combustion Science*, Vol. 12, No. 3, 1986, pp. 163-250.
- [8] Spalding, D.B., Felton, P.G., Turan, A., and Swithenbank, J., "Fundamental Modelling of Mixing, Evaporation and Kinetics in Gas Turbine Combustors", in "Combustor Modelling", AGARD CP 275, October 1979.
- [9] Chiu, H.H., and Zhang, X., "Numerical Modeling of Afterburner Combustion," Papers from the Seventh International Symposium on Air Breathing Engines, September 1985.
- [10] Boretti, A.A. and Martelli, F., "Application of a Fast Pseudo Unsteady Method to Steady Compressible Turbulent Reacting Flows," paper submitted for presentation at the "First National Fluid Dynamic Congress," Cincinnati, Ohio, July 1988.
- [11] Boretti, A.A. and Martelli, F., "Numerical Modeling of Turbulent Combustion in Premixed Flows," paper submitted for presentation at the "National Heat Transfer Conference," Houston, Texas, July 1988.
- [12] Viviani, H., "Pseudo-Unsteady Systems for Inviscid Flow Calculation," ONERA TP No. 1984-69.
- [13] Essers, J.A., "Quasi Natural Numerical Methods for the Computation of Inviscid Potential or Rotational Transonic Flows," *Applied Mathematical Modelling*, Vol. 3, February 1979, pp. 55-66.
- [14] Essers, J.A., "Artificial Evolution Techniques for Transonic Flows," Numerical Methods for Flows in Turbomachinery Bladings, VKI LS 1982-05.
- [15] Boretti, A.A. and Martelli, F., "Soluzione delle equazioni del flusso viscoso comprimibile a basso numero di Mach, 2° Congresso Meccanica Computazionale," Rome, Italy, June 1987.
- [16] Choi, D. and Merkle, C.L., "Application of Time-Iterative Schemes To Incompressible Flow," *AIAA Journal*, Vol. 23, 1985, pp. 1518-1524.
- [17] Schmidt, W. and Jameson, A., "Recent Developments in Finite-Volume Time-Dependent Techniques for Two and Three Dimensional Transonic Flows," Computational Fluid Dynamics, VKI LS 1982-04.
- [18] Coustou, M., "Methode de calcul de l'écoulement inter aubes pseudo-tridimensionnel en regime transsonique," PhD Thesis, VKI, University of Brussels, Belgium, 1976.
- [19] Arts, T., "Cascade Flow Calculations Using a Finite Volume Method," Numerical Methods for Flows in Turbomachinery Bladings, VKI LS 1982-05.
- [20] Peyret, R. and Taylor, T.D., Computational Methods for Fluid Flow, Springer-Verlag, New York, New York, 1985.
- [21] Cushman-Roisin, E., "Analytical, Linear Stability Criteria for the Leap-Frog, Dufort-Frankel Method," *Journal of Computational Physics*, Vol. 53, 1984, pp. 227-239.
- [22] Autret, A., Grandotto, M., and Dekeyser, I., "Finite Element Computation of a Two-Dimensional Backward-Facing Step," *International Journal for Numerical Methods in Fluids*, Vol. 7, 1987, pp. 89-102.
- [23] Smyth, R., "Turbulent Flow Over a Plane Symmetric Sudden Expansion", *Journal of Fluids Engineering*, Vol. 101, September, 1979, pp. 348-353.
- [24] Moon, L.F., and Rudinger, G., "Velocity Distribution in an Abruptly Expanding Circular Duct", *Journal of Fluids Engineering*, Vol. 99, March 1977, pp. 226-230.
- [25] Dupoirieux, F., "Numerical Calculations of Turbulent Reactive Flows and Comparison with Experimental Results," ONERA TP No. 1986-80.

9. ACKNOWLEDGEMENTS

The authors are grateful to ENEL-CRTN of Pisa for their support of this work.

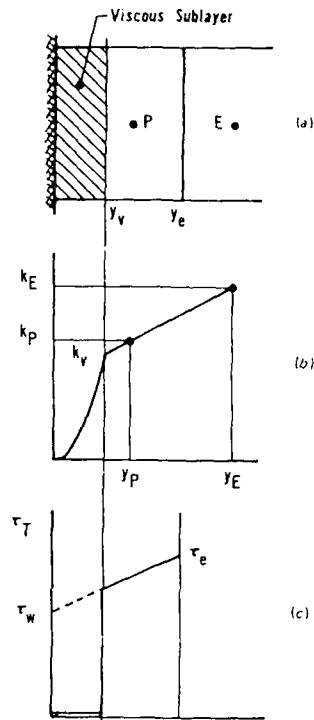


Figure 1 - Near-wall two-layer Chieng and Launder model [3].

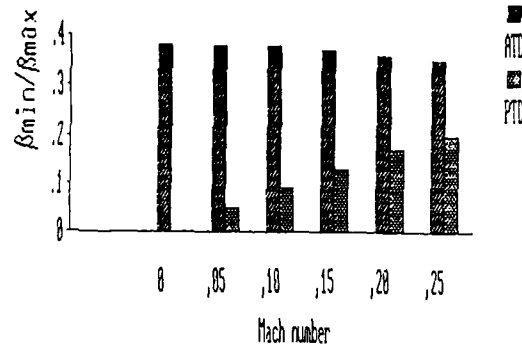


Figure 2 - Minimum and maximum perturbation speed ratios.

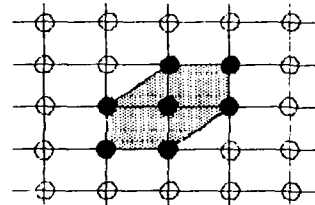


Figure 3 - Hexagonal control volume.

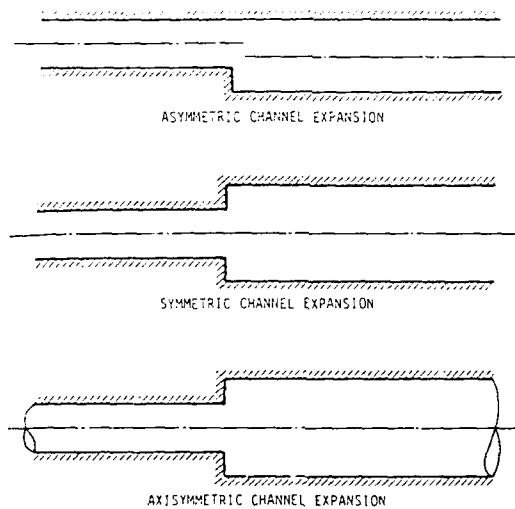


Figure 4 - Flow domain for several isothermal flows.

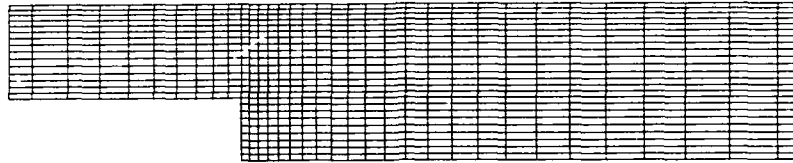


Figure 5 - Backward facing step: mesh adopted.

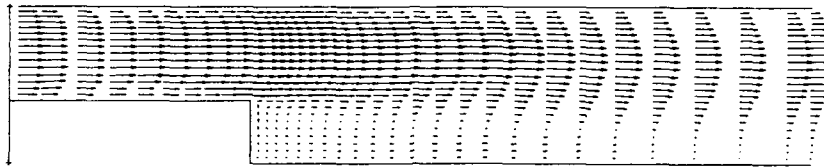


Figure 6 - Backward facing step: predicted velocity field.

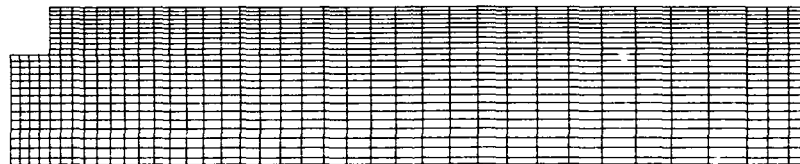


Figure 7 - Axisymmetric expansion: mesh adopted.

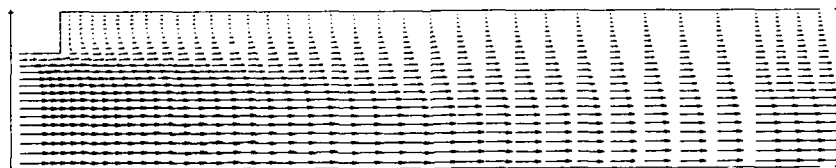
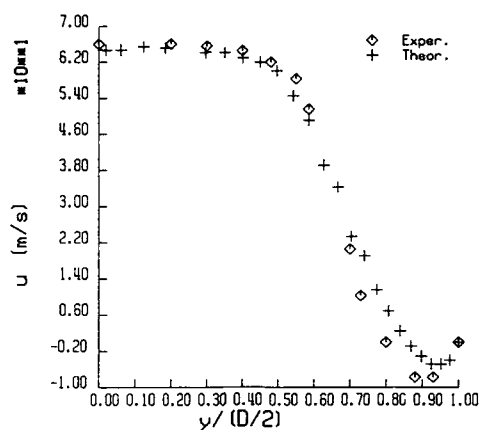
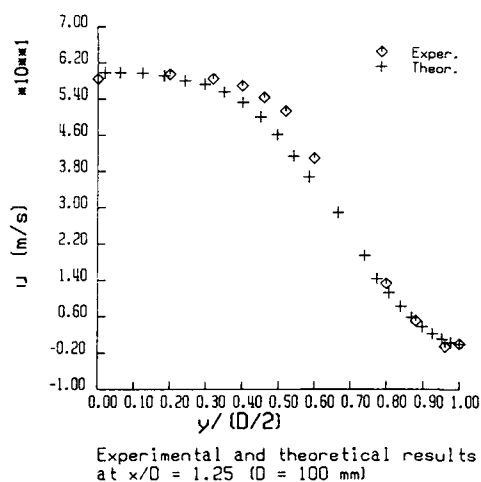


Figure 8 - Axisymmetric expansion: predicted velocity field.



**Figure 9 - Axisymmetric expansion:
comparison of predicted and measured
[24] axial velocities.**



**Figure 10 - Axisymmetric expansion:
comparison of predicted and measured
[24] axial velocities.**

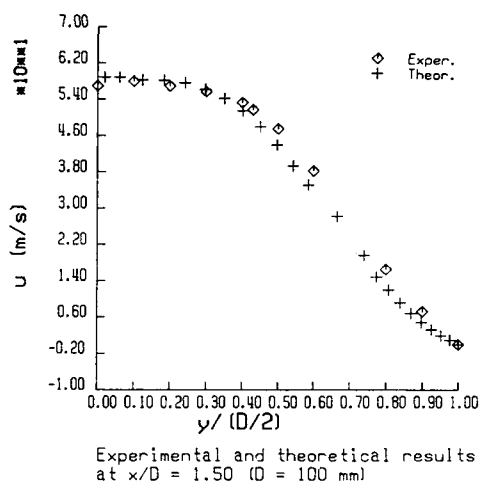


**Figure 11 - Axisymmetric expansion:
comparison of predicted and measured
[24] axial velocities.**

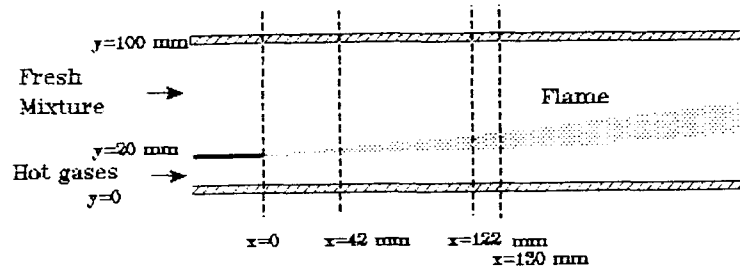


Figure 12 - Flow domain for a reacting flow.



Figure 13 - Pilot flame: mesh adopted.

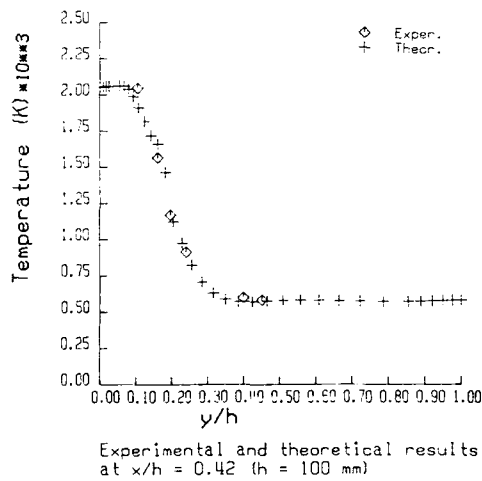


Figure 14 - Pilot flame: comparison of predicted and measured [25] temperatures.

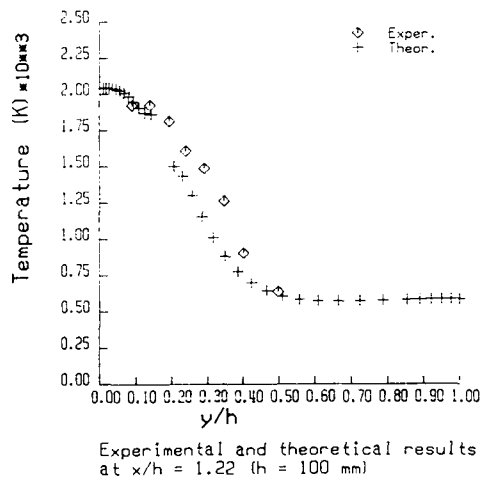


Figure 15 - Pilot flame: comparison of predicted and measured [25] temperatures.

LARGE-SCALE VISCOUS SIMULATION OF LAMINAR VORTEX FLOW OVER A DELTA WING

Bernhard Müller*

FFA, The Aeronautical Research Institute of Sweden,
S-161 11 BROMMA, Sweden

and

Arthur Rizzi

FFA, The Aeronautical Research Institute of Sweden,
S-161 11 BROMMA, Sweden.

&

KTH, Royal Institute of Technology,
S-100 44 STOCKHOLM, Sweden

Abstract

A numerical method has been developed to solve the Navier-Stokes equations for laminar compressible flow around delta wings. A large-scale solution on a mesh of $129 \times 49 \times 65$ points for transonic flow $M_\infty = 0.85$ $\alpha = 10$ deg. and $Re_\infty, C_\mu = 2.38 \times 10^6$ around a 65 deg. swept delta wing with round leading edge is presented and discussed. The results reveal the presence of primary, secondary, and even tertiary vortices. Comparison with experiment shows that the interaction between the primary and secondary vortices is obtained correctly and that these results are a more realistic simulation than the one given by the Euler equations.

Introduction

Numerical solution to the Euler equations is currently being proposed as a model to the problem of leading-edge separation from a delta wing and the consequent formation of a vortex over the wing. The approach seems reasonable enough, and indeed convincing results have been produced, when the separation occurs from a sharp edge¹⁻³. One concern with a solution to finite differences taken on a grid is that the vorticity diffuses because of the numerical method. A mesh with a large number of grid points usually is needed in order to limit the diffusion to a low level. But even then serious reservations arise with this approach if the edge is round because the action of viscosity in the boundary layer now determines precisely where the flow separates, and not a geometrical singularity as in the case of a sharp leading edge.

The comparison of Euler solutions with experimental measurements in an internationally sponsored study⁴ of vortex flow over cropped 65 deg. delta wings with sharp and round leading edges recently demonstrated this point⁴. With the round leading edge a vortex is shed in some numerical Euler solutions but in other solutions the flow is attached around the leading edge. This suggests that the Euler solution may be non

unique. Even when the numerical solution produces a vortex when in reality it is expected, the comparison with the measured surface pressure is not particularly good because the secondary vortex, observed in the experiment but not in the Euler solution, displaces the position of the primary vortex. One concludes that a viscous model is needed for a more realistic simulation.

We have recently developed a numerical method to solve the compressible Navier-Stokes equations for laminar flow over delta wings⁵. We present here some of our latest results from a large-scale Navier-Stokes simulation of transonic flow $M_\infty = 0.85$ $\alpha = 10$ deg. over the round-edge delta wing of the International Vortex Flow Experiment, and compare them with our Euler solution and the measured pressure distributions. The viscous solution contains the secondary vortex as well as other vortices located between the upper surface of the wing and the shear layer shed from its leading edge. The comparison with the experiment shows that the position of the primary vortex and the surface pressure under its core are more accurate in the Navier-Stokes solution than in the Euler solution. Hence the proper interaction between the primary and secondary vortices is obtained.

* Current address: DFVLR, Institute for Theoretical Fluid Mechanics, Bunsenstr. 10, D-3400 Göttingen, F.R. Germany

** The Symposium on the International Vortex Flow Experiment on Euler Code Validation was held in Stockholm, Sweden, 1-3 Oct 1986. The Proceedings are published as Ref. 4 and are available on request to: Librarian, FFA, Box 11021, 161 11 BROMMA, Sweden

Computational Method

The Navier-Stokes equations for an arbitrary stationary cell V with boundary ∂V and outer normal unit vector \mathbf{n} in a Cartesian reference frame read

$$\frac{\partial}{\partial t} \int_V \mathbf{q} \, dV + \int_{\partial V} \mathbf{H}(\mathbf{q}) \cdot \mathbf{n} \, dA = 0 \quad (1)$$

where

$$\mathbf{q} = \begin{pmatrix} \rho \\ \rho \mathbf{v} \\ e \end{pmatrix} \quad \mathbf{H} = \begin{bmatrix} \rho \mathbf{v} \\ \rho \mathbf{v} \mathbf{v} + p \mathbf{I} - \boldsymbol{\tau} \\ (e+p)\mathbf{v} - \boldsymbol{\tau} \cdot \mathbf{v} + Q \end{bmatrix}$$

The notation is standard. The column vector \mathbf{q} is density, momentum, and total energy per unit volume. The gas is air and is considered perfect. Newton's law gives the stress tensor

$$\boldsymbol{\tau} = \mu [\text{grad } \mathbf{v} + (\text{grad } \mathbf{v})^T] + \lambda \mathbf{I} \text{div } \mathbf{v}$$

and Fourier's law the heat flux Q . The viscosity coefficient μ depends on temperature according to Sutherland's law, and the Prandtl number is assumed constant, $Pr=0.72$.

Spatial Discretization

The Navier-Stokes equations (1) are discretized in hexahedrons (Fig. 1) using the finite-volume technique. Since the conservative variables are assumed to be defined by their cell averages, the volume integral in (1) over a cell P is expressed by:

$$\int_{V_P} \frac{\partial \mathbf{q}}{\partial t} \, dV = \frac{\partial \mathbf{q}_P}{\partial t} \int_{V_P} dV \quad (2)$$

The surface integral in (1) over the boundary of cell P is approximated by assuming the mean-value of the flux tensor on each side to be equal to the arithmetic average of the flux tensor in the adjacent cells:

$$\int_{\partial V_P} \mathbf{H} \cdot \mathbf{n} \, dA = \sum_{k=1}^6 \mathbf{H}_{Pk} \cdot \int_{\partial V_{Pk}} \mathbf{n} \, dA \quad (3)$$

where

$$\mathbf{H}_{Pk} = \frac{1}{2} (\mathbf{H}_P + \mathbf{H}_k)$$

∂V_{Pk} denotes the common part of the boundaries of P and its neighbouring cell k .

With the conservative variables given, all terms of the flux tensor are readily available in cell P , except for the gradients of the velocity components and temperature as well as $\text{div } \mathbf{v}$. Following the definition of the conservative variables as cell averages, the gradients in cell P are defined by:

$$\text{grad } \phi_P = \frac{\int_{V_P} \text{grad } \phi \, dV}{\int_{V_P} dV} \quad (4)$$

where $\phi = u, v, w, \text{ or } T$.

Using the gradient theorem, the volume integral in (4) can be expressed by a surface integral, which is approximated similarly to (3):

$$\text{grad } \phi_P = \frac{\int_{V_P} \phi \, \mathbf{n} \, dA}{\int_{V_P} dV} = \sum_{k=1}^6 \phi_{Pk} \frac{\int_{\partial V_{Pk}} \mathbf{n} \, dA}{\int_{V_P} dV} \quad (5)$$

where

$$\phi_{Pk} = \frac{1}{2} (\phi_P + \phi_k)$$

$\text{div } \mathbf{v}_P$ is evaluated similarly to $\text{grad } \phi_P$.

On a Cartesian equidistant grid, the present finite-volume approximation is equivalent to a second-order central difference discretization involving 25 points. It is broader than the conventional finite volume schemes applied to the Navier-Stokes equations which involve 19 points.

Numerical Damping

The spatial discretization constitutes the physical difference operator E_{PH} defined by the negative right hand side of (3) divided by the cell volume. The convective central differences do not damp unphysical oscillations caused by flow discontinuities and waves with short wavelengths, and nor do the dissipative central differences because our broad scheme uncouples neighboring points. Therefore we add numerical damping terms to $E_N(q)$ just as we did for solving the Euler equations*, but we use smaller coefficients. They comprise non-linear second-order differences sensed by the discretized second derivative of the pressure, and linear fourth-order differences of the conservative variables:

$$E_N(q) = (CFL/\Delta t) \{ \chi (\delta_I [s_I(p) \delta_I] + \delta_J [s_J(p) \delta_J] + \delta_K [s_K(p) \delta_K]) - \wedge (\delta_I^2 + \delta_J^2 + \delta_K^2) q \} \quad (6)$$

with CFL the maximum CFL number used (defined below) and Δt the time step. The constants χ and \wedge used lie in the ranges: $0 < \chi < 0.01$ and $0.005 < \wedge < 0.02$. The sensors s_I , s_J and s_K are of similar form, e.g. s_I for a cell indexed by I, J, K :

$$s_I(p_{I+1/2, J, K}) = \mu_I |\delta_I^2 p_{I+1/2, J, K}| / \max_{I', J', K'} |\delta_I^2 p_{I', J', K'}| \quad (7)$$

Here we have used the classical finite-difference operators are defined by:

$$\begin{aligned} \delta_I \phi_{I, J, K} &= \phi_{I+1/2, J, K} - \phi_{I-1/2, J, K} \\ \mu_I \phi_{I, J, K} &= (\phi_{I+1/2, J, K} + \phi_{I-1/2, J, K})/2 \end{aligned} \quad (8)$$

and similarly for J and K .

The numerical damping operator E_N is modified near the wing surface and farfield to ensure its dissipative property also there.

Time Integration

Thus the semi-discrete approximation of the Navier-Stokes equations can be written as:

$$\frac{dq}{dt} = F(q) \quad (9)$$

where

$$F = E_{PH} + E_N$$

Equation (9) represents a large system of first-order ordinary differential equations. We solve it for the steady state by the second-order explicit three-stage Runge-Kutta scheme:

$$\begin{aligned} q^0 &= q^n \\ q' &= q^0 + \Delta t F(q^0) \\ q'' &= q^0 + 1/2 \Delta t [F(q^0) + F(q')] \\ q^{n+1} &= q^0 + 1/2 \Delta t [F(q^0) + F(q'')] \end{aligned} \quad (10)$$

Stability

The stability of explicit Runge-Kutta schemes applied to the semi-discretization (9) of the Navier-Stokes equations has been studied for a scalar linear model equation in Ref. 5. If the coefficients of the model equation are obtained from the maximum moduli of the eigenvalues of the coefficient matrices of the linearized Navier-Stokes equation, the von Neumann stability analysis shows that also the mixed derivatives contribute to the time step limitation even on an orthogonal mesh, contrary to the implication we reached in Ref. 5. We have refined the stability condition for an explicit Runge-Kutta method applied to the present finite-volume discretization of the Navier-Stokes equations. The estimate we now use reads

$$\begin{aligned} \Delta t &\leq \min \{ CFL \nu [|v \cdot S_I| + |v \cdot S_J| + |v \cdot S_K| + c(|S_I| + |S_J| + |S_K|)]^{-1}, \\ &\frac{1}{2} |RK| \nu^2 [\nu(|S_I|^2 + |S_J|^2 + |S_K|^2) + 2\nu(|S_I \cdot S_J| + |S_I \cdot S_K| + |S_J \cdot S_K|) \\ &+ ((\lambda + \mu)/\rho)(|S_I| |S_J| + |S_I| |S_K| + |S_J| |S_K|)]^{-1} \} \end{aligned} \quad (11)$$

where c is the speed of sound, $\nu = \max(\mu, \lambda + 2\mu, \gamma\mu/Pr)/\rho$, v the cell volume, S_I the surface normal in I -direction, etc.

The stability bounds RK and CFL are chosen such that all complex numbers z with $RK < \operatorname{Re}(z) < 0$ and $|\operatorname{Im}(z)| < CFL$ lie inside the stability region of the Runge-Kutta method (see Fig. 2). For the three-stage Runge-Kutta method (10) the following choice is taken for the delta wing fine-mesh case: $CFL=0.5$ and $RK=-1$. In general, $CFL=1.5$ and $RK=-1$ are taken. The factor $1/2$ leaves space on the negative real axis of the stability region to accommodate the numerical damping contribution.

Mesh

The round leading edge delta wing proposed for the International Vortex Flow Experiment on Euler Code Validation has 65° sweep and 15% taper. It is defined by one section in terms of x - and z -coordinates:

$$z = \begin{cases} [0.1183/x - 0.2101x + 0.3501x^2 - 0.3406x^3] & 0 < x < 0.4 \\ \text{NACA 64A005 profile} & x > 0.4 \end{cases}$$

The nose radius is 0.7% , the maximum thickness at 40% is 5% local chord, and the trailing edge is sharp.

We generate an O-O mesh around this wing by the transfinite interpolation method⁷. The fine mesh consists of 129, 49 and 65 grid points in the chordwise I -, near normal J - and spanwise K -directions, respectively, i.e. 410 865 grid points in total. On the wing, the mesh points are clustered near the leading edge and tip and to a less extent also near the trailing edge and symmetry boundary with larger spacings in the mid sections (Fig. 3). The mesh is nearly orthogonal at the wing contour, except for the points near the trailing edge and tip (Figs. 4 and 5). The grid points between the wing and the farfield, which is a hemisphere of radius 3 root chords C_R from mid root-chord, are clustered near the wing to resolve the boundary layer. We estimate that the clustering places about 20 points in the boundary layer.

Initial and Boundary Conditions

For $M_\infty=0.85$, $\alpha=10^\circ$, $Re_{\infty, C_R}=2.38 \times 10^6$, the calculation is started from freestream on a coarse mesh using a large second-order damping coefficient ($\chi=0.1$), which is subsequently reduced to 0.01 . The converged result is interpolated on the medium mesh and so on to the fine mesh.

The O-O mesh topology introduces periodic, symmetry, wing and farfield boundaries to determine bilaterally symmetric flow over a quadrilateral wing. The symmetry boundary lies in the $y=0$ plane. The periodic boundaries extend from the trailing edge and tip of the wing in the positive x - and y -directions, respectively. At periodic boundaries, grid points on upper and lower surfaces are mapped onto each other. The conditions on the conservative variables are

$$Q_{IMAX, J, K} = Q_{1, J, K} ; \quad Q_{I, J, KMAX} = Q_{IMAX - I, J, KMAX - 1} \quad (12a)$$

At the symmetry boundary, ρ, u, w , and e are even functions with respect to y , and v is an odd one:

$$(\rho, u, v, w, e)^T(x, y, z) = (\rho, u, -v, w, e)^T(x, -y, z) \quad (12b)$$

The no-slip condition holds on the wing, which is assumed to be adiabatic. The pressure is obtained by neglecting the viscous terms in the wall normal momentum equation:

$$v_w = 0 ; \quad \frac{\partial T}{\partial n}|_w = 0 ; \quad \frac{\partial p}{\partial n}|_w = 0 \quad (12c)$$

The pressure and the stress tensor at the wing interface of the first cell above the wing are approximated by their values in that cell.

The boundary conditions at the farfield boundary are based on the theory of characteristics for locally one-dimensional inviscid flow. For supersonic inflow or outflow, the locally one-dimensional Riemann invariants, entropy and tangential velocity component, i.e.:

$$\begin{aligned} R_1 &= v \cdot n - \frac{2}{\gamma-1} c ; & R_2 &= v \cdot n + \frac{2}{\gamma-1} c \\ R_3 &= \ln \left(\frac{-P}{\rho^\gamma} \right) ; & R_4 &= v - (v \cdot n) n \end{aligned} \quad (12d)$$

are given from outside or inside the computational region by, respectively:

$$R_m = R_{m_\infty} \quad \text{or} \quad \frac{\partial R_m}{\partial n} = 0 \quad (12e)$$

For subsonic inflow, R_1, R_3 , and R_4 are given from outside and R_2 from inside. R_2, R_3 , and R_4 are determined from inside and R_1 from outside for subsonic outflow.

The conditions (12e) are used to determine R_∞ in a fictitious cell outside the domain of integration either by freestream or by R_∞ in the cell next to the farfield.

This fully discrete explicit scheme has been fully vectorized over all three dimensions for the CYBER 205 supercomputer by the vector-coding concept developed by Rizzi⁴. Using 32-bit word length the resulting computer program operates at 23 CPU micro-seconds per time step and per grid point. Only 30 data quantities need to be stored at each grid point.

Discussion of Computed Solution

We simulate laminar flow over the cropped delta wing for the conditions $M_\infty=0.85$, $\alpha=10$ deg. and $Re_{\infty, c_R}=2.38 \times 10^6$. The streamlines (steady particle paths) originating near the leading edge in Fig. 6 show two distinct regions of swirling flow which lift before the trailing edge. The inboard one is clearly the primary vortex, and is above the outboard region. The other swirling that we see only starts past midchord. For this reason and because it is too far outboard, we hesitate to call it the secondary vortex. We discuss this further below. The side view shows that the shear layer leaving from the cropped tip is less tightly wound, presumably because of the reduced sweep angle of this edge. We remark that there is no indication of an abrupt uplifting of the vortex near the beginning of the cropped tip, as we have seen in the corresponding Euler solution^{1,3}. We attributed that as an effect of the cropped edge.

The line towards which the skin friction lines converge (Fig. 7) clearly indicates the secondary separation at $y/s=0.74$ and confirms that there is a secondary vortex in the numerical solution. This compares reasonably well with the oil flow in Fig. 7, considering that the experiment is done for a wing with a sharp leading edge. The experiment indicates a clear primary attachment line, and one can infer one in the computations up to about 60% chord. Past this point the skin friction lines from near the symmetry plane are swept spanwise outboard, and the suggestion of a primary attachment line is completely lost. Since this is just ahead of the cropped tip, perhaps this effect is linked to the tip. But the discrepancy that we cannot explain is that close to the trailing edge the computed lines sweep outboard from the symmetry plane while the oil flow shows the direction to be streamwise inboard of the primary attachment. The skin friction lines emanating from points a short distance away from the tip and trailing edge turn upstream and apparently terminate in a nodal point of separation on the secondary separation line, also in contrast to the oil flow.

Figure 8 presents the computed skin friction lines on the upper side of the leading edge. Where they are converging, the dashed line nearest the leading edge has been drawn to indicate the primary separation line. Where the skin friction lines diverge, a dashed line suggests the attachment line of, presumably, the secondary vortex. The pattern of diverging streamlines cases just ahead of the cropped tip, and apparently the secondary attachment line terminates there. We believe this effect is strongly influenced by the shape of the tip.

The pressure minimum (Fig. 9a) almost coincides with the secondary separation line, around which large gradients of the modulus of vorticity (Fig. 9b) can be seen where the boundary layer lifts off the surface. Pressure and vorticity are nearly conical up to $x/c_R=0.55$. The structure in the flow near the leading edge between $x/c_R=0.55$ and ~ 0.75 is complex and needs to be discussed further. For this purpose Fig. 10 presents contour curves of constant static C_p , total pressure coefficient $C_{p_t}=1-P_t/P_\infty$ and vorticity modulus drawn in the flat plane $x/c_R=0.80$. The rings of static C_p (Fig. 10a) identify the primary vortex. The overall pattern of these contours is regular except for the region between the primary vortex and the leading edge. The contours total pressure (Fig. 10b) and vorticity modulus (Fig. 10c) show the thinness of the boundary layer on the upper and lower surfaces. They also indicate the lifting up of the boundary layer on the upper surface just under the primary vortex. This is confirmation that secondary separation occurs under the primary vortex where the contour lines of C_{p_t} and vorticity on the upper surface are most dense. Further outboard both sets of contours show another uplifting from the wing surface and could be called a tertiary separation. And even a fourth island of vorticity appears very near the tip.

The comparison of static pressure coefficients (Fig. 11) at the stations $x/c_R=0.3$, 0.6 and 0.8 with experimental data verifies the realism of the main features simulated here, and points out the contrast with the Euler solution. The position of the primary vortex core and the pressure level under it are predicted in good agreement with the experiment, whereas the pressure minimum in the Euler solution lies too close to the leading edge and its suction is much higher. A number of different C_p measurements were taken for different Reynolds numbers. The results of these measurements show a clear dependence on the Reynolds number. Since our simulation is for laminar flow, we compare here with the measurements taken at the lowest Reynolds number because that case contains the largest region of laminar flow. Two distinct minima occur in the viscous simulation which is typical of laminar vortex flow. The second minimum usually is not seen in turbulent flow, and this is consistent with the experimental results presented here, in which the transition to turbulence was observed. The comparison of laminar and turbulent pressure measurements over a delta wing (Fig. 12) illustrates this effect which Kuchemann discusses in his book¹⁰. The third minimum in the computed pressure near the leading edge at $x/c_R=0.6$ (in Fig. 11) may be related to the third vortical structure seen near the tip in Fig. 10c.

The overall comparison of the velocity vectors in Fig. 13 measured by two different techniques (laser¹¹ and probe¹²) and those from the computed solution further support the realism of the calculation. We should point out the even under the best of circumstances such measurements are difficult to carry out for transonic flow. As seen in Fig. 13a laser measurements could not resolve the entire primary vortex core, and the probe measurements just outboard of the leading edge in Fig. 13b are clearly in error. Nevertheless these are the best data we have to work with. Close inspection of this figure does show that the core of the primary vortex in the computed solution is slightly above and inboard of the one found in the probe measurements in turbulent flow. The sketch of the primary vortices in Fig. 12, taken from the laminar and turbulent experiments, explains this difference as being due to the turbulent flow condition present during the probe measurements.

We return now to the question of the complex structure seen in the vorticity contours in Fig. 10. Velocity vectors are needed to bring out the sense of the flow direction. Figure 14 displays them drawn at equispaced intervals (not grid points) in a true plane normal to the leading edge at $x/c_g = 0.70$. (Looking at the vectors in this plane reduces the chances of being misled because the missing component along the leading edge varies the least.) Here (Fig. 14a) we see clearly the primary separation, the vortex core, and the primary attachment point. The secondary and tertiary vortices are seen only crudely because of the coarse spacing of the vectors. With a tighter spacing over a region close to the upper surface, Fig. 14b brings out the velocity profile over the whole upper surface of the wing section and now clearly indicates the secondary and tertiary vortices. In the region just surrounding the leading edge of the wing the velocity vectors in Fig. 14c, even reveal a fourth vortex which might be called a "roller" vortex because it is sandwiched between the shed shear layer and the wing surface. There might be a counter clockwise vortex in the vicinity of the leading edge.

In high Reynolds number flows one expects the boundary layer to be very thin. In order to investigate this matter in our solution, we present diagram plots of vorticity, total pressure, and u component of velocity drawn versus the line segment indicated by the dashed line in the contour plots in Fig. 15. These diagrams indicate the very thin and sharp boundary layer profile supported by our mesh clustered tightly near the wing surface. It is interesting to observe that the maximum of vorticity (Fig. 15a) occurs in the boundary layer on the windward side, presumably because the boundary layer is swept and stretched there. The magnitude of vorticity is much higher in both the windward and leeward side boundary layers than in the core of the primary vortex. This suggests that the standard Baldwin and Lomax model for turbulence could be applied in its usual form without modifying its use of vorticity. The largest loss in total pressure occurs in the leeward boundary layer (Fig. 15b), but here the loss in the core is greater than in the windward boundary layer. The profiles of the u velocity component show that the gradient of u is somewhat steeper through the windward boundary layer than it is through the leeward layer where it is separating. The small plateau in u is a curious feature of this uplifting layer.

Concluding Remarks

The quantitative details of this solution must be analyzed further before one can come to a final judgement about its realism. But from comparison with experimental data we can conclude that the laminar Navier-Stokes equations are a better model than the Euler equations for this class of flow, and that in overall qualitative terms their numerical solution is predicting the interaction between the primary and secondary vortices, and thus the surface pressure, more accurately than the inviscid flow simulation. It remains to be investigated which improvements can be gained by implementing simple transition and turbulence models for high Reynolds number vortical flows.

Acknowledgements

The authors thank Dr. G. Drougge, FFA, for valuable discussions. The development of the Navier-Stokes code was supported in part by the Swedish Board for Technical Development (STU) and by an ONR grant during the first author's sabbatical visit at M.I.T. The actual computations were carried out with the support of the Institute of Mathematics and its Applications (IMA) of the University of Minnesota with funds provided by the National Science Foundation (NSF).

References

- 1 Smith, J.H.B.: "Vortex Flows in Aerodynamics", *Ann. Rev. Fluid Mech.*, Vol. 18, 1986, pp. 221-242.
- 2 Newsome, R.W., and Kandil, O.A.: "Vortical Flow Aerodynamics - Physical Aspects and Numerical Simulation", *AIAA Paper* 87-0205, Jan. 1987.
- 3 Rizzi, A., and Purcell, C.J.: "On the Computation of Transonic Leading-Edge Vortices Using the Euler Equations", *J. Fluid Mech.*, Vol. 181, 1987, pp. 163-195.

- 4 Elsenaar, A., and Eriksson, G. (eds), Proc. Intl. Vortex Flow Experiment on Euler Code Validation, FFA TN, Stockholm 1986.
- 5 Müller, B., and Rizzi, A.: "Navier-Stokes Computation of Transonic Vortices Over a Round Leading Edge Delta Wing, AIAA Paper No. 87-1227, 1987.
- 6 Rizzi, A., and Eriksson, L.-E.: "Computation of Flow around Wings Based on the Euler Equations", J. Fluid Mech., Vol. 148, 1984, pp. 45-71.
- 7 Eriksson, L.-E.: "Generation of Boundary Conforming Grids Around Wing-Body Configurations Using Transfinite Interpolation", AIAA J., Vol. 20, No. 10, Oct 1982, pp. 1313-1320.
- 8 Rizzi, A.: "Vector Coding the Finite-Volume Procedure for the CYBER 205", Parallel Computing, Vol. 2, 1985, pp. 295-312.
- 9 Bannink, W.J. and Houtman, E.M.: "Experiments on the Transonic Flow over a Delta Wing at High Angles of Attack", in Ref. 4, 1986, pp. 37-46.
- 10 Küchemann, D.: "The Aerodynamic Design of Aircraft", Pergamon Press, Oxford, 1978, pp. 390-391.
- 11 Hartmann, K.: "Force and Pressure Measurements Including Surface Flow Visualizations on a Cropped Delta Wing", in Ref. 4, 1986, pp. 63-88.
- 12 Hjeltnberg, L.: "Test on a 55° and 65° Delta Wing at FFA", in Ref. 4, 1986, pp. 89-106.
- 13 Rizzi, A., Drougge, G., and Purcell, C.J.: "Euler Simulation of Shed Vortex Flows over the 65 Degree Delta Wings", in Proc. Intl. Vortex Flow Experiment, (See Ref. 4) pp. 289-344.

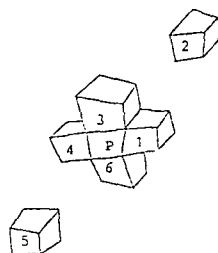


Fig. 1 Basic hexahedron P and neighbouring cells 1 to 6 (2 and 5 set apart)

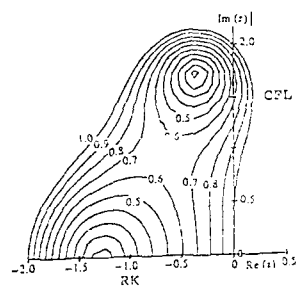
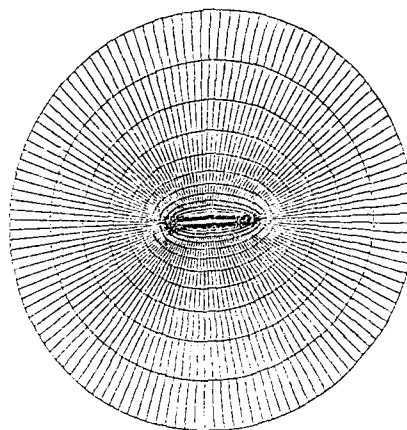
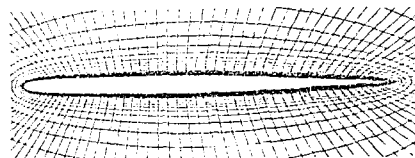


Fig. 2 Contours of constant modulus of growth factors of (10) and stability bounds RK and CFL



a) global view



b) enlargement

Fig. 4 Mesh in plane of symmetry

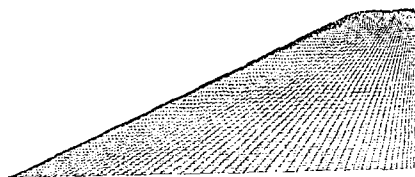
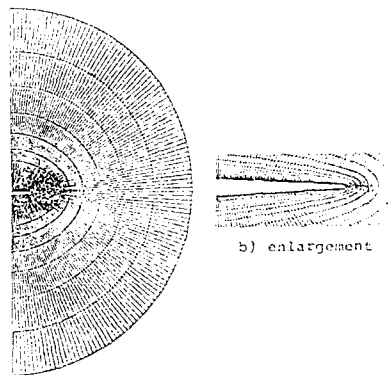


Fig. 3 Surface mesh of 65° swept cropped delta wing

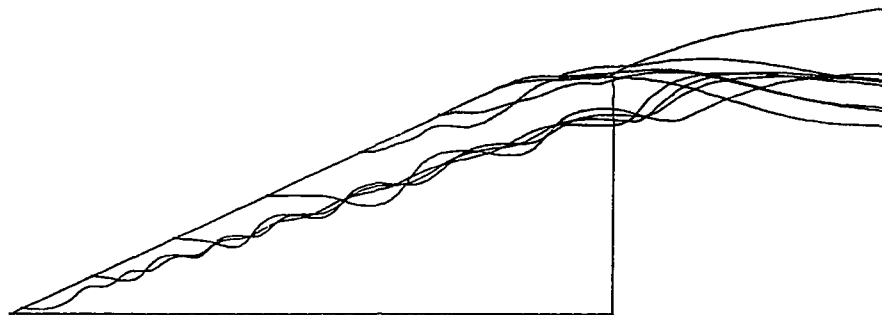


a) global view



b) enlargement

Fig. 5 Mesh in surfaces I=33 and 97 seen from behind (at ~37% local chord on wing)



a) view from above



b) horizontal view towards symmetry plane

Fig. 6 Streamlines originating near the leading edge determined from the solution show multiple vortices over the wing.

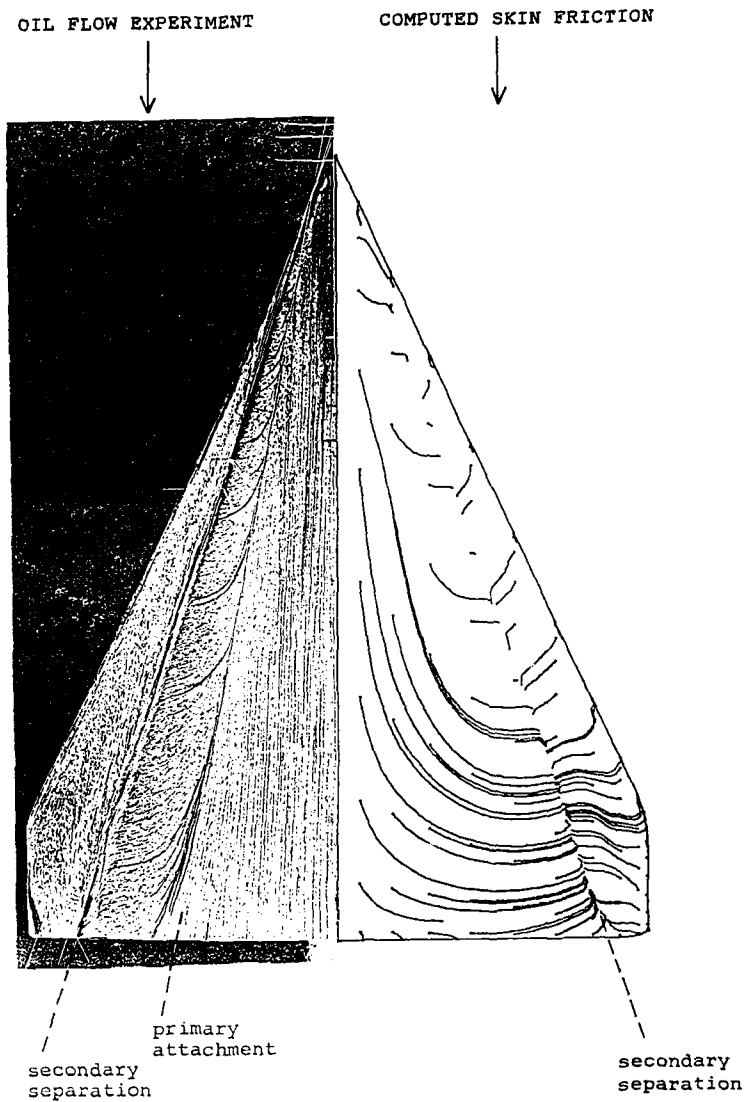


Fig. 7 Comparison of oil flow photograph⁹ with skin friction lines computed in the Navier Stokes solution.

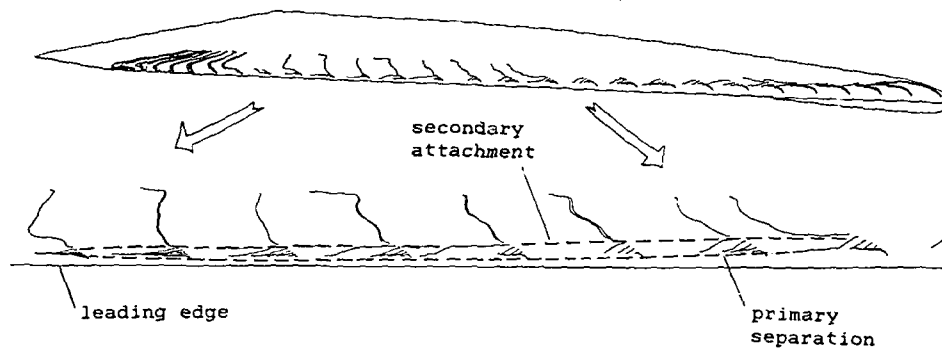


Fig. 8 Skin friction lines on the leading edge indicate the primary separation line and the secondary attachment line.

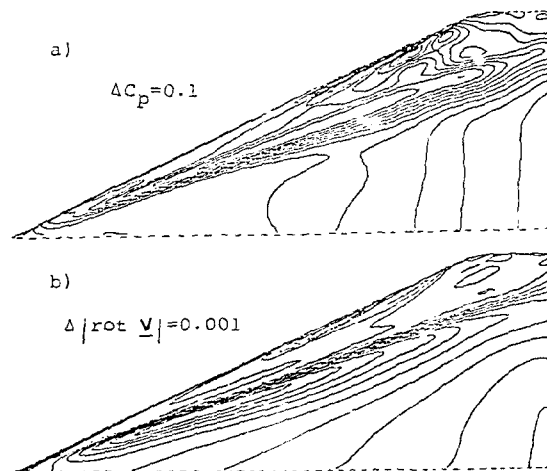


Fig. 9 Leeward surface contour lines of constant C_p and $|\text{rot } \underline{v}|$ for $M_\infty = 0.85$, $\alpha = 10^\circ$, $Re_{\infty, c_R} = 2.78 \times 10^6$

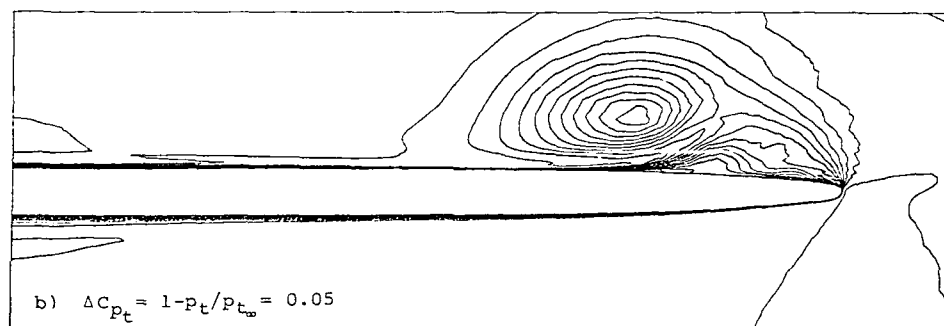
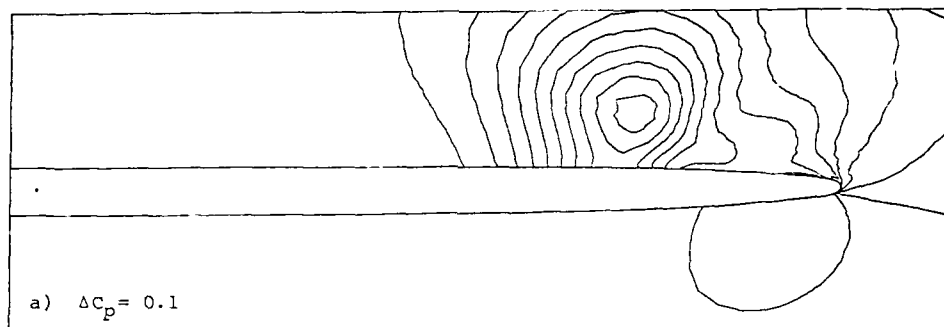


Fig. 10 Contour lines in the plane $x/c_R=0.80$

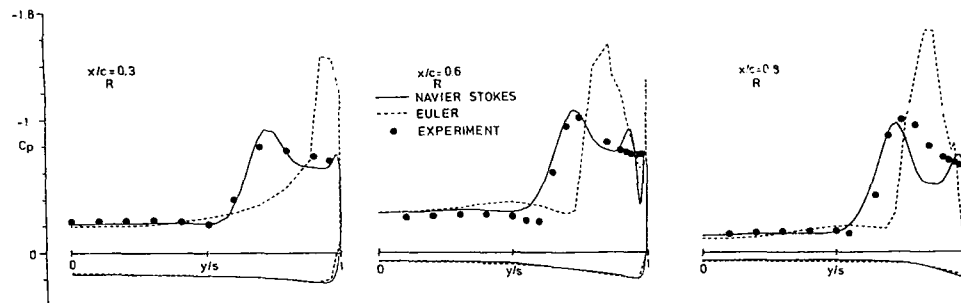


Fig. 11 Comparison of measured surface pressure coefficient with those computed by Euler and Navier Stokes equations.
 $M_\infty = 0.85$, $\alpha = 10^\circ$, $Re_\infty = 2.38 \times 10^6$

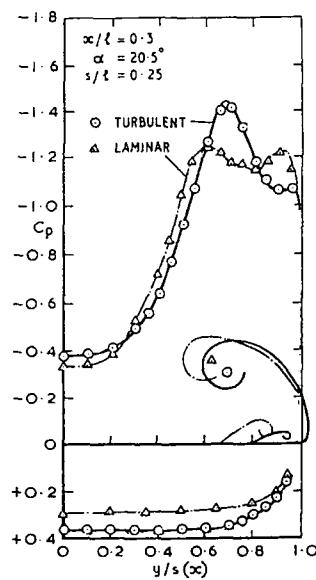


Fig. 12 Differences in measured surface pressures on a delta wing in laminar and in turbulent flow (from Ref. 10).

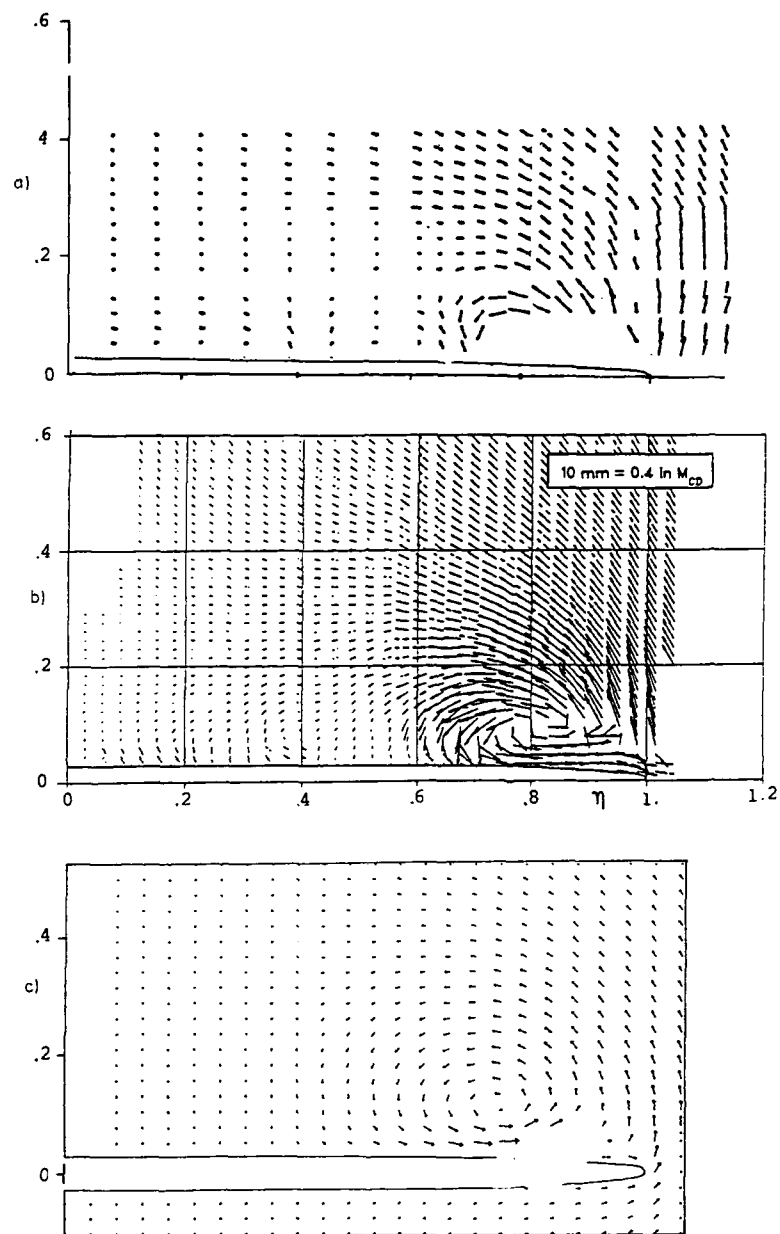


Fig. 13 Comparison of velocity vectors over the wing at $x/c=0.8$ a) from a) laser measurements, b) 7-hole probe measurements, and c) the Navier-Stokes computation

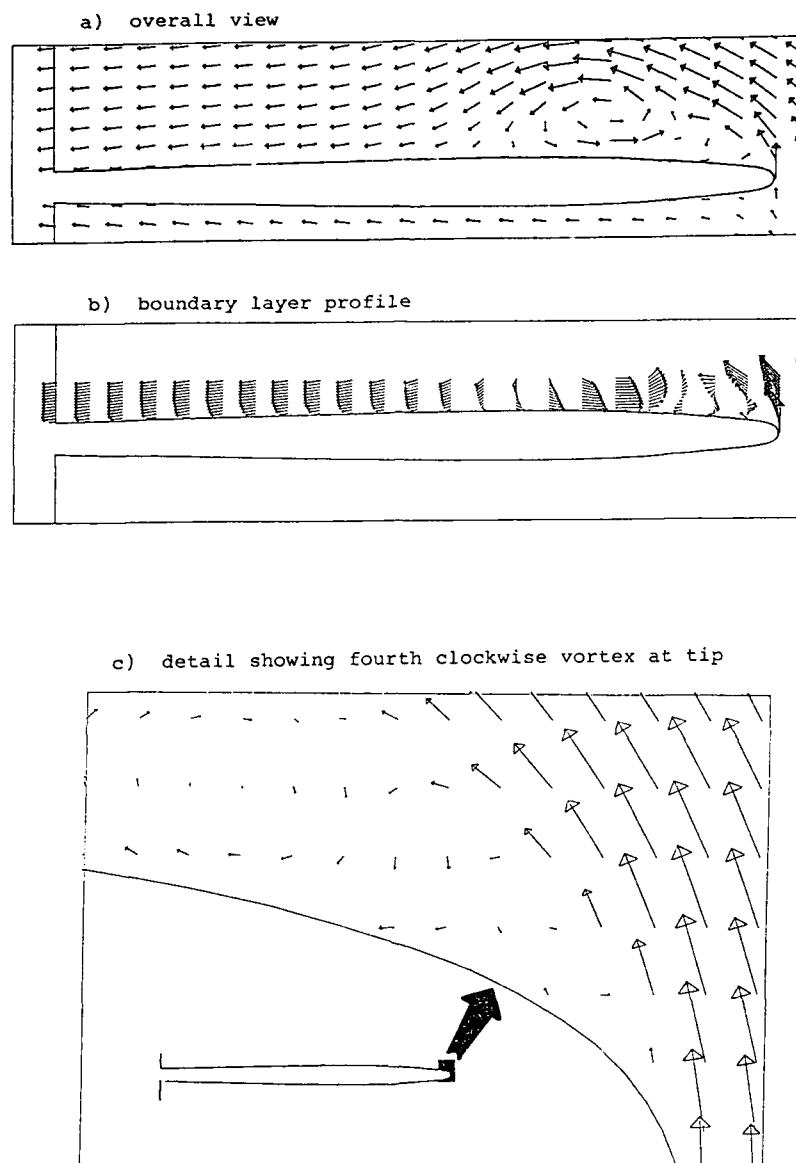


Fig. 14 Velocity vectors drawn in the plane normal to the leading edge at $x/c_R=0.70$

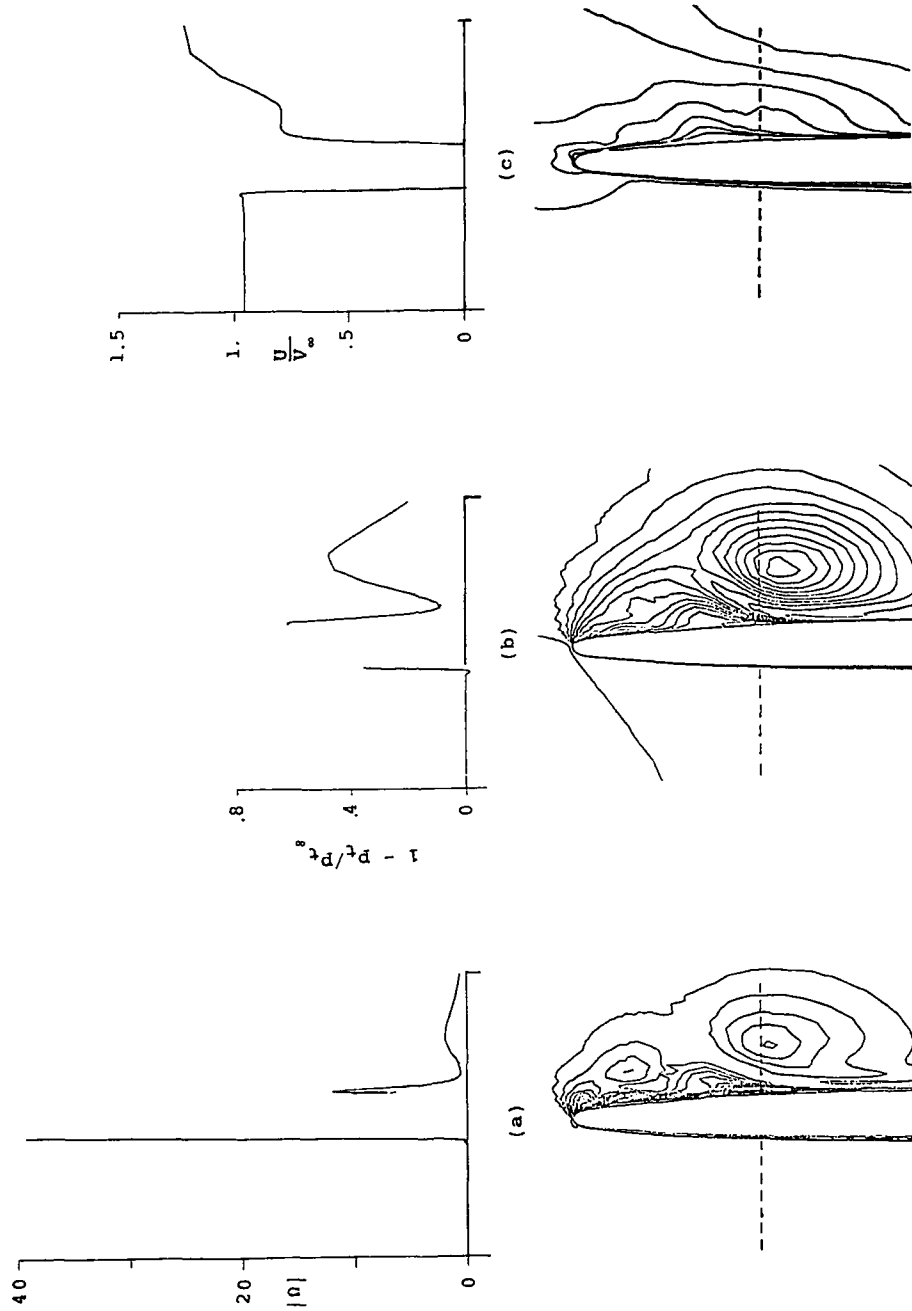


Fig. 15 Profiles through the boundary layer along the dashed line alvorticity moduls, b) total pressure coefficient, c) U/V_∞ velocity component.

INVESTIGATION OF THE ACCURACY OF FINITE VOLUME METHODS FOR 2- AND 3-DIMENSIONAL FLOWS

Rossow, C., Kroll, N., Radespiel, R., Scherr, S.

Deutsche Forschungs- und Versuchsanstalt für
Luft- und Raumfahrt e.V.
Institut für Entwurfsaerodynamik
D-3300 Braunschweig-Flughafen
F.R. Germany

Summary

The accuracy of finite volume methods for the discretization of the unsteady Euler equations in a cartesian coordinate frame is investigated. For finite volume methods, general requirements are derived for a spatial discretization which yields first order accuracy on arbitrary meshes. An error analysis shows that in two dimensions methods based on a cell vertex scheme meet these requirements whereas methods based on a cell centered scheme do not. Numerical results on different two-dimensional meshes confirm the theoretical statement that only cell vertex schemes perform accurately on grids with slope discontinuities.

Using structured coordinate grids for complex three-dimensional flow problems, even cell vertex schemes require additional effort to ensure first order accuracy on arbitrary meshes. The applicability of the cell vertex scheme is demonstrated by the calculation of the flow field in a nozzle and the flow around a powered nacelle.

List of Symbols

c_l	lift coefficient	\vec{q}	velocity vector
c_p	pressure coefficient	R	gas constant
E	total energy	t	time
\vec{F}	tensor of flux density	T	temperature
h	mesh spacing	V	volume
H	total enthalpy	\vec{W}	vector of conserved quantities $= [\rho, \rho u, \rho v, \rho w, \rho E]^T$
$\vec{i}_x, \vec{i}_y, \vec{i}_z$	cartesian unit vectors	x, y, z	cartesian coordinates
Ma	Mach number	α	angle of attack
\vec{n}	unit vector of outward normal	∂V	boundary of control volume V
$O(h^n)$	terms which are at least proportional to h^n		

Introduction

The field of computational fluid dynamics has evolved from the first attempts at solving model fluid flows to the stage where computational methods play an important role in aerodynamic design. With the advent of fast vector computers a significant advance was achieved in this field by developing methods for solving the Euler equations. The use of Euler codes has several motivations. Solutions of the Euler equations give a more physical representation of inviscid subsonic, transonic and supersonic flow fields than potential flow methods. They do not suffer from nonuniqueness problems, which have been observed in potential flow theory. In particular the position of the vortex sheet behind a wing needs not be specified, but it comes out as a part of the solution. In regions where shock waves are present, the Euler equations allow entropy rise through shock waves while mass, momentum and energy are conserved. Furthermore, Euler codes are able to treat embedded regions of different total pressure and total temperature in the flow field without dividing it into different domains, which have to be otherwise patched together by complicated or nonphysical procedures.

The numerical solution of the Euler equations as discretized by the finite volume technique is well known. Finite volume methods are based on the integral form of the governing equations, which ensures the fulfillment of the conservation principles in the discretization. Usually the equations are written in a cartesian coordinate frame, and no global transformation of the system of equations to curvilinear coordinates is necessary. The finite volume discretization technique requires the approximation of the integral over the surface of the control volumes in the computational mesh. There exists a variety of schemes based on the finite volume technique. Generally, however, two basic strategies are applied.

The first strategy uses a cell centered scheme in which the flow quantities are associated with the center of a cell in the computational mesh. Jameson, Schmidt and Turkel [1] applied a cell centered scheme for the calculation of two-dimensional flow fields by solving the Euler equations. In Jameson and Baker [2] further applications of this method to three-dimensional problems are reported. Also Rizzi used in [3] a cell centered

scheme for the calculation of inviscid three-dimensional flows. Due to their simple structure, cell centered schemes are in widespread use in computational fluid dynamics. The second approach employs a cell vertex scheme, where the flow quantities are assigned to the vertices of a cell, i.e. to the mesh nodes. Ni [4] used a cell vertex scheme for the calculation of inviscid two-dimensional flows. Hall [5] applied an extended version of Ni's scheme for the discretization of the two-dimensional Euler equations. Koeck [6] and Denton [7] employed cell vertex schemes for the computation of three-dimensional flows.

Recently the complexity of geometries being investigated has continuously increased. In addition to the calculation of the flow field around a single wing [8], work is more and more focused on the simulation of the flow around complete aircraft configurations, e.g. [2, 9-12]. For such geometries the generation of smooth body-fitted grids is very laborious. Due to the complexity of the configuration under consideration, it may be impossible to generate smooth meshes without singular lines or singular points. Even the use of block-structured meshes [13-16] may not avoid the occurrence of singularities and slope discontinuities.

A difficult question which arises in computational fluid dynamics is the analysis of the numerical error which appears in the discretization of the governing equations. The problem is even more evident when treating complex geometries. As a comparison with exact solutions is usually not possible for complex flows, computation on successively refined grids is used to verify the accuracy of the numerical method. This means of verification requires a priori that the truncation error in the spatial discretization is at least proportional to the mesh spacing, i.e. at least of first order. In order to validate this feature of the spatial discretization the accuracy of finite volume methods has to be assessed mathematically.

In the first part of this study, general requirements are analytically derived which have to be fulfilled to establish first order accuracy of a finite volume method independent of the smoothness of the computational mesh. In the following a cell centered scheme and a cell vertex scheme for the discretization of the two-dimensional Euler equations are compared. The accuracy of the different approaches is analyzed and the derived criteria are confirmed by numerical results. The outcome of this comparison is that only the cell vertex scheme provides the capability to be at least first order accurate on arbitrary meshes. The last topic of the paper concerns three-dimensional flow problems. It is pointed out that a straightforward extension of the two-dimensional cell vertex scheme to three dimensions does not lead to a method of first order on arbitrary meshes, since in three dimensions, the faces of a cell in the computational mesh may be distorted. Furthermore a hexahedral cell may degenerate to a pentahedron or a tetrahedron. A comparison of the results of the calculation of the flow through a nozzle achieved by the application of both cell centered and cell vertex schemes shows the better accuracy of the cell vertex scheme on non-smooth grids. The applicability of the cell vertex scheme is further demonstrated by the calculation of the flow around a powered nacelle. In this case the computational mesh exhibits a polar singularity. However, no transformation of the equations to polar coordinates is necessary.

2. General requirements of finite volume methods

2.1 Governing equations

The three-dimensional Euler equations for unsteady compressible inviscid flows may be written in integral form using a cartesian coordinate system as

$$\iiint_V \frac{\partial}{\partial t} \vec{W} dV = - \iint_{\partial V} \vec{F} \cdot \vec{n} dS \quad (1)$$

where

$$\vec{W} = \begin{bmatrix} \rho \\ \rho u \\ \rho v \\ \rho w \\ \rho E \end{bmatrix}, \quad \vec{F} = \begin{bmatrix} \rho \vec{q} \\ \rho u \vec{q} + p \vec{i}_x \\ \rho v \vec{q} + p \vec{i}_y \\ \rho w \vec{q} + p \vec{i}_z \\ \rho H \vec{q} \end{bmatrix}$$

In equation (1), p , ρ , u , v , w , E and H are the pressure, density, cartesian velocity components, total energy and total enthalpy, respectively. V denotes an arbitrary control volume fixed in time and space and ∂V is the closed boundary of the volume. \vec{F} represents the tensor of flux density and \vec{n} is the outward facing normal along ∂V . The unit vectors of the cartesian coordinate system are given by \vec{i}_x , \vec{i}_y , \vec{i}_z , and the velocity vector is hence

$$\vec{q} = u \vec{i}_x + v \vec{i}_y + w \vec{i}_z \quad (2)$$

Applying the integral mean value theorem, equation (1) can be converted to

$$\left(\frac{\partial \bar{W}}{\partial t}\right)^{av} = - \frac{\iint_V \bar{F} \cdot \bar{n} dS}{\iiint_V dV} \quad (3)$$

The term on the left-hand side of equation (3) represents the integral mean value of the rate of change of \bar{W} in the control volume V , and the right-hand side is the flux per volume of mass, momentum and energy through the surface of V . Together with the equation of state

$$p = \rho RT \quad (4)$$

which relates the pressure to the components of \bar{W} , equation (3) forms a system of five equations for the unknowns ρ , u , v , w and E .

2.2 Finite volume discretization

As equation (3) is valid for an arbitrary control volume, it also holds locally for each cell $V_{i,j,k}$ in the computational mesh

$$\left(\frac{\partial \bar{W}}{\partial t}\right)_{i,j,k}^{av} = - \frac{1}{V_{i,j,k}} \iint_{\partial V_{i,j,k}} \bar{F} \cdot \bar{n} dS \quad (5)$$

where

$$V_{i,j,k} = \iiint_{V_{i,j,k}} dV$$

Denoting the flux of \bar{W} through the surface of the cell $V_{i,j,k}$ by $\bar{Q}_{i,j,k}$

$$\bar{Q}_{i,j,k} = \iint_{\partial V_{i,j,k}} \bar{F} \cdot \bar{n} dS \quad (6)$$

equation (5) reads

$$\left(\frac{\partial \bar{W}}{\partial t}\right)_{i,j,k}^{av} = - \frac{1}{V_{i,j,k}} \bar{Q}_{i,j,k} \quad (7)$$

In a finite volume method the flux $\bar{Q}_{i,j,k}$ is evaluated by approximating the surface integral in equation (6) by numerical integration. Denoting the result of the numerical integration by $\bar{I}_{i,j,k}$, equation (6) now is

$$\bar{Q}_{i,j,k} = \bar{I}_{i,j,k} + \bar{E}_{i,j,k} \quad (8)$$

where $\bar{E}_{i,j,k}$ denotes the error due to the numerical integration. Substituting (8) in (7) gives the approximation of the integral mean value of the rate of change of \bar{W} in each cell

$$\left(\frac{\partial \bar{W}}{\partial t}\right)_{i,j,k}^{av} \approx - \frac{1}{V_{i,j,k}} [\bar{I}_{i,j,k} + \bar{E}_{i,j,k}] \quad (9)$$

Equation (9) shows that for the approximation of the mean rate of change of the flow variables in a control volume one has to deal with error terms of the form

$$\bar{E}_{i,j,k} = \frac{\bar{e}_{i,j,k}}{V_{i,j,k}} \quad (10)$$

If the integral mean value of the rate of change of the flow quantities in a control volume is to be calculated with at least first order accuracy, the error term $\bar{E}_{i,j,k}$ must at least depend linearly on the mesh size h . The volume of a cell is a quantity whose magnitude in an n -dimensional space is proportional to the n -th power of the mesh size h

$$V_{i,j,k} = V(h^n)_{i,j,k} \quad (11)$$

Thus it is evident from equation (10) that the integration error in the numerical integration of $\bar{F} \cdot \bar{n}$ over the surface of a cell must be proportional to h^{n+1}

$$\bar{E}_{i,j,k} = \frac{\bar{e}(h^{n+1})_{i,j,k}}{V(h^n)_{i,j,k}} = O(h) \quad (12)$$

to fulfill the above requirement.

Equation (12) states that in two-dimensional finite volume methods the accuracy of the numerical integration of the term $(\vec{F} \cdot \vec{n})$ over the surface of a cell must be of third order. For three-dimensional methods the error of the numerical integration must be at least of fourth order. Only under these conditions it is assured that the approximation of equation (3) is at least first order accurate on arbitrary meshes.

Note that in the above considerations no assumptions about the location of the flow quantities were made. The relations derived so far are independent of the strategy applied in the finite volume scheme.

3. Two-dimensional flows

3.1 Discretization

In this section the two basic strategies, the cell centered and cell vertex discretization scheme, will be compared through their application to two-dimensional flows. The particular cell centered finite volume method is a scheme according to Jameson [1], whereas the cell vertex scheme is based on the ideas of Hall [5]. A comparison including a detailed error analysis was given in [17] and therefore here only the main features of the different schemes will be discussed.

In order to apply the finite volume methods investigated here, the physical domain is divided into quadrilateral cells by generating a body-fitted grid. A typical cell with corresponding geometrical quantities is shown in Fig. 1. As the faces of a two-dimensional cell are given by straight lines, the normal vectors to the different faces are constants which can be calculated exactly. The numerical evaluation of the flux $Q_{i,j}$ through the surface of a cell is performed by splitting the surface integral of equation (6) into a sum of integrals over the four faces of the cell. Due to the fact that the normal vectors are constants, equation (6) can be written for two-dimensional cells as

$$\vec{Q}_{i,j} = \vec{n}_{i+1/2,j} \cdot \int_{S_{i+1/2,j}} \vec{F} dS + \vec{n}_{i,j+1/2} \cdot \int_{S_{i,j+1/2}} \vec{F} dS + \vec{n}_{i-1/2,j} \cdot \int_{S_{i-1/2,j}} \vec{F} dS + \vec{n}_{i,j-1/2} \cdot \int_{S_{i,j-1/2}} \vec{F} dS \quad (13)$$

The remaining problem is the evaluation of the integration of the flux density tensor over the different faces.

First the cell vertex scheme will be considered. In Fig. 2 four control volumes are sketched which have point i,j as a common vertex. The flow quantities are located at the vertices of the control volumes. The flux density tensor in the midpoints of the faces is obtained by linear interpolation of the quantities at the endpoints of the face. The numerical integration is performed with the trapezoidal rule which is known to be third order accurate. For this reason the approximation of the integral mean value of the rate of change of the flow quantities in a cell is approximated at least with an accuracy of first order. Note that due to the fact that the normal vector on each face can be calculated exactly, accuracy of first order is assured independently of the geometry of the cell. Roe has shown in [18] that for the case that the cells are parallelograms, the approximation of the rate of change in a cell is even second order accurate. Due to the parallelism of opposite faces the first order error terms cancel each other. In order to relate the mean values of the rate of change in a cell to the rate of change at a vertex, a further approximation is made by the use of a distribution formula. The application of this formula assumes the change at a vertex to be a function of all cells having the particular vertex in common. Following Hall [5], the changes in the cells surrounding a vertex are weighted by the volumes of the corresponding cells, and this average is taken to be the change at the particular vertex. For point i,j in Fig. 2 this leads to:

$$\left. \frac{\partial \vec{W}}{\partial t} \right|_{i,j} \approx \frac{\left(\frac{\partial \vec{W}}{\partial t} \right)_{i,j}^{sv} V_{i,j} + \left(\frac{\partial \vec{W}}{\partial t} \right)_{i-1,j}^{sv} V_{i-1,j} + \left(\frac{\partial \vec{W}}{\partial t} \right)_{i,j-1}^{sv} V_{i,j-1} + \left(\frac{\partial \vec{W}}{\partial t} \right)_{i-1,j-1}^{sv} V_{i-1,j-1}}{V_{i,j} + V_{i-1,j} + V_{i,j-1} + V_{i-1,j-1}} \quad (14)$$

This formula is first order accurate on arbitrary meshes. Therefore the accuracy of the approximation of the rate of change at a vertex is always of first order. On cartesian meshes the distribution formula (14) is second order accurate thus leading to a discretization method which is second order accurate on cartesian grids.

Next the cell centered scheme will be discussed. The flow quantities are located at the cell centers (Fig. 3). In order to perform the numerical integration of equation (13) the mean value of the flux density tensor \vec{F} at the midpoint of a face is approximated by averaging the quantities in those cells having the face in common. Multiplication of the mean flux density tensor with the corresponding cell face and normal vector leads as before to numerical integration of (13).

If the averaging of the quantities in neighboring cells gave the exact value of the flux density tensor at the midpoints of the faces, the integration would be third order accurate. For the arrangement of cells sketched in Fig. 4 the averaging does not provide the exact value at the midpoint of a face even for a linearly varying function. The consequence is that the numerical integration of (13) is no longer third order accurate, which in turn leads to errors independent of the mesh size h for the approximation of the rate of change in the control volumes. In [17] it is pointed out that the reduction of the discretization error in cell centered schemes depends only on the smoothness of

the computational grid. On non-smooth grids with slope discontinuities the discretization error will not be reduced when the mesh is refined. Nevertheless on cartesian grids the cell centered scheme is second order accurate and on grids which are sufficiently smooth the cell centered scheme behaves as a scheme of second order accuracy.

3.2 Solution method

In order to establish a fair comparison of both discretization strategies, the same solution method is applied as a framework for the procedures described above. As the schemes use central differences they require an amount of artificial viscosity, and here a blend of fourth and second differences as described by Jameson [1] is added. The integration of the system of ordinary differential equations is carried out by the use of a five-stage Runge-Kutta scheme. Details of the scheme can be found in [19]. In order to drive the solution towards the steady state, acceleration techniques such as local time stepping, implicit averaging of residuals, and enthalpy damping are applied. The cell vertex scheme is further augmented by the use of a multigrid method which is based on the work of Jameson [1] and Hall [5]. Solid wall boundaries in the cell centered scheme are handled by implementation of the normal momentum relation [19]. The cell vertex scheme uses a flow tangency condition similar to [5]. The treatment of the farfield boundaries is based on the concept of Riemann invariants. For lifting cases the effect of a single vortex is added to the freestream flow.

3.3 Numerical Results

The first test case considered is the internal flow over a circular arc of 10% thickness. The onflow Mach number was chosen to be 0.5 so that the flow field remains subsonic. The grid exhibits a slope discontinuity caused by the attachment of the circular arc to the wall (Fig. 5). The isobar patterns delivered by the cell centered scheme exhibit disturbances caused by the discontinuity in the mesh. The results obtained with the cell vertex discretization are given in the same figure. In this case the isobars have smooth slopes and the flow field is symmetric with respect to the inflow and outflow boundaries, as it should be for inviscid subsonic flow. Fig. 6 shows the results for the same problem after a mesh refinement. The disturbances in the cell centered scheme do not vanish, due to the zeroth order errors in the scheme.

The second case for comparison is the transonic flow past the NACA 0012 aerofoil. An O-grid was generated by conformal mapping using 160 by 32 cells and all grid lines possess smooth slopes. Fig. 7 shows the results provided by the application of the different discretization methods. Both schemes deliver almost the same results, as can be seen from the contour pressure distribution and the lift and drag coefficients. In order to check the order of accuracy, a mesh refinement to 320 by 64 cells was performed. The results are given by dashed lines in the same figure. The total pressure losses are almost reduced by a factor of four in both schemes, indicating that both schemes behave as second order accurate schemes.

4. Three-dimensional flows

4.1 Discretization

For derivation of an accurate finite volume method for the calculation of three-dimensional flow fields only cell vertex schemes will be discussed. Compared to the 2-D case additional effort is required in three dimensions when using structured meshes. This is caused by two reasons: first, the faces of three-dimensional cells in structured meshes are not necessarily rectangles but may have a trapezoidal or even triangular shape. Furthermore the vertices of a cell face may not lie in a plane and therefore the normal vector is no longer constant on the face.

If all cell faces are given by triangles, no problems occur to meet the requirement of equation (12), since on a triangle the normal vector is always constant and will not cause any difficulties in the discretization. Additionally simple averaging of the flow quantities at the three vertices leads to a numerical integration which is fourth order accurate. This implies that such a numerical integration of a function, which varies linearly on the cell face, will yield the exact value of the integral. This property is exploited by methods applied to unstructured meshes (e.g. [20]).

When treating quadrilateral rather than triangular cell faces the numerical integration has to be exact for a bilinear function to meet the above requirements [21]. In this case the averaging of the quantities at the four vertices only provides a formula of sufficient accuracy if the cell face is given by a rectangle. Additionally, due to the fact that the normal vector may not be a constant, it is not possible to derive a three-dimensional analog to equation (13). For faces on which the normal vector is not a constant the integration has to include the varying normal vector. In order to overcome these difficulties the cell faces can be subdivided into triangles. Performing this subdivision in an appropriate manner leads to a discretization scheme which is first order accurate on arbitrary meshes. Furthermore, on cartesian meshes the discretization will be second order accurate and therefore on smooth meshes a behaviour of second order can be expected. The subdivision of cell faces into triangles leads to a three-dimensional cell vertex discretization scheme with analogous properties to the two-dimensional scheme. Of course numerical effort will be increased when employing this discretization.

The considerations above only concern the approximation of the integral mean value of the rate of change of the flow variables in a cell. In order to approximate the rate of change at a vertex a distribution formula similar to equation (14) is used.

4.2 Numerical results

In this section numerical results from the application of the cell vertex finite volume method will be presented. The framework of the solution method is a direct extension of the 3-D DFVLR cell centered Euler code [22]. In contrast to the 2-D cell vertex code no multigrid technique is implemented at this time.

The first problem considered is the subsonic flow through a nozzle. Fig. 8 illustrates the nozzle grid. To improve computational efficiency, the symmetry of the configuration was used and the mesh covered only one fourth of the physical domain. The mesh has 80 cells along the axis and 10×10 cells in the cross-sections. The inflow Mach number was chosen as 0.03. The computed results are shown in Fig. 9 by displaying isobars in a series of cross-sections. Even on this coarse mesh the results of the cell vertex discretization scheme do not show any irregularities when following the flow through the nozzle. In order to demonstrate the higher accuracy of the cell vertex scheme, the same flow field was calculated using a cell centered discretization. It should be mentioned that the solution method remained the same and the results are given at corresponding cross-sections. At the region where the circular shape of the cross-sections changes to a rectangular one the non-smoothness of the grid causes disturbances in the flow field obtained from the cell centered scheme. This can be seen in Fig. 9.

The last numerical simulation was chosen to demonstrate the applicability of the cell vertex scheme to complex geometries. The flow field around a powered nacelle during take-off conditions is computed. The grid structure is shown in Fig. 10. As indicated in this figure the core jet is represented by a solid body. As the framework of the solution method allows the use of a multi-block technique, the computational domain is divided into three blocks. From Fig. 10 it can be seen that the grid exhibits two types of singularities: first there is a polar singular line at the symmetry axis. Secondly, at the leading and trailing edge the quasi-streamline grid diverges to form the upper and lower sides of the nacelle. Fig. 11 gives a view of the grid around the nacelle generated by an elliptic system [23]. Fig. 12 displays an enlarged view of the mesh near the leading edge region of the nacelle. Note that the grid lines have a discontinuity in slope at the block boundaries.

In order to simulate take off conditions, results were computed at an angle of attack of 18° and a freestream Mach number of 0.25. No attempt was made to simulate a bending of the core jet due to the angle of attack. Fig. 13 shows the calculated distribution of lines of constant Mach number. As can be seen from the figure no discontinuities of the lines crossing the block boundaries or the singular line at the axis are present. Even the strong discontinuity in the slope of the grid lines at the block boundaries at the leading edge does not cause disturbances. Fig. 14 illustrates this favorable behaviour in an enlarged view of the flow field at the grid singularities. It is worth mentioning that no transformation to cylindrical coordinates was necessary to establish an accurate solution for this flow problem.

5. Concluding remarks

In this paper the accuracy of two- and three-dimensional finite volume methods has been assessed mathematically. A significant result of this error analysis is that on arbitrary meshes an accuracy of at least first order is not always assured for the spatial discretization. It is seen that for two-dimensional flow problems, methods based on a cell vertex scheme establish first order accuracy independent of the smoothness of the grid, whereas methods based on a cell centered scheme do not. These theoretical statements are confirmed by numerical results obtained for different flow problems on smooth and non-smooth meshes.

In the case of three-dimensional flow analysis on structured meshes even cell vertex schemes need additional effort in order to establish an accurate solution method. This is caused by the occurrence of irregular cells such as pentahedrons or tetrahedrons. Furthermore the cell faces may be nonplanar and the normal vector to a face is no longer constant. Subdivision of the cell faces into triangles establishes first order accuracy on arbitrary meshes. For cartesian coordinate grids the discretization is second order accurate and therefore on smooth meshes a behaviour of second order accuracy can be expected.

The higher accuracy of the cell vertex scheme is shown by comparing the calculations of the flow field in a nozzle with both a cell centered and a cell vertex scheme. In order to demonstrate the applicability of the cell vertex scheme to complex geometries, the flow around a powered nacelle is calculated. The grid used in the computations has various singular lines and no deviation of the results near those lines was observed.

6. References

- [1] Jameson, A. Numerical Solutions of the Euler Equations by Finite Volume Methods Using Runge-Kutta Time Stepping Schemes. AIAA-Paper 81-1259 (1981).
- Schmidt, W.
- Turkel, E.

- [2] Jameson, A. Solution of the Euler Equations for Complex Configurations.
Baker, T.J. AIAA-Paper 83-1929 (1983).
- [3] Rizzi, A. Damped Euler Equation Method to Compute Transonic Flow Around Wing-
Body Combinations. AIAA Journal, Vol. 20 (1982), pp. 1321-1328.
- [4] Ni, R.H. Multiple Grid Scheme for Solving the Euler Equations. AIAA-Paper
81-1025 (1981).
- [5] Hall, M.G. Cell Vertex Multigrid Scheme for Solution of the Euler Equations.
Proceedings of the Conference on Numerical Methods for Fluid
Dynamics, Reading, U.K., 1985.
- [6] Koeck, C. Computation of Three-Dimensional Flow Using the Euler Equations and
a Multiple Grid Scheme. Int. Journal for Numerical Methods in
Fluids, Vol. 5 (1985), pp. 483-500.
- [7] Denton, J.D. The Computation of Fully Three-Dimensional Flow through any Type of
Turbomachinery Blade Row. AGARD-LS-140 (1985).
- [8] Test Cases for Inviscid Flow Field Methods. AGARD-AR-211 (1985).
- [9] Moitra, A. Euler Solutions for High-Speed Flow about Complex Three-Dimensional
Configurations. AIAA-Paper 86-0246 (1986).
- [10] Yu, N.J. Flow Simulations for a Complex Airplane Configuration Using Euler
Kusunose, K., Equations. AIAA-Paper 87-0454 (1987).
Chen, H.C.
Sommerfeld, D.
- [11] Sawada, K. Numerical Investigation on Wing/Nacelle Interferences of USB Confi-
Takanashi, S. gurations. AIAA-Paper 87-0455 (1987).
- [12] Kusunose, K. Transonic Analysis for Complex Configurations.
Marcum, D.L. AIAA-Paper 87-1196 (1987).
Chen, H.C.
Yu, N.J.
- [13] Thompson, J.F. Numerical Grid Generation. Proceedings of a Symposium on the Nume-
ed. rical Generation of Curvilinear Coordinate Systems and their Use
in the Numerical Solution of Partial Differential Equations. April
1982 Nashville, Tennessee. (1982).
- [14] Thompson, J.F. Numerical Grid Generation. North Holland, New York (1986)
Warsi, Z.U.A.
Mastin, G.W.
- [15] Weatherhill, N. Grid Generation and Flow Calculations for Aircraft Geometries.
Forsey, C.R. AIAA-Paper 84-1665 (1984).
- [16] Woan, C.J. Three-Dimensional Elliptic Grid Generations Using a Multi-Block
Method. AIAA-Paper 87-0278 (1987).
- [17] Rossow, C. Comparison of Cell Centered and Cell Vertex Finit Volume Schemes.
To be published in Proceedings of 7th GAMM Conference (1987).
- [18] Roe, P.L. Error Estimates for Cell Vertex Solutions of the Compressible Euler
Equations. ICASE Report No. 87-6 (1987).
- [19] Kroll, N. Solution of the Two-Dimensional Euler Equations - Experience with a
Jain, R.K. Finite Volume Code. DFVLR-FB 87-11 (1987).
- [20] Jameson, A. Calculation of Inviscid Transonic Flow over a Complete Aircraft.
Baker, T.J. AIAA-Paper 86-0103 (1986).
Weatherhill, N.
- [21] Chung, T.J. Finite Element Analysis in Fluid Dynamics.
McGraw-Hill, New York, 1978.
- [22] Radespiel, R. Progress in the Development of an Efficient Finite Volume Code for
Kroll, N. the Three-Dimensional Euler Equations. DFVLR-FB 85-31 (1985).
- [23] Radespiel, R. Grid Generation Around Wing-Body-Combination Using a Multi-Block
Structure. AGARDograph on "Current Practices in Numerical Grid Ge-
neration", eds.: J. Thompson and J. Steger, 1987.

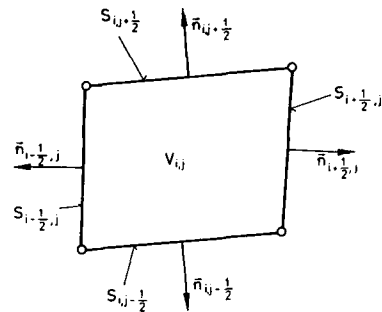


Fig. 1: Definition of two-dimensional cell

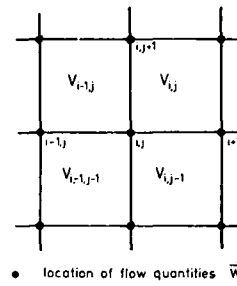


Fig. 2: Finite volume of cell vertex scheme

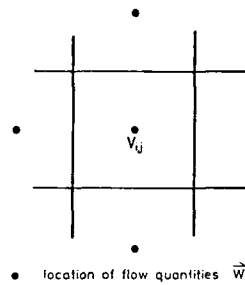


Fig. 3: Finite volume of cell centered scheme

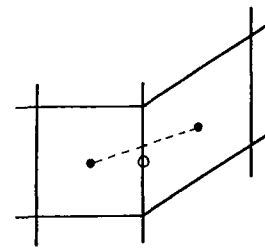


Fig. 4: Cell centered flux balance on skewed grid

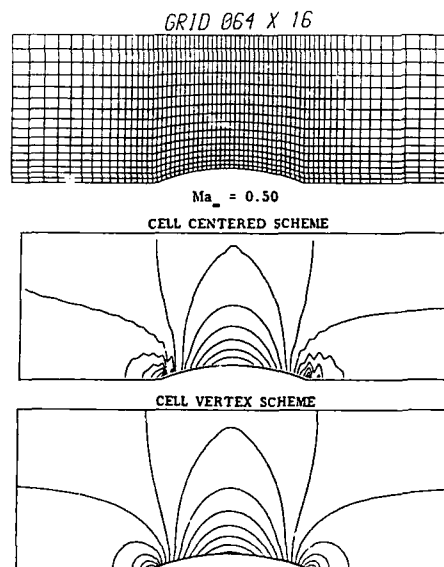


Fig. 5: Internal flow over circular arc

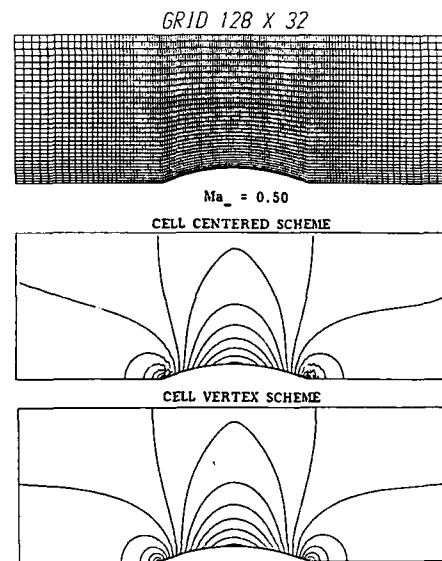


Fig. 6: Effect of grid refinement

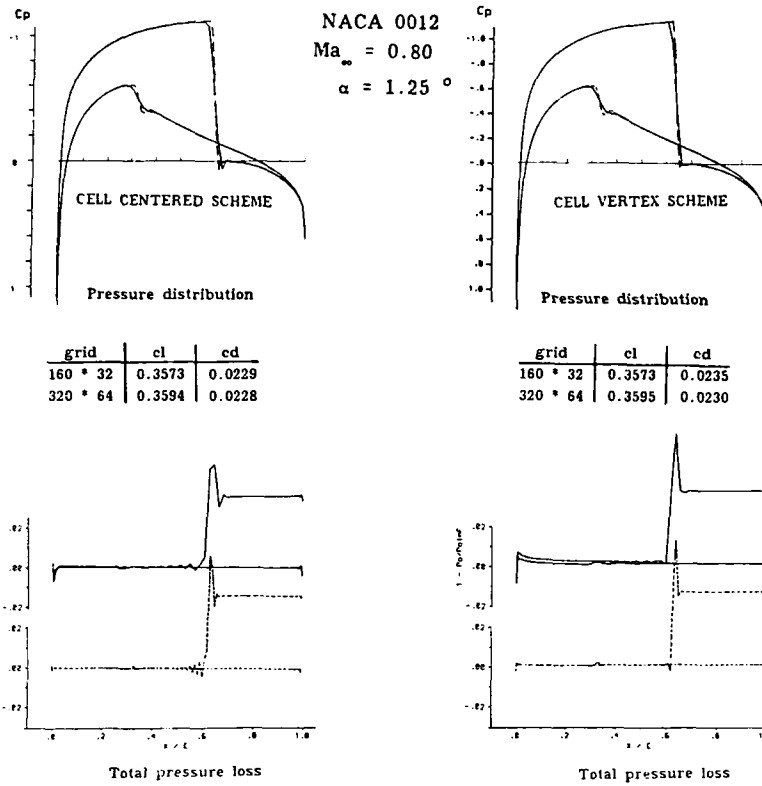


Fig. 7: External flow around NACA 0012 aerofoil

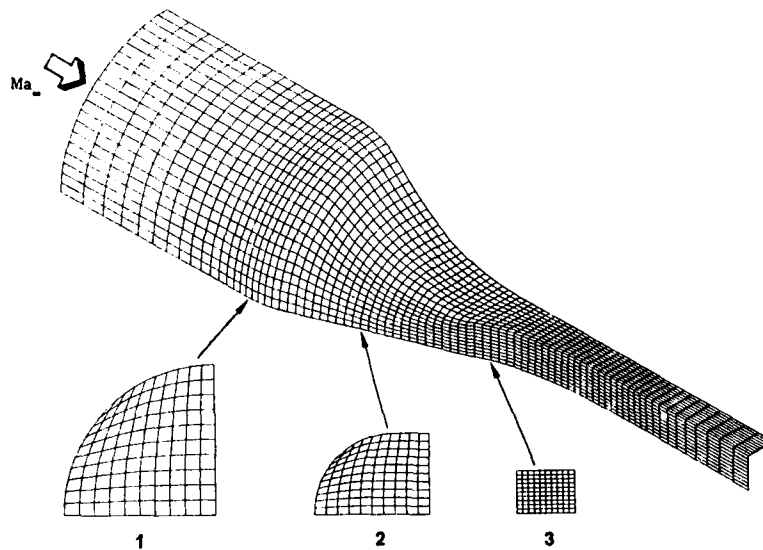


Fig. 8: Coordinate grid for nozzle

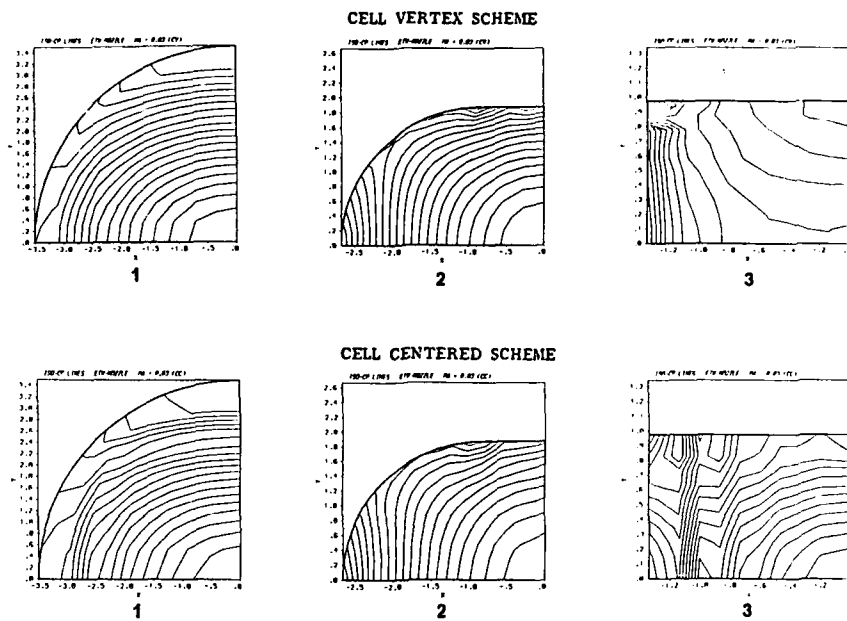


Fig. 9: Nozzle flow field in different cross-sections

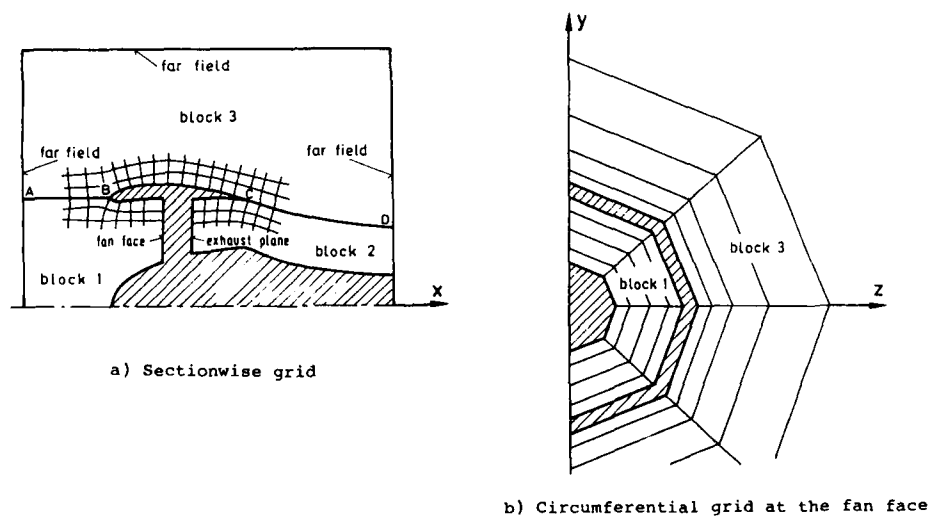


Fig. 10: Grid structure for nacelle configuration

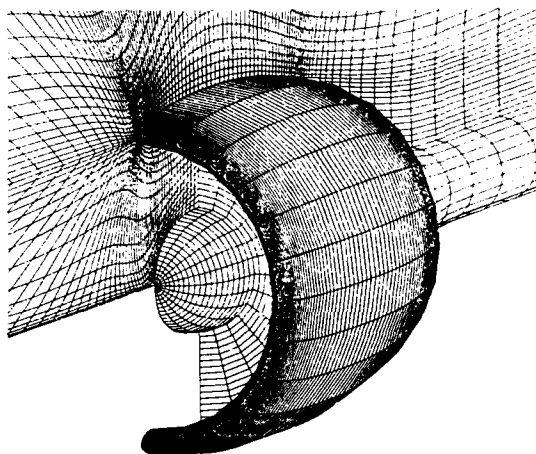


Fig. 11: Coordinate grid around nacelle

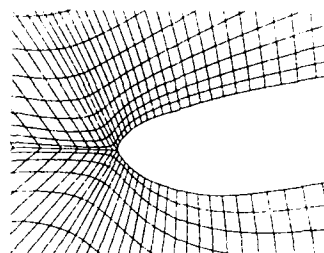


Fig. 12: Enlarged view of the grid at leading edge

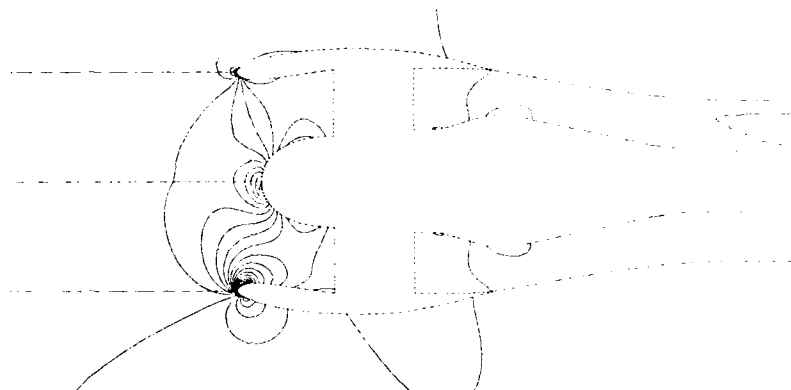


Fig. 13: Mach contours in the symmetry plane of nacelle configuration at $\alpha = 18^\circ$, $Ma_\infty = 0.25$

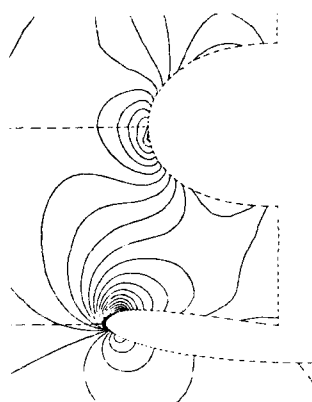


Fig. 14: Enlarged view of Mach contours near grid-singularities

DOCUMENTATION OF SEPARATED FLOWS FOR COMPUTATIONAL FLUID DYNAMICS VALIDATION *)

by

Prof. Dr.-Ing. Dietrich Hummel
 Institut für Strömungsmechanik
 Technische Universität Braunschweig
 Bienroder Weg 3, 3300 Braunschweig
 Federal Republic of Germany

SUMMARY

In recent years a large number of separated flows have been studied at Institute für Strömungsmechanik of TU Braunschweig and a lot of experimental data are available. Some flows are well understood in many details and properly documented, so that they can be used as test cases for computational fluid dynamics validation. The topics of separated flows to be treated here are low speed flows around delta wings, double-delta wings and canard configurations as well as hypersonic flows in axial corners of intersecting wedges. The experimental results are summarized in this paper. The main results are presented and a detailed documentation is provided on where and in which form these results are available.

LIST OF SYMBOLS

A	Aspect ratio ($A = b^2/s$)	α	Angle of attack
M	Machnumber	β	Angle of sideslip
N_{25}	Geometric neutral point	γ	Body half angle (Fig. 12)
Re	Reynoldsnumber ($Re = V_\infty \cdot c_{iw}/\nu$ for wings)	δ	Wedge angle normal to the leading-edge
R_1, R_2	Reattachment points (Fig. 25)	ϵ	Kink angle (Fig. 12)
S	Area	θ	Corner angle (Fig. 24)
S_1, S_2	Separation points (Fig. 25)	λ	Taper ratio ($\lambda = c_d/c_1$)
Tr	Triple point (Figs. 25)	ν	Kinematic viscosity
V_∞	Free-stream velocity	ϕ	Leading-edge sweep (Figs. 13, 24)
Y, Z	Conical coordinates in the measuring plane (Fig. 24), origin at x-axis ($Y = y/x, Z = z/x$)	ψ	Angle between the shear stress direction (local flow direction) at the wall and the conical direction, positive towards the corner center (Fig. 25)
\bar{Y}, \bar{Z}	Conical coordinates in the measuring plane (Fig. 24), origin at the corner	ξ, η, ζ	Dimensionless wing-fixed coordinates ($\xi = x/c_1, \eta = y/s_1, \zeta = z/s_1$)
b	Wing span ($b = 2s$)	$\bar{\xi}, \bar{\eta}, \bar{\zeta}$	Dimensionless aerodynamic coordinates ($\bar{\xi} = \bar{x}/s, \bar{\eta} = \bar{y}/s, \bar{\zeta} = \bar{z}/s$)
c	Chord	Subscripts	
\bar{c}	Mean aerodynamic chord		
c_L, c_D, c_M	Lift-, drag-, pitching-moment-coefficient (based on q_∞, S_W, \bar{c}_W , reference point N_{25} , nose-up positive)	C	canard
c_g	Total pressure coefficient ($c_g = (p - p_\infty)/q_\infty$)	K	kink
c_p	Static pressure coefficient ($c_p = (p - p_\infty)/q_\infty$)	W	τ (Figs. 19-23)
c_q	Dynamic pressure coefficient ($c_q = q/q_\infty$)	W	State at a swept wedge (Figs. 24, 25)
d	Wing thickness	W, u	State at an unswept wedge (Figs. 24, 25)
g	Total pressure	a	Outer section ($y = s$)
l	Model length	d	Maximum thickness
p	Static pressure	i	Inner section ($y = 0$)
q	Dynamic pressure	l	Based on model length
\dot{q}	Local heat transfer rate at the wall	t	Total condition (gas brought to rest isentropically)
s	Wing half span	\bar{n}, \bar{c}	In the \bar{n}, \bar{c} -plane
$s_1(x)$	Local half span	1, 2	Front, rear part (Fig. 13)
v	Local velocity	2	State behind a normal shock (Figs. 25, 26)
x, y, z	Rectangular wing-fixed coordinates origin at wing apex (Figs. 2, 13, 21, 24)	∞	Free-stream conditions
$\bar{x}, \bar{y}, \bar{z}$	Rectangular aerodynamic coordinates, origin at wing trailing-edge		

*) Partly supported under contracts DFG Schl 5/82, Hu 254/2, Hu 254/7, Hu 254/8 and BMVg T/Rf41/90010/91454, TR/Rf41/D0011/D1411.

1. INTRODUCTION

For computational fluid dynamics comparisons with experimental data are essential. In the very beginning of numerical calculations the strategy and the grid type have to be adapted to the physical characteristics of the flowfield. In the course of the calculations various errors may be caused e. g. by neglecting terms in the governing equations, by finite mesh spacing, by the applied difference scheme or finite volume formulation, by artificial viscosity and by the application of numerical boundary conditions. Therefore results of computational fluid dynamics have to be checked by comparison with experimental data. For this purpose experimental investigations have to be provided which are well understood and properly documented. In the last years some international programs have been initiated to collect experimental data on various topics for validation of computational fluid dynamics. Beside this cooperative work in some places single flows or some series of flows have been investigated experimentally and the data obtained can similarly be used as test cases for results of computational fluid dynamics. Since a long time at the Institut für Strömungsmechanik of Technische Universität Braunschweig separated flows have been studied in detail, and a lot of experimental data are available for validation of computational fluid dynamics. It is the purpose of this paper to summarize these experimental investigations, to present the main results and to provide a detailed documentation on where and in which form these results are available.

2. INVESTIGATIONS ON DELTA WINGS AT LOW SPEED

2.1 General properties of the flow

At moderate and large angles of attack the flow separates from the sharp leading-edges of slender wings. These flow separations usually take the form of two free vortex layers joined to the leading-edges of the wing and rolling up to form spiral shaped primary vortices above the upper surface of the wing as sketched in Fig. 1. The vortices over the wing induce additional velocities at the upper surface of the wing. The corresponding pressure distribution which is also drawn in Fig. 1 shows distinctly marked minima beneath the vortex axes. Accordingly an additional lift force occurs which depends non-linearly on the angle of attack. Due to the leading-edge vortices the flow at the wing surface is directed outwards. The steep pressure gradient between the minimum of pressure and the leading-edge causes again flow separation which usually takes the form of a small secondary vortex. At the upper surface of the wing this secondary vortex induces additional velocities. The corresponding modification of the pressure distribution is indicated in Fig. 1b by hatching. At very large angles of attack the lift coefficient reaches a maximum value similar to that in the attached flow case, but the reasons for this behaviour are quite different: Firstly the suction is reduced due to the vertical displacement of the vortices in the rear part of the wing. Secondly the primary vortices experience a sudden change of their structure which is called vortex bursting or even vortex breakdown, which causes an additional strong reduction of the suction on the upper surface of the wing.

This vortex formation is well known since a long time. The first experiments on slender wings are due to H. Winter [1]. The physics of the vortex formation have been studied mainly on delta wings. There exists a very large number of papers on this subject, for instance by D.J. Marsden, R.W. Simpson, W.J. Rainbird [2], N.C. Lambourne, D.W. Bryer [3], D.H. Peckham [4], P.B. Earnshaw, J.A. Lawford [5,6] and D. Hummel [7,8], and the flow over delta wings is also covered by review papers which have been published from time to time for instance by D. Küchemann [9], J.H.B. Smith [10] and D.J. Peake [11].

2.2 Survey of the experimental program at TU Braunschweig

Comprehensive experimental investigations on delta wings have been carried out at the Institut für Strömungsmechanik of Technische Universität Braunschweig. The first papers were aimed at a certain understanding of vortex breakdown and its effects on slender wings. In an early work D. Hummel [12] investigated the flowfield of a leading-edge vortex with vortex breakdown by means of probe measurements. Since the pressure gradient produced by the probe has an influence on the phenomenon under consideration, such experiments are very doubtful. Therefore, vortex breakdown has been generated over the wing by a very strong artificial pressure gradient so that the additional pressure gradient due to the probe was relatively small. The data presented in [12] are the only flow field measurements by a probe which have been carried out in a vortex with vortex breakdown. They will be hopefully replaced in near future by results of Laser-Doppler-Anemometry. In the papers by D. Hummel [12], D. Hummel, P.S. Srinivasan [13] and D. Hummel, G. Redeker [14], a series of sharp-edged delta wings has been investigated by means of three- and six-component measurements in order to investigate the effect of vortex breakdown on the overall characteristics of slender wings. An $A = 1.0$ delta wing of this series has been equipped with a pressure hole system in its surface in order to get more insight into details of the flow. Using this model, the effects of vortex breakdown on the flow at the upper surface have been investigated by means of pressure distribution measurements and oilflow patterns by D. Hummel [15]. In addition the flow situation which leads to the maximum lift coefficient has been analysed by D. Hummel [16] applying pressure distribution measurements and three-component measurements without and with suction in the vortices in order to remove vortex breakdown. By this method the two effects which lead to the maximum lift coefficient were separated and the explanation given in Fig. 1c could be established.

Further investigations on the $A = 1.0$ delta wing have been carried out in the angle of attack regime in which no vortex breakdown is present. A lot of measurements have been performed at an angle of attack $\alpha = 20.5^\circ$, since some theoretical results from J.H.B. Smith [17] for this special angle of attack were available at that time. Investigations by D. Hummel [15], [16] showed the effects of Reynoldsnumber: The overall forces and moments are independent of Reynoldsnumber, but the pressure distribution and the flow at the upper surface depend significantly on Reynoldsnumber. Pressure distribution and boundary layer measurements have been carried out for laminar boundary layers on the upper and lower surface of the wing. From these measurements first of all the bound vortex lines in the lifting surface have been determined by D. Hummel [16]; see also D. Küchemann [18]. Later the boundary layer measurements have been published by D. Hummel [19] as a separate test case for boundary layers on delta wings. Similar

investigations have been carried out by D. Hummel, G. Redeker [20] using artificially turbulent boundary layers. The slope of the bound vortex lines in the vicinity of the trailing-edge of the wing indicated the occurrence of counter-rotating vorticity downstream of the wing trailing-edge as described qualitatively by B.J. Elle, J.P. Jones [21] and D. Hummel, G. Redeker [20]. Therefore the flowfield behind the trailing-edge of the delta wing $A = 1.0$ has been measured at $\alpha = 20.5^\circ$ in different planes by D. Hummel [7], [8]. Since these experiments the flow over a sharp-edged delta wing in the angle of attack range without vortex breakdown may be regarded as fully understood even in details.

2.3 Results for the delta wing $A = 1.0$

The different kinds of measurements which have been carried out on the $A = 1.0$ delta wing are put together in Tab. 1. They can be used for comparisons with computational fluid dynamics and subsequently some guidelines are given for the use of this material.

2.3.1 Windtunnel model [7], [15], [19]

The measurements have been carried out on a sharp-edged delta wing of aspect ratio $A = 1.0$ the geometry of which is shown in Fig. 2. The wing has a flat surface and a narrow triangular cross-section up to $x/c_f = 0.9$ and a trapezoidal cross-section in the region $0.9 < x/c_f < 1.0$. The model is conical with respect to the wing apex as well as with respect to the wing tips. The maximum relative thickness is $d/c_f = 0.021$ at $x/c_f = 0.9$. On both sides of the model pressure tubes are embedded in the surface and the holes for the pressure measurements are drilled on lines $x = \text{const.}$ (sections a to g in Fig. 2). The dimensions of the model are length $c_f = 750$ mm, span $b = 375$ mm, thickness $d = 16$ mm. The geometric neutral point $N_{0.5}$ is situated at $x_{N_{0.5}}/c_f = 0.5$.

The tests have been performed in the 1.3 m Low-speed Windtunnel of Institut für Strömungsmechanik at Technische Universität Braunschweig. This windtunnel has an open working section with a circular cross section of 1.3 m diameter. The angle of attack α has been chosen as the angle between the free-stream and the flat surface (plane $z = 0$) of the model and positive for a free-stream flow from the lower surface, see Fig. 2.

2.3.2 Forces and moments [7], [13], [19]

The results of the three-component measurements are shown in Fig. 3. At very large angles of attack vortex breakdown occurs in the vortices. The movement of the breakdown point as function of the angle of attack may be taken from [13]. The trailing-edge of the wing is reached at $\alpha = 29^\circ$ and for larger angles of attack the aerodynamic characteristics are strongly influenced by vortex breakdown.

The results plotted in Fig. 3 have been obtained for $Re = 2 \cdot 10^5$. Similar tests have been carried out for $6 \cdot 10^5 \leq Re \leq 2 \cdot 10^6$ and no influence of Reynoldsnumber has been found. Therefore these results can be used for all Reynoldsnumbers in this region. This does not mean that there are no Reynoldsnumber effects in details, but if one is interested only in forces and moments on a slender sharp-edged wing the Reynoldsnumber is not an important parameter.

2.3.3 Surface oilflow patterns on the wing [7], [16], [19], [20]

Detailed investigations have been carried out for the angle of attack $\alpha = 20.5^\circ$ since for this special value theoretical results from J.H.B. Smith [17] were available.

A first set of data has been collected for a Reynoldsnumber $Re = 9 \cdot 10^5$. In this case the boundary layers at the pressure side as well as in the unseparated parts of the suction side of the wing were laminar [7], [16], [19]. The surface oilflow pattern from the flat surface of the wing at $\alpha = -20.5^\circ$ is given in Fig. 4a. It shows a typical pressure side flow without any flow separations. The corresponding pattern for $\alpha = +20.5^\circ$ given in Fig. 4b is a typical suction side flow with laminar boundary layers. In this case an early secondary separation takes place at $\eta = \pm 0.68$ and in the region of the secondary vortex detailed flow studies [16] led to the understanding that tertiary separations underneath the secondary vortex are present.

A second set of data has been collected for turbulent boundary layers on the upper surface of the wing. For this purpose the flow was investigated again at a Reynoldsnumber of $Re = 9 \cdot 10^5$, but artificially turbulent boundary layers have been generated by means of turbulence generators as shown in Fig. 5. For this purpose wires, having a relative diameter of $D/s = 0.0053$, were fixed to the wing surface at $\eta = \pm 0.5$. It turned out that the turbulent boundary layer stays longer attached [20]. In this case the secondary separation takes place at $\eta = \pm 0.8$. Only a weak secondary vortex is formed and no tertiary separations are present.

2.3.4 Pressure distributions on the wing [7], [16], [19], [20]

The pressure distribution on the flat pressure side of the wing at $\alpha = -20.5^\circ$ is shown in Fig. 6 [19]. This is a typical lower surface pressure distribution with a high pressure level in the central parts of the wing and accelerated flow towards the leading-edges. In this case no flow separations are present. On rays $\eta = \text{const.}$ the pressure coefficients change in longitudinal direction; therefore the flow is non-conical. The pressure distribution on the flat suction side of the wing at $\alpha = +20.5^\circ$ is shown in Fig. 7 [19]. This is a typical upper surface pressure distribution for a laminar boundary layer. The early secondary separation at $\eta = \pm 0.68$ leads to a strong secondary vortex which produces high suction at $\eta = \pm 0.90$. The displacement effect of the large secondary vortex moves the axis of the primary vortex upwards and more inboard as compared to inviscid flow [20]. Therefore the suction peaks generated by the primary vortex are relatively low and located inboard at $\eta = \pm 0.62$. The flow is again non-conical. According to detailed flow studies [16] the additional suction peaks at $\eta \approx 0.73$ are due to a tertiary vortex underneath the secondary vortex.

The pressure distribution on the flat suction side of the wing at $\alpha = +20.5^\circ$ and turbulent boundary layers is shown in Fig. 8. The secondary separation at $\eta = \pm 0.80$ leads to a small secondary vortex which produces only weak suction close to the wing leading-edge. Correspondingly its displacement effect on the primary vortex is small. Therefore the suction peaks due to the primary vortex are very high and they are located outboard at $\eta = \pm 0.68$.

Concerning comparisons between experimental data and theoretical results the following conclusions can be drawn: For comparisons with inviscid flow theories such as potential flow and Euler solutions

experiments with turbulent boundary layers should be used. Only in this case reasonable agreement can be expected, but in addition one has to bear in mind that a difference between theory and experiment has to remain due to the neglect of viscosity in the theory. On the other hand the pressure distribution for laminar boundary layers can properly be used to check viscous flow calculations such as boundary layer methods as well as solutions of the Navier-Stokes equations.

2.3.5 Boundary layer measurements [19].

Three-dimensional laminar boundary layers on the flat surface of the delta wing $A = 1.0$ have been measured at $\alpha = \pm 20.5^\circ$. The corresponding pressure distributions are shown in Figs. 6 and 7. From these experiments the velocities at the outer edge of the boundary layer were used to determine the bound vortex lines in the lifting surface which have been published in [7], [16], [18]. The detailed boundary layer measurements [19] have been carried out for the three-dimensional flow at all stations x, y according to Fig. 2 in which the static pressure at the wing surface had been determined. For all these stations the distributions of magnitude and direction of the local velocity vector have been measured and the limiting value of the local flow direction at the wing surface has been determined from a quantitative evaluation of the oilflow pattern according to Fig. 4. The paper [19] contains the experimental data for two three-dimensional laminar boundary layer flows namely a typical pressure side flow at $\alpha = -20.5^\circ$ without any flow separation and a typical suction side flow at $\alpha = +20.5^\circ$ with secondary separations at $\eta = \pm 0.68$. For both boundary layers some velocity distributions have been presented in [19], which are not repeated here. These boundary layer measurements are well suited as test cases to check methods for the calculation of three-dimensional laminar boundary layers as well as solutions of the Navier Stokes equations.

Similar experiments have also been carried out for the case of artificially turbulent boundary layers [20]. From these measurements the bound vortex lines could be determined using the velocity vectors at the outer edge of the boundary layer. Unfortunately only a small part of the velocity profiles is covered by the experimental data and therefore these experiments do not provide a similar test case for turbulent boundary layers.

2.3.6 Flowfield measurements [7]

The investigations of the flowfield behind the $A = 1.0$ delta wing at $\alpha = 20.5^\circ$ have been carried out at a Reynoldsnumber of $Re = 2.0 \cdot 10^5$. In this case the lower surface boundary layer was laminar up to the flat ridge near the trailing-edge of the wing. At the upper surface natural transition laminar/turbulent took place at $\xi = 0.43$ and in the rear part of the wing a turbulent boundary layer was present. The flow was attached in the inner region and secondary separation occurred at $\eta = \pm 0.83$ which led to a small secondary vortex.

From the flowfield measurements by means of a 5-holes-probe [7] the total pressure contours are shown in Fig. 9 and the local velocity vectors in Fig. 10 for four different planes behind the wing. Downstream of the trailing-edge the vortex sheet is distinctly warped and a concentrated trailing vortex is formed the rotation of which is opposite to that of the corresponding leading-edge vortex. According to inductions from the primary vortex the counter-rotating trailing vortex moves outwards and upwards and its center follows a helical path around the leading-edge vortex. The existence of the trailing vortex is due to the distribution of vorticity in the lifting surface. This effect is also present in inviscid flow. Therefore the experimental results [7] on the flowfield in the vicinity of the trailing-edge of a delta wing are a widely used test case for all kinds of theoretical representations of the delta wing flow such as potential flow, Euler and Navier-Stokes solutions.

2.4 Results for other delta wings [12], [13], [14]

The delta wing $A = 1.0$ discussed so far is part of a series of delta wings which has been investigated at Institut für Strömungsmechanik of TU Braunschweig. The other wings of this series had aspect ratios $A = 1.6$ and $A = 2.3$, the cross-section shapes were the same as shown in Fig. 2 for the $A = 1.0$ delta wing. The results of the three-component measurements as well as the vortex breakdown positions as functions of the angle of attack may be taken from D. Hummel, P.S. Srinivasan [13]. The results of six-component measurements as well as the locations of vortex breakdown for various combinations of the angle of attack α and the angle of sideslip β have been published by D. Hummel [12] and D. Hummel, G. Redeker [14]. Pressure distribution measurements and surface oilflow patterns in unsymmetrical flow ($\beta \neq 0$) have been carried out only for the $A = 1.0$ delta wing of the series. Some results are available from D. Hummel [12], [15].

2.5 Vortex breakdown flowfield [12]

The structure of a vortex with vortex breakdown has been studied by D. Hummel [12] by means of probe measurements. These investigations have been carried out over an $A = 0.78$ cropped delta wing with a taper ratio $\lambda = 0.125$. At an angle of attack $\alpha = 31^\circ$ vortex breakdown has been generated over the wing by an artificial pressure gradient produced by a large obstacle downstream of the wing, and the additional pressure gradient generated by the probe itself could be regarded as small. A typical result of these measurements is shown in Fig. 11. The velocity distribution is given for different planes perpendicular to the free-stream. Upstream of the breakdown point the velocity increases very much towards the vortex axis whereas downstream of the breakdown point a large region of the retarded flow is present in the vortex center.

Modern methods of computational fluid dynamics such as solutions of the Euler and the Navier-Stokes equations could be applied to delta wing flows with vortex breakdown over the wing. In this case velocity distributions as shown in Fig. 11 should turn out. Although artificial conditions led to the experimental results, the data can nevertheless be used for comparison by a proper adaptation. For this purpose the calculations should be carried out for an angle of attack $\alpha > 31^\circ$, at which vortex breakdown takes place at $\xi = 0.46$ as in the experiments. In this condition the velocity distributions in the vicinity of the

vortex breakdown point should be comparable. It would be very much interesting to see whether methods of computational fluid dynamics, which are able to calculate a maximum lift coefficient $c_{l,max}$ for a delta wing, lead to reasonable results for the velocity distributions in the vortex flow field with vortex breakdown over the wing.

2.6 Test cases

In conclusion the experimental data for delta wings contain the following test cases for comparison with results of computational fluid dynamics:

- Test case 1: Delta wing $A = 1.0$, flowfield at $\alpha = 20.5^\circ$
 Available data: Model geometry
 Aerodynamic coefficients
 Pressure distribution
 Surface oilflow patterns
 Bound vortex lines
 Flowfield behind trailing-edge
 Reference : D. Hummel [7]
- Test case 2: Delta wing $A = 1.0$, laminar boundary layers at $\alpha = \pm 20.5^\circ$ (pressure and suction side)
 Available data: Model geometry
 Aerodynamic coefficients
 Pressure distribution
 Surface oilflow patterns
 Three-dimensional velocity profiles
 Reference : D. Hummel [19]
- Test case 3: Delta wing $A = 0.78$, velocity distribution in a vortex with vortex breakdown
 Available data: Model geometry
 Total pressure contours and dynamic pressure contours in four planes
 Static pressure along vortex axis
 Velocity profiles
 Reference : D. Hummel [12]

3. INVESTIGATIONS ON DOUBLE-DELTA WINGS AT LOW SPEED

3.1 General properties of the flow

For modern fighter aircraft wings with kinked leading-edges such as double-delta wings or strake-wings are mainly used. Basic experiments on this kind of wings are due to W.H. Wentz, M.C. McMahon [23], [24], W. Staudacher [25], J.E. Lamar, J.M. Luckring [26], M.J. Liu et al. [27], U. Brennenstuhl und D. Hummel [28], [29], [30], [31], [34], [37], H.W.M. Hoeijmakers, W. Vaatstra, N.G. Verhaagen [32], N.G. Verhaagen [33] as well as M. Beukenberg and D. Hummel [35], [36]. At low angles of attack two primary vortices are shed on each side of the wing, originating from the wing apex and from the leading-edge kink. For large kink angles this kind of vortex system is present up to high angles of attack until the vortices are destroyed by vortex breakdown. For small and moderate kink angles in the leading-edge the two vortex systems merge into one system with increasing angle of attack. This process is a fundamental feature of the flow over wings with kinked leading-edges. At very high angles of attack vortex breakdown occurs in the joined vortices too, which leads to the wellknown limitations of the aerodynamic coefficients.

3.2 Survey of the experimental program at TU Braunschweig

A large number of experimental investigations on double-delta wings have been carried out at the Institut für Strömungsmechanik of Technische Universität Braunschweig. In these tests a series of wings according to Fig. 12 was used. The wings I to VIII form a subseries having the same front part with a semi apex angle of $\gamma = 10^\circ$ and the same kink position at $x_k/c_f = 0.5$, whereas the kink angle ϵ is varied from -15° (wing I) to 40° (wing VIII). Another subseries is formed by the wings VI, IX and X for which the wing span is kept constant and the kink position x_k/c_f is altered between $x_k/c_f = 0.5$ (wing VI) and $x_k/c_f = 0$ (delta wing X). All wings were manufactured as thin flat plates having a thickness/chord ratio of $d/c_f = 0.006$.

For all these wings three-component measurements have been carried out and the positions of vortex breakdown were determined. The results of these investigations have been published in [28], [29], [30], [31], [34]. Details of the flow have been derived from surface oilflow patterns and from pressure distribution measurements which have been carried out for the subseries of wings VI, IX and X in [28], [34] and the subseries of wings IV to VIII in [29], [34]. In the course of these investigations the merging process of the vortices and its relation to the wing geometry has been studied. It turned out, that within the wing series according to Fig. 12 the wing VI, having an aspect ratio of 2.05, showed the corresponding flow phenomena quite clearly and therefore this planform was chosen for further studies of the merging process of the two vortex systems. Some preliminary flowfield measurements have been performed using a 5 mm probe [28]. Intensive flowfield studies have been carried out by means of a 2 mm probe [29], [31], [34]. The case of two separate vortex systems was measured at $\alpha = 10^\circ$ and the merging process of the two vortex systems was analyzed at $\alpha = 12^\circ$ in several planes perpendicular to the free-stream. In order to detect more details of the flow at a constant probe diameter a half-model of the

double-delta wing A = 2.05 was built and by means of this model the details of the flowfield were determined. Separate vortex systems were measured at $\alpha = 7^\circ$ and merging vortex systems at $\alpha = 11^\circ$ in several planes over the wing [34].

Finally these investigations were extended to include double-delta wings in unsymmetrical flow [35], [36]. For the wings V, VI and VII according to Fig. 12 six-component measurements have been carried out and the positions of vortex breakdown were determined. In addition the status of the flow has been derived from pressure distribution measurements and surface oilflow patterns for various unsymmetrical free-stream flow conditions. It turned out that in unsymmetrical flow a separated vortex system on one side and a merged vortex system on the other side may be present and with increasing angle of attack the different vortices are destroyed gradually by vortex breakdown. For some cases the flowfield has been measured in different planes perpendicular to the free-stream [35], [36].

3.3 Results for the double-delta wing A = 2.05

A survey of all measurements carried out on the double-delta wing A = 2.05 (wing VI of the series according to Fig. 12) is shown in Tab. 2. These experimental data can be used for comparison with computational fluid dynamics and some guidelines how to use this material are given subsequently.

3.3.1 Windtunnel models [28], [31], [34]

The measurements have been carried out on the double-delta wing A = 2.05 according to Fig. 13. Concerning the planform the sweep of the front part is $\phi_f = 80^\circ$ and of the rear part $\phi_r = 60^\circ$ and the leading-edge kink is located at $x_l/c_f = 0.5$. Two different model versions have been used. Model A has a flat plate cross-section with a constant thickness $d/c_f = 0.006$. All edges of this wing are rounded by a radius of half wing thickness. It turned out that this tiny radius was small enough to produce leading-edge separation already at very small angles of attack. The model size is $c_f = 500$ mm. Model B is a half model with triangular cross-sections in the front parts and trapezoidal cross-sections in the rearmost parts of the wing. The maximum thickness $d_{max}/c_f = 0.045$ is located at $x_l/c_f = 0.82$ and the front part the center line thickness increases by an angle $\beta = 1.64^\circ$. The model size is 1500 mm and at all edges the model has a constant thickness of 1 mm. The model has an effective negative camber and the flat surface has been used as suction side during the tests.

All measurements have been performed in the 1.3 m Low-speed Windtunnel of Institut für Strömungsmechanik at Technische Universität Braunschweig. The Reynoldsnumber based on the root chord c_f of the wing was $Re = 1.3 \cdot 10^6$ for tests with model A and $Re = 4.0 \cdot 10^6$ for tests with model B.

3.3.2 Forces and moments [28], [30], [31], [34]

The results of the three-component measurements on model A are shown in Fig. 14. At angles of attack $\alpha < 10^\circ$ the two vortices on each side of the wing are separate and the aerodynamic coefficients depend nonlinearly on the angle of attack. For larger angles of attack $\alpha > 10^\circ$ the vortices join over the wing. This flow phenomenon moves upstream with increasing angle of attack quite rapidly and leads to a considerable reduction in lift and nose-down pitching moment. The movement of the vortex breakdown point within the joined vortices as function of the angle of attack may be taken from [34], [35], [36]. The trailing-edge of the wing is reached at $\alpha = 26^\circ$ and for even larger angles of attack the aerodynamic coefficients are strongly influenced by vortex breakdown.

3.3.3 Pressure distributions [28], [30], [31], [34], [35]

The pressure distribution on the suction side of model A has been measured for various angles of attack. Typical examples are shown in Fig. 15 for the rear part of the wing. At $\alpha = 10^\circ$ in each section two vortices are clearly indicated, which do not merge. The outer vortex which originates from the leading-edge kink is much stronger than the inner one which is no longer fed with circulation downstream of the leading-edge kink. The shape of the pressure distributions in the region between the suction peak and the leading-edge indicate that the boundary layer at the secondary separation line was turbulent. At $\alpha = 12^\circ$ two separate vortices can be detected up to $\xi = 0.75$. More downstream the vortices join quite rapidly and already at $\xi = 0.875$ only a single suction peak is found. For pressure distributions at $\alpha > 12^\circ$ see [34].

3.3.4 Flowfield measurements [29], [31], [34], [35]

The investigations on the structure of the flowfield on the double-delta wing A = 2.05 have been concentrated on the angles of attack $\alpha = 10^\circ$ and $\alpha = 12^\circ$ in order to get a documentation of the two flow states with separated and merging vortex systems. Fig. 17 shows the flowfield on model A downstream of the wing trailing-edge at $\alpha = 10^\circ$, taken from [31]. The two separated vortices are clearly indicated. Additional measurements in planes more upstream and more downstream may be taken from [34]. The counter-rotating vortex related to the outer primary vortex is the trailing vortex which had already been found for the simple delta wing as shown in Figs. 9 and 10. In order to understand the occurrence of the counter-rotating vortex related to the inner primary vortex additional measurements have been carried out on model B at $\alpha = 7^\circ$ in several planes over the wing. It turned out that downstream of the leading-edge kink the vortex sheet between the two primary vortices joins the upper surface boundary layer and more downstream a counter-rotating trailing vortex is formed which originates from a vortex sheet leaving the wing surface close to the inner primary vortex. These details are described in [34]. Concerning comparisons of these results with computational fluid dynamics one has to conclude that both counter-rotating vortices are due to inviscid effects. This means that solutions of the Euler equations or even results according to potential flow theories should contain these counter-rotating vortices.

The flowfield on model A downstream of the wing trailing-edge at $\alpha = 12^\circ$, taken from [31], is shown in Fig. 18. The joined vortex associated by its counter-rotating trailing vortex is clearly indicated. The development of this flow can be taken from additional measurements in several planes located more upstream [31], [34] and further details have been found by measurements on model B in two planes over the

wing at $\alpha = 11^\circ$ [34]. If the angle of attack is increased from $\alpha = 10^\circ$ to $\alpha = 12^\circ$ a sudden change of the flow structure over the wing is observed, which is due to inviscid flow phenomena. Concerning comparisons with computational fluid dynamics it should be expected that this change of the flow structure is described by theory even in the case of inviscid flow.

3.4 Results for other double-delta wings [28], [29], [31], [34], [35]

Similar results as for the $A = 2.05$ double-delta wing, wing VI of the series according to Fig. 12, are also available for other wings of this series. Apart from three-component measurements, which exist for all wings of this series [28], [34], the flow on the $A = 1.31$ (wing V) and the $A = 3.01$ (wing VII) double-delta wing has also been studied quite intensively by means of pressure distribution measurements and surface oilflow patterns in symmetrical [34] and unsymmetrical flow [35], [36]. From these investigations the general flow structure including the occurrence of vortex breakdown may be regarded as fully understood, but flowfield measurements for comparison with computational fluid dynamics do not exist.

3.5 Test cases

In conclusion the experimental data for double-delta wings contain the following test cases for comparison with result of computational fluid dynamics:

Test case 4: Double-delta wing $A = 2.05$, flowfield at $\alpha = 10^\circ$, system of separate vortices

Available data: Model geometry
Aerodynamic coefficients
Pressure distribution
Surface oilflow patterns
Flowfield over and behind the wing
Reference : U. Brennenstuhl [34]

Test case 5: Double-delta wing $A = 2.05$, flowfield at $\alpha = 12^\circ$, system of merging vortices

Available data: Model geometry
Aerodynamic coefficients
Pressure distribution
Surface oilflow patterns
Flowfield over and behind the wing
Reference : U. Brennenstuhl [34]

4. INVESTIGATIONS ON CANARD CONFIGURATIONS AT LOW SPEED

4.1 General properties of the flow

Close-coupled canard-wing configurations play an important role in modern fighter aircraft design as discussed by H. John, W. Kraus [38]. The benefits of such a tail configuration are known since H. Behrbohm [40]. The value of maximum lift coefficient $c_{L,max}$ and the corresponding angle of attack $\alpha(c_{L,max})$ can be considerably increased by adding a delta canard to a delta wing. This advantage is due to favourable interference effects between the vortex systems of canard and wing. A lot of experimental investigations on series of canard-wing combinations have been carried out (see [46]) in order to find practicable configurations. Investigations on the physics of the interfering vortex systems of canard and wing are rare. Some informations may be taken from B.B. Gloss, D.D. Miner [41], J. Er-EI, A. Seginer [42], K. Hartmann [43], L. Hjelmborg [44] and K.A. Bütelfisch et al [45].

4.2 Survey of the experimental program at TU Braunschweig

At Institut für Strömungsmechanik of TU Braunschweig an experimental program on close-coupled canard configurations is in progress. The aim is to get detailed insight into the interference between the vortex systems of canard and wing and to provide data for a comparison with theoretical investigations. In particular it is intended to give a detailed quantitative documentation of the three-dimensional flowfield.

The experimental investigations were started on a configuration with delta planforms $A = 2.31$ for wing and canard. The longitudinal and the vertical distance of the canard as well as its setting angle relative to the wing have been varied systematically. Three-component and pressure distribution measurements have been carried out and additional surface oilflow patterns have been taken on canard and wing for several angles of attack. To identify the main interference effects results for canard-off and canard-on configurations have been compared. The main results of these investigations have been published by D. Hummel, H.-Chr. Oelker [46], [47]. The canard induces at the wing a non-uniform distribution of reduced local angles of attack which leads to a non-conical vortex formation at the wing and to a delay in the occurrence of vortex breakdown. On the other hand the wing produces upwash at the canard, which increases its lift. Another favourable effect at the canard results from longitudinal velocity components induced by the wing which lead again to a delay of canard vortex breakdown. Starting from this basic understanding of the flow an angle of attack of $\alpha = 8.8^\circ$ was chosen for flowfield measurements. In this case no vortex breakdown was present at the configuration. Preliminary results of these investigations have already been included in [46] and [47] for one plane close to the trailing-edge of the wing. The complete flowfield study will be published in [48].

After the formation of the international working group for Euler code validation the investigations have been extended to the new model geometry with an $A = 1.65$ swept canard and a sharp-edged $A = 1.38$ cropped delta wing. Within the international program these investigations form the limiting case for $M = 0$. Three-component and pressure distribution measurements have been carried out and surface oilflow patterns have been taken for various angles of attack. In addition a complete flowfield study has been performed in different planes over the wing. The measurements have already been terminated, the evaluation is in progress and the results will be published as soon as possible.

4.3 Results for the $A = 2.31$ delta canard configuration

The experimental data available for the $A = 2.31$ delta canard configuration are put together in Tab. 3. These results can be used for comparisons with computational fluid dynamics, but the following remarks should be noticed.

4.3.1 Windtunnel model [46], [47], [48]

The measurements have been carried out for a canard-fuselage-wing-configuration which is shown in Fig. 19. Wing and canard have delta planforms of aspect ratio $A_C = A_W = 2.31$ and a corresponding leading-edge sweep of $\phi_C = \phi_W = 60^\circ$. In both cases symmetric parabolic airfoils for the root section and parabolic contours in spanwise direction have been used. All edges are sharp. Both wing and canard are equipped with a tube system underneath the surface and with pressure holes to measure the surface pressure distribution. A very flat fuselage has been chosen, which consists of a cylindrical portion of length $l_F = 8h_F$ and front and rear parts of length $l_{FF} = l_{RF} = 2h_F$. The detailed geometric data may be taken from [46]. The test case to be used for comparison with computational fluid dynamics is the so called "normal configuration" according to [46] which is characterized by a coplanar canard-wing combination having a very small distance between wing apex and canard trailing-edge of $\Delta r/c_{iW} = 0.05$.

4.3.2 Forces and moments [46], [47], [48]

The results of the three-component measurements are shown in Fig. 20. For the canard-off configuration the vortex breakdown point crosses the wing trailing-edge at $\alpha \approx 10^\circ$ and the corresponding reductions in lift and nose-down pitching moment are clearly indicated. For the canard-on configuration due to the favourable interference effects vortex breakdown occurs over the wing not till $\alpha \approx 20^\circ$. On the other hand in the canard vortices vortex breakdown is present at the canard trailing edge at $\alpha > 12^\circ$, but due to favourable wing-induced pressure gradients the burst canard vortices are restored to a non-burst state in the region of the leading-edge of the wing. With increasing angle of attack vortex breakdown moves upstream over the canard very slowly.

4.3.3 Pressure distributions [46], [47], [48]

The pressure distribution on the suction side of canard and wing has been measured for various angles of attack. A typical example is shown in Fig. 21 for $\alpha = 8.8^\circ$. The traces of the leading-edge vortices can clearly be detected from the suction peaks on canard and wing. At this angle of attack no vortex breakdown is present at the configuration. The pressure distribution on the wing of the canard configuration shows in the front part considerably lower suction peaks, which lie closer to the leading-edge than in the non-interfering case. In the rear part of the wing the suction peaks reach again the same level as for the canard-off configuration but their spanwise position is different. The corresponding formation of the leading-edge vortex is therefore distinctly non-conical.

Similar pressure distribution are also available in [46], [47] for angles of attack $\alpha = 14.7^\circ$ and $\alpha = 29.6^\circ$, but for these angles of attack one has to bear in mind, that vortex breakdown is present over the configuration. At $\alpha = 14.7^\circ$ vortex breakdown occurs in the canard vortices between the canard trailing-edge and the wing leading-edge and at $\alpha = 29.6^\circ$ vortex breakdown occurs also in the wing vortices. Comparisons of results of computational fluid dynamics and these experiments for large angles of attack should be made for theories which are able to treat the vortex breakdown phenomenon properly. In all other situations the comparisons should be carried out for $\alpha = 8.8^\circ$ which is a test case without any vortex breakdown.

4.3.4 Surface oilflow patterns [46], [47]

Flow studies have been carried out by means of oilflow patterns on the upper surface of the $A = 2.31$ canard configuration. The result for $\alpha = 8.8^\circ$ is shown in Fig. 22. The non-conical state of the flow on the suction side of the wing is clearly indicated. For this free-stream condition the vortex systems of canard and wing do not merge. It should be noticed that neither the pressure distribution according to Fig. 21 nor the surface oilflow patterns according to Fig. 22 show any indication of the slope of the canard vortices over the wing. This is due to the fact that the canard vortices lie at relatively large distance over the inner portion of the wing.

Similar oilflow patterns are available in [46], [47] for $\alpha = 14.7^\circ$ and $\alpha = 29.6^\circ$. In combination with the pressure distribution they indicate vortex breakdown in the canard and wing vortices.

4.3.5 Flowfield measurements [46], [47], [48]

The investigations on the structure of the flowfield on the $A = 2.31$ delta canard configuration have been concentrated on the angle of attack $\alpha = 8.8^\circ$ in order to get a documentation of the flow state without vortex breakdown at the configuration. A typical result for a plane at the wing trailing-edge is shown in Fig. 23 [46], the flowfield in other planes upstream and downstream of the wing trailing-edge may be taken from [48].

On the righthand side the primary wing vortex is located at $\bar{r} = 0.81$ and a corresponding secondary vortex is found at $\bar{r} = 0.93$. The estimated trace of the vortex sheet is indicated by a dash-dotted line and its position has been determined from local maxima of total pressure loss. Another region of large total pressure reductions is found at some distance over the wing at $\bar{r} = 0.30$ indicating the position of

the canard vortex. The total pressure losses within this vortex are not as large as in the wing primary vortex. This indicates that the canard vortex is the weaker one. The isobars of the canard vortex show an attached region of increased pressure losses which results from the wake of the canard trailing-edge. The measurements in planes over the wing [48] showed clearly that this region contains the remains of a canard secondary vortex as well as those of a counter-rotating canard trailing-edge vortex which is formed downstream of the canard trailing-edge in the same way as for a delta wing according to Figs. 9 and 10. Another interesting phenomenon which has been deduced from the flowfield measurements over the wing [48] is the fact that the vortex sheet originating from the trailing-edge of the canard joins the upper surface of the wing and contacts the upper surface boundary layer in the inner portion of the wing. Underneath the canard vortex the free vortex sheet separates again from the wing boundary layer and rolls up into the canard vortex.

Even for low angles of attack for which vortex breakdown is not present, a rather complicated structure of the flowfield on a canard configuration turned out. Apart from secondary separations and some mixing of the free vortex sheet with the upper surface boundary layer of the wing, the main characteristics of the flowfield on this sharp-edged configuration are dominated by nonviscous effects. Concerning comparisons with computational fluid dynamics important features of this flowfield should be described properly even by inviscid flow theories.

Similar experimental data for overall forces and moments, pressure distributions and surface oilflow patterns are also available for $\alpha = 14.7^\circ$ and $\alpha = 29.6^\circ$ [46], [47], but flowfield measurements exist only for one plane at the wing trailing-edge and $\alpha = 14.7^\circ$. These measurements could also be used for comparison with computational fluid dynamics, but in this case a theory should be used which is able to cover vortex breakdown properly. More flowfield measurements are not available since the disturbances from the probe influence the phenomenon of vortex breakdown considerably.

4.4 Test case

In conclusion the experimental data for the $A = 2.31$ delta canard configuration contain the following test case for comparison with results of computational fluid dynamics:

Test case 6: Delta canard configuration $A = 2.31$, flowfield at $\alpha \approx 8.8^\circ$, no vortex breakdown

Available data:	Model geometry
	Aerodynamic coefficients
	Pressure distribution
	Surface oilflow patterns
	Flowfield over and behind the wing
Reference :	H.-Chr. Oelker, D. Hummel [48]

5. INVESTIGATIONS ON CORNER CONFIGURATIONS IN HYPERSONIC FLOW

5.1 General properties of the flow

Hypersonic flight vehicles are subject to considerable thermal stress due to kinetic heating. High heat transfer rates are not restricted to the nose region and the wing leading-edges, but they occur similarly also in the junctions between wing and body as well as in rectangular air intakes.

Apart from various pressure distribution and heat transfer measurements at the wall of corner configurations the first investigations on the structure of the flowfield are due to A.F. Charwat, L.G. Redekopp [49] for the supersonic flow in a 90° -corner between two wedges. The general features of this type of flow are shown schematically in Fig. 24 for the case of a swept corner configuration. At supersonic free-stream velocity the flowfield can be divided in two parts: In the outer region inviscid flow is predominant. A shock system is formed which consists of the two wedge shocks, the connecting corner shock, two embedded shocks and two slip surfaces. Embedded shocks and slip surfaces are necessary in order to fulfil the shock relations in the vicinity of the two intersecting lines between the wedge shocks and the corner shock. The pressure distribution generated by this shock system has a strong influence on the formation of the viscous layer in the corner region. Due to the embedded shocks flow separations occur in the inward directed viscous flow, which leads to highly non-uniform distributions of static pressure and local heat transfer rate along the walls. In hypersonic flow the shock system is located close to the configuration and a strong interference between the boundary layer flow and the outer shock system takes place. Summaries of the existing knowledge on the three-dimensional flow separations in axial corners are due to R.H. Korkegi [50] and J.J. Peake, M. Tobak, R.H. Korkegi [51].

5.2 Survey of the experimental program at TU Braunschweig

At the Institut für Strömungsmechanik of TU Braunschweig a long-term program on according to Tab. 4 hypersonic flow in axial corners has been started in 1972. The first part of the investigations was concerned with symmetric corners between unswept wedges and wedge angle δ , corner angle θ and free-stream Machnumber M_∞ were varied systematically. For a large number of configurations pressure distributions and heat transfer measurements at the walls as well as pitot pressure measurements in the flowfield have been carried out. The flow at the walls has been visualized by means of an oil-dot technique and the resulting surface oilstreak patterns have been evaluated quantitatively to detect separation and reattachment lines. First results have been published by K. Kipke, D. Hummel [52]. It turned out that the shock system according to Fig. 24 leads to flow separation and to the formation of primary vortices close to the wall which are accompanied in some cases by secondary vortices. In the vicinity of the corner center very high static pressures and heat transfer rates have been found, but these high values could be reduced considerably by increasing the corner angle θ .

In the second part of the program the investigations have been extended to include also a systematic variation of the sweep angle ϕ for symmetric corners of intersecting wedges with different corner angles. These investigations are due to W. Möllenstädt [53], [54]. The results showed the dependence of the shock system and of the flow separations from the sweep angle ϕ . It turned out that the high values of static pressure and heat transfer rate in the corner center can be considerably reduced by sweeping the leading-edges of the wedges.

Almost all results from this experimental program which has been summarized by D. Hummel [55] may be used as test cases for computational fluid dynamics. Some typical results are shown subsequently and some guidelines for the use of this material are given.

5.3 Results

5.3.1 Windtunnel models [52], [53]

All corner configurations according to Fig. 24 were symmetrical with respect to the plane through the apex and the $(\theta/2)$ -line. The corner angles were $\theta = 60^\circ$, 90° and 120° , the wedge angles normal to the leading-edges $\delta = 6.3^\circ$, 8.0° and 10.0° , and the sweep angles of the leading-edges $\phi = -30^\circ$, 0° , 15° , 30° , 45° and 60° . The dimensions of all models were $l = 100$ mm in free-stream direction and $b = 50$ mm perpendicular to it.

The measurements have been performed in the gun tunnel of the Institut für Strömungsmechanik at TU Braunschweig [55]. The free-stream Machnumbers were $M_\infty = 12.3$ and 16.0 , corresponding to Reynoldsnumbers, based on model length l , of $Re_l = 5 \cdot 10^7$ and $Re_l = 1.7 \cdot 10^8$ and the stagnation pressure was 150 bar. Since a nearly conical flowfield was investigated, the pitot pressure and wall pressure measurements, the heat transfer investigations by means of the transient thin skin technique and the evaluation of the oil-dot streaks have been carried out in the plane $x/l = 0.9$ close to the rear end of the model.

5.3.2 Flowfield characteristics [52], [53]

General features of the flowfield in a 90° -corner may be taken from Fig. 25, which shows the results for a -30° (forward) swept configuration. The pitot pressure isobars in the measuring plane are drawn in Fig. 25a. Since the flowfield is symmetric with respect to the $(\theta/2)$ -line the upper part of the diagram shows the measurements and in the lower part the interpretation is given. In the corner region the system of wedge shock, corner shock, secondary or embedded shock and slip surface can be detected. The shocks are characterized by a steep increase of the pitot pressure, which is strongest for the corner shock. Behind the shocks pitot pressure plateaus at different levels are present. For the measured shock positions the strengths of all shocks can be calculated from the shock relations and the corresponding pitot pressure plateau values are in good agreement with the measured ones. The shocks interfere along the line between the wedge shock and the corner shock which is marked in the measuring plane by the triple point Tr . Due to the different pitot pressure levels on both sides the slip surface is also characterized by a pitot pressure jump. The slip surface divides the flow through the corner shock from that through the wedge shock which crosses also the embedded shock. On both sides of the slip surface the same static pressure is present, but different velocities tangential to the slip surface as well as different pitot pressures and therefore different values of the entropy exist. According to Crocco's theorem the slip surface is a vortex sheet. The slip surfaces from both sides tend to meet at the plane of symmetry. Therefore the flow through the corner shock does not reach the inner part of the corner flowfield. The flow behind the embedded shock and in front of the slip surface is not yet parallel to the wall. The corresponding changes in the flow direction towards the corner center is achieved by passing some expansion and compression regions as indicated in Fig. 25a. Finally in the corner center very high pitot pressures have been found, but the peak values in the hatched regions of the flowfield could not be determined due to limitations of the available pressure transducers.

Underneath the wedge shock a decrease of the pitot pressure towards the wall is observed. The onset of the pitot pressure reduction marks the outer edge of the boundary layer. In conical coordinates the flow within the boundary layer is directed inwards. At $Z = 0.1$ oval isobars show a relative pitot pressure minimum, which has been interpreted by K. Kipke, D. Hummel [52] as a total pressure loss due to a vortex in the viscous layer. The corresponding flow separation is caused by the pressure rise due to the embedded shock and it occurs already far upstream at S_1 and the corresponding reattachment line lies at R_1 .

The measured pressure distribution at the wall is shown in Fig. 25b. Its slope is similar to that in two-dimensional flow underneath a shock impinging on a boundary layer. The separation takes place at S_1 far upstream of the point of impingement (l : plateau) and increases downstream to the value at reattachment R_1 (2 : plateau). In the present situation this scheme is modified by the strong vortex in three-dimensional flow, which produces additional negative static pressures at the wall. Underneath the primary vortex a positive pressure gradient in φ -direction is present which leads to a secondary separation at S_2 and corresponding reattachment at R_2 .

The positions of separation and reattachment lines have been taken from oil flow streaks. A quantitative evaluation is shown in Fig. 25d. The angle φ between the wall streamlines and the conical direction is plotted against the coordinate φ . Positive values of φ indicate a flow towards the corner center whereas negative values belong to a flow directed outwards. The effect of the second wedge on the flow at the wall under consideration starts at the conical line A at $\varphi = 0.7$ which may be regarded as an influence of the second wedge shock which is located far more outwards than e. g. the second wedge shock. Fig. 25d indicates that the flow in the corner region converges at the separation lines S_1 and S_2 and diverges at the reattachment lines R_1 and R_2 . At these lines the flow follows the conical lines at $\varphi = 0$. Between S_1 and R_1 a primary vortex is formed and between S_2 and R_2 a smaller secondary vortex is present as sketched schematically in Fig. 25a. This kind of vortex formation is well known from delta wings with subsonic leading-edges, see e. g. D. Hummel [7]. Due to the strong primary vortex a large portion of the viscous layer finally moves outwards and does not reach the corner center. Correspondingly the viscous layer becomes very thin close to the corner center. This means that in the region of R_1 high energy inviscid

flow comes very close to the corner center and causes very high wall pressures and heat transfer rates there.

The measured heat transfer rates are plotted in Fig. 25c. It turns out that in the region of the reattachment line R_1 the heat transfer rate is 7 times as large as on an unswept wedge. A second, relative heat transfer maximum is found in the vicinity of the reattachment line R_2 of the secondary vortex.

5.4 Test cases

In the course of the experimental program a total of 22 flowfields have been measured in detail and 13 of them have been published [52], [53], [55]. They can be used as test cases for comparison with computational fluid dynamics:

Test case 7: Hypersonic flows in corners of unswept wedges at $M_\infty = 16$ for different wedge angles δ and corner angles θ .

Available data: Model geometry
Wall pressure distribution
Wall heat transfer distribution
Flow directions at the wall
Pitot pressure isobars in the flowfield
Reference: K. Kipke, D. Hummel [52]

Test case 8: Hypersonic flows in corners of swept wedges at $M_\infty = 12.3$ for different sweep angles ϕ and corner angles θ .

Available data: Model geometry
Wall pressure distribution
Wall heat transfer distribution
Flow directions at the wall
Pitot pressure isobars in the flowfield
References: W. Möllenstädt [53], [54]

6. CONCLUSIONS

From comprehensive experimental investigations on separated flows carried out at Institut für Strömungsmechanik of TU Braunschweig 8 test cases for computational fluid dynamics validation have been deduced. These are

Test case 1: Delta wing $A = 1.0$, flowfield at $\alpha = 20.5^\circ$, low speed.

Test case 2: Delta wing $A = 1.0$, laminar boundary layers at $\alpha = \pm 20.5^\circ$, low speed

Test case 3: Delta wing $A = 0.78$, velocity distribution in a vortex with vortex breakdown, low speed

Test case 4: Double-delta wing $A = 2.05$, flowfield at $\alpha = 10^\circ$, separate vortices, low speed

Test case 5: Double-delta wing $A = 2.05$, flowfield at $\alpha = 12^\circ$, merging vortices, low speed

Test case 6: Delta canard configuration $A = 2.31$, flowfield at $\alpha = 8.8^\circ$, no vortex breakdown, low speed

Test case 7: Hypersonic flows in corners of unswept wedges at $M_\infty = 16$ for different wedge angles δ and corner angles θ

Test case 8: Hypersonic flows in corners of swept wedges at $M_\infty = 12.3$ for different sweep angles ϕ and corner angles θ

For these test cases the main results are presented and a detailed documentation is provided on where and in which form these results are available.

6. REFERENCES

- [1] H. Winter: Strömungsvorgänge an Platten und profilierten Körpern bei kleinen Spannweiten. Forsch. Ing.-Tas. 6 (1935), 67-71.
- [2] D.J. Marsden, R.W. Simpson, W.J. Rainbird: The flow over delta wings at low speeds with leading-edge separation. College of Aeronautics, Cranfield, Rep. 114 (1958).
- [3] N.C. Lambourne, D.W. Bryer: Some measurements in the vortex flow generated by a sharp leading-edge having 65° sweep. ARC CP 477 (1959).
- [4] D.H. Peckham: Low speed wind-tunnel tests on a series of uncambered slender pointed wings with sharp edges. RAE Rep. Aero 2613 (1958), ARC Rep. Mem. 3186 (1961).

- [5] P.B. Earnshaw, J.A. Lawford: Low-speed wind-tunnel experiments on a series of sharp-edged delta wings. Part I: Forces, moments, normal force fluctuations and positions of vortex breakdown. RAE TN Aero 2780 (1961).
- [6] J.A. Lawford: Low-speed wind-tunnel experiments on a series of sharp-edged delta wings. Part II: Surface flow patterns and boundary layer transition measurements. RAE TN Aero 2954 (1964).
- [7] D. Hummel: On the vortex formation over a slender wing at large angles of incidence. AGARD-CP-247 (1978), 15-1 to 15-17.
- [8] D. Hummel: The vortex wake of a slender wing at large angle of attack. Proc. VIIth Intern. Sympos. 1979, Nat. Akad. Sci. Republ. Korea, 139-180.
- [9] D. Küchemann: Die aerodynamische Entwicklung von schlanken Flügeln für den Überschallflug. Jb. 1962 d. WGLR, 66-77.
- [10] J.H.B. Smith: A review of separation in steady, three-dimensional flow. AGARD-CP-168 (1975), 31-1 to 31-17.
- [11] D.J. Peake: Controlled and uncontrolled flow separation in three dimensions. NAE Aeron. Rep. LR-591 (1976).
- [12] D. Hummel: Untersuchungen über das Aufplatzen der Wirbel an schlanken Deltaflügeln. Z. Flugwiss. 13 (1965), 158-168.
- [13] D. Hummel, P.S. Srinivasan: Vortex breakdown effects on the low-speed aerodynamic characteristics of slender delta wings in symmetrical flow. J. Roy. Aeron. Soc. 71 (1967), 319-322.
- [14] D. Hummel, G. Redeker: Über den Einfluß des Aufplatzens der Wirbel auf die aerodynamischen Beiwerte von Deltaflügeln mit kleinem Seitenverhältnis beim Schiebflug. Jb. 1967 der WGLR, 232-240.
- [15] D. Hummel: Experimentelle Untersuchung der Strömung auf der Saugseite eines schlanken Deltaflügels. Z. Flugwiss. 13 (1965), 247-252.
- [16] D. Hummel: Zur Umströmung scharfkantiger schlanker Deltaflügel bei großen Anstellwinkeln. Z. Flugwiss. 15 (1967), 376-385.
- [17] J.H.B. Smith: Improved calculations of leading-edge separation from slender delta wings. Proc. Roy. Soc. Lond. A 306 (1968), 67-90. RAE Techn. Rep. 66070 (1966).
- [18] D. Küchemann: Entwicklungen in der Tragflügeltheorie. 11. Ludwig-Prandtl-Gedächtnis-Vorlesung. Jahrbuch 1967 der WGLR, 11-22.
- [19] D. Hummel: Experimentelle Untersuchung dreidimensionaler laminarer Grenzschichten an einem schlanken Deltaflügel. Z. Flugwiss. Weltraumforsch. 10 (1986), 133-145.
- [20] D. Hummel, G. Redeker: Experimentelle Bestimmung der gebundenen Wirbellinien sowie des Strömungsverlaufs in der Umgebung der Hinterkante eines schlanken Deltaflügels. Abhandlg. d. Braunschw. Wiss. Ges. 22 (1972), 273-290.
- [21] B.J. Elle, J.P. Jones: A note on the vorticity distribution on the surface of slender delta wings with leading-edge separation. J. Roy. Aero. Soc. 65 (1961), 195-198.
- [22] R.T. Jones: Properties of low-aspect-ratio pointed wings at speed below and above the speed of sound. NACA Rep. 835 (1946).
- [23] W.H. Wentz, M.C. McMahon: An experimental investigation of the flow fields about delta and double-delta wings at low speeds. NASA CR-521 (1966).
- [24] W.H. Wentz, M.C. McMahon: Further experimental investigations of delta and double-delta wings flow fields at low speeds. NASA CR-714 (1967).
- [25] W. Staudacher: Flügel mit kontrollierter Ablösung. DGLR-Vortrag 77-028 (1977).
- [26] J.E. Lamar, J.M. Luckring: Recent theoretical developments and experimental studies pertinent to vortex flow aerodynamics - with a view toward design. AGARD-CP-247 (1978), 24-1 to 24-31.
- [27] M.J. Liu, Z.Y. Lü, C.H. Qiu, W.H. Su, X.K. Gao, X.Y. Deng, S.W. Xiong: Flow patterns and aerodynamic characteristics of a wing-strake configuration. J. Aircraft 17 (1980), 332-338.
- [28] U. Brennenstuhl, D. Hummel: Untersuchungen über die Wirbelbildung an Flügeln mit geknickten Vorderkanten. Z. Flugwiss. Weltraumforsch. 5 (1981), 375-381.
- [29] U. Brennenstuhl, D. Hummel: Weitere Untersuchungen über die Wirbelbildung an Flügeln mit geknickten Vorderkanten. Z. Flugwiss. Weltraumforsch. 6 (1982), 239-247.
- [30] U. Brennenstuhl, D. Hummel: Untersuchungen über die Wirbelbildung an Flügeln mit geknickten Vorderkanten. Forschungsbericht BMVg-FBWT 82-3 (1982).
- [31] U. Brennenstuhl, D. Hummel: Vortex formation over double-delta wings. ICAS-Proceedings 1982, Vol. 2, 1133-1146.

- [32] H.W.M. Hoijmakers, W. Vaatstra, N.G. Verhaagen: Vortex flow over delta and double-delta wings. *J. Aircraft* 20 (1983), 825-832.
- [33] N.G. Verhaagen: An experimental investigation of the vortex flow over delta and double-delta wings at low speed. AGARD-CP-342 (1983), 7-1 to 7-16.
- [34] U. Brennenstuhl: Experimentelle und theoretische Untersuchungen über die Wirbelbildung an Doppeldeltaflügeln. Dissertation TU Braunschweig 1985.
- [35] M. Beukenberg, D. Hummel: Experimentelle Untersuchungen an Doppeldeltaflügeln bei unsymmetrischer Strömung. DGLR-Bericht 86-03 (1986), 146-171.
- [36] M. Beukenberg: Aerodynamische Untersuchungen an Doppeldeltaflügeln bei unsymmetrischer Strömung. Forschungsbericht BMVg-FBWT 87-2 (1987).
- [37] U. Brennenstuhl, D. Hummel: Experimentelle und theoretische Untersuchungen über die Wirbelbildung an Doppeldeltaflügeln. *Z. Flugwiss. Weltraumforsch.* 11 (1987), 37-49.
- [38] H. John, W. Kraus: High angle of attack characteristics of different fighter configurations. AGARD-CP-247 (1978), 2-1 to 2-12.
- [39] W. Kraus: Delta canard configuration at high angle of attack. *Z. Flugwiss. Weltraumforsch.* 7 (1983), 41-46.
- [40] H. Behrbohm: Basic low speed aerodynamics of the short-coupled canard configuration of small aspect ratio. SAAB TN 60 (1965).
- [41] B.B. Gloss, D.D. Miner: Flow visualization study of close-coupled canard-wing and strake-wing configurations. NASA TM X-75663 (1975).
- [42] J. Er-El, A. Seginer: Vortex trajectories and breakdown on wing-canard configurations. *J. Aircraft* 22 (1985), 641-648.
- [43] K. Hartmann: Force and pressure measurements including surface flow visualizations on a cropped delta wing. Proceedings Symposium "International Vortex Flow Experiment on Euler Code Validation", Stockholm 1986, 63-87.
- [44] L. Hjelmerberg: Test on a 55° and 65° delta wing at FFA. Proceedings Symposium "International Vortex Flow Experiment on Euler Code Validation", Stockholm 1986, 89-106.
- [45] K.A. Bütefisch, D. Pallek, J. Reichmuth: Flow field study on a 65° delta wing. Proceedings Symposium "International Vortex Flow Experiment on Euler Code Validation", Stockholm 1986, 107-115.
- [46] D. Hummel, H.-Chr. Oelker: Vortex interference effects on close-coupled canard configurations in incompressible flow. Proceedings Symposium "International Vortex Flow Experiment on Euler Code Validation", Stockholm 1986, 47-61.
- [47] H.-Chr. Oelker, D. Hummel: Experimentelle Untersuchungen an Entenkonfigurationen. DGLR-Bericht 86-03 (1986), 172-191.
- [48] H.-Chr. Oelker, D. Hummel: Investigations on the vorticity sheet of a close-coupled delta-canard configuration. ICAS-Proceedings 1988 (Paper 3.11 R1, to be published).
- [49] A.F. Charwat, L.G. Redekopp: Supersonic interference flow along the corner of intersecting wedges. *AIAA J.* 5 (1967), 480-488.
- [50] R.H. Korkegi: On the structure of three-dimensional shock-induced separated flow regions. *AIAA J.* 14 (1976), 597-600.
- [51] D.J. Peake, M. Tobak, R.H. Korkegi: Three-dimensional interactions and vortical flows with emphasis on high speeds. AGARDograph 252 (1980).
- [52] K. Kipke, D. Hummel: Untersuchungen an längsangeströmten Eckenkonfigurationen im Hyperschallbereich. Teil I: Ecken zwischen ungepfeilten Keilen. *Z. Flugwiss.* 23 (1975), 417-429.
- [53] W. Möllenstädt: Experimentelle Untersuchungen an längsangeströmten Eckenkonfigurationen im Hyperschallbereich. Dissertation TU Braunschweig 1984.
- [54] W. Möllenstädt: Untersuchungen an längsangeströmten Eckenkonfigurationen im Hyperschallbereich. Teil II: Ecken zwischen gepfeilten Keilen. *Z. Flugwiss. Weltraumforsch.* 8 (1984), 405-414.
- [55] D. Hummel: Experimental investigations on blunt bodies and corner configurations in hypersonic flow. AGARD-CP-428 (1987), 6-1 to 6-16.

Tab. 1: Survey of experimental investigations on delta wing $A = 1.0$

Data	$\alpha[^\circ]$	$\beta[^\circ]$	Re	Remarks	References
6-component measurements	0 to 29.4 14.7 to 23.5	-30 to +30 0 to 30	$2 \cdot 10^6$ $2 \cdot 10^6$		[12] [14]
3-component measurements	-10 to +42	0	$(0.9-2.0) \cdot 10^6$		[7],[8],[13],[19]
breakdown position	24 to 42 17 to 42	0 -10 to 30	$2 \cdot 10^6$ $2 \cdot 10^6$		[13] [14]
pressure distribution measurements	20.5 20.5 26.4 26.4 33.0	0 0 5, 15 0 to 30 0	$9 \cdot 10^5$ - $2 \cdot 10^6$ $2 \cdot 10^6$ $9 \cdot 10^5$	laminar artificially turbulent	[7],[8],[16],[19] [7],[8],[20] [12] [15] [16]
boundary layer measurements	20.5	0	$9 \cdot 10^5$	upper and lower surface, laminar	[19]
surface oilflow patterns	20.5 20.5 26.4 26.4	0 0 0 0 to 30	$9 \cdot 10^5$ - $(0.9-2.0) \cdot 10^6$ $2 \cdot 10^6$	laminar artificially turbulent	[7],[8],[16],[19] [7],[8],[20] [15] [15]
bound vortex lines	20.5 20.5	0 0	$9 \cdot 10^5$ -	laminar artificially turbulent	[7],[8],[16] [7],[8],[20]
Flowfield measurements	20.5	0	$2 \cdot 10^6$	4 planes	[7], [8]

Tab. 2: Survey of experimental investigations on double-delta wing $A = 2.05$

Data	$\alpha[^\circ]$	$\beta[^\circ]$	Re	Model	References
6-component measurements	-6 to 40	-5 to 30	$1.3 \cdot 10^6$	A	[35],[36]
3-component measurements	-6 to 40	0	$1.3 \cdot 10^6$	A	[28],[30],[31],[34]
breakdown position	-6 to 40 -6 to 40	-5 to 30 0	$1.3 \cdot 10^6$ $1.3 \cdot 10^6$	A A	[35],[36] [28],[29],[30],[31], [34]
pressure distributions	12 to 30 10 to 30 10 to 30 7, 11	0 0 0 to 20 0	$1.3 \cdot 10^6$ $1.3 \cdot 10^6$ $1.3 \cdot 10^6$ $4.0 \cdot 10^6$	A, 1 section A, 5 sections A, 2 sections B, 5 sections	[28],[30],[31],[34] [34],[37] [35],[36] [34],[37]
surface oilflow patterns	10 to 32 10 to 30 26 7, 11	0 to 20 0 0 to 20 0	$1.3 \cdot 10^6$ $1.3 \cdot 10^6$ $1.3 \cdot 10^6$ $4.0 \cdot 10^6$	A A A B	[36] [28],[29],[30],[31], [34],[35] [35] [34]
Flowfield measurements	10 12 12 10 7 11 10	0 0 0 0 0 0 10, 20	$1.3 \cdot 10^6$ $1.3 \cdot 10^6$ $1.3 \cdot 10^6$ $1.3 \cdot 10^6$ $4.0 \cdot 10^6$ $4.0 \cdot 10^6$ $1.3 \cdot 10^6$	A, 1 plane A, 1 plane A, 4 planes A, 3 planes B, 3 planes B, 2 planes A, 3 planes	[28],[29],[31] [29] [31],[34] [34] [34] [34] [35],[36]

Tab. 3: Survey of experimental investigations on A = 2.31 canard-wing configuration

Data	$\alpha [^\circ]$	$\beta [^\circ]$	Re	Remarks	References
3-component measurements	0 to 40	0	$1.0 \cdot 10^6$	canard off and on	[46],[47]
pressure distribution measurements	8.8 14.7 29.6	0	$1.4 \cdot 10^6$	canard off and on	[46],[47]
surface oilflow patterns	8.8 14.7 29.6	0	$1.4 \cdot 10^6$	canard off and on	[46],[47]
Flowfield visualization	8.8 19.6	0	$7.0 \cdot 10^3$		[46],[47]
Flowfield measurements	8.8 8.8 14.7	0	$1.4 \cdot 10^6$	1 plane 5 planes 1 plane	[46],[47] [48] [46],[47]

Tab.4: Test program for the measurements in corner configurations

Part I: Corners between
unswept wedges
(K. Kipke, D. Hummel [52])

M_∞	12.3		16.0	
δ	6.3°	8.0°	6.3°	10.0°
θ	60°	90°	120°	150°

Part II: Corners between swept
wedges (W. Möllenstädt [54])

M_∞	12.3					
δ	8.0°					
ϕ	-30°	0°	15°	30°	45°	60°
θ	60°	90°	120°	150°	180°	210°

○ heat flux, oil flow pictures

● pitot pressure (flow field), wall pressure, heat flux, oil flow pictures

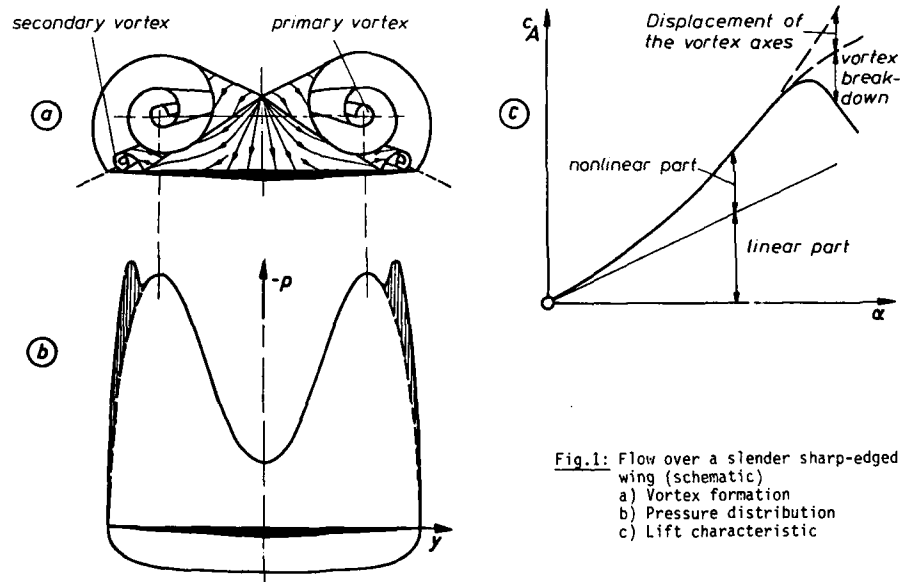


Fig.1: Flow over a slender sharp-edged wing (schematic)
a) Vortex formation
b) Pressure distribution
c) Lift characteristic

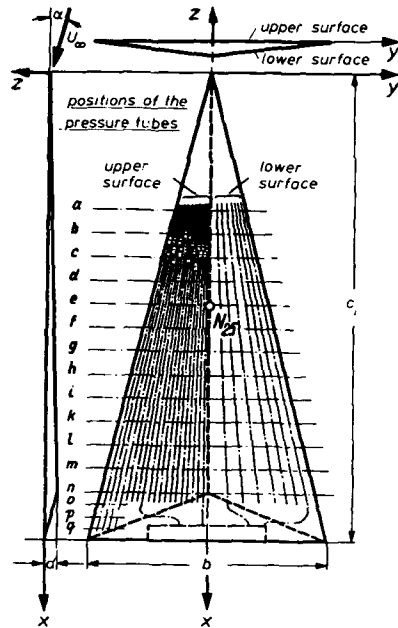


Fig. 2: Windtunnel model of delta wing $A = 1.0$
a : q Cross sections for pressure distribution measurements

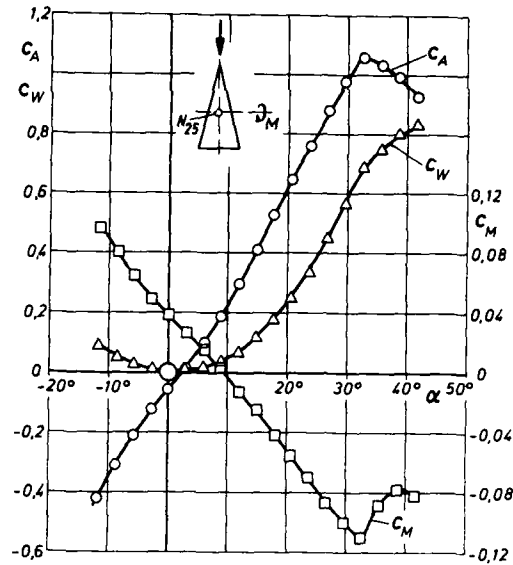


Fig. 3: Results of the three-component measurements on delta wing $A = 1.0$, valid for $6 \cdot 10^5 \leq Re \leq 2 \cdot 10^6$

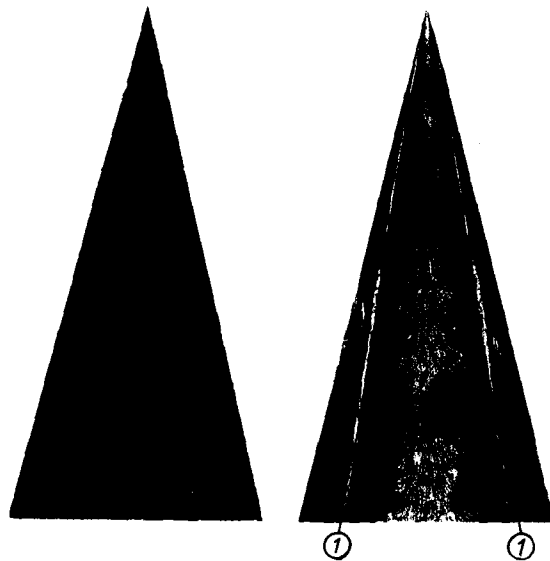


Fig. 4: Oilflow patterns on delta wing $A = 1.0$ at $Re = 9 \cdot 10^5$
(laminar boundary layers)
a) $\alpha = -20.5^\circ$ (flat surface = pressure side)
b) $\alpha = +20.5^\circ$ (flat surface = suction side)
① secondary separation line

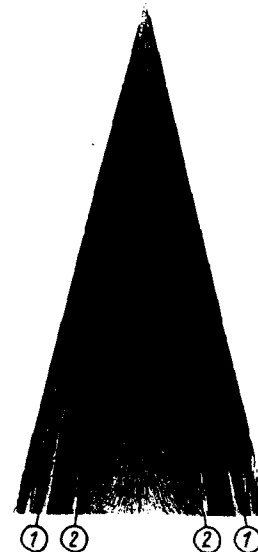


Fig. 5: Oilflow pattern at the upper surface of the $A = 1.0$ delta wing at $\alpha = 20.5^\circ$, artificially turbulent boundary layers
① secondary separation line
② turbulence generators

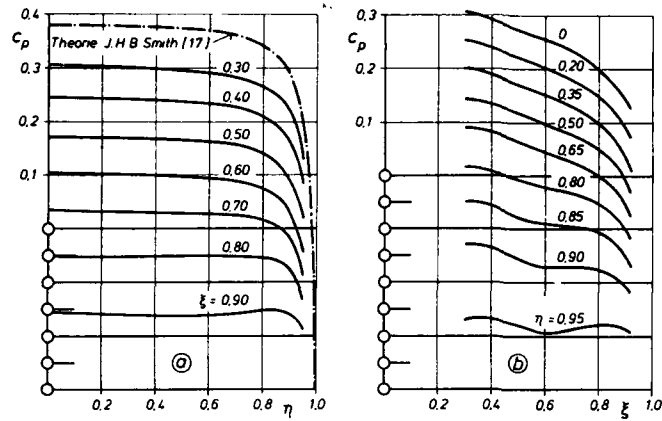


Fig.6: Measured pressure distribution on delta wing $A = 1.0$ at $\alpha = -20.5^\circ$ (flat surface = pressure side) and $Re = 9 \cdot 10^5$
 a) in cross-sections $\xi = \text{const.}$
 b) on rays $\eta = \text{const.}$

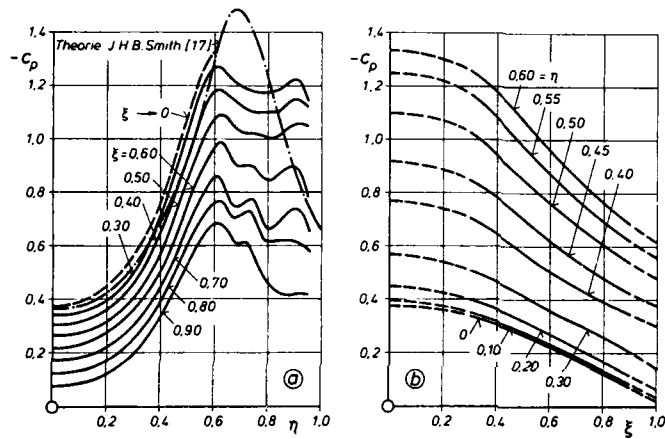


Fig.7: Measured pressure distribution on delta wing $A = 1.0$ at $\alpha = 20.5^\circ$ (flat surface = suction side) and $Re = 9 \cdot 10^5$
 a) in cross-sections $\xi = \text{const.}$
 b) on rays $\eta = \text{const.}$

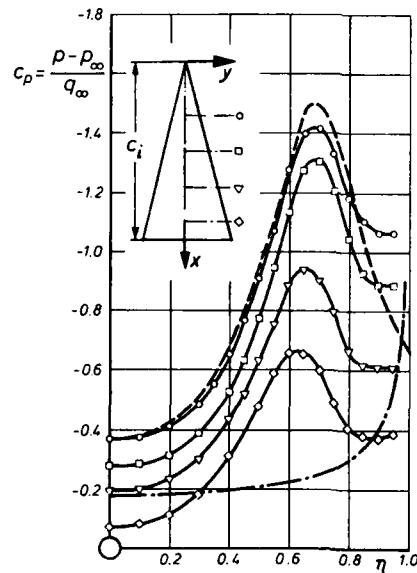


Fig.8: Pressure distribution on delta wing $A = 1.0$ at $\alpha = 20.5^\circ$ (flat surface = suction side), boundary layer: turbulent
 Experiments:

ξ	0.3	0.5	0.7	0.9
Symbol	\circ	\square	∇	\diamond

Theories: ——— J.H.B.Smith [17]
 — · — R.T.Jones [22]

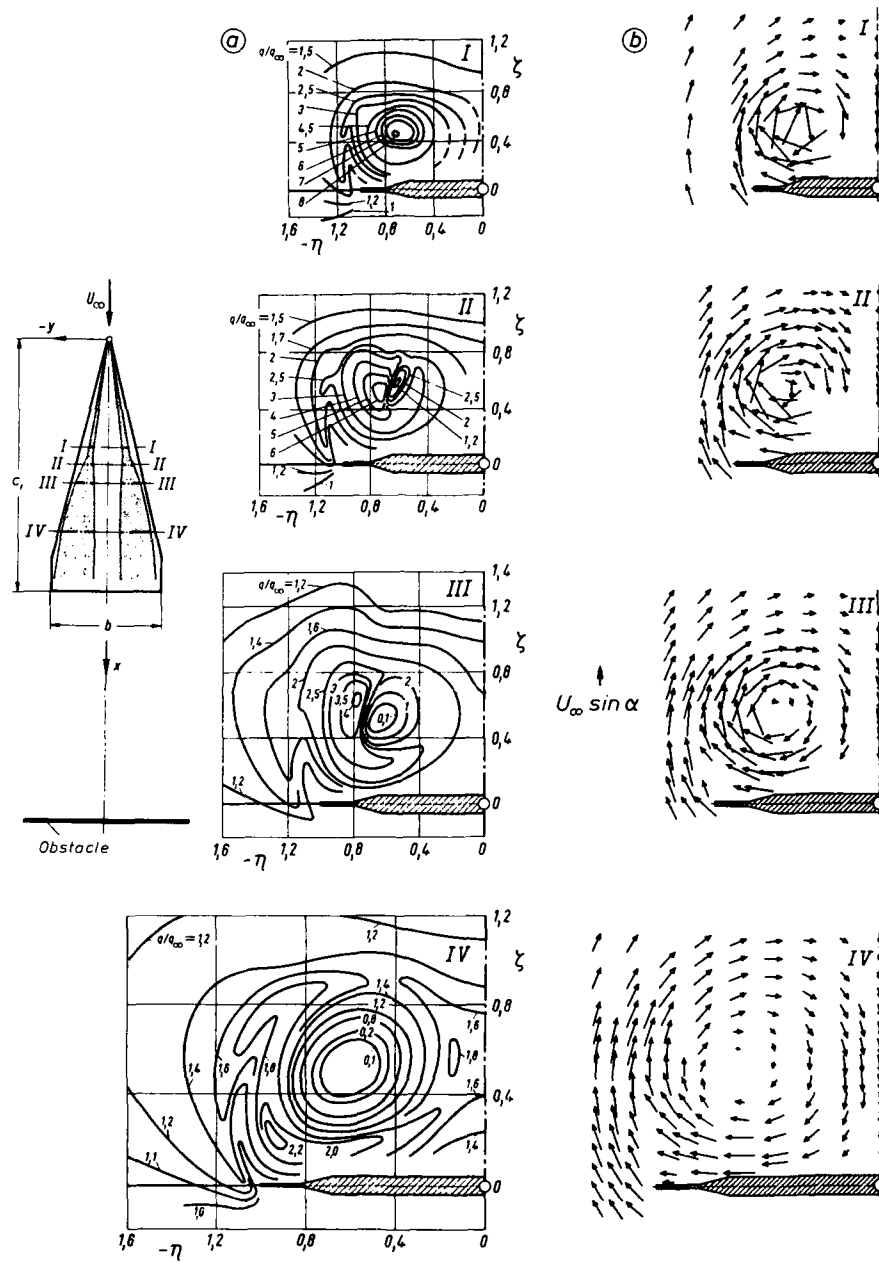
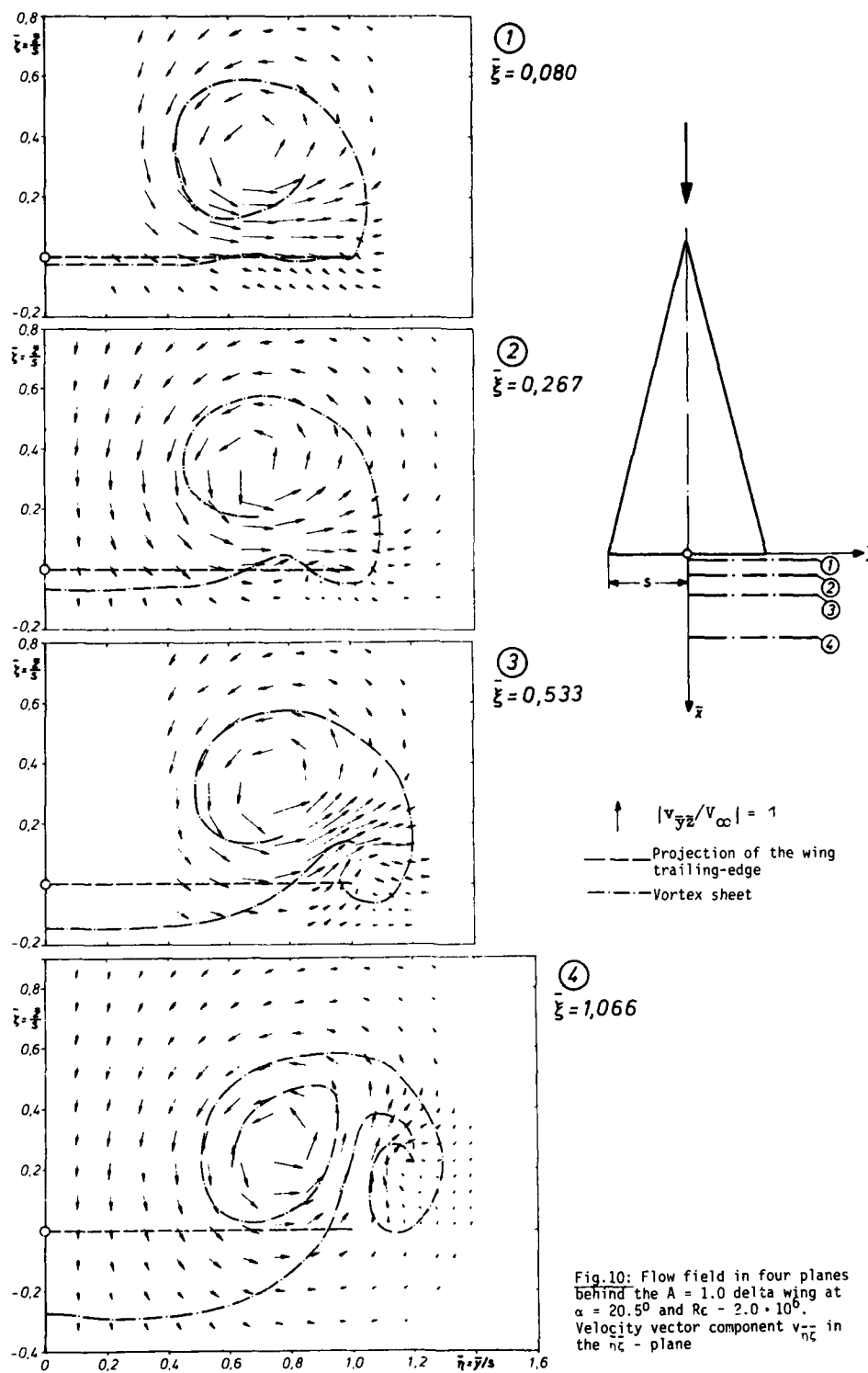
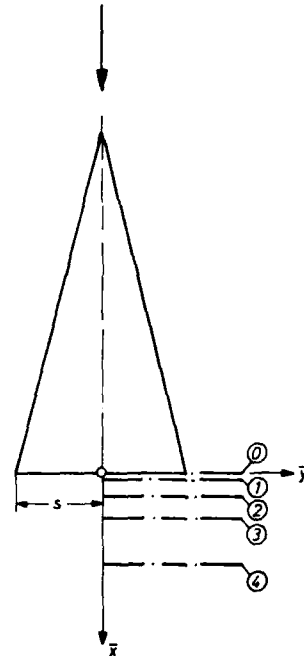
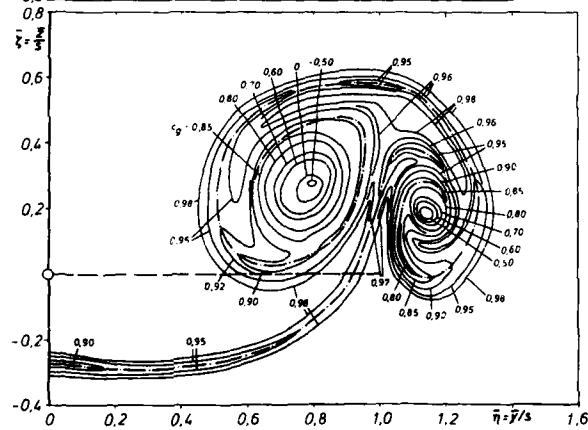
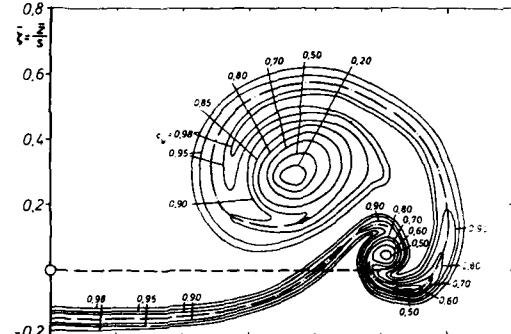
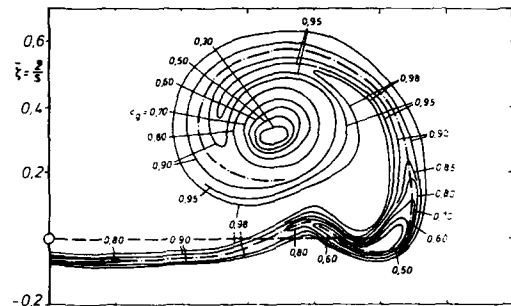
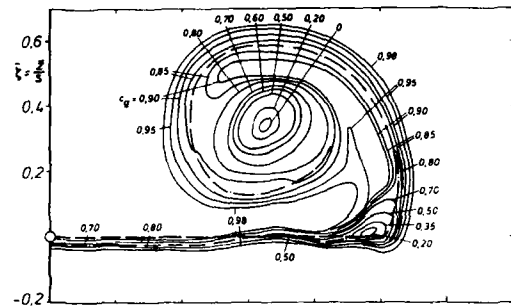
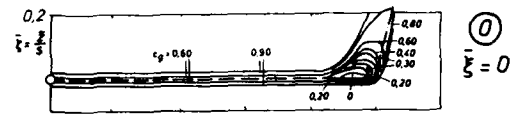


Fig.11: Flow in a vortex with vortex breakdown measured in four planes
 (I : $\xi = 0.425$, II : $\xi = 0.491$, III : $\xi = 0.566$, IV : $\xi = 0.761$) over
 an $A = 0.78$ cropped delta wing at $\alpha = 31^\circ$ with an obstacle behind the wing.
 a) Lines of constant dynamic pressure, $q / q_\infty = \text{const.}$
 b) Velocity component parallel to the measuring planes





--- Projection of the wing trailing-edge
 --- Vortex sheet

Fig.9: Distribution of total pressure in five planes behind the $A = 1.0$ delta wing at $\alpha = 20.5^\circ$ and $Re = 2.0 \cdot 10^6$. Lines $c_g = (g - p_\infty) / q_\infty = \text{const.}$

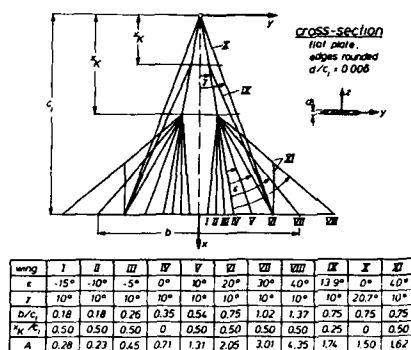
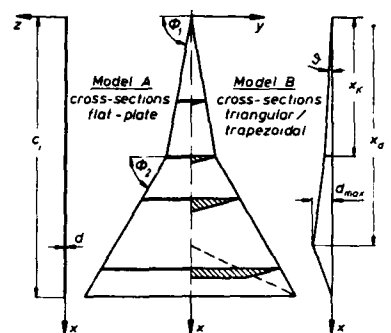
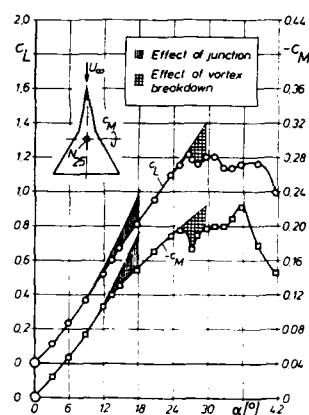
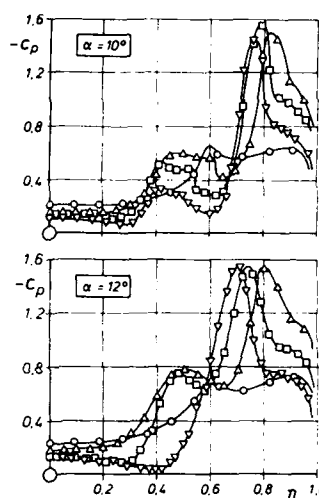
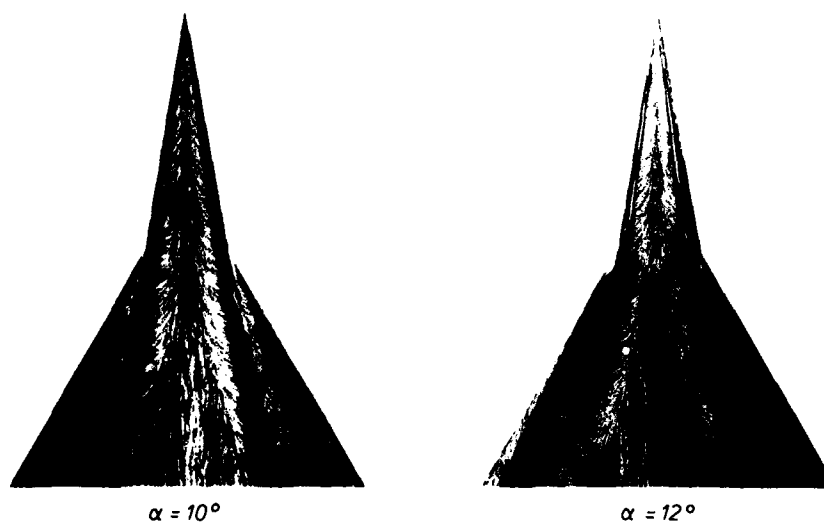


Fig.12: Series of wings with kinked leading-edges

Fig.13: Windtunnel models of double-delta wing $A = 2.05$ Fig.14: Results of the three-component measurements on double-delta wing $A = 2.05$ (model A) at $Re = 1.3 \cdot 10^6$ Fig.15: Pressure distribution on the suction side of double-delta wing $A = 2.05$ (model A)

ϵ	0.500	0.625	0.750	0.875
Symbol	○	△	□	▽

Fig. 16: Oilflow patterns on double-delta wing $A = 2.05$ at $Re = 1.3 \cdot 10^6$

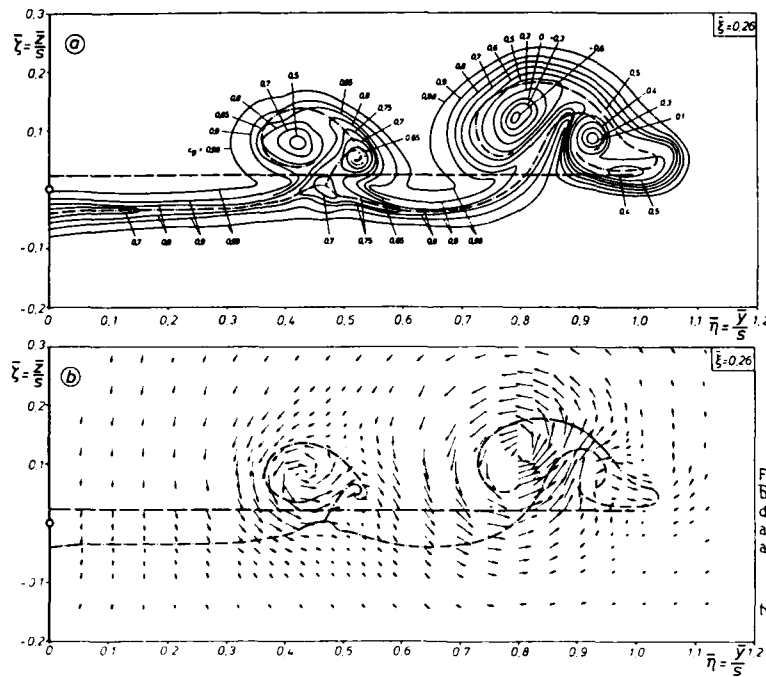


Fig.17: Vortex formation behind the $A = 2.05$ double-delta wing in plane $\xi = 0.26$ at $\alpha = 10^\circ$

a) Lines of constant total pressure coefficient $c_g = (g - p_\infty) / q_\infty = \text{const.}$

b) Velocity vector component $v_{n\xi}$ in the $n\xi$ -plane

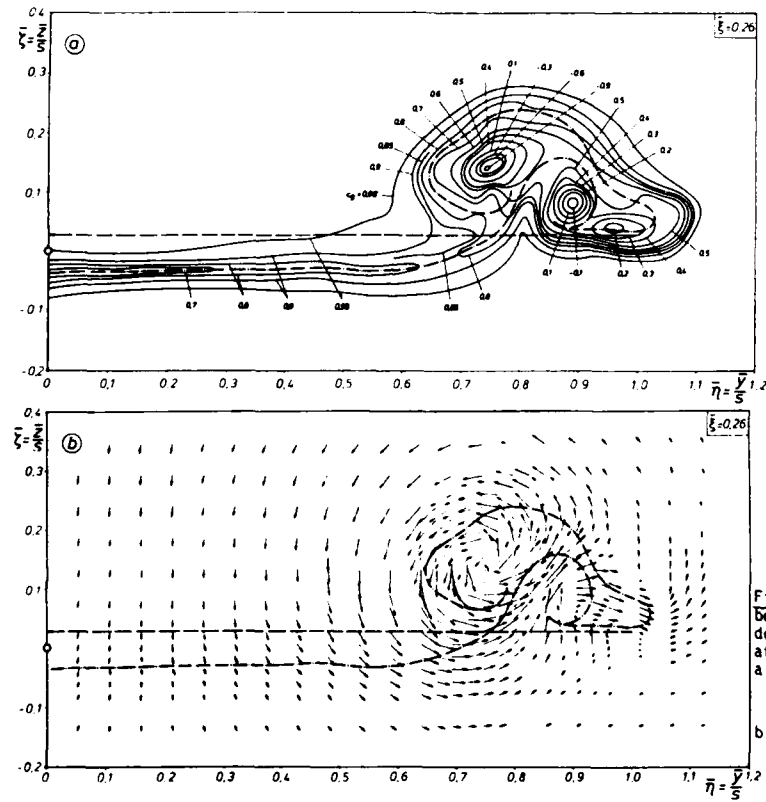


Fig.18: Vortex formation behind the $A = 2.05$ double-delta wing in plane $\xi = 0.26$ at $\alpha = 12^\circ$

a) Lines of constant total pressure coefficient $c_g = (g - p_\infty) / q_\infty = \text{const.}$

b) Velocity vector component $v_{n\xi}$ in the $n\xi$ -plane

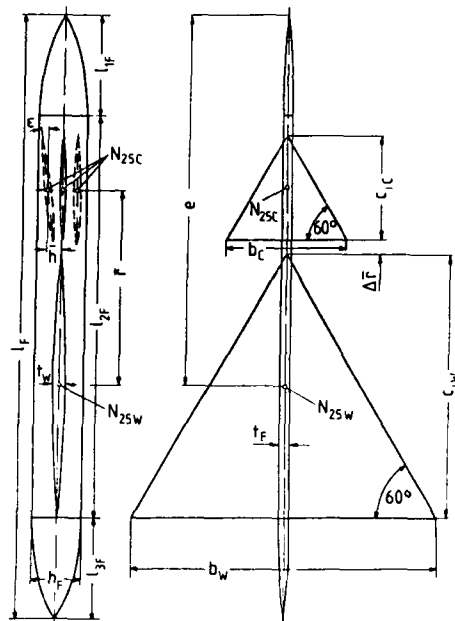


Fig. 19: Canard-wing-fuselage configuration A = 2.31

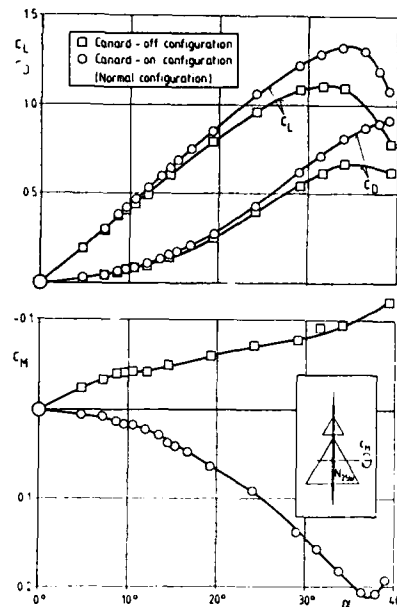


Fig. 20: Results of the three-component measurements for canard-off and canard-on normal configuration at $Re = 10^6$

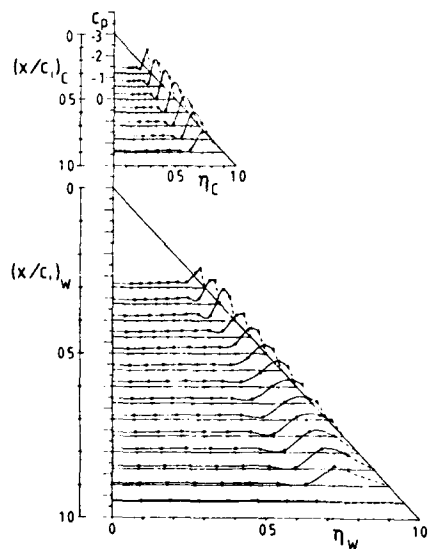


Fig. 21: Upper surface pressure distribution at $\alpha = 8.80$ and $Re = 1.4 \cdot 10^6$ on canard-on configuration A = 2.31

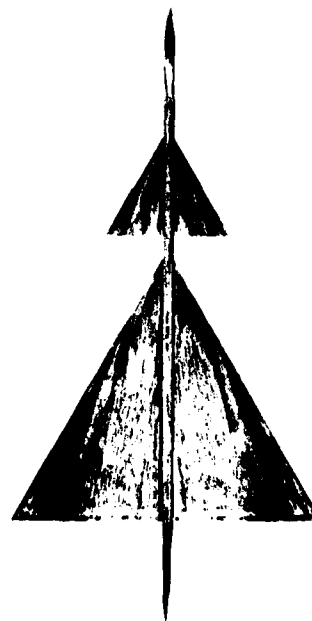


Fig. 22: Upper surface oilflow pattern at $\alpha = 8.80$ and $Re = 1.4 \cdot 10^6$ on canard-on configuration A = 2.31

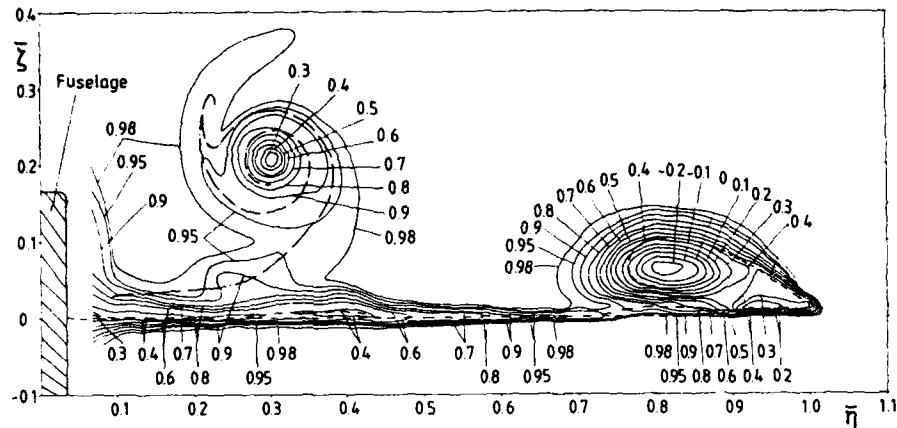


Fig. 23: Total pressure contours $c_q = (q - p_w) / q_\infty = \text{const.}$ behind the $A = 2.31$ delta canard configuration in the plane $\bar{z} = 0.02$ for $\alpha = 8.8^\circ$ and $Re = 1.4 \cdot 10^6$

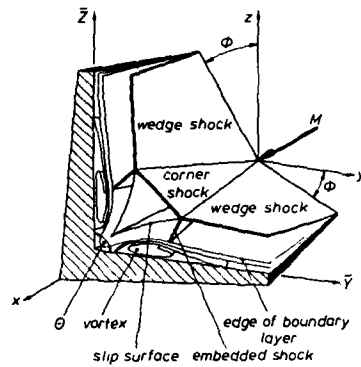


Fig. 24: Schematic view of the hypersonic flow in a swept corner configuration

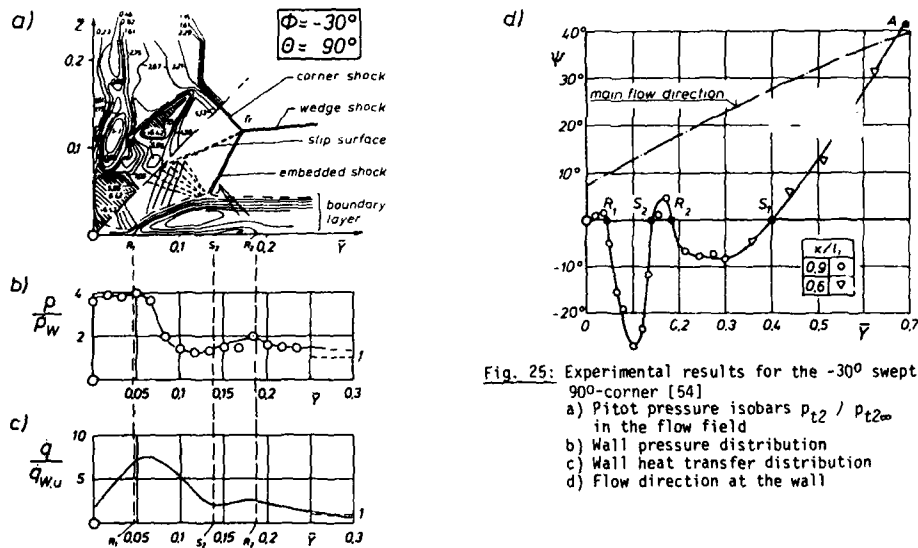


Fig. 25: Experimental results for the -30° swept 90° -corner [54]
a) Pitot pressure isobars $p_{t2} / p_{t2\infty}$ in the flow field
b) Wall pressure distribution
c) Wall heat transfer distribution
d) Flow direction at the wall

Overview of CFD Methods and Comparisons with Flight Aerothermal Data

Kenneth Sutton*, Ernest V. Zoby**, H. Harris Hamilton†
NASA Langley Research Center
Hampton, Virginia 23665-5225
U.S.A.

ABSTRACT

An overview of previously published aerothermal investigations which demonstrate the capabilities of detailed computational fluid dynamics and engineering codes to predict the aerothermal environment about an entry vehicle is presented. The overview consists of a brief discussion of the computational methods and experimental data and includes comparisons between the computed results and data. The overview focuses primarily on analyses of flight data since these data provide the unique capability to assess the real-gas chemistry options in the codes. The computed results are based on a series of codes which are employed by the Aerothermodynamics Branch of the Space Systems Division at the NASA Langley Research Center. The flight data, which were measured on the Reentry F, the Space Shuttle, and the Fire II vehicles, represent a wide range of vehicle configurations and freestream conditions. Also, results of one recent set of ground tests are included since the tests provide data on a model of a pending flight project. The comparisons of the predicted results and data demonstrate the adequacy of the present CFD capabilities and indicate the potential to predict the aerothermal environment about future flight vehicles.

INTRODUCTION

Recent interest in hypersonic vehicles has increased the need for verification and application of computational flowfield techniques in many areas. These prediction techniques are useful for design studies, and they can aid in developing improved methodology for extrapolating wind-tunnel data to flight conditions. Obviously, before any method can be used with confidence, it must be verified as accurately as possible. This is especially true if future mission goals are so demanding that excessive conservatism applied to computational predictions (or experimental data) will inhibit the successful design of these vehicles.

The present paper addresses the verification and application of aerothermal prediction techniques which may be useful in such design studies. One purpose of this paper is to provide an overview of the numerical capabilities and the applicability of a series of computer codes employed by the Aerothermodynamics Branch of the Space Systems Division at the NASA Langley Research Center. These codes, such as a Direct Simulation Monte Carlo method,¹ Navier-Stokes methods,² subsets of the Navier-Stokes equations,³⁻⁵ and engineering methods,^{6,7} have been used to define the flowfield and aeroheating environment over a range of freestream conditions for flight and ground-test configurations. The detailed computational fluid dynamics (CFD) methods are useful also in studies of generic body shapes and provide detailed information such as surface heat-transfer and pressure distributions, force-and-moment values, and shock-layer properties. In general terms, the engineering programs employ various levels of approximation in determining surface pressure, heat-transfer, and real-gas effects. They are typically used for conceptual design because they can be run quickly, and they can be used for extensive parametric studies. Another purpose of this paper is to present a summary of available flight data sources for future reference by the aerospace community and to illustrate the type, quality and extent of these data.

The applicability of the CFD codes has been demonstrated in previous investigations, e.g., Refs. 8-11, by comparisons of the predicted results with flight and ground-test data and with predicted results of other codes. This paper presents an overview of an extensive number of such investigations. The comparisons present a sound approach for code verification and in addition provide the opportunity to assess potential errors or problems associated with the codes.

COMPUTATIONAL METHODS

The codes used by the Aerothermodynamics Branch of the Space Systems Division at the NASA Langley Research Center for flowfield studies are reviewed in this section. One of the functions of this branch is to develop detailed codes which can be used to study various technology areas, such as turbulent flow, radiation, reacting chemistry, low density, and vehicle geometry effects, on the aerothermal environment about an entry vehicle and to assess the effect of these technology areas for various missions. In addition, engineering codes which are based on various levels of approximation are developed to assist researchers in conceptual design and parametric studies of proposed missions. We will briefly describe the engineering and detailed codes used in the present paper.

ENGINEERING CODES

MINIVER: The MINIVER program¹² is a simple engineering code that can be easily used in computer-aided design systems such as AVID.¹³ The code provides a menu for the user to select methods to compute post-shock and local flow properties as well as heating rates. The stagnation-point heating is computed with

*Head, Aerothermodynamics Branch, Space Systems Division.

**Aero-Space Technologist, Aerothermodynamics Branch, Space Systems Division.

†Research Leader, Aerothermodynamics Branch, Space Systems Division.

the Fay-Riddell¹⁴ method; the local laminar values are computed by the Blasius¹⁵ skin-friction method with Eckert reference enthalpy¹⁶ to account for compressibility effects and a modified Reynolds analogy; and the turbulent heating levels can be computed by the Schultz-Grunow¹⁷ skin-friction technique with reference enthalpy and a Reynolds analogy or with the Spalding-Chi¹⁸ skin-friction method and a Reynolds analogy. In addition, several boundary-layer transition criteria are provided. The calculations can be based on perfect gas or equilibrium air chemistry. Angle-of-attack effects are simulated by a tangent-cone or an approximate cross-flow option, and the flow can be computed for two- or three-dimensional surfaces. However, the three-dimensional effects are available only through use of the Mangler transformation (laminar or turbulent) for flat plate to sharp cone conditions. The code does not provide any method to account for the pressure overexpansion or variable-entropy effects on heat transfer along blunted vehicles.

INCHES: The INCHES code⁶ is an approximate combined inviscid and boundary-layer method that was initially developed for engineering calculations of inviscid radiative and convective heating rates for planetary missions. The code uses a modified Maslen technique¹⁹ and computes the axisymmetric zero degree angle-of-attack flowfield over paraboloids, ellipsoids, hyperboloids, and sphere-cones. Variable entropy can be included by using local inviscid properties located a boundary-layer thickness away from the body surface. The code uses the Cohen stagnation-point heating method and Blasius skin-friction coefficient based on momentum thickness with Eckert reference enthalpy and a modified Reynolds analogy to compute local laminar heating. The turbulent heating equation also employs a skin-friction expression based on a momentum thickness. A velocity profile, typically given by the one-seventh power profile, is assumed to compute the required exponents and constants in the skin-friction relation. However, the power-law velocity profile has been shown to be a function of the momentum-thickness Reynolds number. This dependence has been incorporated in the INCHES turbulent heating method. The study of Ref. 6 incorporated angle-of-attack effects (crossflow) based on the DeJarnette and Davis²⁰ method in the heating calculations over the windward and leeward symmetry planes of sphere-cones. At angle of attack, the inviscid shock shape and flowfield are computed based on the equivalent cone value. With the available experimental data, the comparisons of predicted results and data were good. However, a recent investigation⁸ has shown that this technique for accounting for angle-of-attack effects on the laminar heat transfer is not satisfactory for slender blunted cones at small angles of attack, e.g., a 5° cone at 3° angle of attack.

LISC: An approximate method²¹ has been developed for predicting laminar and turbulent heating rates on the windward side of the Space Shuttle Orbiter. The method is based on a "local infinite swept cylinder" (LISC) analysis and includes both equilibrium-air chemistry, variable boundary-layer-edge entropy, and lateral velocity-gradient correlations. The three-dimensional, compressible turbulent boundary-layer equations are solved in terms of time-average mean flow quantities. Following an infinite swept cylinder analysis,²² the flow direction derivatives are assumed to be smaller than the normal or the lateral derivatives and thus can be neglected. Further, if surface curvature effects are neglected, the boundary-layer equations describing the flow at an axial station can be solved along a given cross section independent of other cross sections. The surface pressure at any point along the windward-symmetry plane of the Shuttle Orbiter is calculated using a tangent-cone approximation where the half angle of the cone is equal to the local-flow-deflection angle (i.e., the local-body-deflection angle plus the angle of attack). The real-gas, axisymmetric, flowfield solution over a cone is obtained using a time-asymptotic, numerical procedure with equilibrium thermodynamic properties.²³

DETAILED METHODS

Direct Simulation Monte Carlo

In the Direct Simulation Monte Carlo (DSMC) method, the intermolecular collisions are considered on a probabilistic rather than a deterministic basis. Furthermore, the real gas is modeled by thousands of simulated molecules. The velocity components, internal states, and position coordinates of these molecules are stored and are modified with time as the molecules are concurrently followed through representative collisions and boundary interactions in simulated physical space. The time parameter in the simulation may be identified with physical time in the real flow, and all calculations are unsteady. When the boundary conditions are such that the flow is steady, then the solution is the asymptotic limit of the unsteady flow. The computation is always started from an initial state that permits an exact specification such as a vacuum or uniform equilibrium flow. A discussion of the "variable hard sphere" (VHS) molecular model, the recommended model for the simulation of gases in an engineering context, is given in Ref. 24. Of particular relevance is the discussion of the models that account for internal energy effects and chemical reactions.

Navier-Stokes

SLNS: The steady Navier-Stokes (NS) equations are solved² along the stagnation streamline of a blunt axisymmetric body by integrating a set of coupled nonlinear ordinary differential equations with respect to distance normal to the body. Solution to the nonlinear algebraic equations resulting from a finite-difference approximation of differential equations is obtained by a numerical method known as the successive accelerated replacement method. In this method, the corrections applied to the unknown variable at each of the mesh points are controlled by an acceleration factor which prevents the iteration scheme from diverging. The name successive replacement for the method comes from the fact that new values are used as soon as they are obtained. The method employs an eleven-species kinetics model for air with a wall of arbitrary catalyticity. The thermodynamics and transport properties for air are employed to temperatures of 30,000 K. The flowfield equations are coupled²⁵ to an equilibrium radiation

model, and an approximate electron energy equation is used for the electron temperature. Solutions obtained with this method include surface slip boundary conditions.

LAURA: Program LAURA²⁶ (Langley Aerothermodynamics Upwind Relaxation Algorithm) is used to solve the fully coupled set of governing equations using a finite-volume, symmetric-total-variation-diminishing scheme. The equation set includes the Navier-Stokes equations, eleven-species continuity equations, a total energy conservation equation, and a vibrational/electronic energy conservation equation. The translational and rotational energy modes are assumed to be in equilibrium at temperature T , and the vibrational and electronic modes are in equilibrium at temperature T_v . Flow simulations using the two-temperature model have been implemented for the forebody alone and for the complete flow including the near wake for the Aeroassist Flight Experiment (AFE) configuration (Fig. 1). A two-dimensional or axisymmetric flow option has been added to enable relatively quick parametric studies of the various kinetic and relaxation models available in the code. Two different kinetic models are available as well as some options for defining the mechanisms for vibrational energy relaxation.

Viscous-Shock-Layer

The Viscous-Shock-Layer (VSL) method has been widely used during the last decade for numerical solutions of hypersonic flows over a range of body shapes and freestream conditions. Because of the simplicity of the technique, many physical models have been incorporated into VSL codes for further in-depth study of detailed flowfield calculations. The VSL method has been applied to planetary entry bodies with massive ablation and radiation,²⁷ to slender vehicles with transitional and turbulent flow,²⁸ and to complex reentry vehicles with nonequilibrium chemistry.^{9,29} The VSL approach has received much attention because of the computational advantages it offers. The VSL equations are obtained from the Navier-Stokes equations by retaining terms through the shock layer up to second order in the inverse square root of the Reynolds number. Parabolic approximations are made in both the streamwise and crossflow directions, and the equations can be solved by marching techniques which are efficient in terms of computer time and storage requirements. The VSL method is easier to apply than a matched boundary-layer and inviscid method since no coupling problem exists between inviscid and viscous regions. The equations are limited, however, to attached flow in both the streamwise and crossflow directions, unlike some higher approximations.

A three-dimensional viscous-shock-layer code was developed³⁰ in a nonorthogonal coordinate system which allowed the analysis of nonaxisymmetric bodies and was extended to include equilibrium air and turbulent flow models. Subsequent study indicated the need for modifications and corrections, and the resulting version has been redesignated as VSL84.⁴ A nonequilibrium version (SHTNEQ) of the code was developed³¹ and also was subsequently modified.³¹

Inviscid

The methodology and structure of the HALIS (High Alpha Inviscid Solution) code are presented in detail in Ref. 32. Briefly, the code is a time-asymptotic solution of the Euler equations which utilizes an unsplit MacCormack differencing scheme. The solution space is the volume between the body surface and the bow-shock wave which is treated as a time-dependent boundary condition. This leads to a coordinate system defined by the position of the bow shock and body as well as the spatial derivatives along these surfaces. A spherical coordinate system is used to describe the blunt nose-cap region of the flowfield, while a cylindrical coordinate system is used for the rest of the flowfield. For very blunt vehicles, e.g., the AFE configuration (Fig. 1), a spherical coordinate system is used for the entire inviscid flowfield solution.³³ The HALIS code was written for use on the CDC Cyber 203, a vector processing computer.

For the Shuttle results presented in this paper, the HALIS code was configured in the following manner. There are a total of 145 planes down the vehicle, 15 in the spherical coordinate system, and 130 in the cylindrical coordinate system. There are 39 planes around the body which include two rays of information reflected across the upper and lower symmetry planes, and there are 15 points located along each ray between the body and bow-shock wave.

Boundary-Layer

The AA3DBL (Axisymmetric Analogue for 3-Dimensional Boundary Layer) code⁷ was developed following the procedure of Cooke.³⁴ Therefore, the general three-dimensional boundary-layer equations are first written in a streamline-oriented coordinate system. If the crossflow velocity in the boundary layer is neglected, the boundary-layer equations reduce to the same form as for axisymmetric flow, provided that distance along a streamline is interpreted as distance along an equivalent axisymmetric body and that the metric coefficient that describes the spreading of streamline is interpreted as the radius of an equivalent axisymmetric body. This greatly simplifies the viscous problems and means that approximate three-dimensional heating rates on a body can be computed along individual streamlines independent of what happens along other streamlines.

With the axisymmetric analogue, any axisymmetric boundary-layer method can be applied along an inviscid-surface streamline to obtain an approximate three-dimensional boundary-layer solution. For many aerothermal studies, surface heating rates are the primary objective, and while these heating rates could be obtained from a finite-difference solution of the full axisymmetric boundary-layer equations, this is unnecessary because very accurate results for both laminar and turbulent flow can be obtained more easily from approximate heating relations.³⁵ The heating results can be obtained at only a fraction of the computational effort required for a full boundary-layer solution.

Inviscid-surface streamline paths and the metric coefficient associated with the spreading of the streamlines are needed in the application of the axisymmetric analogue. Previous approaches using a known surface pressure distribution³⁶ were found to be unsatisfactory except for relatively simple cases such as sphere cones. (For a further discussion of this problem, see Refs. 5, 7, and 8.) The reason can be traced to the fact that the streamline metric calculations require first and second derivatives of the pressure. When these derivatives were calculated by finite-difference techniques, they proved to be inaccurate in many cases. A better approach is to use inviscid-surface velocity components, when they are available, to perform the streamline and metric computations. This approach requires only the first derivatives of the velocity components, and they can be generated numerically more accurately than second derivatives.

For the AA3DBL technique,⁷ the velocity components should be calculated by an accurate three-dimensional flowfield solution such as HALIS.³² Boundary-layer edge properties are obtained by interpolating in the inviscid flowfield at a distance equal to the boundary-layer thickness away from the wall. An initial assumption is made for the boundary-layer edge properties (usually equal to the wall values), and then the solution is iterated until the assumed values for the edge properties are equal to the calculated values.

EXPERIMENTAL DATA

Experimental data which were measured on flight vehicles are discussed in this section. The data were obtained over a wide range of vehicle configurations (Fig. 1) and freestream conditions. A brief discussion of the vehicle geometry, experimental technique, and prime data period for each of the flight tests is presented. A discussion of a ground-test model, test conditions, and the corresponding data is also presented since this model represents a possible near-term flight project, the Aeroassist Flight Experiment (AFE).

REENTRY F FLIGHT TEST

Laminar, transitional, and turbulent heating data were measured on a slender conical body during free flight.³⁷ This flight experiment, known as Reentry F, was performed in 1968 to provide accurate measurement of turbulent heating rates on a nearly sharp conical vehicle in regions where Mach number, Reynolds number, freestream enthalpy, and ratios of wall-to-total temperature could not be obtained by ground-based experiments. The Reentry F vehicle (Fig. 1) was a spherically-blunted cone with a half angle (θ_c) of 5° and was 13 ft in length with an initial nose radius of 0.1 inch. A graphite nosetip extended for the first 7.69 inches followed by a conical beryllium frustrum. Temperature measurements were obtained for the prime data period at altitudes between 120,000 and 60,000 ft at a freestream Mach number of approximately 20. These temperature data were reduced to heating rates and compared with data generated by existing prediction techniques. In addition, the measurements provided experimental information on hypersonic boundary-layer transition³⁸ in the flight environment. Today, after nearly 20 years, these data continue to hold importance for the same reasons. They are useful for comparison of prediction techniques, and practical application of transition criteria continues to be of primary importance since transition to turbulence affects both thermal design and aerodynamic performance.

SHUTTLE FLIGHT DATA SYSTEM

Through its first five flights, the Space Shuttle Orbiter had a data acquisition system to record the surface pressures and temperatures on the vehicle through both the ascent and descent phases of its flights. The development flight instrumentation (DFI) system consisted of a matrix of pressure transducers and thermocouples covering the surface of the vehicle.

The pressure transducers were, in general, sized for the pressure levels expected during the peak heating phase of the reentry trajectory, which limited the availability of some pressure data during the latter portion of the reentry. In general, 15-psia and 150-psf transducers provided pressure data through the entire reentry over the range of Mach number and angle of attack of interest ($M_\infty \geq 6$ and $25^\circ \leq \alpha \leq 45^\circ$), whereas the data from the 75-psf gauges are, with some exceptions, only available for $M_\infty > 15$. The only complete sets of pressure data are from the third (STS-3) and fifth (STS-5) Shuttle flights. The reduction and analysis of the flight pressure data follow the procedures outlined in Ref. 39.

Thermocouples which were mounted within the thermal protection system (TPS) and in thermal contact with the surface coating were located at over 200 vehicle surface locations. The measurements provide time histories of TPS surface temperature throughout the entry and are the basis for the determination of convective heating rates. The measured temperature-time histories were smoothed and subjected to an interactive review process to assure that the smoothed data provide an accurate representation of the raw temperature data. An inverse, one-dimensional, transient heat-transfer analysis⁴⁰ was used to determine the convective heating rate to the TPS surface. The importance of using the transient analysis to compute the convective heating rate rather than assuming a radiation equilibrium condition was demonstrated at trajectory times when the heating level was low, e.g., early in the trajectory or late in the trajectory when the convective flux was less than the surface reradiative cooling term. Also, the radiative equilibrium assumption was not adequate for conditions when some transient phenomenon such as boundary-layer transition influenced the vehicle aerothermodynamics. The impact on the computed experimental heating rates due to uncertainties in parameters, such as the thermal properties of the TPS, the surface emittance, temperature measurements, and the thermocouple depth location, was investigated.⁴¹ Such uncertainties were reported to contribute a ± 10 percent error in the measured heating rates.

FIRE II DATA

The Fire II vehicle, launched in 1965, was used to measure the radiative heating and the total (convective plus absorbed radiative) heating to a blunt-nose body at an entry velocity of approximately 36,100 fps.^{42,43} The forebody configuration was a truncated hemispherical shape with a small corner radius (Fig. 1) and had a layered heatshield composed of three beryllium layers with each backed by phenolic asbestos. Heatshields 1 and 2 were ejected during the entry to expose a clean, non-melted surface for the next data period. The dimensions of the heatshields were smaller from heatshield 1 to 3. Heating data were measured at several locations around the body, but the present work considers only the data measured at the centerline location. The vehicle entered at an angle-of-attack of zero degrees; thus, the centerline location was the flow stagnation point.

Two types of radiometers were used to measure the radiative heating.⁴² A total radiometer (thermopile) measured the radiative intensity in the 0.2 to 6.2 eV range, limited by the quartz window. A spectral radiometer measured the spectral intensity, which was then integrated to provide the total intensity in the 2 to 4 eV interval. Only the data for the 0.2 to 6.2 eV range are discussed in the present paper. The error band for the intensity data was estimated to be ± 20 percent.

Thermocouples were installed in the beryllium layers allowing the layers to be used as calorimeters that measured the total heating rate; that is, the sum of the convective heating rate and the absorbed, radiative heating rate.⁴³ The maximum measured value was 1000 Btu/ft²-sec, and the estimated error was ± 44 Btu/ft²-sec at this maximum value.

The Fire II data were categorized in prime data periods for each heatshield; that is, data obtained at times when the outer-surface temperatures of the quartz or beryllium were calculated to not interfere with the measurement and to be below the melt point. The prime data period of intensity measurements for heatshields 2 and 3 was less than 0.5 seconds. Anomalies seen in the data are explained in terms of melting of the materials, exposure of the phenolic asbestos, and ejection of the heatshields.⁴²

AFE (GROUND-TEST DATA)

For future opportunities in near and far space, a new family of vehicles, known as aeroassist vehicles, has been proposed. Walberg⁴⁴ has reviewed several aeroassist vehicle concepts. These vehicles will typically operate in the upper reaches of the atmosphere at higher velocities than those usually encountered by reentry vehicles. The aerodynamic characteristics of these vehicles will be used to execute orbital maneuvers associated with their mission and to reduce the amount of propellant required to make these orbital changes. An aeroassist vehicle of current interest is the aeroassisted orbital transfer vehicle (AOTV), which will be used to transfer payloads from low-to high-Earth orbit and back.

For a better understanding of the flowfields, surface pressures, heating distributions, and aerodynamics of such vehicles, a flight experiment has been proposed by research organizations within NASA and is called the Aeroassist Flight Experiment (AFE). Of the numerous body shapes initially proposed for this vehicle, a configuration⁴⁵ developed by the NASA Johnson Space Center has been selected for the flight project. The AFE body (Fig. 1) is generated by a 60° elliptic cone which has been raked off at a 75° angle. The nose is an ellipsoid which is tangent to the cone at all points of their intersection. The forebody is jointed to a skirt-type afterbody which reduces the flow expansion near the base of the cone and also reduces the heating in this region.

The success of the AFE project will depend on a number of factors, including the proper placement of instrumentation on the vehicle surface and the ability to fly the maximum science weight. Both of these factors are directly impacted by the accuracy of the aerodynamic data base through the determination of two parameters: (1) trim angle of the vehicle and thus the location of the stagnation point on the surface and (2) pitching moment characteristics which will determine what, if any, active control system will be required to stabilize the vehicle.

Data, from three ground-based test facilities located at the Langley Research Center, have been obtained to provide an understanding of the effects of these parameters on the AFE vehicle. The Hypersonic Helium Tunnel Facility⁴⁶ provides a test stream with a ratio of specific heats (γ) of 1.667 at a nominal Mach number of 20. The 31-Inch Mach 10 Tunnel⁴⁷ has a $\gamma = 1.4$ at a nominal Mach number of 10. The Hypersonic CF₄ Tunnel,⁴⁸ which utilizes tetrafluoromethane (Freon 14) to simulate the low- γ effects of real air, provides a nominal freestream Mach number of 6. The model was tested in each of the three ground-based facilities through the angle-of-attack range $-10^\circ \leq \alpha \leq 10^\circ$. The same balance was used in each facility to maintain consistency in the data measurement.

COMPARISON OF PREDICTIONS WITH EXPERIMENTAL DATA

In this section of the paper, highlights from investigations which compare results of the previously discussed flowfield codes and experimental data are presented. These comparisons of predicted results and experimental data are presented primarily at flight conditions. Thus, the chance to assess the real-gas chemistry capabilities in a code is provided with the comparisons. Such an opportunity is not typically available with ground-test results. However, all of these codes have been compared with ground-test data measured on models of the flight vehicles, with other available ground-test data, and with results of other CFD codes.

The comparisons will be presented for the Reentry F vehicle, the Shuttle Orbiter, the Fire II vehicle, and the AFE model, respectively. This order provides a review of aerothermal comparisons for slightly blunted slender vehicles, for a complex blunted winged vehicle, and then for very blunt bodies.

REENTRY F

Figures 2-4 contain comparisons of flight data and heating-rate predictions using a detailed viscous-shock-layer code and engineering codes for two Reentry F trajectory points. Equilibrium air chemistry was used in all of the calculations. Figure 2 presents heating-rate data at an altitude of 120,000 ft with a freestream Mach number of 19.25. The flow in this case was laminar over the entire vehicle, and angle of attack was approximately zero. The comparison between experiment and VSL3D⁸ prediction shows agreement within 10 percent. The heating distribution computed using the INCHES code⁶ is also in similar agreement.

Figures 3 and 4 show the experimental heating-rate data compared with the VSL3D and engineering code predictions, respectively, for a trajectory point at 80,000 ft. The Mach number remained near 20 for this case, but a small angle of attack (0.14°) existed for the flight vehicle. In the MINIVER code,¹² the equivalent-cone approximation was used to account for the pitch. Such a simplifying approximation in the MINIVER solutions is adequate in this case but will not be accurate at larger angles of attack. The data and predictions shown in Figs. 3 and 4 are for the most leeward plane (the primary thermocouple ray). The data show that boundary-layer transition occurred about halfway down the vehicle, and for the present calculations, the transition location was taken at the reported distance.³⁸ In Fig. 3, the overall agreement between heating data and predicted results is excellent except in the transition region.

Figure 4 presents laminar and turbulent heating-rate predictions using the INCHES and MINIVER codes for the same conditions shown in the previous figure. Both engineering codes assume instantaneous transition for this comparison. As shown, the INCHES prediction is in good agreement (within 10 percent) with both the laminar and fully turbulent data. The laminar heating method in MINIVER also yields results in good agreement with the data. After transition, the results of two turbulent heating methods used in MINIVER are compared with the data. The first, based on the Schultz-Grunow skin-friction relation, is in very good agreement with the data. Conversely, the Spalding and Chi skin-friction relation results in turbulent heating rates 15 to 20 percent lower than the data. Similar results have been noted⁴⁹ for the Spalding and Chi relation in other codes.

SHUTTLE ORBITER

The comparisons of predicted results and Shuttle data are shown first for results typical of published inviscid analyses. The pressure comparisons are shown because the data were important in understanding the aerodynamic behavior of the Shuttle entry and because the inviscid code results were necessary for boundary-layer calculations. Next, the nonequilibrium flow results based on the low-density (> 300,000 ft) data are presented. Then, the remaining nonequilibrium results representative of altitudes from approximately 250,000 ft to 160,000 ft are presented. Finally, comparisons are presented typical of lower altitude results that illustrate capabilities to predict off-centerline, lower wing and turbulent heating data.

Shuttle Inviscid Results

The flight data point, $M_\infty = 21.6$, was chosen for comparison because the STS-3 and STS-5 entry trajectories were coincident at this point, providing two sets of flight data. At these high Mach numbers, real-gas effects become important. Thus, both a perfect gas and an effective γ solution have been computed using the HALIS code for comparison with flight data. (The effective γ is the perfect-gas value required to compute the same shock density ratio as obtained for a given equilibrium-air condition.)

The centerline pressure distribution is shown in Fig. 5, where both perfect gas and effective γ HALIS solutions have been plotted along with the STS-3 and STS-5 flight data. The two HALIS solutions are similar up to an x/L value of 0.5, except for the stagnation region which is poorly detailed in this figure. (For detailed plots of pressure distributions in the stagnation region, see Ref. 50.) However, for $x/L > 0.5$, the $\gamma_e = 1.18$ solution produces a lower pressure level along the centerline with the greatest effect occurring in the expansion region on the aft end of the vehicle. The computed solutions are in good agreement with the flight data. At this Mach number, pressure sensors located on the centerline just upstream of and on the body flap are not yet saturated. These pressures have also been plotted on Fig. 5. In Figs. 6(a)-6(e), the chordwise pressure distributions on the lower surface of the wing are compared with the flight data at spanwise locations of 0.4, 0.5, 0.6, 0.7, and 0.8. In all of these figures, the real-gas effects have a large impact on the pressure distributions over the wing surface, and the flight data strongly support the results of the effective γ HALIS solution. At this flight condition, the STS-3 elevon deflection is approximately 5° whereas the deflection is only 2° for STS-5.

Shuttle Nonequilibrium Results

The DSMC calculations for the flow past an axisymmetric representation of the windward centerline of the Space Shuttle Orbiter over an altitude range of 300,000 to 500,000 ft are presented in Ref. 1. The DSMC results were compared with similar results based on a VSL code (HYVIS⁹) and a NS method (SLNS²). Results of those comparisons are presented in Fig. 7 in terms of the heat-transfer coefficient, C_H , ($C_H = 2q/\rho_\infty U_\infty^3$), where q is the heat-transfer rate and ρ_∞ and U_∞ are the freestream density and velocity,

respectively, versus the overall Knudsen number. The DSMC numerical simulations used a five-species model for air (O_2 , N_2 , O , N , and NO) and a noncatalytic wall at temperatures corresponding to the flight measured values. For the DSMC¹ calculations, the wall was also assumed to be diffuse with full thermal accommodations. At an altitude of 300,000 ft, the heat-transfer coefficient computed by both DSMC and HYVIS are in good agreement with the Orbiter flight data. However, as the altitude increased, the HYVIS results, without slip boundary conditions, began to depart rapidly from the DSMC results for λ_∞/r_n values greater than 0.03. (The λ_∞ is the freestream mean-free path length, and the nose radius, r_n , was used as 4.25 ft for the calculations at 300,000 ft). Results of more recent continuum calculations² using the NS equations for the stagnation streamline (SLNS) have been compared with DSMC data for altitudes of 300,000 to 400,000 ft (λ_∞/r_n from 0.028 to 1.22), and the agreement is good for the conditions over which the comparisons are made. Even though all three numerical methods are in agreement with respect to stagnation-point heat transfer at an altitude of 300,000 ft, the investigation of Ref. 1 shows that there are substantial differences in the flowfield structure, and these differences increase with increasing rarefaction. The DSMC calculations of Ref. 1 show that the flowfield disturbance extends a greater distance upstream of the body; that is, the shock wave is of the same order of thickness as the shock layer. The inability of the NS equations to properly describe the shock structure is not surprising, since investigators (e.g., Ref. 51) have shown that the NS equations do not adequately describe the structure of strong planar shock waves for Mach numbers greater than approximately 2.

The results of the calculations shown in Fig. 7 are in good agreement with the flight heating-rate data up to an altitude of 300,000 ft. With increasing altitude, the agreement between flight and calculated heating becomes progressively poorer. While the DSMC calculated heat-transfer coefficient asymptotically approaches a value of 1.0 for large Knudsen numbers, the flight data results never reach a value much greater than 0.22. If an energy accommodation coefficient less than 1.0 is assumed, the agreement is improved, but the discrepancy cannot be totally resolved with realistic values of the accommodation coefficient. The reason for the experimental trend with increasing Knudsen number is not known at present. However, two areas of concern are obvious: one being the accuracy of the flight heating values at low heating conditions and the second being that some event may have occurred in flight that has not been included in the Monte Carlo simulation. The accuracy of the flight heating data is discussed in detail in Ref. 40. Therefore, if it is assumed that the thermocouple measurements and the heating rates deduced from those measurements are reasonably accurate, then the question arises to the cause of the apparent low heating values for Knudsen numbers of the order of 0.1 and greater. Two events that would produce lower heating values are mass addition to the flowfield and the lack of full thermal accommodation. If there is any outgassing as the orbiter encounters the onset of the heating pulse, then this would reduce the heating. It should be noted that a fuel dump occurred prior to entry with fuel from the reaction control jets in the nose region being ejected forward of the orbiter. The effect of mass addition was not considered in the present calculations; however, the effect of the surface reflection model was examined.

For the altitude range from approximately 250,000 to 160,000 ft, the experimental wall temperature measurements and resulting heat-transfer rates obtained during the first flights of the Space Shuttle have been demonstrated^{9,52-54} to be lower than predicted equilibrium values at least over the first 40 percent of the Shuttle length and for much of the altitude range of interest. The flight data from the Catalytic Surface Experiment (CSE),⁵³ which was a Space Shuttle Orbiter experiment by NASA Ames Research Center, have verified that the lower rates can be attributed primarily to the relatively noncatalytic nature of the TPS and not to unknowns in freestream or flowfield quantities and that some degree of nonequilibrium flow persists to altitudes as low as 160,000 ft.

The importance of finite catalytic surface effects (surface reaction-rate coefficient or energy-transfer recombination coefficient) on the heat transfer in a dissociated nonequilibrium environment has long been recognized.⁵⁵ Both temperature-dependent⁵² and constant⁵³ values of the coefficients for surface oxygen and nitrogen recombination have been used to calculate laminar heat fluxes to the Space Shuttle. The reaction rates ($k_{w,O}$ and $k_{w,N}$) were inferred from ground-test arc-jet heat-transfer measurements^{56, 57} conducted at wall temperatures higher than flight-measured values. The heating rates, or surface temperatures, which have been calculated with the existing reaction rates yield only a fair comparison^{9,52,53} with the Shuttle experimental windward-ray thermal data. In fact, at altitudes lower than approximately 210,000 ft, the calculated heating rates are as much as 30 to 40 percent lower than the experimental data.

Results typical of these comparisons were recently presented³¹ and are shown in Fig. 8. The windward-symmetry plane heat-transfer data measured at 234,000 ft are compared with the results of the modified SHTNEQ code³¹ using temperature-dependent reaction rates.⁵⁶ The axisymmetric VSL (HYVIS) code results⁹ using the same rate expressions and employing an "equivalent hyperboloid" concept are also shown on the figure. The predicted results of both codes are shown to be approximately 20 percent lower than the data. However, good agreement is obtained with the predicted results from the nonequilibrium VSL methods based on the 3D and the axisymmetric equivalent body techniques.

The concept that an axisymmetric equivalent body could model the windward-centerline flowfield over the Shuttle at a given angle of attack was proposed in Ref. 58 based on comparisons of ground-test data measured on a Shuttle model at 30° angle of attack. This concept was then verified^{10,59} over an angle-of-attack (AOA) range of 25° to 45°. For this AOA range, a hyperbola with a computed nose radius and body half-angle was used to model the Shuttle windward-symmetry plane coordinates. The primary reason

for the good comparison is that the Shuttle has a rather wide flat-bottom surface with a smoothly decreasing slope, and the equivalent body approximately models the longitudinal and circumferential cross sections.

Also shown on Fig. 8 is a comparison of the data with results predicted by the modified SHTNEQ code using an oxygen recombination-rate expression⁶⁰ determined from STS-2 flight data. A substantial improvement in the comparisons is observed. The rate expression was determined⁶⁰ by a "best" fit to the experimental STS-2 heating rates at altitudes from 260,000 to 234,000 ft. The expression was correlated as a function of the surface temperatures in an Arrhenius form. Based on the data used to develop the rate expressions, improved comparisons similar to those shown in Fig. 8 should not be surprising, but it is important to note that the rate expression is not uniquely dependent on the code used in the analysis process. Good agreement is obtained for calculated results based on codes using different computational techniques.^{31,60} Two encouraging results were observed in the study of Ref. 60. First, the comparisons of the data and predicted results were significantly improved for altitudes lower than 234,000 ft. Secondly, both the STS-2 and STS-3 heating data and predicted nonequilibrium results approached the corresponding equilibrium levels in a very similar manner with decreasing altitude (Figs. 9(a) and 9(b)). An additional illustration of the improved agreement obtained with the Shuttle 3D VSL code³¹ using the rate expression derived from flight data is shown in Fig. 10. The windward-symmetry plane heating-rate data at 199,000 ft are compared with the predicted results. Good agreement is shown.

Since the SHTNEQ code solves the full three-dimensional flowfield over the windward surface, it is of interest to make comparisons between prediction and flight for regions away from the symmetry plane. These comparisons are presented in Fig. 11 at an altitude of 199,000 ft. This figure compares the transverse heating distributions at axial locations (x/L) of 0.098, and 0.592, Figures 11(a) and 11(b), respectively. The predictions shown in these figures are those obtained using the oxygen recombination rate from Ref. 60. In general, the heating-rate predictions for the off-centerline data are quite good and are typically within 10 to 15 percent of the flight data. Also, the trends of the heating distributions in the crossflow direction are in agreement. The peak in heating occurring at the corner between the lower surface and side fuselage is generally predicted.

Shuttle Data at Lower Altitudes

Experimental laminar heating rates from STS-2 measured along the windward-symmetry plane at $M_\infty = 9.15$ are shown in Fig. 12. Heating rates calculated by the LISC,²¹ INCHES,⁶ HYVIS,⁹ VSL84,⁴ and AA3DBL⁷ codes are shown on the figure. The results of the calculations are in reasonably good agreement. While there is some scatter in the experimental data, the predicted results are also in generally good agreement with the data.

Circumferential distributions of heating are presented at two axial stations ($x/L = 0.1$ and 0.4) in Fig. 13. At the two stations, the calculated results are in good agreement with the data. The calculated results are based on the VSL84, AA3DBL, and LISC codes. Note the relatively small differences in the results of the two inviscid-boundary-layer methods^{7,21} and the VSL method.⁴

A unique capability of the AA3DBL method is the capability to accurately predict heating rates on the Shuttle Orbiter wing. A comparison of calculated heating with flight data for the "mid-wing" location ($2y/b = 0.5$) is presented in Fig. 14 as a function of x^*/c (where x^* is the distance from the leading edge and c is the chord length). Two predictions are shown, one for laminar flow and one for turbulent flow. The turbulent calculations were made by starting transition at $x/L = 0.2$. At first glance the flight data appear to behave very strangely; first being laminar, then transitional, then laminar, then transitional, then laminar again, and finally fully turbulent near the trailing edge of the wing. This behavior is quite easily explained when it is realized that the flow at different chord locations on the wing has traveled along different streamlines. Thus, flow along one streamline can be transitional or even turbulent while the flow on adjacent streamlines remains laminar. In fact this behavior fits the transition pattern observed⁶¹ for this case which is illustrated by the transition front locations shown in Fig. 15.

The heating at the more outboard location on the wing ($2y/b = 0.8$) is presented in Fig. 16. The heating pattern for this case is typical of what is expected for a flow undergoing transition. The flow near the leading edge of the wing is laminar, then it undergoes transition, and finally becomes fully turbulent near the trailing edge. The calculated heating in the laminar and turbulent regions of the flow is in reasonably good agreement with the flight data.

Shuttle Turbulent Data

The Shuttle flowfield, based on nonequilibrium calculations,⁹ is at an equilibrium state prior to the onset of boundary-layer transition. For the purpose of investigating both the boundary-layer transition movement and associated turbulent heating levels, laminar and "fully" turbulent results predicted by the INCHES code were compared¹⁰ with the experimental data at numerous freestream conditions from the time corresponding to the onset of the transition front. While this complete set of results is not presented, the turbulent comparisons presented in Fig. 17 are typical. Also shown on the figure are the swept-cylinder (LISC) results²¹ for this condition. The turbulent data from STS-1 are shown to be about 10 percent lower than the STS-2 data. Discrepancies of less than 10 percent are obtained when the predicted results are compared with data for either flight.

FIRE II

The Fire II data are presented in Figs. 18 and 19 for the time histories of the radiative intensity measured from 0.2 to 6.2 eV and of the total heating rate (convective plus absorbed radiative fluxes), respectively. Time of zero seconds for Fig. 19 corresponds to actual trajectory time of 1617.75 seconds. All the measured data for radiative intensity are presented in Fig. 18 without denoting the prime data periods. This omission was done for clarity in presenting the results, and the reader is referred to Refs. 42 and 62 for additional details.

The computational results based on a VSL code²⁵ and a detailed inviscid code⁶² both using equilibrium chemistry and coupled with the Aerotherm radiation code⁶³ are presented also in Fig. 18. These results are in reasonably good agreement with the flight data throughout the trajectory. Results of another VSL code⁶⁴ have been shown²⁵ to be slightly lower than the present results. Comparisons of calculated results with the Fire II data for the radiative intensity in the 2 to 4 eV spectral interval are presented in Refs. 25, 62, and 64. Also, Ref. 62 provides detailed comparisons of the radiative heating for a large ground-based experimental data base and results from the Apollo 4 flight data.

The results from the VSL code²⁵ and from the inviscid code coupled with a convective heating equation⁶² are compared with the total heating-rate data in Fig. 19. Also shown is the calculated convective heating rate. Again, the computed results are in reasonably good agreement with the flight data. At the time of the third heatshield, the heating is dominated by convective heating. At the time of peak heating, heatshield 2, the calculated results are slightly lower and occur slightly earlier than the flight data. The calculations show that 35 percent of the maximum total heating rate is due to absorbed radiation. Furthermore, 70 percent of the absorbed radiation comes from the spectra greater than 6.2 eV. Thus, while the actual measured flight data for radiation, Fig. 18, provided a means to compare theoretical results at a spectral range less than 6.2 eV, the total heating data provide some results to infer a comparison with radiation data for the vacuum ultraviolet region.

The agreement between the calculated results and flight data prior to peak heating was unexpected and is probably fortuitous due to the dominating low-density nonequilibrium flow at the higher altitudes. To explore these effects, the nonequilibrium Navier-Stokes (SLNS²) solution was coupled with the Aerotherm radiation code,⁶³ as described in detail in Ref. 25, and the results are shown also in Figs. 18 and 19. This radiation code is based on the assumption of thermal equilibrium, but several attempts were still made to adapt the code to the nonequilibrium condition. Unfortunately, the efforts are depicted by the large discrepancies shown in the comparisons. The poor nonequilibrium predictions highlight the need for a detailed nonequilibrium radiation code, such as discussed in Ref. 65, that can be fully coupled and exercised efficiently in a detailed flowfield calculation. Two recent studies^{65,66} have shown that results based on chemical and thermal nonequilibrium concepts can provide good agreement with the Fire II radiation data; however, the radiation transport was not coupled to the flowfield solution in these solutions.

AFE MODEL

Heating calculations have been made over the AFE geometry for angles of attack from -10° to 10° . All of the calculations were performed at $M_\infty = 9.86$, $p_\infty = 1.256 \text{ lbs/ft}^2$, and $T_\infty = 94^\circ \text{ R}$, which produced a freestream unit Reynolds number of approximately $0.5 \times 10^6/\text{ft}$. The calculated heat-transfer coefficients from LAURA²⁶ and AA3DBL¹¹ are compared with experimental data obtained in the 31-Inch Mach 10 Hypersonic Tunnel in Fig. 20 to help verify these computational methods for this configuration and to show the types of heating distributions that will occur over this class of vehicle. Boundary-layer edge properties for the AA3DBL code were computed by the HALIS three-dimensional, inviscid flowfield code.

The results for $\alpha = 0^\circ$ are presented in Fig. 20. These data are presented as h/h_{ref} (where h is the heat-transfer coefficient) versus nondimensional surface distance measured from the nose of the body. The data in Fig. 20(a) are located in the pitch plane with positive values of s/L for the lower symmetry plane and negative values of s/L for the upper symmetry plane. The data in Fig. 20(b) are located in a lateral plane passing through the nose. The experimental data were obtained on moderate fidelity stycast models using the phase-change paint technique, and the accuracy is probably ± 20 percent.

In the symmetry plane, (Fig. 20(a)), the predicted heating near the stagnation point is slightly higher for the LAURA code than for the AA3DBL code and should be more accurate since the LAURA code is based on a solution of the full Navier-Stokes equations; however, there are no experimental data available in this region. In the leeward-symmetry plane, the heating data is very low over the entire skirt. The LAURA code results show a slight rise in heating near the end of the cone or the beginning of the skirt (i.e., $x/L = -0.21$) which is caused by the rapid expansion of the flow in this region. Along the windward-symmetry plane, the heating decreases rapidly at first but levels out over the aft portion of the elliptic cone section. As the skirt is approached, both methods predict an increase in heating which peaks near $s/L = 0.77$ which is again caused by a rapid flow expansion. Although the LAURA code results are much higher than the experimental data measurements, regions such as this are subject to much larger than normal errors, and the data, without corrections for three-dimensional conduction effects, would be expected to fall below the theoretical predictions. Both sets of predictions are in reasonably good agreement with the experimental data.

In the lateral plane, (Fig. 20(b)), the AA3DBL results reach a small plateau slightly ahead of the skirt and then fall continuously to a very low value near the base of the body. The LAURA results again

show a peak in heating just ahead of the skirt ($x/L = 0.39$) and then decrease very rapidly. The experimental data show no peak in heating as also noted for the symmetry plane. In general, the predictions are in again reasonably good agreement with the experimental data.

For the AFE model, the HALIS aerodynamic coefficients have been shown³³ to be in good agreement with experimental data taken over a range of Mach numbers and ratios of specific heats (γ); whereas the corresponding results for Newtonian theory are in poor agreement with either the computational or experimental data. The aerodynamics are computed also at a flight condition of maximum dynamic pressure using the HALIS code with an equilibrium air chemistry option to assess the validity of extrapolating ground-test data to flight. The AFE vehicle will fly in the free molecular, transitional, and continuum flow regimes and experience the effects of nonequilibrium chemistry. For the present calculations, the point of maximum dynamic pressure corresponding to the minimum flight altitude was selected to minimize the effects of nonequilibrium chemistry and to be assured of continuum flow. An equilibrium chemistry solution should provide a reasonable simulation of the actual flight condition. The HALIS-calculated results for ground- and flight-test conditions were obtained at angles of attack between -10° and 10° in 5° increments.

The results of these equilibrium calculations for the critical aerodynamic coefficients of pitching moment, C_m , are shown on Fig. 21 along with the computed values at the three tunnel conditions and the Newtonian values for the flight condition. HALIS flight computations indicate that the vehicle trims at zero degrees. Clearly, results from the $M_\infty = 21.5$ helium and $M_\infty = 10$ air tests would misrepresent the aerodynamic and trim characteristics of the AFE vehicle at this flight condition. Surprisingly, from a stability standpoint, the C_{m_α} values at zero degree angle of attack are similar for the Newtonian,

flight, and CF_q curves even though in magnitude, the Newtonian C_m value is seriously in error, whereas the C_m in CF_q is considerably closer to the flight value. From the standpoint of magnitude, the CF_q results are the best approximation to the flight values of C_m for $\alpha \leq 5^\circ$. However, over the same values of α , there are considerable differences in C_{m_α} . Again, these predicted flight values are for air in thermodynamic equilibrium, and the impact, if any, of nonequilibrium chemistry on the vehicle aerodynamics has yet to be determined. Under no circumstances, either for tunnel or predicted flight values, was the use of Newtonian pressures to determine aerodynamics of any practical use for this configuration whose flowfield is dominated by subsonic flow behind the bow-shock wave.

CONCLUSIONS

An overview of previous investigations demonstrating the capabilities of both detailed and engineering codes to predict the aerothermal environment about an entry vehicle has been presented. The overview consists of a brief discussion of the computational methods and the experimental data and presents comparisons of the predicted results and data. The focus is primarily on flight data analyses.

The predicted results are based on a series of computer codes employed by the Aerothermodynamics Branch of the Space Systems Division at the NASA Langley Research Center. The detailed codes range from a Direct Simulation Monte Carlo method to investigate the high-altitude, low-density noncontinuum flow to three-dimensional inviscid plus boundary-layer methods to investigate the lower altitude, continuum conditions. The computational capabilities also include engineering codes which use various levels of approximation to predict the aerothermal environment. The flight data represent measurements over a diverse set of vehicle configurations. Aerodynamic and aeroheating results of recent ground tests are also included because the tests provide data on a model of a pending flight project.

The overview provided the opportunity to demonstrate in a single source the capability of these codes to predict the aerothermal environment about an entry vehicle. Comparisons based on flight data were selected because these results yield the unique chance to assess the coupled real-gas chemistry procedures included in the codes. The analyses of flight data were preceded by studies in which the results of the codes were compared to predictions of other computational methods and existing experimental data. While no one method was used, nor probably should be expected, to predict the whole range of entry environment and vehicle configurations, the collection of codes demonstrated good existing capabilities and future potential for predicting the aerothermal environment about flight vehicles. The overview also illustrated procedures which were and should be used to verify a computational technique.

REFERENCES

- ¹Moss, J. N. and Bird, G. A., "Direct Simulation of Transitional Flow for Hypersonic Re-entry Conditions," Thermal Design of Aeroassisted Orbital Transfer Vehicles, Progress in Astronautics and Aeronautics, edited by H. F. Nelson, Vol. 196, 1985, pp. 113-134.
- ²Gupta, R. N. and Simmonds, A. L., "Hypersonic Low-Density Solutions of the Navier-Stokes Equations with Chemical Nonequilibrium and Multicomponent Surface Slip," AIAA Paper 86-1349, June 1986.
- ³Gnoffo, P. A., "Hypersonic Flows Over Biconics Using a Variable-Effective-Gamma, Parabolized-Navier-Stokes Code," AIAA Paper 83-166, July 1983.
- ⁴Thompson, R. A., "Three-Dimensional Viscous-Shock-Layer Application for the Space Shuttle Orbiter," Thermophysical Aspects of Re-entry Flows; Progress in Astronautics and Aeronautics, edited by J. N. Moss and C. D. Scott, Vol 103, 1986, pp. 541-570.

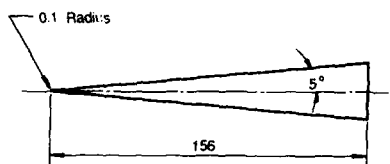
- ⁵Weilmuenster, K. J., "Comparison of Inviscid Flow Computations with Flight Data for the Shuttle Orbiter," Journal of Spacecraft and Rockets, Vol. 22, No. 3, May-June 1985, pp 297-303.
- ⁶Zoby, E. V. and Simmonds, A. L., "Engineering Flowfield Method with Angle-of-Attack Applications," Journal of Spacecraft and Rockets, Vol. 22, No. 4, July-August 1985, pp. 398-404.
- ⁷Hamilton, H. H., DeJarnette, F. R., and Weilmuenster, K. J., "Application of Axisymmetric Analogue for Calculating Heating in Three-Dimensional Flow," Journal of Spacecraft and Rockets, Vol. 24, No. 4, July-August, 1987, pp. 296-302.
- ⁸Thompson, R. A., Zoby, E. V., Wurster, K. E., and Gnoffo, P. A., "An Aerothermodynamics Study of Slender Conical Vehicles," AIAA Paper 87-1475, June 1987.
- ⁹Shinn, J. L., Moss, J. N., and Simmonds, A. L., "Viscous-Shock-Layer Heating Analysis for the Shuttle Windward Plane with Surface Finite Catalytic Recombination Rates," Entry Vehicle Heating and Thermal Protection Systems: Space Shuttle, Solar Starprobe, Jupiter Galileo Probe; Progress in Astronautics and Aeronautics, edited by P. E. Bauer and H. E. Collicott, Vol. 85, 1983, pp. 149-180.
- ¹⁰Zoby, E. V., "Analysis of STS-2 Experimental Heating Rates and Transition Data," Journal of Spacecraft and Rockets, Vol. 20, No. 3, May-June 1983, pp. 232-237.
- ¹¹Hamilton, H. H. and Weilmuenster, K. J., "Calculations of Convective Heating on Proposed Aeroassist Flight Experiment Vehicle," AIAA Paper 86-1308, June 1986.
- ¹²Engel, G. D. and Praharaj, S. C., "MINIVER Upgrade for the AVID System, Vol. I: LANMIN User's Manual," NASA CR-172212, August 1982.
- ¹³Wilhite, A. W., "The Aerospace Vehicle Interactive Design System," AIAA Paper 81-233, January 1981.
- ¹⁴Fay, J. A. and Riddell, F. R., "Theory of Stagnation Point Heat Transfer in Dissociated Air," Journal of Aeronautical Sciences, Vol. 121, No. 25, 1958, pp. 73-85, 121.
- ¹⁵Schlichting, H., Boundary-Layer Theory, 4th Ed., McGraw-Hill, New York, 1960.
- ¹⁶Eckert, E. R. G., "Survey on Heat Transfer at High Speeds," U.S. Air Force, ARL 189, Dec. 1961.
- ¹⁷Schultz-Grunow, F., "A New Resistance Law for Smooth Plates," Luftfahrt Forsch, Vol. 17 (1940), pp. 239-246, (translation) NACA TM 986, 1941.
- ¹⁸Spalding, D. B. and Chi, S. W., "The Drag of A Compressible Turbulent Boundary Layer on a Smooth Flat Plate With and Without Heat Transfer," Journal of Fluid Mechanics, Vol. 18, Pt. 1, Jan. 1964, pp. 117-143.
- ¹⁹Maslen, S. H., "Axisymmetric Hypersonic Flow," NASA CR-2123, 1972.
- ²⁰DeJarnette, F. R. and Davis, R. M., "A Simplified Method for Calculating Laminar Heat Transfer Over Bodies at an Angle of Attack," NASA TN D-4720, 1968.
- ²¹Hamilton, H. H., II, "Approximate Method of Predicting Heating on the Windward Side of Space Shuttle Orbiter and Comparisons with Flight Data," Entry Vehicle Heating and Thermal Protection Systems: Space Shuttle, Solar Starprobe, Jupiter Galileo Probe; Progress in Astronautics and Aeronautics, edited by P. E. Bauer and H. E. Collicott, Vol. 85 1983, pp. 21-53.
- ²²Adams, J. C., Jr. and Martindale, W. R., "Hypersonic Lifting Body Windward Surface Flowfield Analysis for High Angles of Incidence," AEDC TR-73-2, Feb. 1973.
- ²³Tannehill, J. C. and Mugge, P. H., "Improved Curve Fits for the Thermodynamic Properties of Equilibrium Air Suitable for Numerical Computations Using Time-Dependent or Shock Capturing Methods, Part 1 - Final Report," NASA CR-2470, Oct. 1974.
- ²⁴G. A. Bird, "Monte-Carlo Simulation in an Engineering Context, Rarefied Gas Dynamics, Part 1: Progress in Astronautics and Aeronautics, edited by Sam S. Fisher, Vol. 74, 1981, pp. 239-255.
- ²⁵Gupta, R. N., "Navier-Stokes and Viscous-Shock-Layer Solutions for Radiating Hypersonic Flow," AIAA Paper 87-1576, June 1987.
- ²⁶Gnoffo, P. A., McCandless, R. S. and Yee, H. C., "Enhancements to Program LAURA for Computation of Three-Dimensional Hypersonic Flow," AIAA Paper 87-0280, January 1987.

- ²⁷ Moss, J. R., "Advancements in Aerothermodynamics in Support of the Galileo Probe," Proceedings of the Thirteenth International Symposium on Space Technology and Science, August 1982, pp. 613-624.
- ²⁸ Gupta, R. N., Lee, K. P., Moss, J. N., Zoby, E. V., and Tiwari, S. N., "Viscous-Shock-Layer Analysis of Hypersonic Flows Over Long Shuttle Bodies," AIAA Paper 87-2487, August 1987.
- ²⁹ Kim, M. D., Swaminathan, S., and Lewis, C. H., "Three-Dimensional Nonequilibrium Viscous Shock Layer Flows Over the Space Shuttle Orbiter," AIAA Paper 83-0487, January 1983.
- ³⁰ Szema, K. Y., Thareja, R. R., and Lewis, C. H., "Three-Dimensional Viscous Shock-Layer Flows Over Lifting Bodies at High Angle of Attack," AIAA Paper 81-1146, June 1981.
- ³¹ Thompson, R. A., "Comparisons of Nonequilibrium Viscous-Shock-Layer Solutions with Windward Surface Shuttle Heating Data," AIAA Paper 87-1473, 1987.
- ³² Weilmuenster, K. James and Hamilton, H. Harris II, "Calculations of Inviscid Flow Over Shuttle-Like Vehicles at High Angles of Attack and Comparisons with Experimental Data," NASA TP 2103, May 1983.
- ³³ Weilmuenster, K. James and Hamilton, H. Harris II, "A Comparison of Computed and Measured Aerodynamic Characteristics of a Proposed Aeroassist Flight Experiment Configuration," AIAA Paper 86-1366, June 1986.
- ³⁴ Cooke, J. C., "An Axially Symmetric Analogue for Three-Dimensional Boundary-Layers," R. & M. No. 3200, British A.R.C., 1961.
- ³⁵ Zoby, E. V., Moss, J. N., Sutton, K., "Approximate Convective Heating Equations for Hypersonic Flow," Journal of Spacecraft and Rockets, Vol. 18, No. 1, January-February 1981, pp. 64-70.
- ³⁶ DeJarnette, F. R. and Hamilton, H. H. II, "Inviscid Surface Streamlines and Heat Transfer on Shuttle-Type Configurations," Journal of Spacecraft and Rockets, Vol. 10, No. 6, May 1973, pp. 314-321.
- ³⁷ Stainback, P. Calvin, Johnson, Charles B., Boney, Lillian R., and Wicker, Kathleen C., "A Comparison of Theoretical Predictions and Heat-Transfer Measurements for a Flight Experiment of Mach 20 (Reentry F)," NASA TM X-25601972.
- ³⁸ Wright, Robert L. and Zoby, Ernest V., "Flight Measurements of Boundary-Layer Transition on a 5° Half-Angle Cone at a Free-Stream Mach Number of 20 (Reentry F)," NASA TM X-2253, 1971.
- ³⁹ Bradley, P. F., Siemers, P. M. III, and Pruett, C.D., "Comparison of Forward Fuselage Space Shuttle Orbiter Flight Pressure Data to Wind-Tunnel and Analytical Results in the Hypersonic Mach Number Range," AIAA Paper 81-2477, November 1981.
- ⁴⁰ Throckmorton, D. A., "Benchmark Determination of Shuttle Orbiter Entry Aerodynamic Heat-Transfer Data," Journal of Spacecraft and Rockets, Vol. 20, No. 3, May-June 1983, pp. 219-224.
- ⁴¹ Bradley, P. F. and Throckmorton, D. A., "Space Shuttle Orbiter Flight Heating Rate Measurement Sensitivity to Thermal Protection System Uncertainties," NASA TM 83138, 1981.
- ⁴² Cauchon, Dona L., "Radiative Heating Results from the Fire II Flight Experiment at a Reentry Velocity of 11.4 Kilometers per Second," NASA TM X-1402, July 1967.
- ⁴³ Cornette, Elden S., "Forebody Temperatures and Calorimeter Heating Rates Measured During Project Fire II Reentry at 11.35 Kilometers per Second," NASA TM X-1305, November 1966.
- ⁴⁴ Walberg, G. D., "A Survey of Aeroassisted Orbit Transfer," Journal of Spacecraft and Rockets, Vol. 22, No. 1, January-February 1985, pp. 3-18.
- ⁴⁵ Roberts, B. B., "Systems Analysis and Technology Development for the NASA Orbital Transfer Vehicle," AIAA Paper 85-0965, June 1985.
- ⁴⁶ Arrington, J. P., et al., "Longitudinal Characteristics of Several Configurations at Hypersonic Mach Numbers in Conical and Contoured Nozzles," NASA TN D-2489, 1964.
- ⁴⁷ Schaefer, William T., Jr., "Characteristics of Major Active Wind Tunnels at the Langley Research Center," NASA TM X-1130, July 1965.
- ⁴⁸ Midden, Raymond E. and Miller, Charles G. III, "Description and Calibration of the Langley Hypersonic CF₄ Tunnel," NASA TP 2384, March 1985.
- ⁴⁹ Zoby, E. V. and Graves, R. A., "Comparison of Results From Three Prediction Methods With Turbulent Heating Data From Wind-Tunnel and Free-Flight Tests," NASA TM X-2390, September 1971.

- ⁵⁰Weilmuenster, K. James and Hamilton, H. Harris II, "A Comparison of Computed Space Shuttle Orbiter Surface Pressures with Flight Measurements," AIAA Paper 82-0937, June 1982. pp. 843-857.
- ⁵¹Liepmann, H. W., Narasimha, R., and Chahine, M. T., "Structure of a Plane Shock Layer," Physics of Fluids, Vol. 5, No. 11, November 1962.
- ⁵²Scott, C. D. and Derry, S. H., "Catalytic Recombination and the Space Shuttle Heating," Entry Vehicle Heating and Thermal Protection Systems: Space Shuttle Solar Starprobe, Jupiter Galileo Probe; Progress in Astronautics and Aeronautics, edited by P. E. Bauer and H. E. Collicott, Vol. 85, 1983, pp. 123-149.
- ⁵³Rakich, J. V., Stewart, D. A., and Lanfranco, M. J., "Results of a Flight Experiment on the Catalytic Efficiency of The Space Shuttle Heat Shield," Entry Vehicle Heating and Thermal Protection System: Space Shuttle Solar Starprobe, Jupiter Galileo Probe; Progress in Astronautics and Aeronautics, edited by P. E. Bauer and H. E. Collicott, Vol. 85, 1983, pp. 97-123.
- ⁵⁴Scott, C. D., "Effects of Nonequilibrium and Catalysis on Shuttle Heat Transfer," AIAA Paper 83-1485, June 1983.
- ⁵⁵Goulard, R., "On Catalytic Recombination Rates in Hypersonic Stagnation Heat Transfer," Jet Propulsion, Vol. 28, No. 11, November 1958, pp. 737-745.
- ⁵⁶Scott, C. D., "Catalytic Recombination of Nitrogen and Oxygen on High-Temperature Reusable Surface Insulation," Aerothermodynamics and Planetary Entry; Progress in Astronautics and Aeronautics, edited by A. L. Crosbie, Vol. 77, 1981, pp. 192-213.
- ⁵⁷Stewart, D. A., Rakich, J. V., and Lanfranco, M. J., "Catalytic Surface Effects Experiment on the Space Shuttle," Thermophysics of Atmospheric Entry; Progress in Astronautics and Aeronautics, edited by T. E. Horton, Vol. 82, 1982, pp. 248-273.
- ⁵⁸Adams, J. C., Martindale, W. R., Mayne, A. W., Jr., and Marchand, E. O., "Real Gas Scale Effects on Hypersonic Laminar Boundary-Layer Parameters Including Effects of Entropy-Layer Swallowing," Arnold Engineering Development Centers, AFS, TN, AEDC-TR-75-2, 1975.
- ⁵⁹Zoby, E. V., "Approximate Heating Analysis for the Windward-Symmetry Plane for Shuttle-Like Bodies at Large Angle of Attack," Thermophysics of Atmospheric Entry; Progress in Astronautics and Aeronautics, edited by T. E. Horton, Vol. 82, 1982, pp. 229-247.
- ⁶⁰Zoby, E. V., Gupta, R. N., and Simmonds, A. L., "Temperature-Dependent Reaction Rate Expressions for Oxygen Recombination," Thermal Design of Aeroassisted Orbital Transfer Vehicles; Progress in Astronautics and Aeronautics, edited by H. F. Nelson, Vol. 96 of 1985, pp. 445-465.
- ⁶¹Hartung, L. C. and Throckmorton, D. A., "Computer Graphic Visualization of Orbiter Lower Surface Boundary-Layer Transition," AIAA Paper 84-0228, January 1984.
- ⁶²Sutton, K., "Air Radiation Revisited," AIAA Paper 84-1733, 1984.
- ⁶³Nicolet, W. E., "User's Manual for the Generalized Radiation Transfer Code (RAD/EQUIL)" NASA CR-116353, October 1969.
- ⁶⁴Balakrishnan, A., Park, C., and Green, M. J., "Radiative Viscous Shock Layer Analysis of Fire, Apollo, and PAET Flight Data," AIAA Paper 85-1064, 1985.
- ⁶⁵Park, C., "Assessment of Two-Temperature Kinetic Model for Ionizing Air," AIAA Paper 87-1574, June 1987.
- ⁶⁶Bird, G. A., "Nonequilibrium Radiation During Re-Entry at 10 km/s," AIAA Paper 87-1543, June 1987.

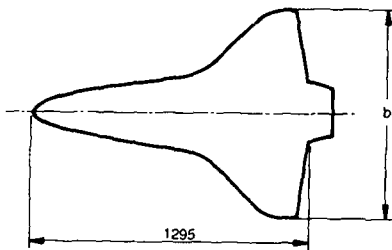
ACKNOWLEDGEMENTS

The authors wish to acknowledge the research and contributions of several co-workers. Without their significant research efforts, this paper would not have been possible. While there has been reference to many investigators, particular notice is made of the following individuals: Mr. James K. Weilmuenster for his development of the HALIS code, which provided the first detailed flowfield studies over the Shuttle windward surface and is currently used to obtain important information for studies of the complex AFE configurations; Mr. Richard A. Thompson for his work with the viscous-shock-layer codes, especially the nonequilibrium Shuttle analyses; Dr. James N. Moss for his significant contributions to both continuum and nonequilibrium analyses; Dr. Peter A. Gnoffo for his development of the LAURA code; and Dr. Roop N. Gupta of Scientific Research and Technology, Inc., in Hampton, VA. for his continuing efforts in radiative and convective nonequilibrium viscous flowfield studies.



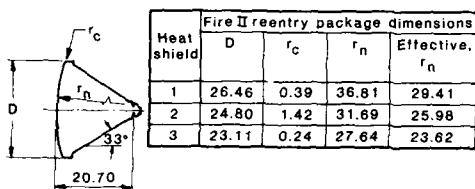
(a) Reentry F.

Fig. 1 Vehicle Geometries. (All dimensions in inches.)



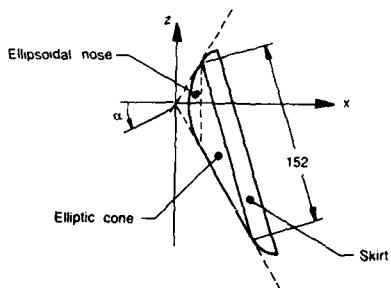
(b) Lower surface of Shuttle Orbiter.

Fig. 1 Continued.



(c) Fire II.

Fig. 1 Continued.



(d) AFE.

Fig. 1 Concluded.

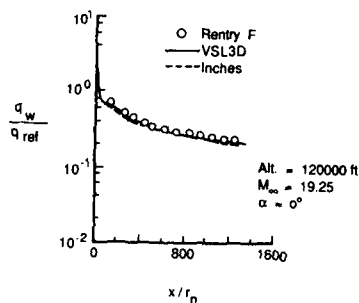


Fig. 2 Comparison of laminar heating-rate predictions with Reentry F flight data.

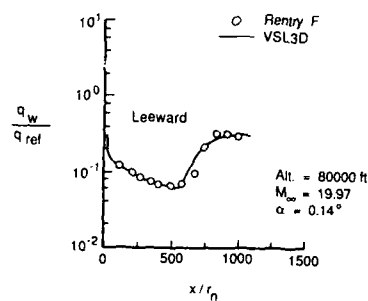


Fig. 3 Comparison of detailed heating-rate predictions with Reentry F flight data.

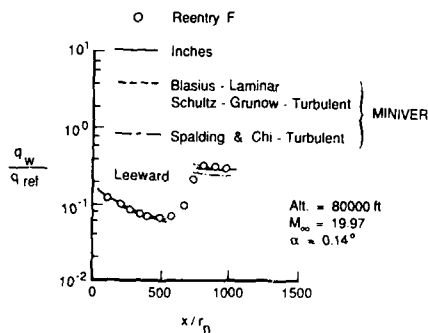
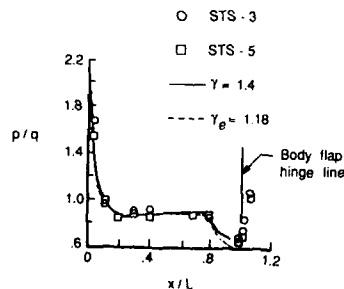


Fig. 4 Comparison of engineering heating-rate predictions with Reentry F flight data.

Fig. 5 Comparison of HALIS/flight centerline pressures on the Shuttle Orbiter; $M_{\infty} = 21.6$, $\alpha = 40$ deg.

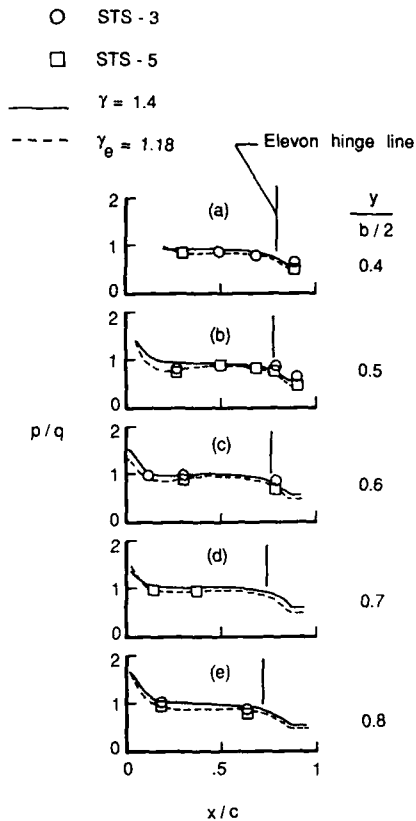


Fig. 6 Comparison of HALIS/flight chordwise pressure distributions on the Shuttle Orbiter wing; $M_\infty = 21.6$, $\alpha = 40^\circ$.

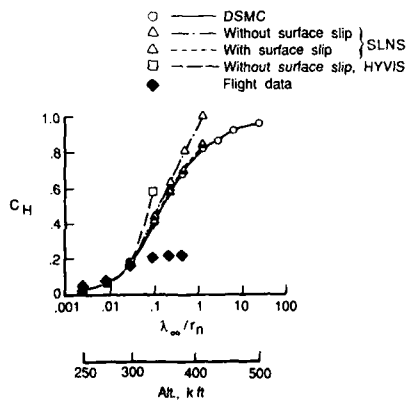


Fig. 7 Stagnation heat-transfer coefficient versus Knudsen number for Shuttle Orbiter.

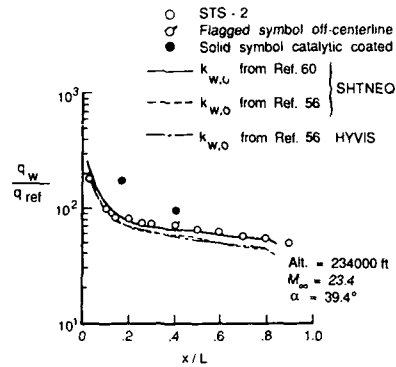


Fig. 8 Comparison of nonequilibrium centerline heating-rate predictions on the Shuttle Orbiter.

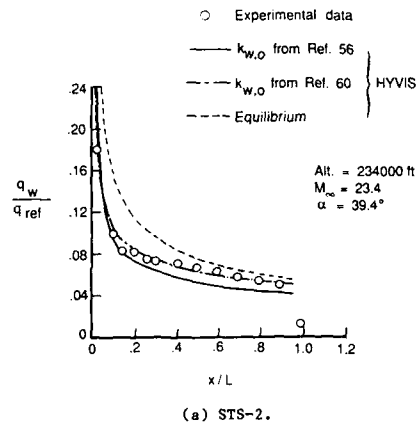


Fig. 9 Comparison of nonequilibrium heating rates for different surface conditions on the Shuttle Orbiter.

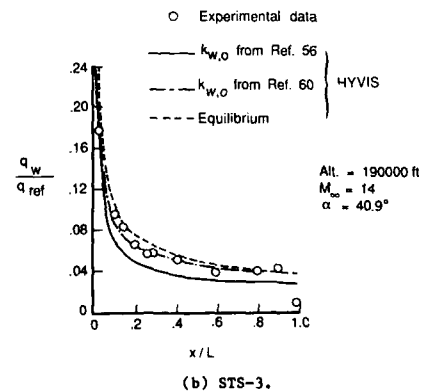


Fig. 9 Concluded.

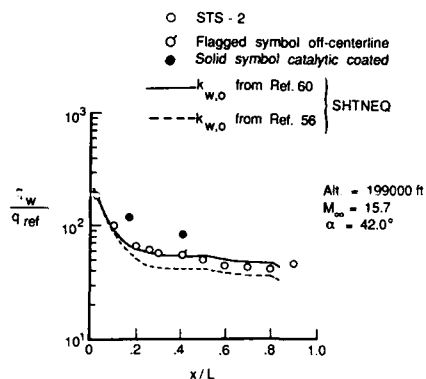


Fig. 10 Comparison of nonequilibrium centerline heating-rate predictions on the Shuttle Orbiter.

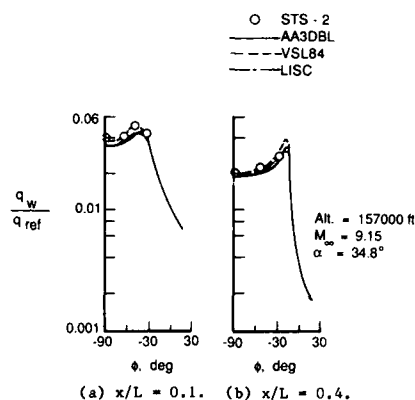


Fig. 13 Circumferential heating-rate distributions on Shuttle Orbiter.

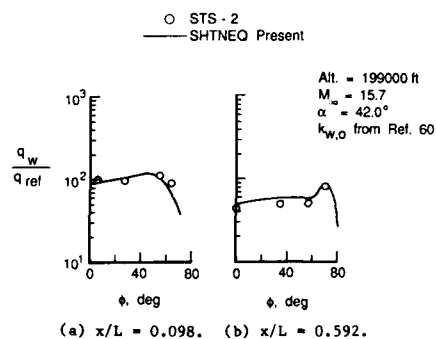


Fig. 11 Nonequilibrium heating-rate predictions in circumferential direction on the Shuttle Orbiter.

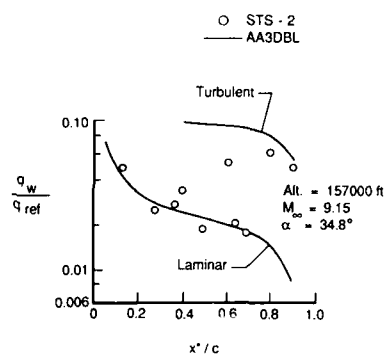


Fig. 14 Streamwise heating-rate distribution on Shuttle Orbiter wing at $2y/b = 0.5$.

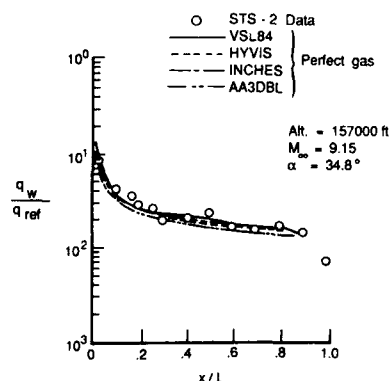


Fig. 12 Comparison of centerline heating-rate predictions with Shuttle flight data.

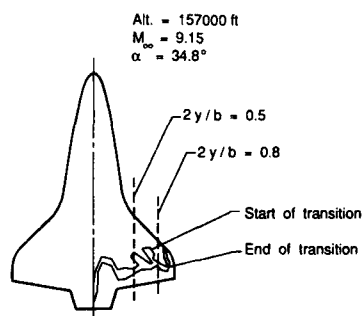


Fig. 15 Transition front on Shuttle Orbiter wing from STS-2 flight.

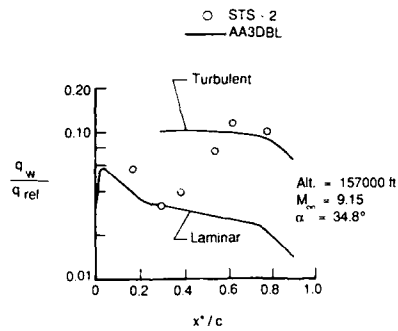


Fig. 16 Streamwise heating-rate distribution on Shuttle Orbiter wing at $2y/b = 0.8$.

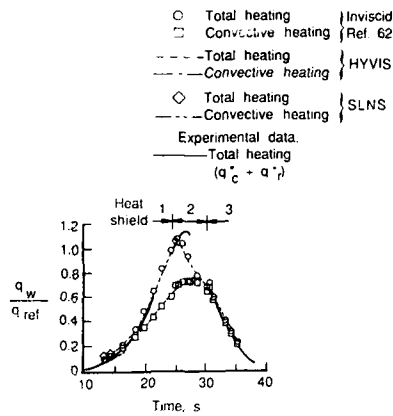


Fig. 19 Comparisons with total heating-rate data from Fire II.

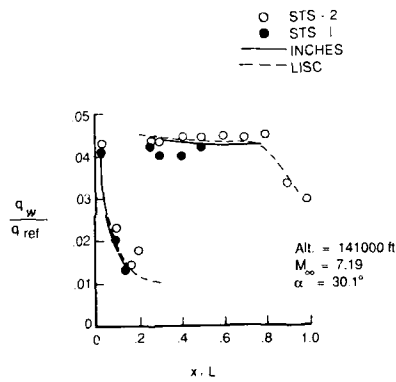


Fig. 17 STS-2 centerline heating-rate distributions.

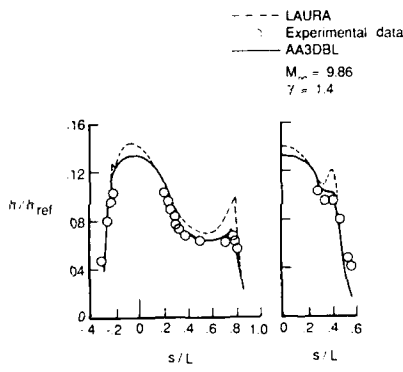


Fig. 20 Comparisons of wind-tunnel heating distributions on AFE configuration.

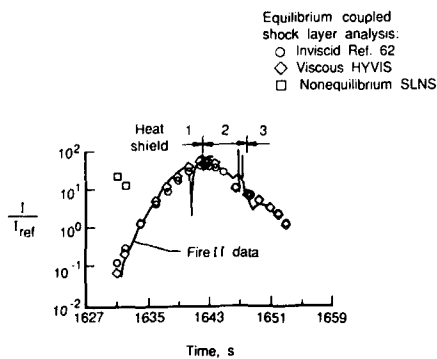


Fig. 18 Comparisons with the radiation intensity data from Fire II.

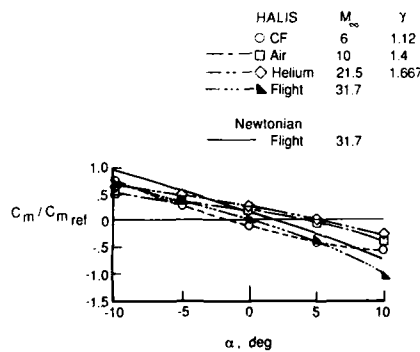


Fig. 21 Comparison of pitching-moment predictions at ground-test and flight conditions for AFE configuration.

REPORT DOCUMENTATION PAGE									
1. Recipient's Reference	2. Originator's Reference	3. Further Reference	4. Security Classification of Document						
	AGARD-CP-437 Volume 2	See Page ii	UNCLASSIFIED						
5. Originator	Advisory Group for Aerospace Research and Development North Atlantic Treaty Organization 7 rue Ancelle, 92200 Neuilly sur Seine, France								
6. Title	VALIDATION OF COMPUTATIONAL FLUID DYNAMICS Volume 2: POSTER PAPERS								
7. Presented at	the Symposium of the Fluid Dynamics Panel in Lisbon, Portugal, 2-5 May 1988.								
8. Author(s)/Editor(s)	Various		9. Date December 1988						
10. Author's/Editor's Address	Various		11. Pages 242						
12. Distribution Statement	This document is distributed in accordance with AGARD policies and regulations, which are outlined on the Outside Back Covers of all AGARD publications.								
13. Keywords/Descriptors									
<table border="0"> <tr> <td>Fluid dynamics</td> <td>Experimental data</td> </tr> <tr> <td>Algorithms</td> <td>Validity</td> </tr> <tr> <td>Computation</td> <td>Comparison</td> </tr> </table>				Fluid dynamics	Experimental data	Algorithms	Validity	Computation	Comparison
Fluid dynamics	Experimental data								
Algorithms	Validity								
Computation	Comparison								
14. Abstract									
<p>AGARD's Fluid Dynamics Panel has sponsored a Symposium with the specific intent of examining activities, both computational and experimental, directed toward validating or calibrating CFD codes over a broad spectrum of fluid-dynamics study areas. The objectives of the Symposium were to identify the level of agreement of numerical solution algorithms and physical models with experimental and/or analytical data, to identify regions of validity for given flow solvers, and to identify flow regions where significant gaps exist and further work is warranted.</p>									

<p>AGARD Conference Proceedings No.437 Volume 2 Advisory Group for Aerospace Research and Development, NATO VALIDATION OF COMPUTATIONAL FLUID DYNAMICS - Volume 2: POSTER PAPERS Published December 1988 242 pages</p> <p>AGARD's Fluid Dynamics Panel has sponsored a Symposium with the specific intent of examining activities, both computational and experimental, directed toward validating or calibrating CFD codes over a broad spectrum of fluid-dynamic study areas. The objectives of the Symposium were to identify the level of agreement of numerical solution algorithms and physical models with</p> <p>P.T.O.</p>	<p>AGARD-CP-437 Vol.2</p> <p>Fluid dynamics Algorithms Computation Experimental data Validity Computation</p>	<p>AGARD Conference Proceedings No.437 Volume 2 Advisory Group for Aerospace Research and Development, NATO VALIDATION OF COMPUTATIONAL FLUID DYNAMICS - Volume 2: POSTER PAPERS Published December 1988 242 pages</p> <p>AGARD's Fluid Dynamics Panel has sponsored a Symposium with the specific intent of examining activities, both computational and experimental, directed toward validating or calibrating CFD codes over a broad spectrum of fluid-dynamic study areas. The objectives of the Symposium were to identify the level of agreement of numerical solution algorithms and physical models with</p> <p>P.T.O.</p>	<p>AGARD-CP-437 Vol.2</p> <p>Fluid dynamics Algorithms Computation Experimental data Validity Computation</p>	<p>AGARD-CP-437 Vol.2</p> <p>Fluid dynamics Algorithms Computation Experimental data Validity Computation</p>
<p>AGARD Conference Proceedings No.437 Volume 2 Advisory Group for Aerospace Research and Development, NATO VALIDATION OF COMPUTATIONAL FLUID DYNAMICS - Volume 2: POSTER PAPERS Published December 1988 242 pages</p> <p>AGARD's Fluid Dynamics Panel has sponsored a Symposium with the specific intent of examining activities, both computational and experimental, directed toward validating or calibrating CFD codes over a broad spectrum of fluid-dynamic study areas. The objectives of the Symposium were to identify the level of agreement of numerical solution algorithms and physical models with</p> <p>P.T.O.</p>	<p>AGARD-CP-437 Vol.2</p> <p>Fluid dynamics Algorithms Computation Experimental data Validity Computation</p>	<p>AGARD Conference Proceedings No.437 Volume 2 Advisory Group for Aerospace Research and Development, NATO VALIDATION OF COMPUTATIONAL FLUID DYNAMICS - Volume 2: POSTER PAPERS Published December 1988 242 pages</p> <p>AGARD's Fluid Dynamics Panel has sponsored a Symposium with the specific intent of examining activities, both computational and experimental, directed toward validating or calibrating CFD codes over a broad spectrum of fluid-dynamic study areas. The objectives of the Symposium were to identify the level of agreement of numerical solution algorithms and physical models with</p> <p>P.T.O.</p>	<p>AGARD-CP-437 Vol.2</p> <p>Fluid dynamics Algorithms Computation Experimental data Validity Computation</p>	<p>AGARD-CP-437 Vol.2</p> <p>Fluid dynamics Algorithms Computation Experimental data Validity Computation</p>

<p>experimental and/or analytical data, to identify regions of validity for given flow solvers, and to identify flow regions where significant gaps exist and further work is warranted.</p> <p>Papers presented and discussions held at the Symposium of the Fluid Dynamics Panel in Lisbon, Portugal, 2-5 May 1988.</p>	<p>experimental and/or analytical data, to identify regions of validity for given flow solvers, and to identify flow regions where significant gaps exist and further work is warranted.</p> <p>Papers presented and discussions held at the Symposium of the Fluid Dynamics Panel in Lisbon, Portugal, 2-5 May 1988.</p>
<p>ISBN 92-835-0489-5 Vol.1 ISBN 92-835-0490-9 Vol.2 ISBN 92-835-0491-7 set of 2 vols.</p>	<p>ISBN 92-835-0489-5 Vol.1 ISBN 92-835-0490-9 Vol.2 ISBN 92-835-0491-7 set of 2 vols.</p>
<p>experimental and/or analytical data, to identify regions of validity for given flow solvers, and to identify flow regions where significant gaps exist and further work is warranted.</p> <p>Papers presented and discussions held at the Symposium of the Fluid Dynamics Panel in Lisbon, Portugal, 2-5 May 1988.</p>	<p>experimental and/or analytical data, to identify regions of validity for given flow solvers, and to identify flow regions where significant gaps exist and further work is warranted.</p> <p>Papers presented and discussions held at the Symposium of the Fluid Dynamics Panel in Lisbon, Portugal, 2-5 May 1988.</p>
<p>ISBN 92-835-0489-5 Vol.1 ISBN 92-835-0490-9 Vol.2 ISBN 92-835-0491-7 set of 2 vols.</p>	<p>ISBN 92-835-0489-5 Vol.1 ISBN 92-835-0490-9 Vol.2 ISBN 92-835-0491-7 set of 2 vols.</p>

AGARD

NATO OTAN

7 rue Ancelle · 92200 NEUILLY-SUR-SEINE

FRANCE

Telephone (1)47.38.57.00 · Telex 610 176

**DISTRIBUTION OF UNCLASSIFIED
AGARD PUBLICATIONS**

AGARD does NOT hold stocks of AGARD publications at the above address for general distribution. Initial distribution of AGARD publications is made to AGARD Member Nations through the following National Distribution Centres. Further copies are sometimes available from these Centres, but if not may be purchased in Microfiche or Photocopy form from the Purchase Agencies listed below.

NATIONAL DISTRIBUTION CENTRES

BELGIUM

Coordonnateur AGARD — VSL
Etat-Major de la Force Aérienne
Quartier Reine Elisabeth
Rue d'Evere, 1140 Bruxelles

LUXEMBOURG

See Belgium

NETHERLANDS

Netherlands Delegation to AGARD
National Aerospace Laboratory, NLR
P.O. Box 126
2600 AC Delft

CANADA

Director Scientific Information Services
Dept of National Defence
Ottawa, Ontario K1A 0K2

NORWAY

Norwegian Defence Research Establishment

DENMARK

Danish Defence Research Board
Ved Løngade

Postage and Fees Paid
National Aeronautics and
Space Administration
NASA-451



Official Business
Penalty for Private Use \$300

Director to AGARD
mas

FR

NASA

National Aeronautics and
Space Administration

GER

Washington, D.C. SPECIAL FOURTH CLASS MAIL
BOOK
20548

GRE

1
/
1
F

L1 001 AGCP-457V289031350026720
DEPT OF DEFENSE
DEFENSE TECHNICAL INFORMATION CENTER
DTIC-DDA-2
CAMERON STATION BLDG 5
ALEXANDRIA VA 223046145

ICELA

D
c/
Rc

Centre

55 Brown Street
Glasgow G2 8EX

ITALY

Aeronautica Militare
Ufficio del Delegato Nazionale all'AGARD
3 Piazzale Adenauer
00144 Roma/EUR

UNITED STATES

National Aeronautics and Space Administration (NASA)
Langley Research Center
M/S 180
Hampton, Virginia 23665

THE UNITED STATES NATIONAL DISTRIBUTION CENTRE (NASA) DOES NOT HOLD
STOCKS OF AGARD PUBLICATIONS. AND APPLICATIONS FOR COPIES SHOULD BE MADE
DIRECT TO THE NATIONAL TECHNICAL INFORMATION SERVICE (NTIS) AT THE ADDRESS BELOW.

PURCHASE AGENCIES

National Technical
Information Service (NTIS)
5285 Port Royal Road
Springfield
Virginia 22161, USA

ESA/Information Retrieval Service
European Space Agency
10, rue Mario Nikis
75015 Paris, France

The British Library
Document Supply Division
Boston Spa, Wetherby
West Yorkshire LS23 7BQ
England

Requests for microfiche or photocopies of AGARD documents should include the AGARD serial number, title, author or editor, and publication date. Requests to NTIS should include the NASA accession report number. Full bibliographical references and abstracts of AGARD publications are given in the following journals:

Scientific and Technical Aerospace Reports (STAR)
published by NASA Scientific and Technical
Information Branch
NASA Headquarters (NIT-40)
Washington D.C. 20546, USA

Government Reports Announcements (GRA)
published by the National Technical
Information Service, Springfield
Virginia 22161, USA



Printed by Specialised Printing Services Limited
40 Chigwell Lane, Loughton, Essex IG10 3TZ

ISBN 92-835-0490-9